

DTIC FILE COPY

4

**Volume III: Engineering Interfaces in
Metal Matrix Composites**

AD-A198 746

**Final Technical Report
June 10, 1988**

contract # N00014-84-K-0495

**James A. Cornie
Principal Investigator**

**DTIC
ELECT
AUG 30 1988
S G D**

DISTRIBUTION STATEMENT A

**Approved for public release
Distribution Unlimited**

**Massachusetts Institute of Technology
77 Massachusetts Avenue, 8-401
Cambridge, MA 02139**

88 10 04 8

Acknowledgements:

We are grateful to

**ONR, Dr. Steven G. Fishman,
DARPA, Dr. Ben Wilcox, and
NADC, Dr. J. Waldman**

for their generous support of the program and to IST/SDIO for their continued support under contract N00014-85-K-0645. We also appreciate the support of the Consortium for the Processing and Evaluation of Inorganic Matrix Composites for aspects of this work.



Accession For	
NTIS CRA&I	<input checked="checked" type="checkbox"/>
DTIC TAB	<input type="checkbox"/>
Unannounced	<input type="checkbox"/>
Justification	
By <i>per lto</i>	
Distribution /	
Availability Codes	
Dist	Avail and/or special
A-1	

CONTENTS:

**VOLUME III: Engineering Interfaces in
Metal Matrix Composites**

Toughness of Interfaces

-Ali S. Argon, Vijay Gupta, Howard S. Landis and James A. Cornie

**Interfaces with Controlled Toughness as Mechanical Fuses
to Isolate Fibers from Damage**

-Vijay Gupta, Ali S. Argon and James A. Cornie

**Intrinsic Toughness of Interfaces Between SiC Coatings
and Substrates of Si or C Fiber**

-Ali S. Argon, Vijay Gupta, Howard S. Landis and James A. Cornie

**In-situ HVEM Study of Fracture in SiC Coated Graphite
Fiber/Aluminum Composites**

-Janez Megusar, Qlong Li, James A. Cornie and K. H. Westmacott

Interface Chemistry of Inorganic Composite Materials

-Andreas Mortensen

On Elastic-Plastic Cracks Between Dissimilar Media

-Edward Zywick

Mechanical Properties of Residually Stressed a-SiC:H Thin Films
-H.S. Landis, Vijay Gupta, and James A. Cornie

TOUGHNESS OF INTERFACES

A.S. Argon, V. Gupta, H.S. Landis*, and J.A. Cornie
Massachusetts Institute of Technology
Cambridge, MA 02139

ABSTRACT

The critical energy release rate for separation of thin coatings from their substrate can be determined accurately in many instances when the coatings are elastic, and are under a state of residual stress. When the thickness of such coatings reaches a critical value, so that the elastic strain energy per unit surface area in them equals the specific work of fracture of the interface, the coating will delaminate from the substrate in quasi-static equilibrium. Through analysis of such delaminations of SiC coatings from single crystal Si substrates and Pitch-55 carbon fibers, the intrinsic toughness of Si-SiC and C-SiC interfaces have been determined, and are in the range of 5.5 J/m².

INTRODUCTION

In metal matrix composites, it is often necessary to protect the reinforcing fiber from damage resulting from fracture of surrounding fibers or from misfitting reaction products between the matrix and the fiber. It has long been appreciated that this is best accomplished by permitting some slippage along the interface between fiber and matrix, or by controlled delamination along this interface. Since other requirements must also be met during the processing of the composite, such as proper wetting along interfaces to avoid porosity, simultaneously controlling the interface toughness becomes very difficult. Therefore, we have proposed that the two functions be separated by the introduction of a second parallel interface, the properties of which can be separately controlled [1]. This becomes possible, with little extra effort, when protective coatings are used on fibers to isolate them from reaction with the matrix. In such cases, the primary interface between the coating and the fiber can be tailored during production of the coated fiber, and controlled to have special toughness properties to govern the decoupling of the fiber from its damaging surroundings, while maintaining full wetting contact along the interface between the coating and the matrix. Thus, the primary interface can be used as a mechanical fuse, as illustrated in Fig. 1. When a crack impinging on a fiber from the outside, either caused by fiber damage in the surrounding regions, or resulting from a reaction misfit wedge, as shown in Fig. 1, if the ratio of the fracture toughness of the primary interface to that of the fiber in the plane of the crack is less than the corresponding ratio of energy release from the surrounding stress field for virtual extensions of the crack along the interface vs. in its plane, the crack will propagate along the interface, instead of going into the fiber. With well bonded fibers, this is not likely to happen without special treatments for the primary interface, requiring deliberate control of the interface toughness. Normally, this requires a decrease in the interface toughness.

*Now with GTE Laboratories, Waltham, Massachusetts

Fig 1

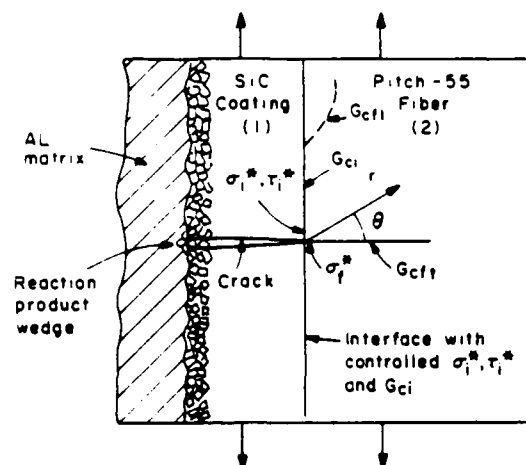


FIG. 1. Sketch showing various possible paths of a crack impinging on an interface between a coating and the underlying fiber.

Since the propagation of a crack either into the fiber or along the interface is accompanied by more or less inelastic dissipation in the matrix or in the fiber itself, the effective reduction of the interface toughness could be achieved in principle by altering the inelastic properties of the matrix or the fiber. This, however, may have other undesirable global consequences. A much more successful procedure, following again along the notion of considering the primary interface as a mechanical fuse, is to control the intrinsic toughness of the primary interface. This should be quite effective, since in such interface fractures, the actual mode of separation is cleavage-like with or without surrounding inelastic dissipation, the latter affects the crack only through its shielding effect. In such instances, the overall toughness G_c of the interface is a sum of the intrinsic toughness G_{co} and the additional specific inelastic work of separation G_p where, however, the latter is directly scaled by the former [2], i.e.,

$$G_c = G_{co} + G_p = G_{co} (1 + K) \quad (1)$$

where

$$K = \frac{dG_p}{dG_{co}} \quad (2)$$

Thus, the task of protection of fibers from damage reduces to two specific related requirements of tailoring the intrinsic toughness of the primary interface between the protective coating and the fiber, and the measurement of this interface toughness. Here, we will report briefly only on special techniques for the determination of intrinsic toughness of interfaces, which has become possible through the analysis of the phenomenon of spontaneous delamination of coatings from substrates. A more expanded discussion of the phenomenon and its special potential for interface toughness determination can be found elsewhere [3].

THE SiC SYSTEM

Vapor Deposition of SiC Coatings

The coating of choice to protect carbon fibers, such as the Pitch-55 fibers, widely used for reinforcement in metal matrix composites, is SiC. It adheres well to carbon fiber and the surrounding metal matrix, and is neutral in reactions with the metal matrix. In the experiments reported here, SiC coatings have been applied to substrates of single crystal Si wafers and Pitch-55 fibers by a plasma-assisted chemical vapor deposition process.

It was found that the ion bombardment energy is the most important single parameter governing the properties of the coatings. Preliminary observations showed that during deposition of SiC on substrates, large concentrations of atomic hydrogen are entrapped in the coatings, which must be removed by annealing the substrate-coating pair at a temperature of 600C for about 30 minutes, if severe porosity problems are to be avoided during the processing of the metal matrix composite. Associated with this problem, it was discovered that the as-deposited hydrogenated SiC coatings are under a state of bi-axial compression, which is relieved during the annealing treatment, and is replaced with a residual bi-axial tensile stress of similar magnitude. It is these residual stresses in the coatings which are responsible for the spontaneous delamination and offer in the process the means for determination of interface toughness.

Coatings with Tensile Misfit

The residual stresses, whether compressive or tensile in SiC coatings on circular disk shaped thin Si single crystals with (111) planes parallel to the plane of the disk were measured by measuring the curvature of the combination of coating and disk. As shown in Fig. 2, if the coatings are in tension, the curvature of the assembly is concave upward in the direction

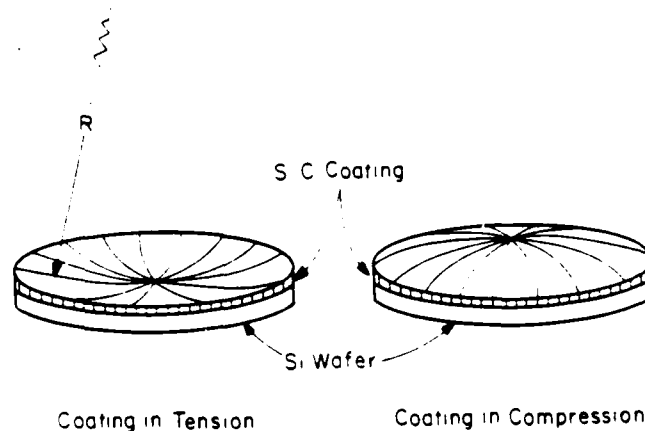


FIG. 2. Bowing of a circular Si wafer with a thin SiC coating: in bi-axial tension, and bi-axial compression.

of the coating, while the opposite is true when the stresses are compressive. By elementary considerations, it is easy to show that for thin

coatings, the residual stress depends only on the thickness t of the coating, and the radius of curvature R of the assembly, but not on the elastic properties of the coating. The residual stress σ is given by an expression [3],

$$\sigma = \frac{E_s h^2}{6(1 - \nu_s) t R} \quad (3)$$

where E_s and ν_s are the Young's modulus and Poisson's ratio of the substrate, and h is the substrate thickness. The measured residual stresses in the coatings in tension or compression are shown in Fig. 3. This established that the residual stress depended only on the ion beam energy and not on the thickness of the coatings.

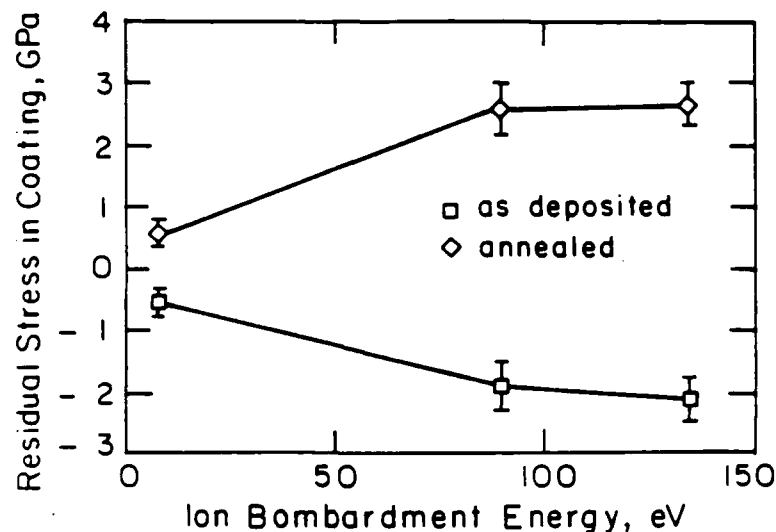


FIG. 3. Measured residual stresses in coatings as a function of ion beam energy for as-deposited coatings in compression and annealed coatings in tension.

In annealing experiments of coatings to drive out the entrapped hydrogen, it was discovered that the resulting coatings in residual tension remained attached to the substrate indefinitely when they were of a thickness less than $0.2 \mu\text{m}$. With larger thicknesses, the coatings developed two families of parallel cracks: one set parallel to the $\langle 110 \rangle$ direction of the Si substrate, the other family parallel to the $\langle 112 \rangle$ direction, orthogonal to the first set. When thicknesses of the coatings exceeded $0.3 \mu\text{m}$, delamination fronts spread out along the interface between coating and substrate bounded by the parallel through-thickness pre-cracks. This produced well delineated long delamination ribbons, which continued to lie flat on the Si substrate, as the one shown in Fig. 4a. A large magnification view of the detached end of the ribbon in Fig. 4b shows a readily measurable gap, which represents the initial tensile misfit displacement in the now delaminated ribbon. Through the measurement of such built-in misfit strains, and the previously measured residual tensile stress, the Young's moduli of the amorphous SiC coatings could be determined from Eqn. (4) below, on the assumption that the Poisson's ratio of the coating is 0.3,

$$E = \frac{(1 - \nu)\sigma}{\epsilon_m} \quad (4)$$

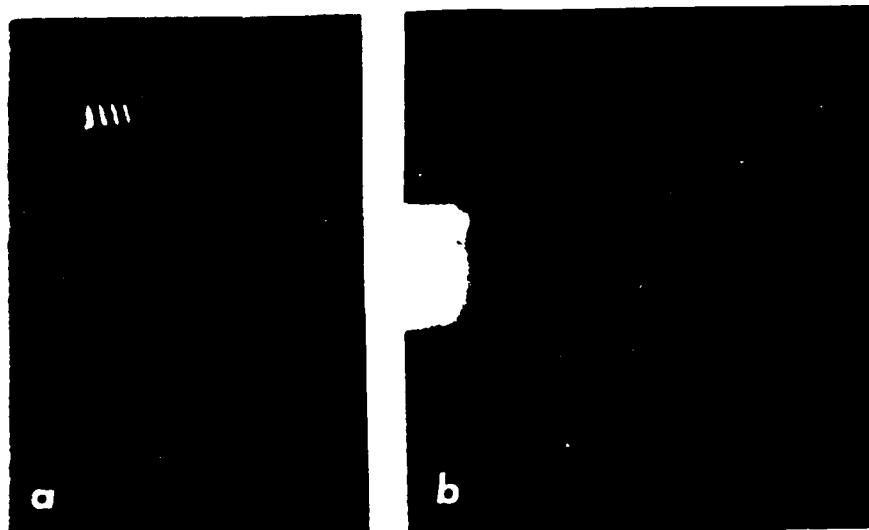


FIG. 4. Example of ribbon-like delamination of an annealed coating in tension: (a) low magnification view showing extent of ribbon, (b) high magnification view showing the initial tensile material misfit displacement.

The calculated moduli are shown in Fig. 5, and indicate that they too depend on the ion beam energy and not on any other parameter.

The observations thus, indicate that the delamination is driven by the elastic strain energy in the coating. In such problems of biaxially stressed thin coatings resulting from a constant material misfit independent of thickness, the elastic strain energy almost entirely resides in the coating, with only a negligible contribution coming from the much thicker substrate [3]. Thus, for very thin coatings where the elastic strain energy per unit area of the interface is less than the interface toughness, the coating remains intact indefinitely. As the thickness of the coating increases, the available elastic strain energy per unit area monotonically increases until it becomes equal to the intrinsic interface fracture separation work per unit area G_{co} . Then, the coating can delaminate away from the substrate under quasi-static conditions, starting from any interface defect or pre-crack. For thicknesses greater than the critical thickness, the delamination will occur with increasing velocity. From elementary considerations, the critical specific fracture separation work G_{co} is given by [3],

$$G_{co} = \frac{\sigma^2(1 - \nu)t_c}{E} = \frac{\epsilon_m^2 E t_c}{(1 - \nu)} \quad (5)$$

where σ , ϵ_m , E , ν , t_c are in order: the bi-axial residual tensile stress, the bi-axial material misfit strain, the Young's modulus, the Poisson's

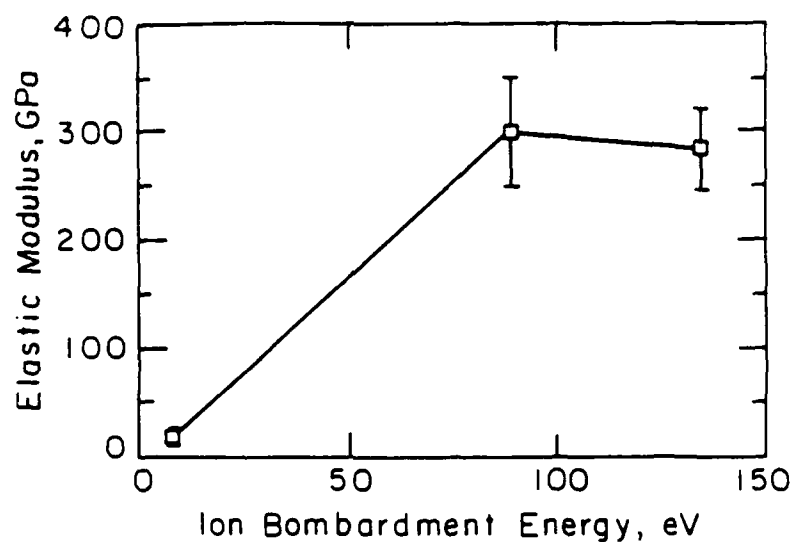


FIG. 5. Dependence of calculated modulus of coatings in tension on ion beam energy.

ratio, and the critical thickness -- all of the coating. This work of interface fracture is shown in Fig. 6. It is found to depend weakly on the ion beam energy, and for large energies, reaches an asymptotic average level of 5.1 J/m^2 .

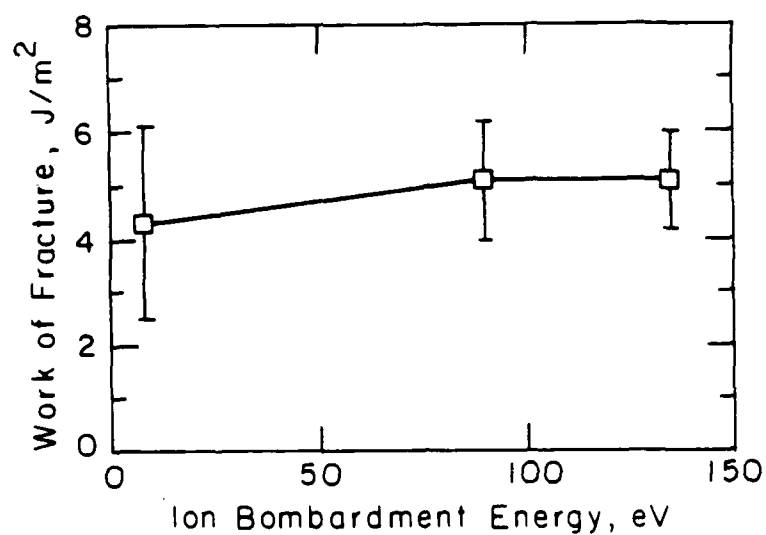


FIG. 6. The dependence of the calculated interface fracture work on ion beam energy for coatings in tension.

Coatings with Compressive Misfit

In the as-deposited coatings, the residual stress is compressive, as stated above. There too, the elastic strain energy stored in the coating per unit area of the interface increases monotonically with thickness of the coating. The delamination of these coatings from the substrate, however, exhibits a very different form. Here, it is found that coatings of considerably greater thickness remain attached intact to the substrate. When they reach a new critical thickness in the range of $1.0 \mu\text{m}$, they are found to separate by forming a blister which lifts off the substrate in a regularly buckled form, as shown in Fig. 7, where a number of blisters in

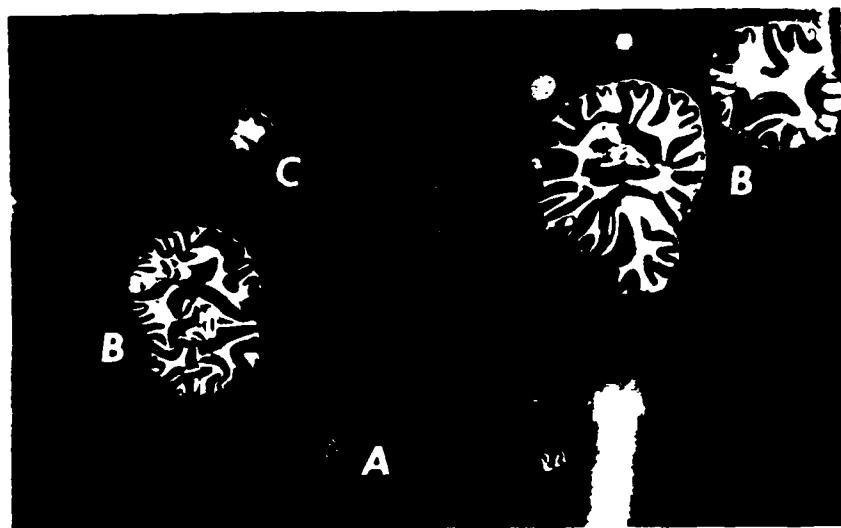


FIG. 7. Delamination blisters in an as-deposited coating in bi-axial compression: (A) smallest size blister just lifting off, (B) large blisters growing radially outward, with a self-similar and regular circumferential buckled front, (C) a blister just large enough to assume a regular circumferential buckled shape.

various stages of separation can be seen. At (A), the blisters are just large enough to produce two half waves of vertical buckling, at (B), large blisters have settled into a form where they propagate radially outward in quasi static equilibrium, with a self-similar circumferential buckling wave length λ . This wave length appears just established in the small blister shown at (C).

Detailed observations of the growth of the blister with Nomarski interference contrast microscopy showed that as the blister front advances radially outward, first the radial residual stress is relieved by slippage of the coating radially inward over a process zone of several microns in width. This is followed by the partial relief of the circumferential stress by the formation of the circumferential buckles, with a wave length λ , that depends on the initial bi-axial residual compressive stress σ given by Eqn. (6) below [3],

$$\lambda = \pi t \sqrt{\frac{E}{3(1 - \nu^2)\sigma(1 - \nu)}} \quad (6)$$

In Eqn. (6), E is the Young's modulus of the coating, t its thickness, and ν its Poisson's ratio, which we take to be 0.3. Since the residual compressive stress can be measured independently from the curvature of the substrate attached to the coating, and λ can be measured from the micrographs, such as Fig. 7, the modulus of the coating can be calculated from Eqn. (6). When this was done for a coating of 1.1 μm thickness with a measured λ of 20 μm , and residual compressive stress of 2 GPa, E was found to be 116 GPa.

Further elementary analysis of the remaining elastic strain energy U_f per unit area of interface in the post buckled shape of the coating establishes it to be [3],

$$U_f = \frac{\pi^4 E t^5}{9(1 - \nu^2)^2 \lambda^4} \quad (7)$$

In the same fundamental parameters, the initial strain energy per unit area of interface is [3],

$$U_i = \frac{\pi^4 E t^5}{9(1 - \nu^2)^2 (1 - \nu) \lambda^4} \quad (8)$$

At the critical thickness t_c , the difference between (8) and (7) should provide for the intrinsic fracture toughness G_{co} of the interface, i.e.,

$$G_{co} = \frac{\nu \pi^4 E t_c^5}{9(1 - \nu^2)^2 (1 - \nu) \lambda^4} \quad (9)$$

Evaluation of the typical case already referred to above gave an interface toughness of $G_{co} = 5.95 \text{ J/m}^2$, which is 14% higher than the value determined for coatings in residual tension. The difference is attributed to the additional slight dissipative work of slippage when relative sliding occurs between coating and substrate during the release of the radial stress.

THE SiC PITCH-55 CARBON FIBER SYSTEM

The same phenomenon of spontaneous delamination also occurs with SiC coatings on Pitch-55 carbon fibers. When such fibers were coated, followed by the annealing treatment of 600C for 30 minutes, the coatings were found to remain stable and intact, if their thicknesses were less than 0.33 μm for coatings deposited at low ion beam energy. When coatings with this history were left in laboratory air with the usual relative humidity of 60% for several months, they were found to undergo copious and complete delamination by cracking and flaking, as shown in Fig. 8.

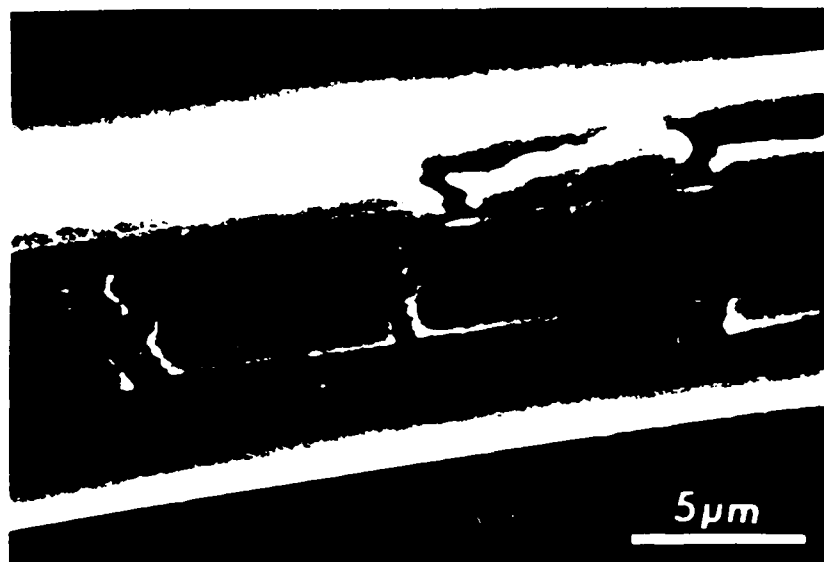


FIG. 8. Flakes of delaminated SiC coatings on a Pitch-55 fiber.

The initial bi-axial misfit strain ϵ_m between coating and fiber could be determined from the ratio of the average gap size between flakes to the average dimension of the flakes. With this information, and the assumption that the modulus of the coating in tension is given uniquely by Fig. 5 as being a function of only the ion beam energy, and the further assumption that the Poisson's ratio remained at 0.3, the elastic strain energy of the coating per unit area could be calculated and equated to the fracture toughness of the interface to simply result in [3],

$$G_{co} = \frac{\epsilon_m E t_c}{(1 - \nu)} \quad (10)$$

for coating thickness to fiber radius ratio $t/R \ll 1$. Evaluation of these results for a typical case of coating with a modulus of 16 GPa, thickness of 0.33 μm , and a misfit strain of 2.7×10^{-2} on a fiber with a radius of 5 μm , the interface toughness was calculated to be $G_{co} = 5.47 \text{ J/m}^2$. This is quite close to the value of 5.1 J/m^2 determined for the SiC-Si pair.

DISCUSSION

We have demonstrated that the phenomenon of spontaneous delamination of coatings under residual stress, from more massive substrates occurs when the elastic strain energy of misfit per unit area equals the intrinsic work of separation of the coating from the interface, delamination can occur quasi-statically. The analysis of the conditions of such delamination provides the much needed information on the intrinsic fracture toughness of the interface. Apart from small differences, which apparently are due to a slight energy dissipation during slippage of the coating over the substrate as the radial stress is relieved first before the tangential stress, in the

case of the growth of the compression blister, the interface toughness is independent of the state of stress in the coating. Furthermore, the toughness of the interface between SiC coatings and carbon fibers is also quite close to that measured for the SiC/Si pair.

Observation of such delamination events is not new. Earlier, Evans and Hutchinson [4] have reported somewhat similar delamination phenomena for interfaces between surface layers and substrates in computer interconnects, but observed a rather different process in the delamination of the layers in compression, which was less informative.

It must be noted that the simplicity of the phenomenon reported above results from the sharply defined nature of the interface, and the condition that the interface toughness is evidently less than the toughness of either the coating or the substrate, so that delamination cracks remain in the interface and do not wander into either of the two adjoining materials. Under this condition, the nature of the stress intensity at the crack tip for the interface crack, which has created quite considerable controversy [5,6], is irrelevant, since the problem can be analysed by overall energetics alone.

On the whole, we conclude that the interface toughnesses reported here are quite meaningful and of an expected magnitude. How these reflect themselves in actual composites is a more complex matter, and require understanding of the other accompanying dissipative processes [1].

ACKNOWLEDGEMENT

This research was supported by the Office of Naval Research under contract N0014-84-K-0495.

REFERENCES

1. V. Gupta, A.S. Argon, and J.A. Cornie, submitted to J. Mater. Science.
2. J.R. Rice, in: Proceedings of First International Conference on Fracture, T. Yokobori, T. Kawasaki, and J.L. Sedlow, eds. (The Japanese Society for Strength and Fracture of Materials, Sendai, Japan), p. 309 (1965).
3. A.S. Argon, V. Gupta, H. Landis, and J.A. Cornie, submitted to J. Mater. Science.
4. A.G. Evans and J.W. Hutchinson, Intern. J. Solids and Structures, 20, 455 (1984).
5. J.R. Rice and G.S. Sih, J. Appl. Mech., 32, 418 (1965).
6. M. Comninou, J. Appl. Mech., 44, 631 (1977).

Submitted to the Journal Of Materials Science

INTERFACES WITH CONTROLLED TOUGHNESS
AS MECHANICAL FUSES TO ISOLATE FIBERS FROM DAMAGE

V. Gupta, A.S. Argon, and J.A. Cornie

Massachusetts Institute of Technology, Cambridge, MA 02139, U.S.A.

ABSTRACT

A source of inadequate performance of Metal Matrix Composites has been the loss of strength due to the reaction layers between the fiber and the surrounding metal matrix. Here, we propose that the traditional diffusion barrier coatings on the fiber can be utilized to serve as mechanical fuses to isolate the impinging reaction zone cracks by interface delamination. Requirements on the interface strength and toughness for the specific tailoring of the fiber/coating interface are given. Special problems associated with the graphite/aluminum system are identified. A double cantilever beam experiment has been developed to measure the work of separation of thin coatings (0.1 to 0.3 μm) from bulk substrates. This test has been successfully applied to measure the work of fracture of the interface between a planar pyrolytic graphite substrate with the same chemistry and closely related microstructure as that of the 10 μm Pitch-55 graphite fiber and SiC coatings on them. A value of 60 J/m^2 was obtained for the critical energy release rate for the PG/SiC interface. Additional measurements of energy release rates in thin layers of glue used to model the aluminum matrix and in PG itself, have given values which account for the high toughness of the main interfaces through the accompanying inelastic deformation work in the glue and the PG while the crack travels along the interface.

I. INTRODUCTION

Composite materials are tailored combinations of materials constructed to exploit the desirable properties of the component parts, while minimizing their weaknesses. The points of particular interest are the attainment of high stiffness and strength under both monotonic and cyclic loading, and other improvements in associated properties, such as desired levels of thermal expansion, damping capacity, resistance to environmental attack; all at minimum weight and acceptable cost.

Since composites combine a multiplicity of component material parts, they contain a high volume density of interfaces. The proper performance of composites in service puts extreme and often conflicting demands on these interfaces. In all of our considerations here, we will view composites as heterogeneous media having a relatively coarse microstructural scale, for which the elastic or plastic properties of the heterogeneities are governed by representative volume elements on a much finer scale. This implies that individual phases can be considered as continua, and that they interact with each other only through their interfaces. Thus, the consideration of choice is micro-mechanics, from which other macro-properties are assumed to be obtainable.

In normal service, interfaces are required to transmit full traction to assure that reinforcing phases such as fibers are fully load bearing to enhance the stiffness of the composite and to promote redundant deformations in a ductile matrix that can markedly increase the overall deformation resistance in it. The difference in the deformation resistance between fibers and matrix results in the development of stress concentrations across the interfaces. These concentrations can initiate cavitation and incipient

fracture phenomena, which sooner or later become unstable and result in the premature termination of service by overall fracture. When such fracture is inevitable, it is desirable that as much dissipative work be associated with it as possible to result in tough and energy absorbing structures. Whether that toughness has the clear characteristics of being associated with the propagation of a single crack, and carrying conventional implications of fracture toughness, or is more diffuse and widespread over the entire structure is important in design, but of secondary consideration here. In all of these terminal phenomena, overall instability can be delayed by the systematic decoupling of the reinforcing elements that are on the verge of becoming critically stressed. To the extent that this can be successfully accomplished, subcritical damage can be spread over larger volume elements, to result in a quasi-plastic response of the entire composite on the large scale. This desired systematic decoupling of the reinforcing fibers or other heterogeneities can be accomplished by controlling the terminal properties of interfaces, to have them act as mechanical fuses at appropriate pre-determined levels of critical tractions. Such fine tuning or "tailoring" of interface properties is in principle possible, but requires a high degree of understanding of both the micro-mechanics of interfaces and the factors that affect their cohesive strength and overall fracture toughness.

In metal matrix composites, where chemical reactions are also possible between the fibers and the metal matrix, forming reaction product layers along interfaces, the positive material misfit that often accompanies such reactions can initiate cracks in the fibers. To protect the fibers from such reaction damage, it is customary to provide them with non-reactive

coatings. Since such coatings are introduced on the fibers under carefully controlled conditions, they can also offer the opportunity for tailoring the strength and toughness of their interfaces with the fiber, to achieve the mechanical fuse action discussed above to isolate damage. Such damage may have originated either among neighboring fibers, and is transmitted across the matrix to the fiber, or it may have been generated by reaction products forming on the outer interface between the matrix and the protective coating.

We report here the results of a combined experimental and theoretical study on such key interfaces between the fibers and their protective coatings. It should be emphasized that the concept of using such interfaces as mechanical fuses is a very general one, and in principle, could be applied to any composite system. However, in this study, we focus on its application to metal matrix composites.

II. INTERFACE MECHANICS

2.1 Metal Matrix Composite Systems

For metal matrix composites, a large number of fiber and matrix systems have been explored. For structural applications at intermediate temperatures, the light metals of aluminum, titanium, and magnesium have been under primary consideration as matrices. While beryllium has most attractive properties in its own right, even without any reinforcement, it has not received much attention because of the difficulties associated with its processing. Of these, aluminum has been the matrix most widely considered. As a f.c.c. metal, it exhibits exceptional ductility, and has a large number of

well developed alloys with impressive properties. Of the various fibers used to reinforce aluminum, such as, boron, Al_2O_3 , SiC , and carbon, the one that will be of primary interest to this investigation is the system of meso-phase pitch base fibers obtained from spun polymer precursors by a sequence of carbonization (1000 - 2000°C) or graphitization (2000 - 3000°C) treatments. Such pitch base fibers have axial fiber Young's moduli that range from 100 - 500 GPa with increasing molecular orientation, increasing long-period of crystalline domains, and increasing density (1.9 - 2.2 g/cm³). In graphitized form, their tensile strengths are of the order of 2 GPa and relatively independent of their stiffness [1]. Figure 1a gives the microstructure of a Pitch-55 (Axial modulus 55×10^6 psi = 385 GPa) fiber, as viewed in a cross section across the axis. The fibers are typically of 10 μm in diameter, and are predominantly available in 500 - 10,000 filament yarns. The long axial grooves along the external cylindrical surface and the microstructure of the transverse section indicate that the principal morphology of the fiber is in the form of randomly corrugated and densely packed lamellae, oriented parallel to the fiber axis. This suggests an idealized fiber morphology, shown in Fig. 1b, with "planes of weakness" terminating roughly at right angles on the external surface. The consequence of this fiber morphology is a very low transverse modulus (14 GPa for the Pitch-55 fiber), and correspondingly low transverse tensile strength as well, estimated to be around 75 MPa on the basis of the usual correlation between modulus and strength. The particular morphology of the fiber also results in low shear stiffness and shear strength in longitudinal shear response to stresses σ_{zr} . Although this has no important consequence in the normal service of the

composite; it can have important beneficial effects in the spreading of damage. Pitch-55 fibers have a density of 2.0 g/cm^3 . The major advantage of Pitch-55 fibers is their chemical inertness due to high carbon content, high density, and high crystallinity. In the case of metal matrix composites for space structures, the attractions of this are the combination of properties which promote thermal dimensional stability, i.e., high Young's modulus, low and negative coefficient of thermal expansion, and high thermal conductivity.

The fibers are usually provided with a SiC coating of roughly $0.2 \mu\text{m}$ thickness, applied by a plasma-assisted chemical vapor deposition process (PACVD) to isolate them from the matrix. The properties of such SiC coatings and means for their placement have been investigated by Landis et al., and will be reported by them elsewhere [2]. Such coatings can be under substantial bi-axial misfit stresses, dependent upon their structure and levels of entrapped hydrogen. These misfit stresses are compressive in the as-deposited form of the coatings, but can be relieved and even turned into tensile stresses upon thermal treatment. They are usually either maintained at zero or slightly compressive levels. The coatings are generally amorphous and have isotropic Young's moduli of about 300 GPa.

As discussed earlier, the overall mechanical properties of the composite are critically dependent on the properties of the key interfaces between the fiber and coating. The general mechanics, and in particular, the problems associated with Gr/Al systems involving the fiber-coating interactions are of a generic nature, and are potentially applicable to many other composite systems as well.

2.2 Fiber-Matrix Interaction

In composites, certain conflicting requirements must be satisfied by the interfaces between fiber and matrix. First, in a successful composite, it is important to decouple the fiber from the matrix during fracture, so as to prevent planar, low energy absorbing fractures. In fact, fiber fracture at random levels, followed by fiber pull out is desirable. This demands that the interfacial strength should not be too high. On the other hand, adequate interfacial strength is required to provide good transverse properties of the composite. Hence, in order to tailor the interfaces to desired properties for them to act as mechanical fuses, it is necessary to bound the interface strength and toughness.

2.3 Transverse Behavior and Lower Bound to the Interface Strength

The interface strength is probed directly when the composite is stressed in the transverse direction. Hence, the interface strength should be high enough, so that transverse service stresses can be transferred to the fiber. Because of the complexity of the stress field at the interfaces in a bundle of fibers, the transverse loading problem has been approached chiefly with numerical techniques. The interfacial stresses developed under transverse tensile loading in composites of Pitch-55 fibers in pure Al matrices has been studied to a considerable extent by Zywicz [3]. Figure 2, relating to their work, shows the geometry of a typical close-packed array of Pitch-55 fibers surrounded by an Al matrix. The relevant results for our consideration are given in Table I, where the stress concentrations in purely elastic and elastic-plastic behavior of the Al matrix are summarized as a

function of volume fraction of fibers for two different modes of tensile loading in the transverse direction, i.e., $\sigma_{xx\infty}$, in the close-packed direction and $\sigma_{yy\infty}$, mid-way between the close-packed directions. The table shows that since the transverse modulus of the fibers is less than that of the aluminum, the fibers have actually a deficiency in load carrying capacity in purely elastic behavior of fibers and matrix, resulting in a stress concentration in the matrix. This, however, is changed when the matrix can undergo plastic deformation, and can continue to load the fibers by plastic drag. Thus, for an equivalent plastic strain of even as small as 0.01, interface stress concentrations ranging from 1.14 to 2.40 appear on the cylindrical fiber surface, depending on fiber volume fraction and are governed by the equivalent plastic resistance of the matrix. Based upon what the equivalent plastic resistance of the matrix is, i.e., whether the matrix is pure Al or an Al alloy, the results in Table I provide a lower bound for the required interface strength, i.e.,

$$\sigma_i^*(\text{lower bound}) > k\sigma_{T\infty} . \quad (1)$$

Where k is the maximum stress concentration factor, and $\sigma_{T\infty}$ is the desired transverse tensile strength of the composite.

2.4 Controlled Delamination of Coatings and Upper Bound to the Interface Strength

The nature of the interface cracking problem is of particular interest, as depicted in Fig. 3, which shows a schematic view of a crack in a SiC coating, terminating on the interface between the coating and the

Pitch-55 fiber. The crack could alternatively have resulted from a matrix strain concentration produced by fractures in the surrounding fibers, a surface notch, or as shown in the figure, by a reaction product produced misfit wedge propping the flanks of the crack open. In all these cases, the principal concern is to protect the fiber from fracturing by penetration of the main crack into the fiber. This is to be achieved by decoupling the fiber at the interface between the coating and the fiber by producing either normal or shear failure at the interface using the concentrated interface stresses $\sigma_{\theta\theta}(\pi/2)$ or $\sigma_{r\theta}(\pi/2)$. The crack deflection process along the interface requires the following conditions to be satisfied by the stress field near the tip of the crack:

- a) The ratio of the fiber tensile σ_f^* strength to the interface cohesive strength σ_i^* should be greater than the ratio of the elastic crack tip stresses probing the plane across the fiber to the stress probing the interface to separate it in tension, i.e., the ratio of $\sigma_{\theta\theta}$ (at $\theta = 0$) to $\sigma_{\theta\theta}$ (at $\theta = \pi/2$). This will lead to the delamination of the interface in tension, provided that such tensile stress can be achieved. This condition leads to an upper bound for the interface cohesive strength.
- b) The ratio of the fiber tensile strength to the interface shear strength τ_i^* should be greater than the ratio of $\sigma_{\theta\theta}$ (at $\theta = 0$) to $\sigma_{r\theta}$ at the interface (i.e., at $\theta = \pi/2$). This will ensure the separation of the interface in shear, and bounds the interface shear strength. When the ratio of the interface cohesive strength to the interface shear strength is less than the ratio

of $\sigma_{\theta\theta}/\sigma_{r\theta}$ at the interface, tensile separation will be preferred. Alternatively, for two possible directions of growth of the crack, i.e., across the fiber vs. along the interface, if the ratio of the energy release rate for growth across the fiber, to growth along the interface is less than the ratio of the work of fracture G_{cft} of transversely across the fiber to work of separation of the interface G_{ci} , then the fracture will follow the interface.

- c) The work of separation of the interface G_{ci} in any appropriate combination of separation across $\sigma_{\theta\theta}$ and $\sigma_{r\theta}$ along the interface should be less than the work of fracture G_{cfl} of the fiber in the longitudinal direction or the coating for the crack to continue to travel along the interface.

Thus, it is of interest to determine the stress $\sigma_{\theta\theta}$ and $\sigma_{r\theta}$ acting across the interface for a crack terminating at right angles on the interface, and establish the energy release rates that result when the crack branches into the interface to relieve these stresses. Furthermore, it is of interest to compare these energy release rates with the release rate for a crack going into the fiber.

Upon the initial successful diversion of the delamination crack along the interface, continued preferential delamination, as opposed to the crack entering the fiber, requires in addition, knowledge of the stress intensity associated with cracks lying on the interface, to satisfy the condition under (c) above.

Although knowledge of these stresses and energy release rates for cracks terminating on the interface or lying along the interface in these bi-material problems should be quite useful for purely elastic behavior, it will be clear that additional considerations will be necessary to understand the interface behavior, when plastic deformation in the fiber or in the matrix outside the coating accompanies the propagation of the delamination crack.

For isotropic bi-material media with a crack terminating at right angles on the interface, a very useful solution has been provided by Swenson and Rau [4] for the Mode I loading of such a crack. As these authors show, such cracks have a singularity which differs fundamentally from that of cracks in homogeneous media, with singularity exponents either larger or smaller than 0.5, depending upon whether the crack is in the stiffer or the more compliant medium. The principal result of their analysis for the changes in stress intensification around the crack tip in a bi-material with semi-infinite extent is reproduced in Fig. 4 for plane strain, Mode I loading, as a function of the shear modulus ratio for a pair of materials having the same Poisson's ratio of 0.3. It is to be noted that, when the crack is in the stiffer medium, as would be the case of interest in this study with a crack in the SiC coating, the intensification of delaminating tensile stress $\sigma_{\theta\theta}(\pi/2)$ decreases, while the delaminating shear stress $\sigma_{r\theta}(\pi/2)$ increases with increasing shear modulus ratio μ_1/μ_2 . In fact, when μ_1/μ_2 exceeds 10, the opening mode stress $\sigma_{\theta\theta}(\pi/2)$ across the interface drops to zero, while the magnitude of $\sigma_{r\theta}(\pi/2)$ has doubled. It is to be noted that in the case of interest here, the ratio between the modulus of the SiC and the axial modulus of the fiber is 1.17, and thus differs only marginally from the isotropic case. This implies that the ratio of the opening mode stress $\sigma_{\theta\theta}(\pi/2)$ across the interface to that in the fiber, i.e., $\sigma_{\theta\theta}(\pi/2)/\sigma_{\theta\theta}(0)$ is roughly 0.35 (as is the ratio $\sigma_{r\theta}(\pi/2)/\sigma_{\theta\theta}(0)$). We note, however, that the Pitch-55 fiber is intensely anisotropic and has a transverse modulus that is only 4% of the axial modulus. Thus, it can be expected that the fiber can readily flex in the transverse direction to release the transverse normal stress $\sigma_{\theta\theta}(\pi/2)$; perhaps completely. This indicates that decoupling the fiber from the coating may prove to be quite difficult, particularly if the interface has no means of responding plastically in shear. Clearly, a full solution of

this bi-material problem with the anisotropy of the fiber fully taken into account is necessary.

The associated bi-material problem of a crack lying in the interface of two elastic media that would be required to follow the path of the delamination crack has been considered by a number of investigators [5,6], and is plagued by oscillatory singularities, the origin of which is not understood. Incorporation of geometrical and material non-linearities are presently being explored, but have so far not led to fully satisfactory results [7]. Solutions of this type, however, will be necessary not only for the problem of continued propagation of delamination cracks, but also in the final interpretation of experimental measurements of interface toughness, as we describe below.

III. CONTROL AND MEASUREMENT OF TOUGHNESS OF INTERFACES

3.1 General Strategy

To use the interface between the fiber and its coating as a reliable mechanical fuse to protect the fiber from damage, requires both control of interface strength and toughness in processing, as well as reliable methods of measuring such strength and toughness. The process of producing high quality coatings of SiC on Pitch-55 fibers and other substrates with the desired properties of interfaces by plasma-assisted chemical vapor deposition has been discussed by Landis, et al. [2]. The actual tailoring of the properties of these interfaces between coating and substrate to place them between the required lower and upper bounds discussed above, is still in progress, and will be reported in the future. Here, we will discuss

primarily the procedures developed for the measurement of interface properties. Of these, the interface cohesive strength and shear strength are difficult to measure, since they will be very sensitive to imperfections and are not likely to be of great value in governing the mode of the delamination of the interface to protect the fiber. For this latter purpose, the work of separation across the interface will be of greater value. From fundamental considerations, it is expected that the actual fracture work of an interface could be dependent on the mixture of the modes that are forcing it apart, i.e., the mixture of the applied Mode I and Mode II, to which the interface crack is subjected. However, since the nature of the singularity related to interface cracks separating two dissimilar materials under any mode of loading is presently associated with uncertainties discussed briefly in Section 2.4 above, we have concentrated attention on the development of reliable and reproducible methods of measurement of the fracture work of an interface by the most convenient means possible. In this quest, however, two limiting approaches have been distinguished. The interfaces which are of interest are expected to be relatively sharply defined along a steep material gradient between the coating and the fiber. The decohesion should then follow along a smooth surface, and have the appearance of a typical cleavage fracture. Thus, the actual intrinsic toughness G_{CO} , i.e., the release rate necessary for the decohesion is expected to be in the range of only 3-5 J/m², which is typical for a cleavage-like fracture in a hard inorganic solid. On the other hand, the energy release rate G_C for an actual interface delamination in a composite is likely to be very much larger, because of the presence of accompanying inelastic deformation in the fiber

and in matrix surrounding the fibers. In such fractures where the eventual separation process is of a cleavage type, the additional energy release rate G_p that is associated with the surrounding inelastic dissipations will be scaled by the intrinsic toughness of the interface G_{co} [8], i.e.,

$$G = G_{co} + G_p = G_{co}(1 + K) , \quad (2)$$

$$\text{where } K = G_p/G_{co} . \quad (3)$$

Therefore, in spite of the much larger dissipations associated with delaminations of interfaces in composites, the fundamental interface property to be controlled is the interface toughness G_{co} , which is expected to be related directly to the reversible work of separation of the interface by the well-known relation

$$G_{co} = \chi_{SiC} + \chi_C - \chi_i \quad (4)$$

where χ_{SiC} and χ_C are the surface free energies of SiC and C and χ_i is the interface energy of SiC and carbon. Hence, in the control of the fuse-like action of the interface between coating and fiber, the reliable measurement of G_{co} and how it may be affected by the processing conditions is of vital importance. Nevertheless, of almost equal importance is the measurement of the interface toughness in the actual composite itself.

In what follows, we will discuss the methods developed to measure the overall toughness G_c of the interfaces in systems very similar to those of the actual composite. The special methods necessary to measure the intrinsic toughness of the interface are discussed in an accompanying communication [9].

3.2 Measurement of Critical Energy Release Rates G_c of Interfaces
in Composites

Measurement of interface fracture work is not a new problem in thin film and coating technology. The literature is replete with practical techniques for the measurement of some average properties of thin film or coating interfaces, recently reviewed by Mittal [10]. Here, we shall develop some special considerations and procedures necessary for the accurate measurement of interface fracture work.

The preferred test for the determination of interfacial properties should measure the state of adhesion directly using simple fundamental procedures of mechanics relatively free of artifacts relying on complex models, based on unverifiable assumptions. For example, in the scratch test [11], the process of scratch formation is complex and cannot be readily explained in terms of pure models. Furthermore, there is no preferential failure at the film/substrate interface, and the size and shape of the stylus can influence the mode of failure in an undeterminable manner. In the periodic cracking technique utilized by Chow, Liu and Penwell [12] and by Davutoglu and Aksay [13], the complex state of stress at the edge of the film in contact with the substrate is not taken into account. More detailed stress field modeling, such as that carried out by Yang and Freund [14] using sliding stress intensity factors, are necessary. The indentation technique of Chiang, Marshall, and Evans [15], requiring the presence of the interface in the vicinity of a plastic zone, is also based on a fairly complicated model, and does not measure the interface work of fracture directly. On the other hand, the double cantilever beam test provides a simple and direct

method to measure the total adhesive fracture work, and has been used earlier by Gilman [16] quite effectively to measure the work of cleavage fracture of bulk materials. However, we have modified it to measure the work of fracture of thin film interfaces in systems structurally and chemically resembling those in the metal matrix composite itself.

IV. INTERFACES IN MODEL COMPOSITE SYSTEMS

4.1 The Pyrolytic Graphite SiC Interface

An important prerequisite in the control of interface properties, such as tensile cohesive strength and the work of fracture, is that these properties should be measurable and the effectiveness of the crack deflection process should be demonstrable.

Performing experiments on actual interfaces in composites would be best, but is very difficult because of the very small diameter of the fiber (c.a. 10 microns). Therefore, it is desirable that the experiments be performed on similar planar interfaces on a larger scale. This requires finding material available in bulk, having the same chemical and morphological characteristics as that of the fiber, which can then be adopted for macroscopic testing procedures.

For this purpose, pyrolytic graphite was chosen as a first approximation to the Pitch-55 fibers. Pyrolytic graphite (PG) is obtained by vapor phase deposition of pure carbon in a temperature range of 1900 - 2500°C. It has a density of 2.2 g/cm^3 , which is approaching the theoretical density of graphitic carbon, i.e., 2.28 g/cm^3 . It grows in polycrystalline, nearly planar spherulitic forms in a layer-like manner, but with a great degree of

anisotropy in the growth direction across which it is very compliant and weak. Its isotropic Young's modulus in the growth planes is 28.5 GPa, and in the growth direction across the layers is only 7 GPa. Figure 5 shows the basis of modeling of the fiber surface with PG. The surface of PG parallel to the C axis resembles the surface of the Pitch-55 fiber. It has the same chemistry of Pitch-55, a somewhat higher density, and rather similar anisotropic morphology that resembles that of the Pitch-55 fibers, as viewed in the circumferential direction. However, the analogy is quantitatively quite different. The Pitch-55 fibers have a stiff direction modulus 13.5 times that of PG, but a compliant direction modulus that is only 2 times that of PG. Thus, the fibers are both far more anisotropic and far stiffer than the PG. Nevertheless, experimentation of relative interface properties and general response of coatings on carbon substrates are far more readily investigated on PG than on individual Pitch-55 fibers, and permit simulation of coating-substrate interactions in bulk.

4.2 The Double-Cantilever Beam Experiment

This experiment was designed to measure the work of separation of a SiC coating of 0.1 - 0.5 micron thickness, deposited on a planar PG substrate. The specimen consists of strips of PG of 6.3 mm width, 3.2 mm thickness, and 150 mm length with the layer planes oriented perpendicular to the surface, as shown in Figure 6. The surfaces of these strips with the given orientation of the planes were metallographically polished in a Syntron vibratory polisher. These polished surfaces were then coated with SiC of near stoichiometric composition, using a plasma-assisted chemical vapor deposition process. The coated strips were annealed at 600°C in a vacuum

oven in order to relieve the residual stresses inside the films. Two of these coated strips were then bonded together using a very tough PermaBond glue (ESP 109 and 110) over 75 mm of their length, so as to create an initial crack of 75 mm between the two strips. This laminate assembly was heated to 200°C to cure the glue. As will become clear below, the glue layer between the two strips has mechanical properties close to those of pure aluminum.

A schematic diagram of the test apparatus is shown in Figure 6. The free ends of the graphite strips were connected to tightly fitting metal cages, which were then connected to the Instron machine load train, as shown in the figure. Load was transferred to the free ends of the cantilever strips by 200 μ m thick tungsten wire. This wire was made taut prior to the testing, using a pin and set screw arrangement, shown in the figure. The double cantilevers were pulled apart with a cross-head speed of 0.5 mm/minute. A plot of load vs. load point displacement was obtained. By initial selection of components, stable testing conditions were obtained, requiring that the unloading stiffness of the specimen is substantially less than the stiffness of the testing machine.

Treating the arms of the crack as cantilever beams and using simple beam theory, the bending force F at the time of the crack propagation can be related to the fracture work of the interface G_c , through the Griffithh criterion by means of the formula:

$$G_c = F^2 L^2 / E I b , \quad (5)$$

where L is the initial crack length, I is the moment of inertia, b is the

width, and E is the modulus of elasticity of the PG strips.

4.3 Double Cantilever Experiment Results

Since the glue and the interface between the glue and the SiC coating is tougher than the interface between PG and SiC coating, the crack preferentially propagates along the latter interface. In some instances, the crack was found to initiate in the glue layer, but jumped to the less tough interface between SiC and PG. In such cases, the portion of the force/crack-length curve pertaining to this type of propagation was not considered. Scanning electron microscopy, such as Fig. 7 of the fracture surface clearly shows the plane of the crack and the regions where the crack deviated from the interface, dipped inside the glue, and came back to the PG/SiC interface. Additional stereo-images of the fracture surface helped to establish better these occasional deviations of the crack path. Figure 8 shows an example of such a stereo-pair. These observations established that the area of the fracture surface through the glue is only a small fraction (about 0.1) of the total fractured area along the interface. To make corrections for such deviations, to obtain the actual energy release rate along the PG/SiC interface, it is necessary to measure the fracture toughness of a comparably thin glue layer. This was accomplished by bonding two high strength steel strips together with the same glue of the same thickness, and prying the strips apart in a double-cantilever beam experiment. This gave a critical energy release rate $G_c = 244 \text{ J/m}^2$ for the glue layer, which was used in making the desired corrections.

Figure 9 shows a typical load extension curve for a crack running along the planar interface between SiC and PG. Three drops in the curve indicate three stable jumps ahead of the crack. The average value of the fracture work G_c (the critical energy release rate) for the interface determined from such experiments, and incorporating corrections for deviations of the path through the glue gave a value of $60 \pm 6.85 \text{ J/m}^2$.

The quoted value of the critical energy release rate G_c along the interface obtained from the double cantilever beam experiment is quite high when compared to an expected level of $3\text{-}5 \text{ J/m}^2$, based on interface energy for hard inorganic solids. These high values must incorporate additional inelastic dissipation when the crack runs along the interface between SiC and PG. Thus, the crack also probes the PG and the glue on both sides, and forces them to undergo plastic relaxation. It is known that the tensile yield strength of the glue is 64 MPa, while the intra-laminar shear strength of the PG is 52 MPa, which translates into a Mises tensile yield strength of 90 MPa. Considering as a crude first approximation the interface cracking to be occurring in a conventional homogeneous material under small scale yielding conditions, we can estimate the inelastically affected layer depth h of material near the fracture surfaces from the well known linear elastic fracture mechanics relation of:

$$h = \frac{1}{2\pi} \frac{G_c}{(1 - \nu^2)Y\epsilon_y} \quad (6)$$

Here, $G_c = 60 \text{ J/m}^2$ is the measured work of fracture, Y is the tensile yield strength of the equivalent homogeneous material (take $Y = 71 \text{ MPa}$ as the average for the glue and the PG), ϵ_y is the elastic strain at yield (~ 0.02

for the glue and ~ 0.013 for the PG, take 0.015), and ν is the Poisson's ratio (≈ 0.3). Evaluation of this expression gives a layer depth of about 10 microns. As a similar first approximation, the plastic work per unit area of fracture, locked-up in the crack surface layers of thickness h , should be of the order of $2\beta Y \epsilon_y h$, where β , which is a constant of integration involving the plastic strain gradient into the surface in the deformed layers, is expected to be in the range of 2-3 (take 2.5). Using the above choices for Y , ϵ_y and h , we estimate the dissipative component G_p of the energy release rate to be 53 J/m^2 , or quite close to what was measured.

In order to gain more confidence in the above explanations, the critical energy release rate for fracture of the PG in the same orientation as in the above tests (i.e. with its weak planes oriented perpendicular to the fracture surface and running parallel to the crack growth direction) was also measured using the double cantilever beam experiment. The measured average value of $G_c = 136 \text{ J/m}^2$ is about twice as large as the critical energy release rates measured for cracks propagating along the PG/SiC interface. Scanning electron microscopy of the fracture surfaces of the PG, as shown in Fig. 10, revealed the layered structure of PG and indicated considerable roughness in the forms of steps between lamina. The measured difference in fracture work between the PG/SiC interface and the PG substrate itself is quite large, indicating that the preferred delamination path should indeed be along the PG/SiC interface, as was observed.

The toughness of the glue layer is worth more consideration. As mentioned above, the thin glue layer exhibited a critical energy release rate at fracture of the order of 244 J/m^2 , and has a flow stress equal to

64 MPa. This is close to the yield strength of unalloyed aluminum, which, however, in bulk form, exhibits energy release rates in plane strain fracture nearly two orders of magnitude higher, with deformation zones being correspondingly thicker. But when tested in confined spaces in thin layers, the fracture work of aluminum is likely to be no larger than what was found for the glue. This indicates that the glue in many respects acts as a good model for the aluminum matrix in the prototype composite. Therefore, we conclude that the double-cantilever beam experiment for the fracture work of the PG/SiC interface, being surrounded by a glue layer and a PG substrate, mimicks the behavior of the actual composite of SiC coated Pitch-55 fibers in an unalloyed aluminum matrix. Table II summarizes all the measured overall critical energy release rates for fracturing along the interface and in the PG as well as in the glue along paths shown in Fig. 11. From these measurements of the properties of the PG/SiC interfaces, we conclude that the overall energy release rates G_c are indeed made up of an intrinsic component G_{c0} and a much larger plastic dissipation component G_p in the surrounding material, as discussed in connection with Eqn. (2), but that G_{c0} is still the fundamental quantity which sets the scale of the overall fracture work.

Therefore, for the purpose of monitoring the toughness properties of the tailored interface, it is essential to find reliable means of measuring the intrinsic toughness level G_{c0} alone. In an accompanying communication [9], we discuss how this intrinsic work of separation of the coatings from its substrate can be measured under nearly ideal conditions of quasi-static delamination of residually stressed coatings under the driving force of the locked-in strain energy of the coating, which produces only negligible

inelastic effects in the substrate.

V. DISCUSSION

The delamination, or fracture toughness of interfaces play a key role in all composites, but particularly so in metal matrix composites, where unwanted reactions between the matrix and the fiber can produce reaction products with material misfit that can severely damage the fiber. This was observed in elegant experiments of Metcalf [17] in the boron fiber aluminum system. Since during the production of composites processing histories that give proper wetting of fibers by the molten matrix and good adhesion are often in conflict with conditions to limit reaction damage, the proposal has been made here to separate functions of proper wetting from careful control of interface mechanical properties. This can be accomplished by tailoring the desired mechanical properties of the interface between the protective coating and the reinforcing fiber, while accepting wetting related reaction damage between the matrix and the outer surface of the protective coating of the fiber. When properly controlled, this permits the pedigreed key interface between the coating and the fiber to act as a mechanical fuse to decouple the fiber from its surroundings by initiating delamination along it.

In this communication, we have discussed techniques for the measurement of the fracture work of such interfaces in simulated conditions of local environments representative of those in the composite itself. The double cantilever beam experiment that was used to measure the fracture work in symmetrical sandwiches of PG/SiC/glue/SiC/PG showed that very substantial inelastic deformation in the PG and the thin glue layer accompanies

the apparent cleavage-like separation of the interface between the PG and the SiC. Since the PG has qualitatively similar inelastic behavior and morphology to that of the Pitch-55 fibers, and the glue has similar yield behavior to that of a pure Al matrix in the composite, the toughness measurements reflect behavior that can be expected from the composite itself. Direct meaningful measurements of fracture work of interfaces between SiC coatings and Pitch-55 fibers in prototype composites have so far not been carried out.

Clearly, additional developments are necessary both for the measurement of intrinsic toughnesses of interfaces, and for the analysis of interface cracks with accompanying inelastic behavior in the surrounding matrix and fibers. In the accompanying communication, we present new developments on the measurement of intrinsic toughness of interfaces [9].

ACKNOWLEDGEMENTS

We gratefully acknowledge DARPA, Office of Naval Research and Naval Air Development Center under Contract No. N00014-84-K and IST/SDIO under Contract No. N00014-85-K-0645 and M.I.T. Consortium for Processing and Evaluation of Metal and Ceramic Matrix Composites for their generous support of this project.

We moreover acknowledge with thanks the help of H. Landis in preparing SiC coatings on substrates, and useful discussions with Dr. T. Erturk during the early phases of this investigation.

REFERENCES

1. R. Bacon, in Proceedings of Conference on "Metal and Ceramic Matrix Composites Processing", vol. II, p. 23 (U.S. Dept. of Defense: Columbus, Ohio) (limited circulation) (1984).
2. H.S. Landis, V. Gupta, and J.A. Cornie, to be published.
3. E. Zywickz, "Local Stress and Deformation due to Fabrication and Transverse Loading", SM Thesis, Dept. Mech. Eng., M.I.T., Cambridge, MA (1986).
4. D.O. Swenson and C.A. Rau, Jr., Intern. J. Fracture Mechanics, 6, 357 (1970).
5. J.R. Rice and G.C. Sih, J. Appl. Mech. 32, 418 (1965).
6. M. Comninou, J. Appl. Mech., 44, 631 (1977).
7. C.F. Shih and R.J. Asaro, submitted to J. Appl. Mech.
8. J.R. Rice, in "Proceedings of the First International Conference on Fracture", edited by T. Yokobori, T. Kawasaki, and J.L. Swedlow (The Japanese Society of Strength and Fracture of Materials: Sendai, Japan), vol. 1, p. 309 (1965).
9. A.S. Argon, V. Gupta, H.S. Landis, J.A. Cornie, this journal.
10. K.L. Mittal, in "Adhesion Measurement of Thin Films, Thick Films, and Bulk Coatings", edited by K.L. Mittal, STP640 (ASTM: Philadelphia), p. 5 (1978).
11. J. Ahn, K.L. Mittal, and R.H. McQueen, in "Adhesion Measurement of Thin Films, Thick Films, and Bulk Coatings", edited by K.L. Mittal, STP640 (ASTM: Philadelphia), p. 134 (1978).

12. T.S. Chou, C.A. Liu, and R.C. Pennell, J. Poly. Sci., 14, 1305 (1976).
13. A. Davutoglu and A.I. Aksay, in "Surfaces and Interfaces in Ceramic and Ceramic-Metal Systems", edited by J. Pask and A.G. Evans, "Materials Science Research (Plenum Press: New York), vol. 14, p. 641 (1981).
14. W. Yang and L.B. Freund, "Shear Stress Concentration Near the Edge of a Thin Film Deposited on a Substrate", to be published.
15. S.S. Chiang, D.B. Marshall, and A.G. Evans, in "Surfaces and Interfaces in Ceramic and Ceramic-Metal Systems", edited by J. Pask and A.G. Evans, "Materials Science Research" (Plenum Press: New York), vol. 14, p. 603 (1981).
16. J.J. Gilman, J. Appl. Phys., 31, 2208 (1960).
17. A.G. Metcalfe, in "Composite Materials: Interfaces in Metal Matrix Composites", edited by A.G. Metcalfe (Academic Press: New York), vol. 1, p. 1 (1974).

TABLE I - Transverse Stress Concentration for Pitch-55 Fibers in an Aluminum Matrix (*)

Elastic Stress Concentration Factors k			
V_f	0.4	0.6	0.8
$\sigma_{rrmax}/\sigma_{xx\infty}$	0.44	0.56	0.74
$\sigma_{rrmax}/\sigma_{yy\infty}$	0.60	0.82	1.04

Elastic-Plastic ($\bar{\epsilon} = 0.01$) Stress Concentration Factors k (**)				
$\sigma_{rrmax}/\bar{\sigma}$	1.14	1.55	2.40	$(\sigma_{xx\infty})$
$\sigma_{rrmax}/\bar{\sigma}$	1.14	1.14	1.33	$(\sigma_{yy\infty})$

(*) Zywicz and Parks [3].

(**) $\bar{\sigma}$ is the Mises equivalent stress.

TABLE II - Total Specific Fracture Work or Critical Energy Release Rate

<u>Fracture Path</u>	<u>G_{IC} (J/m²)</u>
PG/SiC Interface	62.4 \pm 6.8
Permabond Glue	244
Pyrolytic Graphite	136

FIGURE CAPTIONS

- Fig. 1 - (a) Morphology of a 10 micron diameter Pitch-55 fiber revealed on a transverse fracture surface, (b) idealized fiber morphology as a set of corrugated parallel planes running parallel to the fiber axis. The fiber yield strength is expected to be low in longitudinal shear.
- Fig. 2 - A hexagonal packing of aligned fibers in a meta. matrix. The transverse plastic resistance differs in the y direction from that of the x direction.
- Fig. 3 - Sketch showing a potential form of mechanical probing of a fiber by a crack in the coating pried open by a misfit wedge produced by a coating-matrix reaction. To protect the fiber, controlled delamination at the interface is desired.
- Fig. 4 - The effect of shear modulus ratios on crack tip stresses for a crack in one medium ending perpendicularly on the interface, under plane strain loading (from Swenson and Rau [4], courtesy of Pergamon Press).
- Fig. 5 - (a) Scanning electron micrograph of the morphology of a smooth layer plane perpendicular to the "c" axis in pyrolitic graphite showing nodules, (b) idealized rendering of the layer planes in PG.
- Fig. 6 - The double cantilever beam experiment for the measurement of interface toughness.

- Fig. 7 - A SEM micrograph of the fracture surface between a SiC coating and a PG substrate having its surface parallel to the c axis of the PG. The crack propagation direction was parallel to the surface markings: (a) fracture surface viewed toward PG, (b) viewed toward SiC and glue layer.
- Fig. 8 - A stereo-pair of SEM micrographs of the fracture surface between a SiC coating and PG substrate. The crack propagation direction was parallel to the markings.
- Fig. 9 - A typical load (displacement) curve recorded in a double cantilever beam experiment, showing 3 quasi-stable extensions of the crack before it finally ran unstably.
- Fig. 10 - A SEM micrograph of the fracture surface in PG running transverse to the smooth layer planes.
- Fig. 11 - Sketch showing the three possible paths of a crack running parallel to an interface between SiC and PG.

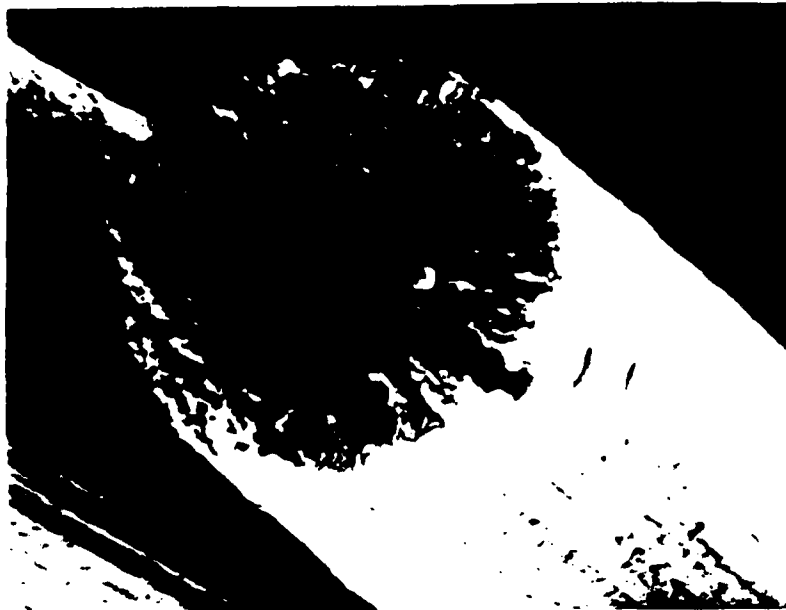


Fig. 1 - (a) Morphology of a 10 micron diameter Pitch-55 fiber revealed on a transverse fracture surface, (b) idealized fiber morphology as a set of corrugated parallel planes running parallel to the fiber axis. The fiber yield strength is expected to be low in longitudinal shear.

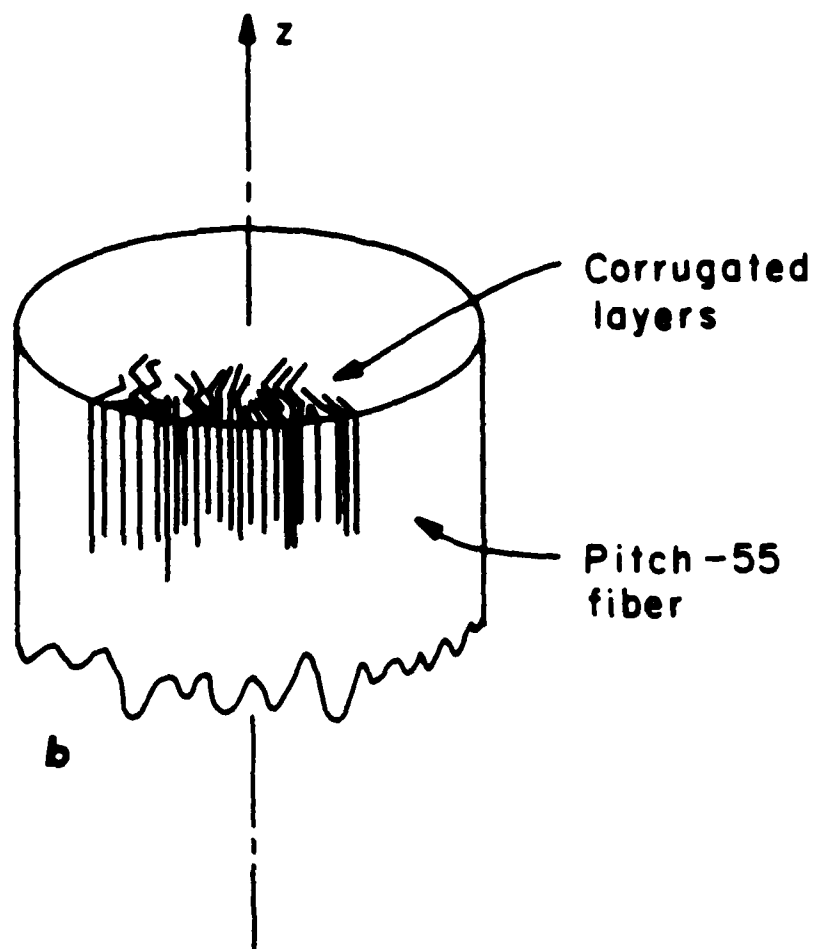


Fig. 1 - (a) Morphology of a 10 micron diameter Pitch-55 fiber revealed on a transverse fracture surface, (b) idealized fiber morphology as a set of corrugated parallel planes running parallel to the fiber axis. The fiber yield strength is expected to be low in longitudinal shear.

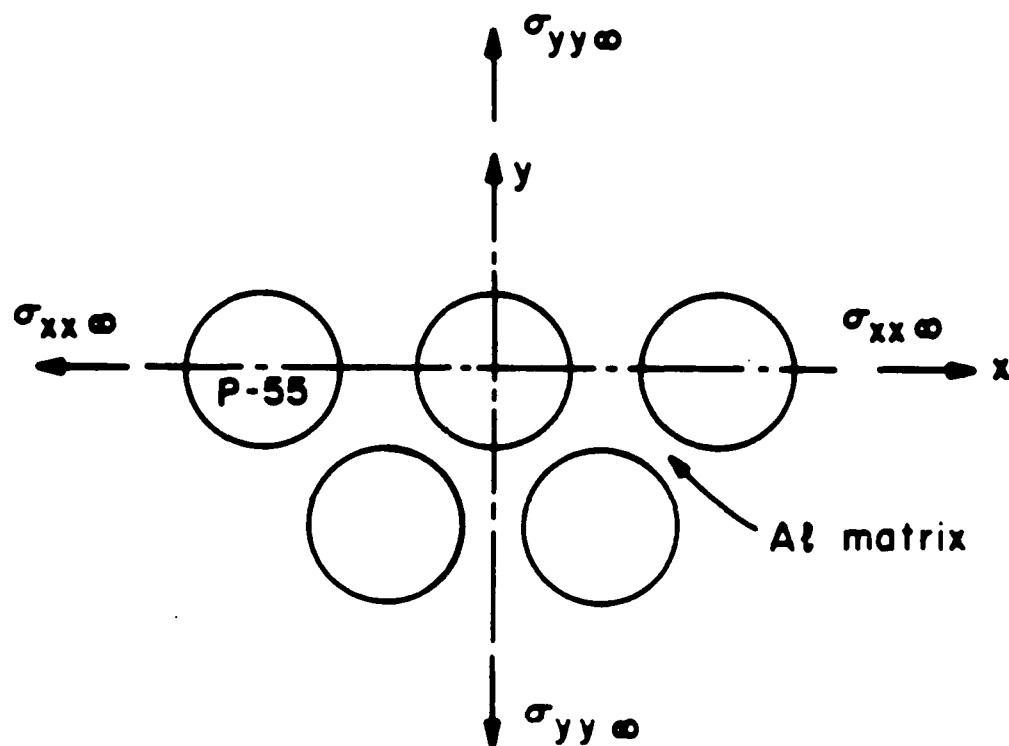


Fig. 2 - A hexagonal packing of aligned fibers in a metal matrix. The transverse plastic resistance differs in the y direction from that of the x direction.

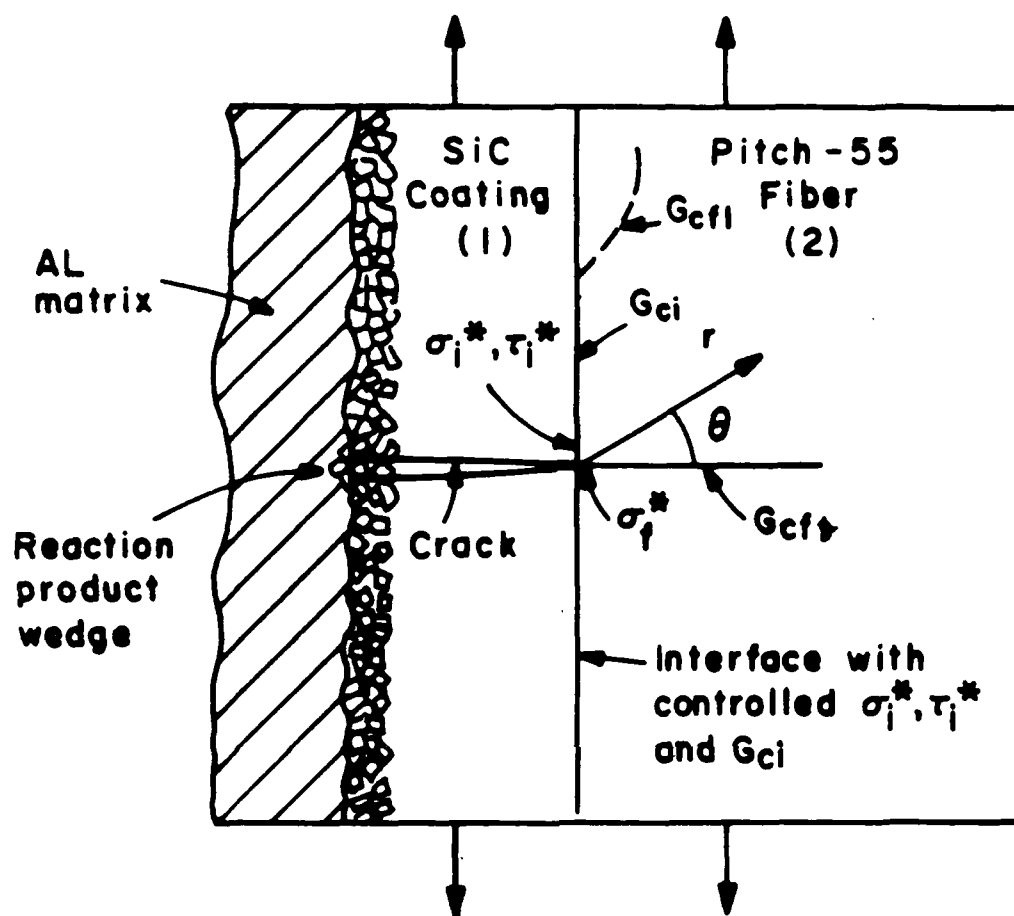


Fig. 3 - Sketch showing a potential form of mechanical probing of a fiber by a crack in the coating pried open by a misfit wedge produced by a coating-matrix reaction. To protect the fiber, controlled delamination at the interface is desired.

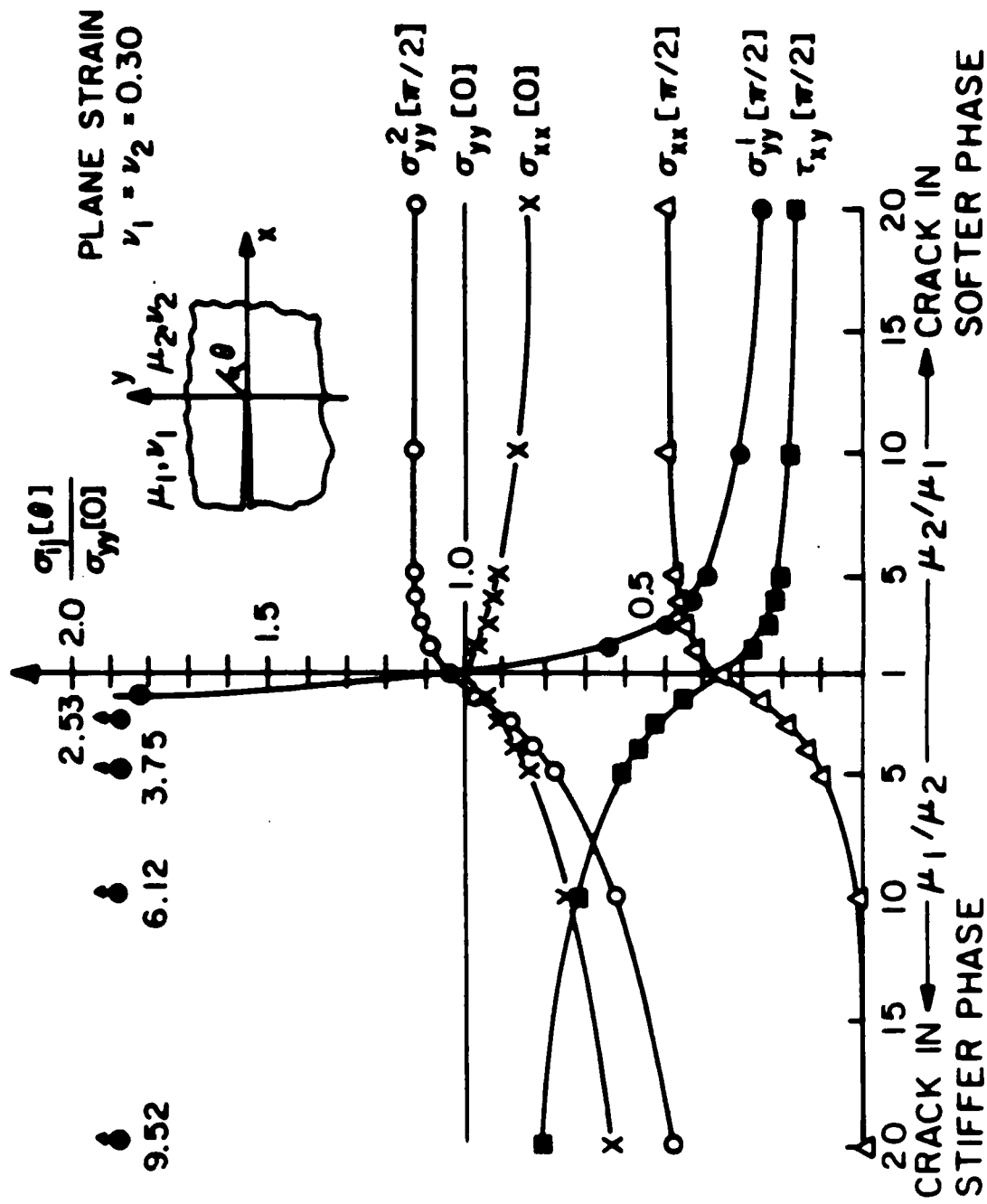


Fig. 4 - The effect of shear modulus ratios on crack tip stresses for a crack in one medium ending perpendicularly on the interface, under plane strain loading (from Swenson and Rau [4], courtesy of Pergamon Press).

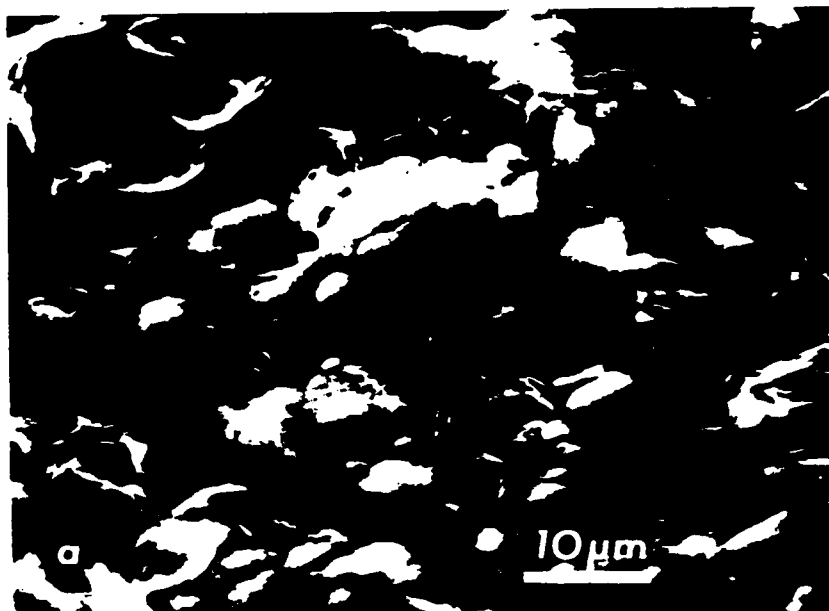


Fig. 5 - (a) Scanning electron micrograph of the morphology of a smooth layer plane perpendicular to the "c" axis in pyrolytic graphite showing nodules, (b) idealized rendering of the layer planes in PG.

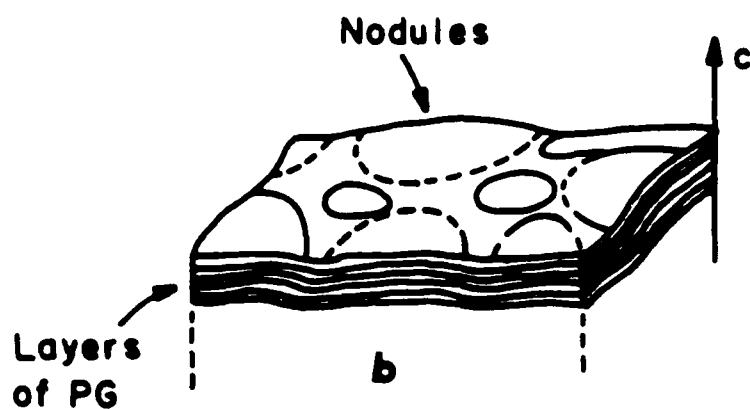


Fig. 5 - (a) Scanning electron micrograph of the morphology of a smooth layer plane perpendicular to the "c" axis in pyrolytic graphite showing nodules, (b) idealized rendering of the layer planes in PG.

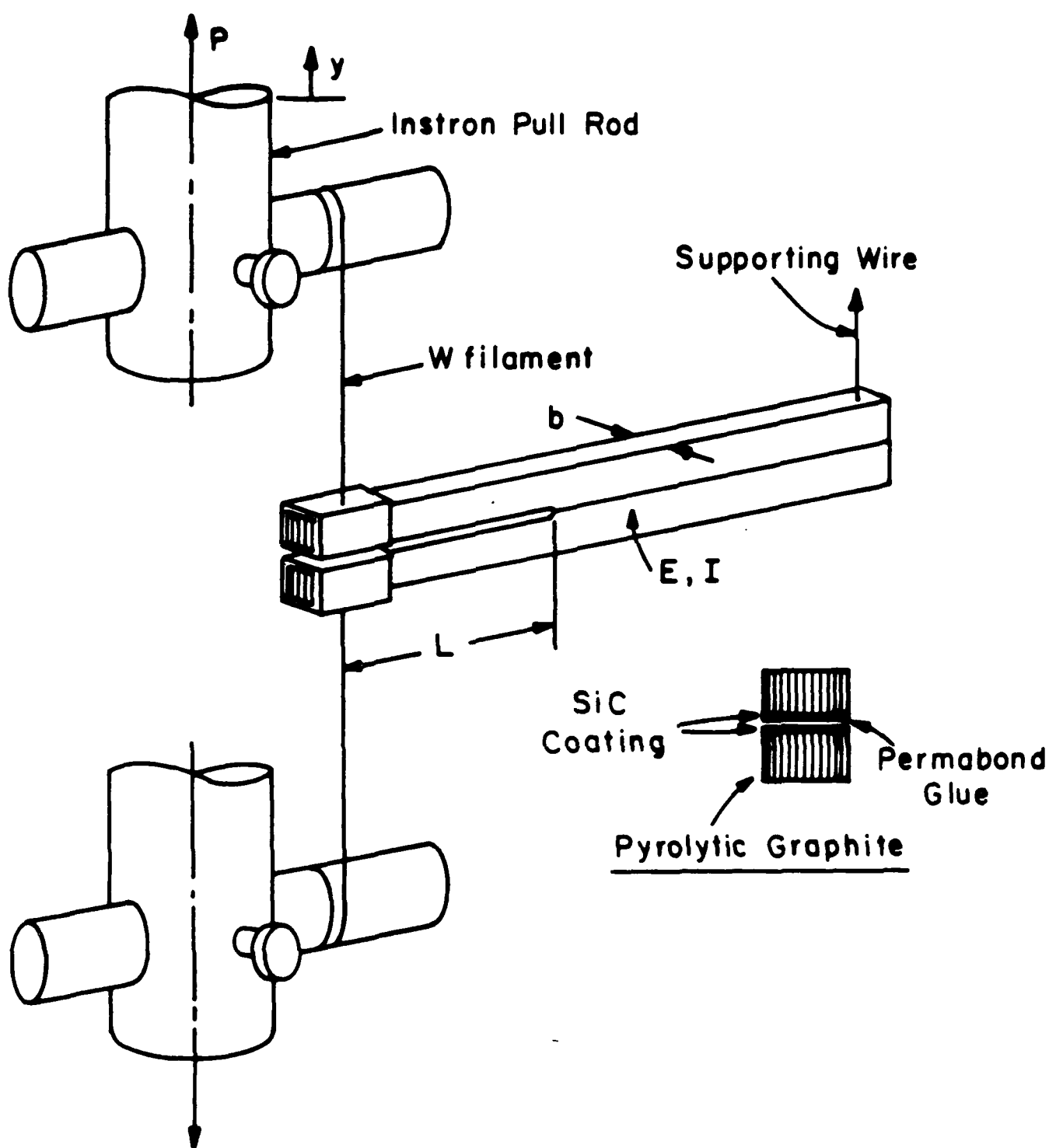


Fig. 6 - The double cantilever beam experiment for the measurement of interface toughness.

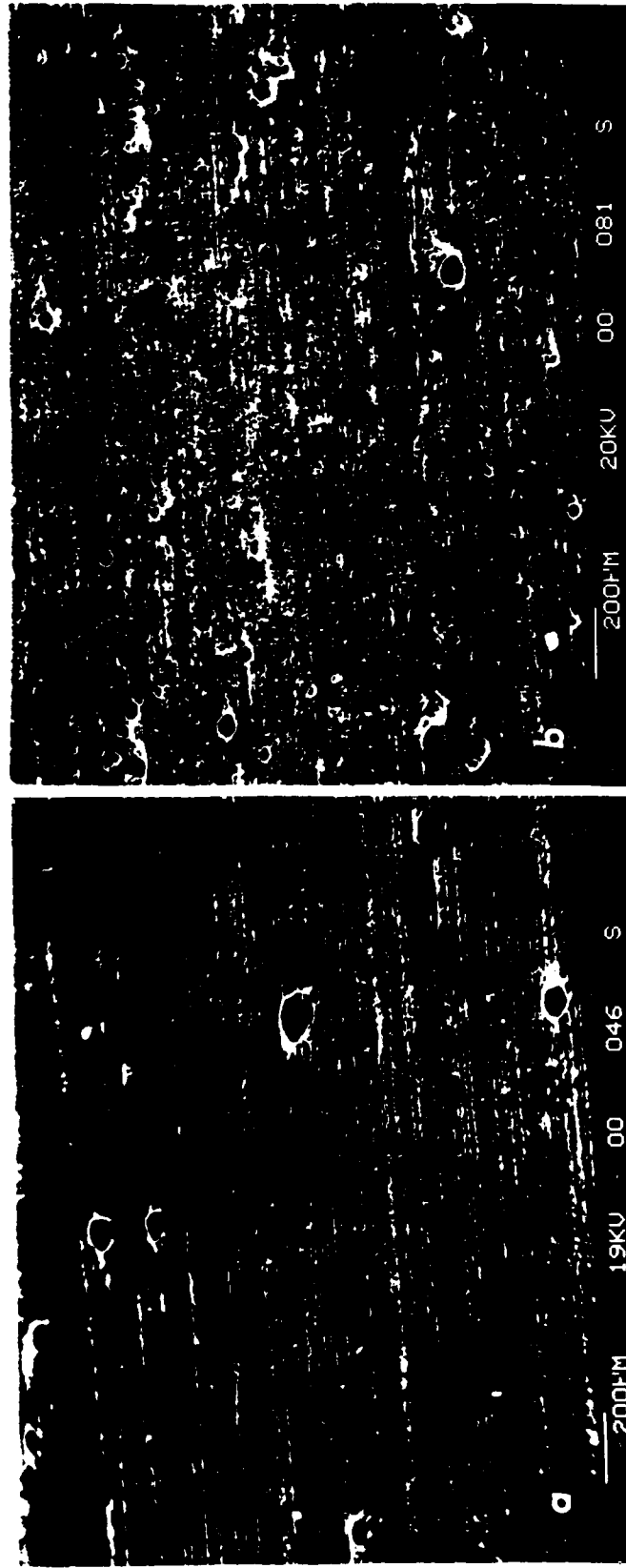


Fig. 7 - A SEM micrograph of the fracture surface between a SiC coating and a PG substrate having its surface parallel to the c axis of the PG. The crack propagation direction was parallel to the surface markings: (a) fracture surface viewed toward PG, (b) viewed toward SiC and glue layer.

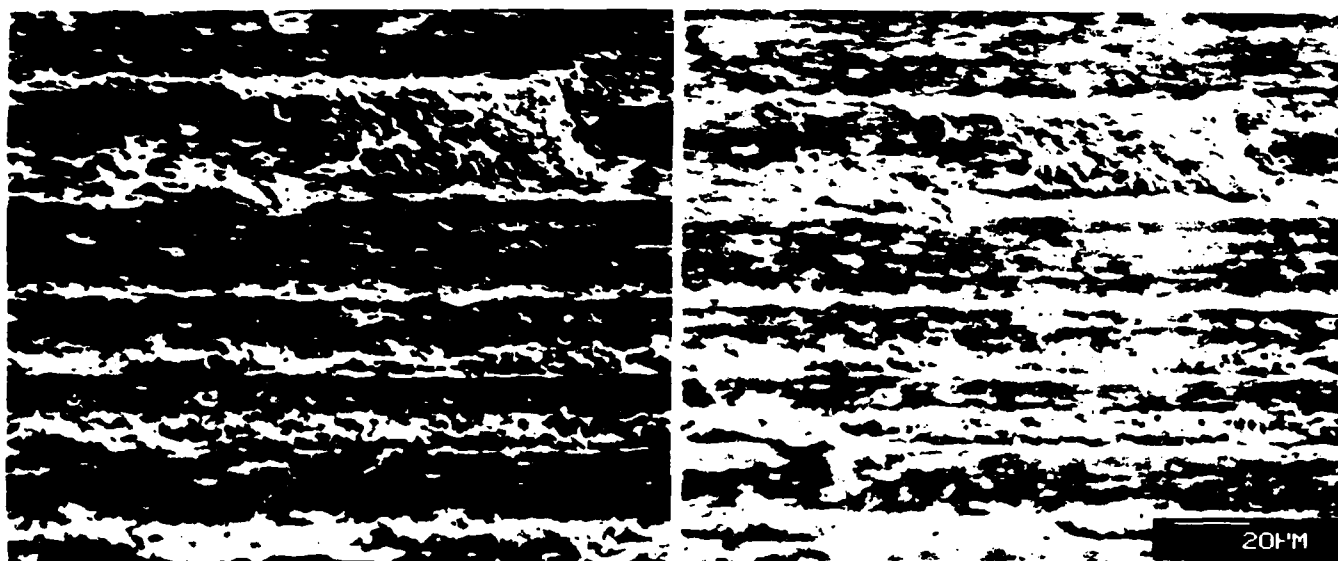


Fig. 8 - A stereo-pair of SEM micrographs of the fracture surface between a SiC coating and PG substrate. The crack propagation direction was parallel to the markings.

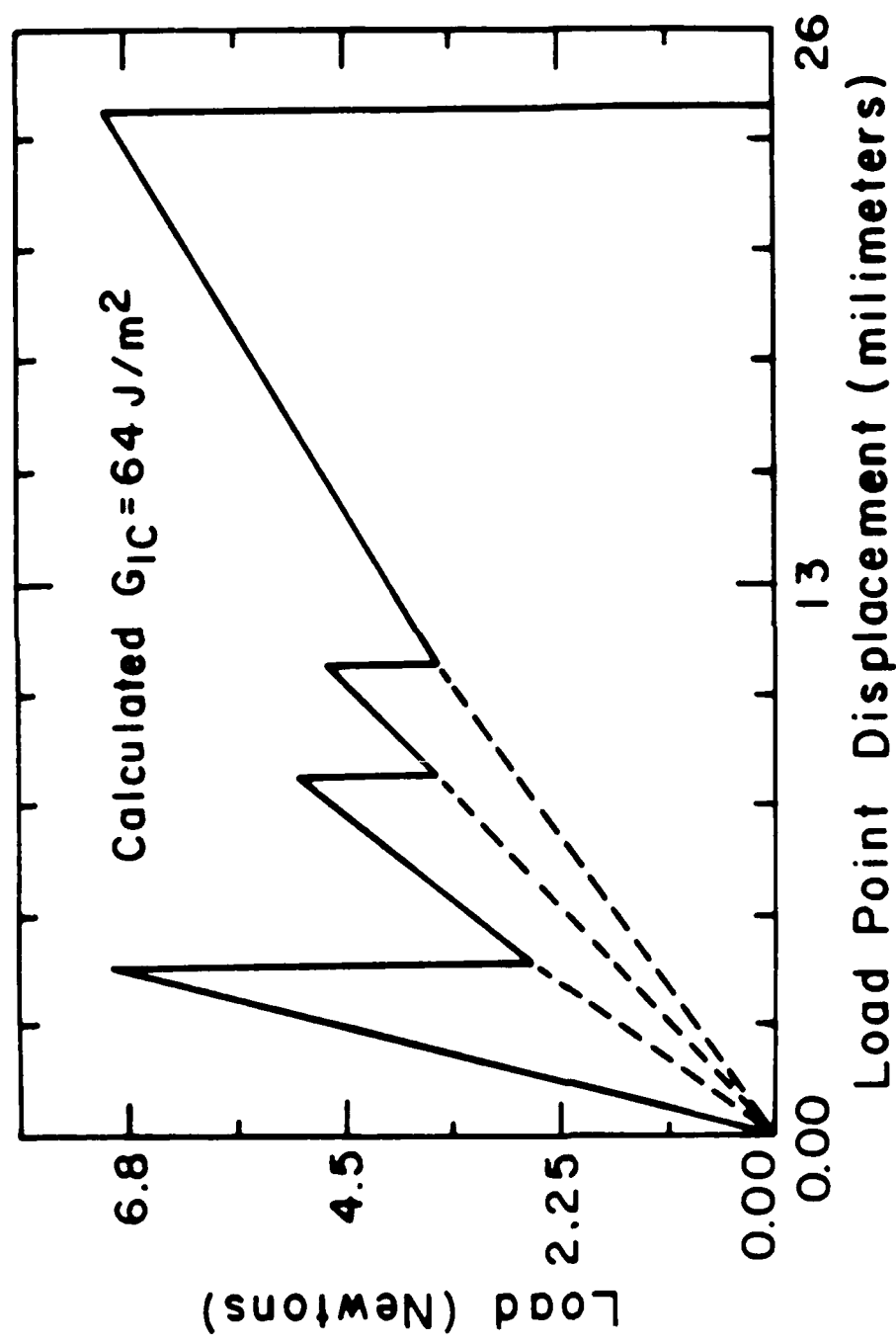


Fig. 9 - A typical load (displacement) curve recorded in a double cantilever beam experiment, showing 3 quasi-stable extensions of the crack before it finally ran unstably.

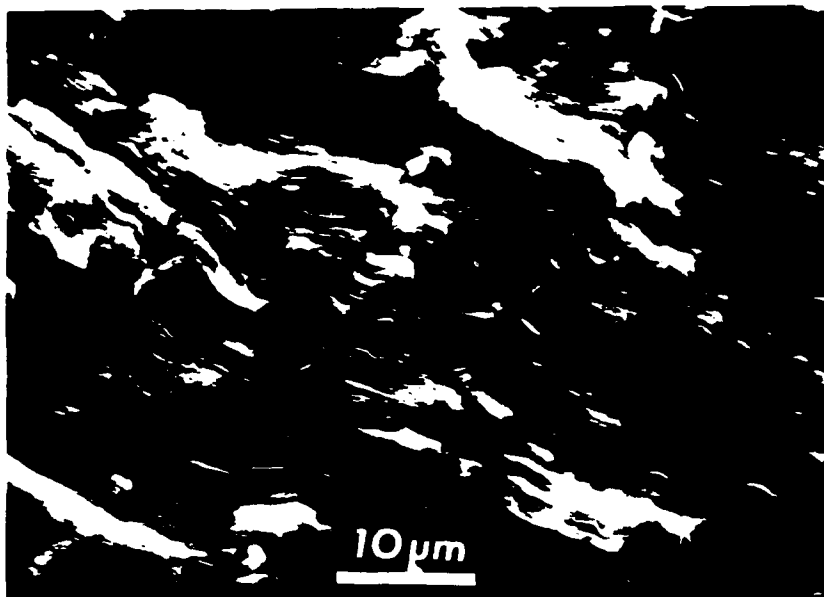


Fig. 10 - A SEM micrograph of the fracture surface in PG running transverse to the smooth layer planes.

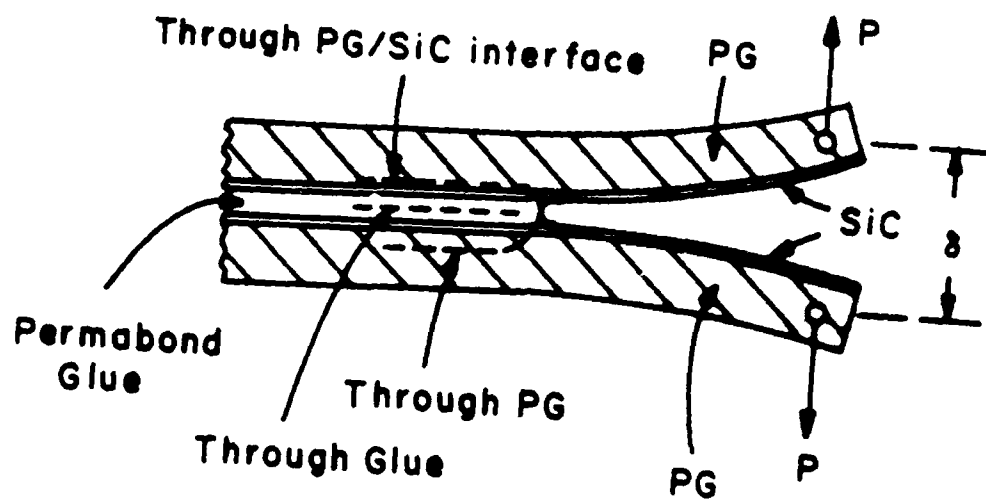


Fig. 11 - Sketch showing the three possible paths of a crack running parallel to an interface between SiC and PG.

INTRINSIC TOUGHNESS OF INTERFACES
BETWEEN SiC COATINGS AND SUBSTRATES OF Si OR C FIBER

A.S. Argon, V. Gupta, H.S. Landis*, and J.A. Cornie

Massachusetts Institute of Technology, Cambridge, MA 02139

ABSTRACT

The critical energy release rate for separation of SiC coatings from single crystal Si substrates or surfaces of carbon fibers, along their well-defined interfaces can be determined quite accurately from analysis of the spontaneous delamination of coatings under bi-axial stress, when such coatings exceed a critical thickness. Direct evaluations have been made of the specific work of delamination along the interface for SiC coatings from single crystal Si substrates, for both the case of coatings under bi-axial compression, as well as under bi-axial tension. The critical energy release rate for coatings in tension was 5.1 J/m^2 , and that for coatings under compression was 5.9 J/m^2 . The higher value of the latter is attributed to relative slippage between coating and substrate before lift-off of the former.

Corresponding determination of the critical energy release rate for delamination of SiC coatings under bi-axial tension from surfaces of anisotropic Pitch-55 carbon fibers gave an answer of 5.5 J/m^2 . These values compare very well with expectations from surface energies of strong solids.

*Now with General Telephone and Electronics Laboratory, Waltham, Massachusetts

I. INTRODUCTION

Relaxation of shear tractions across interfaces and eventual fracture along interfaces are key phenomena affecting the performance of composites reinforced with stiff or less deformable heterogeneities. Particularly, the possibility of controlled delamination along an interface of a reinforcing fiber or platelet before the stresses become too high in them to produce fracture has been recognized for some time as a desirable condition to achieve stable traction-displacement behavior, and to increase overall toughness. In the composites field, key interface properties are usually measured by simple operational procedures, such as a single fiber pull-out test or a relatively macroscopic interlaminar shear test [1]. There have also been other more indirect techniques, such as the periodic cracking of a brittle fiber embedded in a matrix, plastically extended parallel to the fiber [2], or initiating local interface fractures through very local deformations produced by scratches [3] or hardness indenters [4]. In all of these cases, either only average information is obtained for a delamination process in which in reality a front of concentrated stresses and inelastic strain propagate along the interface, or the deformation is even more inhomogeneous and produces local interface separation through the production of plastic misfit which requires the solution of local elasto-plastic boundary value problems for the evaluation of the critical interface conditions. In all of these instances, the critical interface tractions that result in separation are not accurately determinable, while the fracture toughness of the interface itself is usually shrouded by much excess accompanying deformation, often even absent in the failure process occurring in the prototype composite.

In many interface fractures resulting in a clean cleavage-like separation, the critical intrinsic energy release rate G_{co} for separation of the interface (to be referred to here as the intrinsic interface toughness), is accompanied by a much larger term, G_p , reflecting the dissipative additional inelastic deformations in the layers immediately adjacent to the separating interface. While this additional work, G_p , can dominate over the toughness G_{co} , the latter still scales the much larger inelastic dissipation work, so that any factor which affects G_{co} is directly reflected in the magnitude of G_p in an amplified manner [5,6]. In an accompanying communication [6], we have proposed that the toughness of interfaces between protective coatings, such as SiC and fibers such as Pitch-55, can be tailored to initiate controlled delamination to protect the fiber from damage, and thereby act as mechanical fuses. There, we discussed an experimental technique based on the double cantilever beam to measure the overall specific fracture work ($G_{co} + G_p$) of model composite interfaces. Here, we will discuss special techniques on how the much smaller, but key intrinsic toughnesses G_{co} of interfaces can be measured, which must be governed to control composite properties.

II. INTRINSIC MECHANICAL PROPERTIES OF INTERFACES

2.1 Toughness of Coating - Substrate Interfaces

During the study of vapor deposition of SiC coatings on various substrates, it became clear that the intrinsic toughness of an interface between a thin coating and a more massive substrate is directly measurable through the controlled delamination of the coating from the substrate during the relief of the residual stresses in the coating. Such delaminations and

their potential for interface toughness measurement were recognized earlier by Evans and Hutchinson for surface layers under residual compression [7]. Here, we will demonstrate how this technique can be generalized and used for intrinsic interface toughness measurement in cases where the coating is either in residual tension or residual compression, on both model systems as well as on actual prototype interfaces between SiC coatings and Pitch-55 fibers. Before we present the details of such interface toughness determinations, it is necessary to discuss some essential details of the coating process which clarifies the origin of the residual stresses.

2.2 Vapor Deposition of SiC Coatings

Amorphous hydrogenated thin films of SiC were deposited in Pitch-55 fibers and on Si single crystal wafers using a plasma assisted chemical vapor deposition (PACVD) process, the details of which are discussed by one of us elsewhere [8].

It was observed that the processing parameters, especially the ion bombardment energy play a critical role in determining the unique physical and mechanical properties of the SiC deposits. These processing parameters could be adjusted to obtain the necessary toughness properties for the interfaces to optimize their desirable mechanical fuse action discussed in the accompanying communication [6].

Preliminary observations made on such PACVD coatings of SiC on Pitch-55 fibers indicated that in the as-deposited form, the coatings entrap a large concentration of hydrogen, which leaves the coatings under substantial residual compressive stress. When such coated fibers are incorporated into actual metal matrix composites, molten Al must be infiltrated

among them at or around 660°C. This releases the entrapped hydrogen, and results in poor adhesion of fibers to matrix and in unwanted porosity. To prevent this, coatings are given outgassing treatments at 600°C to remove the hydrogen.

If this process is carried to completion in a period of about 30 minutes at 600°C, the coatings acquire a substantial level of residual tensile stress. Thus, the type and magnitude of the residual stress in coatings is an important element in the proper performance of composites, and the factors which influence it are of direct interest.

2.3 Measurement of Residual Stresses in Coatings

The levels of residual stress in SiC coatings applied by the PCVD process were measured through the change of curvature they produce in a 1 inch diameter standard Si single crystal wafer with (100) surfaces and 250 μm thickness when the coating is deposited on the wafer. An initially flat and homogeneous circular disk shaped Si wafer acquires a convex shape with a coating in residual compression on its top surface, as depicted in Fig. 1b, and a concave shape when the coating is in residual tension, as depicted in Fig. 1a. Elementary considerations give readily that the residual biaxial stress σ in the coating depends on the average in-plane elastic modulus E_s and the Poisson's ratio ν_s of the substrate, the thickness h of the substrate, the thickness t of the coating, and of course, the radius of curvature R of the substrate. Provided that the coating is very much thinner than the substrate, i.e. $t/h \ll 1$, this residual stress is (Appendix I):

$$\sigma = \frac{E_s h^2}{6(1 - \nu_s) t R} \quad (1)$$

The residual stress is tensile for a positive curvature (concave upward) and compressive for a negative curvature (convex upward), and is not influenced by the elastic properties of the coating. The thicknesses of the coatings were measured using a Dektak II profilometer by masking portions of the Si wafer with a layer of vacuum grease before the coating was applied. When the masked areas were cleaned with a series of rinses of toluene, acetone, methanol, and finally, ethanol, a sharp surface step emerged at the peripheries of the coated areas left on the wafer. The height of these steps was readily measured by the diamond stylus of the profilometer (under a contact pressure of 25 mg) to an accuracy of 2.5 - 10 nm. Typical coating thicknesses which were measured were between 0.1 - 1.0 μm , and were quite reproducible through control of the deposition conditions. The curvatures of the circular disk shaped wafers with the variously stressed coatings were also measured with the same profilometer. The deformation of the bowed disks during the measurements under the slight pressure of the stylus was negligible.

Since the maximum difference in the Young's modulus in the plane of the (100) wafer is only 16%, no important differences in curvature were detected in any orientation by the profilometer for coatings of uniform thickness.

As shown in Fig. 2, the measured level of biaxial compression in as-deposited fibers was found to be independent of the thickness of the deposit, but increased with increasing ion beam energy in the PACVD apparatus.

Upon annealing of the as-deposited films for a period of 30 minutes at 600C, coupious hydrogen gas evolution from the films was observed, which

resulted in substantial reduction of film thickness. This thickness reduction also increased with increasing ion beam energy, as shown in Fig. 3, indicating that more energetic ion beams result in more built-in material misfit in the films. Residual stress measurements on the wafers after the 30 minutes outgassing treatment at 600°C indicated that in spite of the very large reduction of thickness, the coatings also contract biaxially and acquire a large bi-axial residual tensile stress. As Fig. 2 shows, the measured bi-axial tensile stresses in the outgassed coatings increase with initial ion beam energy in a manner symmetrical to the compressive stress in the as-deposited coatings. Clearly, these residual stresses at around 2 GPa are exceedingly high (around 0.5% of the Young's modulus of the SiC coating).

2.4 Delamination of Coatings from Substrates

It was observed that coatings, whether under a compressive residual stress or a tensile residual stress, delaminated nearly spontaneously from the substrate when their thickness exceeded a well-defined critical value. In both cases, delamination was initiated from interface flaws which appeared to be of circular shape and were most probably a result of occasional local surface contamination. The form of delamination in compression differed significantly from that in tension. In the former case for coatings of thickness substantially under 1 micron, the initially circular delamination patches did not grow. However, when the coating thickness exceeded 1 micron, slow delamination in quasi-static conditions could be observed, which initiated with outward buckling of the coating into one or two fundamental wave lengths, as can be seen in regions A of Fig. 4. These delamination patches grew by development of ever increasingly complex wrinkling patterns,

but rapidly developed a regular delamination front, as shown for the blister at C and for the relatively large blisters in regions B of Fig. 4. The blister then grew, often in neutral equilibrium, as residually stressed layers fed across the blister periphery into a circumferential strip with regularly spaced radial buckling ridges. In the further radial expansion of the delamination front, the principal buckling wave length in the circumferential strip immediately adjacent to the blister front remained unaltered, as can be discerned from Fig. 4 readily by comparing the smallest buckled blisters at A with the largest ones at B, as well as with the other intermediate sized blisters shown in the figure. Figure 4 shows other circular patches, larger than those at A, in which no buckling has occurred. These are likely to be interface flaws, in which the adhesion of the coating to the substrate across the interface has not been fully impaired. No progressive delamination in such regions was observed.

In the outgassed samples, where the residual stress in the coating becomes bi-axial tension, the delamination shows quite different features with increasing thickness of the coating. Three different regimes of delamination have been identified in the coatings deposited under intermediate and high ion beam energies (75 - 150 e.V.), i.e., those in which the measured residual tensile stress was above 2 GPa. In relatively thin deposits (less than 0.2 μm thick) only circular blisters were found by the entrapment of hydrogen gas evolving during the outgassing process. In some instances, particularly for blisters of large radius, the caps of the blisters were found detached from the sample. In samples where the thickness of the coating exceeded 0.2 μm , blister detachment was followed by

formation of cracks in the coatings emanating from the edge of the detached blister hole, as shown in Fig. 5. The initially radial cracks become parallel to one of two perpendicular directions once they are about one diameter away from the hole. The straight cracks away from the holes were found to be parallel to the two $\langle 110 \rangle$ directions in the plane of the Si wafer. These directions are the stiffest in the plane of the (100) wafer, and produce the largest misfit stress, across them in the coating.

In coatings that were thicker than $0.3 \mu\text{m}$, delamination fronts spread out along the interface between the coating and the substrate bounded by the parallel pre-cracks in the coatings radiating away from the holes in the mutually orthogonal $\langle 110 \rangle$ directions, as shown in Fig. 6. In samples with even thicker coatings, the delaminated fraction of the interface steadily increases, as in the case of Fig. 7, until at thicknesses exceeding $0.75 \mu\text{m}$ almost the entire coating has delaminated from the substrate, as is shown in Fig. 8.

Clearly, the driving force for the delamination in both cases of compressive and tensile residual stresses is the elastic strain energy in the coating. As discussed in Section 2.3 above, the residual stress in the coating depends only on the ion beam energy and the concentration of entrapped hydrogen gas in the coating, that results in the bi-axial material misfit, but not on the coating thickness. Furthermore, as is well known, and as we will demonstrate below, when the coating is very much thinner than the substrate, nearly all the elastic strain energy of misfit between coating and substrate is stored in the coating. Thus, as the coating thickness increases

the driving force for delamination increases nearly with thickness. In very thin coatings, the stored elastic strain energy is insufficient to provide for the required elastic energy release rate necessary to form the interface delamination, and no delamination was found to occur in either vacuum or in air. In an intermediate range of thickness, coatings could be preserved intact when stored in a vacuum, but delaminated in time when exposed to the laboratory environment.

With even thicker coatings, delamination occurred very rapidly both in vacuum and in air. Thus, it is expected that the delamination process along the interface is aided by humidity and is subject to static fatigue, well known in silica glasses [9]. This effect, however, will not be pursued further in this communication.

We will demonstrate in Section 2.6 below that the observed delamination phenomenon described above permits the rather accurate determination of the intrinsic interface toughness between a sharply delineated coating and its substrate, as is the case here between SiC and Si. In addition, the very regular and ribbon-like delamination in the case with tensile residual stresses also permits the determination of the Young's modulus of the amorphous SiC coatings. We discuss this below in the following section in preparation of the developments for interface toughness determination.

2.5 The Young's Moduli of Amorphous Coatings in Residual Tension

In samples exhibiting the very regular ribbon-like delamination, it was observed that some of the loose ribbons remained perfectly flat upon delamination and in registry with the rectangular slots, in which they underwent the

contractile strain resulting from the relief of the material misfit causing the residual stress. A particularly clear example of this is shown in Fig. 9a and b. In Fig. 9a, the extent of the delamination ribbon is shown clearly by the bordering parallel cracks in the coating terminating roughly 140 μm below the horizontal crack that initiated the delamination. The termination of the gray region inside the ribbon at the point of termination of the parallel cracks indicates that the extent of delamination in the ribbon is well delineated. The upper portion of the same ribbon, given at a larger magnification in Fig. 9b, shows a well defined gap which represents the overall contraction of the ribbon upon delamination. Observations of this type, which could be made with equal precision at many places on the coating, permitted the accurate determination of the initial bi-axial misfit strain in the coating. The results of such measurements are shown in Fig. 10. They indicated that while the tensile misfit strain was quite large in coatings deposited at low ion beam energy, it was considerably smaller and independent of ion beam energy for energies above 75 e.V.

Since the residual tensile stress in the coatings resulting from this misfit strain could be measured separately through the measurement of the curvature of the Si wafer before any cracks could develop, as discussed in Section 2.3 above, the Young's modulus of the coatings could then be calculated from the equation:

$$E = \frac{(1 - \nu)\sigma}{\epsilon_m} , \quad (2)$$

giving the dependence of bi-axial residual stress σ on the bi-axial misfit strain ϵ_m provided Poisson's ratio ν is known. For an assumed Poisson's ratio of 0.3, the calculated Young's moduli of SiC coatings are plotted in

Fig. 11 as a function of the initial ion beam energy. The modulus goes from a rather low value of about 16 GPa to around 300 GPa for coatings deposited at energies in excess of 75 e.V.

The determination of the Young's modulus of coatings having compressive misfit strain require a different procedure, which will be discussed in Section 2.7 below.

2.6 Work of Separation of Interfaces between Substrates and Coatings with Tensile Misfit

Although the stress intensity for delamination propagating along interfaces between a coating under tensile residual stress and a massive substrate of different elastic properties is complex and difficult to determine [10,11] the associated and far more useful, critical elastic energy release rate G_{co} , which we have referred to as the intrinsic interface toughness can be readily determined if the crack is constrained to remain in the interface. Thus, considering the elastic energy release from the coating and the substrate in response to a quasi-static extension of the interface crack, the desired energy release rate available from the system can be calculated readily by elementary methods from the theory of circular plates in bending (see Appendix I) to be:

$$G_{co} = \frac{\epsilon_m^2 E t}{(1 - \nu)} \left[1 - 4 \left(\frac{1 - \nu_s}{1 - \nu} \right) \left(\frac{E}{E_s} \right) \left(\frac{t}{h} \right) \right], \quad (3)$$

where the second term in brackets gives the fraction of the energy released from the substrate during delamination. In Eqn. (3), ϵ_m is the total misfit strain between coating and substrate E , ν , E_s , ν_s are the Young's moduli and

Poisson's ratios of the coating and substrate respectively, and t and h are the thicknesses of the coating and substrate. For the cases of interest where $\lambda \ll h$, where the total misfit strain is nearly entirely accommodated in the coating, i.e., where

$$\epsilon_m = \frac{\sigma^2(1 - \nu)}{E} . \quad (5)$$

Since σ and E are separately measurable, as discussed in Sections 2.3 and 2.5, the energy release rate is calculable uniquely, provided Poisson's ratio of the coating is known. Thus, as the thickness of the coating increases, the available energy from the system becomes larger. At a given threshold thickness t_c of the coating, when the available strain energy is sufficient to provide for the total specific work of delamination in air, such delamination will occur, and establishes the intrinsic interface toughness G_{co} in air as:

$$G_{co} = \frac{\sigma^2(1 - \nu)t_c}{E} . \quad (6)$$

Since the work of delamination in a vacuum will be substantially larger because of the absence of static fatigue, the critical delamination thickness in vacuum for comparable conditions should be proportionally larger. The observed critical thicknesses for delamination in air are shown in Fig. 12, while the calculated specific work of delamination is shown in Fig. 13. Both of these terms depend somewhat on the ion beam energy. The average value of this work of fracture for high ion beam energies is 5.1 J/m^2 .

2.7 Work of Separation of Interfaces between Substrates and Coatings
with Compressive Misfit

As is shown in Fig. 4 and in the sketch of Fig. 14a, once a sufficiently large portion of the coating is delaminated from the substrate at an initial flaw, it will undergo some release of elastic strain energy by buckling. After undergoing some early and complex buckling shapes, the delamination process settles down into a self similar front, seen established for the blister at C in Fig. 4. In this delamination front, sketched out in Fig. 14a, bi-axially strained coating feeds-in across the circumferential delamination front of the blister, and undergoes nearly complete release of the radial stress. This is seen more clearly in Fig. 15, which shows a blister of intermediate size viewed with Nomarski interference contrast microscopy that is capable of detecting very small changes in elevation by a color contrast. The figure reveals that the blister has an outer ring, which surrounds the buckling front at a radial distance of 5-7 μm ahead of it. The zone between the outer radius of this circular front and the average front of the buckled zone could only be seen with the Nomarski contrast mode of observation because of a slight decrease of elevation of the coating surface different from its outer surroundings, which was still fully attached to the substrate. Such a change results through the release of the radial stress, as postulated, which produces a differential radial strain $\Delta\epsilon_r$ and a differential thickness $\Delta\epsilon_z$, given by:

$$\Delta\epsilon_r = (1 + \nu)\epsilon_m, \quad (7a)$$

$$\Delta \epsilon_z = - \frac{\nu(1 + \nu)}{(1 - \nu)} \epsilon_m \quad (7b)$$

and a decrease in the tangential stress σ_θ by a factor of $(1 - \nu)$ from its initial level of $\sigma_0 E/(1 - \nu)$. As we will see below, the thinning of the film upon the release of the radial stress is of a magnitude that can be detected readily by the Nomarski interference contrast mode of microscopy.

Upon a critical radial displacement of the coating toward the interior of the outer front of the blister, cohesion across the interface is completely lost, and the remaining tangential stress $\sigma_\theta (= (1 - \nu)\sigma)$ is relieved further by the regular circumferential buckling of the film to a wave length λ . The process of delamination with a self similar circumferential buckling mode becomes self sustaining when for a radial increment of delamination, the difference between the initial elastic strain energy in the coating and that remaining in the regular post buckling shape is sufficient to provide for the total work of delamination of the interface in this increment.

The key element of the delamination is the principal circumferential buckling wave length λ , which is directly measurable from micrographs. It relates to the initial tangential stress σ that governs it by the Euler buckling relation of thin strips, (for details of the analysis see Appendix II) as:

$$\lambda = \pi t \sqrt{\frac{E}{3(1 - \nu^2)\sigma(1 - \nu)}}, \quad (8)$$

where E and ν are the Young's modulus and the Poisson's ratio of the coating as before, and σ is the initial bi-axial compressive residual stress in the coating. We note parenthetically that since the initial residual stress σ

is directly measurable from the curvature of the bent wafer and ℓ from the micrographs, the Young's modulus of the hydrogenated coating in its as-deposited form in the PCVD process is calculable directly from Eqn. (8).

Since the substrate is massive and nearly inextensional, once strips of coating traverse across the delamination front their initial displacement misfit in the circumferential direction must be completely relieved by the circumferential buckling. This permits calculation of the steady state post buckling amplitude z_0 , sketched in Fig. 14b as:

$$z_0 = \frac{t}{\sqrt{3(1 - \nu^2)}} . \quad (9)$$

This then permits the calculation of the final elastic strain energy U_f per unit area in the post buckling shape of the tangential strip, just on the blister side of the delamination front to be (see Appendix II):

$$U_f = \frac{\pi^4 E t^5}{9(1 - \nu^2)^2 \ell^4} . \quad (10)$$

Since the initial elastic strain energy U_i per unit area in the bi-axially stressed coating in the same form of representation is:

$$U_i = \frac{\pi^4 E t^5}{9(1 - \nu^2)^2 (1 - \nu) \ell^4} , \quad (11)$$

the elastic strain energy release rate G by this special form of tangential buckling, available to provide for the specific work of delamination of the interface becomes,

$$G = U_i - U_f = \frac{\nu \pi^4 E t^5}{9(1 - \nu^2)^2 (1 - \nu) \ell^4} . \quad (12)$$

Once again, at a critical thickness t_c , this energy becomes sufficient to provide for the quasi-static propagation of the delamination front in neutral equilibrium in air, establishing the intrinsic delamination toughness of the interface G_{co} as:

$$G_{co} = \frac{\nu \pi^4 E t_c^5}{9(1 - \nu^2)^2 (1 - \nu) \ell^4} . \quad (13)$$

As a specific case, we consider the delamination blisters of Fig. 4 of a coating deposited at high ion beam energy, expected to have a bi-axial compressive residual stress of $\sigma = 2\text{ GPa}$, as shown in Fig. 2. The critical thickness of this coating was measured to be $1.1\text{ }\mu\text{m}$, while the average post buckling wave length ℓ in the circumferential direction was measured to be $20\text{ }\mu\text{m}$. Assuming as before a Poisson's ratio of 0.3, we calculate first the Young's modulus from Eqn. (8) to be 116 GPa . Finally, using this value, the critical energy release rate G_{co} (specific work of delamination) is calculated from Eqn. (13) to be 5.9 J/m^2 . This is 14% higher than the average value calculated from the delamination of the coatings under tensile residual stress, and well within the scatter of measurements of that experiment. Thus, we conclude that the intrinsic toughness of the interface between SiC and Si is uninfluenced by the "dehydrogenation" that converts the coatings from having negative misfit to positive misfit.

III. TOUGHNESS OF INTERFACES BETWEEN SiC COATINGS AND PITCH-55 FIBERS

The total work of delaminating a SiC coating from a Pitch-55 carbon fiber can also be determined by a technique very similar to that used for a system of Si wafer and SiC coating under tensile misfit strain. Figure 16 shows a SEM micrograph of an outgassed fiber with a SiC coating of 0.33 μm thickness, initially deposited under conditions of low ion beam energy. The coating showed some small through the thickness cracks, but no delamination during several weeks of storage in air after the regular outgassing treatment of 30 minutes at 600°C. When it was examined again after several months of further storage in laboratory air with the usual level of relative humidity, in the vicinities of 60%, copious delamination of the SiC coating was found, as shown in Fig. 16. The initial bi-axial misfit strain ϵ_m between the coating and the fiber could be determined from the ratio of the average gap size between flakes to the dimensions of the flakes. With knowledge of this, and the assumption that the Young's modulus of the coating was the same as that for similar coatings on Si wafers deposited under the same ion beam conditions, the total energy release rate per unit area of interface could be determined from the sample.

An elementary misfit analysis presented in more detail in Appendix III gives the intrinsic interface toughness G_{co} of the interface to be

$$G_{co} = \frac{\epsilon_m^2 E t_c}{2} \left(\frac{F}{H^2} \right), \quad (14)$$

where ϵ_m is the bi-axial misfit strain between coating and fiber, E the Young's modulus of the coating, t_c the thickness of the coating, and F and H

are complicated functions of ratios of Young's moduli and the coating thickness to fiber radius given as:

$$\begin{aligned}
 F = & 2(1 - \nu) + \left[(3 - 5\nu)\left(\frac{E}{E_r}\right) + 6(1 - \nu)\left(\frac{E}{E_z}\right) \right] \left(\frac{t}{R}\right) \\
 & + \left[(1 - 2\nu)\left(\frac{E}{E_r}\right)^2 + 4(1 - \nu)\left(\frac{E}{E_z}\right)^2 + 2(4 - 7\nu)\left(\frac{E}{E_r}\right)\left(\frac{E}{E_z}\right) \right] \left(\frac{t}{R}\right)^2 \\
 & + 2 \left[(1 - 2\nu)\left(\frac{E}{E_r}\right)\left(\frac{E}{E_z}\right)\left(\frac{E}{E_r} + \frac{2E}{E_z}\right) \right] \left(\frac{t}{R}\right)^3 .
 \end{aligned} \tag{15}$$

$$\begin{aligned}
 H = & (1 - \nu) + \left[(1 - 2\nu)\left(\frac{E}{E_r}\right) + 2(1 - \nu)\left(\frac{E}{E_z}\right) \right] \left(\frac{t}{R}\right) + 2(1 - 2\nu)\left(\frac{E}{E_r}\right)\left(\frac{E}{E_z}\right)\left(\frac{t}{R}\right)^2
 \end{aligned} \tag{16}$$

In Eqns. (15) and (16), (E/E_r) and (E/E_z) are the ratios of the Young's modulus of the coating to the transverse modulus of the fiber and the axial modulus of the fiber respectively; ν is the Poisson's ratio of both the fiber and the coating (assumed to be the same), and t/R is the ratio of the thickness of the coating to the fiber radius.

As a specific example, we evaluate the critical energy release rate of the coating related to the case of Fig. 16 of a coating applied to a fiber under low ion beam conditions in the PACVD apparatus. This should result in a coating with Young's modulus of $E = 16$ GPa. The initial misfit strain, as measured from the gaps between the fragments of the coatings was found to be $\epsilon_m = 2.7 \times 10^{-2}$ in the axial direction. Since the axial and radial Young's moduli E_z and E_r of the fiber were 385 GPa and 14 GPa respectively,

$E/E_r = 1.14$ and $E/E_z = 4.16 \times 10^{-2}$. Furthermore, the thickness of the SiC coating was $0.33 \mu\text{m}$ and the fiber radius $5 \mu\text{m}$, giving $t/R = 6.6 \times 10^{-2}$. Thus, for assumed Poisson's ratios of 0.3, the values of the functions F and H can be calculated to be 1.53 and 0.734 respectively. This gives for the intrinsic interface toughness $G_{CO} = 5.5 \text{ J/m}^2$, which is very close to the corresponding value measured for the delamination of the interface between SiC and a Si substrate, presented in Sections 2.6 and 2.7 above.

IV. DISCUSSION

In the preceding, we have demonstrated that the "spontaneous" delamination phenomenon of thin misfitting coatings, from their substrates, can be used very effectively to determine the toughness of the interface between them. When the elastic strain energy per unit area due to the misfit in the coating begins to exceed the intrinsic interface toughness, i.e., the specific work of separation of the coating from the substrate along the interface, the coating delaminates from the interface flaws. Since no instability is involved, the delamination, once started, can propagate under quasi-static conditions. Observations indicate that the critical thickness of a coating for delamination in vacuum is larger than the corresponding thickness for delamination in laboratory air with the usual levels of relative humidity. Thus, a static fatigue or stress corrosion cracking effect appears to be present in the delamination. This aspect of the delamination still needs to be studied further.

When the coatings are in residual tension, the delamination occurs in a sequence of events, beginning with cracking of the coating in long parallel rows, followed by delamination of the ribbons of coating between the

parallel cracks. Since the substrate Si wafers had {100} plane surfaces in which the two orthogonal <110> directions are 16% stiffer than the <100> directions, the resulting larger misfit stresses in the <110> directions produce these orthogonal pre-cracks in the coatings. The misfit strain could be measured quite accurately from the relaxed size of the delaminated loose ribbon lying flat in the rectangular cavity of pre-cracking. This, together with the independent measurement of the residual tensile stress through the curvature of the sandwich of coating and substrate, permitted the determination of the elastic modulus of the coatings, which is essential for the determination of the energy release rate.

When the coatings are in residual compression in the hydrogenated state, immediately upon coating, the delamination exhibited rather unusual and hitherto unreported forms. When the coating exceeded the critical thickness required to provide the energy release rate, delamination occurred by the enlargement of blisters having self similar circumferential fronts, in which first, the radial stress is released by translation of the coating relative to the substrate in the radial direction by an amount

$$\Delta u_r = \Delta r \Delta \epsilon_r, \quad (17)$$

where Δr is the width of the radial stress release zone of about 5 μm thickness, shown in Fig. 15, and $\Delta \epsilon_r$ is the radial strain difference between coating and substrate in this zone, given by Eqn. (7a). For the typical case considered in Section 2.7 above, where for a residual compressive stress of 2 GPa and a coating modulus of 116 GPa, giving an initial misfit

strain of 1.21×10^{-2} , the relative displacement in the inner border of the radial stress release zone is obtained to be about 60 nm. The associated reduction in thickness calculated from Eqn. (7b) is about 7.5 nm, which is well within the range of detection of the Nomarski contrast mode of microscopy. Since the color contrast in this radial strip of release of the radial stress is uniform, it must be concluded that there is little shear traction acting across the interface, but that the coating is still attached to the substrate even after a relative slippage of about 250 interatomic distances. If this interpretation is indeed correct, it must be concluded that for flat interfaces, there is little reduction of the cohesive strength of an interface due to large relative shear displacements across it. Although this is quite natural for flat grain boundaries, it is surprising for the interfaces between crystalline Si and amorphous SiC. Finally, however, as the relative displacements across this strip mount, small departures from flatness should produce normal stresses acting across the interface to produce full delamination and the quite regular circumferential buckling that is so readily apparent. It is interesting to note that the buckled blisters require only one independent measurement for the complete solution of the problem. Considering that the thickness of the coating and the wave length of the circumferential buckling are readily determinable by microscopy, only the residual compressive stress in the coating needs to be measured separately by measuring the radius of curvature of the sandwich of Si wafer and SiC coating. Then, the Young's modulus of the coating can be determined from Eqn. (8), making the energy release rate determinable uniquely from Eqn. (13).

The measurement of real interest for metal matrix composites, however, is the interface toughness between a SiC coating and a Pitch-55 carbon fiber, which could be determined by a similar analysis, provided the modulus of the coating depends only on the energy of the ion beam and not on any other property of the substrate or condition of deposition. This point needs to be verified further by additional experiments with planar surfaces of Pitch-55 type material in thin strips permitting residual stress measurement by curvature change. Meanwhile, in the absence of this information, the determined interface toughness of 5.5 J/m^2 is, within experimental error, identical to that between SiC and Si. Furthermore, in the latter case, there was no effect on the interface toughness of substantial residual stresses in the plane of the coating, whether tensile or compressive. The overall average value of the interface toughness for the three experiments is 5.5 J/m^2 . It is interesting to note further, that the interface toughness in the case of the Pitch-55 fiber is about 7% higher than that of the SiC-Si interface with coatings in tension. Since some plastic flow could take place in the fiber on planes parallel to the axis, this difference may be due to this effect. Moreover, the interface toughness for the case of delamination of coatings with compressive stress, where apparently considerable relative translation occurs in the radial direction across the interface before lift-off of the coating by buckling, the interface toughness is 17% larger than that for the case with the coating in tension where such sliding apparently does not occur.

We conclude that the interface toughness measurements are quite meaningful and of the expected order. Thus, taking the overall average

value of 5.5 J/m^2 , we equate it to $\gamma_{\text{SiC}} + \gamma_{\text{Si}} - \gamma_{\text{int}}$, where the symbols stand for the specific surface energies of SiC and Si, and the interface energy between SiC and Si respectively. The measured magnitudes of G_{co} are well in the range of what can be expected from well-bonded strong solids.

ACKNOWLEDGEMENT

We gratefully acknowledge DARPA, Office of Naval Research and Naval Air Development Center under Contract No. N00014-84-K and IST/SDIO under Contract No. N00014-85-K-0645 and the M.I.T. Consortium for Processing and Evaluation of Metal and Ceramic Matrix Composites for their generous support of this project.

We are also grateful to Dr. Jerome Cuomo of IBM for his advice on PACVD facility design.

REFERENCES

1. K.L. Mittal, in "Adhesion Measurement of Thin Films, Thick Films, and Bulk Coatings", edited by K.L. Mittal, STP 640 (ASTM: Philadelphia), p. 5 (1978).
2. T.S. Chow, C.A. Liu, and R.C. Penwell, J. Polymer Sci., 14, 1305 (1976).
3. J. Ahn, K.L. Mittal, and R.H. McQueen, in "Adhesion Measurement of Thin Films, Thick Films, and Bulk Coatings", edited by K.L. Mittal, STP 640 (ASTM: Philadelphia), p. 134 (1978).
4. S.S. Chiang, D.B. Marshall, and A.G. Evans, in "Surfaces and Interfaces in Ceramic and Ceramic Metal Systems", edited by J. Pask and A.G. Evans, "Materials Science Research" (Plenum Press: New York), vol. 14, p. 603 (1981).
5. J.R. Rice, in "Proceedings of First International Conference on Fracture", edited by T. Yokobori, T. Kawasaki, and J.L. Swedlow, (The Japanese Society for Strength and Fracture of Materials: Sendai, Japan), vol. 1, p. 309 (1965).
6. V. Gupta, A.S. Argon, and J.A. Cornie, J. Mater. Sci., in this issue.
7. A.G. Evans and J.W. Hutchinson, Intern. J. Solids and Structures, 20, 455 (1984).
8. H.S. Landis, "Amorphous Hydrogenated Silicon Carbide by Plasma Enhanced Chemical Vapor Deposition for Metal Matrix Composite Applications", Ph.D. Thesis Department of Materials Science and Engineering, M.I.T., Cambridge, MA (1987).
9. S.W. Freiman, in "Glass Science and Technology", edited by D.R. Uhlmann and N.J. Kreidl (Academic Press: New York), vol. 2, p. 21 (1980).
10. J.R. Rice and G.S. Sih, J. Appl. Mech., 32, 418 (1965).
11. M. Comninou, J. Appl. Mech., 44, 631 (1977).

APPENDIX I - Residual Stress Measurements in Thin Coatings

1.1 Residual Stress

Consider a thin circular wafer with {100} plane surfaces, having a thickness h , an in-plane isotropic modulus of E_s , and a Poisson's ratio of ν_s . An amorphous isotropic coating of thickness t of SiC with modulus E_c and Poisson's ratio ν_c is attached to the substrate. Due to the condition of deposition, the coating incorporates a bi-axial misfit strain ϵ_m , which we take to be tensile. This puts it under a state of residual tensile stress $\sigma_r (= \sigma_\theta)$, which is of interest. As all elastic misfit problems, the solution is obtained by detaching the coating from the substrate, as shown in Fig. I-1, and considering the deformations necessary to attach them together again. Thus, considering the coating to be so thin as to be under a uniform stress σ_r , by equilibrium, the substrate would be subjected to a compressive stress $\sigma_r(t/h)$ and a bending moment per unit length of periphery of:

$$M = (\sigma_r t)(t + h)/2 , \quad (I-1)$$

This bending moment produces a spherical curvature in the substrate wafer given by:

$$\frac{1}{R} = \frac{M}{D_s(1 + \nu_s)} \quad \therefore \quad D_s = \frac{E_s h^3}{12(1 - \nu_s)^2} , \quad (I-2a,b)$$

and a surface strain at the interface of:

$$\epsilon_r = \frac{h}{2R} . \quad (I-3)$$

The average compressive stress in the wafer produces an average radial compressive strain of:

$$\epsilon_r = \frac{(1 - \nu_s)\sigma_r t}{hE_s} . \quad (I-4)$$

The sum of all radial strains at the interface in the coating and the substrate must be equal to the initial misfit strain ϵ_m , i.e.,

$$\epsilon_m = \frac{(1 - \nu_c)\sigma_r}{E_c} + \frac{(1 - \nu_s)\sigma_r t}{hE_s} + \frac{t(t + h)h\sigma_r}{4D_s(1 + \nu_s)} , \quad (I-5)$$

where the first term is the radial strain in the coating. Thus,

$$\epsilon_m = \left[\frac{(1 - \nu_c)}{E_c} + \frac{4(1 - \nu_s)}{E_s} \left(\frac{t}{h} \right) + \frac{3(1 - \nu_s)}{E_s} \left(\frac{t}{h} \right)^2 \right] \sigma_r . \quad (I-6)$$

On the other hand, from Eqn. (I-2a and b), the bi-axial stress σ in the coating is:

$$\sigma = \sigma_r = \frac{E_s h^3}{6t(1 - \nu_s)(t + h)R} \approx \frac{E_s h^2}{6t(1 - \nu_s)R} \left(1 - \frac{t}{h} \right) . \quad (I-7)$$

Thus, through the measurement of the radius of curvature of the bent wafer, the residual stress in the coating is determinable from Eqn. (I-7).

1.2 Elastic Strain Energy

The elastic strain energy stored in the sandwich of stretched coating, and compressed and bent substrate is determinable in a straight forward way

from the theory of thin circular plates.

The strain energy in the coating is:

$$\frac{(1 - \nu_c) \sigma^2 t}{E_c} . \quad (I-8)$$

In the substrate, the elastic strain energy is partly in bending, of a magnitude of:

$$\frac{3(1 - \nu_s) t^2}{E_s h} \left(1 + 2 \left(\frac{t}{h} \right) \right) \sigma^2 , \quad (I-9)$$

and partly in compression, of a magnitude of:

$$\frac{(1 - \nu_s) h}{E_s} \sigma^2 \left(\frac{t}{h} \right)^2 . \quad (I-10)$$

Thus, the total elastic strain energy U in the sandwich is the sum of all three terms, which for quantities including second order terms is:

$$U = \frac{\epsilon_m^2 E_c t}{(1 - \nu_c)} \left[1 - 4 \frac{(1 - \nu_s)}{(1 - \nu_c)} \frac{E_c}{E_s} \left(\frac{t}{h} \right) \right] . \quad (I-11)$$

where the total misfit strain is

$$\epsilon_m = \frac{\sigma(1 - \nu_c)}{E_c} \left[1 + 4 \frac{(1 - \nu_s)}{(1 - \nu_c)} \frac{E_c}{E_s} \left(\frac{t}{h} \right) \right] . \quad (I-12)$$

In Eqn. (I-11), the second term in the brackets is the fraction of the energy contributed to the total through the bending and compression of the

substrate. For $t/h \ll 1$, this contribution is clearly negligible. This gives for the elastic energy release rate in delamination

$$G_{co} = U \approx \frac{\epsilon_m^2 E_c t}{(1 - \nu_c)} , \quad (I-13)$$

which was used in the interpretation of results.

APPENDIX II - Interface Toughness from Buckled Blisters

As explained in the text, the coating inside a blister lifts off through the propagation of a circumferential buckling front with a characteristic circumferential wave length of λ .

Initially, under bi-axial compression, the stresses in the coating are:

$$\sigma_r = \sigma_\theta = \frac{E\epsilon_r}{(1-\nu)} = \frac{E\epsilon_\theta}{(1-\nu)} = \frac{E\epsilon_m}{(1-\nu)}, \quad (\text{II-1})$$

where E and ν are properties of the coating, and ϵ_m the total misfit strain.

Upon traverse of the outer fringe of the blister through an element of coating, the radial stress is fully released; this reduces the tangential stress down to:

$$\sigma_\theta = E\epsilon_\theta. \quad (\text{II-2})$$

As the element of coating traverses through the buckling front, it undergoes a characteristic Euler buckling that responds to the new level of tangential stress, and establishes a circumferential buckling wave length of

$$\lambda = \pi t \sqrt{\frac{E}{3(1-\nu^2)\sigma_\theta}}. \quad (\text{II-3})$$

In the post buckling shape, circumferential line elements in the coating become longer by an amount of $\lambda\epsilon_m$ over a wave length of buckled coating

$$\Delta\lambda = \lambda\epsilon_m = \frac{-2t^2}{3\lambda(1-\nu^2)}. \quad (\text{II-4})$$

This establishes the amplitude of buckling along a circumferential line element. Thus, in reference to Fig. 14b,

$$\Delta l = \int_0^l \left(\sqrt{1 + \left(\frac{dz}{d\phi} \right)^2} - 1 \right) d\phi = \frac{\pi^2 z_0^2}{l} , \quad (\text{II-5})$$

for a sinusoidal buckling shape.

$$z = z_0 \sin \left(\frac{2\pi\phi}{l} \right) , \quad (\text{II-6})$$

giving for the amplitude

$$z_0 = \frac{t}{\sqrt{3(1 - \nu^2)}} , \quad (\text{II-7})$$

The final elastic strain energy in the post buckling shape per unit width in the radial direction is:

$$U_f = \int_0^l \frac{M^2}{2EI} d\phi \quad \therefore \quad M = EI \frac{d^2 z}{d\phi^2} , \quad (\text{II-8a,b})$$

$$\text{giving } U_f = \frac{4EI\pi^4 z_0^2}{l^3} = \frac{\pi^4 E t^5}{9l^3 (1 - \nu^2)^2} , \quad (\text{II-9})$$

The initial elastic strain energy in the bi-axially strained coating per strip of unit width and length l is:

$$U_i = \frac{(1 - \nu)\sigma_z^2 l t}{E} = \frac{-2Et^5}{9(1 - \nu^2)^2 (1 - \nu) l^3} , \quad (\text{II-10})$$

$$\text{where } \sigma_{\theta} = \frac{\pi^2 E t^2}{3(1 - \nu^2)(1 - \nu) \ell^2} , \quad (\text{II-11})$$

the initial tangential stress was substituted to obtain the final result. Finally, the energy release rate (per unit area of coating) is obtained by subtraction of (II-9) from (II-10), and dividing by ℓ , i.e.:

$$G_{co} = \frac{\nu \pi^4 E t^5}{9(1 - \nu^2)^2 (1 - \nu) \ell^4} . \quad (\text{II-12})$$

APPENDIX III - Interface Toughness of Coatings on Pitch-55 Fibers

Consider a Pitch-55 type fiber of radius R with an axial modulus E_z , a radial modulus E_r , and Poisson's ratio ν with an isotropic coating of thickness t , with a modulus E and Poisson's ratio ν , having a total tensile bi-axial misfit strain ϵ_m relative to the fiber. As indicated in Fig. III-1, we take the unknown misfit stresses in the coating to be σ_θ and σ_z , and since $t/R \ll 1$ will be the case, neglect radial stresses. The corresponding stresses in the fiber that result from equilibrium are given in the figure.

By straight forward analysis, the strains in the coating and the fiber are:

$$\epsilon_{\theta c} = \sigma_\theta/E - \nu\sigma_z/E \quad \therefore \quad \epsilon_{zc} = \sigma_z/E - \nu\sigma_\theta/E , \quad (\text{III-1a,b})$$

$$\epsilon_{\theta f} = - (1 - \nu)t\sigma_\theta/E_r R + 2\nu t\sigma_z/E_z R , \quad (\text{III-2a})$$

$$\epsilon_{zf} = 2\nu t\sigma_\theta/E_r R - 2t\sigma_z/E_z R . \quad (\text{III-2b})$$

The matching of the fiber to the coating requires

$$\epsilon_{\theta c} - \epsilon_{\theta f} = \epsilon_m \quad \therefore \quad \epsilon_{zc} - \epsilon_{zf} = \epsilon_m . \quad (\text{III-3a,b})$$

This gives by elementary methods

$$\sigma_\theta = \frac{\epsilon_m E}{H} \left[1 + 2\left(\frac{E}{E_z}\right)\left(\frac{t}{R}\right) \right] , \quad (\text{III-4a})$$

$$\sigma_z = \frac{\epsilon_m E}{H} \left[1 + \frac{E}{E_r} \left(\frac{t}{R}\right) \right] , \quad (\text{III-4b})$$

$$\text{where } H = (1 - \nu) + \left[(1 - 2\nu) \frac{E}{E_r} + 2(1 - \nu) \frac{E}{E_z} \right] \left(\frac{t}{R} \right) + 2(1 - 2\nu) \left(\frac{E}{E_r} \right) \left(\frac{E}{E_z} \right) \left(\frac{t}{R} \right)^2 . \quad (\text{III-5})$$

The elastic strain energy in the fiber and coating per unit length are:

$$U_f = (\sigma_{\theta f} \epsilon_{\theta f} + \sigma_{zf} \epsilon_{zf}/2) \pi R^2 , \quad (\text{III-6a})$$

$$U_c = (\sigma_{\theta}^2 + \sigma_z^2 - 2\nu\sigma_{\theta}\sigma_z) \pi R t / E . \quad (\text{III-6b})$$

By elementary methods, using the results above, the total elastic strain energy per unit length of fiber can be readily obtained as:

$$U = \frac{\pi R t \epsilon_m^2 E}{H^2} F , \quad (\text{III-7})$$

$$\begin{aligned} \text{where } F = & 2(1 - \nu) + \left[(3 - 5\nu) \left(\frac{E}{E_r} \right) + 6(1 - \nu) \left(\frac{E}{E_z} \right) \right] \left(\frac{t}{R} \right) , \\ & + \left[(1 - 2\nu) \left(\frac{E}{E_r} \right)^2 + 4(1 - \nu) \left(\frac{E}{E_z} \right)^2 + 2(4 - 7\nu) \left(\frac{E}{E_r} \right) \left(\frac{E}{E_z} \right) \right] \left(\frac{t}{R} \right)^2 \\ & + 2(1 - 2\nu) \left(\frac{E}{E_r} \right) \left(\frac{E}{E_z} \right) \left(\frac{E}{E_r} + 2 \left(\frac{E}{E_z} \right) \right) \left(\frac{t}{R} \right)^3 \end{aligned} \quad (\text{III-8})$$

This gives finally the energy release rate per unit area of interface, if delamination were to occur at the interface to completely unload both fiber and coating:

$$G_{co} = U/2\pi R = \frac{\epsilon_m^2 EtF}{2H^2} . \quad (III-9)$$

This was used to evaluate the results of cracking and delamination of coatings from fibers.

FIGURE CAPTIONS

- Fig. 1 - Change of curvature in a circular Si wafer with a thin coating of SiC in biaxial tension (a), or in biaxial compression (b).
- Fig. 2 - Measured residual stress in a CVD SiC coating as a function of ion beam energy in both as-deposited hydrogenated coatings (compression) and coatings annealed at 600°C for 30 min. (tension).
- Fig. 3 - Thickness strain (negative) in hydrogenated coatings upon annealing at 600°C for 30 min.
- Fig. 4 - Blisters in the as-deposited coatings of SiC when the coatings are of a critical thickness: (A) blisters just large enough to buckle upwards, (B) large and growing blisters with well established buckling fronts remaining self similar in growth, (C) smallest regular blister.
- Fig. 5 - Detached blisters act as nucleation sites of through-the-thickness cracks in the coatings under tensile biaxial stress, but of insufficient thickness for delamination.
- Fig. 6 - Delamination of ribbons from substrate, following the through-the-thickness pre-cracking of coatings under biaxial tension when the coating is thick enough for delamination to begin.
- Fig. 7 - Regular delamination patterns in the form of long ribbons in a coating of more than sufficient thickness for delamination to occur relatively rapidly.
- Fig. 8 - Nearly complete and "spontaneous" delamination in a coating of 0.8 μ m thickness.

- Fig. 9 - Misfit strain in coatings with bi-axial tensile stress is measurable by comparing the relaxed ribbon dimensions with those of the frame into which they initially fitted: (a) long delamination ribbon, (b) displacement of end of ribbon upon relief of misfit strain.
- Fig. 10 - Dependence of biaxial misfit strain on ion beam energy in annealed coatings under biaxial tension.
- Fig. 11 - Dependence of Young's modulus on ion beam energy in annealed coatings under biaxial tension.
- Fig. 12 - Dependence of critical coating thickness for delamination on ion beam energy in annealed coatings under biaxial tension.
- Fig. 13 - Dependence of critical energy release rate on ion beam energy in annealed coatings under biaxial tension.
- Fig. 14 - Sketch of idealized circumferential buckling of a delaminating coating in a blister in an as-deposited hydrogenated coating under biaxial compression: (a) perspective view, (b) buckled coating viewed in the radial direction.
- Fig. 15 - A large buckled blister in a coating in the process of undergoing delamination, viewed with the Normarski interference contrast mode of microscopy. The outer ring surrounding the buckled center is the zone in which radial slippage occurs to relieve the radial stress.
- Fig. 16 - An SEM micrograph of a fragmented and delaminated annealed coating of critical thickness of SiC on a Pitch-55 fiber. The misfit strain is determinable from the gaps between the flakes.

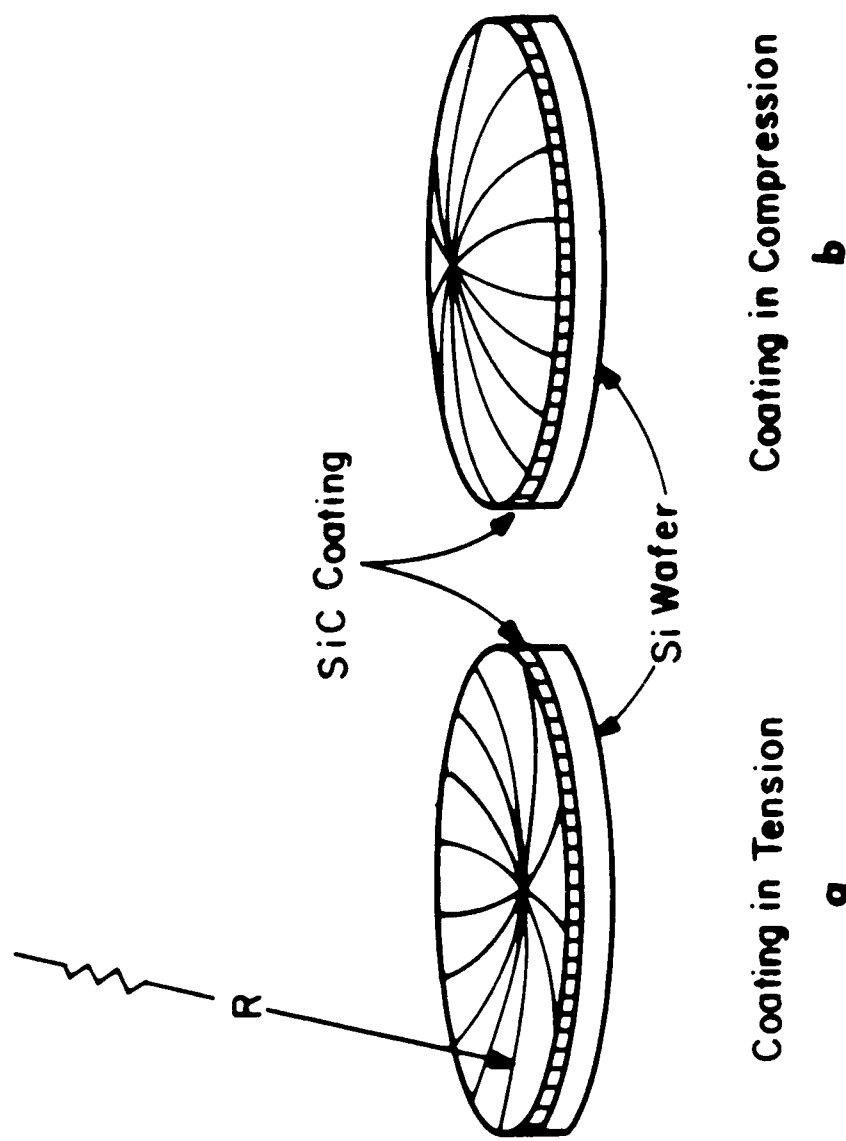


Fig. 1 - Change of curvature in a circular SiC wafer with a thin coating of SiC in biaxial tension (a), or in biaxial compression (b).

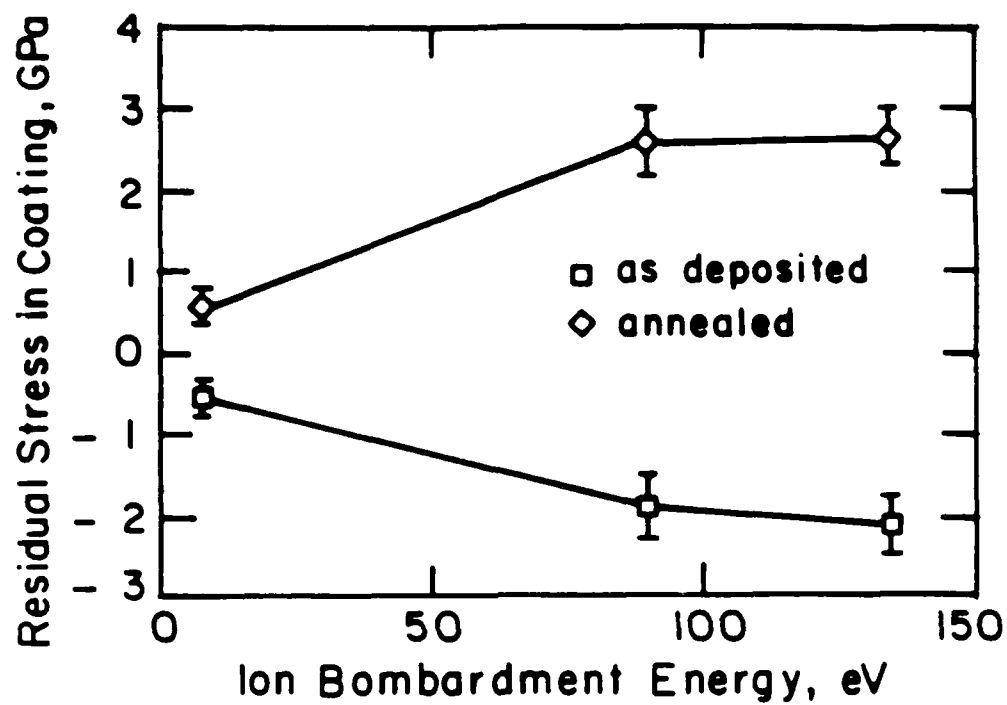


Fig. 2 - Measured residual stress in a CVD SiC coating as a function of ion beam energy in both as-deposited hydrogenated coatings (compression) and coatings annealed at 600°C for 30 min. (tension).

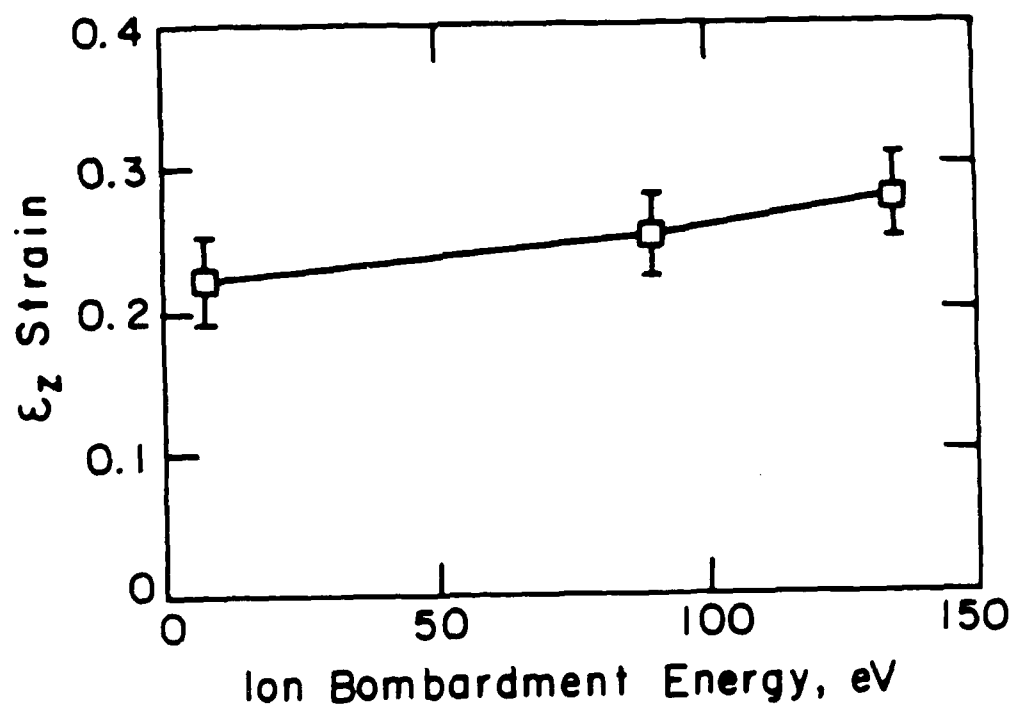


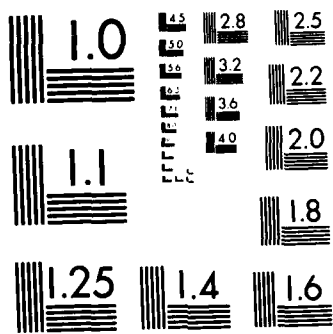
Fig. 3 - Thickness strain (negative) in hydrogenated coatings upon annealing at 600°C for 30 min.

75-1190-746

ENGINEERING INTERFACES IN METAL MATRIX COMPOSITES
(VOLUME 3)(U) MASSACHUSETTS INST OF TECH CAMBRIDGE
J A CORNIE 10 JUN 88 N00014-84-K-8495

UNCLASSIFIED

F/G 11/6.1 NL



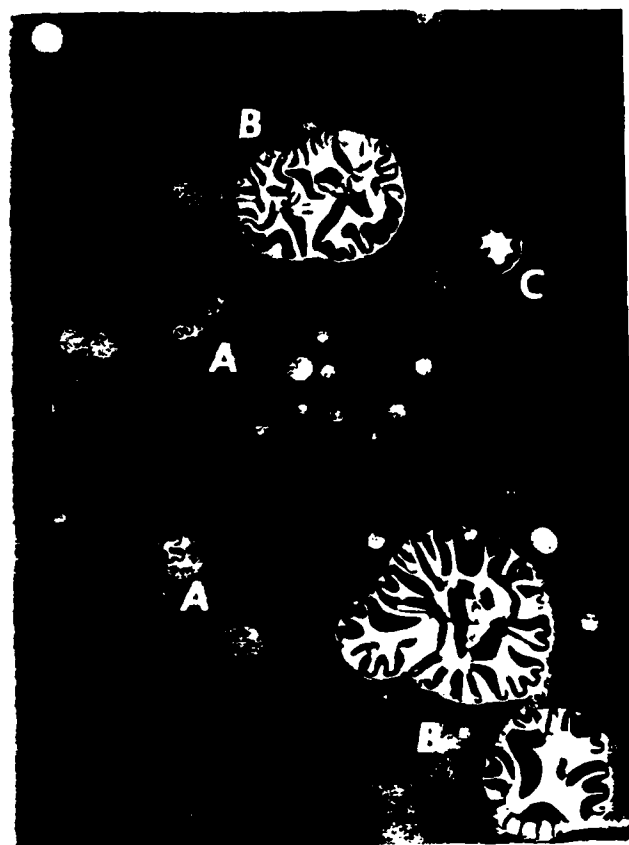


Fig. 4 - Blisters in the as-deposited coatings of SiC when the coatings are of a critical thickness: (A) blisters just large enough to buckle upwards, (B) large and growing blisters with well established buckling fronts remaining self similar in growth, (C) smallest regular blister.



Fig. 5 - Detached blisters act as nucleation sites of through-the-thickness cracks in the coatings under tensile biaxial stress, but of insufficient thickness for delamination.



Fig. 6 - Delamination of ribbons from substrate, following the through-the-thickness pre-cracking of coatings under biaxial tension when the coating is thick enough for delamination to begin.



Fig. 7 - Regular delamination patterns in the form of long ribbons in a coating of more than sufficient thickness for delamination to occur relatively rapidly.

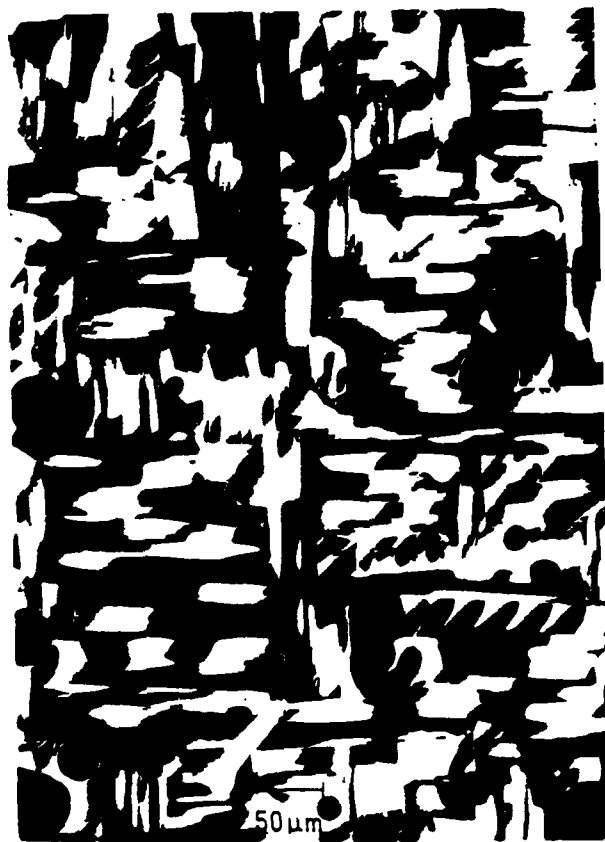


Fig. 8 - Nearly complete and "spontaneous" delamination in a coating of 0.8 μm thickness.

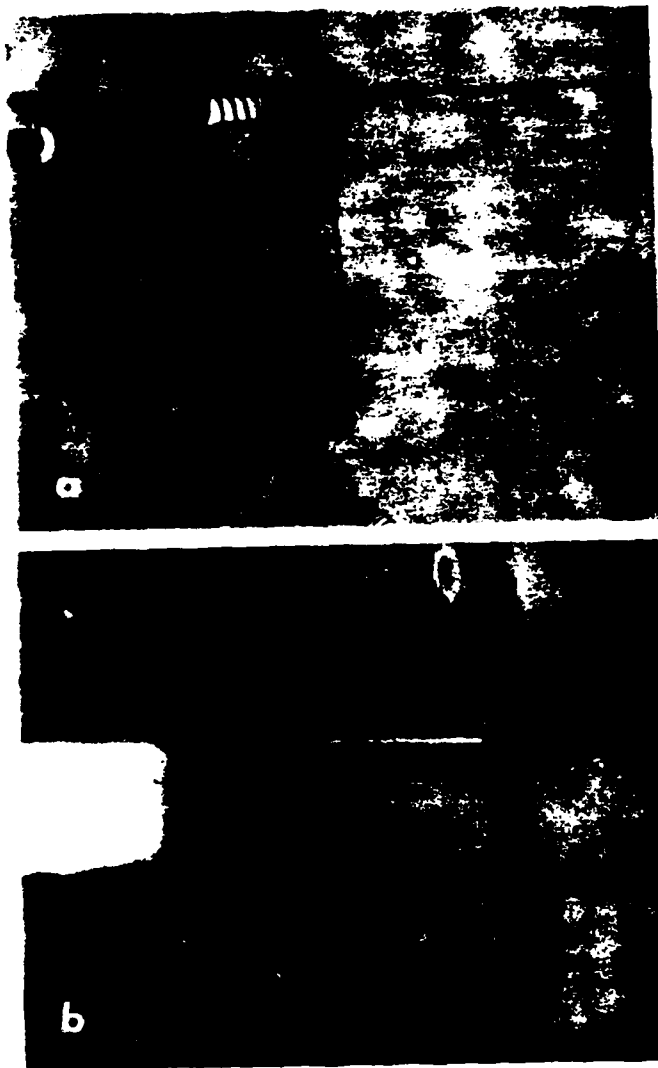


Fig. 9 - Misfit strain in coatings with biaxial tensile stress is measurable by comparing the relaxed ribbon dimensions with those of the frame into which they initially fitted: (a) long delamination ribbon, (b) displacement of end of ribbon upon relief of misfit strain.

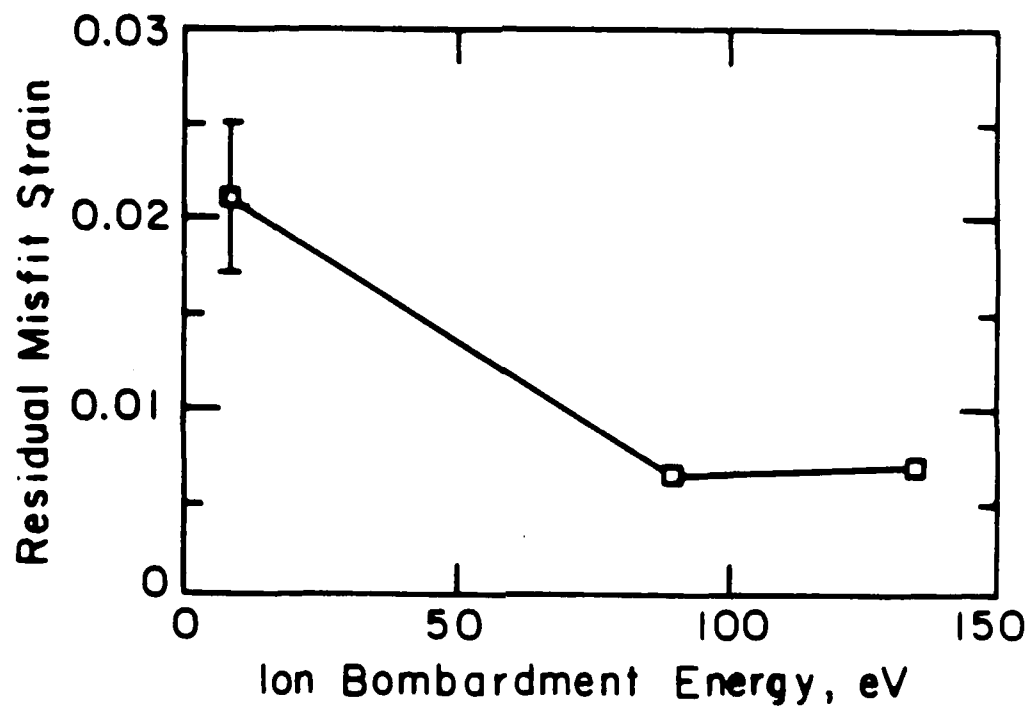


Fig. 10 - Dependence of biaxial misfit strain on ion beam energy in annealed coatings under biaxial tension.

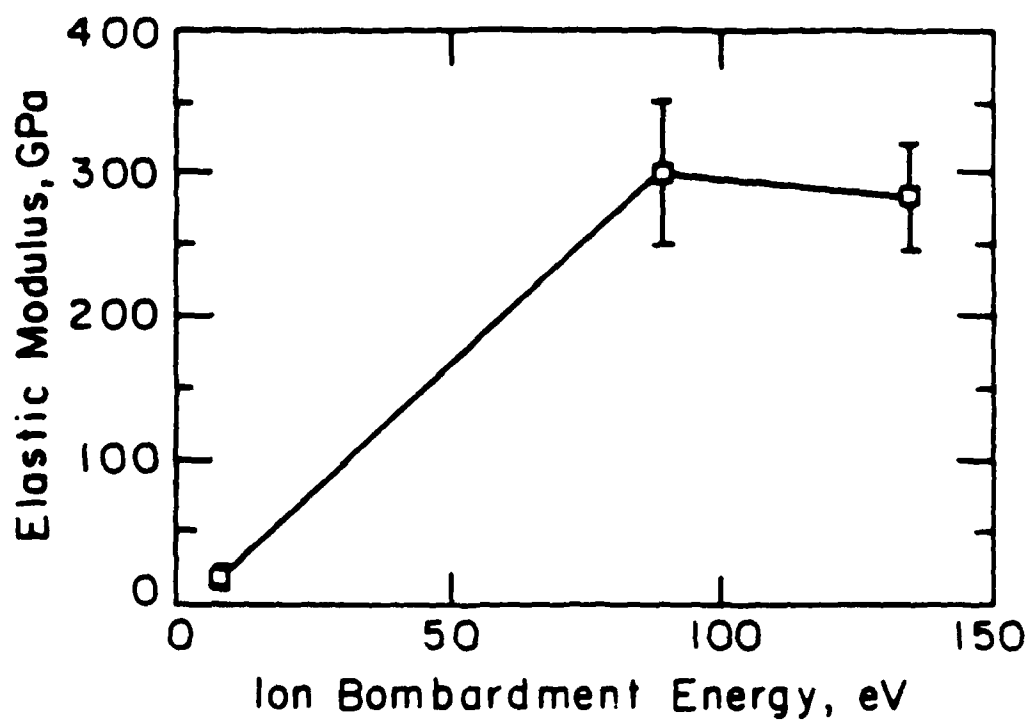


Fig. 11 - Dependence of Young's modulus on ion beam energy in annealed coatings under biaxial tension.

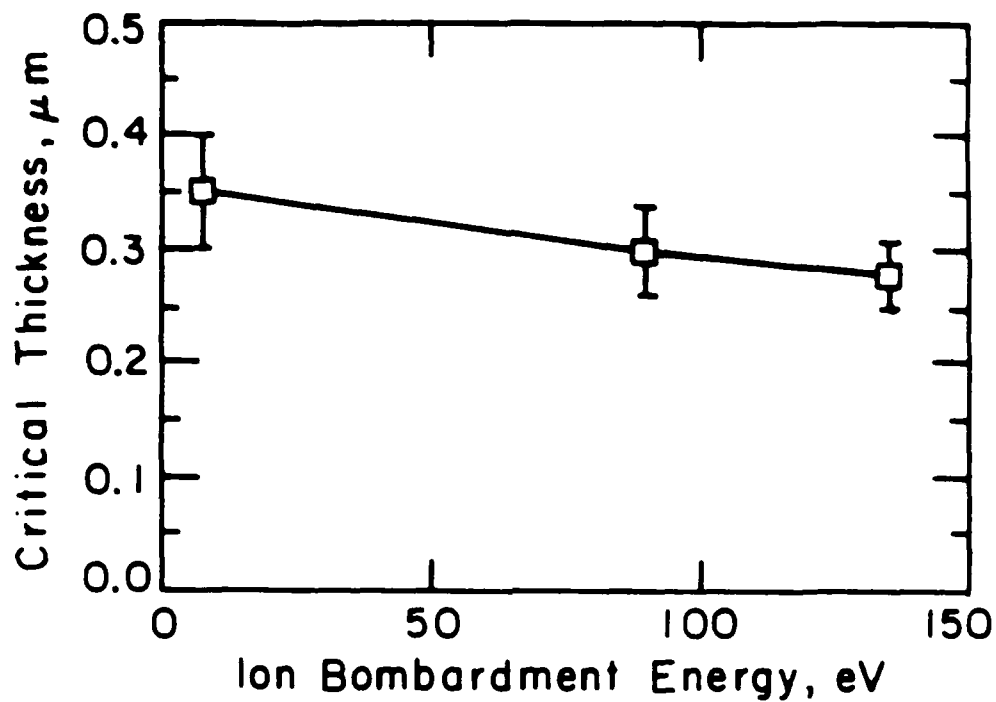


Fig. 12 - Dependence of critical coating thickness for delamination on ion beam energy in annealed coatings under biaxial tension.

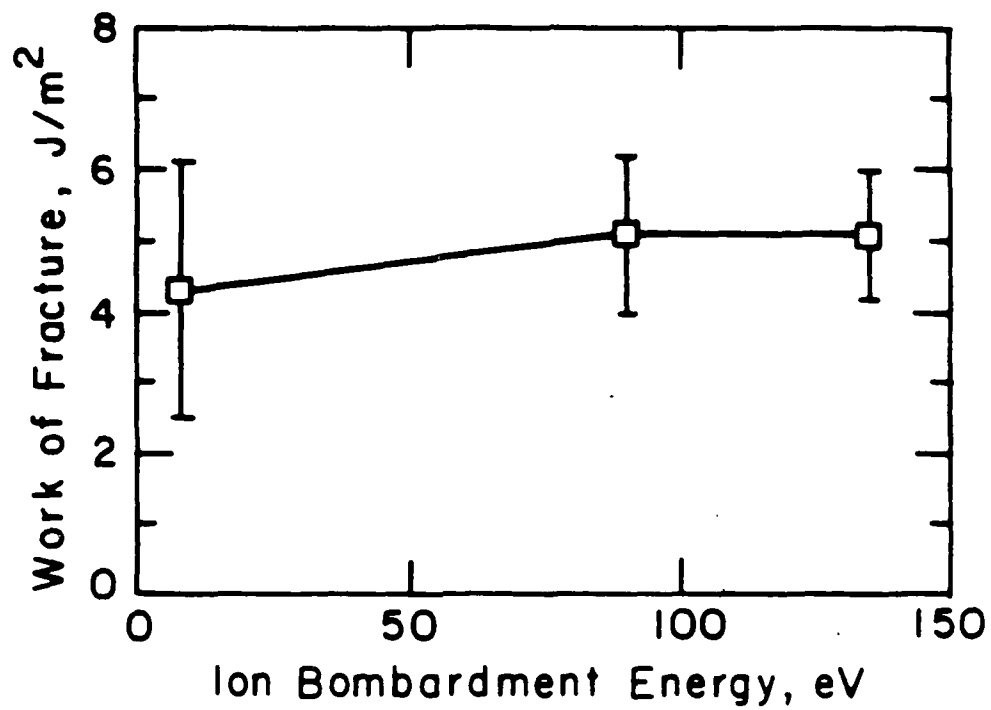
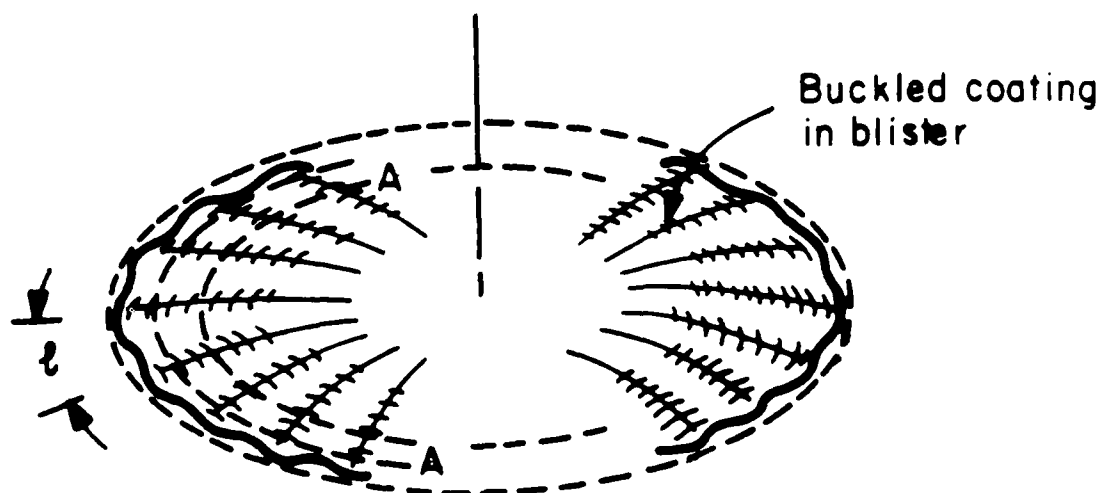
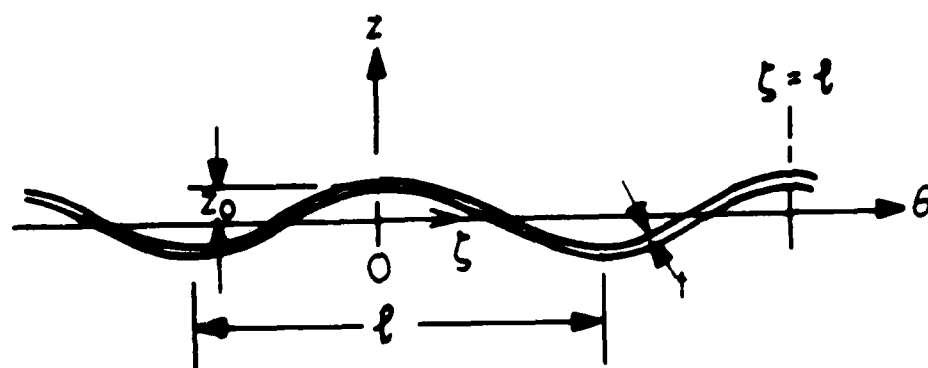


Fig. 13 - Dependence of critical energy release rate on ion beam energy in annealed coatings under biaxial tension.



(a)



Section A-A

(b)

Fig. 14 - Sketch of idealized circumferential buckling of a delaminating coating in a blister in an as-deposited hydrogenated coating under biaxial compression: (a) perspective view, (b) buckled coating viewed in the radial direction.

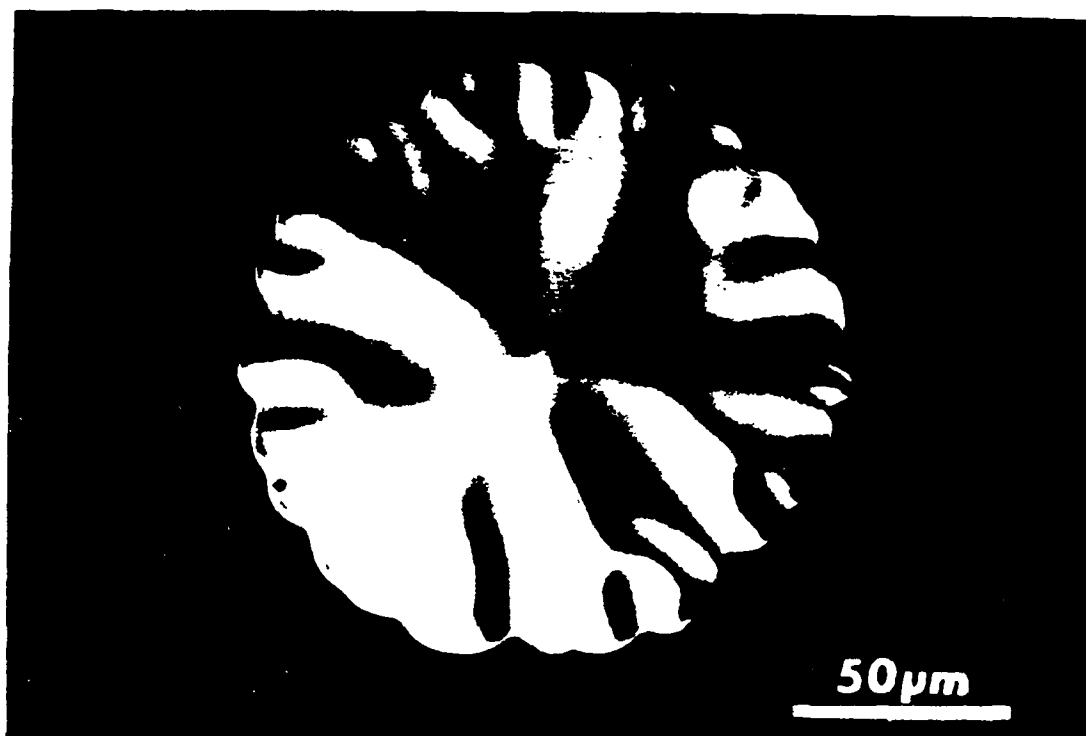


Fig. 15 - A large buckled blister in a coating in the process of undergoing delamination, viewed with the Normarski interference contrast mode of microscopy. The outer ring surrounding the buckled center is the zone in which radial slippage occurs to relieve the radial stress.

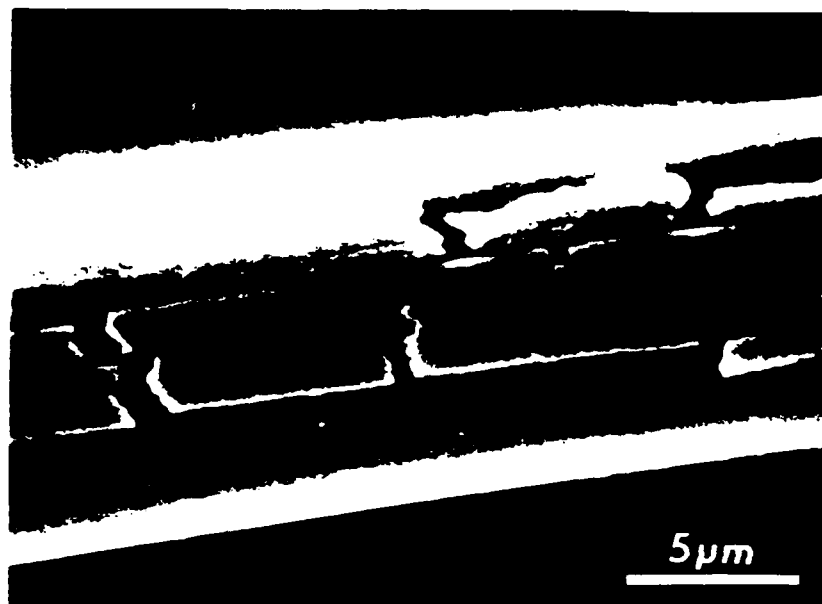


Fig. 16 - An SEM micrograph of a fragmented and delaminated annealed coating of critical thickness of SiC on a Pitch-55 fiber. The misfit strain is determinable from the gaps between the flakes.

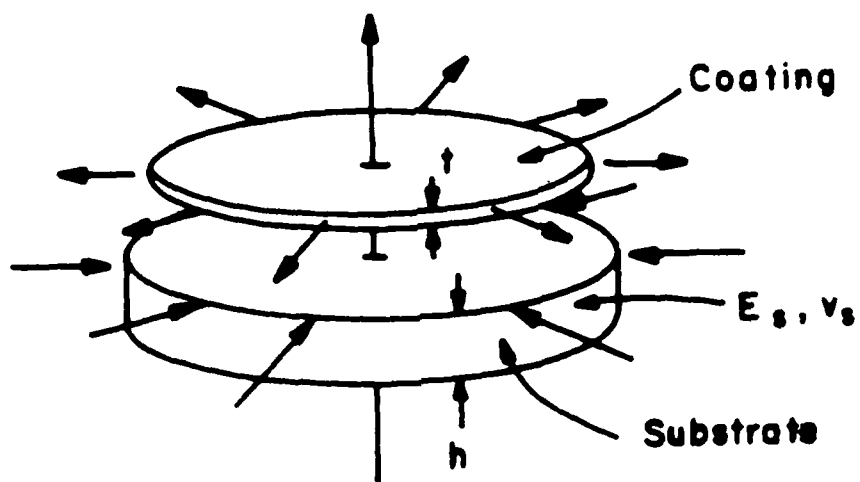


Fig. I-1 Misfit between coating and substrate in round disk.

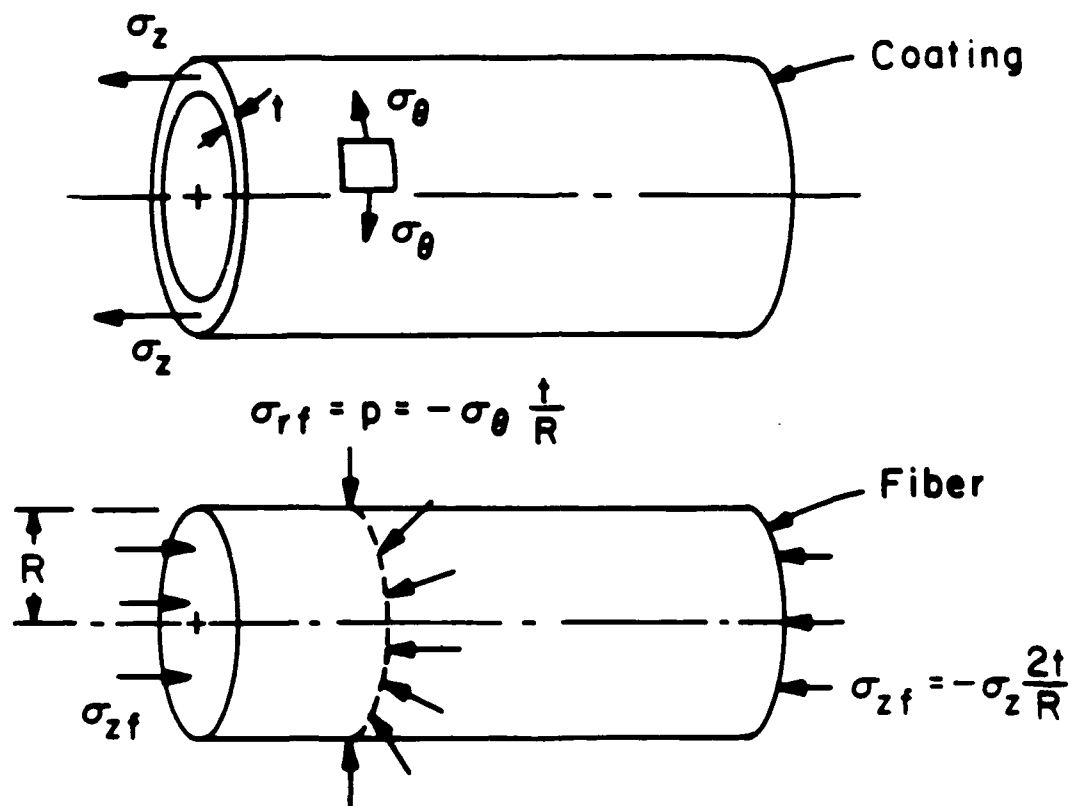


Fig. III-1 Misfit between coating and fiber.

Mechanical Properties of Residually Stressed a-SiC:H Thin Films

H. S. LANDIS, V. GUPTA and J. A. CORNIE

ABSTRACT

Amorphous hydrogenated silicon carbide produced by the glow discharge deposition of silane and methane can exhibit compressive residual stresses as large as 2.7 GPa. Vacuum annealing below the crystallization temperature causes tensile stresses of the same magnitude to develop as hydrogen is liberated from the deposit. Independent measurements of the residual stress and strain in the annealed coatings, and the stress and Young's modulus in the as-deposited coatings, allow determination of the strain energy density and the interfacial work of fracture.

I. INTRODUCTION

It is possible to produce thin films of a variety of materials at very low substrate temperatures by plasma enhanced chemical vapor deposition (PECVD) [1]. In particular, the glow discharge decomposition of silane and methane produces crystallographically amorphous silicon-carbon alloys whose stoichiometry can be controlled by the Si/C ratio in the feed gas [2-5]. As-deposited coatings exhibit compressive residual stresses, which can be quite large if the coating has been subjected to energetic ion bombardment during growth [6-17].

Deposits generally contain large amounts of hydrogen, on the order of 20 atom percent [2]. Depending on the composition, much of the hydrogen can be liberated by vacuum anneals below the crystallization temperature. The effects of dehydrogenation on the electronic and chemical properties of these materials, particularly a-Si:H, have been investigated by other researchers [18-32]. Hydrogen serves to saturate "dangling bonds" in the disordered material, localizing defects and producing an effective mobility gap. The liberation of hydrogen by vacuum heat treatments below the crystallization temperature does increase the density of unpaired electrons, as measured by electron paramagnetic resonance (EPR), but only slightly [33-38]. Proton paramagnetic resonance (PPR) studies suggest that local reconstruction of the amorphous tetrahedral network occurs, even though crystallization does not [39].

As might be expected, the liberation of 15 to 30 atom percent of the coating also has a large effect on the residual stress state of these materials. These stresses, and their influence on the mechanical behavior of the coating/substrate composite, are the principal focus of this paper.

II. EXPERIMENTAL

All depositions were performed in a custom plasma enhanced chemical vapor deposition facility [40] at a base pressure of 2×10^{-6} Torr (figure 1). The substrate temperature during deposition is always less than 100°C. Parallel six inch diameter shielded electrodes are driven by separate 13.56 MHz power supplies equipped with automatic matching networks. This configuration allows independent control over the total power input into the plasma and the DC offset on the substrate electrode.

The effective ion bombardment energy (IBE) during deposition is determined as follows. The DC potential of the substrate electrode with respect to ground is measured during deposition. The ion energy distribution with respect to ground is later separately measured with the substrate electrode floating and all of the RF power applied to the upper electrode. This is done by energy dispersive mass spectrometry, after Kohler et al [41,42]. The DC plasma potential in volts is numerically equal to the peak in the ion energy distribution in electron volts. The effective ion bombardment energy (in eV) during deposition is approximated as the difference between the substrate and plasma potentials in volts (see figure 2). There are three main assumptions involved in this technique. First, only singly charged ions are present in the discharge. Second, ion/neutral collisions in the sheath have a negligible effect on the ion energy distribution. Third, the plasma potential depends on the reactor geometry and the total RF power, but not on the partitioning of the power between the electrodes.

Semiconductor purity (99.9995%) gases are introduced into the chamber at a total pressure of 50 mTorr. An argon discharge is first used to sputter the native oxide from the (100) silicon wafer substrates. Silane and methane are

then added to the discharge while the pressure is maintained at 50 mTorr. After the deposition is complete (five to ten minutes) the reactive gas flow is ceased and the discharge extinguished. The silicon/carbon ratio was determined by X-ray photoelectron spectroscopy, and is approximately 1:1 ($\pm 5\%$) for all of the a-SiC:H coatings discussed. The deposition conditions used for three types of coatings (high, moderate and low ion bombardment energy) are presented in Table 1.

The film thickness is determined by use of a mechanical profilometer and a second wafer that has been masked to produce a sharp step. The residual stress in the film is determined by measuring the radius of curvature of the wafer/coating couple and applying the relation [43]

$$\sigma_1 = \frac{E_2 t_2^2}{6(1-\nu_1) t_1 R} \quad \text{Eqn. 1}$$

Here σ is the stress, E the elastic modulus, t the thickness, ν Poisson's ratio and R the radius of curvature. The subscript 1 refers to the coating and 2 to the substrate. The indicated simplification is valid for thick substrates ($t_2 \gg t_1$). Deposits made by PECVD from silane and methane typically contain large amounts of hydrogen [2,18]. The hydrogen content of these films is determined by monitoring the pressure rise as the coatings are heated in a sealed evacuated chamber of known volume [44].

The residual strain is determined by two techniques which will be described in the next section. Other materials parameters such as elastic modulus and the strain energy density were calculated from the standard relations.

$$E_1 = \frac{\sigma_{1x}(1-\nu_1)}{\epsilon_{1x}} = \frac{\sigma_{1y}(1-\nu_1)}{\epsilon_{1y}} = \frac{\sigma_1(1-\nu_1)}{\epsilon_1} \quad \text{Eqn. 2}$$

$$\omega_1 = \frac{1}{2} \sigma_{1x} \epsilon_{1x} + \frac{1}{2} \sigma_{1y} \epsilon_{1y} = \sigma_1 \epsilon_1 \quad \text{Eqn. 3}$$

The subscripts x and y refer to the two orthogonal in-plane directions (z will refer to the surface normal). By symmetry $\sigma_{1x} = \sigma_{1y} = \sigma_1$ and $\epsilon_{1x} = \epsilon_{1y} = \epsilon_1$. In Equation 3, ω_1 is the strain energy density in the coating. Stresses normal to the plane of the deposit are neglected in this plane stress approximation.

The deposition rates (normalized with respect to the total RF power input) for the three types of coatings are presented in Table 2, along with several other deposition and materials properties. Vacuum anneals in the temperature range 300-935°C liberate large quantities of hydrogen from the deposit (figure 3). The loss of such a large amount of material from the deposit causes a substantial decrease in the coating thickness, as can be seen in figure 4 for the standard anneal (600°C, 30 min. in vacuum). Although the shrinkage associated with dehydrogenation is not isotropic, there are non-zero components in the plane of the coating. This in-plane shrinkage causes the compressive residual stresses that are found in the as-deposited coatings to be transformed into tensile residual stresses. (See figure 5.)

Selected area diffraction by TEM (using a JOEL 200 CX) indicate that the coatings are crystallographically amorphous in both the as deposited state and after annealing. A typical diffraction pattern is presented in figure 6. The primary characteristics, a diffuse halo and no apparent bright spots, are found for all three types of coatings, both as-deposited and after the standard anneal. This implies that the deposits remain amorphous even through the restructuring associated with the 600 °C dehydrogenation anneal.

Optical microscopy provides much more information about the effects of dehydrogenation on the mechanical behavior of a-SiC:H deposits. Tensile residual stresses in annealed low IBE coatings thicker than about 0.35 μm

cause the deposit to break up into nearly equiaxed sections that can then delaminate, as is visible in figure 7.

Moderate and high IBE deposits exhibit a much different behavior. The circular defects in figure 8 are blisters that form during vacuum annealing as hydrogen accumulates at the substrate/coating interface, particularly at areas where the interface has been weakened by particulate contamination. The high pressures that result cause the film to plastically deform into circular blisters. (These blisters can be virtually eliminated by careful substrate cleaning and slow ramp rates for the vacuum anneals.)

If the coating thickness exceeds about $0.1\text{ }\mu\text{m}$ these blisters act as nucleation sites for through-the-thickness cracks. As can be seen in figure 8, propagation is favored in the $\langle 110 \rangle$ directions, the crystallographically stiff directions of the silicon substrate. As these cracks can extend over large distances, the coating is effectively scribed into many long rectangular sections.

For annealed thicknesses greater than about $0.30\text{ }\mu\text{m}$ moderate and high IBE coatings spontaneously delaminate at the substrate interface. The driving force for this fracture is the release of stored residual strain energy. The critical thickness for delamination depends on the residual stress state in the coating, and thus on the ion bombardment energy and the dehydrogenation anneal. (See Table 2 and figure 5.) Because delamination of a compressively stressed coating is mechanically constrained and requires a Euler instability to be reached [45,43] the critical thickness for as-deposited coatings is substantially larger than the critical thickness for delamination of the corresponding coatings under tensile stress.

By careful examination of dehydrogenated coatings just thicker than the critical thickness for dehydrogenation, it is possible to determine the residual strain in the coating. The rectangular section in the center of figure 9 is a region



of dehydrogenated moderate IBE a-SiC that has delaminated over a length L , but still lies flat against the Si substrate. The distance ΔL represents the change in length that results from the relaxation of the residual stress over the length L . Consequently the residual strain in the coating (before delamination) is given by the simple relation

$$\epsilon_1 = \frac{\Delta L}{L} \quad \text{Eqn. 4}$$

A similar sort of measurement is possible with annealed high and low IBE a-SiC, although the generally equiaxed fracture pattern of the low IBE material significantly increases the uncertainty in the measurement. (See Table 2 and figure 10.) Independent measurement of the residual stress and residual strain in annealed coatings allows the calculation of the total strain energy density in the deposit [40], using Eqn. 3. For thin coatings, or more specifically for $t_1 E_1 \ll t_2 E_2$, the strain energy in the substrate does not significantly contribute to the total strain energy in the composite [40]. Experimental determination of the minimum, or critical thickness for delamination, denoted t_c , allows calculation of the intrinsic fracture toughness of the interface. Variations of these techniques can be applied to other substrate materials, including small diameter fibers of use in composite materials. The measurement the work of fracture of compressively stressed coatings requires a different technique, involving a buckling analysis on areas of compressive delamination. (See figure 11.) These matters will be discussed more thoroughly in the following section.

III. RESULTS AND DISCUSSION

The residual stresses in the SiC coatings, as presented in figure 5, are independent of the thickness of the deposit, but strongly dependent on the ion

bombardment energy and the dehydrogenation anneal. Tensile residual stresses in annealed coatings on polished (100) silicon wafers cause delamination failure if the coating is thick enough to supply the strain energy necessary for the work of fracture of the interface. This is illustrated in figure 9 for an annealed moderate ion bombardment energy film 0.35 μm thick. Similarly, a high ion bombardment energy specimen 0.28 μm thick in figure 12a shows a ribbon of SiC approximately 160 μm long that has delaminated but now lies flat against the substrate. Figure 12b shows that the relaxed length is approximately 1.1 less than the original length, yielding a relaxation strain of -0.69%. This implies that the strain in the intact areas of the coating is 0.69%. Observations of many similar delamination failures, in annealed low, moderate and high ion bombardment energy coatings yield the strain measurements presented in Table 2. Through the measurement of these residual tensile strains, and the previously measured residual tensile stress, the Young's moduli of the dehydrogenated amorphous SiC coatings can be determined from Eqn. 2, assuming a value of 0.3 for ν_1 , the Poisson's ratio of the coating.

The calculated moduli are given in Table 2, and have been found to be generally independent of the thickness of the coating. Since the strain energy in the substrate is negligible for coating thicknesses much less than the substrate thickness [40], the stored strain energy in the substrate/coating system is a linear function of the coating thickness, and the critical specific fracture separation work G_{c0} (the intrinsic toughness of the interface) is given by [43]

$$G_{c0} = \frac{\sigma_1^2 (1 - \nu_1) t_1}{E_1} \quad \text{Eqn. 5}$$

and is presented in figure 13 for annealed low, moderate and high ion bombardment energy a-SiC on (100) silicon substrates. The critical coating

thickness t_c , for a given set of deposition and annealing conditions, is determined by observing the minimum thickness at which delamination occurs in a specimen with copious through-the-thickness cracks already present.

In as-deposited coatings the residual stresses are compressive. The delamination of these coatings occurs by the formation of a blister which begins to lift off the substrate in a regularly buckled form, as in figure 11. These blisters propagate radially outward in quasi static equilibrium with a self-similar circumferential buckling wavelength λ . Considering that the film completely relieves its radial stress as the blister grows radially outward and buckles under the circumferential stress, the wavelength λ can be related the Young's modulus and the initial biaxial residual stress σ by Eqn. 6 [43].

$$\lambda = \pi t_1 \sqrt{\frac{E_1}{3(1-\nu_1^2)\sigma_1(1-\nu_1)}} \quad \text{Eqn. 6}$$

Again assuming a value of 0.3 for the Poisson's ratio of the coating, the Young's modulus of the as-deposited coatings can be determined by measuring λ , t_1 and σ_1 . When this was done for an as deposited high ion bombardment energy of 1.1 μm thickness with a measured λ of 20 μm and compressive residual stress of approximately 2 GPa, E was found to be 116 GPa.

Further, the intrinsic fracture toughness of the interface can be determined by subtracting the strain energy stored per unit area of the interface in the buckled coating from the initial strain energy in the biaxially stressed coating. This leads to an expression for G_{c0} , given by Eqn. 7 [44].

$$G_{c0} = \frac{\nu_1 \pi^4 E_1 t_1^5}{9(1-\nu_1^2)^2 (1-\nu_1) \lambda^4} \quad \text{Eqn. 7}$$

Evaluating this intrinsic toughness for the as deposited high IBE a-SiC:H

coating described above yields a work of fracture of 5.9 J/m^2 . The difference between this value and the 5.1 J/m^2 for the annealed coating could be due to the difficulty of determining the critical coating thickness, or a slight additional dissipative work associated with sliding of the coating over the substrate during the release of the radial stress, or could be a real effect from the atomic rearrangements associated with dehydrogenation [33-39].

The same phenomenon of spontaneous delamination also occurs with a-SiC:H coatings on Pitch-55 carbon fibers. For low ion bombardment a-SiC:H, annealed for 30 minutes at 600°C in vacuum, coatings less than $0.33 \mu\text{m}$ were found to remain intact for periods of months, while thicker coatings were found to undergo copious delamination by cracking and flaking, as in figure 14. The residual strain was determined from the ratio of the average gap size between the flakes to the average dimension of the flakes. This technique yields a value for ϵ_1 of 2.7%, which is not too different from the value obtained for similar coatings on silicon (Table 2). Assuming that the elastic modulus of the coating is not a function of the substrate material but only the deposition and annealing conditions, the intrinsic interfacial fracture toughness for this fiber/coating system can also be rigorously determined [43]. Assuming that E_1 is indeed 19 GPa, the Poisson's ratio of the substrate ν_1 is 0.3, the critical coating thickness is $0.33 \mu\text{m}$, and the fiber is $10 \mu\text{m}$ in diameter and has the reported mechanical properties [43,46] one obtains $G_{c0} = 5.5 \text{ J/m}^2$.

V. APPLICATIONS

In many ways, the techniques and procedures outlined in the previous sections are more important than the specific measurements made in the a-SiC:H system. Of the many parameters influencing the microscopic fracture

behavior of composite materials, the most fundamental and the most inaccessible is the intrinsic interfacial work of fracture. It is largely this quantity that determines the magnitude of the stress field about the crack tip, and thus the plastic zone size. The size of the plastic zone ahead of the crack tip, together with the intrinsic interfacial toughness, determines the total, or extrinsic work of fracture. It is this extrinsic quantity that is measured by conventional techniques [47].

Specifically, due to the very local nature of the strain field which drives the crack tip in the residually stressed coatings, the plastic zone size in the vicinity of the crack tip will be quite small, and hence the G_{c0} obtained from the delamination process described in the previous sections is essentially the intrinsic toughness of the interface. Consequently, for modelling purposes, we can use this interface toughness as a fundamental materials parameter in any system where failure occurs at such an interface. One such class of materials is metal matrix composites. Fiber coatings are often utilized to prevent chemical reaction at the interface [48,49], promote wetting during matrix infiltration [49,50], and improve the fracture properties of the composite [51]. Amorphous hydrogenated silicon carbide is a promising coating material in all of these regards [40]. It is much more than an additional bonus that the most fundamental parameter affecting the microscopic fracture behavior, the intrinsic toughness of the failing interface, can be independently determined in the manner discussed above.

VI. CONCLUSIONS

The residual stress state in amorphous hydrogenated silicon carbide produced by plasma enhanced chemical vapor deposition is strongly influenced

by the ion bombardment energy during deposition and subsequent thermal treatments. These stresses, both tensile and compressive, can be determined from the curvature of the substrate/coating couple. The residual tensile strain can be determined if a partially delaminated region can be found that lies flat against the substrate. Independent measurement of the stress and strain allows calculation of the coating elastic modulus, if a value is assumed for Poisson's ratio. Knowledge of the residual stress and strain, coupled with the critical coating thickness for interfacial delamination, allows calculation of the interfacial work of fracture. If it is assumed that the elastic modulus does not depend on the substrate used, then the interfacial work of fracture can be determined for coatings under tensile stress on other substrates. In addition, the interfacial work of fracture of compressively stressed amorphous coatings on thick, flat substrates can be determined by an inverse buckling analysis, as is described elsewhere by Argon and Gupta [43].

VI. REFERENCES

1. T. D. Bonifield, "Deposition Technologies for Films and Coatings, Developments and Applications", eds. R. F. Bunshah et. al., Noyes Publications (1982), p. 365.
2. H. Wiedner et. al., Phys. Stat. Sol. B 92 p. 99 (1979).
3. H. Yoshihara et. al., Thin Solid Films 40 p. 1 (1981).
4. R. A. Roy and R. Messier, J. Vac. Sci. Tech. A 2 p. 312 (1984).
5. Y. Murayama and T. Takao, Thin Solid Films 40 p. 309 (1977).
6. D. A. Anderson, Phil. Mag. 35 (1) p. 17 (1977).
7. C. Weissmantel et. al., Thin Solid Films 61 p. L5 (1979).
8. C. Weissmantel et. al., Thin Solid Films 63 p. 315 (1979).

9. B. Meyerson and F. W. Smith, J. Non-Cryst. Solids, 35.36 p. 435 (1980).
10. A. Pan and J. E. Greene, Thin Solid Films 78 p. 25 (1981).
11. J. A. Thornton and D. W. Hoffman, J. Vac. Sci. Tech. 18 (2) p. 203 (1981).
12. E. H. Hirsch and I. K. Varga, Thin Solid Films 69 p. 99 (1980).
13. A. Kasdan and D.P. Goshorn, J. Vac. Sci. Tech. A 1 p. 437 (1983).
14. D. S. Yee et. al., J. Vac. Sci. Tech. A 3 p. 2121 (1985).
15. T. C. Huang et. al., J. Vac. Sci. Tech. A 3 p. 2161 (1985).
16. E. Kay, J. Vac. Sci. Tech. A 4 p. 462 (1986).
17. S. S. Sun, J. Vac. Sci. Tech. A 4 p. 572 (1986).
18. M. H. Brodsky, M. Cardona and J. J. Cuomo, Phys. Rev. B 16 (8) p. 3556 (1977).
19. J. C. Knights et. al., Phil. Mag. B 37 (4) p. 467 (1978).
20. D. K. Biegelsen et. al., Phys. Rev. B 20 (12) p. 4839 (1979).
21. J. C. Knights et. al., J. Non-Cryst. Solids 32 p. 393 (1979).
22. J. C. Knights, J. Non-Cryst. Solids 35.36 p. 159 (1980).
23. R. J. Nemanich and J. C. Knights, J. Non-Cryst. Solids 35.36 p. 243 (1980).
24. D. K. Biegelson et. al., J. Non-Cryst. Solids 35.36 p. 285 (1980).
25. A. J. Leadbetter et. al., Solid State Commun. 33 p. 973 (1980).
26. A. J. Leadbetter et. al., Solid State Commun. 38 p. 957 (1981).
27. J. A. Reimer et. al., J. Vac. Sci. Tech. 19 (1) p. 53 (1981).
28. B. A. Scott et. al., J. Appl. Phys. 54 p. 6853 (1983).
29. C. J. Fang et. al., J. Non-Cryst. Solids 35.36 p. 255 (1980).
30. D. Weaire and F. Wooten, J. Non-Cryst. Solids 35.36 p. 495 (1980).
31. R. Mosseri et. al., J. Non-Cryst. Solids 35.36 p. 507 (1980).
32. A. Hiraki et. al., J. Non-Cryst. Solids 35.36 p. 519 (1980).
33. K. J. Matysik, C. J. Mogab and B. G. Bagley, J. Vac. Sci. Tech. 15 (2) p. 302

(1978).

34. J. A. Reimer, et al., Solid State Commun. 37 p. 161 (1981).
35. K. Zellama et al., J. Non-Cryst. Solids 35,36 p. 225 (1980).
36. P. John, et. al., J. Non-Cryst. Solids 35,36 p. 237 (1980).
37. W. Beyer and H. Wagner, J. Non-Cryst. Solids 59,60 p. 161 (1983).
38. M. Reinelt et al., J. Non-Cryst. Solids 59,60 p. 169 (1983).
39. I. Haller, Appl. Phys. Lett. 37 p. 282 (1980).
40. H. S. Landis, Ph.D. thesis, Materials Science and Engineering, MIT (1988).
41. K. Kohler et al., J. Appl. Phys. 57 p. 59 (1985).
42. K. Kohler et al., J. Appl. Phys. 58 p. 3350 (1985).
43. A. S. Argon et al., J. Mat. Sci. (1988) under submission.
44. J. J. Hajjar, B.S. thesis, Electrical Engineering and Computer Science, MIT (1983).
45. A. G. Evans and J. W. Hutchinson, Intern. J. Solids and Structures, 20 p. 455 (1984).
46. R. Bacon, Proceedings of the Metal and Ceramics Composites Processing Conference, 13-15 November, 1984. Batelle Columbus Laboratories, Columbus, Ohio.
47. V. Gupta et al., J. Mat. Sci. (1988) under submission.
48. J. A. Cornie, "Failure Modes in Composites IV", Proc. TMS/AIME, Chicago 1978, eds. J. Cornie and F. Crossman, p. 236.
49. M. F. Amateau, J. of Composite Materials 10 p. 279 (1976).
50. H. Katzman, J. Mat. Sci. 22 p. 144 (1987).

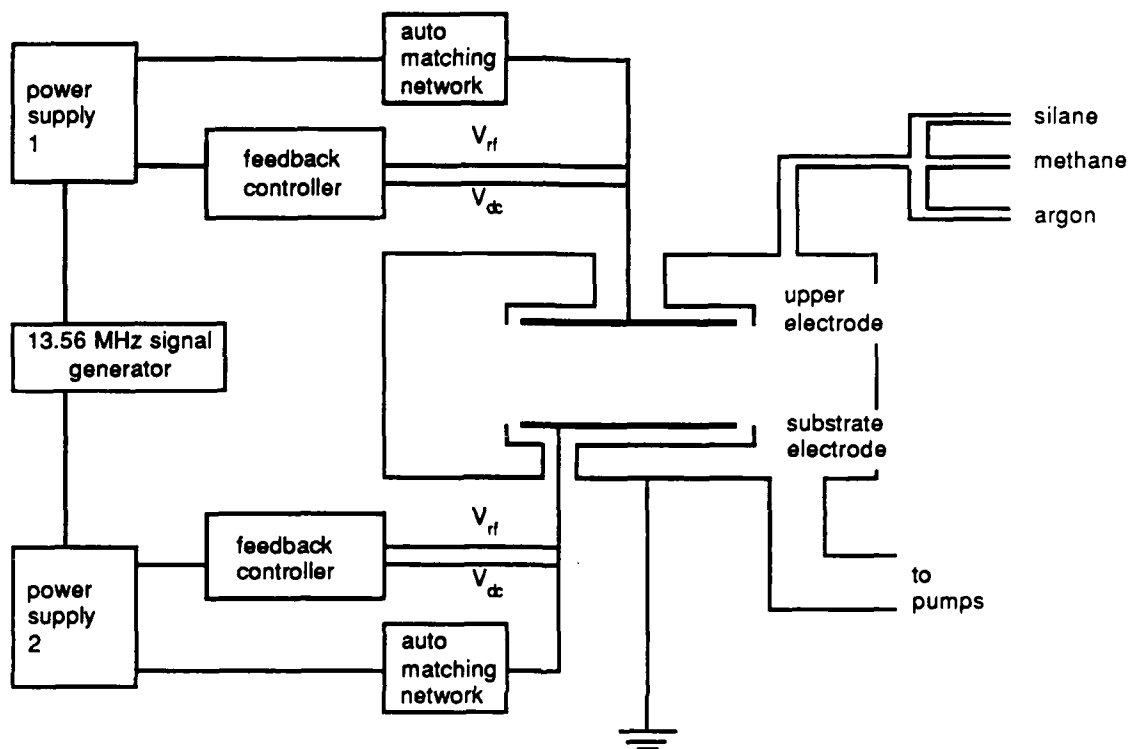


Figure 1. Schematic diagram of the Plasma Enhanced Chemical Vapor Deposition System used to fabricate the thin films.

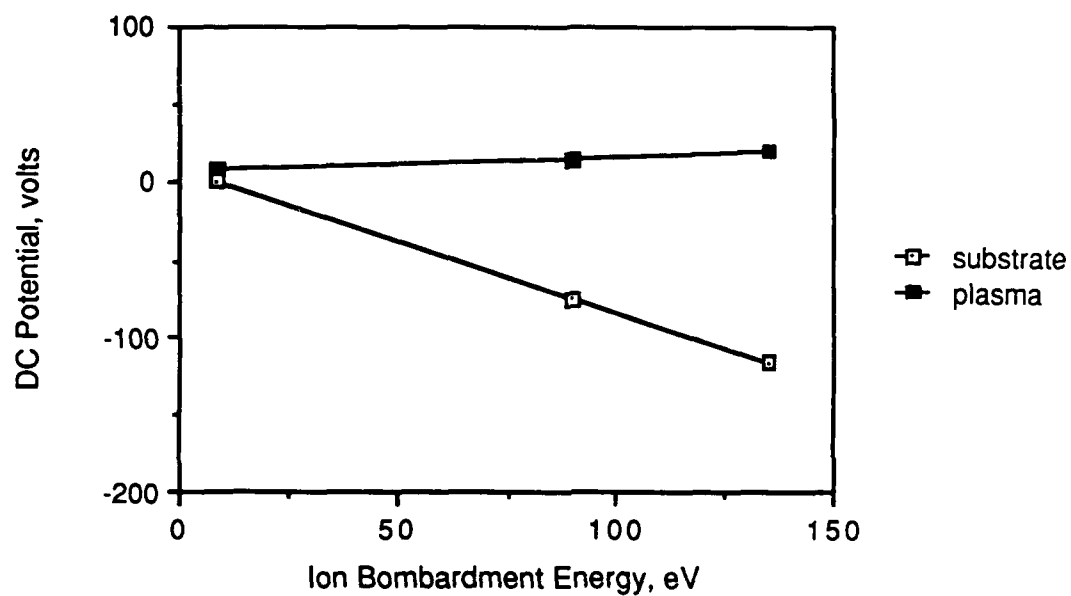


Figure 2. The ion bombardment energy is approximated using the difference between the DC potential on the substrate during deposition and the plasma potential with all of the RF power applied to the upper electrode.

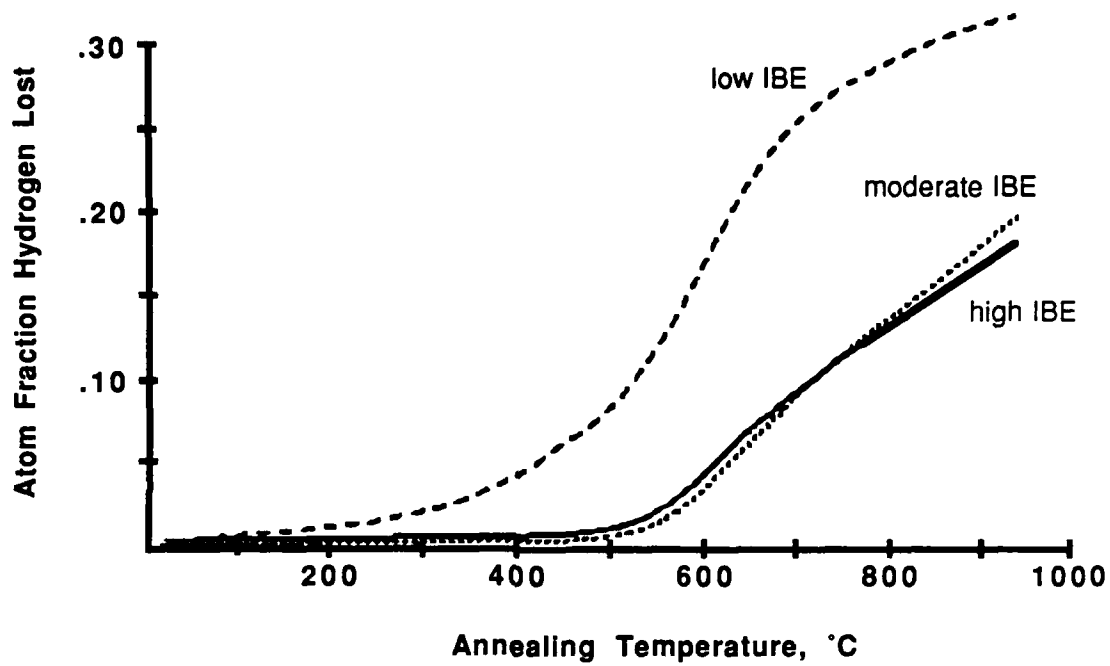


Figure 3. Hydrogen evolution spectra for low, moderate and high IBE a-SiC:H.

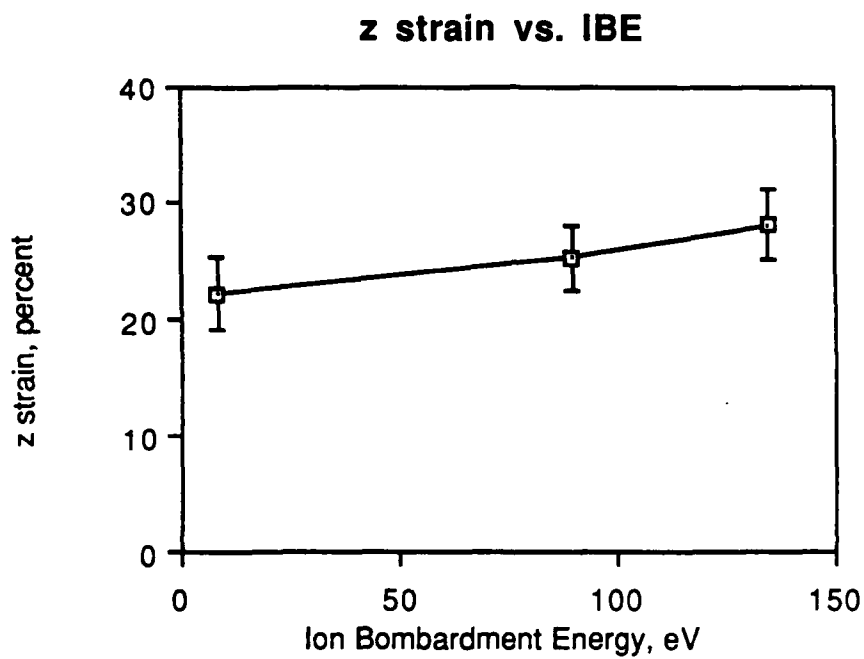


Figure 4. Percent decrease in deposit thickness due to the standard anneal (600°C, 30 min. in vacuum) as a function of the ion bombardment energy.

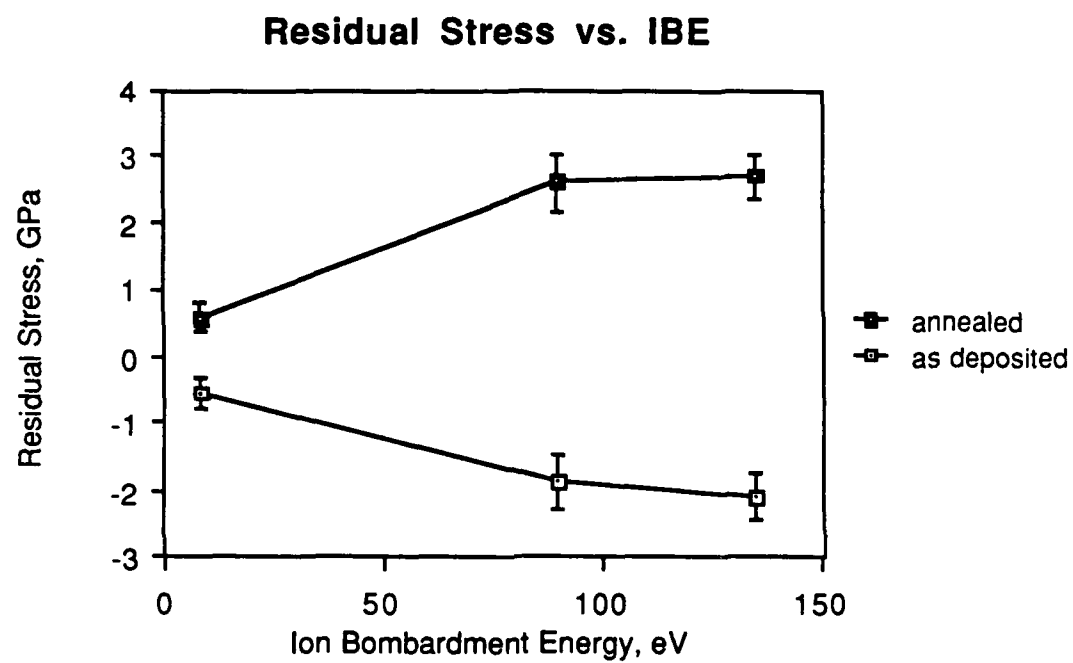


Figure 5. As-deposited and annealed residual stress as a function of ion bombardment energy.

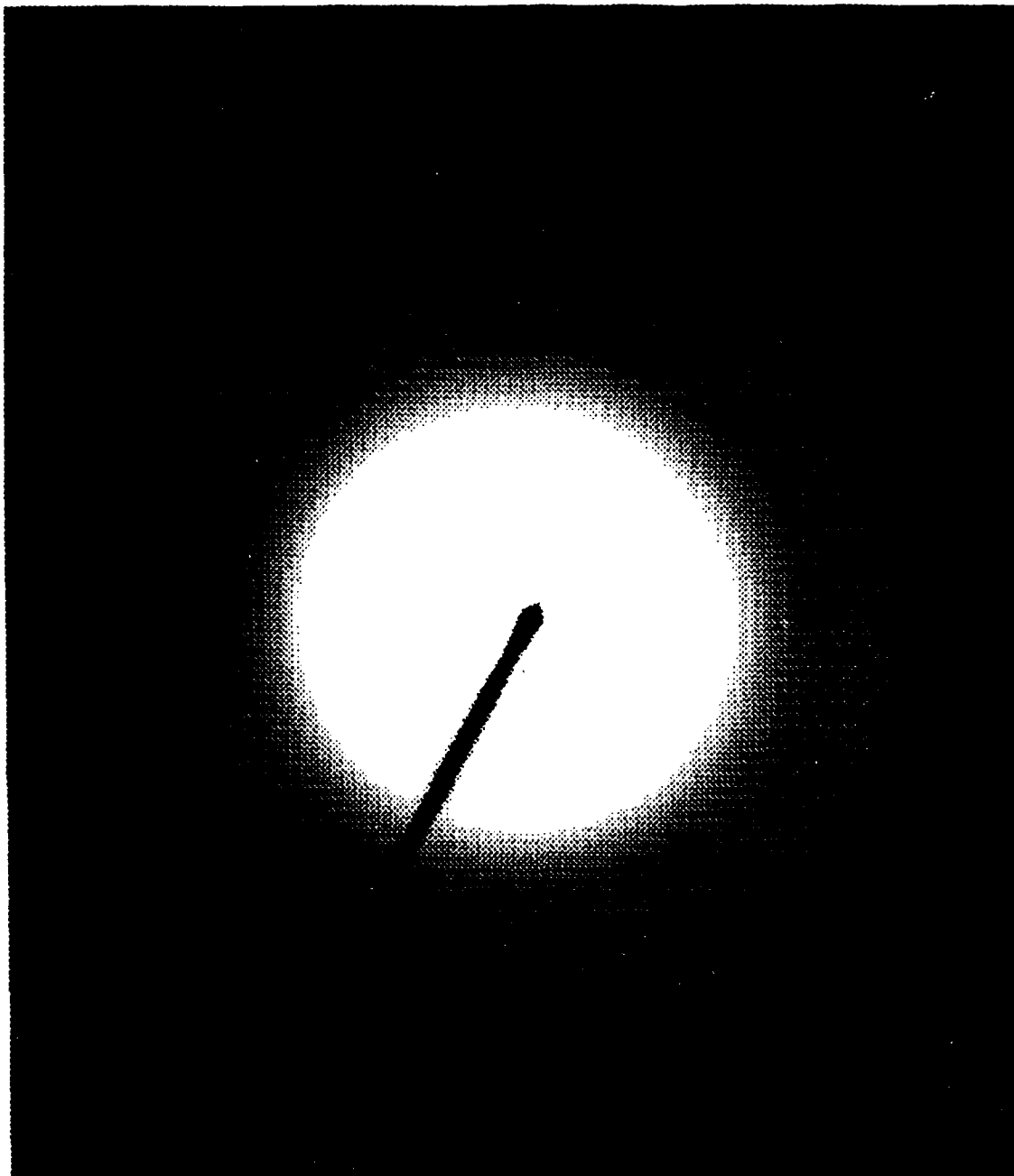


Figure 6. Selected area diffracton pattern of annealed moderate IBE a-SiC:H by TEM.



10 μm

Figure 7. Low IBE annealed a-SiC:H, 0.42 μm thick. Residual tensile stresses in the deposit cause fracture and delamination if the coating thickness is greater than about 0.35 μm .

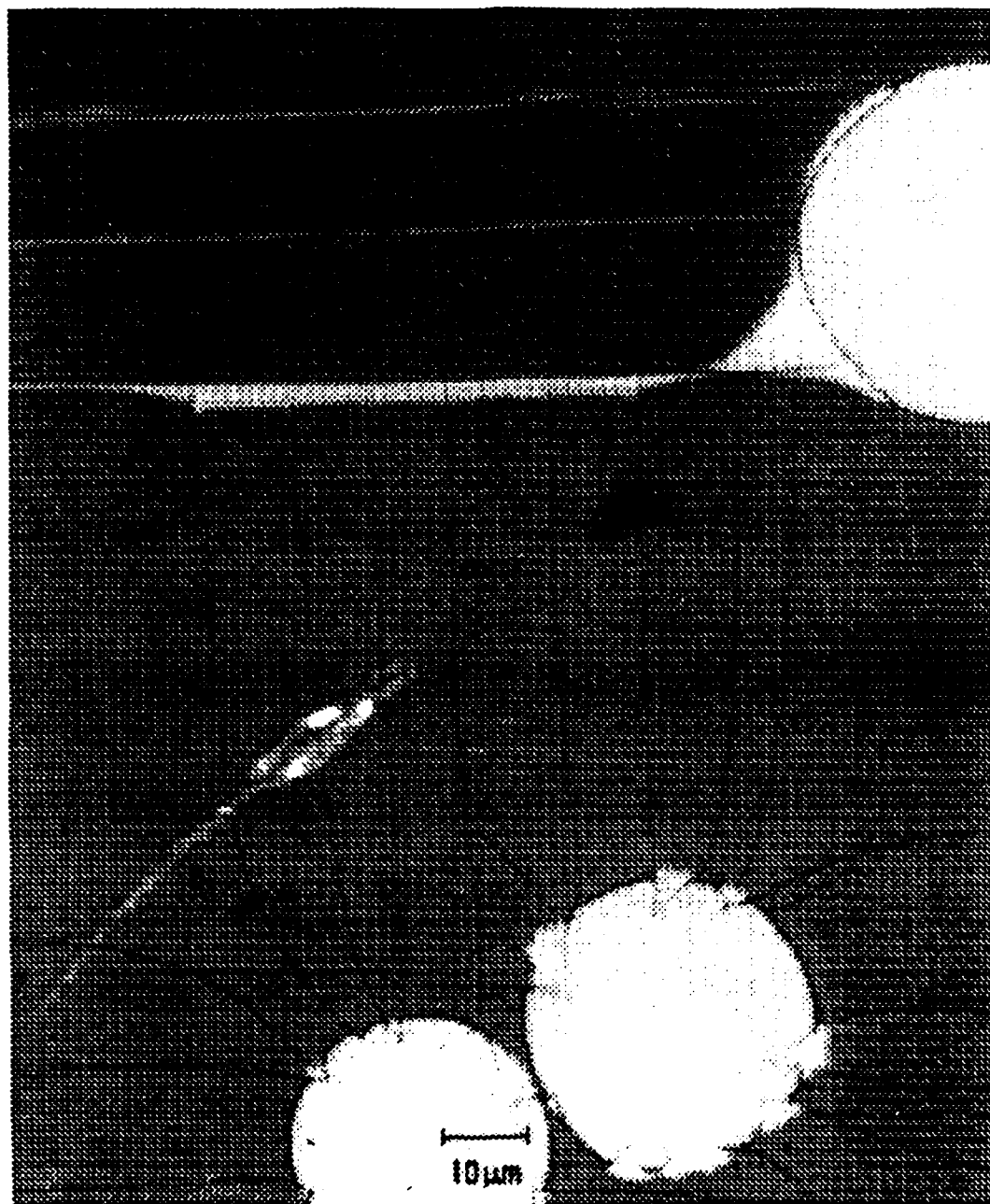
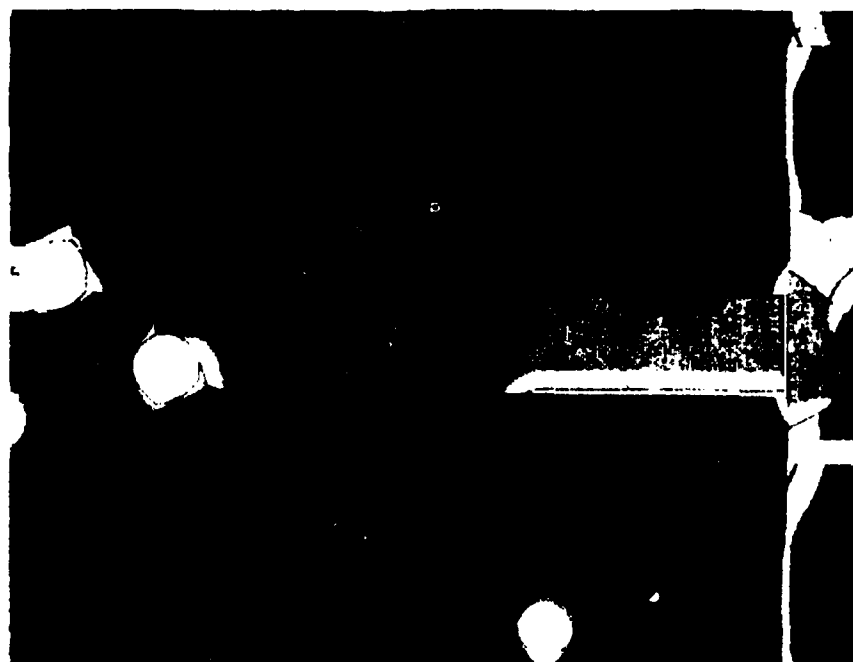


Figure 8. High IBE annealed a-SiC:H, 0.13 μm thick. The circular defects are blisters formed by the accumulation of liberated hydrogen at the substrate/coating interface. These defects act as nucleation sites for through-the-thickness cracks, which propagate in the $\langle 110 \rangle$ directions of the silicon substrate.



100 μm

Figure 9. Moderate IBE annealed a-SiC:H, 0.32 μm thick. The delaminated length L is 355 μm , and the change in length ΔL is 2.3 μm . The strain in this specimen is approximately 0.66%.

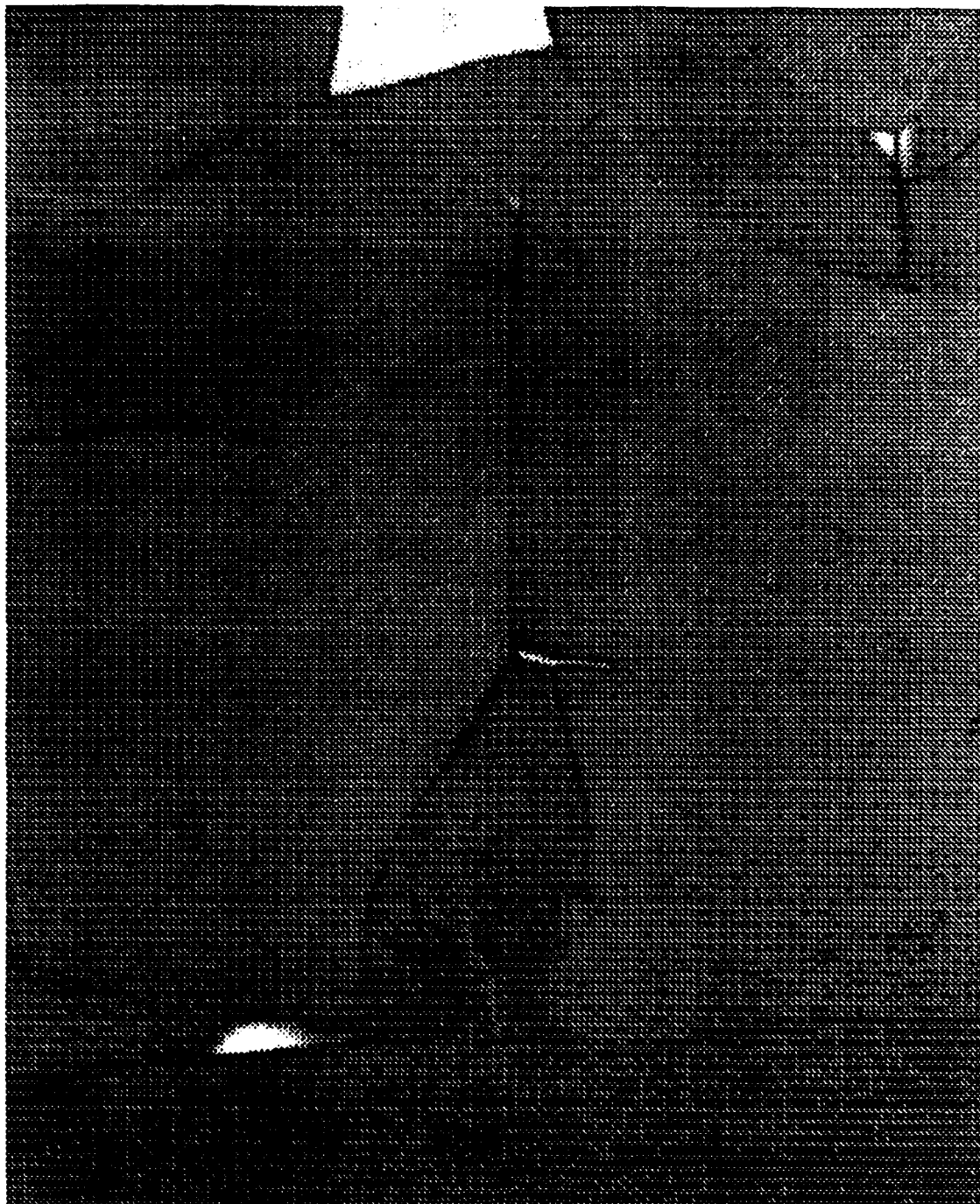


Figure 10. Low IBE annealed a-SiC:H, 0.35 μm thick. The absence of through-the-thickness cracks running along orthogonal $\langle 110 \rangle$ directions makes the determination of the residual strain more difficult in these specimens.



Figure 11. Measurement of the circumferential buckling wavelength λ allows calculation of the Young's modulus of compressively delaminated coatings.

a.



b.

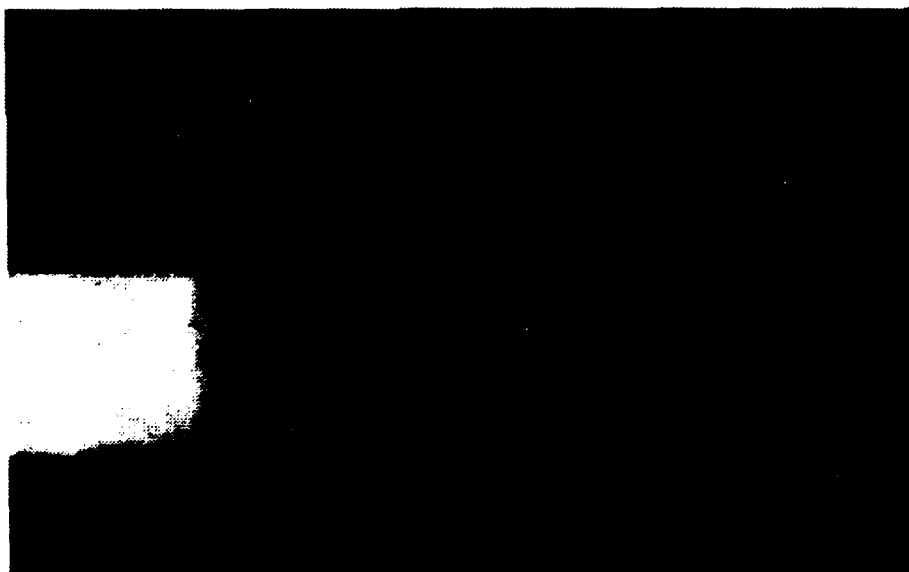


Figure 12. High IBE annealed a-SiC:H, 0.29 μm thick. The delaminated length L is 145 μm (a) and the change in length ΔL is 0.97 μm (b). The residual strain in this specimen is 0.67%.

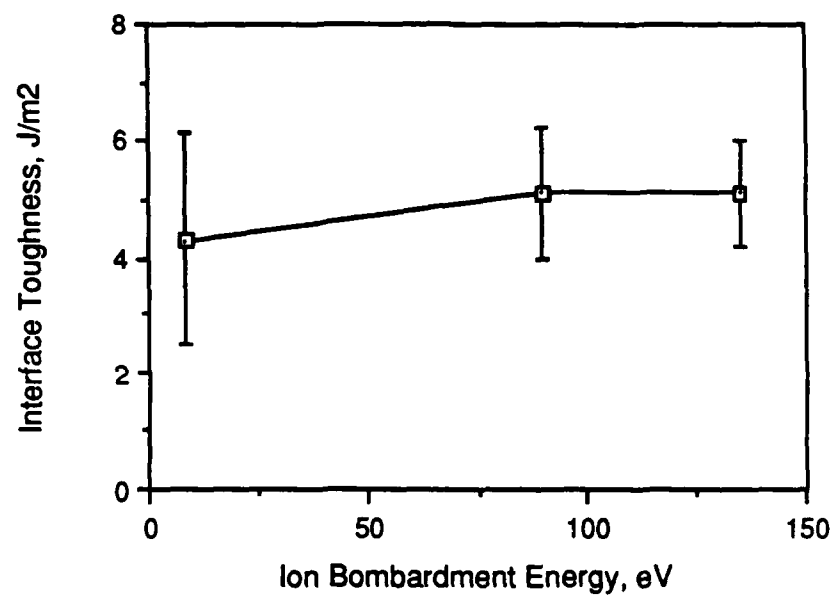


Figure 13. Critical specific fracture separation work, or the intrinsic interface toughness, G_{c0} .

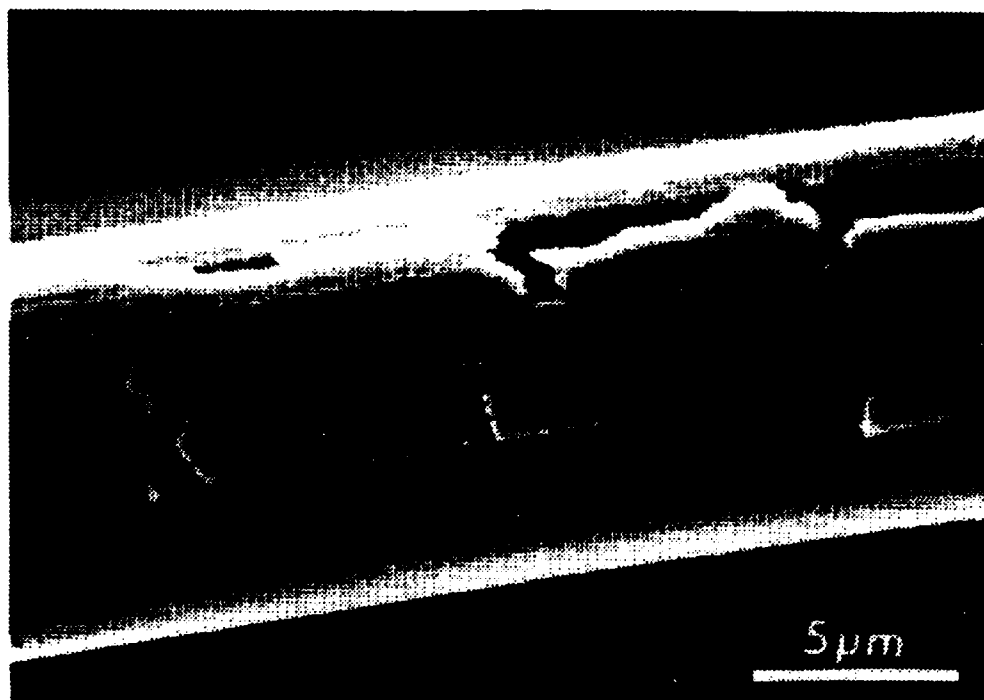


Figure 14. SEM micrograph of 0.33 μm thick annealed low IBE a-SiC:H on a 10 μm diameter P-55 pitch based graphite fiber.

Table 1. Deposition conditions

	low IBE	moderate IBE	high IBE
gas flow			
silane	4.2 sccm	4.2 sccm	4.2 sccm
methane	6.7 sccm	6.7 sccm	6.7 sccm
argon	10.9 sccm	10.9 sccm	10.9 sccm
pressure	50 mTorr 6650 Pa	50 mTorr 6650 Pa	50 mTorr 6650 Pa
RF power			
target	100 W	100 W	100 W
substrate	gnd	25 W	50 W
IBE	8 ± 3 eV	90 ± 10 eV	135 ± 15 eV

Table 2. Materials Properties of a-SiC:H

	low IBE	moderate IBE	high IBE
stress, GPa			
as-depos.	-0.55±.20	-1.9±.39	-2.1±.32
annealed	0.58±.19	2.6±.42	2.7±.33
t_{crit} , μm			
annealed	0.35±.05	0.30±.04	0.28±.03
strain, %			
annealed	2.1±.4	0.65±.03	0.68±.03
E, GPa			
annealed	19±7.2	300±51	285±37
G_C , J/m ²			
annealed	4.3±1.8	5.1±1.1	5.1±.9

In Situ HVEM Study of Fracture in the SiC Coated Graphite Fiber/ Aluminum Composite

J. MEGUSAR, Q. LI, AND J. A. CORNIE,
Massachusetts Institute of Technology, Cambridge, MA

K. H. WESTMACOTT
University of California, Berkley, CA

Presented at the 12th Annual Conference on Composites and Advanced Ceramics
Cocoa Beach, Florida, January 17-20, 1988

A SiC coated graphite fiber/ aluminum composite was processed by plasma enhanced chemical vapor deposition (PECVD) of silicon carbide followed by the aluminum pressure infiltration. Miniature tensile specimens were tested in-situ in the high voltage electron microscope at the NCEM. Preliminary studies showed that fracture in the SiC coated graphite fiber/ aluminum composite advances by decohesion of the graphite fiber/ amorphous SiC interface. These studies on deformation and fracture will serve, in addition to data on interface composition and structure, as a basis for modeling interface properties.

In-situ high voltage electron microscopy (HVEM) study of fracture in the SiC coated graphite fiber/aluminum composite is a part of the ongoing research on tailoring and modeling of interfaces in metal matrix composites. These observations will serve, in addition to data on interface composition and structure, as a basis for modeling interface properties.

As a model system, graphite fibers were coated with a layer of the amorphous SiC by using plasma enhanced chemical vapor deposition (PECVD) and embedded in the pure aluminum matrix by pressure infiltration. Miniature tensile specimens of the SiC coated GR/Al composite were tested in-situ in the high voltage electron microscope at the NCEM, Lawrence Berkley Laboratory. Observations on fracture initiation and propagation were

video recorded. In this paper, we will present and discuss these observations as they relate to the interfaces in the SiC coated GR/Al composite. Further more, we will discuss other experiments in progress which are also aimed at advancing our understanding of deformation and fracture behavior in metal matrix composites.

EXPERIMENTAL PROCEDURE

Processing of the SiC coated GR/Al composite included coating the graphite fibers and pressure infiltration of the metal matrix. Graphite fibers, grade Pitch 55, were coated with a thin layer of silicon carbide by plasma enhanced chemical vapor deposition. The process of the PECVD system used has been described elsewhere [1]. Coated graphite fibers were annealed for 0.5 hour at 873 K to remove hydrogen. Graphite preforms were preheated to 623K and pressure infiltrated by pure aluminum (99.9%) at 3.6 MPa over a period of 1.5 minutes. The temperature of the liquid aluminum prior to infiltration was 963K. Details of the pressure infiltration technique used have been described elsewhere [2].

Microstructural characterization was carried out by using JEOL 200CX transmission electron microscope. TEM discs were prepared by dimple grinding technique, followed by ion thinning at 4KV and at a liquid nitrogen temperature.

Miniature tensile specimens were tested in-situ in the KRATOS 1.5 MeV high voltage electron microscope at the National Center for Electron Microscopy (NCEM) at the Lawrence Berkley Laboratory. Straining experiments were carried out at room temperature and at 1.5 MeV accelerating voltage. Miniature tensile specimens had the following dimensions: 9mm length x 1 mm width (gauge section) x 0.1 mm thickness. Several tensile specimens were prepared, with the gauge section reduced to several microns by subsequent ion thinning.

RESULTS

Figure 1 is a low magnification TEM micrograph showing the graphite fiber, SiC coating and the aluminum matrix in the SiC coated GR/Al composite. The SiC coating is $\sim 0.13 \mu\text{m}$ thick and its structure is fully amorphous under the given processing conditions. There are two interfaces of interest: a) Interface 1, between the polycrystalline graphite fiber and the amorphous SiC coating, and b) Interface 2, between the amorphous SiC coating and the aluminum matrix. High resolution electron microscopy studies to characterize the structure of these interfaces are in progress [3]. Analytical electron microscopy [3] showed no evidence of appreciable diffusion occurring during plasma enhanced chemical vapor deposition of the SiC layer on graphite fibers. Pressure infiltration, on the other hand, resulted in an interdiffusion layer, approximately 40 nm wide, at the amorphous SiC/aluminum interface.

In-situ HVEM observations on fracture in the SiC coated GR/Al composite were video recorded and the important results are shown in Figures 2, 3 and 4. A relatively low magnification (2,500x) was chosen for this preliminary study in order to obtain an overall view, including several graphite fibers, of the fracture process. Figure 2 (top) shows the initiation of the fracture, with graphite fibers oriented perpendicular to the tensile axis. Specimen thickness was $\sim 1 \mu\text{m}$. The fracture path in a fully separated specimen is shown Figure 2 (bottom). It is evident that crack advanced along the graphite fiber/aluminum interface. Electron diffraction of the aluminum side of the fracture surface revealed a broad halo around the central spot, indicative of the amorphous SiC. This suggests, that separating took place along the graphite fiber/ amorphous SiC interface rather than along the amorphous SiC/ aluminum interface. Figures 3 and 4 are dark-field micrographs showing crack initiation and early stages of crack propagation in the SiC coated GR/Al composite. In particular, Figure 3 shows several touching fibers which are inclined to the tensile axis. (In this case, foil thickness exceeded $5 \mu\text{m}$ and it resulted in a somewhat lower resolution.) Graphite fibers shown in Figure 4 are perpendicular or inclined to the tensile axis.

Observations from Figures 3 and 4 confirmed that fracture in the SiC coated GR/Al composite propagated along the graphite fiber/aluminum interface rather than through graphite fibers. Graphite fibers in the present study were either perpendicular or inclined to the tensile axis, and their distribution in the aluminum matrix varied from single and well separated fibers to clusters of touching fibers.

AES survey scans were taken on a graphite fiber in one of the fracture specimens. Figure 5 (top) is a SEM fractograph of the specimen shown in Figure 3 and it indicates the location (A) where the AES scans were taken. A strong carbon peak and a small oxygen peak in Figure 5 (bottom) confirm the TEM observations, namely, that the decohesion took place along the graphite fiber/ amorphous SiC interface.

DISCUSSION

In general, properties of the composite materials depend critically on the properties of interfaces. In optimizing the mechanical behavior of the metal matrix composites, for example, one has to consider a transfer of load from the metal matrix to the reinforcing fibers to maximize strength and, on the other hand, a deflection of crack at the fiber/ metal matrix interface in order to maintain the composite integrity [4]. This requires a careful tailoring of the interface properties. Such tailoring should be based on a detailed knowledge of the interface structure and composition and on a thorough understanding of the deformation and fracture processes.

Preliminary in-situ HVEM studies reported in this paper showed that, under the given processing conditions, the fracture in the SiC coated GR/Al composite advances by decohesion of the graphite fiber/ amorphous SiC interface. These experiments also showed that crack propagation in the SiC coated GR/Al composite is sufficiently slow to allow an experiment in which the specimen is strained incrementally and the microstructure (i.e. dislocation structure) then examined by tilting the specimen to establish appropriate

diffraction conditions. In this way, it should be possible to study deformation processes associated with fracture initiation and propagation. There is also evidence of thermo-visco-plastic residual stresses in the as-cast graphite fiber/ aluminum composite [5] leading to dislocation generation in the aluminum matrix. New specimens of the SiC coated GR/Al composite have been processed, with the inter-fiber spacing increased up to ten times the fiber diameter in order to avoid overlapping of the deformation fields associated with individual graphite fibers. An in-situ HVEM straining experiment is being planned to study dislocation generation in these specimens.

An independent straining experiment has been initiated in which the JEOL 200CX electron microscope is operated in a scanning mode [6]. Plastic strains at the aluminum/ fiber interface and the extent of the plastic zone are being studied during the stepwise straining of the miniature tensile specimens. The results of these studies will be integrated with the in-situ HVEM observations on dislocation generation and will serve, in addition to data on interface structure and composition, as a basis for modeling interface properties.

ACKNOWLEDGMENTS

We gratefully acknowledge Dr. H. S Landis and Dr. L. J. Masur for their assistance with the composite processing and Mr. D. Ackland for his assistance with the in-situ HVEM straining experiments.

This research was sponsored by the Office of Naval Research, under Contract No. N00014-84-K-0495.

REFERENCES

- [1] H. S. Landis, Ph.D. Thesis, M.I.T., 1987.
- [2] L. J. Masur, Ph.D. Thesis, M.I.T., 1987.
- [3] Q. Li, J. Megusar, H. S. Landis, L. J. Masur and J. A. Cornie, unpublished data, 1988.
- [4] T. Erturk, V. J. Gupta, A. Argon, and J. A. Cornie, "Tailoring Interface Properties for Damage Containment in Graphite/ Aluminum Metal Matrix Composites", Proceedings of the 6th International Conference on Composite Materials ICCM-VI, Imperial College, London (Pub. by Elsevier Applied Science), pp. 2.156-2.168, 1987.
- [5] E. Zywiec, "Thermo-Visco-Plastic Residual Stresses in Metal Matrix Composites", M.S. Thesis, M.I.T., 1986.
- [6] Q. Li, J. Megusar and J. A. Cornie, unpublished data, 1988.

FIGURE CAPTIONS

- Figure 1 - TEM micrograph showing the graphite fiber, amorphous SiC coating and aluminum matrix in the SiC coated GR/Al composite.
- Figure 2 - TEM micrograph showing a fracture path in the SiC coated GR/Al composite, with graphite fibers oriented perpendicular to the tensile axis.
- Figure 3 - TEM micrograph showing initiation and propagation of fracture in the SiC coated GR/Al composite, with graphite fibers inclined to the tensile axis.
- Figure 4 - TEM micrograph showing initiation and propagation of fracture in the SiC coated GR/Al composite, with graphite fibers perpendicular or inclined to the tensile axis.
- Figure 5 - SEM fractograph (top) of the specimen shown in Figure 3; AES survey scan on a graphite fiber (bottom).

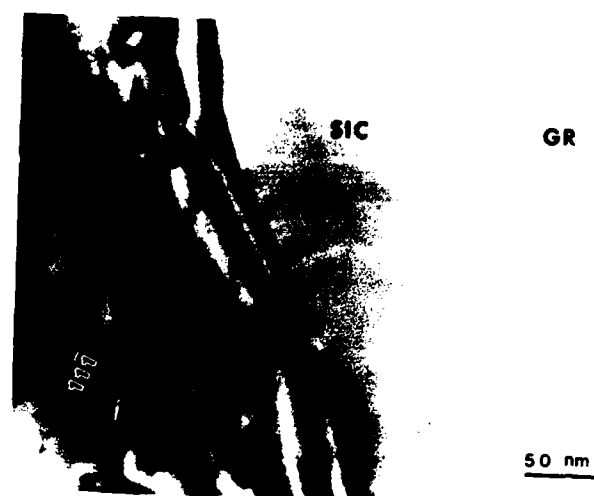


Figure 1 - TEM micrograph showing the graphite fiber, amorphous SiC coating and aluminum matrix in the SiC coated GR/Al composite.

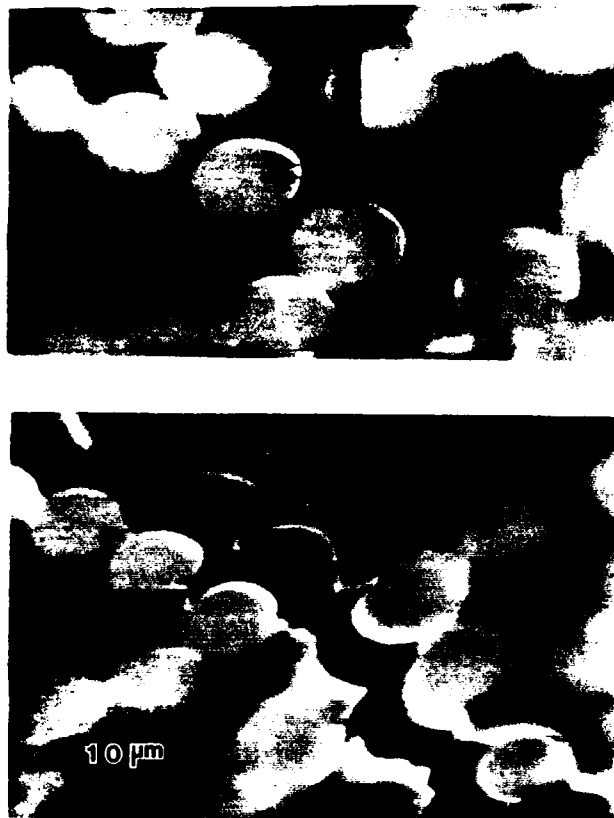


Figure 2 - TEM micrograph showing a fracture path in the SiC coated GR/Al composite, with graphite fibers oriented perpendicular to the tensile axis.

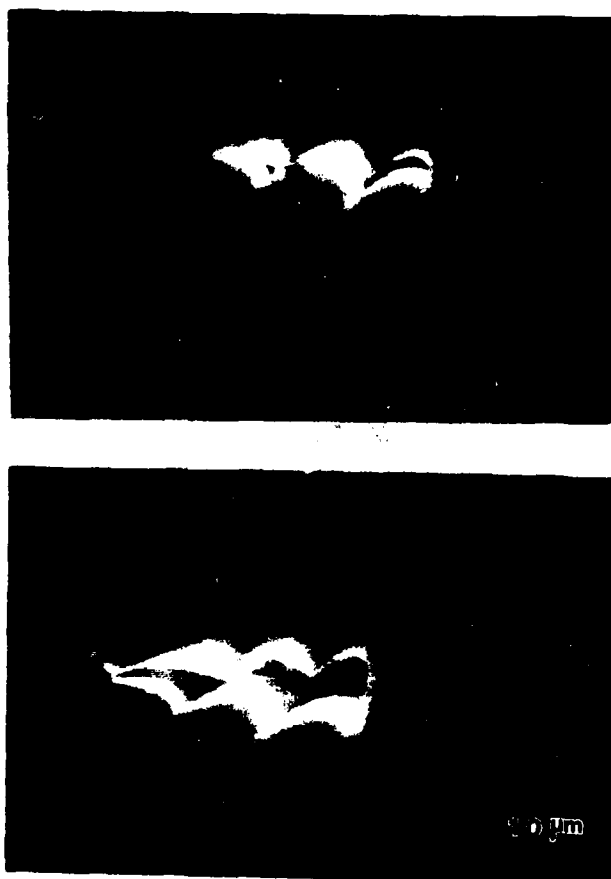


Figure 3 - TEM micrograph showing initiation and propagation of fracture in the SiC coated GR/Al composite, with graphite fibers inclined to the tensile axis.

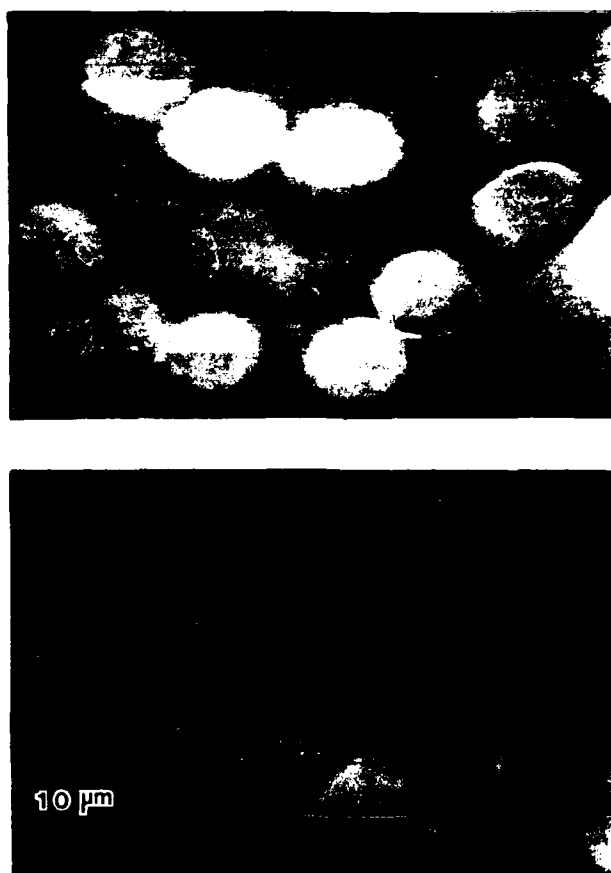


Figure 4 - TEM micrograph showing initiation and propagation of fracture in the SiC coated GR/Al composite, with graphite fibers perpendicular or inclined to the tensile axis.

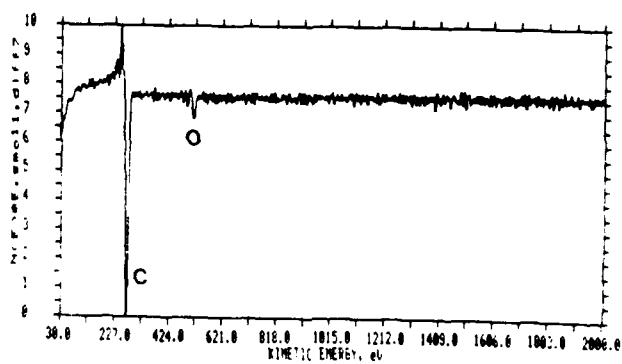
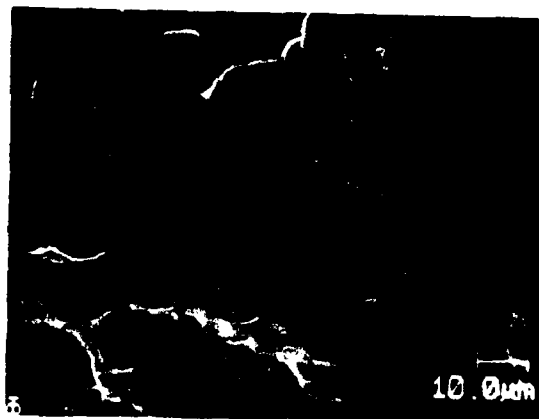


Figure 5 - SEM fractograph (top) of the specimen shown in Figure 3; AES survey scan on a graphite fiber (bottom).

INTERFACE CHEMISTRY OF INORGANIC COMPOSITE MATERIALS

Andreas Mortensen

Department of Materials Science and Engineering
 Massachusetts Institute of Technology, Cambridge, MA 02139, USA.

ABSTRACT

Interfaces in metal and ceramic composites differ from interfaces in polymer matrix composites inasmuch as: (i) fiber degradation due to chemical reaction with the matrix at processing temperatures is frequent and (ii) bonding at the interface is generally chemical in nature (i.e. features primary chemical bond formation across the interface). Elementary analysis of requirements placed on the interface for mechanical property optimization indicate that, for toughening by fiber debonding and pull-out, very weakly bonded interfaces are needed. Sufficiently weak interfaces can be obtained by using interfacial layers of materials such as graphite or boron nitride which feature strongly anisotropic chemical bonding. Several tough inorganic composite utilize such interfaces. With large fibers in ductile matrices, however, strong interfaces are desirable if the matrix can provide sufficient resistance to crack propagation.

1. INTRODUCTION

The interface in polymer matrix composites is at this day engineered to a level of sophistication that is rather impressive in comparison with what is generally achieved with inorganic matrix composites. The chemistry of thermosetting polymer resin bonding to hydrophilic glass fiber surfaces via silane coupling agents, as well as the various oxidative treatments that are applied to carbon fibers, have been shown to influence processing and properties of polymer matrix composites to a significant degree via complex chemical tailoring of the bond between the matrix and the fiber (Plueddemann 1974; Hull 1981; Knox 1982; Chawla 1987). Reasons for this state of affairs are numerous and include the head-start research on polymer matrix composites has had, as well as composite processing temperatures that are much lower and do not present fiber-matrix chemical compatibility problems. There are, however, a few other differences between these two types of composites which may point to a slightly different approach in chemical tailoring of the interface for inorganic composites.

Since the volume on interfaces in metal matrix composites edited in 1974 by Metcalfe, no review of interface chemistry nearly as extensive has been published for either metal or ceramic composites, in spite of the fact that such a work would presently be very different in scope and content. Many of the concepts, of the chemical processes, etc. described in that volume still are true and relevant today, such as the recurrent concern with excessive fiber-matrix reactivity in inorganic composites, which places severe restrictions on possible materials systems and processing conditions. New reinforcements, new processing methods and novel characterization

techniques, coupled with a better understanding of the requirements placed on the interface in composites have however emerged since then, justifying a summary of the topic that would be both more extensive, more multidisciplinary and longer: a task much beyond what is attempted here. The present article will therefore seek to briefly summarize in very broad terms where the question stands at present. Specifically, the logic underlying some of the most successful inorganic composites produced to date will be outlined, to provide some indication of how the properties of inorganic composites can be improved by proper chemical engineering of their interface. For simplicity, the discussion is limited to the case of parallel fiber reinforced composites.

2. MECHANICAL REQUIREMENTS AT THE INTERFACE

The first requirement we place on the interface is evidently that the strength of the fibers be preserved. This requirement precludes chemical reactions between the fibers and the matrix that lead to the formation of too thick a reaction layer of low strain to failure, or to the creation of notches on the fiber surface. This requirement, although rather obvious from the point of view of the mechanics of the interface, may be far from obvious from the point of view of processing, as illustrated for example in SiC whisker reinforced RBSN (reaction bonded silicon nitride, Haggerty 1988), Fig. 1. Fiber degradation by chemical reaction with the matrix is still the most frequent cause for poor inorganic composite properties.

Assuming now that fiber strength is preserved, we can place several conflicting requirements on the interface.

2.1. The interface must not be too strong if a strong composite in which toughening mechanisms specific to composite materials and opposing fracture perpendicular to the fibers are to be exploited. This principle has been theoretically and experimentally proven by numerous authors, as summarized in various articles and monographs (Hull 1981; Kelly 1970, 1971; Kelly and Macmillan 1986; Wells and Beaumont 1985 a&b; Evans and McMeeking 1986; Chawla 1987). Resulting fracture energies are very high: polymer matrix composites can feature apparent fracture energies as high as those of unreinforced metals (Ashby and Jones 1980).

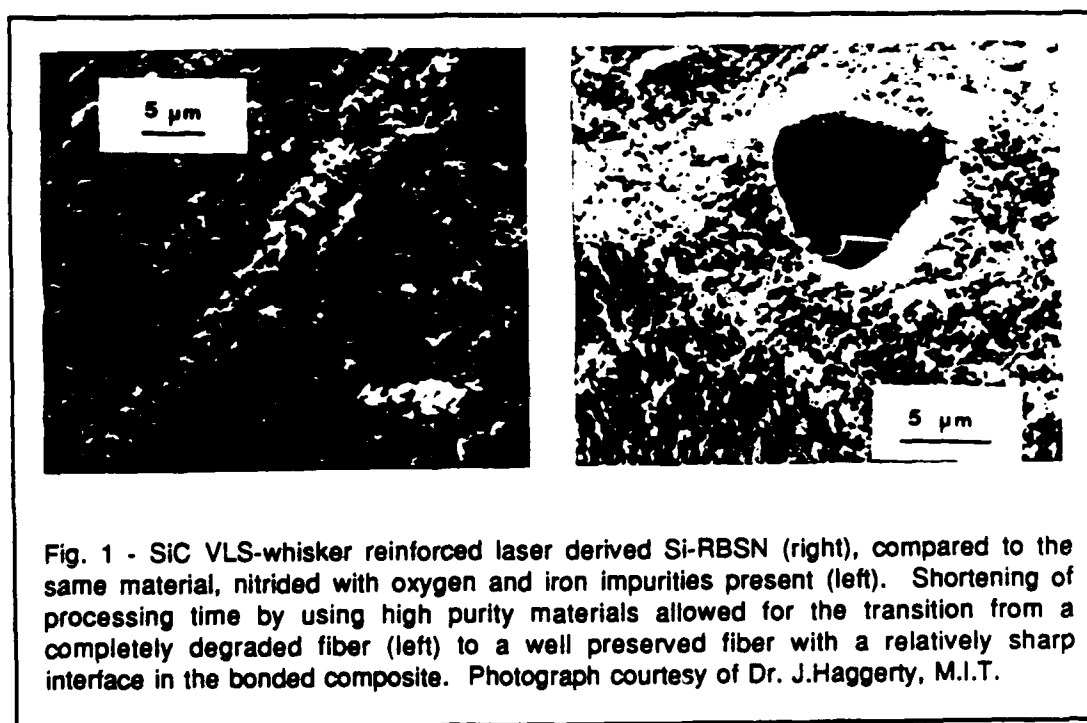


Fig. 1 - SiC VLS-whisker reinforced laser derived Si-RBSN (right), compared to the same material, nitrided with oxygen and iron impurities present (left). Shortening of processing time by using high purity materials allowed for the transition from a completely degraded fiber (left) to a well preserved fiber with a relatively sharp interface in the bonded composite. Photograph courtesy of Dr. J.Haggerty, M.I.T.

The dependence of strength and toughness on the interface varies according to the system and its modeling. One can simplify the role of the interface by consideration of two parameters: the resistance of the interface to initial fracture and its resistance to sliding motion of the matrix against the fiber after debonding. The latter parameter, τ , is mostly a function of physical properties of the interface, in particular its smoothness after debonding. Although τ , as well as other parameters (such as fiber flaw size and distribution) that intervene in composite toughening mechanisms can be varied by chemical tailoring of the interface, the connection between these parameters and interface chemistry is not obvious and has to date not been extensively exploited.

Composite toughening mechanisms are dependent on initiation of debonding at the fiber-matrix interface. Initiation of such debonding has been analyzed by Kendall (Kendall 1975 & 1976; Kelly and Macmillan 1986) in terms of an energy balance, leading to the result that for crack deflection to occur at a planar interface perpendicular to a short crack in an elastically homogeneous material, the fracture energy g_i of the interface must be less than a value given by:

$$\frac{g_i}{g} < \frac{1}{4\pi(1-\nu^2)} \quad (1)$$

where g is the fracture energy of the material, and ν its Poisson ratio. This relation has been modified by Kendall (1975) to account for the effect of crack length as well as differences in modulus across the interface, all effects resulting in variations of this ratio by a factor significantly less than an order of magnitude. Agreement with experimental work by Kendall (1975, 1976) on model samples of rubber was very good. Equation (1) may be an oversimplification of the problem (the effect of elastic inhomogeneity across the interface on crack tip stresses is appreciable, as discussed by Swenson and Rau 1970; Erdogan 1972; Shorshorov, Ustinov, Zirlin and Olefirenko 1979; Erturk, Gupta, Argon and Cornie 1987), but it does indicate that very low values of the interfacial fracture energy g_i are required for crack deflection to occur.

There is little question that for tough brittle matrix composites, these energy absorption mechanisms that are specific to composite materials and rely on weak interfaces are important. With ductile matrix composites, however, the desirability of weak interfaces is less evident since the matrix itself can contribute significantly to the work of fracture by plastic deformation. In W-Cu and B-Al composites, fracture energy has been shown to increase with increasing fiber diameter, matrix volume fraction and matrix ductility. Data clearly indicate that the main contribution to fracture energy in these composites emanates from matrix deformation (Cooper and Kelly 1967; Olster and Jones 1974; Prewo 1976, 1980; McDanells and Signorelli 1976; Kelly and Macmillan 1986). However, most fibers that are present candidates for low cost metal matrix composite reinforcement are rather small in diameter, usually below 20 μm . From data by Cooper and Kelly (1969), the fracture energy of copper reinforced with 50 volume per cent tungsten fibers 20 μm in diameter would be below 10 kJ/m^2 , which is already in the low range for metals (Ashby and Jones, 1980). A weak interface for initiation of crack deflection may therefore also be desirable in a large number of fiber reinforced metals of current interest, because fiber diameters are now usually small.

2.2. The interface must not be too weak. This requirement is primarily dictated by the desire to preserve off-axis strength. Otherwise, the composite will fail at the interface, much as the carbon fiber reinforced aluminum sample in Fig. 2. An illustration is provided by comparing the transverse strength of two aluminum matrix composites: one, in which the reinforcement was 35 Vol% Fiber FPTM alumina fibers and the matrix Al-3Li, exhibited a transverse strength of 142 MPa with fracture mainly through the matrix, indicating a very strong interfacial bond (resulting

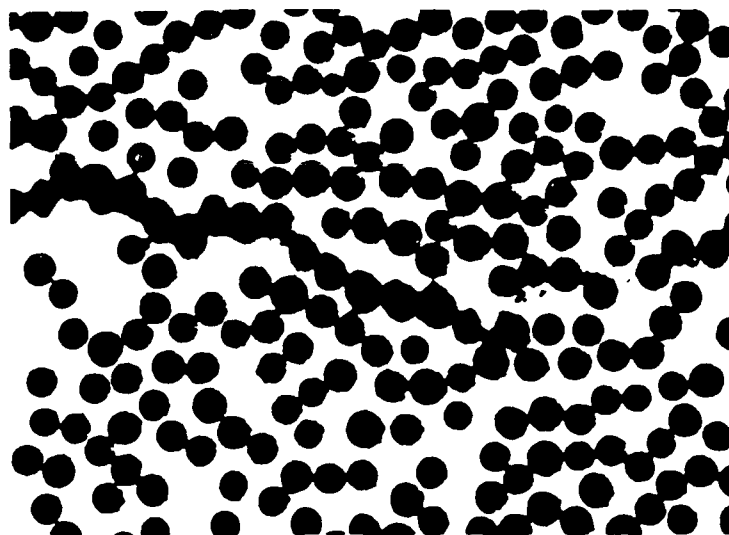


Fig. 2 - Interrupted transverse tension test in Pitch 55 carbon fiber reinforced 2024 aluminum. Fracture initiated at the interface, which is weak in this composite. Average fiber diameter is 10 μm . Photograph courtesy of Prof. T.Erturk, University of Lowell and Dr. J. Cornie, MIT.

from reaction of Li with the Al_2O_3 fibers, Page and Leverant 1985); the other, where aluminum alloys were reinforced with 43 volume percent Pitch 55 carbon fibers, exhibited much lower transverse strengths between 42 and 14 MPa, with fracture mostly through or near the interface as in Figure 2 (Erturk, Cornie and Dixon 1986). Variations of such magnitude can also result from variations in fiber distribution, in particular by suppression of fiber to fiber contact points (Towata and Yamada 1986 a & b), or from differences in matrix strength. Whether fracture takes place along a row of touching fibers as in Fig. 2 or involves some crack propagation through the matrix, analysis of the problem when the interface is weak must again include g_i (neglecting here any dependence of g_i on crack propagation mode). Low g_i results in low composite transverse strength.

It is realized that the present discussion is centered about a simplified description of the incidence of interface properties on composite strength and toughness. On this most elementary level, however, it is clear that for many inorganic composites, there exists an optimum in the bond strength that is desired at the interface, and that the nature of this optimum will vary significantly with the matrix (assuming fibers are brittle). With matrices unable to contribute significantly to composite toughening, that optimum will be at a very low value of g_i . When the matrix can blunt cracks and increase the work of fracture, a strong interface is desired. Chemical tailoring of the interface will therefore hinge upon attainment of a wide range of values of g_i for the various composites discussed here. It therefore is of interest to address the general character of bonding at the interface in inorganic composites.

3. CHEMICAL NATURE OF INTERFACES

3.1. Sharp interfaces. Interfaces that are sharp on the atomic scale are generally classified into several categories, according to the nature of the bond across the interface. The classification more or less follows that of chemical bonds in general, and distinguishes between physical and chemical bonds. The nature of the bond is important in determining the work of adhesion, i.e. the energy expenditure that is necessary to break the bond at the interface. This

work of adhesion is equal to g ; if the interface is brittle, i.e. if no other energy expenditure is necessary to break the interface.

Physical bonding has been shown to be the principal mechanism for cohesion at the interface formed between numerous substrates and low surface tension liquids such as water and organic solvents. The work of adhesion and wetting angles have been quantified, based on various analyses of van der Waals attraction between two surfaces. Theoretically, the treatment of the bond is well established, and its energy can be calculated by use of the London formula, or more complete continuum approaches that have been reviewed by several authors (Krupp 1967; Naidich 1981; Adamson 1982; Delannay, Frozen and Deryttere 1986). The resulting bond energy is lower than 0.6 J/m^2 , and is temperature independent (Naidich 1981). This type of bond is reversible in that debonding and bond formation can be obtained any number of times at the same interface. Hydrogen bond formation can also be included in this category, since resulting works of adhesion are not much higher than with dispersion forces, and since the bond is also reversible (Pritchard 1969). According to Plueddeman's analysis (1974) of silane sizings on glass fibers, the bond between the silane coupling agent and several types of fiber is of the hydrogen bond type when water is present at the interface, which correlates well with observed mechanical properties of these composites and the fact that the fiber-matrix bond has indeed been observed to be reversible (Hull 1981).

Chemical bonding, on the other hand, involves the formation of primary chemical bonds across the interface. The work of adhesion that results is an order of magnitude or two higher, and is temperature dependent. Extensive experimental data has been gathered to prove that wetting and adhesion between ceramics and metals is strongly dependent on primary chemical bonds that are broken or formed in the process, even in cases where no interfacial reaction products are formed (Pask and Fulrath 1962; Naidich and Kolesnichenko 1964; Naidich 1981; McDonald and Eberhart 1965; Ramqvist 1965, 1966, 1969; Warren 1968; Samsonov, Panasyuk and Kozina 1968; Rhee 1970; Goretzki, Exner and Scheuermann 1971; Pepper 1976; Petzow, Suga, Ellsner and Turwitt 1984; Oki, Choh and Hibino 1985; Choh, Kammel and Oki 1987). The nature of the bond itself and hence the work of adhesion vary considerably with the materials forming the interface, and theoretical treatments are thus more system-specific (McDonald and Eberhart 1965; Gubanov and Dunaevskii 1977; Miedema and den Broeder 1979; Warren 1980; Naidich 1981; Delannay et al. 1987).

A contribution to adhesion can arise from electrostatic forces resulting from electron exchange between the two solids (Krupp 1967; Deryagin, Krotova and Smilga 1978). The magnitude of this contribution to the work of adhesion (which could rigorously be viewed as a form of chemical bonding) varies considerably from system to system, and is estimated by Krupp (1967) to be generally negligible because of the high charge densities needed. Experimental work by Mendez, Finello, Walser and Marcus (1982) has, however, demonstrated the importance of electrostatic attraction pressures across an $\text{Al}/\text{Al}_2\text{O}_3/\text{carbon}$ interface.

Whereas for polymer matrix composites, physically bonded interfaces of low adhesion energy are attainable, chemical bonding is generally found with systems and temperatures involved in metal and ceramic matrix composites fabrication. Examples of interfaces where bonding between metals or ceramics can be attributed solely to van der Waals interaction exist, but are rare. These include bonds formed between carbon and metals such as copper, silver, gold, lead or tin that are inert with respect to carbon (Naidich 1981), bonds between sapphire and silver (Pepper 1976), or bonds between ceramic substrates and thin metallic films (Benjamin and Weaver 1959, 1960, 1961, 1963). An example of a sharp boundary across which bonding is chemical in nature is given in Fig. 3. The calculated work of adhesion of the interface between an amorphous silicon carbide coating and a carbon fiber is about 5.5 J/m^2 (Argon, Gupta, Landis and Cornie 1988), clearly higher than can be obtained by physical bonding alone. Another example of a sharp chemically bonded interface can be found with C/Mg composites, where no pull-out was observed in squeeze-cast carbon fiber reinforced magnesium composites, indicating strong bonding at an interface that was sharp when examined in the transmission electron microscope (Diwanji and Hall 1986).



Fig. 3 - Interface between Pitch 55 fiber and an amorphous coating of SiC deposited on the fiber by plasma enhanced chemical vapor deposition. Measurement of bond strength by Argon et al. (1988) gave a work of fracture $g_i = 5.5 \text{ J/m}^2$. Photograph courtesy of Dr. J. Megusar and Mr. Q. Li, M.I.T.

3.2. Thicker interfaces. These result from prolonged interaction of the two phases, with formation of diffusion layers or chemical compounds at the interface. As mentioned above, because matrix and reinforcement are generally reactive and their fabrication involves exposure to elevated temperatures, they very often react to some degree. Such interaction will generally result in a strong interface, and may weaken the fiber either through formation of notches (as is the case with aluminum carbide platelet formation on carbon or silicon carbide fibers), or by formation of too thick an interfacial coating of low strain to failure that adheres well to the fiber (Metcalf 1974; Shorshorov et al. 1979; Ochiai and Murakami 1979 & 1981; Ochiai, Urakawa, Ameyama and Murakami 1980). A comprehensive case by case review of the problem of fiber/matrix reactions is beyond the scope of this article, and references on the subject can be found elsewhere (Metcalf 1974; Chawla 1987; Mortensen, Cornie and Flemings 1988).

In summary, interfaces in inorganic matrix composites are generally strong because they tend to involve chemical bond formation. Another characteristic is that the bond strength is therefore time and temperature dependent, sometimes even in systems that do not form extended interfacial reaction layers. If the kinetics of chemical bond formation are sluggish, the strength of the interface may then be varied as a function of time, which has in some cases been exploited to control the properties of the composite. Examples of time dependent bond strengths with no concomitant interfacial reaction layer formation include work of adhesion of thin metallic films on ceramic substrates (MacDonald and Eberhart 1965; Benjamin and Weaver 1960, 1961), and electroformed and annealed tungsten-copper composites (Cooper and Kelly 1967; Ochiai et al. 1980). Examples of interfaces featuring time dependent bond strengths in which a reaction layer is formed are, however, much more numerous. A last characteristic of the interfaces in inorganic composites is that in most (but not all, Pepper 1976) cases, bonding is irreversible.

4. CONSEQUENCES FOR COMPOSITE PROPERTY OPTIMIZATION

To obtain debonding at the interface, adopting the simplified analysis of equation (1), it becomes clear that if g is not very high, a very weak interface is indeed necessary to obtain a tough composite. Roughly, g_i should be at least ten times smaller than g , which is low to begin with if we equate this term with the fracture energy of a generally brittle fiber. A lower bound on g_i is given by the work of adhesion at the interface $W_a = \gamma_{fa} + \gamma_{ma} - \gamma_{fm}$, where γ denotes surface energy and subscripts f, a and m denote fiber, ambient atmosphere and matrix respectively. With formation of a chemical bond at the interface, its work of adhesion will be at least on the order of 1 to 10 J/m², which is within an order of magnitude of g for most brittle ceramic materials (Kingery, Bowen and Uhlmann 1976; Ashby and Jones 1980). Any ductility in one of the two neighboring phases at the interface will furthermore increase g_i significantly (Petzow, Suga, Elssner and Turwitt 1984). Because most interfaces in inorganic composites comprise a chemical bond, it is unlikely that a satisfactorily low g_i can be obtained without resorting to deliberate tailoring of the interface properties. This can be accomplished by introducing, at the interface, a thin layer of a third phase with low intrinsic toughness, or such that bonding with matrix or fiber will be very weak. Using the relationship

$$g \approx \frac{E b}{10} \quad (2)$$

for true brittle fracture toughness where E is Young's modulus and b is the interatomic spacing (Cottrell 1964; Kelly and Macmillan 1986) it is seen that an order of magnitude's difference between g_i and g would require a bond strength within such an interfacial layer that is unusually low for the materials under consideration: the scale over which Young's modulus for inorganic materials varies is hardly more than one order of magnitude (Ashby and Jones, 1980), and b varies over an even smaller range. It seems therefore that the most attractive materials for interface optimization are to be found among those for which the bonding structure is highly anisotropic: graphitic or turbostratic carbon, boron nitride or perhaps sapphire. A thin layer of graphite at the interface, with basal planes oriented parallel to the surface of the fiber, is ideal in that it provides very low bond strength transverse to the interface ($E \approx 10$ GPa; Riggs, Shuford and Lewis 1982), with very high bond strength parallel to the interface ($E \approx 1000$ GPa; Riggs et al. 1982). This layer will be intrinsically weak, and will also be likely to form a weak bond with neighboring phases. Interfacial layers of carbon, either graphitic with basal planes parallel to the interface or in one case, amorphous, have been used in several of the most successful inorganic composites produced to date:

1 - It has been found that the strength of SiC filaments fabricated by chemical vapor deposition on a substrate fiber can be doubled by depositing a thin layer of approximately pure carbon on the surface of the fiber. This finding forms the basis for the remarkable properties of AVCO's SCS series of silicon carbide monofilaments (UTS > 4 GPa). The increase in strength that results from this thin (< 1 μ m) layer of carbon has been attributed to the healing effect it exerts on uncoated SiC filament surface defects (Cornie, Suplinskas and DeBolt 1981; Nutt and Wawner 1985). The structure of the fibers and their coating has been investigated in detail by Nutt and Wawner (1985), who found that the carbon layer consisted mostly of pyrolytic type graphite with its basal planes oriented parallel to the fiber surfaces. These fibers thus contain, before incorporation into any matrix, a very weak crack-deflecting surface layer, and should yield elevated values of fracture toughness so long as this layer is not degraded by interfacial chemical reactions with the matrix. With various protective barriers over the carbon layer (most often in the form of carbon-rich Si-C coatings), these fibers have been combined with aluminum alloys (Cornie et al. 1981, Nutt and Wawner 1985), titanium alloys (Naslain, Paillet and

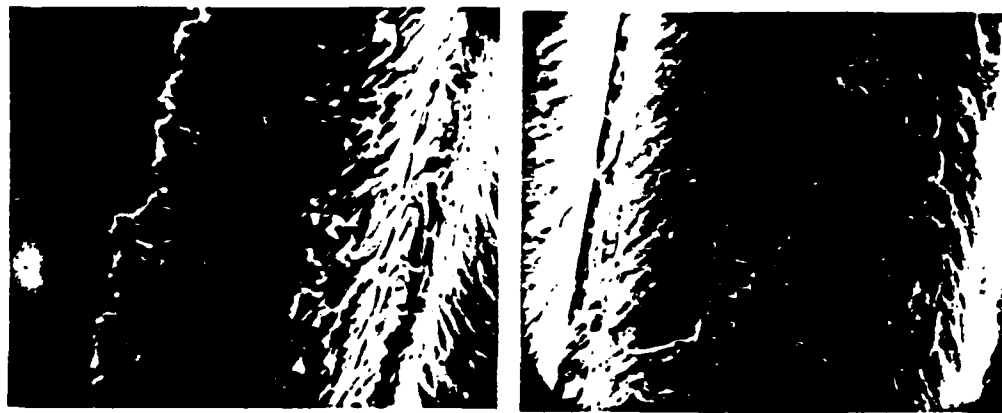


Fig. 4 - Debonded SCS-2 silicon carbide filaments in a cast aluminum alloy 357 matrix composite. The matrix side of the fracture surface (left) is still bonded to a thin crazed layer of the fiber coating, indicating that fracture was through the fiber coating. A denuded fiber from the same sample (right) displays uneven cracking through the SCS coating. 20 μ m

Quenisset 1979; Smith, Froes and Cammett 1982; Quenisset, Soumelidis and Naslain 1985; Martineau, LePetitcorps, Pailler and Naslain 1985), titanium aluminide (Brindley 1987), glass matrices (Prewo 1980; Prewo, Brennan and Layden 1986) as well as reaction bonded silicon nitride (Corbin, Rossetti and Hartline 1986). In cases where the carbon layer survived processing, fiber debonding was observed on fracture surfaces, which took place at the interfacial carbon-rich interfacial layer as seen in Fig. 4. In ceramic matrix composites, the presence of this carbon layer resulted in composites with high strength and toughness. In metal matrix composites, such interfacial debonding is, however, less essential for high toughness since matrix ductility can contribute significantly to composite toughening with these rather large diameter filaments ($d=140 \mu\text{m}$).

2 - The structure of carbon fibers varies depending on the diverse heat-treatments that have been used in their production. Detailed examination by transmission electron microscopy of PAN (polyacrylonitrile-derived) carbon fibers heat treated at various temperatures have shown that type I fibers (high modulus, elevated heat treatment temperature) contain a skin layer between 150 and 250 nm thick of highly oriented turbostratic graphite with relatively large crystallite sizes and basal planes parallel to the surface. This skin layer is absent in type II fibers (lower modulus, lower heat treatment temperature; Bennett and Johnson 1979; Johnson 1980). Differences in surface structure, in particular in the type of exposed bonds, influence the initial chemical reactivity of the fibers. Their chemical affinity to oxygen, silicon carbide or aluminum decreases as the modulus of the fibers increases (Amateau and Dull 1977; Baker and Bonfield 1978; Kohara and Muto 1986; Maruyama and Rabenberg 1986; Chawla 1987; Katzmann 1987). This can be explained by a higher degree of perfection in the orientation of basal planes as the modulus of the fiber increases, especially at the fiber periphery where basal planes become more parallel to the surface. As the number of exposed graphite plane edges is reduced, fiber reactivity decreases. After infiltration by aluminum using the TiB process, it has been found that fiber pull-out increases, transverse strength decreases and longitudinal composite strength increases as fiber modulus increases in PAN carbon-aluminum composites (Amateau 1976; Amateau and Dull 1977; Goddard 1978; Shindo 1986; Honjo and Shindo 1986; Shindo and Honjo 1986; Murakami, Nakao, Imataki, Shindo, Honjo and Ochiai 1986). Depositing a layer of pyrolytic carbon on PAN II fibers, thus creating a surface skin similar to that in type I fibers, has been shown to increase fiber strength and to render PAN II fibers essentially similar to PAN I fibers in aluminum: rule of mixtures longitudinal strengths are observed, with increased pull-out and decreased transverse strength. Interpretation of the results is complex and involves

consideration of several phenomena other than the weakness of bonding with and within the outer skin of the carbon fibers: (i) the fibers react with aluminum and the extent of fiber degradation will vary with the orientation of the basal planes at the surface of the fibers; (ii) as the modulus of the fiber is increased, the requirements placed on the interface vary (for a simplistic analysis, combine equations (1) and (2)). Nonetheless, the presence of a layer of carbon with basal planes parallel to the fiber surface, whether initially present in the fibers or deposited onto their surface, has invariably resulted in longitudinal strengths in agreement with rule of mixtures predictions, as well as extensive debonding and pull-out of carbon fibers in aluminum.

3 - In ceramic matrix composites, toughening mechanisms must rely on crack deflection. Weak interfaces are therefore essential for attainment of high longitudinal composite strength and toughness in these composites. Extremely good properties have indeed been achieved on such materials by several authors, in particular by researchers at UTRC, using SiC fibers or whiskers to reinforce several glass or "ceraming" glass matrices (Prewo and Brennan 1980, Brennan and Prewo 1982; Prewo et al. 1986; Brennan 1986, 1987; Prewo 1986, 1987). Detailed studies of the interface by Brennan (1986, 1987) have shown that achievement of high strength and toughness, with extensive fiber debonding and pull-out, was contingent upon the presence of a thin layer of carbon at the interface which either resulted from fiber-matrix interaction when using non-stoichiometric polymer precursor derived fibers and appropriate matrix compositions, or by deliberate coating of the fibers with carbon. Exposure to air at temperatures at or above 1273 K results in brittle composites, due to degradation of this carbon-rich layer and replacement by a strongly bonded interface (Prewo 1986, Luh and Evans 1987, Grande, Mandell and Hong 1988). Chemical reactions leading to formation of the carbon layer are complex, and result in multilayered interfaces as seen on Fig. 5. The very low values of $g_i \leq 0.4 \text{ J/m}^2$ measured by Marshall and Evans (1985) on these composites from debond lengths observed after matrix cracking are on the order of the value derived from equation (2) with $b = 3.4 \text{ \AA}$ and $E = 10 \text{ GPa}$ typical of the weak bond in graphite (the carbon rich layer in these composites contains other elements and is reported to be amorphous, however). Use of alumina or silicon nitride reinforcements with similar matrices by the same authors led to brittle failure in the absence of a carbon rich layer (Prewo et al. 1986) *.

Such composite property optimization via a weak interface is not a valid approach for all inorganic composites, however. As pointed out earlier, a price must be paid when using weak interfaces for crack deflection along the fiber, principally in the form of significantly reduced off-axis properties. In several metal matrix composite systems with large fiber diameters, increased interface bond strength has led to increased composite strength and fracture energy, until fiber degradation began due to fiber/matrix chemical reactions (McDanel and Signorelli 1976; Zaboletskii, Salibekov, Kansevich, Lyuttsau and Fadyukov 1978; Naslain et al. 1979; Quenisset et al. 1985). In these cases, the limit in permissible interfacial strength is much higher than with composites that rely on crack deflection for longitudinal toughness. Coatings of interest for such composites should mainly aim to preserve the strength of the fibers and facilitate processing of the composite. Numerous examples of such coatings exist, such as the outer Si-C coating on AVCO's SCS fibers (Cornie et al. 1981; Nutt and Wawner 1985). Other approaches to the problem involve slowing down the kinetics of fiber degradation via judicious choice of processing methods. Some fabrication methods use solid metal, preferably coated with its oxide, in conjunction with processing methods that preserve this oxide and use low temperatures. The diffusion bonding process for Al-B is an example (Metcalf 1974; Hall, Kyono and Diwanji 1987). Other approaches include casting liquid metal around cold fibers, a

* With carbon fibers in glass, the differences found in aluminum matrices between high strength and high modulus fibers have not been observed. In fact, the high strength fibers gave somewhat better results in work by Phillips (1974). Phillips interprets these data on the basis of mechanical keying effects with no chemical bond at the interface, due to tensile residual stresses at the interface. This interpretation fits the data nicely, and indicates that differences between the fibers in these composites are probably linked more to their coefficients of thermal expansion than to their interface chemistry.

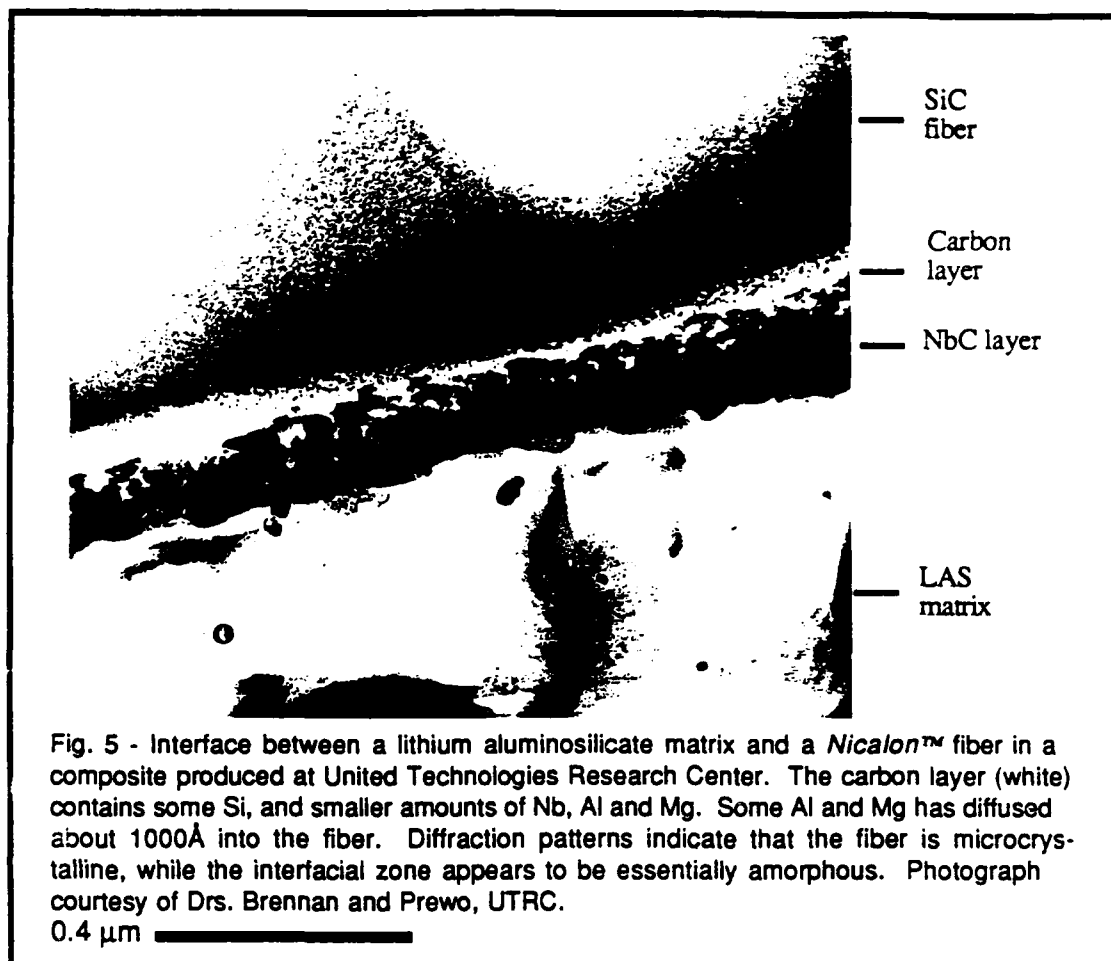


Fig. 5 - Interface between a lithium aluminosilicate matrix and a *Nicalon*TM fiber in a composite produced at United Technologies Research Center. The carbon layer (white) contains some Si, and smaller amounts of Nb, Al and Mg. Some Al and Mg has diffused about 1000Å into the fiber. Diffraction patterns indicate that the fiber is microcrystalline, while the interfacial zone appears to be essentially amorphous. Photograph courtesy of Drs. Brennan and Prewo, UTRC.

0.4 μm

method that has been pioneered by Fukunaga and Goda (1985) with 99.99% aluminum and *Nicalon*TM silicon carbide fibers.

It must be emphasized that tailoring of interface chemistry is also strongly dictated by the processing of the composites. For cast composites, for example, wetting of the fiber by the matrix is a critical issue, to lower pressures involved in the process and to fully infiltrate the fiber preform, in particular at fiber contact points (Mortensen and Cornie 1986, Mortensen et al. 1988). Composite processing may in certain instances place requirements on interface chemistry that conflict with optimization of composite properties. For example, chemical reactions between ceramic fibers and molten metals aid wetting, which most often will result in poor composite properties due to fiber degradation or too strong an interface. It is also emphasized that the present analysis of the interface is simple, and that all fundamentally important aspects of processing-structure-property relationships in inorganic composites that are not directly related to interface chemistry have been ignored in this review. Residual stresses in the composite, the complexity of a proper mechanical treatment of the interface, as well as the influence of geometrical distribution of the fibers should all be taken into account in a less concise treatment of the problem.

5. CONCLUSION

For strong and tough fiber reinforced inorganic materials, the interface must presently seek satisfaction of several requirements:

- 1 - The properties of the fibers must be preserved, i.e. extensive chemical reactions between fiber and matrix must be prevented;
- 2 - Where fiber debonding is necessary for longitudinal strength and toughness, a weak interface is desirable;
- 3 - A strong interface is desirable for good transverse properties;
- 4 - Ease of fabrication, including good wetting of the fibers if the matrix is combined in the liquid state, depends critically on interface chemistry for most economical processing methods.

The criteria to be satisfied will vary, depending on the fiber, the matrix and the application of the composite. There is, therefore, no given set of rules dictating chemical engineering of the interface for optimized properties. However, the bond at the interface is generally chemical in nature, i.e. primary chemical bonds are formed across the interface. This rather general feature of the bond in inorganic composites dictates certain current approaches for interface chemistry control in these composite materials:

(i) where a weak interface is necessary for composite toughness, the strong anisotropy in bonding of certain materials, especially graphite, offers a solution to the problem of crack deflection at the interface. Thin layers of such materials are presently used at the interface of several inorganic composites.

(ii) where the matrix contribution to composite toughness is important, a strong bond is desirable. This category includes that of metal matrix composites with large fibers. In cases where fiber degradation may occur due to chemical reaction with the matrix, protective coatings at the interface and/or careful processing methods are used.

There is at present a surge of interest in the characterization of interfacial properties in inorganic composites (Marshall 1984, Grande et al. 1988, Argon et al. 1988), which will hopefully elucidate on a more quantitative level the requirements we place on the interface. These characterization methods, coupled with a more sophisticated understanding of the interplay between the various processing-structure-property relationships in inorganic composites, will hopefully point to novel ways of controlling and optimizing the interface chemistry of these materials.

ACKNOWLEDGEMENTS

The author is grateful to Dr. James A. Cornie at MIT, Dr. Karl M. Prewo at UTRC and Prof. Kenneth C. Russell at MIT for several interesting discussions on the topic, and to Drs Brennan, Prewo, Cornie, Megusar, Haggerty, Prof. Erturk and Mr. Q. Li for micrographs included in this article. Support from the Aluminum Company of America in the form of the author's chair at MIT is gratefully acknowledged as well.

REFERENCES

- Adamson, A. W. (1982). *Physical Chemistry of Surfaces*, 4th edition. (Wiley-Interscience, New-York) Chapter 6.
- Amateau, M. F. (1976), Progress in the development of aluminum composites using liquid infiltration technology *J. of Composite Materials* **10** (1976), 279-296.
- Amateau, M. F. and Dull, D. L. (1977) The effect of processing on the transverse strength of graphite-aluminum composites In: *Failure Modes in Composites IV* Edited by J.A.Cornie and F.W.Crossman, Proc. TMS/AIME Conf. (Chicago Ill.), 336-358.
- Argon, A. S., Gupta, V. J., Landis, H. S. and Cornie, J. A., Intrinsic toughness of interfaces between SiC coatings and substrates of Si or C fiber, submitted *J. of Materials Science*, 1988.

- Ashby, M. F. and Jones, D. R. H., (1980) Engineering Materials: An Introduction to their Properties and Applications, (Pergamon, Oxford) pages 32 and 126.
- Baker, S. J. and Bonfield, W. (1978) Fracture of aluminium coated carbon fibers *J. of Materials Science* **13**, 1329-1334.
- Benjamin, P. and Weaver, C. (1959) Condensation energies for metals on glass and other substrates *Proc. Roy. Soc. London* **A252**, 418-430.
- Benjamin, P. and Weaver, C. (1960) Adhesion of metal films to glass *Proc. Roy. Soc. London* **A254**, 177-183.
- Benjamin, P. and Weaver, C. (1961) The adhesion of evaporated metal films on glass *Proc. Roy. Soc. London* **A261**, 516-531.
- Benjamin, P. and Weaver, C. (1963) The adhesion of metals to crystal faces *Proc. Roy. Soc. London* **A274**, 267-273.
- Bennett, S. C. and Johnson, D. J. (1979) Electron-microscope studies of structural heterogeneity in PAN-based carbon fibers *Carbon* **17**, 25-39.
- Brennan, J. J. and Prew, K. M. (1982) Silicon carbide fibre reinforced glass-ceramic matrix composites exhibiting high strength and toughness *J. of Materials Science* **17**, 2371-2383.
- Brennan, J. J. (1986) Interfacial Characterization of glass and glass-ceramic matrix/Nicalon SiC fiber composites Tailoring Multiphase and Composite Ceramics, edited by R.E.Tressler, G.L.Messing, C.G.Pantano and R.E.Newnham (Plenum Publishing Corporation) 549-560.
- Brennan, J. J. (1987) Interfacial characteristics of glass-ceramic matrix/SiC fiber composites Interface Science and Engineering 1987 (Lake Placid, N.Y.)
- Brewer, W. D. (1982) Metallurgical and tensile property analysis of several silicon carbide/titanium composite systems In: Mechanical Behavior of Metal-Matrix Composites, edited by J.E.Hack and M.F.Amateau (TMS/AIME Proc. Conf. Dallas, Texas), 39-50.
- Brindley, P. K. (1987) SiC reinforced aluminide composites *Mat. Res. Soc. Symp. Proc.* **81**, 419-424.
- Choh, T., Kammel, R. and Oki, T. (1987) Wettability of graphite to liquid aluminum and the effect of alloying elements on it *Zeitschrift für Metallkunde* **77**, 286-290.
- Corbin, N. D., Rossetti Jr., G. A. and Hartline, S. D. (Jul-Aug. 1986) Microstructure/property relationships for SiC filament-reinforced RBSN *Ceramic Engineering and Science Proceedings* **8**, 958-968.
- Cornie, J. A., Suplinskas, R. J. and DeBolt, H. (1981) "Surface Enhancement of Silicon Carbide Filament for Metal Matrix Composites", ONR Contract N00014-79-C-0691, Summary Report.
- Cooper, G. A. and Kelly, A., (1967) Tensile properties of fibre-reinforced metals: fracture mechanics *J. Mech. Phys. Solids* **15**, 279-297.
- Cottrell, A. H. (1964) Strong Solids *Proc. Roy. Soc. London* **A282**, 2-9.
- Chawla, K. K. (1987) Composite Materials - Science and Engineering (Springer Verlag).
- Delannay, F., Frozen, L. and Deryttere, A. (1987) Review - the wetting of solids by molten metals and its relation to the preparation of metal-matrix composites *J. of Materials Science* **22**, 1-16.
- Deryagin, B. V., Krotova, N. A. and Smilga, V. P. (1978) Adhesion in Solids (Consultants Bureau).
- Diwanji, A. P. and Hall, I. W. (1986) Mechanical properties and the fibre/matrix interface in squeeze-cast graphite-magnesium metal matrix composites Proc. of the Sixth International Conference on Composite Materials ICCM 6, edited by F.L.Mathews, N.C.R.Buskell, J.M.Hodgkinson and J.Morton (Elsevier, London), Vol. 2, 265-274.
- Erdogan, F. (1972) Fracture problems in composite materials *Engineering Fracture Mechanics* **4**, 811-840.
- Erturk, T., Cornie, J. A. and Dixon, R. G. (1986) Interfaces in Metal Matrix Composites edited by A.K.Dhingra and S.G.Fishman, (Proc. Conf. New Orleans TMS/AIME), 239-253.
- Erturk, T., Gupta, V. J., Argon, A. and Cornie, J. A. (July 1987) Tailoring interface properties for damage containment in graphite/aluminum metal matrix composites In: Sixth International Conference on Composite Materials ICCM 6, (London) Vol. 2, 156-168.
- Evans, A.G., and McMeeking, R.M. (1986), On the toughening of ceramics by strong reinforcements *Acta Metallurgica* **12**, 2435-2441.
- Fukunaga, H. and Goda, K. (1985), Formation and role of the solidified layer on a fiber during the fabrication of fiber reinforced metal by the liquid process *J. Japan Inst. Metals* **49**, 78-83.
- Goddard, D. M. (1978) Interface reactions during preparation of aluminium matrix composites by the sodium process *J. of Materials Science* **13**, 1841-1848.
- Goretzki, H., Exner, H.E. and Scheuermann, W., (1971), Electronic structure of refractory carbides and its relation to wetting Modern Developments in Powder Metallurgy Vol. 4: Processes, edited by H.H.Hausner, Plenum Press, 327-337.
- Grande, D. H., Mandell, J. F., Hong, K. C. C., (1988) Fibre-matrix bond strength studies of glass, ceramic and metal matrix composites *J. of Materials Science* **23**, 311-328.

- metal matrix composites *J. of Materials Science* **23**, 311-328.
- Gubanov, A. I. and Dunaevskii, S. M. (1977) Adhesion of a metal and an ionic crystal *Sov. Phys. Solid State* **19** (5), 795-797.
- Haggerty, J. (1988) MIT, Reaction bonded ceramic matrix composites, private communication.
- I.W.Hall, T.Kyono and A.Diwanji, (1987), On the fibre/matrix interface in boron/aluminum metal matrix composites *J. of Materials Science* **22**, 1743-1748.
- Honjo, K. and Shindo, A. (1986) Interfacial behavior of aluminum matrix composites reinforced with ceramics-coated carbon fibers "Composite Interfaces" *Proc of the First Int. Conf. on Composite Interfaces ICCI-1, Cleveland*, edited by H.Ishida and J.L.Koenig (Elsevier, North-Holland) ,101-107.
- Hull, D. (1981) *An Introduction to Composite Materials*, (Cambridge Solid State Science Series, Cambridge University Press), Chapters 1&3.
- Johnson, D. J. (1980) Recent advances in studies of carbon fibre structure *Phil. Trans. Roy. Soc. London* **A294** 443-449.
- Katzman, H. A. (1987) Fibre coatings for the fabrication of graphite-reinforced magnesium composites *J. of Materials Science* **22**, 144-148.
- Kelly, A. (1970) Interface effects and the work of fracture of a fibrous composite *Proc. Roy. Soc. London* **A319**, 95-116.
- Kelly, A. (1971) *Strengthening Methods in Crystals*, edited by A.Kelly and R.B.Nicholson (Applied Science Publishers, London) 433-484.
- Kelly, A. and Macmillan, N. H. (1986) *Strong Solids*, third Edition (Clarendon Press, Oxford).
- Kendall, K. (1975) Transition between cohesive and interfacial failure in a laminate *Proc. Roy. Soc. London* **A344**, 287-302.
- Kendall, K. (1976) Interfacial cracking of a composite *J. Materials Science* **11**, 638-644.
- Kingery, W.D., Bowen, H.K. and Uhlmann, D.R.(1976) *Introduction to Ceramics*, Second Edition, J.Wiley & Sons, N.Y., Chapter 15.
- Knox, C. E. (1982) *Handbook of Composites*, Edited by G.Lubin (Van Nostrand Reinhold) 136-195.
- Kohara, S. and Muto, N., (1986) Degradation of PAN-based carbon fibers by molten aluminum *Comp '86: Eng. Appl. of New Composites* Proc. Conf. University of Patras, 25-29 Aug. 1986.
- Krupp, H. (1967) Particle adhesion - theory and experiment *Advan. Colloid Interface Science* **1**, 79-110.
- Luh, E.Y. and Evans, A.G.(1987), High temperature mechanical properties of a ceramic matrix composite *J. Am. Ceram. Soc.* **70**, 466-469.
- Martineau, P., Le Petitcorps, Y., Pailler, R., and Naslain, R. (1985) The SiC/Ti metal matrix composites: correlation between the filament composition and the composite thermomechanical behavior In: "Developments in the Science and Technology of Composite Materials", *Proc. First European Conference on Composite Materials ECCM 1*, edited by A.R.Bunsell, P.Lamicq and A.Massiah (EACM, Bordeaux), 725-731.
- Marshall, D. B., (1984) An indentation method for measuring matrix-fiber frictional stresses in ceramic composites *Comm. of the American Ceramic Soc.*, **67** (12), C-259-C-260.
- Marshall, D. B. and Evans, A. G., (1985) Failure mechanisms in ceramic-fiber/ceramic-matrix composites *J. of the American Ceramic Society* **68**, 225-231.
- Maruyama, B. and Rabenberg, L. (1986) Oxidation model of interface reactions in aluminum/graphite composites In: *Interfaces in Metal Matrix Composites*, edited by A.K.Dhingra and S.G.Fishman, Proc. Conf. New Orleans 1986 (TMS/AIME), 233-238.
- McDanel, D. L. and Signorelli, R. A. (1976) Improved impact-resistant boron/aluminum composites for use as turbine engine fan blades In: *Failure Modes in Composites III*, edited by T.T.Chiao and D.M.Schuster, Proc. Conf. Las Vegas 1976, (TMS/AIME), 27-57.
- McDonald, J. E. and Eberhart, J. G. (1965) Adhesion in aluminum oxide-metal systems *Trans. Metallurgical Society of AIME* **233**, 512-517.
- Mendez, H., Finello, D., Waiser, R. and Marcus, H. L.(1982) Correlation of electronic state and fracture path of aluminum-graphite interfaces *Scripta Metallurgica* **16**, 855-858.
- Metcalfe, A.G. (1974) *Composite Materials Volume 1 - Interfaces in Metal Matrix Composites*, edited by A.G.Metcalfe (Academic Press, N.Y.), Chapters 1 and 3.
- Miedema, A.R. and den Broeder, F.J.A. (1979) On the interfacial energy in solid-liquid and solid-solid metal combinations *Zeitschrift für Metallkunde* **70**, 4-20.
- Mortensen, A. and Cornie, J.A. (1986), On the infiltration of metal matrix composites *Metallurg.Trans.* **18A**, 1160-1163.
- Mortensen, A., Cornie, J. A. and Flemings, M. C. (February 1988) Solidification of metal matrix composites

- Journal of Metals*, 12-19.
- Murakami, Y., Nakao, K., Imataki, T., Shindo, A., Honjo, K. and Ochiai, S. (1986) Effect of interfacial conditions of the tensile strength of carbon fiber-6061 aluminum alloy composites Composites 1986: Recent Advances in Japan and the United States: Proc. Japan-US CCM3 edited by K.Kawata, S.Umekawa and A.Kobayashi., (Japan Society for Composite Materials), 761-766.
- Naidich, Y.V. and Koiesnichenko, G.A. (1964) Investigation of the wetting of diamond and graphite by molten metals and alloys III Soviet Powder Metallurgy and Metal Ceramics 1 (19), p.191.
- Naidich, J.V. (1981) The wettability of solids by liquid metals Prog. Surf. Membr. Sci. 14, 353-484.
- Naslain, R., Pailler, R. and Quenisset, J.-M. (1979) Chapter XV, Introduction aux Matériaux Composites Vol.2 - Matrices Métalliques et Céramiques, edited by R.Naslain, (Éditions du C.N.R.S.), 313-383.
- Nutt, S.R. and Wawner, F. E. (1985) Silicon carbide filaments: microstructure J. Materials Science 20 1953-1960.
- Ochiai, S. and Murakami, Y., Tensile strength of composites with brittle reaction zones at interfaces J. of Materials Science 14 (1979) pp.831-840.
- Ochiai, S., Urakawa, S., Ameyama, K. and Murakami, Y. Experiments on fracture behavior of single fiber-brittle zone model composites Metallurg.Trans. 11A, 525-530.
- Ochiai, S. and Murakami, Y. (1981) Theoretical prediction of tensile strength of fibers as a function of thickness of brittle zones on fiber surfaces Metallurg.Trans. 12A 1 1161.
- Oki, T., Choh, T. and Hibino, A. (1985) Wettability of aluminium at SiC and the effects of silicon, manganese, iron and copper J. of the Japan Institute of Metals 49, 1131-1137.
- Olster, E.F. and Jones, R.C. (1974), Interfaces in Metal Matrix Composites, edited by A.G.Metcalf, Academic Press, N.Y., Chapter 7.
- Page, R. A. and Leverant, G. R. (1985) Relationship of fatigue and fracture to microstructure and processing in alumina fiber reinforced metal matrix composites In: Proc of the Fifth Int. Conf.on Composite Materials ICCM 5, edited by W.C.Harrigan, J.Strife and A.Dhingra (TMS/AIME, San Diego), 867-886.
- Pask, J. A., Fulrath, R. M. (1962) Fundamentals of glass to metal bonding VII J. of the American Ceramic Society 45 (12), 592-596.
- Pepper, S. V. (1976) Shear strength of metal sapphire contacts J. of Applied Physics, 47 (3), 801-808.
- Petzow, G., Suga, T., Elssner, G. and Turwitt, M. (1984) Nature and structure of metal-ceramic interfaces In: Sintered Metal-Ceramic Composites, edited by G. S. Upadhyaya, (Elsevier Science Publishers, Amsterdam, 3-18.
- Phillips, D. C. (1974) Interfacial bonding and the toughness of carbon fibre reinforced glass and glass-ceramics J. Materials Science 9, 1847-1854.
- Plueddeman, E. P. (1974) Composite Materials Vol. 6: Interfaces in Polymer Matrix Composites, edited by L.J.Brouman and R.H.Krock (Academic Press) Chapter 6.
- Prewo, K. M. (1976) The development of impact tolerant metal matrix composites In: Failure Modes in Composites III, edited by T.T.Chiao and Schuster, Proc. Conf.Las Vegas, (TMS/AIME), 1-26.
- Prewo, K. W. (1980) The importance of fibers in achieving impact tolerant composites Phil. Trans. Roy. Soc. London A294, 551-558.
- Prewo, K. M. and Brennan, J. J. (1980) High-strength silicon carbide fibre-reinforced glass-matrix composites J. of Materials Science 15 463-468 and 1201-1206.
- Prewo, K. M., Brennan, J. J. and Layden, G. K. (1986) Fiber reinforced glasses and glass-ceramics for high performance applications American Ceramic Society Bulletin 65 305-313&322.
- Prewo, K. M. (1986) Tension and flexural strength of silicon carbide fibre-reinforced glass ceramics J. of Materials Science 21, 3590-3600.
- Prewo, K. M. (1987) Fatigue and stress rupture of silicon carbide fibre-reinforced glass-ceramics J. of Materials Science 22, 2695-2701.
- Pritchard, W. H. (April 1969) The role of hydrogen bonding in adhesion In: Aspects of Adhesion 6, Proc. Conf. at the City University, London, edited by D.J.Alnier (University of London Press), 11-23.
- Quenisset, J.-M., Soumelidis, P. and Naslain, R. (1985) Fatigue crack propagation in titanium based 1D composites reinforced by boron, boron carbide and SiC filaments In: "Developments in the Science and Technology of Composite Materials", Proc. First European Conference on Composite Materials ECCM 1, edited by A.R.Bunsell, P.Lamicq and A.Massiah (EACM, Bordeaux), 571-576.
- Ramqvist, L. (1965) Wetting of metallic carbides by liquid copper, nickel, cobalt and iron International Journal of Powder Metallurgy 1 (4), 2-21 and (1966) 2 (2) p. 34.
- Ramqvist, L. (1969) Preparation, properties and electronic structure of refractory carbides and related compounds

Jernkontorets Annaler **153**, 159-179.

- Rhee, S.K. (1970) Wetting of ceramics by liquid aluminum *J. of the American Ceramic Society* **53** (7) 386-389.
- Riggs, D.M., Shuford, R. J. and Lewis, R. W. (1982) Handbook of Composites, edited by G. Lubin, (Van Nostrand Reinhold), 196-271.
- Samsonov, G.V., Panasyuk, D. and Kozina, G.K. (1968) Wetting of refractory carbides with liquid metals *Soviet Powder Metallurgy and Metal Ceramics*, **7**, 874-878.
- Shorshorov, M. Kh., Usunov, L. M., Zirlin, A. M., Olefirenko, V. I. and Vinogradov, L. V. (1979) Brittle interface layers and the tensile strength of metal matrix composites *J. of Materials Science* **14**, 1850-1861.
- Shindo, A. and Honjo, K. (1986) Surface treatment of carbon fibers as reinforcements for aluminum matrix composites In: Composites '86: Recent Advances in Japan and the United States: Proc. Japan-US CCM-3, edited by K. Kawata, S. Umekawa and A. Kobayashi (Japan Society for Composite Materials, Tokyo), 767-774.
- Shindo, A. (1986) Chemical property of carbon fiber surface and interfacial compatibility of composites In: "Composite Interfaces", Proc. of the First Int. Conf. on Composite Interfaces ICCI-1, Cleveland, edited by H. Ishida and J.L. Koenig (Elsevier, North-Holland), 93-100.
- Smith, P. R., Froes, F. H., and Cammett, J. T. (1982) Correlation of fracture characteristics and mechanical properties for titanium matrix composites In: "Mechanical Behavior of Metal-Matrix Composites", Proc. Conf. Dallas, edited by J.E. Hack and M.F. Amateau (TMS/AIME, Texas), 143-168.
- Swenson, D. O. and Rau Jr., C. A. (1970) The stress distribution around a crack perpendicular to an interface between materials *Int. Journal of Fracture Mechanics* **6**, 357-365.
- Towata, S.-I. and Yamada, S.-I. (1986-a), Mechanical properties of aluminum alloy composites with hybrid reinforcements of continuous fiber and whisker or particulate Composites '86: Recent Advances in Japan and the United States: Proc. Japan-US CCM-3, edited by K. Kawata, S. Umekawa and A. Kobayashi (Japan Society for Composite Materials, Tokyo), 497-503.
- Towata, S.-I. and Yamada, S.-I. (1986-b), Mechanical properties of aluminum alloys reinforced with silicon carbide fibers and whiskers or particulates *Trans. Japan Institute of Metals* **27**, 709-716.
- Warren, R. (1968) The interaction between liquid platinum and some transition metal carbides *J. of Nuclear Materials* **25**, 117-119.
- Warren, R. (1980) Solid-liquid interfacial energies in binary and pseudo-binary systems *J. of Materials Science* **15**, 2489-2496.
- Wells, J. K. and Beaumont, P. W. R. (1985-a) Debonding and pull-out processes in fibrous composites *J. Materials Science* **9**, 1275-1284.
- Wells, J. K. and Beaumont, P. W. R. (1985-b) Crack-tip energy absorption processes in fibre composites *J. Materials Science* **9**, 2735-2749.
- Zaboletskii, A. A., Salibekov, S. E., Kansevich, I. A., Lyuttsau, V. G. and Fadyukov, E. M. (1978) Effect of processing factors on some properties of silumin/silicon-carbide-fiber composite materials *Soviet Powder Metallurgy and Metal Ceramics* **17**, 51-54.

ON ELASTIC-PLASTIC CRACKS
BETWEEN DISSIMILAR MEDIA

by

EDWARD ZYWICZ

B.S.E.M., UNIVERSITY OF ILLINOIS, 1983

S.M.M.E., MASSACHUSETTS INSTITUTE OF TECHNOLOGY, 1986

SUBMITTED IN PARTIAL FULFILLMENT
OF THE REQUIREMENTS FOR THE
DEGREE OF
DOCTOR OF PHILOSOPHY
IN MECHANICAL ENGINEERING

at the

MASSACHUSETTS INSTITUTE OF TECHNOLOGY
May 1988

©Massachusetts Institute of Technology, 1988

Signature of Author _____

Edward Zywicz

Department of Mechanical Engineering
May 31, 1988

Certified by _____

David M. Parks

Professor David M. Parks
Thesis Supervisor

Accepted by _____

Professor Ain Ants Sonin, Chairman
Departmental Committee on Graduate Studies

On Elastic-Plastic Cracks Between Dissimilar Media

by

Edward Zywicz

Submitted to the Department of Mechanical Engineering
on May 31, 1988 in partial fulfillment of the
requirements for the Degree of Doctorate of Philosophy in
Mechanical Engineering

Abstract

The asymptotic elastic behavior of interfacial cracks occurring between two dissimilar isotropic media is reviewed. Distinct solutions, based on differing assumptions regarding crack-tip boundary conditions, can be generated. The assumption of traction-free crack-tip faces generally leads to oscillatory singular asymptotic fields which mathematically cause crack-face interpenetration, an inconsistency which can be alleviated by alternatively assuming asymptotic (frictionless) contact. Both cases produce singular crack-tip stresses which cannot be sustained in materials capable of limited plastic flow, and small scale yielding (SSY) should be considered.

Conditions for SSY within surrounding dominant elastic regions of both traction-free and frictionless contact are considered, and the subset of admissible loads producing physically realistic conditions are identified for each crack-tip idealization. Approximate closed form expressions for the plastic zone size and shape are obtained as the locus of points where the elastically-calculated Mises stress equals the tensile yield strength, σ_y . In defining elastic and plastic traction-free crack-tip fields, both a magnitude and phase angle are required. The SSY interfacial load phase angle (ILPA), defined as $\zeta_0 = \angle K + \epsilon \ln(K\bar{K}/\sigma_y^2 \pi \cosh^2(\pi\epsilon))$ where $\angle K$ is the phase angle of the complex traction-free stress intensity factor K and ϵ is the bi-material constant, naturally arises when calculating the approximated plastic zone and conveniently defines the phase angle of the inelastic traction-free fields. The traction-free crack-tip plastic zone size and shape as well as ζ_0 periodically evolve as $|K|$ increases, while the closed crack-tip plastic zone shape differs little from the homogeneous mode II shape and only depends functionally on the closed bi-material stress intensity factor K_{II}^c and weakly on the bi-material constant.

Precise SSY numerical calculations for an elastic/perfectly-plastic material atop a rigid or elastic substrate indicate that the plane-strain asymptotic traction-free crack-tip stress fields in the plastically-deforming material are composed of various elastic and plastic sectors. Deep within the plastic zone, no oscillatory stress variations occur, however, a cusp in the slip-line field couples portions of the stress state to the radial distance for certain loads. Generally the maximum interfacial tractions occur for negative ζ_0 when inelastic sectors completely surround the crack-tip. For positive ζ_0 an elastic crack-face sector grows as the ζ_0 increases, and the interfacial shear strains in the plastically deforming medium are small, independent of the actual interfacial sector type. Crack-face contact within the plastic zone may occur at values of ζ_0 when elastic contact outside the plastic zone does not occur. The closed bi-material crack-tip asymptotic stress fields in plane-strain for an elastic/perfectly-plastic material bonded

to a rigid substrate are composed of two fan and two constant state sectors in the deforming region. Compressive crack-face tractions persist even when contained inelastic deformation is included.

Asymptotic interfacial and crack-face tractions appear constant in the crack tip region, but both normal and shear tractions jump at the crack-tip. The asymptotic elastic potential for the lower-elastic stress state is logarithmically singular for non-zero asymptotic interfacial shear tractions, thus inelastic crack-tip deformation in the "elastic" region is anticipated for deformable media. Validity conditions regarding use of an elastic lower half-space and linearized kinematics and the formation of a blunted crack-tip are presented.

Thesis Supervisor: Dr. David M. Parks

Title: Associate Professor of Mechanical Engineering

Acknowledgement

I would like to thank Prof. Abeyaratne, Prof. Argon, and Prof. Rice for being on my thesis committee and for their help in addressing the problem undertaken herein.

I want to extend my thanks to my friends, fellow grad-students, and co-workers for many helpful discussions, some related to and others unrelated to engineering, and for making the environment pleasant and quite bearable during my stay at MIT. I also appreciate all the help Richard Stringfellow gave in helping me revise this thesis.

I wish to acknowledge the generous donations of the Data General Corporation, and the academic license provided from Hibbit, Karlsson, and Sorsensen, Incorporated.

And lastly, I must address the issue of my advisor, Prof. D. M. Parks. In my years working for him, he has let me bounce and spin much as a pinball does in a pinball machine. Sometimes it felt as though I was rebounding aimlessly among the bumpers. But, in times of trouble he always redirected my course with just enough care and (usually) persistence to aim me toward the right pins. And on several occasions when I appeared to be stalling out, it was not below him to cheat and *tilt* a little. For all that I have learned from him and for his guidance, I would just like to let him know that I truly appreciate it.

The work described herein was supported in part by the Office of Naval Research under grant No. N00014-84-K0495, 'Interfaces in Metal Matrix Composites,' and in part by NSF under contract DMR 84-18718.

Table of Context

Abstract	2
Acknowledgement	4
Table of Context	5
 Chapter 1 : Introduction and Statement of Problem	 10
1.1 Introduction	10
1.1.1 Interfacial Fracture Mechanics Length Scales	11
1.1.2 Considerations of Interface and Crack-Tip Idealizations	13
1.1.3 Homogeneous Fracture Mechanics	15
1.2 Statement of Purpose	17
1.2.1 Statement of Boundary Problem	18
 Chapter 2 : Elastic Interfacial Cracks	 21
2.1 History and Solution Discussion	21
2.1.1 Traction-Free Crack Faces	21
2.1.1 Closed Crack-Tip Faces	28
2.2 Inferred Plastic Behavior	34
2.2.1 Traction-Free Crack Faces	36
 P2 Abstract	 37
P2.1 Introduction	38
P2.2 SSY Plastic Zone Approximation	39
P2.3 Discussion	41

P2.3.1 Mathematical Considerations	41
P2.3.2 Zone Growth Considerations	45
P2.3.3 Comparisons	45
P2.3.4 Valid Solution Domain	47
P2.4 Conclusion	57
P2 References	60
P2.A Appendix A : Mises Equivalent Stress Derivation	61
P2.B Appendix B : Interfacial Crack Example	64
2.2.1.1 Additional Discussion	66
2.2.2 Closed Frictionless Crack-Tip Fields	67
2.2.2.1 Plastic Zone Approximation	67
2.2.2.2 Mathematical Features	69
2.2.2.3 Valid Solution Domain	69
2.2.2.4 Comparisons	72
2.2.2.5 Contact Length Approximation	74
2.2.2.6 Conclusion	74
2.3 Small Scale Contact	75
2.3.1 Loading Restrictions for SSC	76
2.3.2 Correspondence of K_{II}^c to K	77
2.3.3 Accuracy of Contact Length Estimation	79
2.3.4 SSC Summary	81
2.4 Overview	82
2.4.1 Load Map	82
2.4.2 Conclusion	85
Chapter 3 : Description of Solution Technique	87
3.1 Crack-Tip Model Formulation	87

3.1.1 Traction-Free Crack-Tip Faces: Boundary Layer Approach	89
3.1.1.1 Theoretical Considerations	90
3.1.1.2 Boundary Layer Verification	93
3.1.2 Closed Crack-Tip Faces	100
3.2 Elastic/Perfectly-Plastic Constitutive Relationship	100
3.2.1 Kinematics	101
3.2.2 Notation	101
3.2.3 Constitutive Relationship	102
3.2.4 Constitutive Integration Operator	102
3.3 FE Model Considerations	106
3.3.1 Traction-Free Crack-Tip Face Model	107
3.3.1.1 Boundary Layer Implementation	107
3.3.1.2 FE Mesh	108
3.3.1.3 Procedures	111
3.3.2 Traction-Free Crack-Tips: Existence of Stress Oscillations Within the Plastic Zone	112
3.3.3 Closed Crack-Tip Faces	113
 Chapter 4 : Elastic-Plastic Interfacial Crack-Tip Fields	 114
4.1 Asymptotic Crack-Tip Forms	114
4.1.1 Summary of Slip-Line Theory	115
4.1.2 Stationary and Quasi-Static Crack-Tip Forms	116
4.2 Traction-Free Crack-Tip Model	123
4.2.1 Deformable Upper Half-Plane	124
4.2.1.1 Asymptotic Crack-Tip Behavior	124
4.2.1.2 Assemblage of Crack-Tip Fields	136
4.2.1.3 Interfacial Traction and Crack-Tip Fields	137
4.2.1.4 Comparison	138

4.2.1.5 Asymptotic Strain Distribution and CTOD	139
4.2.1.6 Path Dependence of J -Integral	145
4.2.2 Solution in the Lower Elastic Half-Plane	146
4.2.2.1 Formulation of an Elasticity Potential	148
4.2.2.2 Asymptotic Characteristics	155
4.2.2.3 Comparison	157
4.2.3 Parametric Study	157
4.2.3.1 Plastic Crack-Tip Fields and Interfacial Traction	161
4.2.3.2 Strain Distribution and CTOD	167
4.2.3.3 Path Dependence of J -Integral	170
4.2.3.4 Conclusion	171
4.3 Closed Crack-Tip Model	173
4.3.1 Plastic Field	173
4.3.2 Elastic Field	178
4.3.3 Conclusion	182
4.4 Limitations	182
4.4.1 Physical Attributes	184
4.4.2 Evolutionary Limitations	185
 Chapter 5 : Summary and Discussion	 190
5.1 Summary	190
5.2 Discussion	196
5.2.1 Crack-Face Contact	196
5.2.2 Unifying ILPA	197
5.2.3 Anticipated Experimental Observations	198
5.2.4 Influence of Material Properties on Separation	201
5.2.5 Suggested Additional Work	203

References	205
Appendix A : Boundary Layer Formulation	210
A.1 Energy Considerations	211
A.1.1 Formulation of Equivalent Stiffness Matrix	211
A.1.2 Evaluation of Spring Constants	216
A.2 Boundary Considerations	217
Appendix B : Elastic Wedge Stress Potential	220
Appendix C : User-Written Software	223
C.1 Elastic/Perfectly-Plastic UMAT	223
C.2 Traction-Free Crack-Tip Model	232
C.2.1 Spring Coefficients	232
C.2.2 MPC Subroutine	238
C.3 Closed Crack-Tip : MPC Subroutine	244

Chapter 1

Introduction and Statement of Problem

1.1 Introduction

Efforts in the creation, design, and manufacturing of advanced materials, such as metal matrix composites (MMC), laminated composites, ceramics, and metallic polycrystallines, which may or may not contain second phase particles, have been hampered, from the viewpoint of mechanical performance, due to a lack of knowledge about the processes occurring along the interfaces separating the individual constituents or microstructural boundaries. It is widely recognized that laminated materials can have unique failure modes attributable solely to their layered structure. For example, multi-layered electronic boards are known to fail from thermal cycling along their lamination joints. In MMC, the fiber-matrix interface is the controlling factor in overall composite strength and toughness (Cooper and Kelly, 1969; Ochiai and Murakami, 1981). The approaches used to assess the interfacial stresses have been either: to assume a perfect mathematical interface, which allows the evaluation of the necessary interfacial tractions to preserve overall integrity of the interface; or to postulate the existence of a crack-like defect and analyze it using conventional linear elastic fracture mechanics (LEFM) approaches (*e.g.*, in MMC see Buchholz and Herrman, 1983; Ioakimidis and Theocaris, 1979). No extreme analytical problems are typically encountered in investigating ideal interfaces, but that approach sheds little light on the actual chain of events

in the failure process. On the other hand, LEFM does describe the strength of the singularity, but it also predicts infinite interfacial stresses upon extrapolation to the crack tip. Additionally, the linear material behavior and infinitesimal strain assumptions may be violated near the crack tip. From the mechanical property design viewpoint (*e.g.*, types and thicknesses of fiber coatings in MMC, desirable second phase particles in metallic alloys, binder properties for ceramics), knowledge of the actual interfacial stresses are important, especially in front of a crack, in order to prevent catastrophic material failure or to control the failure mode.

Since the exact failure sequence of bonded dissimilar media remains as yet not fully understood, two major issues pertaining to interfacial separation remain. Of course the primary question is: "what are the interfacial bi-material crack-tip tractions leading to separation?" Because crack deflection is also a possibility, identifying the local crack-tip stress and strain fields are important, especially when non-linear material constitutive relations are used.

1.1.1 Interfacial Fracture Mechanics Length Scales

The size scales associated with problems in which some form of interfacial separation is experienced span a very large range. The geophysical size scale in plate tectonics represents a reasonable upper bound. Here the crust of the earth, which is made up of plate-like structures floating atop a viscous jelly-like mantle, continuously moves, causing massive quantities of potential energy to be stored up as elastic strain energy and released at local premordial fracture or fault sites (Hobbs, Means, and Williams, 1976). In these circumstances the transition or interfacial zone between the two plates may be many meters wide and consist of a variety of different geomorphic media. At more common engineering size scales are the fracture phenomena associated with welding metal structures together. In the welding process two separate pieces are joined together by fusing their common boundary, possibly introducing a filler agent. Due to the melting and solidification process during fusing, the material properties of

the weld usually differ substantially from that of the surrounding bulk material, and flaws may be introduced and embedded into the weld. (Attention is specifically focused upon those flaws which are in or adjoins to and lay parallel to the weld.) The size of the interfacial zone is the weld thickness, which may or may not be small compared to the surrounding structure or flaw. For many diffusion type interfaces, such as seen in Gr/Al MMC, where reactive fiber or coating material is consumed by the matrix, the fracture path is thought to follow the weakest portion of the deteriorated interface. In these cases the interfacial size is governed by the diffusion and product reaction kinetics of the coating and matrix species, and the interface size may be relatively small. For example, Everett *et al.* (1986) determined that a thin aluminum coating, applied by physical vapor deposition to a polycrystalline pyrolytic graphite sample, creates an "intermixing zone" approximately 70 to 80 nm thick. A slightly smaller interfacial zone length is obtained for brittle intergranular fracture, as often occurs in polycrystalline metals and ceramics. In metallic polycrystallines there often exist grain boundary defects, such as decoherent boundaries, carbides or sulfides, which weaken the boundary. In ceramics, the consolidation process never yields perfectly dense ceramics, thus many voids exist along the grain boundaries which act as nucleation sites. The size of the interfacial zone in intergranular fracture is approximately the size of the grain boundary, and for metallic polycrystallines the grain boundary is typically on the order of ten Burger's vectors (approximately 2.5 nm). At about the same size scale are the initial phenomena associated with certain types of ductile fracture in metals. Here a second phase particle, such as a carbide or oxide, embedded in the matrix acts as a nucleation site for void formation. When sufficient tractions exist along the particle surface or the necessary deformation accumulates in the matrix, the boundary between the particle and the matrix separates, and after sufficient additional loading, gives way to a completely separated particle and a micro void. Again, the interfacial zone thickness may be on the order of several Burger's vectors.

The ability to resolve the fracture phenomena is limited to the minimum size scale

chosen to describe the individual constituents. In continuum mechanics, a representative volume is chosen whose macro-response sums up all the individual micro features within it (Fung, 1977). For inelastic deformation in metals, the nature of discrete slip events requires a representative volume which has a characteristic dimension of several hundred to several thousand Burger's vectors. (For metals, an average Burger's vector is approximately 2.5×10^{-10} m.) This means that deformable metallic or intermetallic based interfacial zones which are only several Burger's vectors thick cannot be accurately represented by the usual continuum models and require additional considerations to be properly modeled. For thicker interfaces, such as in the Gr/Al system discussed earlier, an average material response may be obtainable and used to define a "thin", but finite, transitional layer between the constituents. However, defining the material constitutive behavior across this diffusion zone must be accomplished by use of a discrete "averaged" layer, rather than by a continuous boundary layer. As the thickness of the interfacial zone increases, the use of continuous "continuum interfaces" becomes justifiable.

1.1.2 Considerations of Interface and Crack-Tip Idealizations

For many physical situations, several continuum modeling simplifications can be made. If the interfacial constitutive behavior is not substantially different from that of either one of the adjoint media, it can be approximated by using the properties of that adjoint medium and by merely extending that material's domain. The interface can be idealized as a perfect zero-thickness mathematical interface which is required to carry the interfacial tractions and maintain the local strain compatibility requirements. For weaker interfaces, interfacial sliding or opening may be allowed after sufficient traction or strain levels are achieved. An alternative approach to interfaces is to prescribe a traction-displacement relationship along the interface, which allows for different shear and normal traction-displacement behavior and allows the interface to separate (Nutt and Needleman, 1987). Use of these continuum models requires that the flaw mod-

eled and the limit of stress and strain resolution be very large compared to the actual interfacial thickness and the appropriate continuum length scale.

For relatively "thin" and "strong" interfaces, a perfect zero-thickness mathematical interface can be used to obtain "upper" limits to the stress and deformation in the crack-tip vicinity. An upper limit is produced in the sense that in order for the interface and surrounding regions to maintain their integrity, they must be capable of withstanding these stresses and deformations. Although such interface models are not capable of accurately describing the entire crack-tip deformation process, they do provide some insight into the conditions just prior to crack growth.

In the study of homogeneous fracture mechanics, attention is typically focused upon the asymptotic behavior of the fields as the crack tip is approached. Under certain conditions the crack-tip fields are described for a wide range of loadings, materials, and geometries by a single set of field equations whose magnitudes are scaled by the material properties and a stress intensity factor. Small scale yielding (SSY) is the most commonly referred class of crack-tip loading conditions for materials capable of inelastic deformation. In SSY use of asymptotic solutions is acceptable as long as the extent of non-linear deformation is contained within a region which is "small" compared to the next characteristic geometrical dimension in the problem. Crack and ligament length, specimen thickness or width, and distance to the point of load application are just a few examples of characteristic geometrical dimensions in a problem. In SSY the fields far away from the inelastic crack-tip deformation, but at distance small compared to the geometrical dimension, are well reproduced by the elastic asymptotic solutions (Rice, 1974). Within the SSY crack-tip idealization, a variety of work describing the fields within the inelastic zone has been performed.

In continuum fracture mechanics, the crack tip is commonly modeled as mathematically sharp. In actuality, crack-tip opening and blunting occurs in many microscopically ductile materials (*e.g.*, cast iron, aluminum, and copper), resulting from continuous deformation or discrete slip steps. For strain hardening materials in SSY, McMeeking

(1977) showed that the crack-tip opening displacement (CTOD) is linearly dependent upon the strength of the surrounding singularity, as measured by the J -Integral (Rice, 1968a). McMeeking also showed that by normalizing the radial distance from the crack-tip by the CTOD, the steady state values of the normalized stress and strain distributions are independent of J . In general, at radial distances large compared to the blunted CTOD, the crack-tip stress and strain behavior appears as if the crack tip is mathematically sharp, even though local crack-tip blunting may be occurring.

1.1.3 Homogeneous Fracture Mechanics

In conventional homogeneous fracture mechanics, the next step after LEFM in determining continuum crack-tip stresses has been to account for contained material non-linearity effects. For the homogeneous mode III case, Hult and McClintock (1956) solved exactly the small scale yielding continuum crack-tip stress field for an elastic/perfectly-plastic material idealization. They analytically calculated the actual size and location of the plastic zone along with the stress and strain distribution in the crack-tip plastic zone and in the surrounding elastic region. Recognizing that similar behavior should occur in the planar modes I and II, various approximate methods were developed in an attempt to account for crack-tip plasticity. In order to correct the plane-stress mode I stress intensity factor for local crack-tip inelastic deformation, which mathematically lengthens the apparent crack size, Dugdale (1960) postulated that the crack-tip yielded region could be idealized as a concentrated zero-thickness yield strip extending from the crack tip. He postulated that the only non-zero stress component was the stress normal to the crack face and that its value was equal to the tensile flow strength of the material. To determine the actual crack-tip stress intensity factor K_I , Dugdale first calculated the size of the yield strip, c , and defined an effective crack length, l_e , to be equal to the original crack length, l , plus the length of the yield strip(s); i.e., $[l_e = l + c]$. To model the yield strip, he imposed the appropriate closing tractions on the effective crack tip(s) over a distance which corresponded to the yield

strip length (c). By superimposing the actual far-field loads, he was then able to determine the elastic stress intensity factor for his crack model. Using different crack-tip plasticity idealizations, others [Barenblatt (1962); Bilby, Cottrell, and Swinden (1963)] have used similar "matched asymptotic boundary layer" approaches to alter the effective crack to achieve better elasticity solutions. For an in-depth explanation and historical review of crack-tip "strip" models for contained inelastic deformation and their physical interpretation, the reader is referred to Kanninen and Popelar (1985).

To describe the continuum crack-tip fields deep within the actual crack-tip plastic zones, other methods were utilized. Based upon various assumptions, Rice (1968b) postulated that the Prandtl (slip-line) distribution represented the stress state at a plane-strain mode I crack tip, and numerical calculations performed by Rice and Tracey (1973) showed that the crack-tip stress distribution for an elastic/perfectly-plastic mode I crack was indeed well characterized by the Prandtl distribution. The Prandtl slip-line model assumes the material is perfectly plastic and that a stress potential can be constructed which satisfies the necessary boundary conditions (traction-free crack tips) and equilibrium requirements. Although this model allowed for determination of the finite stress field, the strain field is undefined. However, in certain regions of the stress field, a portion of the strain field behavior could be inferred. For example, in a fan region the behavior of the $\gamma_{r\theta}$ strain component is found to be singular ($\gamma_{r\theta} \propto 1/r$, where r is the radial distance from the crack tip). Thus, the inclusion of material non-linearities was not sufficient to remove all crack-tip stress and strain singularities.

Hutchinson (1968) and Rice and Rosengren (1968) considered the continuum structure of the planar crack-tip fields for power-law strain-hardening materials using deformation theory [strain \propto (stress) n]. (These fields shall henceforth be referred to as HRR fields.) From the compatibility, constitutive, and equilibrium relationships, the necessary requirements for the existence of a strain potential and a stress potential were established. By using the boundary conditions and assuming a separable form, an eigenvalue problem emerged whose solution determined the radial dependences of the

stress, displacement, and strain fields. Using the characteristic root, a fourth order differential equation was numerically solved to determine the actual angular dependences of these fields. The overall magnitude of the stress and strain fields were determined by their radial and angular dependences and scaled by the strength of the crack-tip singularity, as measured by the path independent J -Integral (Rice, 1968a). For finite values of the strain-hardening exponent, both the stress and strain fields were found to be singular as the crack tip was approached, and as observed previously, the inclusion of non-linear material constitutive behavior does not remove all singularities at the mathematically sharp crack tip. Although perfect plasticity can be considered by taking the limit as $n \rightarrow \infty$, no unique strain field was identifiable.

Development of HRR type singularity fields involves several key assumptions. A total deformation theory of plasticity is used along with linear kinematics (small strain theory) and a monotonically increasing stress-strain relationship. For deformation theory to accurately describe the constitutive behavior, no local stress unloading is admissible and the loading at all material points must be nearly radial. Thus the application of deformation theory is generally restricted to proportional loading. Since small strain theory is used, these solutions do not incorporate any field characteristics which are attributable to crack-tip blunting, and they are only applicable at limited, finite distances from the crack tip. Also, it should be noted that the HRR fields are obtained by retaining only the dominant term in the stress and strain potentials.

1.2 Statement of Purpose

The basic interfacial SSY crack tip characteristics for a specific set of loading and geometric conditions and material idealizations will be provided. The stationary crack-tip fields for specific material idealizations will be represented via closed form expressions, based upon natural dimensional and dimensionless variable groupings. First, a general non-linear idealized bi-material boundary value (BV) problem will be identified, including specific constitutive relationships. Known solutions to the linear elastic BV problem

will be reviewed and implications concerning the non-linear BV problem behavior and associated natural groupings will be extracted from the asymptotic elasticity solutions. From this assembled parametric framework, far-field loadings which produce the geometrical idealizations considered in the BV problem (traction-free crack-tip faces or closed crack-tip faces) will be stated. Next, a discussion of the solution technique for solving the non-linear problem will be presented. Representative forms for the general crack-tip fields will be presented and assembled to construct the complete crack-tip fields for various material choices. Inferred trends of the constructed fields, as functions of material variables, will be identified. Limitations regarding the applicability of these results, will be expressed in terms of the mathematical assumptions made in solving the BV problem and in terms of physical material characteristic associated with interfacial crack problems. Finally, speculative implications, relevant to all interfacial fracture mechanics problems, concerning separation mechanisms will be made.

1.2.1 Statement of Boundary Value Problem

The mechanics problem considered herein is a plane-strain interfacial crack between two isotropic solids, as depicted in *Figure 1.1*. The interface or diffusion boundary layer between the two solids is idealized as having zero thickness. The constitutive response for the material in the upper half (Region 1) is idealized as being elastic/perfectly-plastic, and the material in the lower half is considered to have a linear elastic constitutive relationship. Far-field applied loads are restricted to SSY and to those which result in either traction-free crack faces or crack faces which have (frictionless) contact over a large region, compared to their plastic zone size. (This restriction is enforced only from the edge of the plastic zone outwards away from the crack tip.) The far field loads are assumed to produce a set of displacements near the crack tip which can be represented by a continuous family of self-similar modes whose magnitudes are scaled by the crack-tip singularity. Hence, the family of boundary condition modes which are considered are limited to those which satisfy the general isotropic bi-material crack

problem with either traction-free crack faces or closed crack-tip faces.

The objectives of analyzing these BV problems are: (a) to determine the size, shape, and growth characteristics of the plastic zone in Region 1; (b) to identify the SSY asymptotic elastic and plastic fields deep within the plastic zone; (c) to identify the evolution of strains near the interface as well as the evolution of interfacial tractions with applied load.

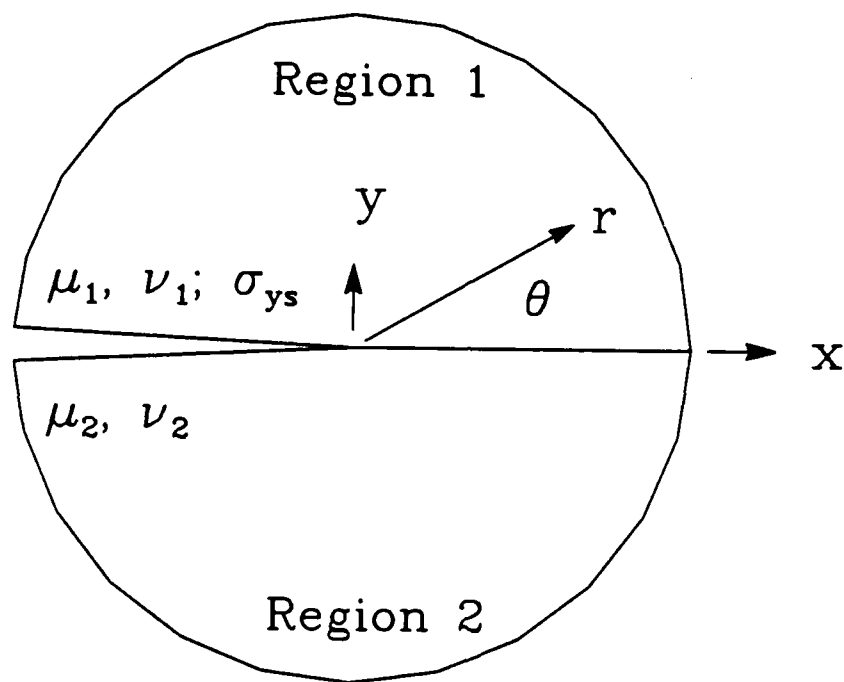


Figure 1.1 Schematic traction-free bi-material interfacial crack-tip region, including polar (r, θ) and Cartesian (x, y) coordinates and domain numbering convention.

Chapter 2

Elastic Interfacial Cracks

2.1 History and Solution Discussion

Applied mechanics can provide a framework for modeling interfacial cracks. Within this framework, there currently exist two specific geometric idealizations which are used to investigate the local interfacial crack-tip fields around a mathematically perfect zero-thickness interface. Both idealizations require continuity of interfacial tractions and displacements, with the basic difference between the two being the physical interpretation given to the near-tip crack faces. The first model assumes that the crack faces are "traction-free" while the other assumes that the crack faces are in "contact," but free to slide relative to one another (frictionless). The following sections review the important aspects of each crack-tip model.

2.1.1 Traction-Free Crack Faces

The asymptotic solution for a traction-free crack tip located between two elastically dissimilar isotropic media was first addressed and partially solved by Williams (1959). He used for the Airy stress function a general power series expansion about the crack tip of the form

$$\phi = r^2 \sum_j A_j r^{\lambda_j} F_j(\theta, \lambda_j), \quad (2.1)$$

where r is the radial distance from the crack tip, θ is the angle measured from the interface, A_j and λ_j are admissible constants, and $F_j(\theta, \lambda_j)$ is an admissible function.

Enforcing displacement and traction continuity across the interface and traction-free crack-tip faces lead to an eigenvalue problem composed of eight simultaneous equations from which λ_j and acceptable forms of $F_j(\theta, \lambda_j)$ were determined. Williams first assumed that λ_j was a real number and was unable to obtain a solution to the characteristic equation. He concluded that λ_j must be a complex number and found that two possible series solutions exist:

$$\lambda_j = \begin{cases} j \pm i \frac{1}{\pi} \coth^{-1}(D) \\ (j + \frac{1}{2}) \pm i \frac{1}{\pi} \tanh^{-1}(D) \end{cases} \quad j = 0, \pm 1, \pm 2, \pm 3, \dots, \quad (2.2)$$

where for plane strain

$$D = \frac{2\mu_1 \left(1 - \frac{\nu_2}{1-\nu_2}\right) - 2\mu_2 \left(1 - \frac{\nu_1}{1-\nu_1}\right) - (\mu_1 - \mu_2)}{2\mu_1 \left(1 - \frac{\nu_2}{1-\nu_2}\right) + 2\mu_2 \left(1 - \frac{\nu_1}{1-\nu_1}\right)}. \quad (2.3)$$

Here μ_k is the shear modulus, ν_k is Poisson's ratio, and the subscript k is 1 in the upper domain and 2 in the lower domain. In Eq.(2.2), both sets of roots exist only when $D = 1$, and both have infinite imaginary components ($\coth^{-1}(\pm 1) = \tanh^{-1}(\pm 1) = \pm \infty$). For commonly used engineering materials (i.e., those with positive Poisson's ratio less than 1/2), $|D| < 1/2$; thus, only the series associated with $\tanh^{-1}(D)$ is defined. Since \coth^{-1} is not defined for arguments with a magnitude less than unity, the set of roots with integer real portions ($\Re(\lambda_j) = j$) must be excluded from the total solution.

In deriving the characteristic equation for the case of purely real roots, it is speculated that at some point Williams incorrectly divided through by $\sin(\pi\lambda_j)$. This led him to conclude erroneously that no purely real roots [$\Re(\lambda_j) = \lambda_j$] exist, when, quite to the contrary, the solution to $\sin(\pi\lambda_j) = 0$ actually produces an acceptable set of whole integer roots. (Note, division by $\sin(\pi\lambda_j)$ is only valid if $\sin(\pi\lambda_j) \neq 0$!) Thus, the complete solution to the bi-material interfacial crack problem with traction-free crack tips consists of half-integer complex powers of r , termed "Williams type," and real whole integer powers of r . For cracks with $D = 0$, the complete set of roots for the homogeneous crack problem is recovered.

Rice (1988) has subsequently assembled the asymptotic expansion of a complete interfacial crack solution consisting of the Williams series [with eigenvalues $\lambda_j = (j +$

$1/2) + i(1/\pi) \tanh^{-1}(D)]$ and a material dependent constant multiplying the real whole-integer power series ($\lambda_j = j$). In terms of standard Muskhelishvili (Muskhelishvili, 1953) functions the general solution is given by

$$\phi'_1(z) = e^{-\pi\epsilon} z^{-\frac{1}{2}-i\epsilon} \sum_N a_N z^N + \frac{2C_2}{C_1 + C_2} \sum_M b_M z^M, \quad (2.4)$$

$$\Omega'_1(z) = e^{\pi\epsilon} z^{-\frac{1}{2}+i\epsilon} \sum_N \bar{a}_N \bar{z}^N - \frac{2C_2}{C_1 + C_2} \sum_M \bar{b}_M \bar{z}^M, \quad (2.5)$$

$$\phi'_2(z) = e^{\pi\epsilon} z^{-\frac{1}{2}-i\epsilon} \sum_N a_N z^N + \frac{2C_1}{C_1 + C_2} \sum_M b_M z^M, \quad (2.6)$$

and

$$\Omega'_2(z) = e^{-\pi\epsilon} z^{-\frac{1}{2}+i\epsilon} \sum_N \bar{a}_N \bar{z}^N - \frac{2C_1}{C_1 + C_2} \sum_M \bar{b}_M \bar{z}^M. \quad (2.7)$$

In these expressions, the bi-material constant, ϵ (imaginary part of the complex root λ_j), is defined as

$$\epsilon = \frac{1}{2\pi} \ln \left[\frac{\frac{\eta_1}{\mu_1} + \frac{1}{\mu_2}}{\frac{\eta_2}{\mu_2} + \frac{1}{\mu_1}} \right] \quad (2.8)$$

and

$$C_k = \frac{\eta_k + 1}{\mu_k}, \quad (k = 1, 2). \quad (2.9)$$

Here $z = x + iy = re^{i\theta}$ is the location measured from the crack tip, $\eta_k = 3 - 4\nu_k$ for plane strain and $\eta_k = (3 - \nu_k)/(1 + \nu_k)$ for plane stress, and the subscript k is used again to refer to the material in the upper half when equal to 1 and to the material in the lower half when equal to 2. The individual stress components are related to the Muskhelishvili stress potentials by the following relationships:

$$\sigma_{zz} + \sigma_{yy} = 2[\phi' + \bar{\phi}'] \quad (2.10)$$

and

$$\sigma_{yy} - \sigma_{zz} + i2\sigma_{zy} = 2[(\bar{z} - z)\phi'' - \phi' + \Omega']. \quad (2.11)$$

Discarding infinite energy terms and retaining only the most dominant term as $r \rightarrow 0$, the local crack-tip stresses behave as follows:

$$\sigma(r, \theta) \sim \frac{1}{\sqrt{r/2a}} \left\{ A(\theta) \cos[B(\theta) + \epsilon \ln \frac{r}{2a}] + C(\theta) \sin[D(\theta) + \epsilon \ln \frac{r}{2a}] \right\}, \quad (2.12)$$

where $r/2a$ is the radial distance from the crack tip normalized with respect to crack length, θ is the angle measured from the interface, and $A(\theta)$, $B(\theta)$, $C(\theta)$, and $D(\theta)$ are functions dependent upon loading, material constants, and angle θ .

Complete solutions to various problems concerning cracks between dissimilar media were obtained by England (1965), Erdogan (1965), and Rice and Sih (1965) using Kolosov-Muskhelishvili and other transformations to express the stress potentials. Additionally, Rice and Sih calculated stress intensity factors for a semi-infinite crack with point loads and for a finite crack between two semi-infinite media loaded by wedge forces or remote far-field loads.

The in-plane two-dimensional bi-material stress intensity factor, K , as defined by Hutchinson, Mear, and Rice (1987), is given by

$$K = \lim_{r \rightarrow 0} \sqrt{2\pi r} \frac{[\sigma_{yy}(r, \theta = 0) + i\sigma_{xy}(r, \theta = 0)]}{r^{i\epsilon}}, \quad (2.13)$$

where $\sigma_{yy}(r, \theta = 0)$ and $\sigma_{xy}(r, \theta = 0)$ are the interfacial normal and shear stresses, respectively. Note, the elastic material properties enter into the stress intensity factor via the bi-material constant, unlike the homogeneous case. Since K is a complex number, it can be written as

$$K = K_I + iK_{II}, \quad (2.14)$$

where K_I and K_{II} are the real and imaginary components of the stress intensity factor, respectively. Using the definition

$$K = (k_I + ik_{II})\sqrt{\pi} \cosh(\pi\epsilon), \quad (2.15)$$

Rice and Sih's (1965) original stress intensity factors, k_I and k_{II} are interpreted in a consistent manner. Table 2.1 contains the stress intensity factors for several geometries (Shih and Asaro, 1987).

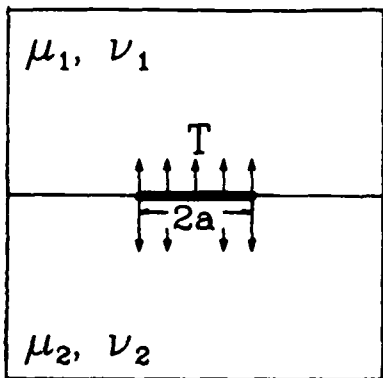
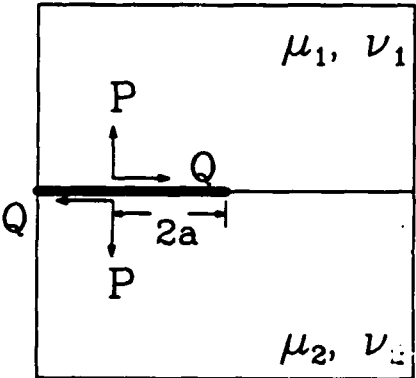
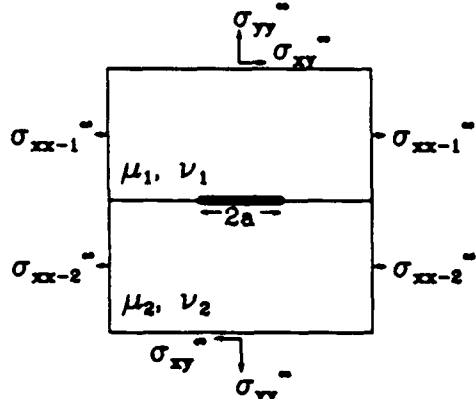
Crack Geometry	Stress Intensity Factor	Reference
<p>Infinite Plate</p> 	$K = T (1 + i2\epsilon) \times \sqrt{\pi a} (2a)^{-i\epsilon}$	<p>England, 1965</p>
<p>Semi-Infinite Plate</p> 	$K = (P + iQ) \cosh(\pi\epsilon) \times (2a)^{-i\epsilon} / \sqrt{\pi a}$	<p>Rice and Sih, 1965</p>
<p>Infinite Plate</p> 	<p>For crack tip at $x = a$, $K = (1 + i2\epsilon) (\sigma_{yy}^{\infty} + i\sigma_{zy}^{\infty}) \times \sqrt{\pi a} (2a)^{-i\epsilon}$</p>	<p>Rice and Sih, 1965</p>

Table 2.1 Bi-material stress intensity factor for various interfacial crack geometries.

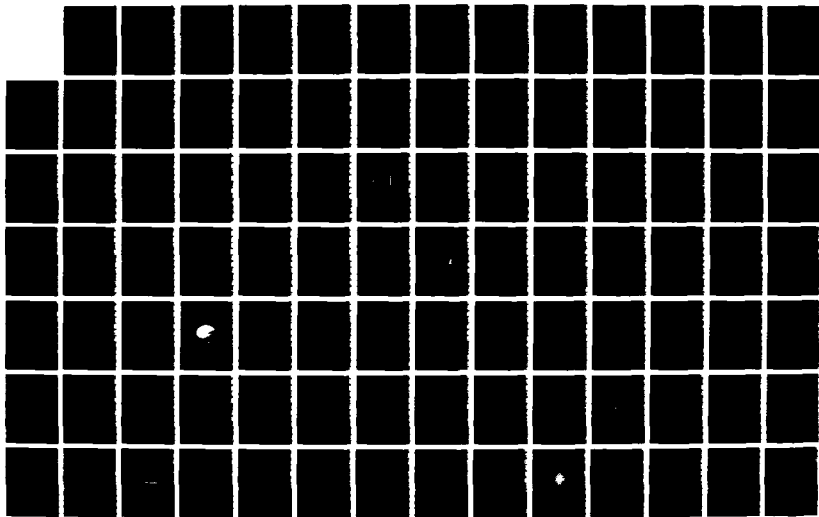
NO-8136 746

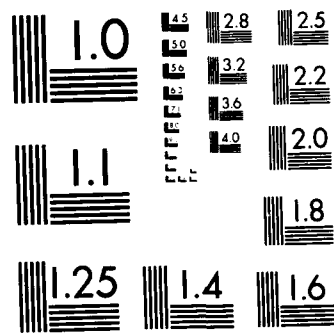
ENGINEERING INTERFACES IN METAL MATRIX COMPOSITES
(VOLUME 3)(U) MASSACHUSETTS INST OF TECH CAMBRIDGE
J A CORNIE 10 JUN 88 N00014-84-K-0493

379

UNCLASSIFIED

F/G 11/6.1 NL





Using Griffith's virtual work argument, Willis (1971) formally calculated the increment of elastic energy dissipation associated with an increment of crack-face advancement for the general anisotropic crack. (He evaluated the elastic energy release rate.) Willis did this by formulating a "stress concentration vector," whose components are K_I , K_{II} , and K_{III} , and equated it with the the specific surface energy to establish a "stability relationship." For the planar isotropic case, Rice (1988) gave the energy release rate in terms of the complex stress intensity factor as

$$\mathcal{G} = \frac{C_1 + C_2}{16 \cosh^2(\pi\epsilon)} \mathbf{K} \bar{\mathbf{K}}, \quad (2.16)$$

where \mathcal{G} is the energy release rate per unit thickness.

Although the asymptotic stress fields and stress intensity factors are easily calculated, their interpretation is not straightforward as in the homogeneous case. For example, the elasticity solution for the bi-material traction-free crack-tip problem possesses some unusual characteristics. Asymptotically, the stress, strain, and displacement fields oscillate with radial distance, and this oscillation in the displacement field causes the crack faces to contact and mathematically interpenetrate. England (1965), using the asymptotic solution for an internally pressurized Griffith crack with length $2a$, calculated the crack-face contact length, δ , by determining the distance from the crack tip to where crack-face interpenetration would occur. For this geometry he found that

$$\frac{\delta}{2a} = 1.26 \times 10^{-4}. \quad (2.17)$$

Since England's calculation was evaluated for $\epsilon = 0.1748$, the maximum value of the bi-material constant in plane strain for materials with positive Poisson's ratio, he concluded that for more realistic property choices the contact distance would be even smaller. For the same Griffith crack geometry but loaded by remote tensile and shear tractions, Rice (1988) calculated values of $\delta/2a$ which were appreciably larger than Eq.(2.17) for certain loading conditions.

Additional complications exist in the definition of the stress intensity factor \mathbf{K} . Rice (1988) pointed out that the interpretation of K_I and K_{II} is ambiguous since K_I and K_{II}

individually do not correspond physically to a pure opening mode or a pure shear mode. Furthermore, the choice of physical units used in determining the numerical value of the stress intensity factor affects the ratio of K_I and K_{II} for any given boundary value problem. Using the definition of K given by Hutchinson, Mear, and Rice (1987) in Eq.(2.13) results in the following generic stress intensity factor:

$$K = \sigma^\infty C e^{-i\epsilon \ln l} \sqrt{\pi l}, \quad (2.18)$$

where σ^∞ is a resultant traction expressed as a complex number with the dimensions of stress, C is a non-dimensional complex geometric constant, and l is the characteristic geometric length of the problem, such as crack or ligament length, distance from the crack tip to point of load application, etc. Examining Eq.(2.18) reveals that when different length units (e.g., m, inches, cm) are assigned to l , $\angle K$ changes. [Here $\angle()$ refers to the phase angle of the complex argument $()$, and the $\angle K$ is chosen such that $-\pi < \angle K < \pi$.] Thus, an infinite number of stress intensity factors, all with different ratios of K_I to K_{II} (and different units), could exist which all yield identical stress states. *This implies that the decomposition of K is meaningless since only in the degenerate case, when $\epsilon = 0$, does modal decomposition of K_I and K_{II} take on any unique or significant meaning.*

The units associated with the bi-material stress intensity factor are unique in that they differ from the homogeneous stress intensity factor by $l^{-i\epsilon}$. For example, typical units of K may be $\text{MPa}(\text{m})^{0.5-0.0332i}$. To remove this uncommon dimension, $(\text{m})^{-0.0332i}$, Shih and Asaro (1987) defined a stress intensity vector Q such that, as $r \rightarrow 0$ on $\theta = 0$, $\sigma_{yy} + i\sigma_{zy} \rightarrow Q(r/l)^{i\epsilon}/\sqrt{2\pi r}$. This expression differs from Eq.(2.13) by the factor $l^{-i\epsilon}$. This approach uniquely identifies $\angle K$, and when used in Shih and Asaro's elasticity expressions produces, at a fixed point, the identical stress state as compared with the previous definition. However, several problems arise in using Shih and Asaro's stress intensity vector Q . The choice of l becomes ambiguous when several geometric lengths exist. For example, in a compact tension specimen (CTS), at least three lengths exist which could be used, namely the thickness, the width, and the crack or ligament length,

and uncertainties clearly exist regarding the appropriate choice of the normalizing length dimension. Second, Shih and Asaro's definition may yield confusion because two different loadings which produce identical stress intensity vectors only produce identical crack-tip stress fields when ϵ is the same for both cases. Although the definition of Hutchinson *et al.* requires additional unusual dimensions to be carried along; the possible non-uniqueness problem is totally circumvented. Therefore, for convention, the definition given by Hutchinson *et al.*, Eq.(2.13), is used in the remainder of this study.

2.1.2 Closed Crack-Tip Faces

In an attempt to eliminate the unsatisfactory aspects of the oscillatory singularity in the traction-free crack-tip model, various other crack-tip models have been proposed. Comninou (1977a) included a frictionless contact zone at the crack tip of a Griffith crack which transmitted only compressive normal tractions and required both traction and displacements to be continuous over the intact interface. Comninou then formulated a singular integral equation to describe the dislocation density which was necessary to produce closed crack tips. She also used the Williams technique of expressing a general power series Airy stress function, Eq.(2.1), about a closed crack tip with crack-face friction (Comninou, 1977b) and without crack-face friction (Comninou, 1977a). By enforcing continuity of tractions and displacements across the interface and by requiring continuous (compressive) normal tractions and normal displacements on the closed crack face, an eigenvalue problem of eight simultaneous equations arose from which acceptable values of λ_j and forms of $F_j(\theta, \lambda_j)$ were determined.

The results of her numerical solution of the singular integral equation and her frictionless crack-tip expansion agreed, demonstrating that as $r \rightarrow 0$, the dominant stress field around the closed crack tip is given by

$$\sigma_{rr} = \frac{-K_{II}^c}{4\sqrt{2r}} \left\{ 5(1 \mp \beta) \sin \frac{\theta}{2} - (3 \pm \beta) \sin \frac{3\theta}{2} \right\}, \quad (2.19)$$

$$\sigma_{\theta\theta} = \frac{-K_{II}^{\epsilon}}{4\sqrt{2r}} \left\{ 3(1 \mp \beta) \sin \frac{\theta}{2} + (3 \pm \beta) \sin \frac{3\theta}{2} \right\}, \quad (2.20)$$

and

$$\sigma_{rr} = \frac{K_{II}^{\epsilon}}{4\sqrt{2r}} \left\{ (1 \mp \beta) \cos \frac{\theta}{2} + (3 \pm \beta) \cos \frac{3\theta}{2} \right\}, \quad (2.21)$$

where, using Comninou's convention for numbering material domains,

$$\beta = \frac{\mu_2(\eta_1 - 1) - \mu_1(\eta_2 - 1)}{\mu_2(\eta_1 + 1) + \mu_1(\eta_2 + 1)}. \quad (2.22)$$

Here K_{II}^{ϵ} is the strength of the singularity, and the *upper* and *lower* signs are used in the lower and upper material domains, respectively. To ensure compressive tractions in the contact zone, loadings are restricted such that $K_{II}^{\epsilon} > 0$ for $\beta > 0$ and $K_{II}^{\epsilon} < 0$ for $\beta < 0$.

A note of caution: Comninou reversed the ordering of the material domains as compared to the convention used by Williams (1957), and others. *Figure 2.1* shows the crack-tip geometry Comninou assumed. *In her work the material in the upper domain is referred to by the subscript 2, and the material in the lower domain is referred to by the subscript 1.* Switching the ordering of the material domains changes the sign of the bi-material constants β and ϵ . For convention, in the present work β will be defined with the subscript 1 in the *lower* domain, and ϵ will be defined with the subscript 1 in the *upper* domain. Using this convention, β is related to ϵ via

$$\epsilon = \frac{1}{2\pi} \ln \left[\frac{1 - \beta}{1 + \beta} \right]. \quad (2.23)$$

Along the interface, the shear component is the only dominant asymptotic stress term that is non-zero, and it behaves as $\sigma_{r\theta}(r, \theta = 0) = K_{II}^{\epsilon}/\sqrt{2r}$. This implies that the additional load carried by the interface, which results from the presence of the crack, is asymptotically only supported by interfacial shear tractions. Note that the interface still supports normal tractions which arise from the far-field loading and from the complete local solution, even in the crack-tip vicinity, and these normal tractions may be on the order of 25 times the tensile far-field opening traction (Comninou, 1977a). The

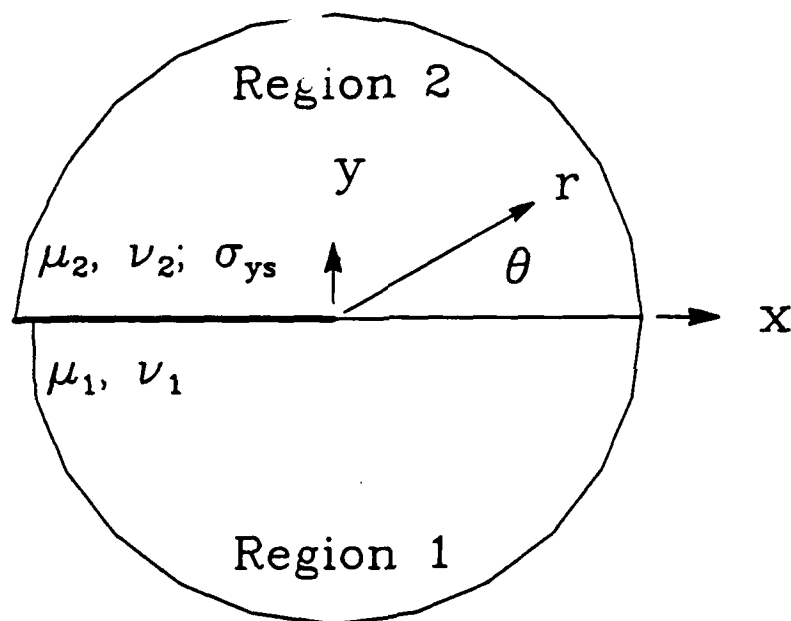


Figure 2.1 Schematic closed bi-material interfacial crack-tip region, including polar (r, θ) and Cartesian (x, y) coordinates and domain numbering convention.

(compressive) normal traction in the contact zone is singular — $\sigma_{yy} = -K_{II}^c \beta / \sqrt{2r}$ as the crack tip is approached — and is bounded as the crack opening (gap) is approached. To be precise, Comninou mathematically requires the normal traction to be equal to zero in the contact zone at the point where crack opening initiates. [A standard moving Hertzian contact boundary condition (Johnson, 1985).]

The complete set of admissible roots for Comninou's Williams type crack-tip expansion contains two series with *real* values. The two admissible series of roots which produce finite crack-tip strain energy and no concentrated crack-tip forces are

$$\lambda_j = \left\{ j + \frac{1}{2}, \right. \quad (2.24)$$

where j is a non-negative integer. (Note, this spectrum of admissible roots is the same as that found for the homogeneous crack problem.) The other roots of interest are $\lambda = 0$, which corresponds to a uniform (domain wise constant) stress field, and $\lambda = 1/2$, which represents a positive square-root stress field ($\sigma \propto \sqrt{r}$). The constraints on the uniform stress field are that σ_{yy} , σ_{zy} , and ϵ_{zz} are continuous along the interface. To satisfy these conditions a "stress jump across (the) interface" (Rice and Sih, 1965) is generally required, and because the crack faces are free of shear traction, $\sigma_{zy} = 0$. It is interesting to note that all half-integer roots ($\lambda = j + 1/2$) in the closed crack-tip expansion, produce no normal interfacial tractions [$\sigma_{rr}(r, \theta = 0) = \sigma_{\theta\theta}(r, \theta = 0) = 0$].

Comninou calculated a stress intensity factor, K_{II}^c , for her model. It is obtained by taking the limit as $r \rightarrow 0$ in the crack-tip region, and is given as

$$K_{II}^c \equiv \lim_{r \rightarrow 0} \left\{ \sqrt{2r} \sigma_{zy}(r, \theta = 0) \right\}. \quad (2.25)$$

Note, Eq.(2.25) produces stress intensity factors having the same dimensions as in the homogeneous case, but differs from the usual homogeneous stress intensity factor definitions by a factor of $\sqrt{\pi}$. (Comninou (1977a) actually calculates two stress intensity factors for her model, however the stress intensity factors are always proportional to each other for $\beta \neq 0$ and are used nearly interchangeably to scale a single set of crack-tip field equations.) Excluding the compressive contact tractions, the crack-tip

fields can be regarded as being quasi-homogeneous "mode II." In other words, for the homogeneous case, $\beta = 0$, the stress state expressed in Eqs.(2.19) to (2.21) reduces to that found for homogeneous mode II loading (Comninou, 1977a).

Gautesen and Dundurs (1987) were able to solve exactly an additional integral in Comninou's formulation for the case of remote tensile loading of a Griffith crack geometry. By writing equivalent series expansions and using some appropriate small argument approximations, they found that, for $\beta > 0$ ($\epsilon < 0$), the total normal stress directly ahead of the closed crack tip is equal to

$$\sigma_{yy}(r = 0^+, \theta = 0) = \frac{\sigma_{yy}^\infty \beta_0}{\pi k_g} \sqrt{1 + \frac{\beta_0^2}{\pi^2}} \left[1 + O(k_g^2) \right], \quad (2.26)$$

where

$$\beta_0 = \ln \left[\frac{1 + \beta}{1 - \beta} \right] = -2\pi\epsilon \quad (2.27)$$

and

$$k_g^2 = 16 \exp \left\{ -\frac{\pi^2}{\beta_0} \left[\frac{2}{\pi} \tan^{-1} \left(\frac{\beta_0}{\pi} \right) + 1 \right] \right\}. \quad (2.28)$$

Here σ_{yy}^∞ is the far-field opening stress. They show that for opening loads, as $\beta \rightarrow 0$ (or alternatively as $\epsilon \rightarrow 0$), the extent of the crack-tip contact vanishes. Additionally, the stress intensity factor K_{II}^c for $\beta > 0$ ($\epsilon < 0$) of such a Griffith crack loaded by the far-field stress σ_{yy}^∞ is given by

$$K_{II}^c = \sigma_{yy}^\infty \sqrt{a} \left\{ \sqrt{1 + \frac{\beta_0^2}{\pi^2}} + O(k_g^2) \right\}, \quad (2.29)$$

where $2a$ is the crack length. For the range $0 < \beta \leq 0.5$ ($0 > \epsilon \geq -0.175$), $K_{II}^c/(\sigma_{yy}^\infty \sqrt{a})$ varies by less than 6%.

When the contact zone is small compared to crack length, results from Comninou's model are consistent with those found by others. For remote tensile loading, she determined that the contact zone is smaller than the maximum first contact calculated by England. She further found that the global stress field away from the immediate

crack-tip region still contains the oscillatory singularity and is not significantly different from the stress field previously obtained. Also, the inclusion of contact zones in Comninou's model eliminates the oscillatory nature of the singularity in the very near crack-tip field.

For arbitrary far-field shear, σ_{xy}^∞ , and normal, σ_{yy}^∞ , loading of a Griffith crack geometry, the crack-face contact length is not always small compared to crack length and the oscillatory stress field may never be recovered, even at relatively large distances from the crack-tip. Comninou and Schmueser (1979) found that for a Griffith crack geometry with $\beta > 0$, at fixed values of σ_{yy}^∞ , the contact length at the right hand crack tip increases when positive remote shear is applied, and for fixed values of σ_{xy}^∞ , increases as the level of remote normal stress decreases to compressive levels. Simultaneously, as the contact length at the right hand crack tip increases, the contact length at the left hand crack tip decreases. Table 2.2 lists the right hand contact length δ for various combinations of far-field loads applied to a Griffith crack geometry. (The notation used is the same as that used previously to define K for the infinite plate in Table 2.1.) For a pure far-field shear load ($\sigma_{yy}^\infty = 0$) and for a compressive normal load, substantial contact lengths exist. Any predictions based upon a "traction-free crack-tip" model for the right hand crack tip under positive shear, with even modest levels of applied normal stress (say for $\beta = 0.5$, $\sigma_{yy}^\infty \leq 3\sigma_{xy}^\infty$), are ill-founded and clearly unjustifiable, since the contact length is so large (e.g., for $\beta = 0.5$, $\delta/2a > 0.1$).

$\sigma_{yy}^\infty/\sigma_{xy}^\infty$	$\delta/2a$
0.50	0.068
0.25	0.23
0	0.33
-0.25	0.60
-0.50	0.78
-0.75	0.88
-1.00	0.92

Table 2.2 Contact lengths at the right hand crack tip of a Griffith crack geometry loaded by far-field stress; $\beta = 0.5$ and $\sigma_{xy}^\infty > 0$ (Comninou and Schmueser, 1979).

In addition to Comninou, others have included various crack-tip models in an attempt to remove the oscillatory singularity and accurately account for contact. For certain geometries and loadings, Atkinson (1982) showed, by several examples, that the elastic energy release rate is virtually unaffected by the precise details of the very near crack-tip model used. In general, such crack-tip modeling may remove the oscillatory behavior locally, but does not remove all the singularities at the crack tip. As with all infinitesimal elasticity solutions, they are only valid in the region where the assumptions of linear material response as well as small strains and rotations, are not violated.

2.2 Inferred Plastic Behavior

From the expressions for the local elastic asymptotic crack-tip stresses, it is clear that unbounded stresses arise as the crack tip is approached. The applicability of linear elastic models must therefore be examined in terms of the mathematical assumptions and the material idealizations used in deriving them. Based upon the tensile behavior of most polycrystalline metals, it is clear that linear elasticity is not an appropriate idealization very near the crack tip, where unbounded stresses are predicted, because nonlinear deformation is anticipated. The inclusion of continuum non-linear material behavior, such as power law strain-hardening or elastic/perfectly-plastic, allows for better representation of the actual material response for many materials and situations. When continuum length assumptions apply, local crack-tip plasticity is typically found embedded within the singular elasticity fields and separated by a transitional "boundary layer." The parametric framework which describes the non-linear to linear material transition should be obtainable by considering the elastic field along the transition boundary. The aim of this section is to describe the boundary characteristics of the continuum non-linear zone in terms of far-field loads and material properties by assuming that the non-linear zone boundary can be approximated by the loci of points whose elastically-calculated Mises equivalent stress, $\bar{\sigma}$, is equal to the tensile

yield strength of the material, σ_y . Using this assumption and the two asymptotic elasticity solutions, Eqs.(2.4) to (2.7) and Eqs.(2.19) to (2.21), a consistent parametric framework for describing the plastic-zone characteristics is assembled.

Several quantities are needed in this framework. First, a representative plastic zone characteristic dimension r_p , given in terms of the far-field applied load and material properties, is required in order to determine if SSY conditions are satisfied. It will be shown that a natural choice for the characteristic dimension is $r_p = K\bar{K}/\sigma_y^2 \pi \cosh^2(\pi\epsilon)$ for the traction-free crack-tip model and $r_p^c = 3K_{II}^c/2\sigma_y^2$ for the closed crack-tip face model. In general, σ_y is the tensile yield strength of the material in either domain, but henceforth shall refer to the tensile yield strength of the plastically deformable material in the upper domain of *Figures 1.1* and *2.1*. Next, it is necessary to determine the size and shape of the plastic zone, in terms of the applied load. It will be shown that traction-free crack-tip plastic zone growth occurs in a periodic manner with respect to increasing stress intensity factor K , and the tractions along the plastic zone boundary also change in a periodic manner, because the tractions simultaneously evolve with the plastic zone. In the closed crack-tip model, it will be shown that the plastic zone growth is self-similar, and that the size of the plastic zone can be scaled by the closed crack-tip characteristic plastic zone dimension r_p^c . Because a single unique plastic zone shape does not exist during loading for the traction-free model, as it does for the closed crack-tip model, an additional quantity describing the phase of the plastic zone will be introduced. The interfacial load phase angle (ILPA), ζ_0 , defined as

$$\zeta_0 = \angle K + \epsilon \ln \left[\frac{K\bar{K}}{\sigma_y^2 \pi \cosh^2(\pi\epsilon)} \right], \quad (2.30)$$

accounts for all possible loading combinations while it compensates for plastic zone growth within the oscillatory field. It uniquely characterizes the plastic zone shape, plastic zone tractions, and determines whether crack-face contact is occurring at the plastic zone edge.

Finally, and most importantly, conditions defining the applicability of each model as well as any possible combination of models, will be identified. It will be assumed that

the traction-free crack-tip model is the governing model, in regards to identifying when each model is appropriate. It is chosen because it analytically exists in closed form and all necessary quantities used in the closed crack-tip face model can be approximated from it when the contact length is small compared to crack length. For certain loading conditions, it will be shown that the closed crack-tip face model is applicable because significant crack-face contact exists. Based upon the value of the ILPA, explicit domains for which the characteristic plastic zone dimension in each model is acceptable, as compared to the length of the crack-face opening or closure, will be identified.

It will be shown that these two continuum interfacial crack-tip models will describe most, but not all, possible crack loadings. For certain circumstances, even when the size of the plastic zone is small compared to crack length, neither of these interfacial crack-tip models will appropriately describe the actual crack-tip behavior. Justification for use of this framework will be made by comparing its elastically based predictions against various precise solutions for actual strain hardening materials. This agreement will warrant the use of this framework for all monotonically increasing strain hardening constitutive relationships [strain \propto (stress)ⁿ] which include an initial linearly elastic ($n = 1$) range.

2.2.1 Traction-Free Crack Faces

The following section is a paper submitted to the Journal of Applied Mechanics by the author and Prof. D. M. Parks which derives an approximate expression for the plastic zone from the asymptotic Williams type oscillatory elasticity solution. It discusses predicted plastic zone size, shape, and growth characteristics, introduces various key bi-material interfacial variables, and gives formal validity conditions, in terms of K , material properties, geometry, and bi-material interfacial variables, for the applicability of the traction-free crack tip BV problem outlined in Chapter 1.

For consistency, all equations, figures, and sections referenced from this paper will be identified using the prefix (P2.).

ELASTIC YIELD ZONE AROUND AN INTERFACIAL CRACK TIP

by
Edward Zywick
and
David M. Parks

Department of Mechanical Engineering
Massachusetts Institute of Technology
Cambridge, Massachusetts 02139 USA

Abstract

A closed form approximate solution for a small scale yielding (SSY) plastic zone around a planar interfacial crack-tip, occurring between two dissimilar ideally-bonded elastic half-spaces, is obtained by equating the elastically-calculated Mises equivalent stress with the material yield strength, σ_y . The dimensionless parameter $\zeta(\theta)$, which is defined as $\zeta(\theta) = \angle K + \epsilon \ln r_p(\theta)$, where $\angle K$ is the phase angle of the complex stress intensity factor K , ϵ is the bimaterial constant, and $r_p(\theta)$ is the polar representation of the plastic zone radius, naturally arises. The SSY interfacial load phase angle (ILPA), defined as $\zeta_0 = \angle K + \epsilon \ln (K\bar{K}/\sigma_y^2 \pi \cosh^2(\pi\epsilon))$, leads to periodic zone growth. The ILPA characterizes the overall applied load phase by combining the oscillatory radial phase shift, attributable to the increase in zone size due to increased loading, with $\angle K$. At a particular angle θ_0 from the uncracked interface, the plastic zone radius thus calculated is independent of $\angle K$, proportional to $K\bar{K}$, and has no oscillatory radial phase dependence. The derived plastic zone expression reproduces the shape characteristics, and it modestly reproduces the zone size when compared with solutions for an elastic/perfectly-plastic solid adjoint to an elastic solid. As the strain hardening exponent in the plastically deforming medium decreases, agreement between the approximation and various accurate numerical solutions improves. In the limiting case when $\epsilon = 0$, the well-known homogeneous elastic solutions for pure mode I and mode II are recovered, as well as all possible mixed mode combinations. Approximate validity conditions for the existence of Williams type asymptotic fields (traction-free crack faces) are presented.

1 Introduction

Much effort has recently been focused on interfaces which exist between dissimilar media, with specific attention being directed toward media separation or fracture events. Publications on the subject, such as Shih and Asaro (1987), Hutchinson *et al.* (1987), and Rice (1988) clarify several aspects of the original oscillatory stress solution obtained by Williams (1959) for an interfacial crack and attempt to apply or further extend traditional (homogeneous) fracture mechanics approaches to interface cracking phenomena. Elastic interfacial crack-tip fields between isotropic media are well characterized, although only a limited number of geometries have had their stress fields and stress intensity factors solved exactly. Ting (1986) has presented a rigorous framework for determining the degree of singularity and the asymptotic characteristics for the general interfacial crack between two elastic anisotropic materials. When non-linear material responses are included, no explicit unifying characterization presently exists to unite the various fracture parameters. However, dimensional analysis by Rice (1988) and by Shih and Asaro (1987) lead to symbolic functional relationships consistent with the present results.

Insight concerning contained crack-tip inelastic deformation zones (in the small scale yielding, SSY, sense) can be obtained by considering the characteristics contained within the elasticity solution. One approximate method which has been used to determine the plastic zone shape and size around a crack tip in a homogeneous medium is equating the elastically-calculated Mises or Tresca equivalent stress with the yield stress of the material (McClintock and Irwin, 1965; Rooke, 1963). The locus of all points satisfying this condition is considered to be the plastic zone boundary which separates the exterior elastic region from the interior plastically yielding region. The changes in plastic zone size and shape with respect to the applied load or stress intensity factor(s) can then be estimated from this expression.

The goal of this work is to present a closed form approximate plastic-zone solution for an interfacial crack between isotropic linear elastic media, and propose various dimensional and dimensionless quantities, which naturally arise in the derivation, as interfacial fracture parameters that uniquely characterize the interface crack-tip region. Comparisons will be made between the approximate solution and various precise numerical solutions to demonstrate its accuracy. Conditions which determine the validity of this expression will be stated.

2 SSY Plastic Zone Approximation

The problem considered is a planar interfacial crack, as shown in *Figure 1*, whose constituents have shear moduli μ_j ($j = 1, 2$) and Poisson's ratios ν_j . (Subscripts 1 and 2 refer to the upper and lower domains, respectively.) Far field loads produce a local elastic stress field which is well characterized by the complex stress intensity factor K and asymptotic interfacial crack-tip stress fields. Following Hutchinson *et al.* (1987), the stress intensity factor is defined such that as, as $r \rightarrow 0$ on $\theta = 0$, $\sigma_{yy} + i\sigma_{zy} \rightarrow Kr^{\epsilon}/\sqrt{2\pi r}$. For the interfacial "Griffith" crack configuration, this definition for K differs from that given by Shih and Asaro (1987) by the complex term $e^{-i\epsilon \ln 2a}$. (See Rice (1988) for calculated examples of K for various geometries and for the interfacial stress fields.) The bimaterial constant, ϵ , which modulates the stress and displacement oscillation period, is defined as

$$\epsilon = \frac{1}{2\pi} \ln \left[\frac{\left(\frac{\kappa_1}{\mu_1} + \frac{1}{\mu_2} \right)}{\left(\frac{\kappa_2}{\mu_2} + \frac{1}{\mu_1} \right)} \right], \quad (1)$$

where $\kappa_j = 3 - 4\nu_j$ for plane strain and $\kappa_j = (3 - \nu_j)/(1 + \nu_j)$ for plane stress.

The general stress field for an isotropic elastic solid can be represented by the Muskhelishvili potential representation (Rice, 1988),

$$\sigma_{zz} + \sigma_{yy} = 2 [\phi' + \bar{\phi}'] \quad (2)$$

and

$$\sigma_{yy} - \sigma_{zz} + i2\sigma_{zy} = 2 [(\bar{z} - z)\phi'' - \phi' + \Omega']. \quad (3)$$

Retaining only the dominant asymptotic term as $r \rightarrow 0$, the plane strain elastic potentials in the upper domain are

$$\phi'_1 = a_0 e^{-\pi\epsilon} z^{-\frac{1}{2}-i\epsilon}, \quad (4)$$

and

$$\Omega'_1 = \bar{a}_0 e^{\pi\epsilon} z^{-\frac{1}{2}+i\epsilon}. \quad (5)$$

Using Eqs.(2) to (5), an expression for the Mises equivalent stress in region 1 can be obtained. (Appendix A contains the complete general series potential functions and

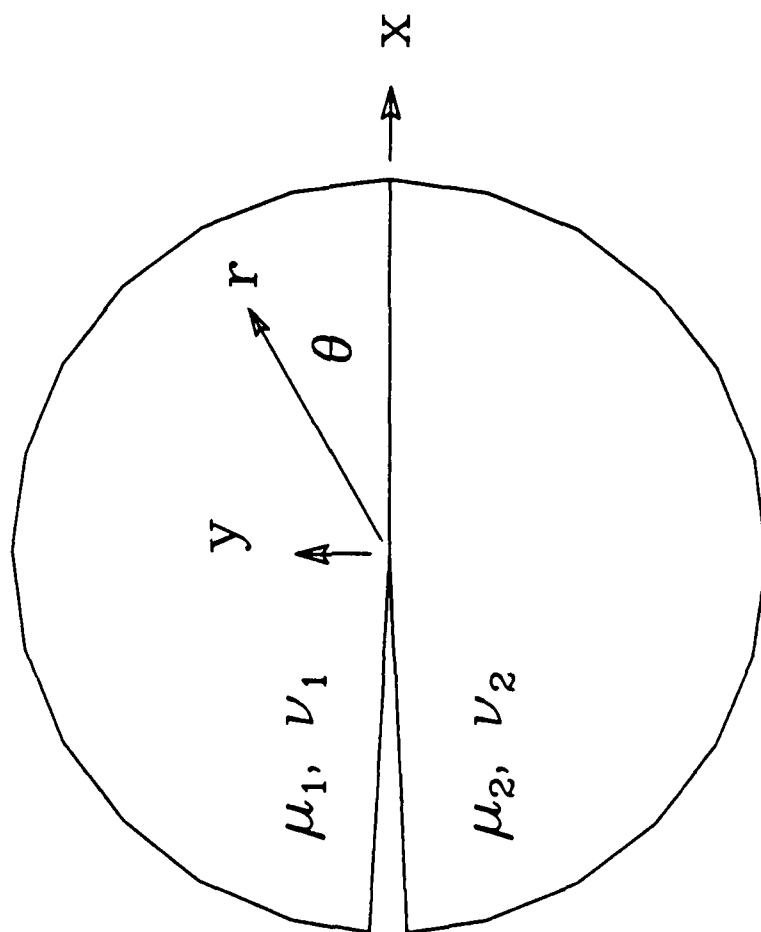


Figure 1 Schematic interfacial crack tip.

formally calculates the Mises equivalent stress.) Equating the Mises equivalent stress, $\bar{\sigma}$, Eq.(A.27) with the material yield strength, σ_{ys} , and solving for the radius yields

$$r_p(\theta) = \frac{K\bar{K}}{\sigma_{ys}^2 \pi \cosh^2(\pi\epsilon)} \frac{1}{8} \times \left\{ \cos 2\zeta(\theta) \left[-3(1 + \cos 2\theta) - 6\epsilon \sin 2\theta + (8D - 6)e^{2\epsilon(\theta-\pi)} \cos \theta \right] \right. \\ \left. + \sin 2\zeta(\theta) \left[3 \sin 2\theta - 6\epsilon(\cos 2\theta - 1) - (8D - 6)e^{2\epsilon(\theta-\pi)} \sin \theta \right] \right. \\ \left. + e^{2\epsilon(\theta-\pi)} \left[\left(\frac{3}{2} - 6\epsilon^2 \right) (\cos 2\theta - 1) + 6\epsilon \sin 2\theta + (8D - 3) \right] + 3e^{2\epsilon(\pi-\theta)} \right\}, (6)$$

where

$$D = \nu_1^2 - \nu_1 + 1 \quad (7)$$

and

$$\zeta(\theta) = \angle K + \epsilon \ln r_p(\theta). \quad (8)$$

Here θ is the angle measured from the interface, $r_p(\theta)$ is the plastic zone radius from the crack tip, and $\angle K$ is the phase angle of the (complex) stress intensity factor defined with a branch cut at $\theta = \pi$ such that $\pi > \angle K > -\pi$. ($\angle K = \arctan(\Im K / \Re K)$), which in the homogeneous case, $\epsilon = 0$, reduces to $\angle K = \arctan(K_{II}/K_I)$). For plane stress conditions, Eqs.(6) and (8) are still valid; however, Eq.(7) is redefined as $D = 1$ and the plane stress value for ϵ must be used.

This approximation is valid only when a dominant elastic crack field exists and the maximum extent of the plastic zone is small compared to crack length (l) or other characteristic dimensions (maximum $r_p \ll l$). Further clarification will be stipulated in section 3.4.

3 Discussion

3.1 Mathematical Considerations

Several interesting mathematical features arise from Eq.(6). Foremost, the dimensionless $\zeta(\theta)$ is naturally obtained in the derivation. It removes the dimensional problems associated with assigning length units in K definitions (Rice, 1988) since $\zeta(\theta)$ is invariant as long as $r_p(\theta)$ and K are expressed with the same length units. Recall the generic K ,

$$\mathbf{K} = \mathcal{Q}^{\infty} C e^{-i\epsilon \ln l} \sqrt{\pi l}, \quad (9)$$

where \mathcal{Q}^{∞} is the far field load expressed as a complex number, C is a dimensionless complex geometric constant, and l is the characteristic dimension. Examination of Eq.(9) reveals that when different length units are used to express l , the $\angle \mathbf{K}$ changes. Eq.(9) can be rewritten as

$$\mathbf{K} = \|\mathcal{Q}^{\infty}\| \times \|C\| e^{i(\phi - \epsilon \ln l)} \sqrt{\pi l}, \quad (10)$$

where $\| \quad \|$ denotes the magnitude of a complex expression,

$$\phi = \angle \mathcal{Q}^{\infty} + \angle C, \quad (11)$$

and

$$\angle \mathbf{K} = \phi - \epsilon \ln l. \quad (12)$$

Substituting Eqs.(6), (11), and (12) into Eq.(8) yields

$$\zeta(\theta) = \phi - \epsilon \ln l + \epsilon \ln \left\{ \frac{\mathbf{K} \bar{\mathbf{K}}}{\sigma_y^2 \pi \cosh^2(\pi \epsilon)} g(\theta, \epsilon, D, \zeta(\theta)) \right\}, \quad (13)$$

where $g(\theta, \epsilon, D, \zeta(\theta))$ is a non-dimensional function. Using Eq.(10), $\mathbf{K} \bar{\mathbf{K}}$ can be expressed as

$$\mathbf{K} \bar{\mathbf{K}} = \|\mathcal{Q}^{\infty}\|^2 \times \|C\|^2 \pi l. \quad (14)$$

Furthermore, Eq.(13) can be rearranged and simplified by using Eq.(14), and it reduces to

$$\zeta(\theta) = \phi + 2\epsilon \ln \left\{ \frac{\|\mathcal{Q}^{\infty}\| \times \|C\|}{\sigma_y \cosh(\pi \epsilon)} \sqrt{g(\theta, \epsilon, D, \zeta(\theta))} \right\}. \quad (15)$$

From Eq.(15) it is clear that $\zeta(\theta)$ is dimensionless and independent of length units used to express \mathbf{K} . This is true as long as a single length measure is assigned to all l used when evaluating \mathbf{K} in, e.g., Eq.(10).

For a wide range of engineering interface material properties, an angle θ_0 exists for which the coefficients

$$P_1 = -3(1 + \cos 2\theta) - 6\epsilon \sin 2\theta + (8D - 6)e^{2\epsilon(\theta - \pi)} \cos \theta \quad (16)$$

and

$$P_2 = 3 \sin 2\theta - 6\epsilon(\cos 2\theta - 1) - (8D - 6)e^{2\epsilon(\theta-\pi)} \sin \theta, \quad (17)$$

which multiply the trigonometric functions of $2\zeta(\theta)$ in Eq.(6), are both zero. Alternatively, a single expression for determining θ_0 is obtained by requiring the magnitude of the coefficient multiplying the term JJ in Eq.(A.22) to be zero. Thus, when $\theta = \theta_0$,

$$4(8D - 6)e^{2\epsilon(\theta_0-\pi)}(-3 \cos \theta_0 - 6\epsilon \sin \theta_0) + (18 - 72\epsilon) \cos \theta_0 + 72\epsilon^2 \sin 2\theta_0 + (8D - 6)^2 e^{4\epsilon(\theta_0-\pi)} + 72\epsilon^2 + 18 = 0. \quad (18)$$

Figure 2 shows the plane strain θ_0 , numerically obtained from Eq.(18), for various ν from 0 to 0.5 for the complete range of ϵ , assuming non-negative ν in each material. Note that, θ_0 is generally not the same under plane strain conditions as it is under plane stress conditions since, under each condition ϵ and D have different definitions. The existence of θ_0 indicates that radially, at angle θ_0 :

- (a) Plastic zone growth is independent of the applied loading phase, $\angle K$.
- (b) The elastically-calculated Mises equivalent stress does not oscillate.
- (c) The plastic zone radius is proportional to $K\bar{K}$.

Substituting Eq.(6) into Eq.(8), and defining the SSY interfacial load-phase angle (ILPA), ζ_0 , as

$$\zeta_0 = \angle K + \epsilon \ln \frac{K\bar{K}}{\sigma_y^2 \pi \cosh^2(\pi\epsilon)}, \quad (19)$$

yields

$$\begin{aligned} \zeta(\theta) = \zeta_0 + \epsilon \ln \left\{ \cos 2\zeta(\theta) \left[-3(1 + \cos 2\theta) - 6\epsilon \sin 2\theta + (8D - 6)e^{2\epsilon(\theta-\pi)} \cos \theta \right] \right. \\ \left. + \sin 2\zeta(\theta) \left[3 \sin 2\theta - 6\epsilon(\cos 2\theta - 1) - (8D - 6)e^{2\epsilon(\theta-\pi)} \sin \theta \right] \right. \\ \left. + e^{2\epsilon(\theta-\pi)} \left[\left(\frac{3}{2} - 6\epsilon^2 \right)(\cos 2\theta - 1) + 6\epsilon \sin 2\theta + (8D - 3) \right] \right. \\ \left. + 3e^{2\epsilon(\pi-\theta)} \right\} - \epsilon \ln(8). \end{aligned} \quad (20)$$

Eq.(20) reveals that $\zeta(\theta)$ can be additively decoupled into a load-phase dependent quantity, ζ_0 , and a transcendental angular dependent function. Alternative definitions of ζ_0 , differing trivially by a pure constant, are possible. Such a constant could be chosen, *e.g.*, to approximately normalize the angular function to unity. Eq.(19) is a convenient expression for the SSY ILPA since it is an explicit single term representing

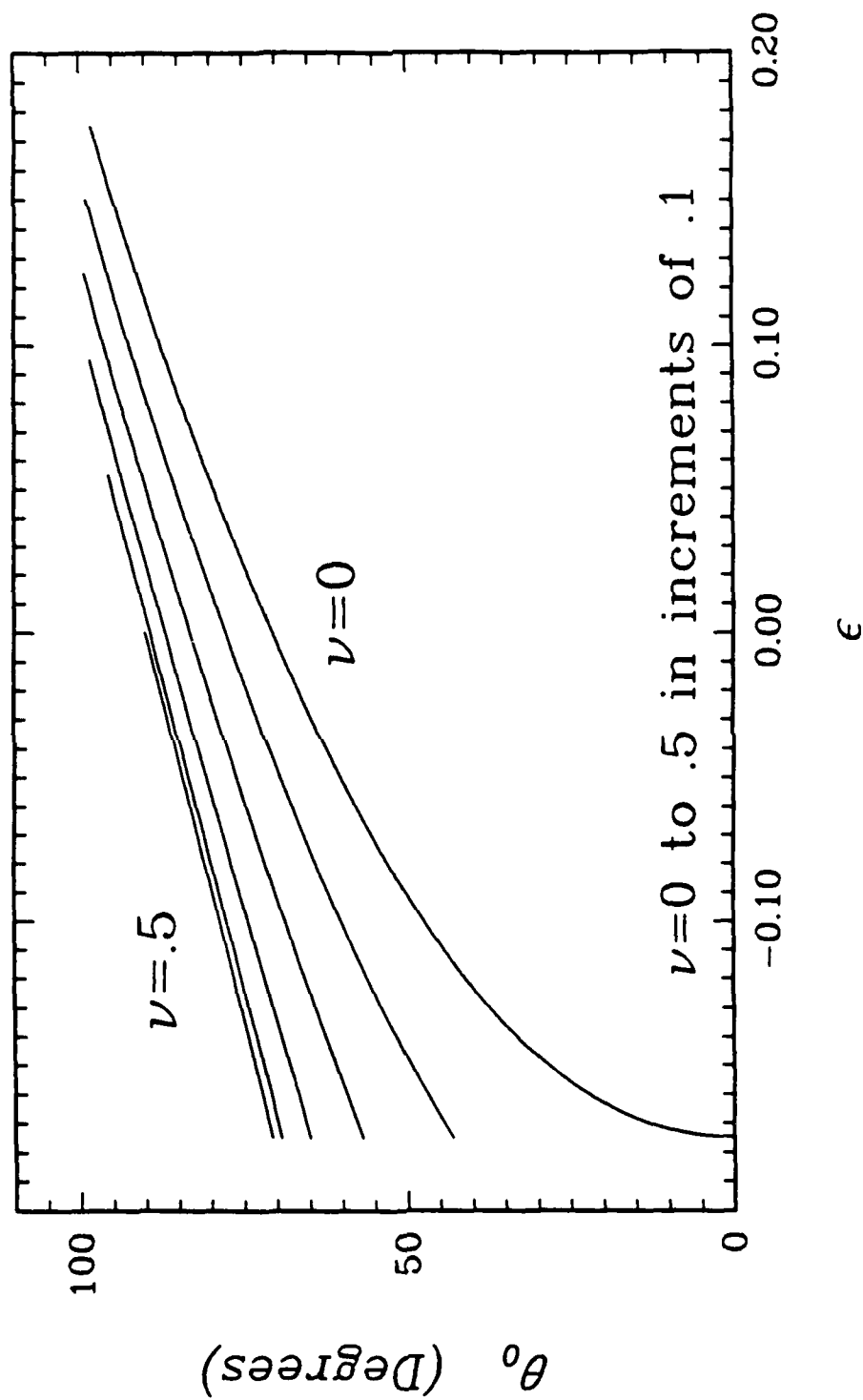


Figure 2 The angle θ_0 is shown for plane strain conditions over the complete range of ϵ for various values of ν from 0 to 0.5 in increments of 0.1.

the total load-phase angle and is common in all $\zeta(\theta)$. The ILPA totally describes the phase angle of the load by summing the loading phase shift, which is attributable to the change in zone size due to increases in loading, and the load-phase angle ($\angle K$).

Another useful expression is obtained by evaluating Eq.(20) at $\theta = \theta_0$, in which case

$$\zeta(\theta_0) = \zeta_0 + \epsilon \ln \left\{ \frac{1}{8} \left(3e^{2\epsilon(\pi-\theta_0)} + e^{2\epsilon(\theta_0-\pi)} \left[\left(\frac{3}{2} - 6\epsilon^2 \right) (\cos 2\theta_0 - 1) + 6\epsilon \sin 2\theta_0 + (8D - 3) \right] \right) \right\}. \quad (21)$$

This expression may prove to be beneficial in investigating the effects of various material dependent parameters, since it does not contain any radially oscillatory terms, and it represents a real value of $\zeta(\theta)$.

3.2 Zone Growth Considerations

From the above expressions, the overall plastic zone growth characteristics with respect to increasing applied load (K) during SSY, can be outlined. After sufficient initial loading has been applied to produce a continuum size plastic zone, the expressions for r_p become valid and applicable. Examination of Eqs.(6) and (20) shows that zone growth is quasi-proportional to $(K\bar{K}/\sigma_y^2)$, and that the zone shape periodically repeats itself with every π increase in ζ_0 . For (very) large cracks, it is possible that the plastic zone may repeat its shape during loading. For every discrete value of ζ_0 , a unique zone shape and a unique set of tractions along r_p exist. Figure 3 shows the plastic zone at various values of ζ_0 for $\epsilon = .170$ and $\nu = .342$. This suggests that ζ_0 uniquely describes the very local crack-tip fields within the zone as long as all previous loading experiences affect the current plastic state in the same manner. For the loading case where several cycles of ζ_0 have occurred, this would appear to be true. Since two loadings with unequal tractions can produce identical plastic zones, (e.g. $\zeta_0 = 90^\circ$ and $\zeta_0 = -90^\circ$ produce tractions with opposite signs), a full 2π evaluation of ζ_0 is required to determine all the local fields.

3.3 Comparisons

In the limiting homogeneous elastic case ($\epsilon = 0$), comparison with numerical solutions (Shih, 1974) indicate that the plastic zone shape and size for pure mode I and mode II, as well as for various mixed modes, are recovered. Comparing the approximate homogeneous plastic zones with plastic zones numerically obtained for strain hardening

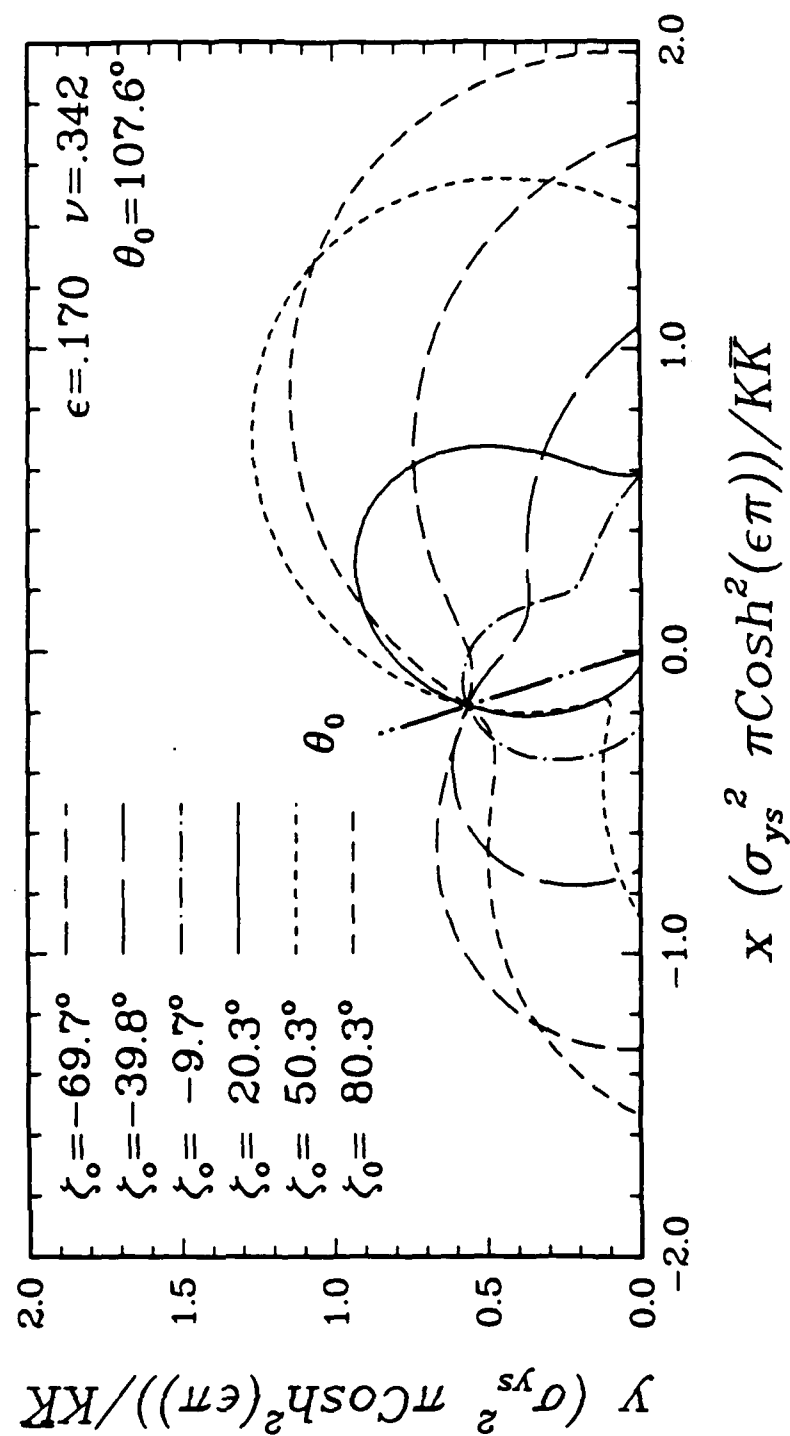


Figure 3 Approximate plastic zones for various ζ_0 values.

material shows that as the strain hardening exponent, n , increases (strain \propto (stress) n), the elastic approximation overestimates the plastic zone size behind the crack tip and underestimates it ahead of the crack tip. This is accompanied by slight distortional effects which tend to rotate the strain hardening plastic zone lobes toward the region in front of the crack as compared to the elastic approximation.

Figures 4 to 7 show finite element (FE) calculations of SSY plastic zones for an interfacial crack tip with an elastic/perfectly-plastic medium adjoint to an elastic medium (Zywickz, 1988), and the approximate plastic zones for several values of ϵ , ν_1 , μ_1 , and $\angle K$. Although the precise shape is not reproduced, the general size and distribution of the lobe(s) as well as their position(s) are well represented by the simple approximation. Examining Figure 5 shows that the size scale is significantly different from that of the other figures, demonstrating the accuracy of the approximation in predicting overall size. Figures 4 to 7 represent the worst case comparisons since perfect plasticity formally represents a strain hardening exponent of $n = \infty$. The jaggedness of the finite element calculated plastic zones is attributable to extrapolation/approximation errors and mesh discretization. Thus, the jaggedness should only be interpreted as an artifact of the discretization and plotting procedure. Figures 8 and 9 show FE calculations of plastic zones for a Ramberg-Osgood strain hardening material, with strain hardening exponents $n = 3$ and $n = 10$, respectively, adjoint to a rigid material (Shih and Asaro, 1987), and the approximate plastic zones for several load levels. These FE calculations were performed for a Griffith type crack, similar to the one shown in Figure 11, with $\epsilon = .0935$, $2a = 2m$, and $\nu_1 = .3$, where the stress intensity factor for the geometry and loading is $K = 1.803\sigma^\infty e^{0.1201i}(m)^{\frac{1}{2}-0.0935i}$. Here σ^∞ represents the remote stress normal to the crack face (the σ_{yy} stress as shown in Figure 11), and σ_0 is the reference stress (or yield stress). The overall sizes and shapes are well characterized by the (asymptotic) approximation. As in the homogeneous case, when the strain hardening exponent is decreased, the elastic approximation becomes more precise. (Recall, the Ramberg-Osgood material idealization produces a linear elastic response for $n = 1$.) Although the plastic zone radii are not all identically the same at θ_0 , the extent of the plastic zone in the vicinity of θ_0 is indeed approximately the same for all loadings (ζ_0).

3.4 Valid Solution Domain

The plastic zone approximation is based upon the assumption that a dominant (Williams type) field exists, as defined in Eqs.(4) and (5), near the crack tip and transitionally

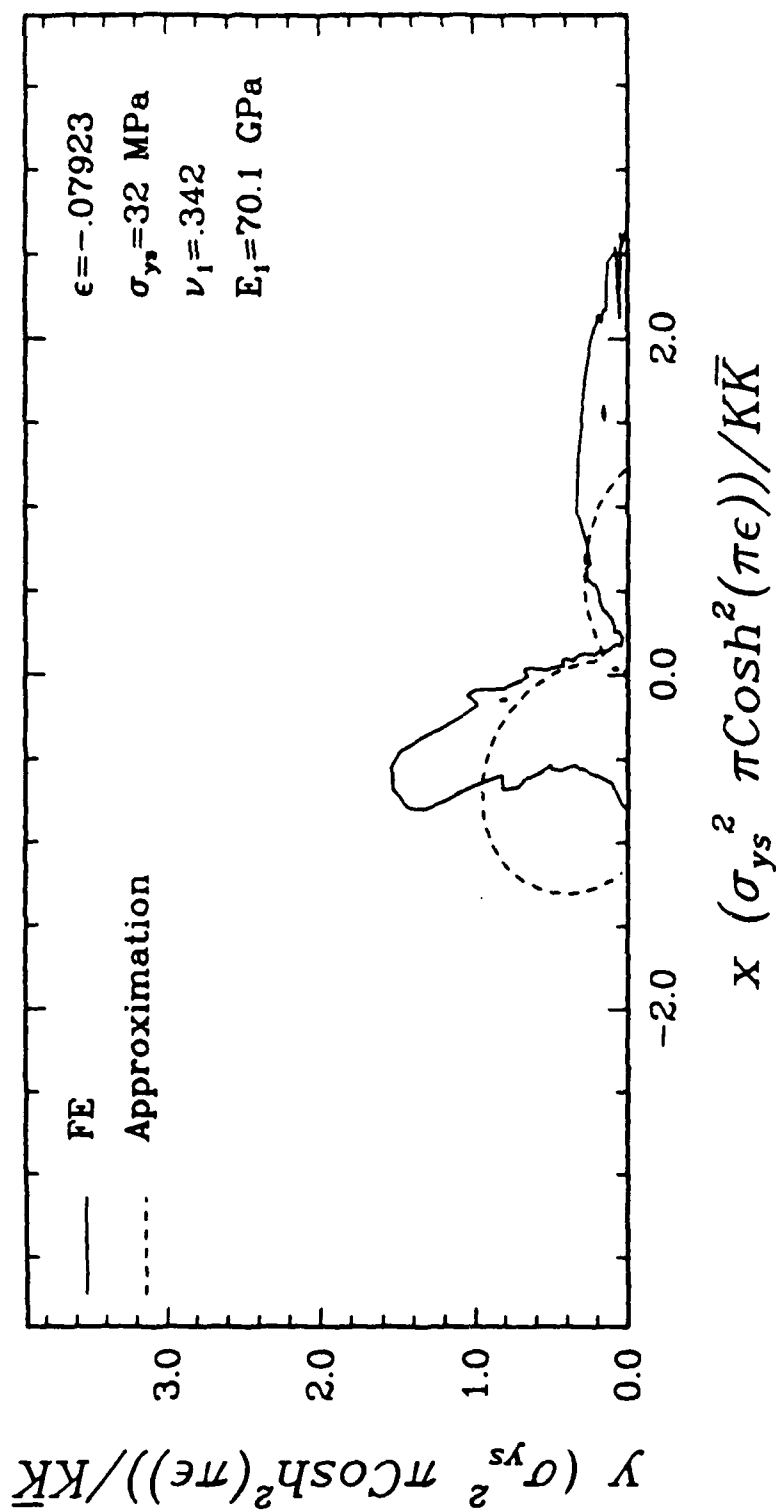


Figure 4 Plastic zone comparison between the elastic approximation and a finite element solution for an elastic/perfectly-plastic medium adjoint to an elastic medium; $K = 50e^{-0.4636i} \text{ MPa(m)}^{\frac{1}{2} + 0.07923i}$, $\zeta_0 = -0.432 (-24.7^\circ)$.

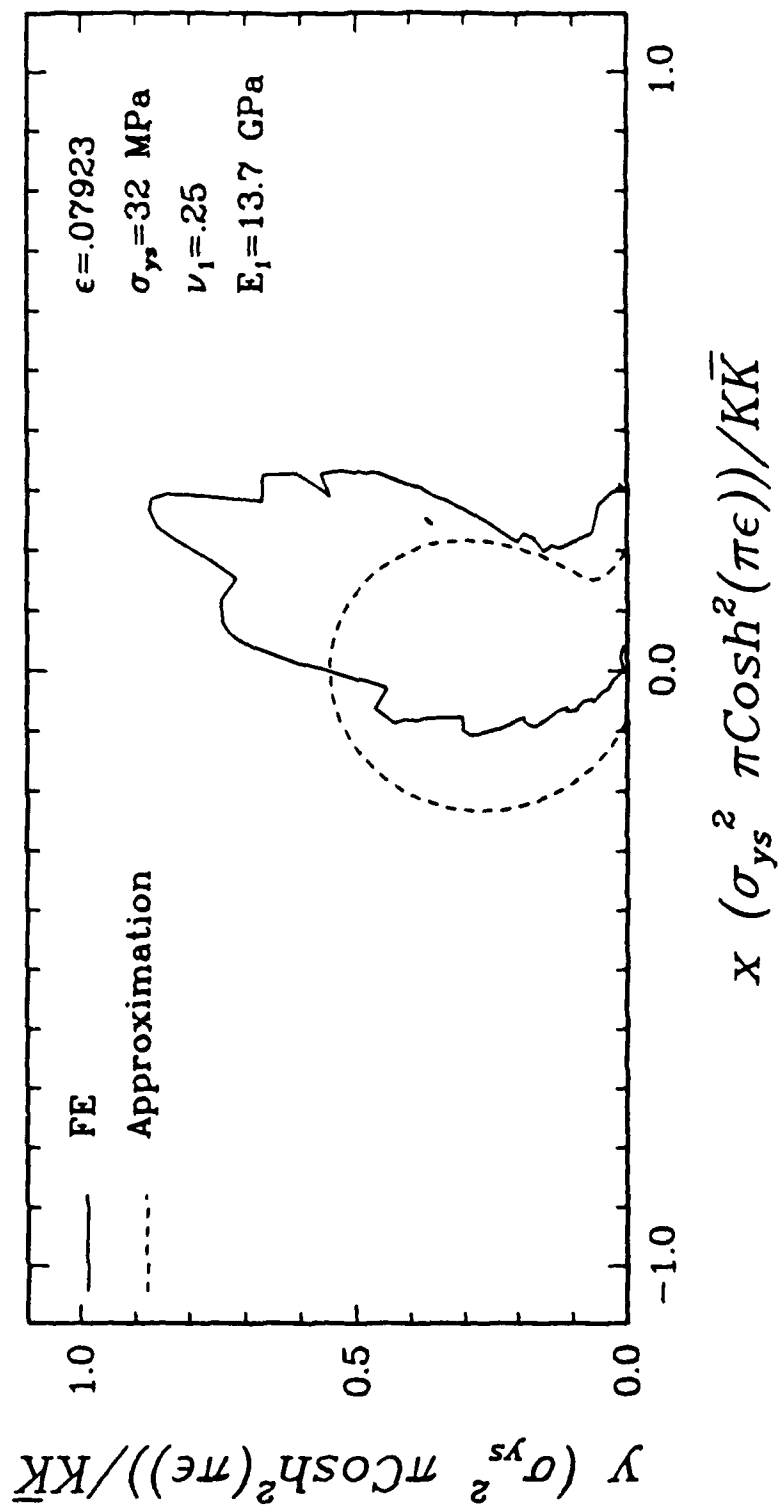


Figure 5 Plastic zone comparison between the elastic approximation and a finite element solution for an elastic/perfectly-plastic medium adjoint to an elastic medium; $K = 30e^{-0.9272i} \text{MPa(m)}^{\frac{1}{2} + 0.0793i}$, $\zeta_0 = -1.004 (-57.5^\circ)$.

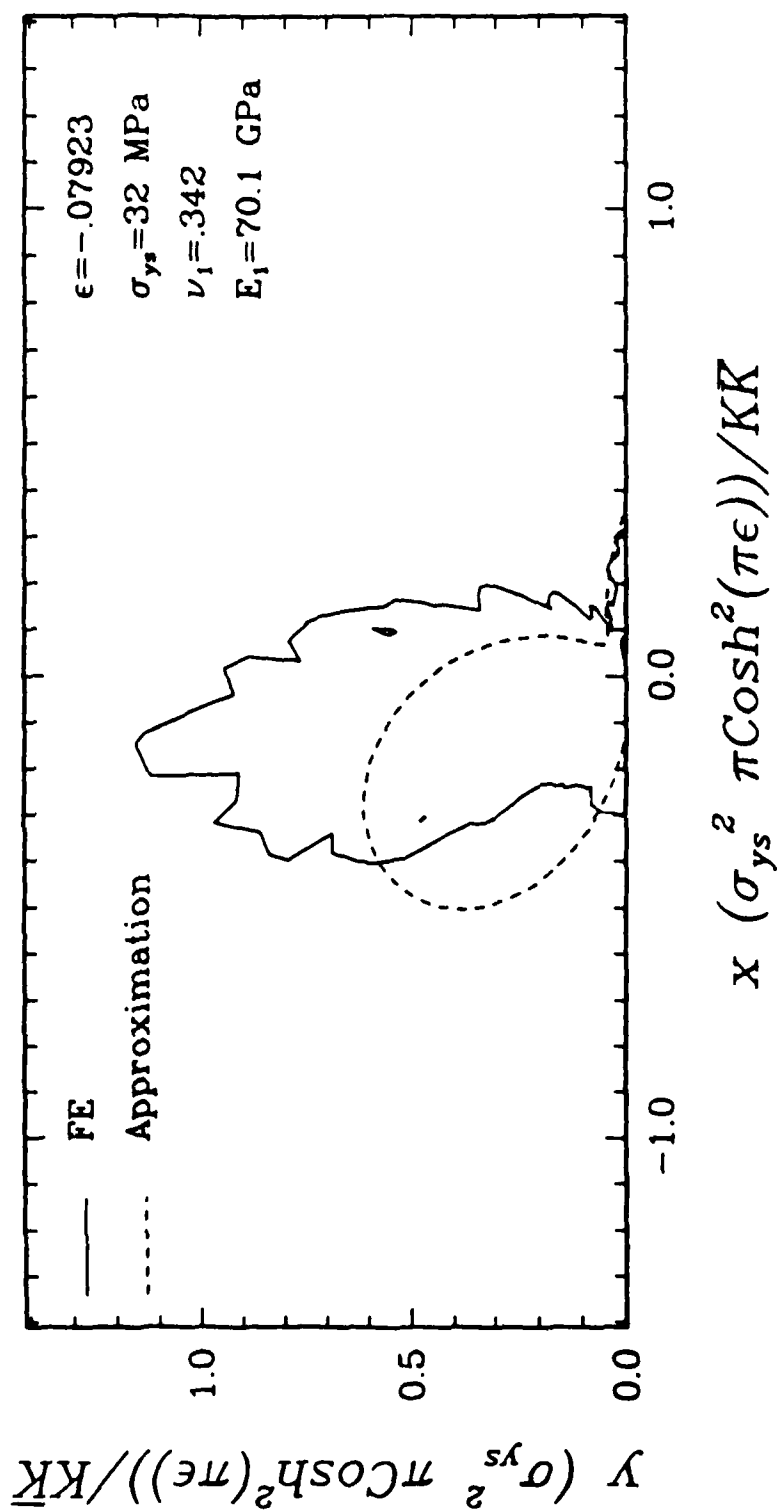


Figure 6 Plastic zone comparison between the elastic approximation and a finite element solution for an elastic/perfectly-plastic medium adjoint to an elastic medium; $K = 56.7 e^{-0.07923} \text{ MPa}(\text{m})^{\frac{1}{2}}$, $\zeta_0 = -0.007 (-.42^\circ)$.

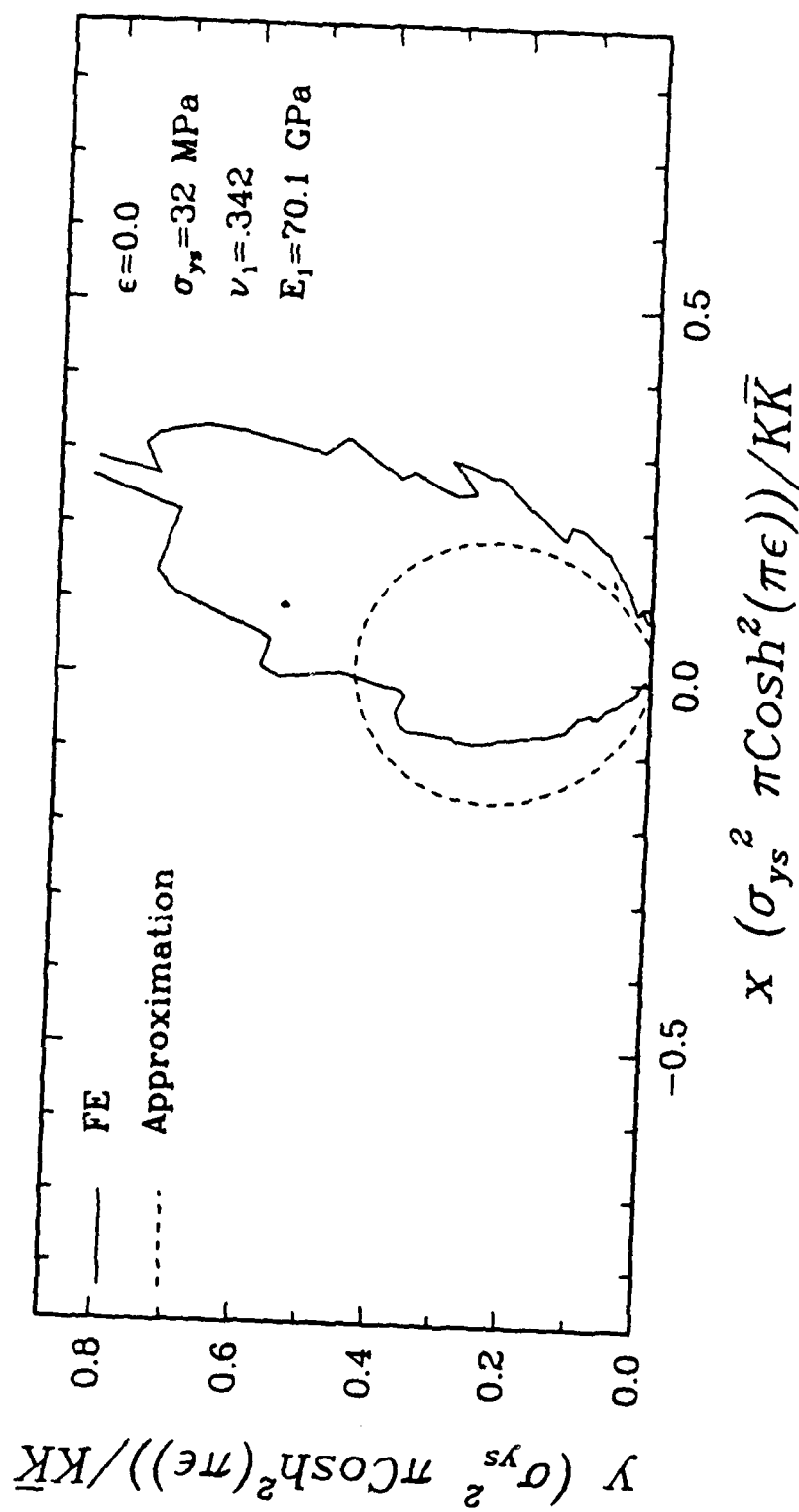


Figure 7 Plastic zone comparison between the elastic approximation and a finite element solution for an elastic/perfectly-plastic medium adjoint to an elastic medium; $K = 63.4 e^{-0.0i} \text{ MPa(m)}^{\frac{1}{2} + 0.0i}$, $\zeta_0 = 0$.

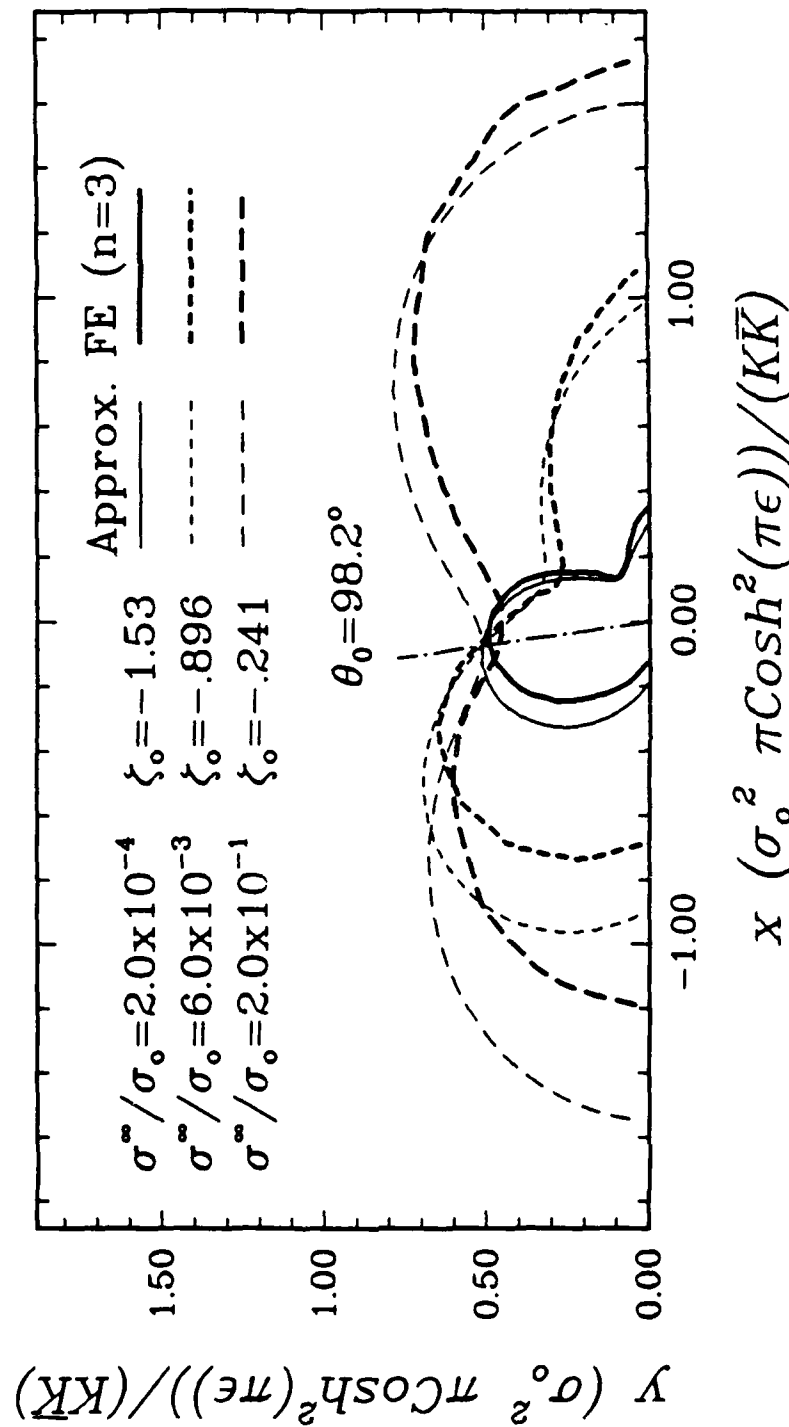


Figure 8 Plastic zone comparisons between the elastic approximation and a finite element solution for a strain hardening material, $n = 3$, (Shih and Asaro, 1987) for various ζ_o ; $K = \sigma^\infty 1.8025 e^{0.1201 \zeta_o} (m)^{\frac{1}{2} - 0.0935 \zeta_o}$, $\epsilon = .0935$, $\nu = .3$.

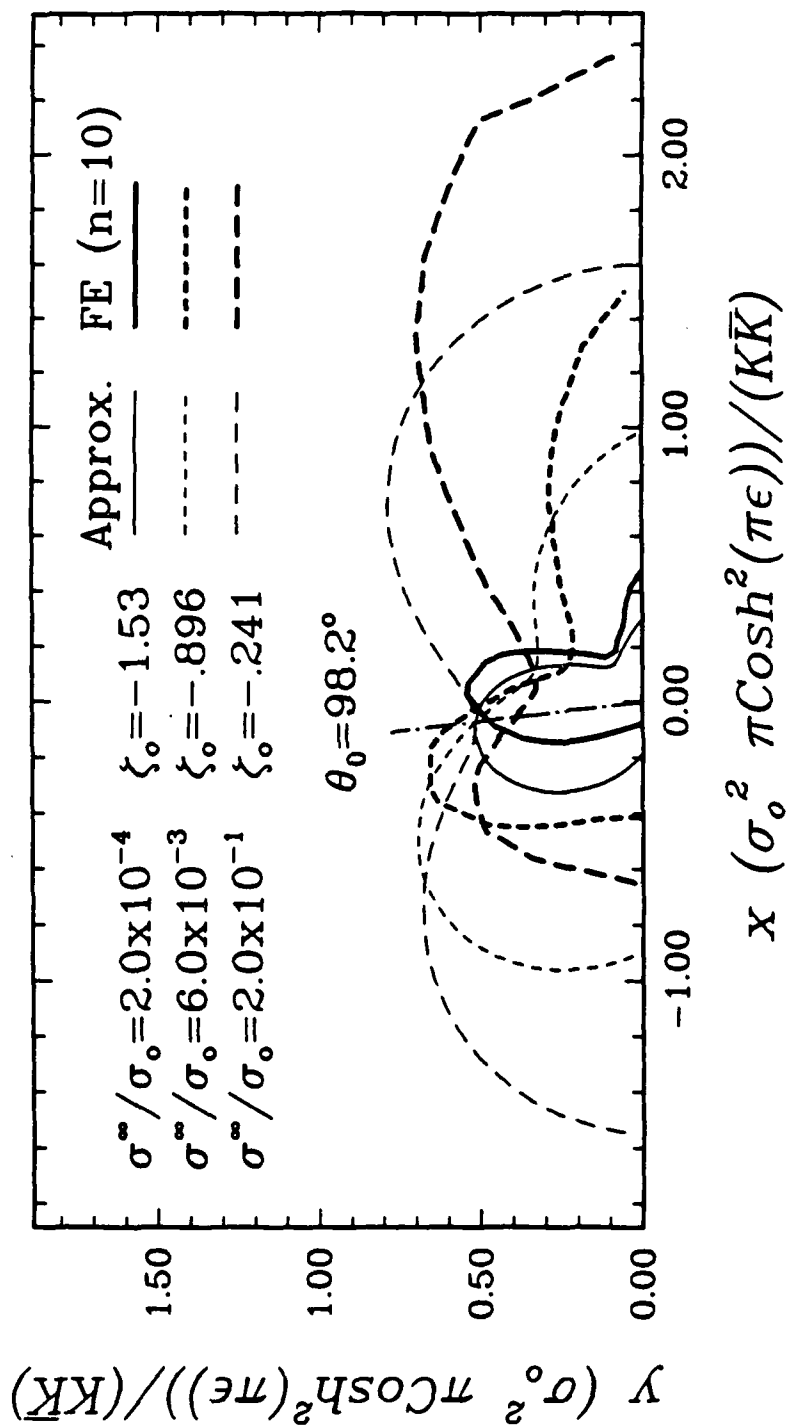


Figure 9 Plastic zone comparisons between the elastic approximation and a finite element solution for a strain hardening material, $n = 10$, (Shih and Asaro, 1987) for various ζ_0 ; $K = \sigma^\infty 1.8025 e^{0.1201 \zeta_0 (m)^{\frac{1}{3}} - 0.0935 \zeta_0}$, $\epsilon = .0935$, $\nu = .3$.

along the plastic zone boundary. This section develops a methodology, based upon exact elasticity solutions for a Griffith crack, for determining approximately when such a Williams type field exists, and thus defining the valid domain for the characterization of the plastic zone in terms of ζ_0 , K , and material parameters.

In examining the exact elasticity solution for an interfacial crack between two semi-infinite media (Rice and Sih, 1965), the stress potentials can be additively decoupled into singular terms and homogeneous far field terms, and reduced to obtain the dominant asymptotic potentials. Consider Φ , the ϕ'_1 stress potential for the Griffith crack, given by Rice and Sih (1965) which is,

$$\begin{aligned} \Phi = & \frac{(z - i2\epsilon a)}{\sqrt{z^2 - a^2}} \left(\frac{z + a}{z - a} \right)^{i\epsilon} \frac{\sigma_{yy}^\infty - i\sigma_{zy}^\infty}{1 + e^{2\pi\epsilon}} \\ & + \frac{\sigma_{xx}^\infty + \sigma_{yy}^\infty}{4} - \frac{\sigma_{yy}^\infty}{1 + e^{2\pi\epsilon}} + i \left(\frac{\sigma_{zy}^\infty}{1 + e^{2\pi\epsilon}} + \frac{2\mu_1\omega_1^\infty}{1 + \kappa_1} \right). \end{aligned} \quad (22)$$

Here the crack tips are located at $z = \pm a$, and ω_1^∞ is the far field rotation in Region 1. In the region near the crack tip, the stress potential can be represented by

$$\Phi \approx \Phi_{near} = P \left[\frac{(z - i2\epsilon a)}{\sqrt{z^2 - a^2}} \left(\frac{z + a}{z - a} \right)^{i\epsilon} \right], \quad (23)$$

where

$$P = \frac{\sigma_{yy}^\infty - i\sigma_{zy}^\infty}{1 + e^{2\pi\epsilon}}. \quad (24)$$

To obtain the asymptotic potential, substitute $z = a + x$ in to Eq.(23) and assume $\|x\| \ll a$ which yields

$$\Phi_{asympt.} = P \left[\frac{a(1 - i2\epsilon)}{\sqrt{2ax}} \left(\frac{2a}{x} \right)^{i\epsilon} \right] = \bar{K} \frac{x^{-i\epsilon}}{\sqrt{2\pi x}} \frac{1}{1 + e^{2\pi\epsilon}}. \quad (25)$$

Using Eq.(A.23), Eq.(25) can be shown to be identical to Eq.(4).

By considering one potential of the exact elasticity solution for a Griffith type crack, Eq.(22), an error parameter can be constructed which represents the discrepancy between the exact solution and the (Williams type) dominant asymptotic solution, Eqs.(4) and (5). Normalizing Eq.(25) by the singular portion of Eq.(22), Eq.(23), yields

$$N = \frac{\Phi_{asympt.}}{\Phi_{near}} = \left(1 + \frac{\hat{x}}{.5 - i\epsilon} \right)^{-1} (1 + \hat{x})^{.5 - i\epsilon}. \quad (26)$$

Here $\hat{x} = x/2a$ is the normalized distance with respect to crack length, and N represents the portion of the singular potential term represented by the asymptotic potential, given by Eq.(25). Evaluating Eq.(26) along the interface at $\hat{x} = 0.1$ yields $N = 0.874$ for $\epsilon = 0$ while for the extreme values $\epsilon = \pm 0.1748$ (positive ν), $N = 0.889e^{\pm 0.0694i}$. For all ϵ , as $\hat{x} \rightarrow 0$, $N \rightarrow 1$. This, in conjunction with the previous observations, indicates that the asymptotic expression reproduces the singular term reasonably well over the entire domain where the singular potential term dominates. (From Eq.(22), it can be shown that at $\hat{x} \approx 0.13$, the singular term contributes to the total stress potential an amount, equal in magnitude, to that of the homogeneous term. For $|\hat{x}| < 0.13$, the singular portion dominates.)

Based upon the previous discussion, the asymptotic representation, Eqs.(4) and (5) or Eq.(25), is representative in the crack-tip region where

$$\frac{l}{10} \geq r \geq 0. \quad (27)$$

Here l is the characteristic dimension. (Note, a slight modification has been made for convenience, and that is to limit the domain to $l/10$ instead of $l/8$.) Such a conclusion is also typical of homogeneous crack solutions.

A second condition must also be satisfied if Eqs.(4) and (5) are to depict the actual dominant asymptotic behavior; namely, that any perturbations within the dominant asymptotic solution domain must be small compared to that domain and occur near the crack tip. Using a St. Venant's type argument, this can be expressed mathematically as

$$r_{\text{perturbation,max}} \leq \frac{3l}{100}. \quad (28)$$

Such perturbations could include plastic zones and crack-face contact and interpenetration, if present. (Note, Williams type fields, Eqs.(4) and (5), are based upon the condition that the crack faces are traction-free.) Eq.(28) represents a very conservative restriction and, depending upon the actual conditions, it may be appropriate to relax it somewhat.

The asymptotic crack-tip opening displacement (CTOD), Δu , as a function of r (Hutchinson *et al.*, 1987) is

$$\Delta u(r) = u(r, \theta = \pi) - u(r, \theta = -\pi) = \frac{(C_1 + C_2)K r^{1/2} \sqrt{r}}{2\sqrt{2\pi}(1 + i2\epsilon) \cosh(\pi\epsilon)}, \quad (29)$$

where

$$u(r) = u_y(r) + iu_z(r), \quad (30)$$

and C_j are defined according to Eq.(A.7). Following Eq.(A.24), ζ is introduced and is defined as

$$\zeta = \angle K + \epsilon \ln r. \quad (31)$$

Substituting Eq.(31) into Eq.(29) yields

$$\Delta u(r) = \frac{(C_1 + C_2) \|K\| \sqrt{r} e^{i\zeta}}{2\sqrt{2\pi} \cosh(\pi\epsilon)(1 + i2\epsilon)}. \quad (32)$$

Crack face interpenetration occurs when, $\Delta u_y < 0 \Rightarrow \Re \Delta u < 0$ or,

$$\cos \zeta + 2\epsilon \sin \zeta < 0. \quad (33)$$

The critical values ζ_0 , the beginning and ending points of interpenetration, occur when

$$\cos \zeta_0 + 2\epsilon \sin \zeta_0 = 0 \quad (34)$$

or,

$$\tan \zeta_0 = -\frac{1}{2\epsilon}. \quad (35)$$

Note that for the homogeneous case, the condition represented by Eq.(33) occurs any time a negative mode I loading is applied.

The previous condition on r , Eqs.(27) and (28), coupled with the oscillatory crack face behavior, can be restated as valid solution domain conditions in terms of ζ (via Eq.(31)), K , and material parameters. Thus, Williams type fields, Eqs.(4) and (5), will exist transitionally along the plastic zone boundary if and only if

$$\cos \zeta + 2\epsilon \sin \zeta > 0 \quad \begin{cases} \epsilon > 0 & \zeta_0 \leq \zeta \leq \zeta_{max} \\ \epsilon < 0 & \zeta_{max} \leq \zeta \leq \zeta_0 \end{cases} \quad (36)$$

and

$$\frac{K\bar{K}}{\sigma_y^2 \pi \cosh^2(\pi\epsilon)} \leq .03l, \quad (37)$$

where

$$\zeta_{max} = \angle K + \epsilon \ln(.1l). \quad (38)$$

The condition depicted by Eq.(36) requires that no crack face contact or interpenetration occurs between the plastic zone boundary and the maximum valid extent of the dominant asymptotic domain. It also assumes that the size of the plastic zone along the crack face can be approximated by the characteristic length, $K\bar{K}/\sigma_y^2 \pi \cosh^2(\pi\epsilon)$. *Figure 10* shows for plane strain the values of ζ , as a function of ϵ , which will not produce crack face interpenetration. For Eq.(36) to be true, both ζ_0 and ζ_{max} , as well as the entire path which connects them, must be in the unshaded region of *Figure 10*. Note that for $\epsilon = 0$ (homogeneous case) the admissible range is $|\zeta_0| < \pi/2$, corresponding to $K_I > 0$.

Conditions represented by Eqs.(36) to (38) are necessary, but not sufficient conditions for a Williams type field to exist. Crack closure beyond $l/10$ is possible and must be ruled by other considerations such as global geometrical and loading factors or by other solutions. However, for a (remotely loaded) Griffith crack, Comninou and Schmueser (1979) showed crack closure is continuous from the crack tip outwards; thus if closure exists beyond $l/10$, it will occur within $l/10$ (with respect to one crack tip). Henceforth, Eqs.(36) to (38) are also sufficient validity conditions for a Griffith type crack.

4 Conclusion

An approximate expression for the plastic zone around an interfacial crack-tip has been presented. It modestly reproduced the characteristic size and shape, as compared to various precise numerical solutions, with increasing accuracy as the strain hardening exponent approached unity. The overall crack-tip plastic zone size was found to be quasi-proportional to $(K\bar{K}/\sigma_y^2)$. Plastic zones were found to change shape with applied load in a periodic manner dependent upon interfacial load-phase angle (ILPA), ζ_0 . The ILPA was identified as a comprehensive single load-phase angle which determines the zone shape and tractions along the zone boundary, and may uniquely identify the behavior within the zone. Conditions for determining applicability of this expression were stated in terms of ζ_0 and ζ_{max} , where ζ_{max} is dependent upon the characteristic length in the problem.

From the previous derivations it appears that the ILPA (ζ_0), ϵ , (possibly ν), and the magnitude of K (expressed as $K\bar{K}$ or J , where J is the J -Integral), are the local interfacial fracture mechanics variables needed to describe interfacial SSY behavior.

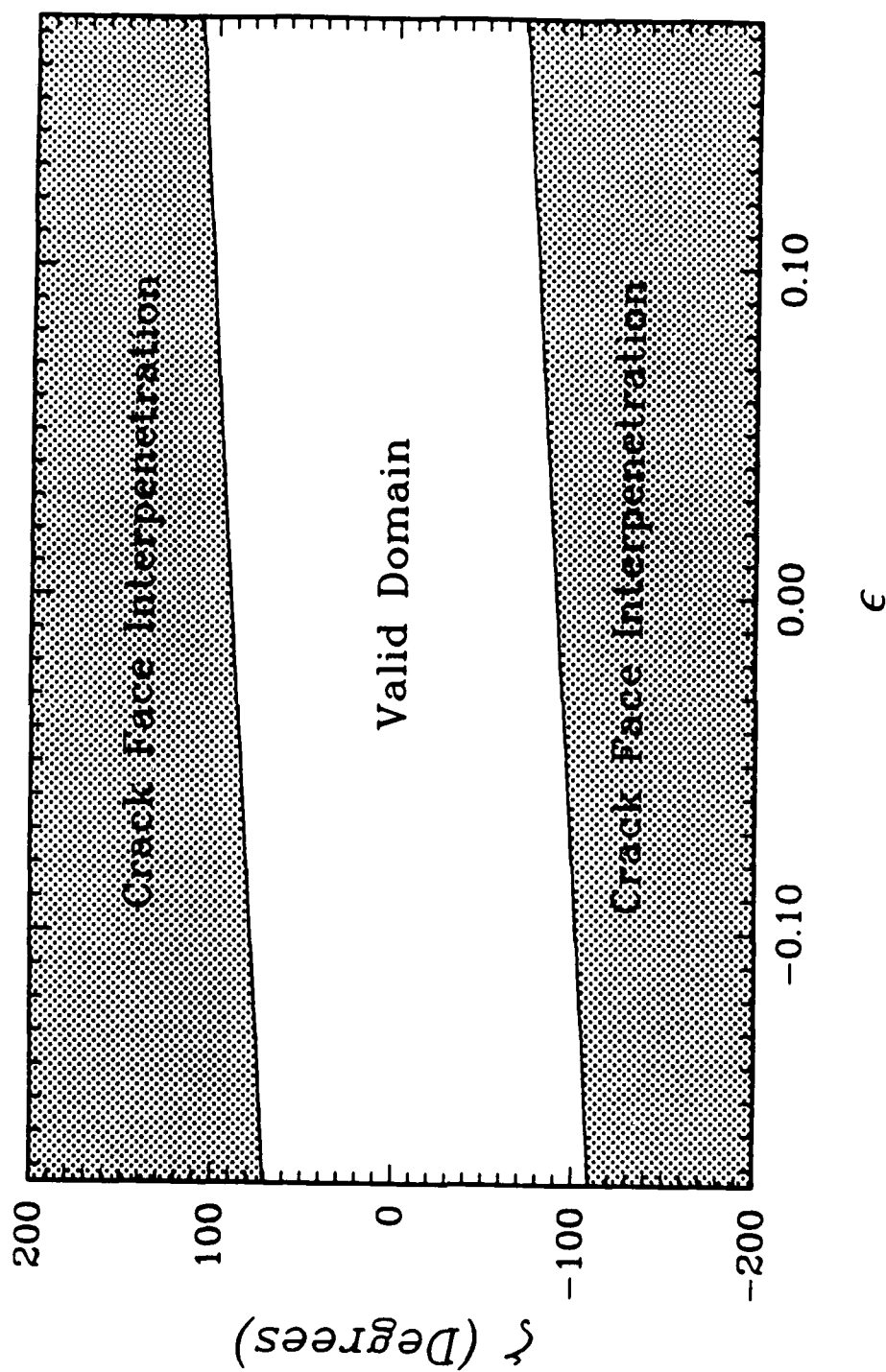


Figure 10 Crack-face interpenetration is shown as a function of ζ and ϵ , for plane strain conditions.

Following homogeneous fracture mechanics, it seems natural to construct interfacial fields analogous to HRR or slip-line fields, utilizing the same material idealizations and similar framework, but with the degree of local (plastic) mode mixity being now dependent upon ζ_0 . Using ζ_0 and the magnitude of the singularity as conditions describing the plastic zone boundary, the characteristics deep within the zone should be identifiable.

To familiarize the readers with the application of these concepts to interfacial fracture mechanics, a hypothetical example is included in Appendix B. It demonstrates how to determine various local crack-tip quantities.

Acknowledgments

Special gratitude is expressed to Prof. J. R. Rice for useful discussions. This work was supported by ONR under grant N00014-84-K-0495.

References

- Brown, S. B., Kim, H. K., and Anand, L., 1987, "An Internal Variable Constitutive Model for Hot Working Metals", Reports of Research in Mechanics of Materials, MIT, Cambridge; (submitted to International Journal of Plasticity).
- Comninou, M., and Schmueser, D., 1979, "The Interface Crack in a Combined Tension-Compression and Shear Field", ASME Journal of Applied Mechanics, Vol. 46, pp.345-348.
- Hertzberg, R. W., 1976, *Deformation and Fracture Mechanics of Engineering Materials*, J. Wiley, New York, pp.20.
- Hutchinson, J. W., Mear, M., and Rice, J. R., 1987, "Cracks Paralleling an Interface Between Dissimilar Media", Harvard University, Div. of Applied Science, Cambridge, (to appear in the ASME Journal of Applied Mechanics).
- McClintock, F. A., and Irwin, G. R., 1965, "Plasticity Aspects of Fracture Mechanics", *Fracture Toughness Testing and Its Applications*, ASTM STP 381, ASTM, Philadelphia, pp.84-114.
- Rooke, D. P., 1963, "Elastic Yield Zone Round a Crack Tip", Royal Aircraft Establishment, Farnborough, Tech. Note CPM 29.
- Rice, J. R., 1988, "Elastic Fracture Mechanics Concepts for Interfacial Cracks", ASME Journal of Applied Mechanics, Vol. 55, pp. 98-103.
- Rice, J. R., and Sih, G. C., 1965, "Plane Problems of Cracks in Dissimilar Media", ASME Journal of Applied Mechanics, Vol. 32, pp. 418-423.
- Shih, C. F., and Asaro, R., 1987, "Elastic-Plastic Analysis of Cracks on Bimaterial Interfaces; Part 1: Small Scale Yielding", Brown University, Providence, (to appear in the ASME Journal of Applied Mechanics).
- Shih, C. F., 1974, "Small-Scale Yielding Analysis of Mixed Mode Plane-Strain Crack Problems", *Fracture Analysis*, ASTM STP 560, ASTM, Philadelphia, pp.187-210.
- Ting, T. C., 1986, "Explicit Solution and Invariance of the Singularities at an Interface Crack in Anisotropic Composites," International Journal of Solids and Structures, Vol. 22, No. 9, pp.965-983.
- Williams, M. L., 1959, "The Stresses Around a Fault or Crack in Dissimilar Media", Bulletin of the Seismological Society of America, Vol. 49, pp.199-204.
- Zywicz, E., 1988, "On Elastic-Plastic Cracks Between Dissimilar Media", Ph. D. Thesis in progress, MIT, Mechanical Engineering, Cambridge.

Appendix A Mises Equivalent Stress Derivation

An asymptotic expression for the Mises equivalent stress around an interfacial plane strain crack tip, as a function of r and θ , is derived.

The general series potential functions for an interface crack, as expressed by Rice (1988), are

$$\phi'_1 = e^{-\pi\epsilon} z^{-\frac{1}{2}-i\epsilon} f(z) + 2C_2 g(z)/(C_1 + C_2), \quad (\text{A.1})$$

$$\phi'_2 = e^{\pi\epsilon} z^{-\frac{1}{2}-i\epsilon} f(z) + 2C_1 g(z)/(C_1 + C_2), \quad (\text{A.2})$$

$$\Omega'_1 = e^{\pi\epsilon} z^{-\frac{1}{2}+i\epsilon} \bar{f}(z) - 2C_2 \bar{g}(z)/(C_1 + C_2), \quad (\text{A.3})$$

and

$$\Omega'_2 = e^{-\pi\epsilon} z^{-\frac{1}{2}+i\epsilon} \bar{f}(z) - 2C_1 \bar{g}(z)/(C_1 + C_2), \quad (\text{A.4})$$

with

$$f(z) = \sum_{n=0}^{\infty} a_n z^n, \quad (\text{A.5})$$

$$g(z) = \sum_{n=0}^{\infty} b_n z^n \quad (\text{A.6})$$

and

$$C_j = (1 + \kappa_j)/\mu_j. \quad (\text{A.7})$$

Here μ_j are the shear moduli, $\kappa_j = 3 - 4\nu_j$ for plane strain and $\kappa_j = (3 - \nu_j)/(1 + \nu_j)$ for plane stress, ν_j are the Poisson's ratios, and the subscripts 1 and 2 refer to the domains above and below the interface, respectively.

From Eqs.(2) and (3) the individual stress components can be expressed as

$$\sigma_{zz} = \frac{1}{2} (B + \bar{B}), \quad (\text{A.8})$$

$$\sigma_{\theta\theta} = \frac{1}{2} (A + \bar{A}), \quad (\text{A.9})$$

and

$$\sigma_{zy} = \frac{-i}{2} (A - \bar{A}), \quad (\text{A.10})$$

where

$$A = (\bar{z} - z)\phi'' + \bar{\phi}' + \Omega', \quad (\text{A.11})$$

and

$$B = 2\phi' + \bar{\phi}' - \Omega' - (\bar{z} - z)\phi''. \quad (\text{A.12})$$

Here $i = \sqrt{-1}$ and a bar denotes the complex conjugate. For plane strain isotropic elastic solids, the Mises equivalent stress is

$$\sigma^2 = (\sigma_{xx}^2 + \sigma_{yy}^2)D + (\sigma_{xx}\sigma_{yy})F + 3\sigma_{xy}^2, \quad (\text{A.13})$$

with

$$D = \nu^2 - \nu + 1 \quad (\text{A.14})$$

and

$$F = 2\nu^2 - 2\nu - 1, \quad (\text{A.15})$$

where ν is the Poisson's ratio of the solid. For plane stress isotropic elastic solids Eq.(A.13) is still valid, but Eqs.(A.14) and (A.15) are redefined as $D = 1$ and $F = -1$, respectively. After substituting Eqs.(A.8) to (A.10) into Eq.(A.13) and doing some complex algebra, Eq.(A.13) is written as

$$\sigma^2 = \frac{1}{2} \Re \{ (D - 3)AA + (D + 3)A\bar{A} + DB\bar{B} + DBB + FAB + F\bar{A}\bar{B} \}. \quad (\text{A.16})$$

Further simplification is obtained by using Eqs.(A.11) and (A.12), so that Eq.(A.16) becomes

$$\begin{aligned} \sigma^2 = \Re \{ & 3(\bar{z} - z)(z - \bar{z})\phi''\bar{\phi}'' - 6(\bar{z} - z)\phi''\bar{\phi}' + 6(\bar{z} - z)\phi''\bar{\Omega}' \\ & + (8D - 6)\phi'\phi' + (8D - 3)\phi'\bar{\phi}' + 3\Omega'\bar{\Omega}' - 6\Omega'\bar{\phi}' \}. \end{aligned} \quad (\text{A.17})$$

The asymptotic potential functions for the upper domain, Eqs.(4) and (5), are obtained by considering the dominant term in Eqs.(A.1) and (A.3) as $r \rightarrow 0$. At this point attention shall be focused upon the solution in the upper domain since the lower domain solution is obtainable by substituting $-\epsilon$ for ϵ . Differentiating Eq.(4), using $z = re^{i\theta}$, expanding out Eqs.(4) and (5), and defining

$$J = a_0 r^{-i\epsilon}, \quad (\text{A.18})$$

we obtain

$$\phi'_1 = J e^{i(\theta-\pi)} e^{-i\frac{\epsilon}{2}} r^{-\frac{1}{2}}, \quad (\text{A.19})$$

$$\phi''_1 = J e^{i(\theta-\pi)} e^{-i\frac{\epsilon}{2}} r^{-\frac{3}{2}} \left(-\frac{1}{2} - i\epsilon\right), \quad (\text{A.20})$$

and

$$\Omega'_1 = J e^{i(\pi-\theta)} e^{-i\frac{\epsilon}{2}} r^{-\frac{1}{2}}. \quad (\text{A.21})$$

Substituting Eqs.(A.19) to (A.21) into Eq.(A.17) yields

$$\begin{aligned} \sigma^2 = \frac{1}{r} \Re \left\{ J J \left[(-3 - i6\epsilon)(e^{-i2\theta} - 1) - 6 + e^{2i(\theta-\pi)}(8D - 6)(\cos \theta - i \sin \theta) \right] \right. \\ \left. + J \bar{J} \left[e^{2i(\theta-\pi)}(1 - \cos 2\theta) \left(\frac{3}{2} + 6\epsilon^2 \right) - e^{2i(\theta-\pi)}(-3 - i6\epsilon)(e^{-i2\theta} - 1) \right. \right. \\ \left. \left. + e^{2i(\theta-\pi)}(8D - 3) + 3e^{2i(\pi-\theta)} \right] \right\}. \end{aligned} \quad (\text{A.22})$$

The constant a_0 is related to the complex stress intensity factor \mathbf{K} (Rice, 1988) via

$$a_0 = \frac{\bar{\mathbf{K}}}{2\sqrt{2\pi} \cosh(\pi\epsilon)}. \quad (\text{A.23})$$

Defining ζ as

$$\zeta = \angle \mathbf{K} + \epsilon \ln r, \quad (\text{A.24})$$

and using Eq.(A.18), we find

$$J J = \frac{\mathbf{K} \bar{\mathbf{K}}}{8\pi \cosh^2(\pi\epsilon)} (\cos 2\zeta - \sin 2\zeta), \quad (\text{A.25})$$

and

$$J \bar{J} = \frac{\mathbf{K} \bar{\mathbf{K}}}{8\pi \cosh^2(\pi\epsilon)}. \quad (\text{A.26})$$

The complete expression for the Mises equivalent stress is obtained by substituting Eqs.(A.25) and (A.26) into Eq.(A.22) and is

$$\begin{aligned} \sigma^2 = \frac{\mathbf{K} \bar{\mathbf{K}}}{r 8\pi \cosh^2(\pi\epsilon)} \left\{ \cos 2\zeta \left[-3(1 + \cos 2\theta) - 6\epsilon \sin 2\theta + (8D - 6)e^{2i(\theta-\pi)} \cos \theta \right] \right. \\ \left. + \sin 2\zeta \left[3 \sin 2\theta - 6\epsilon(\cos 2\theta - 1) - (8D - 6)e^{2i(\theta-\pi)} \sin \theta \right] \right. \\ \left. + e^{2i(\theta-\pi)} \left[\left(\frac{3}{2} - 6\epsilon^2 \right)(\cos 2\theta - 1) + 6\epsilon \sin 2\theta + (8D - 3) \right] \right. \\ \left. + 3e^{2i(\pi-\theta)} \right\}. \end{aligned} \quad (\text{A.27})$$

Appendix B Interfacial Crack Example

A detailed hypothetical example demonstrating the procedures to characterize a plane strain interfacial Griffith-type crack between 1100-O Aluminum and 1080 Steel is presented. The geometry considered is shown in *Figure 11*, and the material properties are listed in *Table 1*. From Eq.(1), $\epsilon = .03373$. For this geometry, with the appropriate σ_{yy} , imposed such that the interface remains straight, the stress intensity factor for the right hand crack tip in terms of the far field stresses is (Rice, 1988)

$$K = (\sigma_{yy} + i\sigma_{xy}) (1 + i2\epsilon) (2a)^{-i\epsilon} \sqrt{\pi a}.$$

The stress intensity factor for the left hand crack tip is the same as for the right hand crack tip because the applied load is symmetric. Substituting in for the numerical values $\sigma_{yy} = 1$ MPa, $\epsilon = 0.03373$, and $2a = 0.0508$ m yields,

$$K = .2831e^{-0.03315i} \text{MPa(m)}^{\frac{1}{2}-0.03373i}.$$

Using Eq.(19), the ILPA is $\zeta_0 = -.33982$ radians (-19.47°). The characteristic plastic zone length $K\bar{K}/\sigma_{ys}^2 \pi \cosh^2(\pi\epsilon) = 1.577 \times 10^{-6}$ m. Evaluating Eq.(37) indicates that the characteristic plastic zone length is sufficiently small compared to crack length. (Alternatively, from Eqs.(6), (19), and (20) the maximum size of the plastic zone is 8.88×10^{-6} m and occurs at $\theta = 122^\circ$. Comparing r_p to the crack length gives, $r_p/2a = 1.748 \times 10^{-4}$.) From Eq.(38), $\zeta_{max} = -.2113$ radians (-12.11°). Checking Eq.(36) indicates that no crack face interpenetration is anticipated. Thus, at this loading all the SSY conditions and the assumption of no crack face interpenetration are satisfied.

Material	μ (GPa)	ν	σ_{ys} (MPa)
1100-O Al	26.1	.342	42.†
1080 Steel	80.7	.300	585.

Table 1 Material properties for 1100-O Aluminum and 1080 Steel (Hertzberg, 1976).

†Brown *et al.*, 1987.

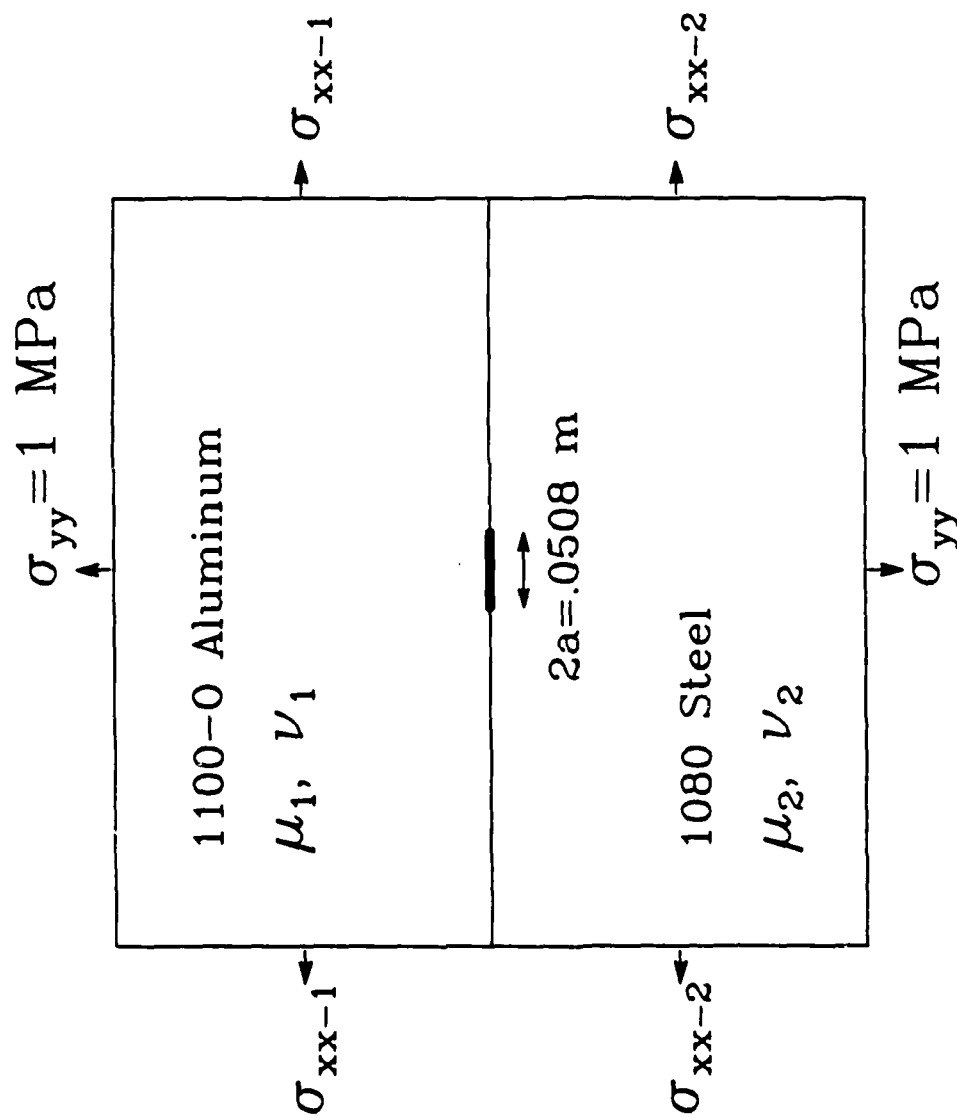


Figure 11 Geometry for a Griffith type interfacial crack.

Additional Discussion

Several additional comments can be made concerning the traction-free crack-tip plastic zone approximation. The oscillatory characteristic plastic zone dimension (r_p) is chosen to be equal to $K\bar{K}/\sigma_y^2 \pi \cosh^2(\pi\epsilon)$. This choice of r_p for the plastic zone size is a compromise because it roughly corresponds to twice the size of the smallest plastic zone (i.e., $\zeta_0 \approx 0^\circ$) and half the size of the largest plastic zone (i.e., $\zeta_0 \approx \pm 90^\circ$). This compromise in the choice of r_p affects the definition of ζ_0 , Eq.(P2.19), and the admissible loading conditions expressed in Eqs.(P2.36) and (P2.37). As pointed out earlier, the precise additive decomposition of ζ into ζ_0 and the transcendental angular function is arbitrary. Altering the chosen characteristic dimension r_p only adds a constant to ζ_0 for fixed values of ϵ . The actual choice of ζ_0 appears rather insignificant because changes in loading conditions (i.e., altering the ratio of far-field shear stress to normal stress) and zone growth show up as relative changes in ζ_0 .

Since ζ_0 is used in Eq.(P2.36) to define the extent of the plastic zone along the crack face, any overestimation of r_p may allow elastic contact to occur between the edge of the actual plastic zone and the radius identified by the (overestimated) nominal plastic zone. Based upon the elastic approximation for $\epsilon = 0.1748$, the maximum difference in ζ_0 between using the characteristic plastic zone dimension r_p and the maximum actual $r_p(\theta)$ from the elastic approximation is less than 7° . For smaller magnitudes of ϵ , the difference in ζ_0 is less. Additionally, the inclusion of a strain-hardening material idealization, $n > 1$, produces plastic zones which are greater than the elastic approximation. For example, when an elastic/perfectly-plastic constitutive idealization is used, the maximum "actual" plastic zone calculated is nearly equal to r_p for values of ζ_0 near 0° . (See *Figures P2.6 and P2.7*.) Thus, overestimation of r_p may not pose a problem in all circumstances. Finally, when loading conditions produce an elastically predicted plastic zone size which marginally does or does not satisfy the non-contact crack-face conditions, Eq.(P2.36), a more accurate determination of plastic zone size and actual contact length is necessary.

In consideration of the actual plastic zone size predicted by the elastic approximation, the maximum plastic zone limitation expressed by Eq.(P2.37), is not as conservative as might first appear. The maximum size of the plastic zone for $\zeta_0 = 0^\circ$ and $\zeta_0 = 60^\circ$, from *Figure P2.3*, is approximately $0.5r_p$ and $2r_p$, respectively. Because little difference exists between the actual maximum plastic zone size and r_p , use of r_p is acceptable in the condition requiring the plastic zone size be small compared to the size of the zone where the asymptotic elastic field is valid, Eq.(P2.37).

2.2.2 Closed Frictionless Crack-Tip Fields

Following the derivation of the approximate plastic zone for the asymptotic traction-free crack-tip (Williams type) elastic field, an asymptotic elastic approximation for the plastic zone around a closed frictionless crack tip between two dissimilar isotropic elastic media will be derived. From it, growth characteristics and validity conditions will be obtained and expressed in terms of K_{II}^* , material properties, and geometry.

Plastic Zone Approximation

The problem considered here is a planar interfacial crack, as shown in *Figure 2.1*, whose constituents have shear moduli μ_j ($j = 1, 2$) and Poisson's ratio ν_j . Note that in the definition of β , the subscripts 1 and 2 now refer to the lower and upper material domains, respectively. Far-field loads produce a closed crack-tip region, and the closed crack-tip field is well characterized by the dominant asymptotic stress field given by Comninou (1977a), Eqs.(2.19) to (2.21).

For isotropic linear elastic plane-strain conditions, the second invariant of the stress tensor, the Mises equivalent tensile stress, $\bar{\sigma}$, is expressed as

$$\bar{\sigma}^2 = (\sigma_{rr}^2 + \sigma_{\theta\theta}^2)D + (\sigma_{rr}\sigma_{\theta\theta})F + 3\sigma_{r\theta}^2, \quad (2.31)$$

where, as before,

$$D = \nu^2 - \nu + 1 \quad (2.32)$$

and

$$F = 2\nu^2 - 2\nu - 1. \quad (2.33)$$

Since the stress field for the upper region is obtained by substituting " $-\beta$ " in place of " β " into the expressions for the lower region, attention is focused upon the lower region only. Substituting the dominant stress expressions, Eqs.(2.19) to (2.21), into Eq.(2.31) yields

$$\bar{\sigma}^2(r, \theta) = \left\{ \frac{K_{II}^2}{r} \frac{1}{32} \right\} \times \left\{ \frac{(1 - \beta)^2}{+6(1 - \beta)(3 + \beta) \cos(2\theta)} \left[3 + (64D - 48) \sin^2\left(\frac{\theta}{2}\right) \right] + 3(3 + \beta)^2 \right\}, \quad (2.34)$$

where β , the Dundurs constant, is given by Eq.(2.22). The approximate plastic zone shape is taken to be the locus of points satisfying $\bar{\sigma} = \sigma_{ys}$, where σ_{ys} is the tensile yield strength of the material. The polar description of the plastic zone shape is given by

$$r_p(\theta) = \left\{ \frac{K_{II}^2}{\sigma_{ys}^2} \frac{1}{32} \right\} \times \left\{ \frac{(1 - \beta)^2}{+6(1 - \beta)(3 + \beta) \cos(2\theta)} \left[3 + (64D - 48) \sin^2\left(\frac{\theta}{2}\right) \right] + 3(3 + \beta)^2 \right\}. \quad (2.35)$$

Here θ is the angle measured from the intact interface. For plane-stress conditions, Eq.(2.35) is still valid, but Eq.(2.32) is redefined as $D = 1$ and the plane-stress value for β must be used.

In deriving the plastic zone approximation, Eq.(2.35), it is assumed that the stress state along the plastic zone boundary is completely characterized by the dominant asymptotic stress field, given by Eqs.(2.19) to (2.21), and that all other stress contributions are negligible compared to the leading asymptotic term. At the tip of a Griffith crack loaded by remote tension, large normal interfacial tractions, as high as 25 times the remote far-field tensile stress, are obtained (Comninou, 1977a; Gautesen and Dundurs, 1987), and the presence of the normal interfacial traction is thought to be attributable to the admissible constant stress field ($\lambda = 0$). Evaluating the dominant asymptotic radial stress, Eq.(2.19), at $\theta = 90^\circ$, and using the value of K_{II} for a Griffith crack loaded in remote tension, Eq.(2.29), the dominant asymptotic stress component behaves as

$$\sigma_{rr}(r, \theta = 90^\circ) = -\sigma_{yy}^\infty \sqrt{\frac{a}{r}}, \quad (2.36)$$

where $2a$ is the crack length. Assuming that the observed normal interfacial tractions represent the magnitude of the σ_{yy} stress component in the constant stress field, the constant stress field contribution to the overall stress field is small for radial distances $\sqrt{a/r} \gg P$, where P is the maximum normal interfacial traction normalized by σ_{yy}^∞ . In light of these possibly high normal interfacial tractions, the validity of Eq.(2.35) in SSY may be limited to loadings where $\sqrt{a/r_p(\theta)}_{\text{maximum}} \gg P$, for $\sigma_{yy} \neq 0$. Inclusion of the $\lambda = 0$ term in the description of the crack-tip fields, as described in the homogeneous case by Larsson and Carlsson (1973) and Rice (1974), could significantly enlarge the range of load amplitudes for which SSY analyses remain accurate.

Mathematical Features

The mathematical features describing the plastic zone are relatively simple and straightforward, as compared to those describing the oscillatory traction-free crack-tip plastic zone. Plastic zone growth is self-similar with similarity length scale K_{II}^2/σ_{ys}^2 , and no oscillatory effects exist within the plastic zone region. The plastic zone shape and growth characteristics for the bi-material closed crack-tip solution are nearly identical to the well known homogeneous mode II solution, and in fact, in the degenerate case, $\beta = 0$, the asymptotic homogeneous mode II solution is completely recovered. Figure 2.2(a) shows the approximated plastic zone shapes for various values of β , with fixed Poisson's ratio, while (b) shows these shapes for several values of the Poisson's ratio, for $\beta = -0.20$. The approximated plastic zone shape differs little from that obtained in the homogeneous case, even for the extreme cases of $\beta = \pm 0.5$. From Figure 2.2, it appears that the plastic zone shape and growth characteristics are only weakly dependent upon β and ν .

Valid Solution Domain

The plastic zone approximation is based upon the assumption that a dominant field, as defined by the asymptotic expressions Eqs.(2.19) to (2.21), exists near the closed

Approximate Plastic Zone

Closed Crack-Tip Face

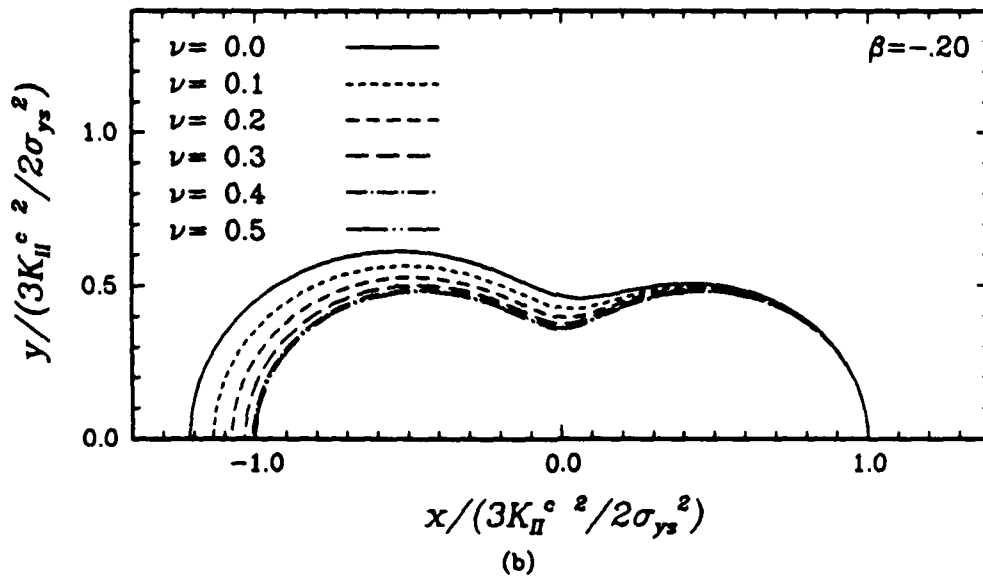
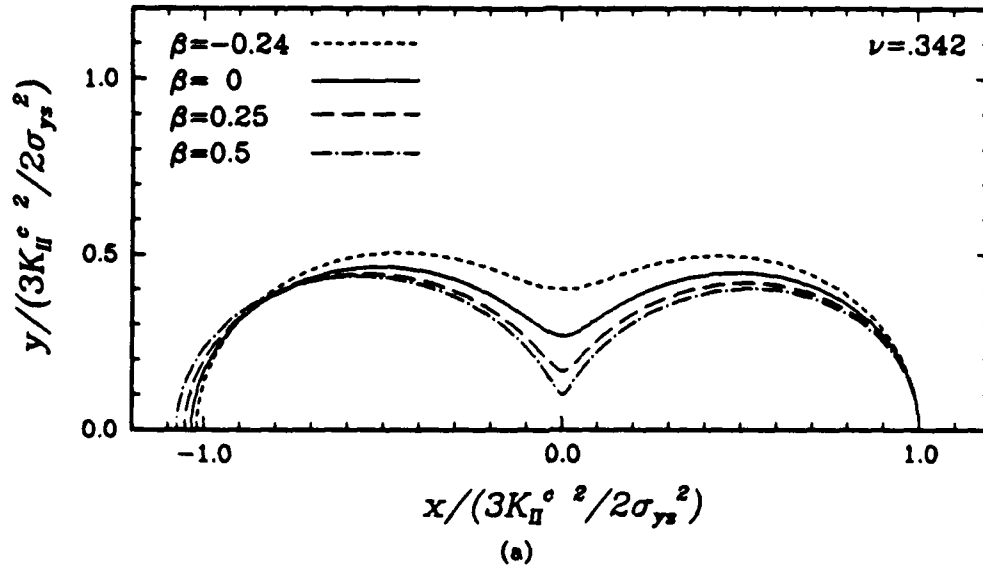


Figure 2.2 Approximate contact SSY plastic zones [Eq.(2.35)] (a) for various values of β with $\nu = 0.342$ and (b) for $\beta = -0.20$ with ν ranging between 0 and 0.5.

crack tip and transitionally along the plastic zone boundary. For this to be true, two conditions must be satisfied. First, crack-tip closure must exist and the crack-tip closure length must be the relevant characteristic dimension. Using the CTOD expression for the oscillatory stress field given in Eq.(P2.32), crack-face contact is estimated, in terms of ζ , by assuming that it occurs whenever $\Delta u_v \leq 0$ or

$$\cos \zeta + 2\epsilon \sin \zeta \leq 0. \quad (2.37)$$

The second condition which must be satisfied, if Eqs.(2.19) to (2.21) are to describe the actual field existing transitionally along the plastic zone, is that any perturbations within the field must be small and be centered about the crack tip. Again, such perturbations include non-linear crack-tip zones. Using a conservative restriction, this is mathematically expressed, via a St. Venant's type argument, as

$$r_{\text{perturbation max}} \leq \frac{3\delta}{100}, \quad (2.38)$$

where δ is the length of the closed crack-tip face. The numerical value used in Eq.(2.38) is based upon the same assumptions as Eq.(P2.28), namely we suppose that the dominant asymptotic solution is appropriate for radial distances $r < \delta/10$ and restrict perturbations within this dominant field to at most $\sim 1/3$ of the latter dimension. The characteristic plastic zone dimension r_p^c chosen for the closed crack-tip model is $3K_{II}^c{}^2/2\sigma_{ys}^2$, which roughly corresponds to the approximated maximum radial extent of the plastic zone.

The previous conditions of closure and (plastic) perturbation zone length are now restated in terms of ζ . Closed crack-tip fields exist transitionally along the plastic zone boundary if and only if

$$\cos \zeta + 2\epsilon \sin \zeta \leq 0 \quad \begin{cases} \epsilon > 0 & \zeta_0^c \leq \zeta \leq \zeta_6 \\ \epsilon < 0 & \zeta_6 \leq \zeta \leq \zeta_0^c \end{cases} \quad (2.39)$$

and

$$\frac{3K_{II}^c{}^2}{2\sigma_{ys}^2} \leq \frac{3\delta}{100}, \quad (2.40)$$

where

$$\zeta_0^c = \angle K + \epsilon \ln\left(\frac{3K_{II}^c}{2\sigma_y^2}\right) \quad (2.41)$$

and

$$\zeta_\delta = \angle K + \epsilon \ln(\delta). \quad (2.42)$$

The conditions expressed in Eq.(2.39) require that continuous crack-face contact exists from the edge of the plastic zone to the end of the contact length. Eq.(2.39) assumes that the plastic zone, along the crack face, can be approximated by the closed crack-tip plastic zone dimension r_p^c . For a more consistent and convenient relationship in small scale contact (SSC), but a somewhat more conservative restriction, ζ_0 can be used in place of ζ_0^c in Eq.(2.39). (SSC will be discussed in Section 2.3.) Use of ζ_0 in SSC is more conservative because the oscillatory characteristic plastic zone dimension r_p is smaller than the closed crack-tip characteristic dimension r_p^c , thus requiring that crack-face closure exist, theoretically, deeper within the plastic zone.

Comparisons

Plastic zones for precise solutions of an elastic/perfectly-plastic material idealization and for the elastic approximation correlate reasonably. The location of yielding integration points, obtained from a finite element calculation for an elastic/perfectly-plastic medium bonded to a rigid medium, and the associated approximated plastic zone are shown in *Figure 2.3* for a closed interfacial crack tip. In the figure, the yielding points near the crack-tip are not plotted. The approximation does not reproduce the exact shape, but the general size and distributions of the various features are well represented. The scale of this figure shows that the closed crack-tip characteristic plastic zone dimension of $r_p^c = 3K_{II}^c/2\sigma_y^2$ is indeed appropriate. Since perfect plasticity formally represents a strain hardening exponent of $n = \infty$, *Figure 2.3* depicts a "worst case" comparison. As observed previously in the traction-free crack-tip case, an elastic approximation increasingly overestimates the plastic zone behind the crack tip and

Bi-material Crack-Tip

Plastic Zone

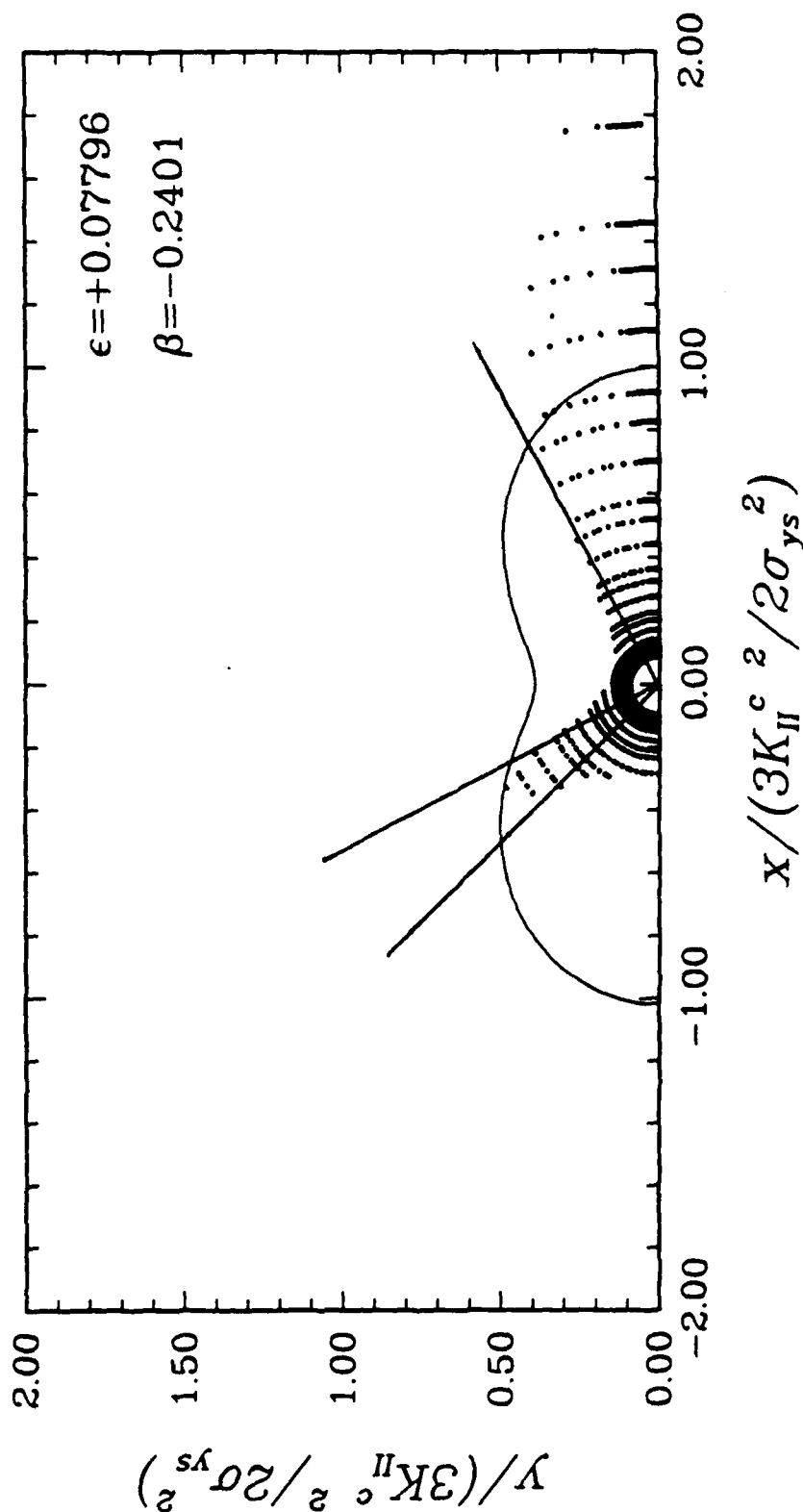


Figure 2.3 Approximate plastic zone, along with the location of actively yielding integration points, from a finite element calculation of contact SSY in an elastic/perfectly-plastic material atop a rigid substrate. Radial lines are boundaries between centered fan and constant state regions of slip-line field.

underestimates the plastic zone size ahead of the crack tip as the strain hardening exponent, n , increases [strain \propto (stress) n]. For materials with smaller values of n , the discrepancy between the elastic approximation and the exact solution should be less.

Contact Length Approximation

At this point no attention has been given to determining the exact length of the contact zone, δ . An estimation of δ can be made using the definition of ζ , Eq.(P2.31), and the critical value ζ_c , Eq.(P2.34), which represent the beginning and ending points of interpenetration. By setting $\zeta = \zeta_c$ and assuming contact occurs any time interpenetration is predicted, the contact length is estimated to be

$$\delta = \exp \left[\frac{1}{\epsilon} \left\{ \tan^{-1} \left(\frac{1}{-2\epsilon} \right) + m\pi - \angle K \right\} \right], \quad (2.43)$$

where m is an integer determining the branch cut used for the \tan^{-1} function, which is obtained by considering the sign of ϵ and the length of δ . Verification of the branch cut can be made by checking if ζ_c satisfies the contact closure conditions given in Eq.(2.37).

Conclusion

An asymptotic planar approximation for the plastic zone around an interfacial crack tip with closed frictionless crack-tip faces has been presented. This approximation captures the general plastic zone characteristics with increased accuracy as the strain-hardening exponent approaches unity. Under SSY assumptions, plastic zone growth was found to be proportional to the characteristic plastic zone dimension $3K_{II}^2/2\sigma_{ys}^2$, and the plastic zone shape was uniquely determined by the bi-material constant ϵ , expressed in an alternative fashion as β , and the Poisson's ratio of the yielding material. Conditions for determining the applicability of this plastic zone expression and for approximating the crack-tip closure length δ were derived from the traction-free crack-tip model.

Explicit conditions for the existence of closed crack-tip zones and their associated inelastic crack-tip behavior were assembled. However, no analytical relation between K_{II} and the far-field loads or K was made. This means that for a particular geometry,

the characteristic crack-tip field is identifiable, but the magnitude and extent of any non-linear behavior can not be quantified. Thus, the precise conditions necessary for SSY for a particular geometry were not determined. (Section 2.3 formulates explicit relationships between K_{II}^c and K for a limited subset of loading conditions for which SSC exists.)

Based upon this derivation, it appears that the governing local interfacial fracture mechanics variables needed to investigate SSY behavior for closed crack-tip faces are ϵ (or β), the ILPA (ζ_0), the magnitude of K_{II}^c , and possibly ν . Because the magnitude of K_{II}^c enters only in determining the plastic zone size and appears as $K_{II}^c{}^2$, it can be replaced by J , where J is the value of the J -Integral. Using the same parametric framework assembled here to approximate the plastic zone and the conditions along the plastic zone boundary, the SSY behavior deep within the plastic zone should be addressable.

2.3 Small Scale Contact

Thus far the traction-free crack-tip model and the closed crack-tip model have been analyzed separately. There exist circumstances for which the elastic (and plastic) closed crack-tip model exists embedded within the traction-free crack-tip model. Under the appropriate loading conditions, the crack-face contact is appropriately small such that the traction-free crack-tip model describes the fields within a small proximity near the crack tip. The actual asymptotic crack-tip fields are defined by the closed crack-tip face model. Separating the two crack-tip models is a boundary layer which transmits the surrounding traction-free crack-tip stress field as "pseudo far-field" loads to the local closed crack-tip model. This section formally addresses small scale contact (SSC) and the correspondence of the various individual model parameters for such a circumstance.

2.3.1 Loading Restrictions for SSC

The requirements for SSC are that the elastic oscillatory traction-free crack-tip field exists in a region surrounding the crack tip and that the resulting contact is small compared to the distance over which that the oscillatory elastic field dominates. It was established in Section P2.3.4 Eqs.(P2.26), that the asymptotic oscillatory elastic field represents the actual crack-tip behavior for radial distances r from the crack tip [Eq.(P2.27)] such that

$$r_{\text{perturbation}_{\text{max}}} \ll r \leq l/10, \quad (2.44)$$

where l is the characteristic geometric length dimension in the problem. Eq.(2.44) is applicable if all perturbations within the crack-tip vicinity are small. Expressing this perturbation limit in terms of the contact length size δ , yields

$$\delta \leq \frac{3l}{100}. \quad (2.45)$$

The previous SSC conditions, Eqs.(2.44) and (2.45), are now restated in terms of ζ , K , and the material properties. First, no (additional) contact may exist from the end of the contact zone, $r = \delta$, to the outer edge of the oscillatory field, $r = l/10$. Using the definition for the value of ζ at the outer edge of the elastic field, ζ_{max} [Eq.(P2.38)], and the definition of ζ at the end of the contact length, ζ_δ [Eq.(2.42)], SSC exists if and only if

$$\cos \zeta + 2\epsilon \sin \zeta > 0 \begin{cases} \epsilon > 0 & \zeta_{\text{max}} \leq \zeta \leq \zeta_\delta \\ \epsilon < 0 & \zeta_\delta \leq \zeta \leq \zeta_{\text{max}} \end{cases} \quad (2.46)$$

and Eq.(2.45) is satisfied. Although multiple crack-tip contact zones do not actually occur [Shield (1982) showed that Comninou's solution for the contact length was unique.], the approximate asymptotic expression for Δu , Eq.(P2.32), predicts multiple contact zones as $r \rightarrow 0$, and thus Eq.(2.46) is a necessary mathematical condition when Eq.(P2.32) is used as a closure criterion.

Within the framework of SSC, the admissibility of SSY is not excluded. The SSY requirements established for the general closed crack-tip model must be met in addition

to the SSC requirements. [i.e., The characteristic plastic zone size r_p^c must be small compared to the contact length δ , Eq.(2.40).] For SSY to exist during SSC, Eqs.(2.40), (2.45), and (2.46) must all be satisfied. Using the relationship between K_{II}^c and K derived in the next section, the characteristic plastic zone sizes in SSC are related to one another by $r_p^c/r_p = (3/2) \cosh^2(\pi\epsilon)$. Also, for SSY in SSC, the maximum difference between ζ_0 , Eq.(2P.19), and ζ_0^c , Eq.(2.41), is less than 7°.

2.3.2 Correspondence of K_{II}^c to K

Unfortunately, since the singular integral formulation presented by Comninou cannot be totally evaluated in closed form, no connection between the elastic K and K_{II}^c has been made, under any conditions. However, for a Griffith crack under far-field tensile stress, K_{II}^c can be directly related to K by using the exact solution of Gautesen and Dundurs (1987), Eq.(2.29), and the expression for K from Table 2.1. Solving for σ_{yy}^∞ from the stress intensity factor K and substituting it into Eq.(2.29) results in

$$K_{II}^c \cong \frac{K \sqrt{1 + \left(\frac{\beta_0}{\pi}\right)^2} (2a)^{i\epsilon}}{\sqrt{\pi} (1 + i2\epsilon)} \cong \sigma_{yy}^\infty \sqrt{a} \sqrt{1 + 4\epsilon^2}, \quad (2.47)$$

for $0 \leq \beta \leq 0.5$. [The predicted contact length δ for this geometry is $\delta/2a \leq 1.2 \times 10^{-4}$ (England, 1965; Comninou, 1977a), thus SSC conditions exist for this geometry.]

Connections between the elastic K and K_{II}^c can be made for other SSC cases by taking advantage of the path independent nature of the J -Integral (Rice, 1967). For the Griffith crack geometry it has been shown that, with sufficient loading to produce a small contact zone compared with crack length, the oscillatory stress field is recovered sufficiently far away from the contact zone (Comninou, 1977a; Atkinson, 1982); i.e., SSC conditions exist. Since both crack-tip models have path-independent J -Integrals and both fields dominate over some distance, a direct evaluation of K_{II}^c is obtainable from K by evaluating the J -Integral in regions where each model is dominant, and equating them. Recall that for elastic materials the J -Integral is equal to the energy release rate \mathcal{G} . After some manipulation of material constants, the energy release rate given by Comninou (1977a) for the closed crack-tip face model, is

$$\mathcal{G} = \frac{K_{II}^{\epsilon 2} \pi (C_1 + C_2)}{16 \cosh^2(\pi \epsilon)}. \quad (2.48)$$

Recalling the energy release rate given by Rice (1988) for the traction-free crack-tip model, Eq.(2.16), and assuming that such a crack-tip configuration as just described exists, we find that for SSC

$$K_{II}^{\epsilon} = \pm \sqrt{\frac{1}{\pi} \mathbf{K} \bar{\mathbf{K}}}, \quad (2.49)$$

where the sign of K_{II}^{ϵ} must be determined by other conditions. [See discussion following Eq.(2.22).]

To verify Eq.(2.49), the Griffith crack described above was considered. The stress intensity factor K_{II}^{ϵ} was evaluated by Eq.(2.29) and then used to calculate the energy release rate via Eq.(2.48). Simultaneously, \mathbf{K} was evaluated using its value for a Griffith crack from Table 2.1, and then the energy release rate was calculated with Eq.(2.16). The two energy release rates were identical, proving that Eq.(2.49) was indeed correct for a Griffith crack in SSC.

Using this approach, a generalization of Eq.(2.47) to include far-field shear loading of a Griffith crack in SSC is made. First, all assumptions regarding SSC must be met. Using Eq.(2.49) and the value of \mathbf{K} for a Griffith crack from Table 2.1, the closed crack-tip stress intensity factor for the right hand crack tip of a Griffith crack in SSC is

$$K_{II}^{\epsilon} \cong \pm \sqrt{(\sigma_{yy}^{\infty 2} + \sigma_{xy}^{\infty 2}) \times (1 + 4\epsilon^2)} a. \quad (2.50)$$

The sign of K_{II}^{ϵ} is determined using the conditions for compressive normal crack-face tractions on the right hand crack tip of a Griffith crack, namely $K_{II}^{\epsilon} < 0$ for $\epsilon > 0$ and $K_{II}^{\epsilon} > 0$ for $\epsilon < 0$. Observe that for $\sigma_{xy}^{\infty} = 0$, Eq.(2.50) reduces to Eq.(2.29). Verification that the contact zone length is small compared to crack length is done by using the approximation for δ , Eq.(2.43), and the contact conditions given by Eq.(2.39).

Unfortunately, due to the non-uniqueness in defining $\angle \mathbf{K}$, obtaining \mathbf{K} from K_{II}^{ϵ} is not as simple. If K_{II}^{ϵ} and δ are known and $\delta/2a$ is "small," \mathbf{K} can be estimated

by determining $\|\mathbf{K}\|$ from Eq.(2.49) and by determining $\angle\mathbf{K}$ by inverting Eq.(2.43). For certain geometries, \mathbf{K} can be estimated at one crack-tip, and then inferred values of \mathbf{K} for the other crack-tip can be obtained by consideration of the stress intensity factor for that geometry. However, further work on closed form definitions of (K_{II}^c, δ) will allow for more complete relationships between K_{II}^c and \mathbf{K} .

Finally, due to the unfortunate numbering of material domains describing β in the closed crack-tip face model and ϵ in the traction-free crack-tip model, various minus signs may enter into the analytical solution when converting from one model to the other. Extreme caution must be used to prevent accidental sign errors, as the author discovered.

2.3.3 Accuracy of Contact Length Estimation

This section considers the accuracy of the asymptotic prediction for crack-face contact, as expressed by Eqs.(P2.33), (2.37), and (2.43). Using the stress intensity factor \mathbf{K} for a Griffith crack (geometry and loading) from Table 2.1, Eq.(P2.33), and the condition represented by Eq.(P2.35), the crack-face contact length for the right hand crack tip, normalized by crack length, is given by

$$\frac{\delta}{2a} = \exp \left\{ \frac{m\pi + \psi}{\epsilon} \right\}, \quad (2.51)$$

where

$$\tan \psi = \frac{\sigma_{yy}^{\infty}}{\sigma_{xy}^{\infty}} \quad \left(-\frac{3\pi}{2} < \psi < \frac{\pi}{2} \right) \quad (2.52)$$

and m is an integer. The actual branch cut, which determines the value of m , is obtained by considering the sign and magnitude of ψ and ϵ , and the range of $\delta/2a$ of the crack tip being investigated. (The restriction on admissible values of ψ is chosen so that approximately $|\angle\mathbf{K}| < \pi$.) Figure 2.4 shows the crack-tip contact length for $\epsilon = -0.1748$ ($\beta = 0.5$), as a function of ρ [$\rho = (2/\pi) \tan^{-1}(\sigma_{xy}^{\infty}/\sigma_{yy}^{\infty})$] for the asymptotic traction-free crack-tip approximation (with branch cut $m = 0$) and for Comninou's solution (Comninou and Schmueser, 1979). Agreement between the two solutions is

Crack-Face Contact

Right Crack Tip

$$\epsilon = -0.1748 \quad (\beta = 0.5)$$

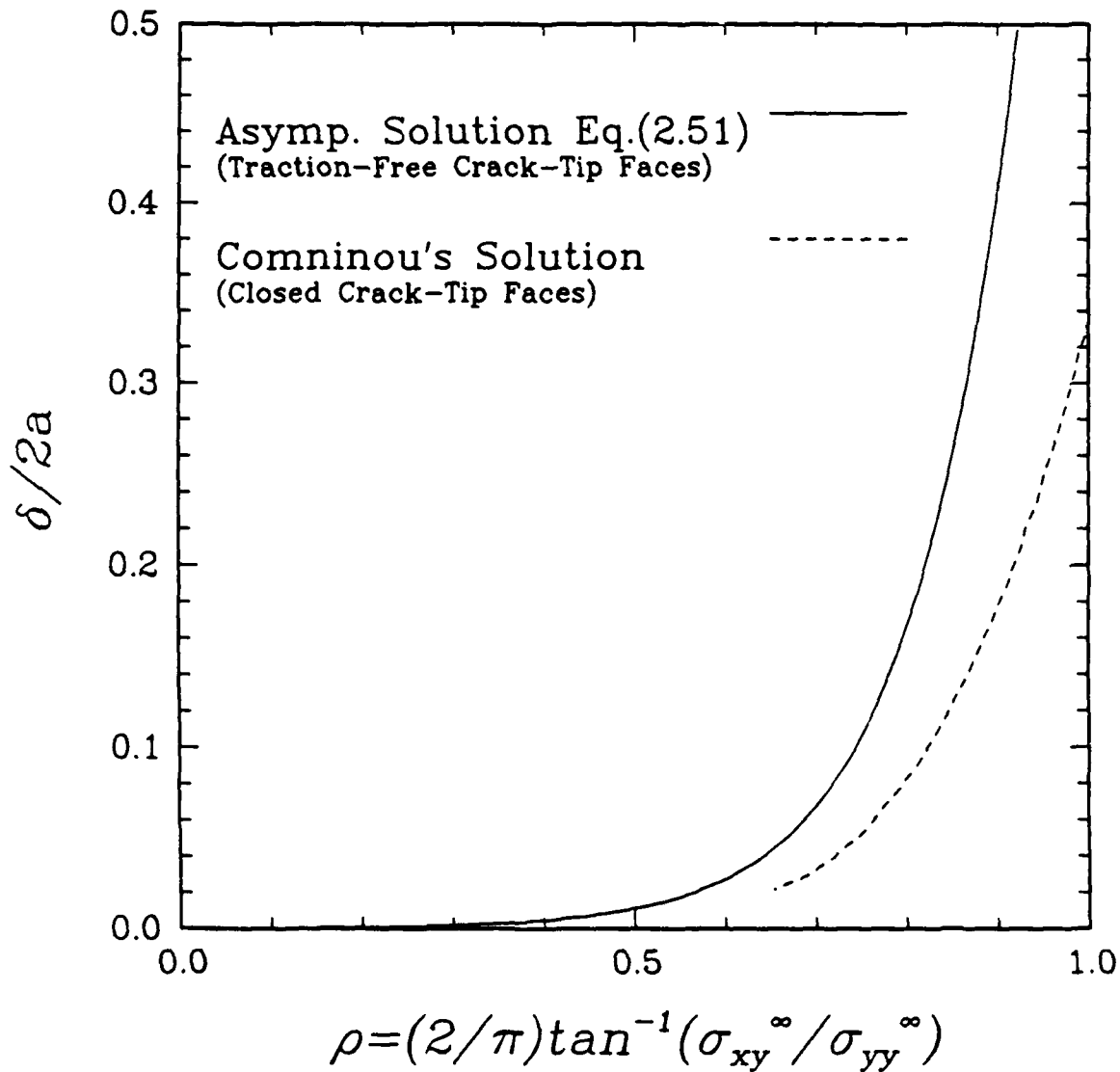


Figure 2.4 Normalized crack-face contact length $\delta/2a$ for the right hand crack-tip of a Griffith crack geometry with far-field positive shear (σ_{xy}^{∞}) and tensile normal (σ_{yy}^{∞}) loads. The solid line is the back extrapolated contact length from the traction-free crack-tip model [Eq.(2.37)] and the dashed line is the solution the for frictionless closed crack-tip model from Comninou and Schmueser (1979).

clearly sufficient to justify using the approximation for $\rho < 0.85$. Since the asymptotic expression Eqs.(2.43) and (2.51) overestimate the contact length, the validity condition represented in Eq.(P2.33) is also conservative with respect to crack-face contact.

Based upon the previous comparison, the contact length approximations, Eqs.(2.43) and (2.51), yield reasonable results for $\epsilon = -0.1748$ when ψ or Φ ($\Phi = \{\tan^{-1}(1/ - 2\epsilon) + m\pi - \angle K - \epsilon \ln(l)\}$) are greater than 0.24 (13.5°). For this range, the previous comparison shows that the predicted contact length only overestimates the "actual" contact length by less than a factor of two. For values of Φ and ψ less than 0.24, closure length predictions for $\epsilon = -0.1748$ are no longer reasonable. However, for Φ and ψ less than 0.24 and $\epsilon = -0.1748$, a minimum contact length of $\delta/2a = 0.13$ exists. For $\epsilon = +0.1748$ with branch cut $m = -1$, Φ and ψ must be greater than -0.24 (-13.5°) in order for Eqs.(2.43) and (2.51) to yield reasonable overestimated contact lengths (within a factor of two). As the magnitude of the bi-material constant ϵ approaches zero, the minimum (or maximum) angles of Φ and ψ , for which reasonable overestimated contact lengths are obtained, also approaches zero. If loading conditions produce a plastic zone size which marginally violates or satisfies the restriction given by Eq.(P2.36) or Eq.(2.39), or the contact conditions in Eqs.(2.45) and (2.46), more precise solutions for δ should be consulted, *e.g.*, Comninou (1977a, 1978) and Comninou and Schmueser (1979).

2.3.4 SSC Summary

Explicit conditions which produce SSC were formally identified in terms of ζ , K , and material properties. Under SSC conditions, an explicit relationship between the closed crack-tip face stress intensity factor, K_{II}^c , and the traction-free crack-tip stress intensity factor, K , was derived for a specific geometry. Based upon equal energy release rates, a more general extension of this relationship was given. Finally, the accuracy of the predicted contact length, in terms of the oscillatory traction-free crack-tip field, was compared against that of precise full-field closed crack-tip solutions. This comparison

identified the loading range for which the contact length approximation, Eq.(2.43), was sufficiently accurate to provide useful results and define SSC.

2.4 Overview

2.4.1 Load Map

To help visualize when crack-tip conditions exist for each model, with or without plasticity, consider the load map shown in *Figure 2.5* (conceived by Prof. D. M. Parks). This map denotes the various model domains for the right hand crack tip of a Griffith crack geometry, as a function of the far-field loading combinations. The appropriate crack-tip model for monotonically and proportionally increasing far-field loads is obtained by constructing a ray from the origin the desired load point. For all load excursions which terminate in the SSY traction-free crack-tip domain, an undefined intermediate state exists when the plastic zone r_p is less than, but nearly the same size (order of magnitude) as, the contact length dimension δ . The crack-tip behavior in this intermediate state is not defined by either model. Although not clearly visible in *Figure 2.5*, all traction-free crack-tip loadings produce SSC unless plasticity is included.

In the load map, the loadings which produce acceptable SSY conditions are those contained within the $r_p/2a = 0.03$ circle. The line separating the SSY traction-free crack-tip region from the intermediate undefined region, $r_p = 3\delta$, is the locus of points producing plastic zones three times larger than the accompanying elastically predicted contact length. The corresponding boundary of the closed crack-tip SSY region is defined by the $r_p^c/2a = 0.03$ circle, where r_p^c is approximated by r_p , and the $r_p = 0.3\delta$ line. (The closed crack-tip boundary is defined by $r_p = 0.3\delta$ instead of $r_p = 0.03\delta$, as suggested by Eq.(2.40), because K_{II}^c is not explicitly known nor is the extent that the K_{II}^c -field represents the far field solution known.) Between the $r_p = 3\delta$ and $r_p = 0.3\delta$ lines is an "uncertain" region where it is unclear whether sufficient plastic deformation would occur under the dominance of either elastic crack-tip model.

The precise location and distribution of each sector in the load map is significantly

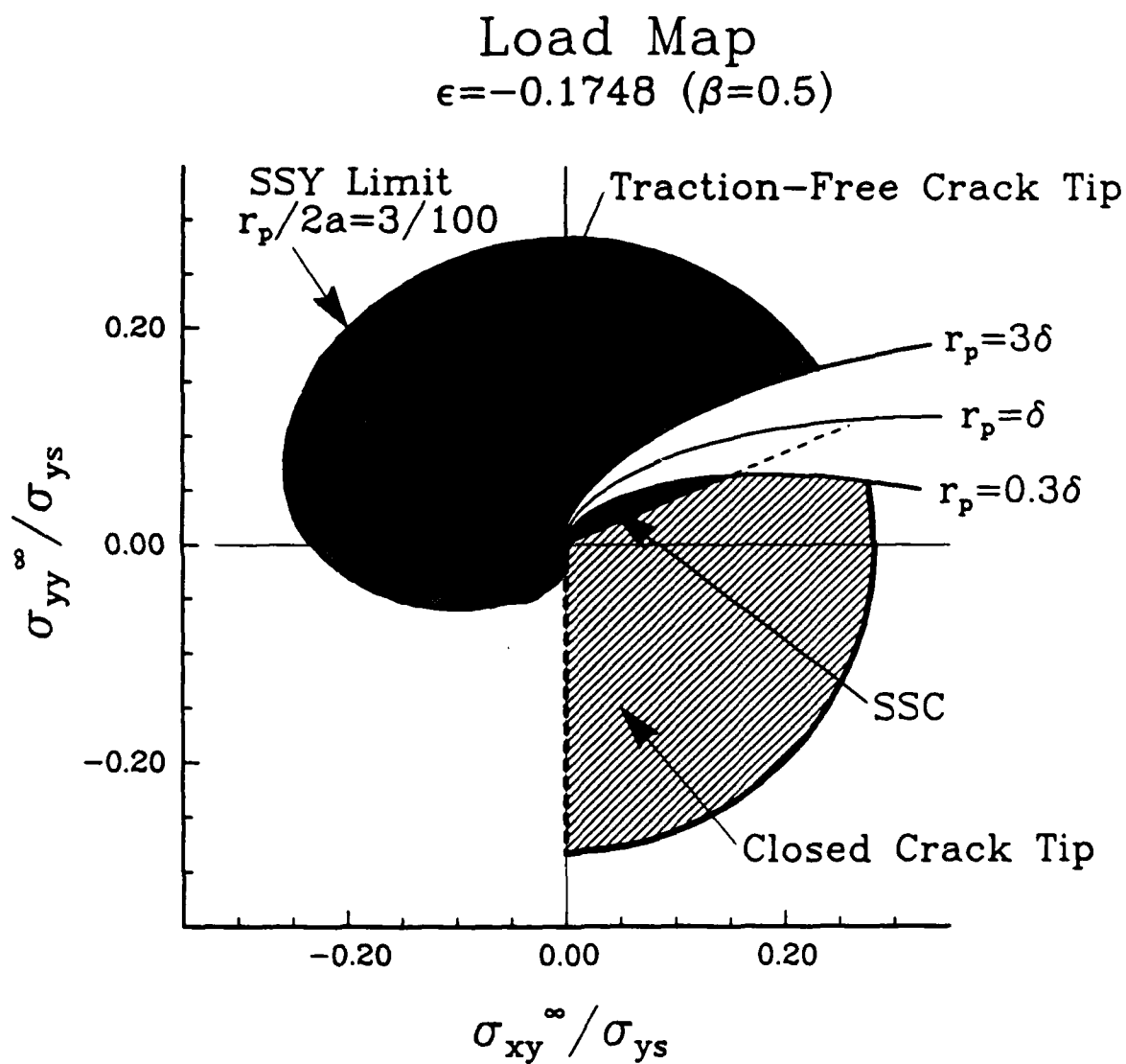


Figure 2.5 Load map for right crack-tip of a Griffith crack geometry with far-field normal (σ_{yy}^{∞}) and shear (σ_{xy}^{∞}) loads, showing approximate SSY limits for traction-free and closed frictionless crack-face conditions; $\beta = 0.5$ and $\epsilon = -0.1748$.

influenced by the value of ϵ . For smaller magnitudes of ϵ , the family of boundary-contact lines compress toward the abscissa, eventually coinciding there for $\epsilon = 0$. For positive values of ϵ , the family of boundary-contact lines appear as mirrored reflections across the ordinate axis. For all values of ϵ , the SSC region is a very small subset of the closed crack-tip domain with the SSC SSY domain being even smaller.

The load map is constructed in the following manner. The characteristic plastic zone size r_p is obtained, as a function of far-field load, by substituting the stress intensity factor for the Griffith crack, from *Table 2.1*, into the characteristic plastic zone size $r_p = K\bar{K}/\sigma_{ys}^2 \pi \cosh^2(\pi\epsilon)$. This yields

$$\frac{r_p}{2a} = \left(\left(\frac{\sigma_{yy}^\infty}{\sigma_{ys}} \right)^2 + \left(\frac{\sigma_{sy}^\infty}{\sigma_{ys}} \right)^2 \right) \frac{1 + 4\epsilon^2}{2 \cosh^2(\pi\epsilon)}. \quad (2.53)$$

To maintain SSY conditions Eq.(P2.37) requires $r_p \leq 0.032a$. The set of points which satisfy Eq.(2.53) when $r_p/2a = 0.03$ defines the SSY limit, to within the approximation that r_p can be used to define the maximum extent of the plastic zone. The boundary lines are obtained by determining the appropriate loads which produce a characteristic plastic zone size f times the contact length ($r_p/2a = f \times \delta/2a$), for a fixed ratio of $\sigma_{yy}^\infty/\sigma_{sy}^\infty$. Using the contact length approximation for a Griffith crack, Eq.(2.51), and Eq.(2.52), the equation describing the boundary lines is given by

$$\frac{2f \cosh^2(\pi\epsilon)}{1 + 4\epsilon^2} \exp \left\{ \frac{m\pi + \psi}{\epsilon} \right\} = \left(\frac{\sigma_{yy}^\infty}{\sigma_{ys}} \right)^2 + \left(\frac{\sigma_{sy}^\infty}{\sigma_{ys}} \right)^2. \quad (2.54)$$

In *Figure 2.5* the branch cut is chosen to be zero since $\epsilon < 0$.

It was noted by Rice (1988) that for a Griffith crack, the behavior at the left hand crack tip with negative applied shear stress is identical to that at the right hand crack tip when an equivalent positive shear stress and normal stress is applied. By considering the work of Comninou and Schmueser (1979) and the observation made by Rice, it is concluded that for $\epsilon < 0$ the contact length at the right hand crack tip, δ_r , decreases as negative shear stress is applied, but the left hand crack-tip contact length, δ_l , increases. This increase in δ_l reduces the actual open crack length to an effective crack size of $2a_{eff} = 2a - \delta_l$. The (modified) SSY boundary for $\sigma_{sy} < 0$ shown in *Figure 2.5*, is

constructed by determining the locus of points which satisfy $r_p/2a_{eff} = 0.03$. [When $\sigma_{xy}^\infty < 0$, the value of δ used is based upon the more precise values of Comninou and Schmueser (1979).] Additionally, when $\sigma_{xy} = 0$ and $\sigma_{yy} < 0$, the crack is completely closed and no singularities exist at either crack tip.

Finally, in constructing the load map, 10° was added to the actual value of ψ used in Eq.(2.54) to calculate $\delta/2a$. For small angles of ψ , the additional 10° produced contact lengths which were closer to those determined by Comninou and Schmueser (1979) and allowed for a better representation of the closed crack-tip and SSC boundaries. For large angles of ψ , no noticeable effects were produced in the load map because of the actual size of $\delta/2a$.

2.4.2 Conclusion

From examination of the elasticity solutions for the two crack-tip models considered and the load map, it is evident that a single crack-tip model is not completely capable of capturing the linear elastic portion of crack-tip behavior under arbitrary loading conditions. Rather, one must first identify the relevant characteristic dimensions in the problem; *i.e.* crack length, contact length and plastic zone size, and then choose a model which gives the correct physical interpretation on these size scales. As pointed out earlier, both models produce physically unrealistic predictions when extrapolated outside their applicable (linear elastic) domain. For example, under the appropriate far-field loads, the traction-free crack-tip solution produces crack-face interpenetration. Additionally, singularities exist at the crack tip in both models, clearly invalidating their linear elastic material assumptions in the very near crack-tip region; *i.e.*, isotropic linear elastic material response, small strains, and small rotations. Obviously additional crack-tip models are necessary to bridge the gap between these two elasticity models, such as closed crack-tip models with crack-face friction, as well as other models which incorporate more physically realistic material idealizations.

At this juncture, plastic zone growth for two continuum crack-tip models has been

investigated by using elastic approximations for the plastic zone. Loadings have been only loosely restricted to those which produce a plastic zone that is small compared to the next relevant characteristic dimension (e.g., contact length or crack length) in the problem and to those which have crack faces continuously apart or in continuous contact from the plastic zone edge to the end of the next relevant characteristic dimension. (Henceforth, the set of admissible planar interfacial cracks is limited to those which fit the two models discussed.) Plastic zone size, shape, and growth characteristics, with respect to applied increasing loads, have been identified and parametrized into convenient dimensional and dimensionless quantities. In terms of these quantities, explicit conditions which approximately determine the applicability of each model have been given. In fact, these models remain appropriate outside their identified domains providing the underlying conditions on which the governing assumptions are based (i.e., contacting or traction-free crack-tip faces), are not violated. Since the validity conditions are based upon asymptotic or approximate formulae, certain geometries may warrant more precise analyses.

The elastically-calculated yield zone and associated inelastic characteristic lengths are based on a Mises yield criterion, but the mathematical approach of determining the loci of points in an elastic field which satisfies a yield criterion is not limited to the Mises criterion. Any other yield criteria, such as the single crystal Schmid criteria, the generalized (anisotropic) Hill criterion, or pressure sensitive transformation criteria, that describes the initiation of an inelastic deformation mechanism, like transformation plasticity, micro-cracking, single crystal slip, and Coulomb friction controlled sliding (in granular materials), can be used to estimate the extent of non-linear behavior contained in an elastic field and qualitatively correlate far-field and local-field quantities. This approximate approach may be quite useful in investigating other phenomena like bi-crystal grain boundaries, micro-delamination or damage in fiber reinforced composite laminates, and any other system where difficulties arise in precisely determining the complete exact response.

Chapter 3

Description of Solution Technique

In this chapter, the individual components which are assembled together to solve the BV problem outlined in Chapter 1 are described. The first section discusses the numerical model in terms of imposed boundary conditions, elastic and plastic domains, and the governing global variational principle, along with modeling simplification-reduction techniques. The second section presents the elastic/perfectly-plastic constitutive relationship along with discussion concerning notation, kinematics, and the constitutive integration operator used. The final section discusses the details of the actual finite element (FE) procedures and meshes used for each of the crack-tip models.

3.1 Crack-Tip Model Formulation

The asymptotic local crack-tip behavior of all numerical models are numerically investigated using, to some extent, the FE approach proposed by Hilton and Hutchinson (1971) for cracks in homogeneous media. Consider the schematic crack-tip region shown in *Figure 3.1*. Near the crack tip, as compared to the characteristic geometric dimension, unique "K"-fields emerge, that asymptotically describe the elastic stress, strain, and displacement fields (within the limits outlined in Section 2.2). The core region is defined to lie within Γ^∞ such that the value of K , along with Eqs.(P2.2) to (P2.5), or the value of K_{II}^c , along with Eqs.(2.19) to (2.21), completely characterizes the linearly elastic fields in the region enclosed by Γ_∞ . The core region is then extracted by cutting

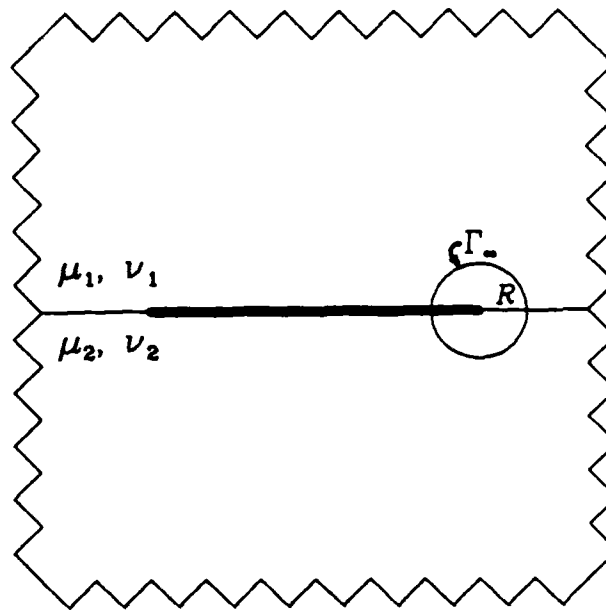


Figure 3.1 Schematic bi-material interfacial crack-tip region, showing core region and domain numbering convention.

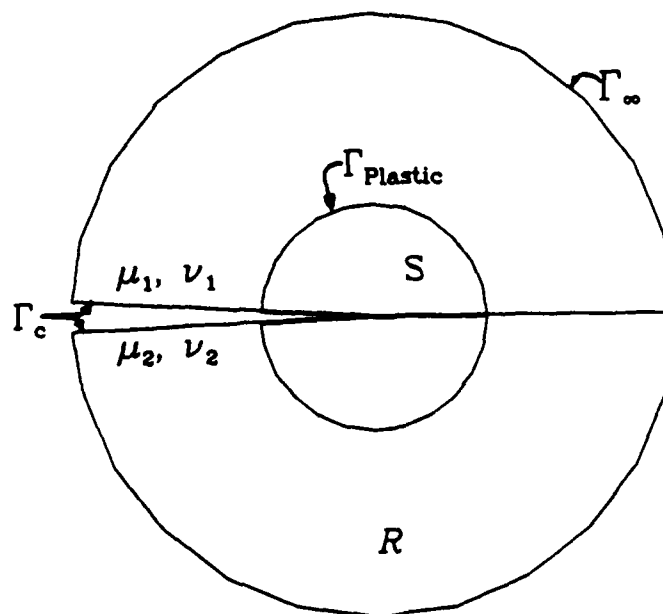


Figure 3.2 Schematic traction-free bi-material interface crack-tip core region, including the elastic (R) and plastic (S) domains and the crack-face (Γ_c), plastic ($\Gamma_{plastic}$), and core (Γ_∞) boundaries.

along Γ_∞ , as shown in *Figure 3.1*. By imposing tractions along Γ_∞ of the extracted core region consistent with Eqs.(P2.2) to (P2.5) or Eqs.(2.19) to (2.21) and scaled by the appropriate \mathbf{K} or \mathbf{K}_{II}^c , the fields within the core region are totally recovered. Alternatively, displacements can be imposed on Γ_∞ to yield the same results. For the traction-free crack-tip model, the displacements are obtained using Eqs.(P2.4), (P2.5), and the following (Muskhelishvili, 1953)

$$2\mu_k (u_x + iu_y) = n_k \phi_k + (\bar{z} - z) \bar{\phi}_k' - \bar{\Omega}_k, \quad (3.1)$$

where $z = x + iy = re^{i\theta}$ is measured from the crack tip, u_x and u_y are Cartesian based displacements, and the remaining terms have the same meaning as before. For the closed crack-tip face model, the dominant asymptotic displacement field can be obtained from the power series expansion (Comninou, 1977a), and in polar coordinates is given by

$$u_r = -\frac{\mathbf{K}_{II}^c \sqrt{2r}}{8\mu_j} \left\{ (2n_j - 1) (1 \mp \beta) \sin \frac{\theta}{2} - (3 \pm \beta) \sin \frac{3\theta}{2} \right\} \quad (3.2)$$

and

$$u_\theta = -\frac{\mathbf{K}_{II}^c \sqrt{2r}}{8\mu_j} \left\{ (2n_j + 1) (1 \mp \beta) \cos \frac{\theta}{2} - (3 \pm \beta) \cos \frac{3\theta}{2} \right\}, \quad (3.3)$$

where the upper and lower signs are used in the lower and upper material domains, respectively.

This approach eliminates the need to model the entire structure containing the crack and allows more mesh refinement in the immediate crack-tip vicinity. Local crack-tip material non-linearities are acceptable, via a St. Venant type argument, as long as they are confined to a zone which is small ($\sim 10\%$) with respect to Γ_∞ (Larsson and Carlsson, 1973; Rice, 1974).

3.1.1 Traction-Free Crack-Tip Faces: Boundary Layer Approach

In addition to the model reduction technique proposed by Hilton and Hutchinson, a further model simplification was used for the traction-free crack-tip model. What follows is a theoretical interpretation and description of this additional method.

Theoretical Considerations

Additional model reduction and computational savings were obtained for the traction-free crack-tip model using Sham's boundary layer method (Sham, 1983). *Figure 3.2* shows a schematic crack-tip core region where Γ_∞ and $\Gamma_{Plastic}$ denote the outer edge of the model and the maximum extent of the plastic zone, respectively. The region \mathcal{R} , by definition of $\Gamma_{Plastic}$, remains elastic during the entire analysis. The boundary layer method reformulates this problem while maintaining the stress, strain, and displacement fields and taking advantage of the elastic region \mathcal{R} . For brevity, a short outline of Sham's boundary layer method follows, and the reader is referred to Sham (1983) for a more complete description.

The boundary layer method recasts the simplification proposed by Hilton and Hutchinson (1971) by altering the physical model depicted in *Figure 3.2*. Consider the boundaries Γ_∞ and $\Gamma_{Plastic}$ to be circles of radii r_∞ and $r_{Plastic}$, respectively, centered about the crack tip. For any value of r_∞ chosen such that $r_\infty \gg r_{Plastic}$, the elastic field within Γ_∞ is reproduced by enforcing Eqs.(2.4) and (2.5) via Eq.(3.1) along Γ_∞ . For convenience, the boundary Γ_∞ will be relocated to $r_\infty = \infty$. Therefore the restriction that $\Gamma_{Plastic}$ be located at a distance close to the crack tip, with respect to Γ_∞ , shall be trivially satisfied for all finite values chosen for $r_{Plastic}$.

To describe the elastic region between Γ_∞ and $\Gamma_{Plastic}$, additional series terms which account for the non-linearities altering the fields within $\Gamma_{Plastic}$ must be included in addition to Eqs.(P2.4) and (P2.5). Using the general series potential identified by Rice (1988), Eqs.(P2.A.1) to (P2.A.4), an inner or Laurent series expansion for the potentials can be constructed. This is accomplished by redefining Eqs.(P2.A.5) and (P2.A.6) to be

$$f(z) = \sum_{N=-\infty}^0 a_N z^N, \quad (3.4)$$

and

$$g(z) = \sum_{M=-\infty}^{-2} b_M z^M. \quad (3.5)$$

Note that an outer series expansion would produce unbounded stresses, strains, and displacements as $r \rightarrow \infty$, while an inner series yields terms which are bounded or tend to zero as $r \rightarrow \infty$. Also, the first term, $M = -1$, for the $g(z)$ expression is excluded since it physically represents point loads applied at the crack tip. For convenience, Eq.(3.4) additively decomposes into

$$f(z) = f^K(z) + f^T(z) = a_0 + f^T(z), \quad (3.6)$$

where

$$f^T(z) = \sum_{N=-\infty}^{-1} a_N z^N. \quad (3.7)$$

Since Eq.(3.5) contains no terms associated with the K-field, Eq.(3.5) should be interpreted as the definition of $g^T(z)$; i.e., $g^T(z) = g(z)$. All terms with the superscript K shall refer to quantities, which assume that only the K-field is present (terms of order $r^{(-1/2) \pm i\epsilon}$ in stress) and those with the superscript T shall be used to identify all the quantities associated with the remaining outer expansion of the inner series terms. Using the potentials represented by Eqs.(P2.A.1) to (P2.A.4), along with Eqs.(3.4) and (3.5), and the displacement relationship, given by Eq.(3.1) the complete field in S can be expressed in terms of the coefficients a_N and b_N .

The boundary layer method requires solving the field equations within Γ_∞ by minimizing the modified rate potential function, given by Sham (1983) as

$$\bar{\Pi} = \int_S \Phi(\dot{\xi}) dS + \int_R \Phi(\dot{\xi}^T) dS - \int_{\Gamma_{Plastic}} (\mathbf{n} \cdot \dot{\sigma}^K(t)) \cdot \dot{\mathbf{u}}^T ds. \quad (3.8)$$

Here Φ is the strain rate potential, $\dot{\xi}$ is the strain tensor, \mathbf{n} is the unit outward normal vector, $\dot{\sigma}^K(t)$ is the stress rate tensor attributable to the K-field, and $\dot{\mathbf{u}}$ is the velocity vector.

The modified potential can be interpreted on a term by term basis. The integral $\int_R \Phi(\dot{\xi}^T) dS$ corresponds to the elastic strain rate energy in the region between $\Gamma_{Plastic}$ and Γ_∞ attributable to the lower order terms. It can be given explicitly in the form $\frac{1}{2} \dot{\mathbf{q}}^T \mathbf{S} \dot{\mathbf{q}}$, where \mathbf{q}^T is the vector of generalized degrees of freedom [the unknown

coefficients a_N and b_M from Eqs.(2.2) and (2.3)], \dot{q}^{eT} is time derivative of q^{eT} , and S is an appropriate stiffness matrix. Since the region \mathcal{R} is elastic, the stiffness matrix S is independent of time and is more conveniently evaluated from the associated relationship $\frac{1}{2}q^{eT}Sq^{eT} = \int_{\mathcal{R}} \Phi(\epsilon^T) dS$ where Φ is now the strain energy density function. In Appendix A.1 the stiffness matrix S is calculated using the known analytical expressions found in Eqs.(P2.A.1) to (P2.A.4), (3.4), and (3.5). (Note, in Appendix A the stress potential χ is used instead of Ω . The two stress potentials are related via $\chi'' = \Omega' - \phi' - z\phi''$.) An equivalent line integral along the boundary Γ_{∞} , $\Gamma_{Plastic}$, and the crack face (Γ_c), Eq.(A.7), is used to evaluate the surface integral. In evaluating the line integral, it can be shown [Eqs.(A.13) and (A.14)] that the only non-zero contribution arises along the $\Gamma_{Plastic}$ boundary. The next integral in Eq.(3.8), $\int_{\Gamma_{Plastic}} (\mathbf{n} \cdot \dot{\sigma}^K(t)) \cdot \dot{\mathbf{u}}^T ds$, can be explicitly expressed as $\dot{q}^{eT} \dot{\mathbf{F}}^e(t)$, where $\mathbf{F}^e(t)$ is the vector of integrated work conjugate forces to the (T -terms) generalized degrees of freedom. The time derivative of the work conjugate force vector, $\dot{\mathbf{F}}^e(t)$, can be written in component form as

$$\dot{F}_j^e(t) = \int_{\Gamma_{Plastic}} (\mathbf{n} \cdot \dot{\sigma}^K(t)) \cdot \dot{\mathbf{u}}_j^T ds, \quad (3.9)$$

where $\dot{\mathbf{u}}_j^T(r, \theta, \epsilon)$ is the j th component of the known velocity mode shape vector; (i.e., the components of the velocity mode shape vector are related to the velocity vector via $\dot{\mathbf{u}}_j^T(r, \theta, \epsilon) = \dot{q}_j^{eT} \dot{\mathbf{u}}_j^T(r, \theta, \epsilon)$, with no summation on j .) The term $\dot{\sigma}^K(t)$ is dependent only on time via the scaling variable $\dot{\mathbf{K}}(t)$ and is otherwise known. Since $\dot{\mathbf{K}}(t)$ is known, and is chosen to be of the form $\dot{\mathbf{K}}(t) = \mathbf{K}_0 \dot{L}(t)$, where $\dot{L}(t)$ is a real scalar function of time, $\dot{\mathbf{F}}^e(t)$ need only be evaluated as \mathbf{F}_0^e at $\mathbf{K}(t=0) = \mathbf{K}_0$ and then scaled by $\dot{L}(t)$ as $\dot{\mathbf{F}}^e(t) = \mathbf{F}_0^e \dot{L}(t)$. The remaining integral in Eq.(3.8) corresponds to the standard rate potential such that $\dot{\sigma} = \partial \Phi(\dot{\epsilon}) / \partial \dot{\epsilon}$ within the region inside $\Gamma_{Plastic}$, and is evaluated using finite elements.

To maintain a well posed mathematical BV problem, the additional lower order terms in \mathcal{R} must be accompanied by additional mode shapes along the $\Gamma_{Plastic}$ boundary. In region \mathcal{R} , $2(N+M-1)$ additional unknowns, contained in the vector q^{eT} , are added to give the complete representation. The addition of these terms compensates for any

deviations from K -fields which may occur in R due to nonlinearities within S . At the same time, $2(N+M-1)$ additional constraint equations are imposed along $\Gamma_{Plastic}$, thus making it a well posed mathematical problem. As the behavior in region S deviates from the asymptotic dominant field, Eqs.(2.4) and (2.5), lower order mode shapes are activated by making amplitude coefficients in q^{*T} non-zero. However, this occurs at the expense of adding additional strain deformation in region R such that equilibrium and compatibility between the two regions is achieved via Eq.(3.8).

By consideration of the previous observations, the modified potential energy function was incorporated into the FE code *ABAQUS* (Hibbitt, 1984). At the outer edge of the FE boundary, taken to be $(\Gamma_{Plastic})$, constraint equations, written in the form of a user-defined multiple point constraint (MPC) subroutine, were used to enforce nodally the admissible displacement eigenmodes in accordance with Eqs.(P2.A.1) to (P2.A.4), (3.1), (3.4), and (3.5). The amplitudes for the dominant singular (K -field) modes were externally prescribed, $K = K_0 L(t)$, while for the other modes, the coefficients (generalized degrees of freedom - q^{*T}) were considered solution dependent unknowns. Connected to the lower order coefficients, q^{*T} , was a spring-element network which had equivalent stiffness S . The complete boundary condition and spring network derivation is formally given in Appendix A. The actual MPC subroutine is listed in Appendix C. The integrated work conjugate forces F_0^e were obtained from the reaction forces of an initial elastic FE analysis, which had all the lower order generalized degrees of freedom zeroed ($q^{*T} = 0$) and an appropriate K_0 value imposed. The vector of generalized reaction forces required to sustain $q^{*T} = 0$ was taken as F_0^e .

Boundary Layer Verification

To verify the boundary layer method implementation, two *homogeneous* test problems were first performed. These were the same two problems considered by Needleman and Sham (1980): (a) a semi-infinite crack with point loads applied normal to the crack face at $x = -a$; and (b) a semi-infinite crack with the crack tip translated such that it

was located at $x = a$. Figures 3.3 and 3.4 show the two geometries.

An equivalent inner series expansion about the origin ($z = 0$) which exactly represents their potentials can be explicitly given for these geometries. For the point load the stress potential functions are given by

$$\phi' = \Omega' = \frac{P}{2\pi(z+a)} \sqrt{\frac{a}{z}} = \frac{P}{2\pi} \sum_{n=1}^{\infty} \frac{a^{(n-1/2)}}{z^{(n+1/2)}} (-1)^{n+1}. \quad (3.10)$$

By comparing these potentials with those used in Eqs.(A.1) to (A.4), the series coefficients are related to the components in $q^{\epsilon T}$ via

$$q_n^{\epsilon T} = \frac{P}{2\pi} \frac{a^{n-\frac{1}{2}} (-1)^{n+1}}{2(n-\frac{3}{2})(n-\frac{1}{2})}, \quad (3.11)$$

for $n = 1$ to ∞ . For the translated crack tip the stress potential functions are

$$\phi' = \Omega' = \frac{K_I}{2\sqrt{2\pi(z-a)}} = \frac{K_I}{2\sqrt{2\pi z}} + \sum_{n=1}^{\infty} f_n \frac{a^n}{z^{(n+1/2)}}, \quad (3.12)$$

where f_n are known constants. Again, by comparing these potentials with those used in this analysis, Eqs.(A.1) to (A.4), the coefficients $q_n^{\epsilon T}$ can be obtained in terms of f_n . Unlike Eqs.(2.4) and (2.5), neither of these expansions contain any whole powers of z .

To verify the boundary layer implementation, homogeneous elastic FE analyses were performed and comparisons between the analytically determined coefficients and the FE calculated coefficients, $q^{\epsilon T}$, were made. Table 3.1 lists the analytical and FE determined coefficients for the two geometries. In both problems the outer boundary of the FE mesh had a radius of 1.0(m). Thus the ratio of $a/|z|$ in the series expansion was 0.3981 for the point load example and was 0.10 for the translated crack tip example.

The FE determined coefficients shown in Table 3.1 are in good agreement with the analytically determined coefficients for the higher order terms, but the agreement diminishes for lower order terms. (Note that lower order terms correspond to components in $q^{\epsilon T}$ with "larger" subscripts.) For the translated crack, this deterioration is attributed to inaccuracies in determining $F^{\epsilon}(t)$, mesh construction, series truncation, and numerical noise. The reaction forces F_0^{ϵ} for the translated crack were obtained by sewing up the crack face such that the crack tip was artificially located at $x = 0$ and by

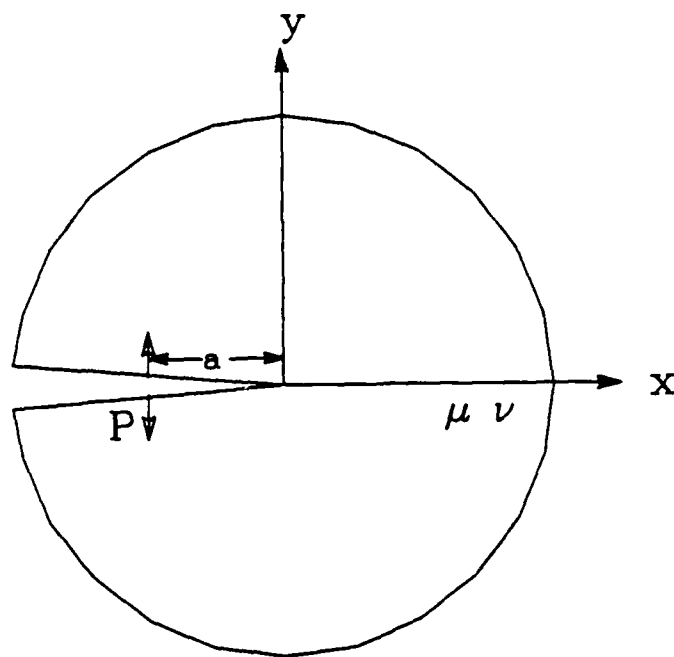


Figure 9.3 Schematic homogeneous crack-tip region with opening crack-face point loads (P) applied at a distance a from the crack-tip.

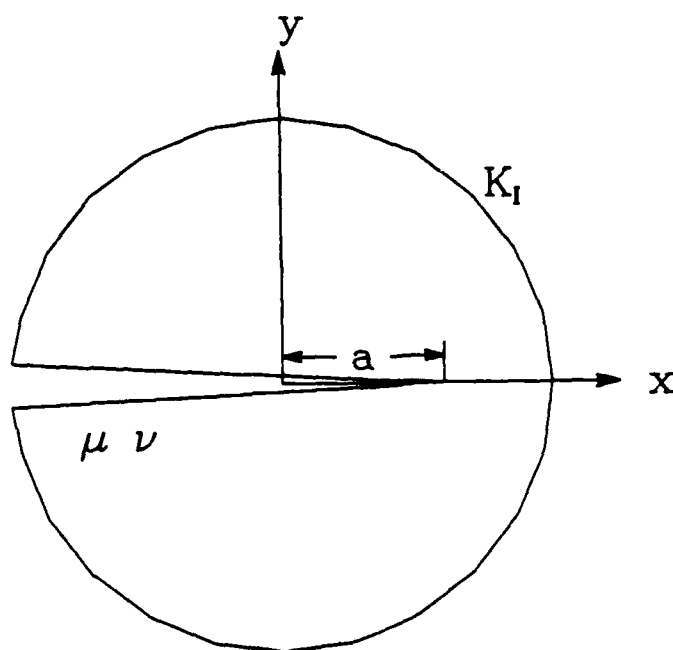


Figure 9.4 Schematic homogeneous crack-tip region and coordinates, showing translated crack tip at $x = a$.

applying K_0 in an initial elastic analysis. Since, in the translated crack case, the mesh was designed to have the crack tip at $x = a$, and no refinement of the mesh existed at $x = 0$, inaccuracies in F_0^* may have arisen. Similarly, the mesh used in the point load case was not refined where the point loads were applied. (This will not be an issue during the actual SSY analysis because the forces F_0^* will be found for the actual unsewed and untranslated meshes.) It was assumed that since the higher order terms matched, the implementation was performed correctly and the dominant behavior was captured even though numerical noise existed.

Coefficient	Analytical [Eq.(3.11)]	FE
q_1	-.2008	-.20084
q_2	-2.6559E-2	-2.6651E-2
q_3	2.0731E-3	2.1220E-3
q_4	-3.2279E-4	-3.6204E-4
q_5	5.6005E-5	8.0071E-5
q_6	-3.3130E-6	-2.0285E-5

(a)

Coefficient	Analytical [Eq.(3.12)]	FE
q_1	-1.9394E-2	-1.9947E-2
q_2	4.6966E-4	4.9868E-4
q_3	7.2501E-6	8.3145E-6
q_4	6.5413E-8	3.1183E-7
q_5	-1.2820E-8	1.5594E-8

(b)

Table 3.1 Analytical and numerical coefficients for a plane-strain crack-tip problem with: (a) opening normal point loads applied at $x = -0.3981$; (b) the crack tip translated to $a = 0.1$.

To verify that the bi-material portion of the boundary layer formulation was correctly implemented, various independent tests were conducted. First, several (bi-material) elastic cases with various material combinations were loaded by prescribing a specific value of K and setting all inner series coefficients equal to zero ($q^{eT} = 0$).

Boundary node displacements, which correspond to the dominant asymptotic solution, were compared with the known analytical solution. Because the user written MPC subroutine, used in prescribing the displacements, was coded in a manner such that one index determined all the powers of the root being imposed (i.e., $\lambda_j = (j + 1/2) + i\epsilon$ where j is the index of interest), it was felt that, the coding for that entire family of roots was performed correctly, as long as the limits on this index were chosen correctly and one specific index value yielded the correct results. In a similar fashion, the whole-integer (real) root set [$\Re(\lambda_j) = \lambda_j = j$] was verified by prescribing K and setting all but one value of q^{eT} equal to zero. The coefficient not set equal to zero was the one producing a domain-wise uniform stress parallel to the interface ($M = 0$ term). (In the actual potentials used, Eqs.(A.1) to (A.4), the constants multiplying the coefficients (q^{eT}) in the displacement relationship were not *trivially* zero when $M = 0$.) Again, since the results of this one specific case were correct and the coding was written in an unbiased manner with respect to indices, it was felt that the coding for the entire set of whole-integer real roots was performed correctly.

In a similar spirit, the spring stiffness constants were verified. For the homogeneous case, several specific spring stiffnesses were analytically and numerically integrated to ensure proper coding. Once again, a single index was used to generate the stress potentials, thus guaranteeing that the entire set of spring stiffness coefficients were determined correctly. *Complex* FORTRAN coding was utilized in such a manner that if the homogeneous case was performed correctly and the bi-material potentials were correct, then the bi-material spring constants would also be determined correctly. Additionally, several spring constants were integrated via other methods to provide an additional check. All homogeneous tests were performed using the actual bi-material subroutines and programs, but with identical elastic properties in each domain.

A crack-face point load elasticity problem, similar to the one used previously, was considered to ensure that the boundary layer extension for bi-materials was implemented correctly. *Figure 3.5* shows the crack-tip geometry and the direction and loca-

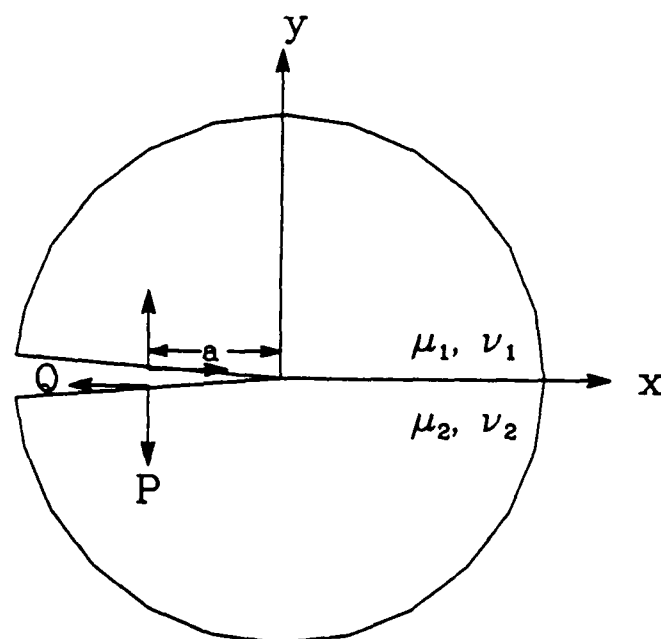


Figure 9.5 Schematic bi-material interfacial crack-tip region with crack-face opening (P) and shearing (Q) point loads applied at a distance a from the crack-tip, showing coordinates and domain numbering conventions.

tion of the crack-face point loads P and Q . From Rice and Sih (1965), the ϕ'_1 stress potential function for this configuration is given by

$$\phi'_1 = \Omega'_1 = \frac{P - iQ}{2\pi e^{\pi\epsilon}} \frac{1}{z + a} \left(\frac{a}{z}\right)^{\frac{1}{2} + i\epsilon} \quad (3.13)$$

and the equivalent inner series expansion about the origin ($z = 0$) is expressed as

$$\phi'_1 = \Omega'_1 = \frac{P - iQ}{2\pi e^{\pi\epsilon}} \frac{1}{z} \left(\frac{a}{z}\right)^{i\epsilon} \sum_{n=1}^{\infty} \left(\frac{a}{z}\right)^{n-\frac{1}{2}} (-1)^{n+1}. \quad (3.14)$$

By comparing this expansion of the ϕ'_1 potential with the general potential used in Eqs.(A.1) to (A.4), the series coefficients $q_n^{\epsilon T}$ in the general potential, Eqs.(A.1) to (A.4), are determined to be

$$q_n^{\epsilon T} = \frac{P - iQ}{4\pi e^{\pi\epsilon}} \frac{[\cos(\epsilon \ln a) + i \sin(\epsilon \ln a)]}{\left[\left(\frac{1}{2} - n\right) - i\epsilon\right] \left[\left(-n - \frac{1}{2}\right) - i\epsilon\right]} a^{n+\frac{1}{2}} (-1)^n, \quad (3.15)$$

for $n = 0$ to ∞ .

A plane-strain FE analysis was used to evaluate the bi-material point load problem. It used the elastic properties of aluminum in the upper region and steel in the lower region, and the bi-material constant was $\epsilon = 0.03220$. (See Table 4.3 for the elastic constants used.) The crack face was loaded with several different combinations of points loads P and Q , while maintaining $K = 0$, and only positive values of P were considered. The values of the analytical and FE determined coefficients for the case where loads of magnitude $P = Q = 1$ are applied at $x = -0.3981$ are listed in Table 3.2. (The FE mesh had a radius of 1.0(m) which yielded a ratio of $a/|z| = 0.3981$.) The discrepancy between the coefficients can be attributed to the coarse mesh, lack of mesh refinement near the point loads, and the fact that the Laurent series expansion was truncated after only six terms. It was assumed that since each individual component and the complete implementation was verified for both homogeneous and bi-material cases, the boundary layer method was extended and implemented correctly for the bi-material problem.

Coefficient	Analytical [Eq.(3.15)]	FE
q_1	$-.17456 + i.18557$	$-0.1747 + i0.1855$
q_2	$-2.0939 \times 10^{-02} + i2.6627 \times 10^{-02}$	$-2.1073 \times 10^{-02} + i2.6346 \times 10^{-02}$
q_3	$1.7809 \times 10^{-03} - i2.0330 \times 10^{-03}$	$1.7875 \times 10^{-03} - i1.9540 \times 10^{-03}$
q_4	$-3.0828 \times 10^{-04} + i3.4306 \times 10^{-04}$	$-3.1094 \times 10^{-04} + i2.9619 \times 10^{-04}$
q_5	$6.8632 \times 10^{-05} - i7.5474 \times 10^{-05}$	$6.3699 \times 10^{-05} - i5.2252 \times 10^{-05}$
q_6	$-1.7453 \times 10^{-05} + i1.9061 \times 10^{-05}$	$-1.4279 \times 10^{-05} + i3.4650 \times 10^{-06}$

Table 3.2 Analytical and numerical coefficients for a plane-strain bi-material crack-tip problem with point load, $P = Q = 1$, applied at $x = -0.3981$.

3.1.2 Closed Crack-Tip Faces

The asymptotic local crack-tip behavior for the closed crack-tip face model was numerically investigated with the FE method proposed by Hilton and Hutchinson (1971). Since no parametric study was to be performed and no numerically difficult oscillatory stress fields exist in the closed crack-tip elasticity solution, Sham's boundary layer approach was not utilized. The displacements were obtained via Eqs.(3.2) and (3.3), rotated into a Cartesian coordinate frame, and imposed along Γ_∞ , the FE mesh boundary. For the FE analysis, the displacements, Eqs.(3.2) and (3.3), were incorporated into a user-written MPC subroutine and nodes along Γ_∞ were constrained with a free node, whose displacement was associated with the value of K_{II}^c , via the MPC. As before, the magnitude of K_{II}^c was scaled with $L(t)$. Appendix C contains a listing of the MPC subroutine used.

3.2 Elastic/Perfectly-Plastic Constitutive Relationship

This section describes the constitutive relationship used, as well as the integration operator and the associated notation. The material relationship was incorporated in the FE analysis via a user-written subroutine called UMAT. A listing of the UMAT subroutine is included in Appendix C.

3.2.1 Kinematics

It is assumed that infinitesimal strain theory (linearized kinematic theory) is used. It is therefore assumed *a priori* that all strains and physical rotations are small such that all rotation tensors can be approximated by the identity tensor and that the symmetric part of the (spatial) velocity gradient can be approximated by the strain rate.

3.2.2 Notation

Using Gurtin's notation convention (Gurtin, 1981), the evolution equation and the definition of various relevant variables are as follows. The Cauchy stress rate tensor, $\dot{\sigma}$, is given by

$$\dot{\sigma} = \mathcal{L}[\dot{\xi} - \dot{\xi}^p], \quad (3.16)$$

with the fourth order elasticity tensor \mathcal{L} , defined as,

$$\mathcal{L} = 2\mu I + (\kappa - \frac{2}{3}\mu) \mathbf{1} \otimes \mathbf{1}, \quad (3.17)$$

where $\dot{\xi}$ is the total strain rate tensor, $\dot{\xi}^p$ is the plastic strain rate tensor, I is the fourth order identity tensor, $\mathbf{1}$ is the second order identity tensor, and κ is the bulk modulus. (Note that the strain tensor is designated with ξ since the usual symbol associated with it is used to define the bi-material constant.) The deviatoric stress rate tensor, $\dot{\sigma}'$, is given by

$$\dot{\sigma}' = \dot{\sigma} - \frac{1}{3} \text{tr}(\dot{\sigma}) \mathbf{1}. \quad (3.18)$$

Similarly, the strain rate tensors can also be decoupled into deviatoric and hydrostatic parts. The Mises equivalent stress, $\bar{\sigma}$, is defined as

$$\bar{\sigma} = \sqrt{\frac{3}{2} \sigma' \cdot \sigma'}, \quad (3.19)$$

and \mathbf{N} , the instantaneous normal to the yield locus at the current stress state, is given by

$$\mathbf{N} = \sqrt{\frac{3}{2}} \frac{\sigma'}{\bar{\sigma}}. \quad (3.20)$$

3.2.3 Constitutive Relationship

The elastic/perfectly-plastic continuum constitutive relationship is based upon several assumptions. It assumes that elastically, as well as plastically, the material is isotropic and that all plastic deformation is volume preserving (incompressible). The yield locus, in the π -plane, is spherical (i.e., not pressure sensitive) and does not translate or change size with plastic flow (i.e., no isotropic or kinematic hardening). All plastic flow occurs only in the direction instantaneously normal to the yield locus, at the current point. The flow rule, Δ , is defined as

$$\Delta = \begin{cases} 1 & \text{If } \bar{\sigma} = \sigma_y \text{ and } \mathbf{N} \cdot \{\mathcal{L}[\dot{\boldsymbol{\epsilon}}]\} \geq 0 \\ 0 & \text{Otherwise.} \end{cases} \quad (3.21)$$

where σ_y is the tensile yield strength of the material. The interpretation of the flow rule is that $\dot{\boldsymbol{\epsilon}}^p$ is non-zero only when $\Delta = 1$. The portion of this constitutive relationship describing plastic straining, written in rate form, is

$$\dot{\boldsymbol{\epsilon}}^p = \Delta \{\mathbf{N} \otimes \mathbf{N}\} [\dot{\boldsymbol{\epsilon}}]. \quad (3.22)$$

The stress rate $\dot{\boldsymbol{\sigma}}$ is obtained by substituting the definition for $\dot{\boldsymbol{\epsilon}}^p$, Eq.(3.22), directly into Eq.(3.16) as

$$\dot{\boldsymbol{\sigma}} = \{\mathcal{L}\} [\{I - \mathbf{N} \otimes \mathbf{N}\} [\dot{\boldsymbol{\epsilon}}]]. \quad (3.23)$$

To facilitate the incorporation of this constitutive relationship into the numerical model, an incremental form is utilized. This incremental form is exact only in the limit that

$$\lim_{\Delta t \rightarrow 0} (\Delta \boldsymbol{\epsilon}) = \frac{\partial \boldsymbol{\epsilon}}{\partial t} \Delta t = \dot{\boldsymbol{\epsilon}} \Delta t. \quad (3.24)$$

3.2.4 Constitutive Integration Operator

The elastic/perfectly-plastic material response is numerically integrated using the Rice-Tracey Mean Normal integration operator (Rice and Tracey, 1973). The material response is integrated under the assumption that during an increment in time, Δt , between the n th and $(n + 1)$ th state, $\dot{\boldsymbol{\epsilon}}$ remains constant such that

$$\epsilon_{n+1} - \epsilon_n = \int_n^{n+1} \dot{\epsilon} dt \approx \dot{\epsilon} \Delta t = \Delta \epsilon. \quad (3.25)$$

The deviatoric stress σ'_{n+1} at the $(n+1)$ state is given by

$$\sigma'_{n+1} = \sigma'_n + \Delta \sigma' \quad (3.26)$$

and, when $\Lambda = 0$,

$$\Delta \sigma' = 2\mu \Delta \epsilon', \quad (3.27)$$

where σ'_n is the deviatoric stress at the n th state, $\Delta \sigma'$ is the deviatoric stress increment, and $\Delta \epsilon'$ is the postulated deviatoric strain increment tensor.

An increment in stress where the initial stress state is elastic and the final state is yielding ($\Lambda = 1$) is now considered, and *Figure 3.6* schematically shows such a stress state in the π -plane. The initial elastic stress state σ'_n does not satisfy the yield condition and lies within the $R = \sigma_y$ sphere. The increment in deviatoric stress, $\Delta \sigma'$, is obtained by traveling from the original stress state along the path of the elastic predictor, $2\mu \Delta \epsilon'$, until the yield surface is reached. The fraction of the total elastic predictor which must be traveled to reach the yield surface is α , and α is given by

$$\alpha(\Delta \epsilon') = \frac{-(\Delta \epsilon' \cdot \sigma'_n) \pm \sqrt{(\Delta \epsilon' \cdot \sigma'_n)^2 - (\Delta \epsilon' \cdot \Delta \epsilon') [(\sigma'_n \cdot \sigma'_n) - \sigma_y^2]}}{\mu (\Delta \epsilon' \cdot \Delta \epsilon')} \quad (3.28)$$

The correct root of α is the one that lies between 0 and 1. Once the yield surface is reached, an intermediate state T^* is constructed using the remaining portion of the elastic predictor $(1 - \alpha)2\mu \Delta \epsilon'$ and the stress state at the yield surface, $\sigma'_n + \alpha 2\mu \Delta \epsilon'$. The intermediate state T^* is defined as

$$T^*(\Delta \epsilon) = 2\sigma'_n + (1 + \alpha)2\mu \Delta \epsilon', \quad (3.29)$$

where N^* , the normalized direction of T^* , is defined as

$$N^*(\Delta \epsilon) = \frac{T^*(\Delta \epsilon)}{2\sqrt{\frac{1}{2}T^*(\Delta \epsilon) \cdot T^*(\Delta \epsilon)}}. \quad (3.30)$$

The deviatoric stress increment $\Delta \sigma'$ is then obtained by projecting $(1 - \alpha)2\mu \Delta \epsilon'$, the remaining fraction of the elastic predictor, onto a vector normal to N^* such that

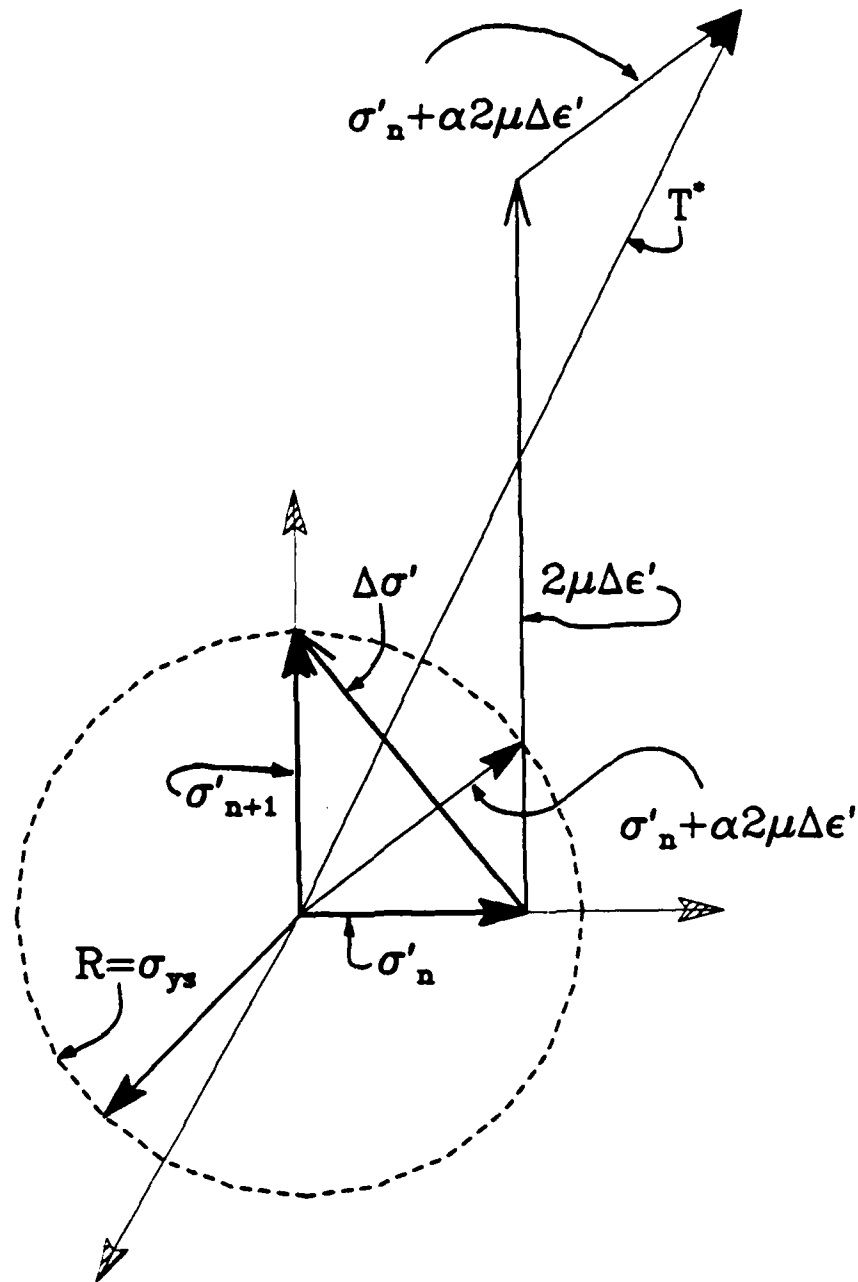


Figure 3.6 Schematic π -plane representation of a stress increment obtained by the Rice-Tracey mean normal integration operator; showing the various vectorized (tensor) stress states and the yield sphere.

$$\Delta \sigma' = 2\mu \{ I - (1 - \alpha) 2N^* \otimes N^* \} [\Delta \epsilon']. \quad (3.31)$$

This operator always places σ'_{n+1} exactly on the yield surface for any strain increment with $\bar{\sigma} \leq \sigma_y$, and elastic predictor state having $\sqrt{\frac{3}{2} (\sigma'_n + 2\mu \Delta \epsilon') \cdot (\sigma'_n + 2\mu \Delta \epsilon')} \geq \sigma_y$. To obtain the updated total stress, σ_{n+1} , the hydrostatic stress must also be integrated. Since ϵ_{n+1} is postulated as being known (given), the hydrostatic stress is trivially obtained and is

$$\sigma_{n+1} - \sigma'_{n+1} = \{ \kappa \mathbf{1} \otimes \mathbf{1} \} [\epsilon_{n+1}]. \quad (3.32)$$

Using Eqs.(3.26), (3.31), and (3.32), the total $(n+1)$ th stress state, when $\Lambda = 1$ during an increment, is given by

$$\sigma_{n+1} = \left\{ \begin{array}{l} 2\mu (I - (1 - \alpha) 2N^* (\Delta \epsilon) \otimes N^* (\Delta \epsilon)) \\ + (\kappa - \frac{2\mu}{3}) (\mathbf{1} \otimes \mathbf{1}) \end{array} \right\} [\Delta \epsilon] + \sigma_n. \quad (3.33)$$

Eq.(3.31) is general and valid for all stress states except when both σ_n and σ_{n+1} lie within the yield radius. In conjunction with Eq.(3.27), Eqs.(3.28) to (3.33) describe the stress state for all possible loading increments.

In addition to calculating the final stress state, a material Jacobian, defined as

$$J = \frac{\partial \Delta \sigma}{\partial \Delta \epsilon}, \quad (3.34)$$

is also required for the global Newton-Rapson (FE) iteration procedure (Hibbitt, Karlsson, and Sorensen, 1987). The Jacobian for this operator is given by,

$$J = G_1 I + (\kappa - \frac{G_1}{3}) \mathbf{1} \otimes \mathbf{1} + G_2 N^* \otimes N^* + G_3 N^* \otimes \gamma + G_4 N^* \otimes \Delta \epsilon' + G_5 \Delta \epsilon' \otimes \gamma, \quad (3.35)$$

where,

$$G_1 = 2\mu - (1 + \alpha)(1 - \alpha) \frac{4\mu^2}{r^*} (N^* \cdot \Delta \epsilon'), \quad (3.36)$$

$$G_2 = 4\mu(\alpha - 1) - (1 + \alpha)(1 - \alpha) \frac{16\mu^2}{r^*} (N^* \cdot \Delta \epsilon'), \quad (3.37)$$

$$G_3 = 4\mu(N^* \cdot \Delta \epsilon') + (1 - \alpha) \frac{16\mu^2}{r^*} (N^* \cdot \Delta \epsilon')^2 - (1 - \alpha) \frac{4\mu^2}{r^*} (\Delta \epsilon' \cdot \Delta \epsilon'), \quad (3.38)$$

$$G_4 = -(1 + \alpha)(1 - \alpha) \frac{4\mu^2}{r^*}, \quad (3.39)$$

$$G_5 = (1 - \alpha) \frac{4\mu^2}{r^*} (N^* \cdot \Delta \epsilon'), \quad (3.40)$$

$$\gamma = -\frac{[2\mu\alpha^2 \Delta \epsilon' + \alpha \sigma'_n]}{2\mu\alpha (\Delta \epsilon' \cdot \Delta \epsilon') + (\sigma'_n \cdot \Delta \epsilon')}, \quad (3.41)$$

and

$$r^* = \sqrt{\frac{1}{2} T^* \cdot T^*}. \quad (3.42)$$

Use of the mathematically exact (generally) non-symmetric Jacobian would require that the FE procedure solve the complete set of equations, as opposed to a symmetric subset. This procedure would be considerably more costly, and thus a symmetrized (approximate) Jacobian is used (Bathe, 1982). The symmetrized Jacobian, J_{sym} , is defined as

$$\begin{aligned} J_{sym} = & G_1 I + (\kappa - \frac{G_1}{3}) 1 \otimes 1 + G_2 N^* \otimes N^* + G_3 \frac{1}{2} (N^* \otimes \gamma + \gamma \otimes N^*) \\ & + G_4 \frac{1}{2} (N^* \otimes \Delta \epsilon' + \Delta \epsilon' \otimes N^*) + G_5 \frac{1}{2} (\gamma \otimes \Delta \epsilon' + \Delta \epsilon' \otimes \gamma). \end{aligned} \quad (3.43)$$

The use of this Jacobian yielded nearly quadratic global convergence, as would be expected in a Newton-Raphson method. (Aside: A radial return operator [Krieg and Krieg, 1977] was also tried, but yielded very poor convergence. It is speculated that because the Jacobian for the Mean-Normal operator is based upon an intermediate stress state halfway between σ'_{n+1} and σ'_n , it does not result in the same sort of radial softening that would be predicted using a radial return Jacobian. This (relative) radial stiffening is thought to retard small to modest changes in the direction of σ'_{n+1} during iterations.)

3.3 FE Model Considerations

This last section is divided into three parts. The first part discusses the "simplified," but efficient, FE model used to obtain the characteristics of the traction-free crack-tip model for different loadings ($\angle K$) and material combinations considered. Since this

mesh would subsequently be used many times and each run represents a substantial investment in CPU time (due to the complexity of the oscillatory elastic fields), much effort was spent on designing it. The second FE model discussed is again a traction-free crack-tip model, however, the purpose this model was to unequivocally determine whether or not oscillatory stress fields, analogous to those found in the elastic solution, exist within the elastic/perfectly-plastic deformation zone. Material properties were chosen and the mesh design was performed in such a manner to yield the maximum amount of information with only a relatively modest investment in computational time. Although many of the same details from the first model were utilized, the goal was to maintain simplicity and thereby ensure an unquestionable result. The third section concerns itself with the FE model assembled to investigate the closed crack-tip face model. Since little complexity was anticipated based upon the elastic solution, a simple, but sufficient, FE model was assembled.

3.3.1 Traction-Free Crack-Tip Face Model

Boundary Layer Implementation

Various common features were incorporated in all the traction-free crack-tip FE models that used the boundary layer method. The FE code *ABAQUS* (Hibbitt, 1984) was used with the user-added subroutines UMAT and MPC. Slight modifications when needed were made in the UMAT to obtain only an elastic response. The boundary layer formulation series were truncated after the first seven half-integer (Williams type) terms ($N = 0, -1, -2, \dots, -6$), and after five even-integer terms ($M = -2, -3, -4, \dots, -6$), where the variables N and M refer to the indices in Eqs.(3.4) to (3.7) or Eqs. (A.1) to (A.4). The term $N = 0$ corresponds to the dominant asymptotic power, and the power $M = -1$ was excluded from the formulation since it represents an applied concentrated crack-tip force and produces infinite far-field elastic strain energy in the boundary layer formulation. The vector q^T was represented by 24 degrees of freedom (12 "free" nodes each with two active degrees of freedom). These free nodes, which actually behave as

Lagrange multipliers in the FE program, were the vertices in the spring network and the nodes to which all outer FE boundary nodes were constrained.

FE Mesh

Prior to elaborating on the actual meshes used, the procedure used to evaluate mesh accuracy will be outlined.

In order to judge the capability of the FE meshes to reproduce at least the elastic K -fields, elastic test runs were performed on each mesh by imposing assorted values of K with $q^{eT} = 0$. The averaged nodal stresses were then examined in the radial and circumferential directions and compared to the dominant asymptotic stress expressions. To evaluate the radial dependence, the stress components were plotted against the natural logarithm of the radial distance r . Excluding the first and last elements, the numerical and analytical results were usually indistinguishable. For a better comparison, the stresses were normalized (multiplied by \sqrt{r}) and plotted against the natural logarithm of the radial distance. In this way, any discrepancy existing in the phase or period between the analytical and numerical solutions would be immediately obvious. One particularly beneficial result emerged from this plotting procedure. The numerically obtained stresses alternatively overestimated and then underestimated the analytical solution, from node to node, with a mean value which was coincidental with the analytical solution. The magnitude of these oscillations (local maximum to minimum) decreased as the number of elements used in the radial direction increased. The oscillation magnitude is thought to represent the actual discretization error attributable to the inability of the element to reproduce the approximate $1/\sqrt{r}$ stress distribution. This parameter was used to estimate when sufficient mesh refinement was achieved. In addition to this measure, the interfacial tractions between the domains were examined to ensure continuity. Finally, numerically obtained elastic energy release rates were compared against theoretical values.

All traction-free crack-tip models had the same geometrical mesh design. An actual

mesh is shown in *Figure 3.7* without the inner core elements. All crack-tip elements were collapsed into a triangular geometry. To maintain physical significance, interface elements were incorporated into the crack-face region, as necessary, to prevent crack face interpenetration during the transient portion of the analysis. (Prior to "steady-state.") The mesh contained 18 and 25 elements circumferentially in the elastic and elastic/perfectly-plastic regions, respectively, with a high concentration of elements around the interface. The mesh contained five logarithmically spaced elements per each of its three concentric rings. Each ring spanned a decade, with the inner ring extending all the way to the crack tip. The outer mesh boundary was located at $R = 1.0$ m in order to circumvent computational difficulties associated with the boundary layer formulation. Plane-strain elements were used.

Two different meshes, differing only in element type, were employed. The initial mesh consisted of 8-node isoparametric elements with full 3×3 Gaussian integration in the elastic region and 8-node isoparametric fully integrated linear pressure hybrid elements in the elastic/perfectly-plastic domains. This mesh was run on ABAQUS, version 4.5.174, and was used for almost all ζ_0 and material combinations considered, since it was relatively small (645 elements) and efficient to run. (Each iteration required approximately 8 minutes per iteration on a FX-8 Alliant mini-supercomputer running on one computational element. Typical job times were around 100 CPU hours.) If sufficient global convergence or resolution of stresses was not achievable, which often happened due to oscillatory pressure noise, the following alternative model was used.

This FE model used plane-strain 9-node isoparametric elements with selective integration in both domains. Full 3×3 Gaussian integration was performed on the deviatoric stresses along with 2×2 Gaussian integration of the pressure, values of which were interpolated-extrapolated to the 3×3 Gaussian points. This model was analyzed with ABAQUS, version 4.6.160, and reduced the time per iteration to about 4 minutes on the Alliant FX-8 mini-super computer. Use of this model significantly reduced the pressure noise as compared to the hybrid 8-node elements used previously.

Representative Mesh

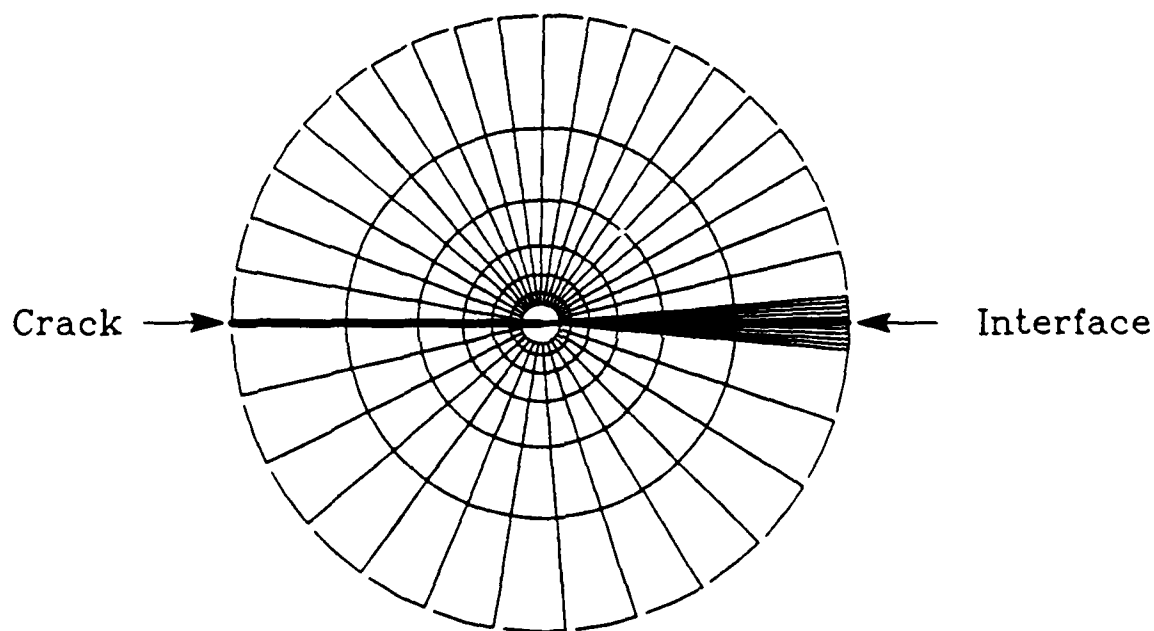


Figure 9.7 Representative finite element crack-tip mesh (excluding actual crack-tip elements), showing circumferential element distribution, crack-face and interface locations, and radial spacings of elements.

Due to the substantial time savings, this model completely replaced the initial model described above.

Procedures

The procedures used in all analyses performed with the boundary layer method were identical. An initial linear run, in terms of constitutive and kinematic theories, was done with the appropriate K_0 applied to determine the reaction force vector F_0^r and to check the assemblage of the model. Comparisons between the numerically obtained J -Integral by the virtual crack extension method (VCEM) and the theoretical value, Eq.(2.16), were made and typically only differed by 0.1%. The actual non-linear analysis used a "STATIC" time procedure with infinitesimal strain theory (HKS, 1987). Loading was accomplished by prescribing "displacements" to the K -term free nodes, in a square root fashion with respect to internal analysis time, to achieve quasi-linear plastic zone growth. The reaction forces from the initial elastic run were imposed as concentrated loads on the T -term free nodes and were scaled using the same amplitude-time function as the K -term displacements. The static parameter CYCLE, which is the maximum number of iterations that can be performed during a time increment before a smaller time increment is tried, was set to 9. This parameter also controls the increase in time increment size by reviewing the number of iterations in the previous two increments necessary to achieve an acceptable solution, and if the number of iterations is less than $([CYCLE/2] - 1)$, the time increment size is increased. An initial suggested time increment size was provided such that at no time during the first increment was the yield condition satisfied anywhere in the mesh. The error tolerance PTOL, which is the maximum acceptable residual nodal force after all element contributions and applied loads are summed up, is set to 1.0×10^{-5} MN. This value of PTOL corresponds to 0.02% of $\sigma_y \cdot l \cdot t$, where l and t are the radial length and thickness of the smallest (radial) element, respectively. The solution procedure iterates until the PTOL condition is satisfied throughout the mesh, cutting back the time increment

size as necessary. Loading was done until the plastic zone nearly touched the FE mesh boundary.

3.3.2 Traction-Free Crack-Tips: Existence of Stress Oscillations Within The Plastic Zone

This section describes the FE model used to investigate the extent of stress oscillations occurring within the plastic zone of a traction-free crack tip. It was assumed that the lower region was rigid ($\mu_2 = \infty$), and that the upper material had the elastic properties of aluminum [$\mu = 26.1$ MPa and $\nu = .342$ (Hertzberg, 1976)] with a yield strength of 32.5 MPa. This results in a bi-material constant of $\epsilon = 0.07796$. Based upon this value of ϵ , a mesh spanning 36 decades in the radial direction would be required to achieve one complete period of elastic stress oscillation. It was felt that plastic deformation extending one-quarter of the elastic period would be sufficient to determine the extent, if any, of plastic stress oscillations. Therefore, mesh spanning 12 decades, which allowed for 3 decades of elastic material outside the plastic zone, was utilized.

Since this model considered the bottom medium to be rigid, only the upper region needed to be modeled. To simulate the rigid lower region, all nodes along the intact interface were pinned. The mesh has 25 elements spanning the circumferential direction, with the same distribution as shown in *Figure 3.7*. Because of the appreciable radial extent of this mesh, only three logarithmically spaced, 9-node selectively reduced elements spanned each of its twelve concentric rings. Crack-tip element geometry, identical to that described previously, was used at the crack-tip. To avoid numerical solver problems associated with large differences in element stiffnesses, the boundary layer method was not employed. Instead, displacements consistent with the dominant asymptotic **K**-field were imposed along the Γ_∞ boundary. The Γ_∞ boundary itself was located at $r = 1.0 \times 10^5$ m. All nodes along this boundary were constrained via a user written MPC to prescribe the nodal displacements.

The procedural aspects of this model were basically the same as before. Again, the elastic/perfectly-plastic material behavior was incorporated with the same UMAT.

The error tolerance **PTOL** used for this analysis was set to 5.0×10^{-8} MN and was 0.7% of $\sigma_{ys} \cdot l \cdot t$. The value of **CYCLE** was varied between 7 and 9, depending upon the progress of the analysis. Loading was applied by scaling the displacement of the **K**-field node in a square root fashion with respect to internal analysis time, to achieve quasi-linear plastic zone growth. The $\angle K$ prescribed was chosen to be $\angle K = 35.0^\circ$. This was necessary to keep the value of ζ_0 within the valid domain during loading; i.e., ζ_0 always satisfied the no crack-face contact conditions predicted by Eq.(P2.33).

3.3.3 Closed Crack-Tip Faces

The FE model used to investigate the crack-tip fields around the closed crack tip utilized many of the same features as the previous FE model. The subroutines UMAT and MPC were included in the analysis. The material in the lower region was assumed to be rigid ($\mu_2 = \infty$), thus only the upper crack-tip region was modeled. The actual mesh used 25 9-node isoparametric elements in the circumferential direction. Radially, the mesh had four concentric rings with five logarithmically spaced elements per each of its four rings. Again, the outer boundary of the mesh was set at $r = 1.0$ m. Since the lower half was rigid, the edge of the mesh corresponding to the intact interface was clamped. Along the crack face, interface elements were attached, thus allowing for possible gap formation. The nodes along the outer edge of the mesh were constrained in accordance with Eqs.(3.2) and (3.3) by a closed crack-tip user-written MPC. Loading was accomplished by prescribing the displacement to the K_{II} -term node in a square root fashion with respect to internal analysis time. The FE model was loaded until the maximum extent of the plastic zone reached $r = 0.1$ m. Since the "STATIC" analysis procedure was used, the **CYCLE** parameter was set to 9, and the error tolerance parameter **PTOL** was set to 1.0×10^{-6} MN (0.02% of $\sigma_{ys} \cdot l \cdot t$).

Chapter 4

Elastic-Plastic Interfacial Crack-Tip Fields

In this chapter the results obtained from the various numerical crack-tip calculations for the BV problem stated in Chapter 1 will be described. The behavior of each crack-tip model will be outlined along with the assumed material idealizations. In order to organize the vast quantity of numerically obtained information into a more manageable format, explicit representation forms will be used which reconstruct all or portions of the actual solution in terms of only a few variables. The characteristics and notation of the representative forms will be introduced and discussed. The local crack-tip fields for all the various material combinations and loadings will be presented via these representative forms and in terms of the dimensional framework outlined in Chapter 2. "Geographical" inner bounds of inelastic crack-tip fields are established from evaluating limitations imposed by the underlying mathematical assumptions.

4.1 Asymptotic Crack-Tip Forms

The purpose of this section is to present the anticipated asymptotic crack-tip forms by reviewing in detail those forms obtained for the cases of a homogeneous stationary crack and for homogeneous quasi-static crack growth. This review is focused solely upon isotropic elastic/perfectly-plastic media whose yield criteria are described by the Mises yield condition. In general, the only restriction placed on the value of the Poisson's

ratio is that it must be positive ($0 < \nu \leq 0.5$). Anticipated differences between the homogeneous and bi-material behavior of the crack-tip forms is discussed along with the conditions necessary to properly assemble these forms into the complete crack-tip fields. Finally, because slip-line theory is used extensively to describe various deforming portions of the crack-tip regions, a brief review of slip-line notation is made.

4.1.1 Summary of Slip-Line Theory

To familiarize the reader with slip-line theory and to assign notation, a short summary follows. The reader is referred to Hill (1983) and Kachanov (1974) for a more complete description and comprehensive derivation.

For a plane-strain rigid/perfectly-plastic material state, two families of curves, referred to as α -lines and β -lines, uniquely describe the material stress state and are derived from equilibrium arguments and the yield criterion. (Slip-line theory is loosely analogous to stream functions used to describe inviscid flow in fluid dynamics.) Along an α -line

$$p + 2k\phi = C_\alpha, \quad (4.1)$$

while along a β -line

$$p - 2k\phi = C_\beta. \quad (4.2)$$

Here p is the mean pressure [$p = -(1/3)\text{tr}(\sigma)$], k the material yield strength in shear ($k = \sigma_{ys}/\sqrt{3}$), ϕ is the angle measured from the positive x-axis to the α -line in an anti-clockwise direction, and C_α and C_β are constants associated with each α -line and β -line, respectively. The stress components are obtained by considering the angle ϕ of the α -line or β -line at the material point of interest and are given by Hill (1983) as

$$\sigma_{xx} = -p - k \sin 2\phi, \quad (4.3)$$

$$\sigma_{yy} = -p + k \sin 2\phi, \quad (4.4)$$

and

$$\sigma_{xy} = k \cos 2\phi. \quad (4.5)$$

The value of p is determined from Eqs.(4.1) and (4.2) and by the slip-line constants, C_α and C_β . Once the constants C_α and C_β along an α - and a β -line are determined at some point, usually via boundary conditions, the complete stress state within the slip-line field can be evaluated. *Figure 4.1* shows a representative element with respect to a family of slip lines along with the associated stress state. Although slip-line theory does not completely describe the strain state in a body, it does describe certain features of the deformation. The α and β characteristic slip-lines are orientated parallel to the direction of maximum shear stress, and they represent directions of zero extension. (i.e., no normal strain is produced in directions parallel to slip lines.

Rigid-plastic slip-line theory is often used to describe elastic/perfectly-plastic materials capable of compressible elastic deformation ($\nu \neq 0.5$) and incompressible plastic deformation. To use rigid-plastic slip-line fields for these materials, it is assumed that the effect of elastic strains are negligible. This assumption is only valid in the asymptotic sense that

$$\dot{\underline{\epsilon}}^P = \left\{ \lim_{t^P \rightarrow \infty} \dot{\underline{\epsilon}}^T \right\}, \quad (4.6)$$

where $\dot{\underline{\epsilon}}^T$ is the total strain rate, and $\underline{\epsilon}^P$ and $\dot{\underline{\epsilon}}^P$ are the total plastic strain and strain rate components, respectively. In general, the use of slip-line theory and accompanying representative forms for elastically compressible materials does not necessitate that the elastic strain components are zero.

4.1.2 Stationary and Quasi-Static Crack-Tip Forms

The admissible plane-strain asymptotic crack-tip fields have been reviewed extensively for stationary and quasi-static homogeneous cracks in isotropic elastic/perfectly-plastic media; e.g., Rice (1982), Rice, Drugan, and Sham (1980), Rice and Tracey (1973), and Nemat-Nasser and Obata (1984). For a stationary crack with $\nu = 0.5$, Nemat-Nasser and Obata identified that three distinct crack-tip sectors may exist; namely an elastic

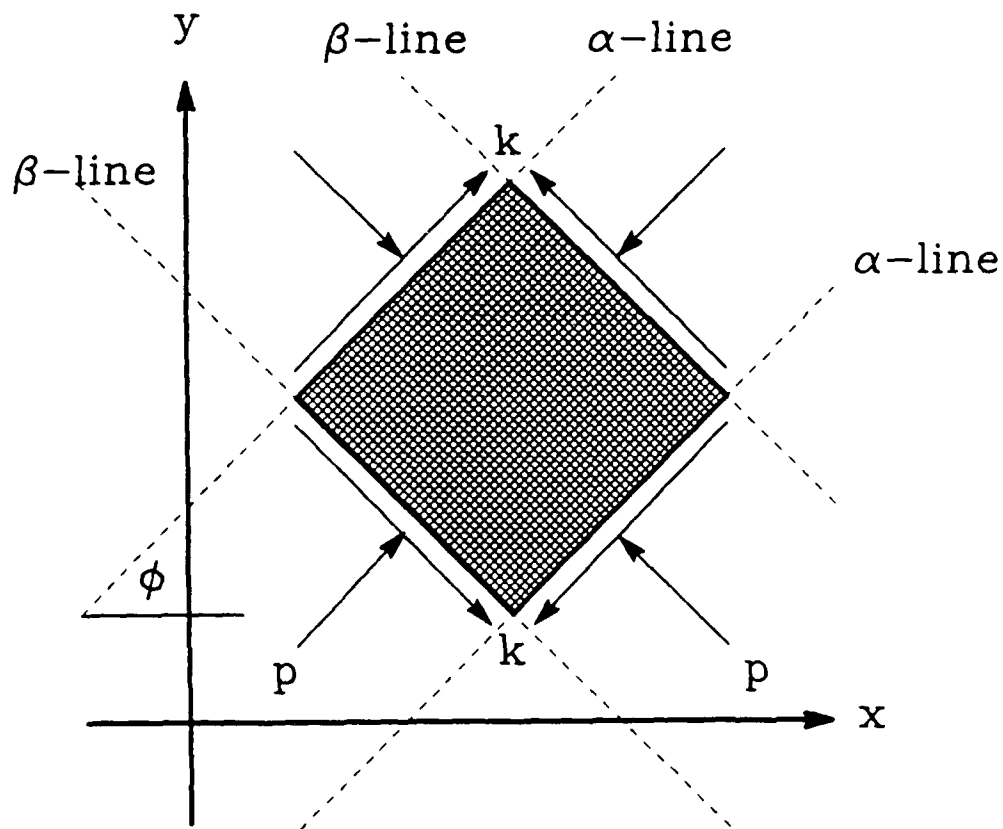


Figure 4.1 Schematic slip-line field element, showing the normal pressure (P) and shear (k) stress states, the orientation of α - and β - lines and the inclination angle ϕ with respect to the coordinates.

sector, a yielding constant state sector, and a yielding centered fan sector. (Nemat-Nasser and Obata showed all the admissible combinations of these sectors, but their asymptotic analysis does not determine which assemblage is appropriate for a specific problem.) An elastic sector which has not experienced any prior plastic deformation is representable by a planar elastic wedge with constant, but not necessarily identical, tractions on each of its sides. To produce finite stresses at the crack-tip and to eliminate any net crack-tip forces, the angular function associated with the singular radial stress component is taken to be zero; i.e., $\sigma_{rr}(r, \theta) = P(\theta) + Q(\theta)/r \Rightarrow Q(\theta) = 0$. Appendix B contains the Airy stress potential and stress distribution for such a wedge. The yielding sectors, formally identified by Rice and Tracey (1973), are obtained from the equilibrium equations and the yield criterion. The stress distribution in the constant state is characterized as having stress components σ_{xx} , σ_{yy} , and σ_{xy} constant everywhere in the sector such that the yield criterion is satisfied. Generally, in constant state regions $\sigma_{\theta\theta}(r, \theta) \neq \sigma_{rr}(r, \theta)$. In centered fan sectors, however, the stress distribution is $\sigma_{rr}(r, \theta) = \sigma_{\theta\theta}(r, \theta)$ and $\sigma_{r\theta} = \text{constant}$, where in the absence of the other deviatoric stress components, $\sigma_{r\theta}$ alone satisfies the yield criterion. When elastic strains are negligible compared to plastic strains or when $\nu = 0.5$, the stress distribution in a centered fan is given by $\sigma_{r\theta} = \pm k$, and $\sigma_{rr}(r, \theta) = \sigma_{\theta\theta}(r, \theta) = (A - 2\phi/\sqrt{3})\sigma_{y0}$, where A is a constant. In terms of rigid-plastic slip-line theory (Hill, 1983), a centered fan is a sector where α -lines emanate radially from the crack tip with circular and concentric β -line arcs (or vice versa), while in constant state sectors the α - and β -lines are straight and normal to each other. Thus in a fan region $\phi = \theta + b$, where b is a constant.

Rice (1982) summarizes the asymptotic distribution of velocities and strain rates for quasi-static crack growth in each of the three previously identified sectors. By setting the crack-tip velocity equal to zero, the predominant behavior of each sector is obtained for the stationary case. Excluding rigid rotations, the non-zero velocity components in a stationary centered fan are

$$V_r = \frac{\partial f(\theta, t)}{\partial \theta} \quad (4.7)$$

and

$$V_\theta = -f(\theta, t), \quad (4.8)$$

and the only non-zero strain rate component is

$$\dot{\epsilon}_{r\theta} = \frac{1}{2r} \left(\frac{\partial^2 f(\theta, t)}{\partial^2 \theta} + f(\theta, t) \right). \quad (4.9)$$

Here V_r and V_θ are the radial and hoop velocity components, respectively, t is time, and $f(\theta, t)$ is a function whose form cannot be determined from an asymptotic analysis. Integration of the strain rates over a finite period of time produces finite strain for all strain components except for the $\epsilon_{r\theta}$ component. Integration of Eq.(4.9) with respect to time yields

$$\epsilon_{r\theta}(\theta, r) = \frac{\gamma_{r\theta}(r, \theta)}{2} = \frac{1}{2} A(\theta, t) \frac{\gamma_0}{R} + C_1(\theta). \quad (4.10)$$

In this equation, $A(\theta, t)$ is defined such that $\partial A(\theta, t)/\partial t = [(\partial^2 f(\theta, t)/\partial^2 \theta) + f(\theta, t)]$ and represents the unknown angular distribution of shear strain, while γ_0 is the shear yield strain of the material, $C_1(\theta)$ is a bounded constant of integration usually taken to be equal to zero, and $R \equiv r/r_p$, where r_p is the characteristic plastic zone dimension and r is the radial distance from the crack tip. In a centered fan $\epsilon_{r\theta} \propto 1/r$ as $r \rightarrow 0$. At the plastic zone boundary, $R = 1$, the shear strain must be approximately equal to γ_0 , thus $A(\theta, t)$ is of order unity.

The non-singular yielding constant state sector behaves in a significantly different manner. It is best described in an auxiliary (m, n) coordinate system whose axes are chosen to lie parallel to the α - and β - lines and whose origin is at the crack tip. The x and y components of the (x, y) coordinate frame, shown in *Figure 4.1*, are related to the components in the $m - n$ coordinate frame by

$$x = m \cos \phi - n \sin \phi \quad (4.11)$$

and

$$y = m \sin \phi + n \cos \phi. \quad (4.12)$$

As $r \rightarrow 0$, the constant state velocity components in the m and n directions are given by

$$V_m = g(n) \quad (4.13)$$

and

$$V_n = h(m), \quad (4.14)$$

respectively. Here $g(n)$ and $h(m)$ are functions whose precise forms cannot be determined from an asymptotic analysis. In a constant state region, the only non-zero strain component as $r \rightarrow 0$ is $\dot{\epsilon}_{mn}$, and it is related to the velocity field via

$$\dot{\epsilon}_{mn} = \frac{1}{2} \left(\frac{\partial g(n)}{\partial n} + \frac{\partial h(m)}{\partial m} \right). \quad (4.15)$$

Integration of the strain rates over a discrete time interval produces finite strains for all components. Plane-strain conditions require that $\epsilon_{ss} = 0$, but for elastically compressible materials (those with $\nu \neq 0.5$) a transient period exists for which $\epsilon_{ss}^{Plastic} \neq 0$. During this transient period finite plastic strains accumulate, and therefore in a constant state region it is generally expected that $\epsilon_{ss}^{Plastic} \neq 0$.

The strain rates in an isotropic elastic sector are obtainable from the elastic wedge potential, given in Appendix B, by interpreting the boundary tractions H , T , Q , and K as applied traction rates; i.e., \dot{H} , \dot{T} , \dot{Q} , and \dot{K} . From Eqs.(B.9) to (B.11) and by use of the elasticity tensor \mathcal{L} defined in Eq.(3.17), the non-zero strain rate components for an isotropic elastic wedge are

$$\begin{aligned} \dot{\epsilon}_{rr} = & \left(\frac{1-\nu^2}{E} \right) \{ \dot{K} - 2\dot{T}\gamma - 2\dot{a}_2(\cos 2\gamma + 1) - 2\dot{c}_2(\sin 2\gamma + 2\gamma) \} \\ & - \left(\frac{\nu(1+\nu)}{E} \right) \{ \dot{K} - 2\dot{T}\gamma + 2\dot{a}_2(\cos 2\gamma - 1) + 2\dot{c}_2(\sin 2\gamma - 2\gamma) \}, \end{aligned} \quad (4.16)$$

$$\begin{aligned} \dot{\epsilon}_{\theta\theta} = & \left(\frac{1-\nu^2}{E} \right) \{ \dot{K} - 2\dot{T}\gamma + 2\dot{a}_2(\cos 2\gamma - 1) + 2\dot{c}_2(\sin 2\gamma - 2\gamma) \} \\ & - \left(\frac{\nu(1+\nu)}{E} \right) \{ \dot{K} - 2\dot{T}\gamma - 2\dot{a}_2(\cos 2\gamma + 1) - 2\dot{c}_2(\sin 2\gamma + 2\gamma) \}, \end{aligned} \quad (4.17)$$

and

$$\dot{\epsilon}_{r\theta} = \left(\frac{2(1+\nu)}{E} \right) \{ 2\dot{c}_2(\cos 2\gamma - 1) - 2\dot{a}_2 \sin 2\gamma \}. \quad (4.18)$$

In these expressions the coefficients \dot{a}_2 and \dot{c}_2 are given by Eqs.(B.7) and (B.8) when H , T , Q , and K are interpreted as \dot{H} , \dot{T} , \dot{Q} , and \dot{K} . Integration of the strain rates, Eqs.(4.16) to (4.18), over a finite time interval produces finite strains in elastic sectors.

Having identified the three basic admissible sectors, asymptotic crack-tip behavior is obtainable by assembling a combination of these sectors in a manner consistent with the far-field conditions. Rice (1982) states that the necessary requirements for assembling these sectors are that " $\sigma_{r\theta}$, $\sigma_{\theta\theta}$, and u_θ must be continuous along radial lines emanating from the crack tip and that any discontinuities in yielding sectors must be consistent with the flow rule." An additional constraint, given by Kachanov (1974), is that "the [energy] dissipation be positive everywhere in the slip-line field."

Before proceeding, several additional observations regarding the behavior and assemblage of the sectors should be made. In yielding regions with incompressible plasticity where the plastic strains are large compared to the elastic strains, the "apparent" Poisson's ratio is $\nu_a \approx 0.5$; i.e., $(1/3)\text{tr}(\sigma) \approx (\sigma_{rr} + \sigma_{\theta\theta})/2$. In general, fan sectors have large plastic strains as $r \rightarrow 0$ ($\epsilon_{r\theta} \propto 1/r$); therefore in a fan region the apparent Poisson's ratio is $\nu_a \approx 0.5$, and $\sigma_{r\theta} \approx \pm k$. Compressible elastic sectors in which there are no residual strains cannot be adjacent to fan sectors (when, at the border, $A(\theta, t) \neq 0$ in the fan region). If $\sigma_{r\theta}$ is equal to $\pm k$ at the elastic sector boundary, the requirement of continuous $\sigma_{\theta\theta}$ produces an Mises equivalent stress greater than the yield stress in the elastic sector. This is true even if a jump in σ_{rr} is allowed between the fan and elastic sector. In general, it is necessary to have a constant state sector between an elastic sector (with no residual strains) and a fan, and the apparent Poisson's ratio across this constant state varies from $\nu_a \neq 0.5$ on the elastic boundary, where plastic strains are negligible, to $\nu_a = 0.5$ on the fan border, where plastic strains dominate.

To verify that an elastic sector with no residual strains and $\nu \neq 0.5$ cannot exist next to a fan which has an apparent Poisson's ratio of $\nu_a \approx 0.5$, consider the following

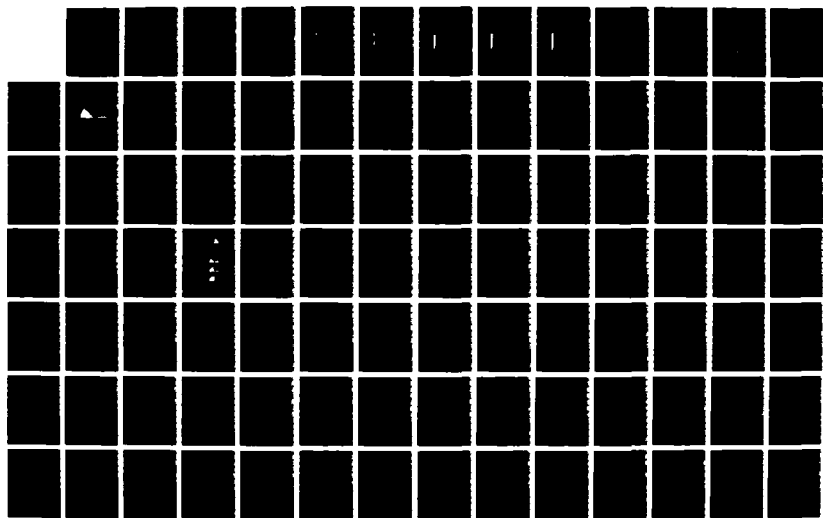
70-4130 P46

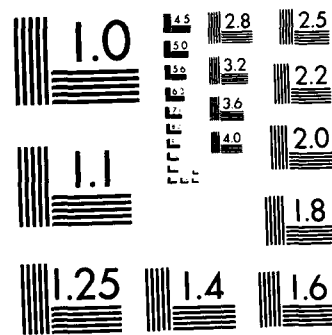
ENGINEERING INTERFACES IN METAL MATRIX COMPOSITES
(VOLUME 3)(U) MASSACHUSETTS INST OF TECH CAMBRIDGE
J A CORNIE 10 JUN 88 N00014-84-K-0493

473

UNCLASSIFIED

F/G 11/6.1 ML





argument. Evaluate the Mises equivalent stress in the elastic sector at the postulated elastic-fan border. At such a point σ_{rr} must be equal to $\pm k$. Substituting this value into the expression for the Mises equivalent stress, Eq.(2.31), yields

$$\bar{\sigma}^2 = (\sigma_{rr}^2 + \sigma_{\theta\theta}^2)D + (\sigma_{rr}\sigma_{\theta\theta})F + \sigma_{y_0}^2, \quad (4.19)$$

where $D(\nu)$ and $F(\nu)$ are given in Eqs.(2.32) and (2.33), respectively. For $\bar{\sigma} \leq \sigma_{y_0}$ (for $\sigma_{\theta\theta} \neq 0$),

$$\left(\frac{\sigma_{rr}}{\sigma_{\theta\theta}}\right)^2 + \frac{F}{D} \left(\frac{\sigma_{rr}}{\sigma_{\theta\theta}}\right) + 1 \leq 0. \quad (4.20)$$

For positive values of ν , the ratio F/D varies from -1 to -2, and the condition required by Eq.(4.20) has real solutions only when $F/D = -2$ ($\nu = 1/2$) and $\sigma_{rr} = \sigma_{\theta\theta}$.

Prior to discussing the bi-material asymptotic crack-tip fields, it is useful to examine several additional features present in the homogeneous analysis. For a stationary homogeneous plane-strain crack subjected to tensile opening loads (mode I), the crack-tip field is that of the classic Prandtl distribution (Hill, 1983). In the Prandtl field, all crack-tip material points are in either yielding constant states or centered fan regions and remain in their respective sectors during the entire loading history. Additionally, the Prandtl stress distribution is independent of the far-field load magnitude as long as SSY conditions exist, although the actual extent of the distribution is dependent on the load magnitude. In the growing quasi-static (opening) case, the crack-tip distribution remains constant with respect to the moving crack tip; however, any material point which does not lie in the plane of the advancing crack front accumulates strains in each of the four quasi-static crack-tip regions (Rice, 1982). Therefore, it is necessary to account for these accumulated residual strains when assembling the crack-tip fields from an instantaneous stress distribution. In general the instantaneous stress distribution of a plane-strain elastic sector with fixed tractions is different for regions which do or do not have out-of-plane residual strains. (In plane strain the out-of-plane stress must account for any residual out-of-plane strains.)

It is anticipated that the major difference between the homogeneous and traction-free bi-material crack-tip fields will result from the continuous shift, in plastic zone

shape and tractions along the plastic zone boundary, which arises with increasing load. The shift between solutions should occur in a continuous fashion with respect to ζ_0 , in a manner analogous to the continuous shift observed in homogeneous crack-tip fields by Shih (1974) for mixed-mode loading between pure mode I and mode II. A continuous evolution with increasing applied load has the potential to alter residual strains and thereby significantly influence stresses in elastic sectors. Also, such continuous evolution may produce oscillatory plastic bi-material crack-tip fields, as observed by Shih and Asaro (1987) for nonlinear elastic strain hardening bi-material interfacial cracks.

Thus far, discussion has been limited to asymptotic forms which are typically interpreted as occurring "at" the crack tip. This interpretation is only a first order approximation and does not address the possibility that away from the crack tip a cusp may form between different sectors. Although such cusps are not found in stationary homogeneous crack solutions, recent work by Narasimhan, Rosakis, and Hall (1987) indicates that a cusp forms ahead of a growing plane-stress homogeneous crack tip, and that the boundary of the cusp separates the regions in which the equations of stress are hyperbolic and elliptic, respectively.

4.2 Traction-Free Crack-Tip Model

The numerical results for the traction-free crack-tip model will be presented in this section, and in conjunction with the previously identified asymptotic forms, approximate local crack-tip fields will be assembled. Discussion will be initially focused on the "high resolution," quarter wave-length model so that the transitional period of plastic flow can be quantified from the elastic-plastic boundary towards the crack-tip to the establishment of a "steady-state," and so that the extent of oscillatory behavior, if any, can be identified. Interfacial tractions and strain distributions will be tracked as a function of ζ_0 , as well as the finite crack tip opening displacement, δ_{CTOD} . A general elastic potential which describes the lower elastic domain will be identified, although not directly from the quarter wave-length model. All results will be analyzed at an

instantaneously fixed value of ζ_0 . In general, steady state and transitional behavior shall refer to spatial and not chronological (analysis or loading time) behavior.

4.2.1 Deformable Upper Half-Plane

Asymptotic Crack-Tip Behavior

The behavior within the deforming bi-material crack-tip zone is similar to that found in homogeneous crack-tip plastic zones. *Figures 4.2 to 4.6* show the location of yielding integration points ($\bar{\sigma} \geq 0.99\sigma_{ys}$), as a function of angle θ from the interface and normalized radial distance $R \equiv r/r_p$ from the crack tip, at several values of ζ_0 between 1.34° and 30.04° for $\epsilon = 0.07796$ and $\nu = 0.342$. In these figures, the location of integration points whose stress state is that of a fan sector, namely $|\sigma_{r\theta}| \geq 0.99k$ and $|(\sigma_{\theta\theta} - \sigma_{rr})/\sigma_{ys}| < 0.02$, are identified by + marks. The fan region dominates the yielding crack-tip fields at small values of R , and *once a fan has developed, the stresses along a ray are independent of radial distance*. Radially as $R \rightarrow 0$, oscillatory stress fields do not exist after a fan sector develops. As is common in the homogeneous fields, a transitional layer exists between the plastic zone boundary and the steady-state fan region. *Figure 4.7* shows the development of stress as a function of R at $\theta = 3.1^\circ$ from the elastic region ($R > 1$) to deep within the plastic zone ($R \ll 1$) for $\zeta_0 = 30.04^\circ$. As seen from *Figures 4.2 to 4.6* and *4.7*, the establishment of a fan usually occurs only deep within the plastic zone at radial distances smaller than approximately 1% to 5% of the *actual plastic zone radius at that angular location*. The behavior of the inelastic transition region between the plastic zone boundary and the establishment of fans or "steady-state" constant state sectors is similar to that of a constant state region, however in such transition regions the associated α - and β - lines have a large but finite radius of curvature. Henceforth, regions where the curvature of α - and β -lines is very small with respect to unity shall be identified as "quasi-constant state regions."

All features seen in the bi-material fields are not present in the homogeneous asymptotic fields. A large elastic sector exists from the crack face ($\theta = 180^\circ$) to $\theta \approx 135^\circ$ for

Bi-material Crack Tip Plastic Zone $\epsilon=0.07796$

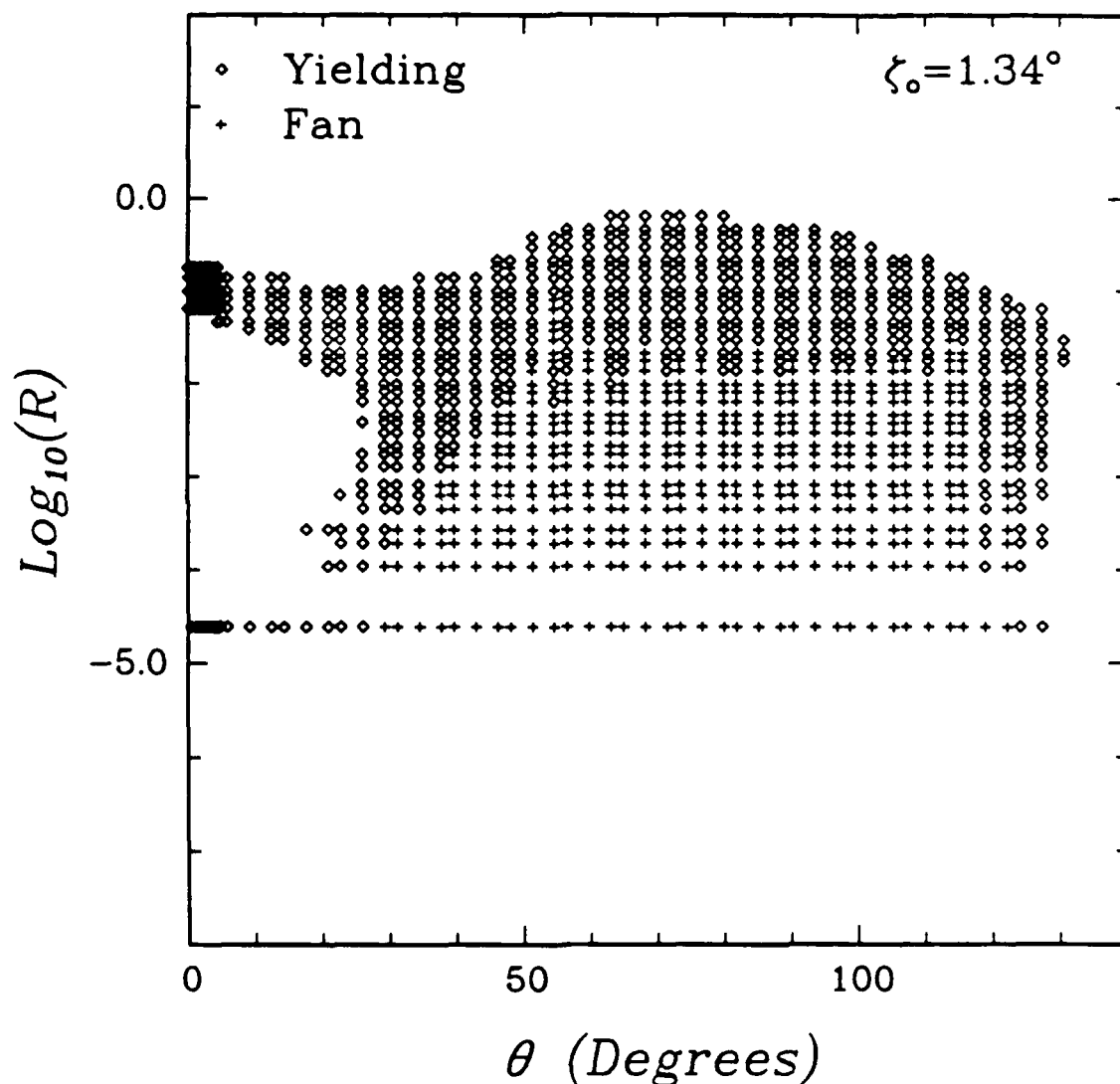


Figure 4.2 Locations of actively yielding ($\bar{\sigma} > 0.99\sigma_{ys}$) integration points around a traction-free bi-material crack-tip for $\epsilon = 0.07796$ and $\zeta_0 = 1.34^\circ$; elastic/perfectly-plastic material bonded to a rigid substrate. Locations indicative of a fan stress state ($|\sigma_{r\theta}| \geq 0.99k$ and $|(\sigma_{\theta\theta} - \sigma_{rr})/\sigma_{ys}| < 0.02$) are shown by a "+".

Bi-material Crack Tip Plastic Zone $\epsilon=0.07796$

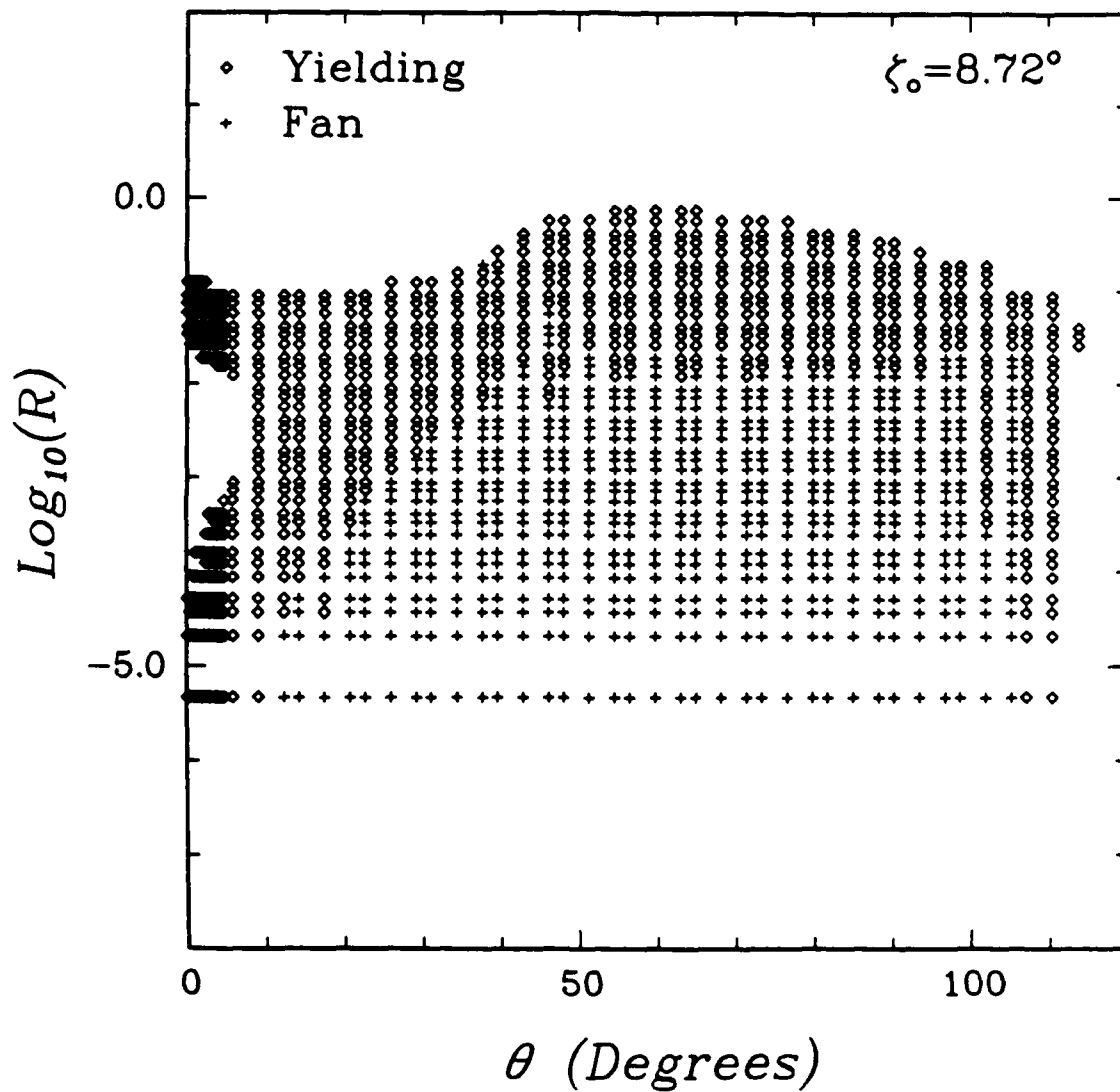


Figure 4.9 Locations of actively yielding ($\bar{\sigma} > 0.99\sigma_{ys}$) integration points around a traction-free bi-material crack-tip for $\epsilon = 0.07796$ and $\zeta_0 = 8.72^\circ$; elastic/perfectly-plastic material bonded to a rigid substrate. Locations indicative of a fan stress state ($|\sigma_{\theta\theta}| \geq 0.99k$ and $|(\sigma_{\theta\theta} - \sigma_{rr})/\sigma_{ys}| < 0.02$) are shown by a "+".

Bi-material Crack Tip Plastic Zone $\epsilon=0.07796$

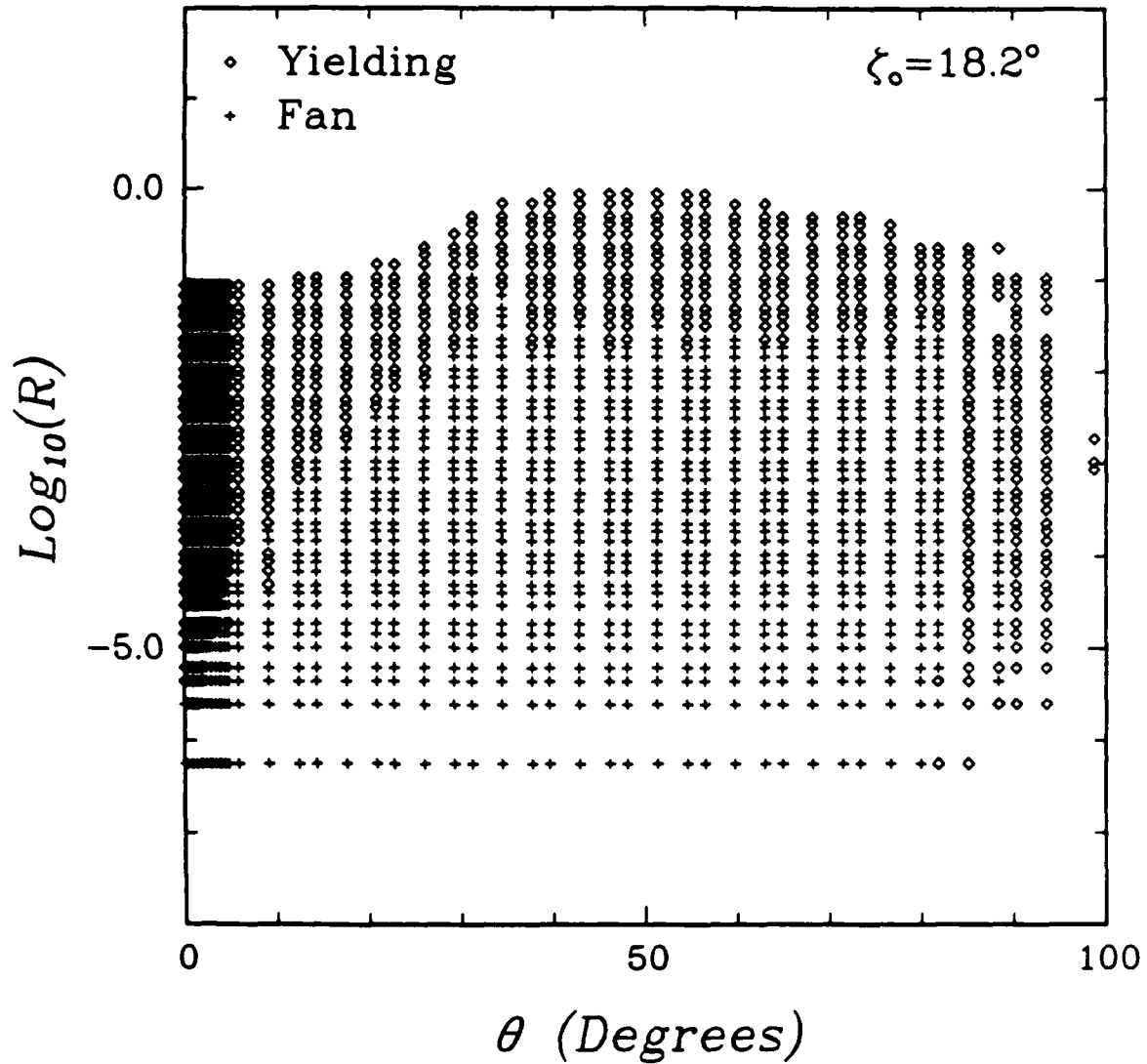


Figure 4.4 Locations of actively yielding ($\bar{\sigma} > 0.99\sigma_{ys}$) integration points around a traction-free bi-material crack-tip for $\epsilon = 0.07796$ and $\zeta_0 = 18.2^\circ$; elastic/perfectly-plastic material bonded to a rigid substrate. Locations indicative of a fan stress state ($|\sigma_{r\theta}| \geq 0.99k$ and $|(\sigma_{\theta\theta} - \sigma_{rr})/\sigma_{ys}| < 0.02$) are shown by a "+".

Bi-material Crack Tip Plastic Zone $\epsilon=0.07796$

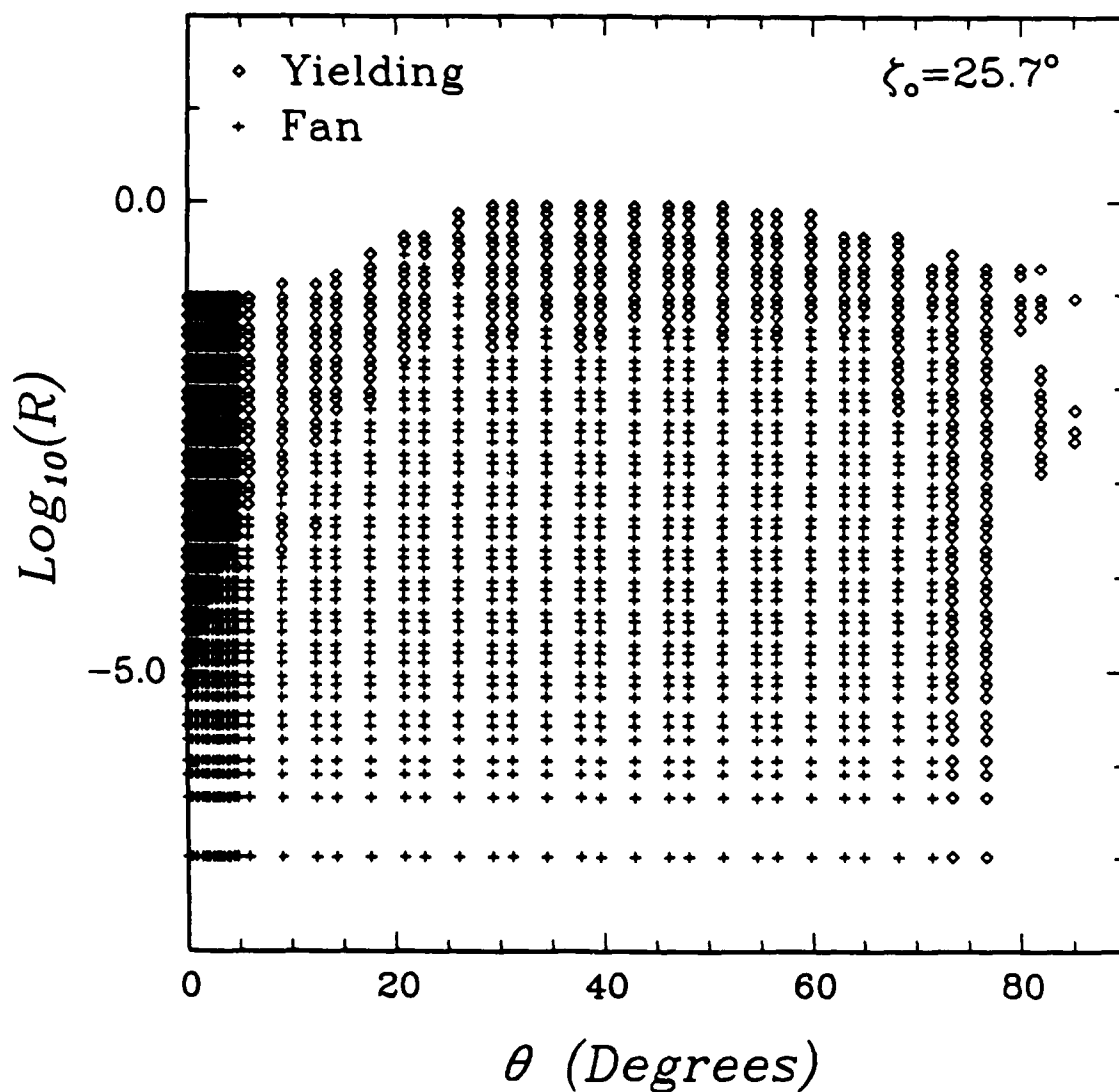


Figure 4.5 Locations of actively yielding ($\bar{\sigma} > 0.99\sigma_{ys}$) integration points around a traction-free bi-material crack-tip for $\epsilon = 0.07796$ and $\zeta_0 = 25.7^\circ$; elastic/perfectly-plastic material bonded to a rigid substrate. Locations indicative of a fan stress state ($|\sigma_{r\theta}| \geq 0.99k$ and $|(\sigma_{\theta\theta} - \sigma_{rr})/\sigma_{ys}| < 0.02$) are shown by a "+".

Bi-material Crack Tip Plastic Zone $\epsilon=0.07796$

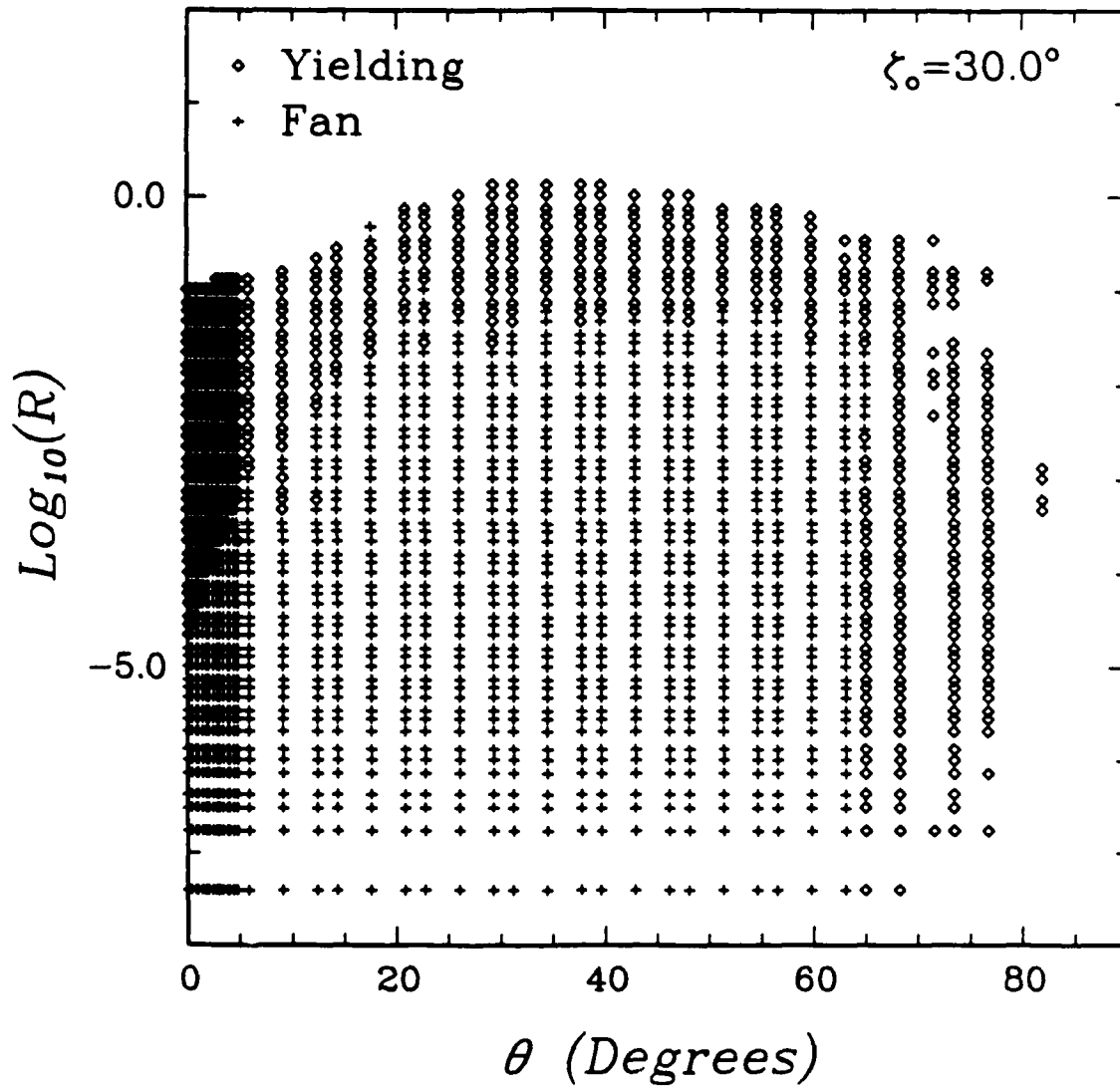


Figure 4.6 Locations of actively yielding ($\bar{\sigma} > 0.99\sigma_{ys}$) integration points around a traction-free bi-material crack-tip for $\epsilon = 0.07796$ and $\zeta_0 = 30.0^\circ$; elastic/perfectly-plastic material bonded to a rigid substrate. Locations indicative of a fan stress state ($|\sigma_{\theta\theta}| \geq 0.99k$ and $|(\sigma_{\theta\theta} - \sigma_{rr})/\sigma_{ys}| < 0.02$) are shown by a "+".

Bi-material Crack-Tip Stresses $\zeta_0 = 30.0^\circ$ $\epsilon = 0.07796$

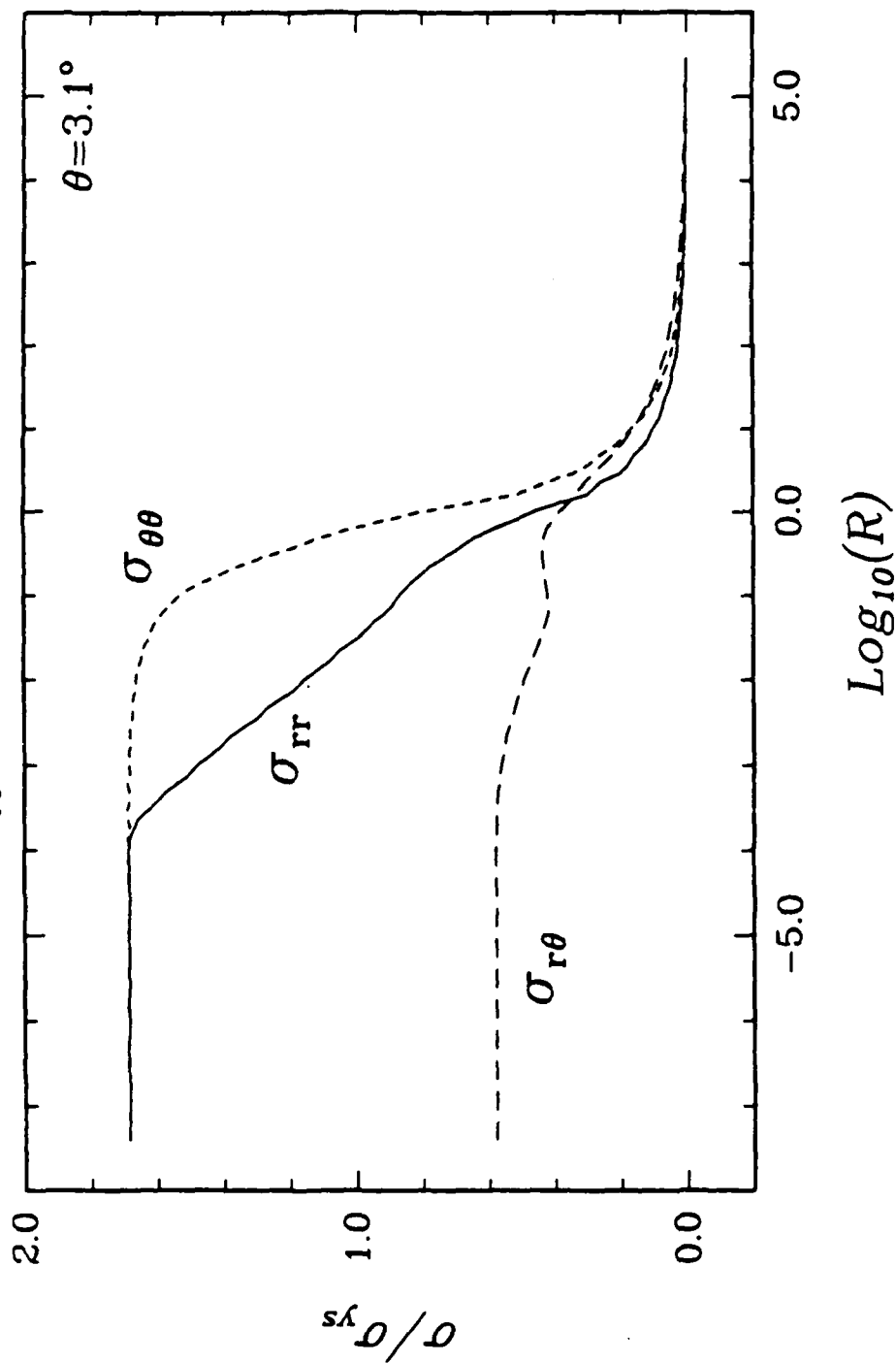


Figure 4.7 Radial variation of normalized stress components for a traction-free bi-material crack-tip (elastic/perfectly-plastic material atop a rigid substrate) under SSY conditions at $\theta = 3.1^\circ$; $\epsilon = 0.07796$ and $\zeta_0 = 30.0^\circ$.

$\zeta_0 = 1.34^\circ$ and to $\theta \approx 73^\circ$ for $\zeta_0 = 30.0^\circ$. Such elastic sectors are not observed in stationary homogeneous crack fields nor are they predicted from the elastically-calculated plastic zone boundary derived in Section 2.2.1. The location of actively yielding integration points and the corresponding elastically-calculated plastic zone shape [from Eq.(P2.6)] for $\epsilon = 0.07796$ ($\nu = 0.342$) at $\zeta_0 = 1.34^\circ$ and $\zeta_0 = 30.0^\circ$ are plotted in *Figures 4.8* and *4.9*, respectively. (Due to the presence of the crack-face elastic sector, the plastic zone shape predicted by the elastic approximation when $\zeta_0 \geq 0$ is less representative of the actual zone shape, especially near the crack-face region.) Recall that for $\epsilon > 0$, ζ_0 increases at fixed $\angle K$ when $\|K\|$ increases. At material points in the crack-face elastic sector which are very near the crack tip, prior plastic deformation would produce residual strains. At radial distances far from the crack tip relative to the characteristic plastic zone size, no residual plastic strains accumulate in the crack-face elastic wedge. Furthermore, an unloaded elastic sector exists along the interface spanning a maximum of about 22° for $\zeta_0 = 1.34^\circ$ and approximately 8° for $\zeta_0 = 8.72^\circ$. The interfacial elastic sector is small and barely visible in *Figure 4.8*, but is more easily seen in *Figures 4.2* and *4.3*. (Again, this feature is not predicted by the elastically-calculated plastic zone; however, for $\zeta_0 \approx 0$, the approximated plastic zone does have a local minimum or rounded "kink" in its shape near $\theta \approx 30^\circ$, and this rounded kink may be related to the development of the interfacial elastic wedge.) Active plasticity exists both radially ahead and behind this elastic sector, indicating that the material points within this elastic region once reached yield, deformed plastically, unloaded to an elastic state, and will again yield and deform plastically.

The presence of a cusp in the crack-tip field is another feature of the bi-material fields which is not observed in the stationary homogeneous asymptotic fields. At small to modest angles from the interface, the length of the transition region from the elastic-plastic boundary to the fan region increases with decreasing θ , producing a cusp in the slip-line field. The cusp itself is not a characteristic slip-line, but merely a boundary line separating two regions. The characteristic α - and β - lines appear continuous and

Bi-material Plastic Zone

$$\zeta_0 = 1.34^\circ \quad \epsilon = 0.07796$$

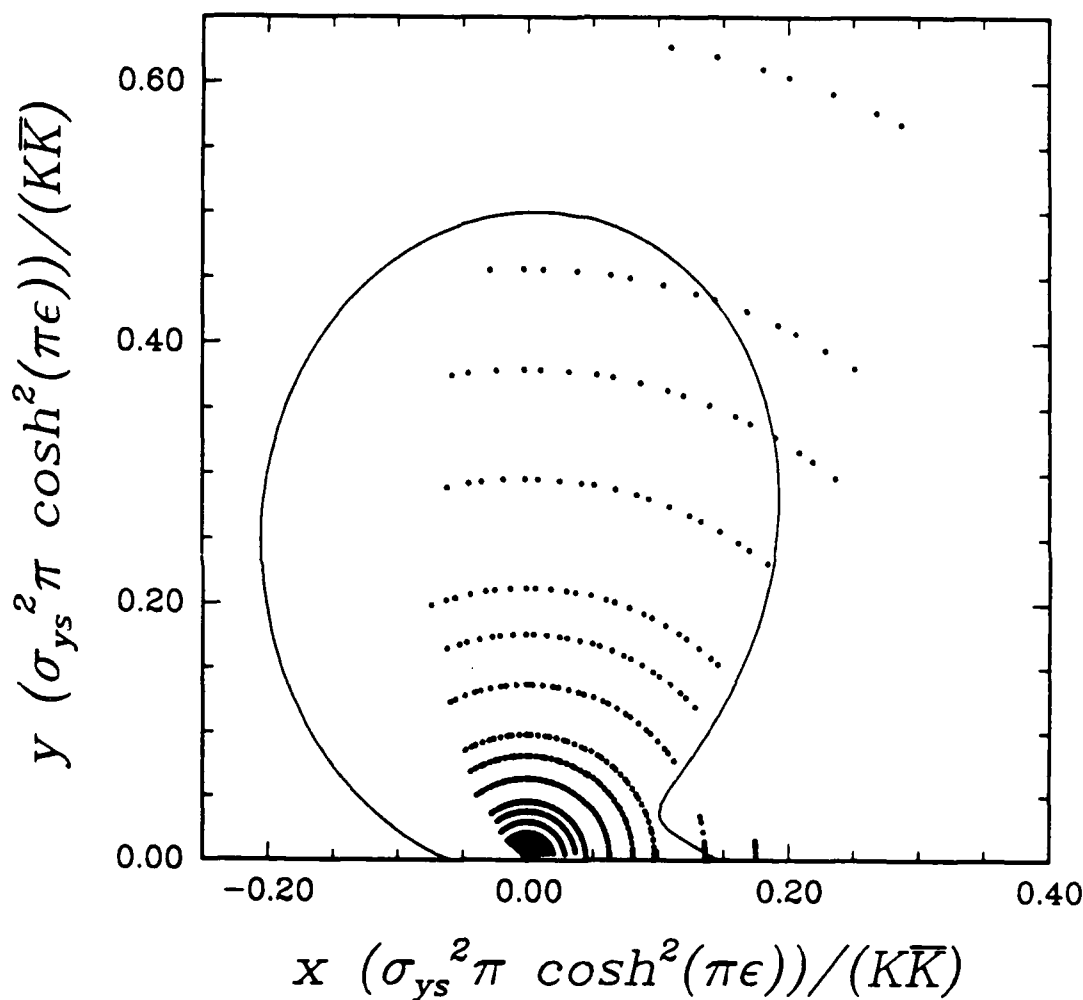


Figure 4.8 Approximate plastic zone, along with the location of actively yielding integration points, from a finite element calculation of traction-free SSY in an elastic/perfectly-plastic material atop a rigid substrate; $\epsilon = 0.07796$ and $\zeta_0 = 1.34^\circ$.

Bi-material Plastic Zone

$\zeta_0 = 30.0^\circ$ $\epsilon = 0.07796$

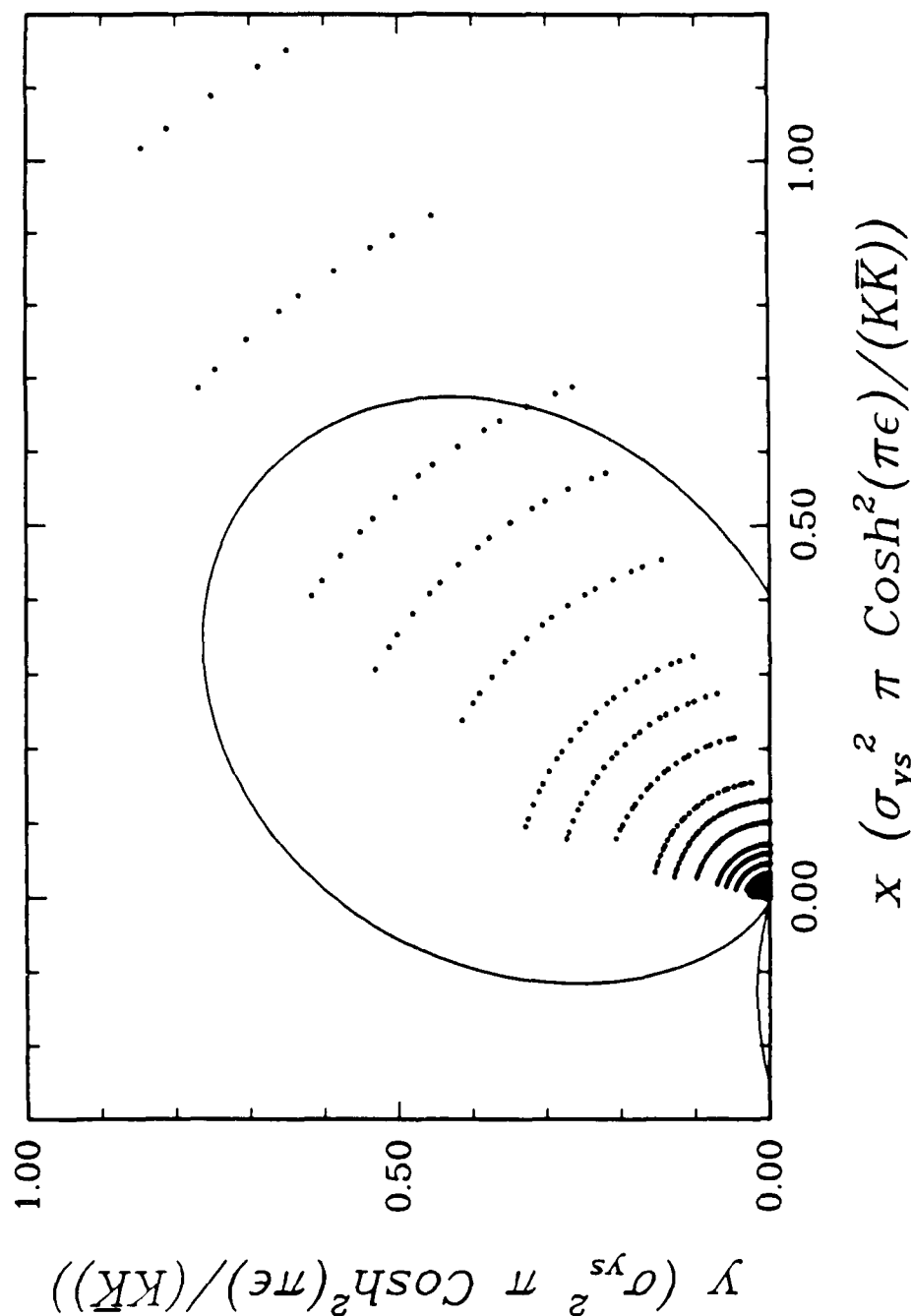


Figure 4.9 Approximate plastic zone, along with the location of actively yielding integration points, from a finite element calculation of traction-free SSY in an elastic/perfectly-plastic material atop a rigid substrate; $\epsilon = 0.07796$ and $\zeta_0 = 30.0^\circ$.

smooth across the cusp. The behavior of the material between the interface and the fan sector; i.e., the material between the cusp and interface, behaves as a quasi-constant state region or, for values of ζ_0 between 1.34° and about 11° , as an unloaded elastic sector. (The value of 11° is obtained by linearly extrapolating the maximum angular extent of the elastic sector as a function of ζ_0 from data at $\zeta_0 = 1.34^\circ$ and $\zeta_0 = 8.72^\circ$.)

Even with a cusp present, the local angular stress distribution at a given value of R is reconstructed by properly assembling the three asymptotic forms identified in Section 4.1.2. Figure 4.10 shows a schematic crack-tip field for a traction-free crack-tip. The crack-tip distribution deep within the plastic zone is determined by the values of the slip-line angles ξ , γ , η , α , and ξ_1 as a function of R . From Figures 4.2 to 4.6, it appears that the slip-line angles ξ and γ are independent of R for $R \ll 1$, but due to the presence of the cusp, the slip-line angles α , η , and ξ_1 are dependent upon R . In the limit as $R \rightarrow 0$, it appears that $\alpha = 0$, suggesting from a purely mathematical point of view, the asymptotic crack-tip fields should be constructed with $\alpha = 0$.

At this point, a definition of "asymptotic SSY bi-material crack-tip field" is necessary. In homogeneous fracture mechanics, the asymptotic fields are those which emerge as r tends toward zero, with the restriction that r remains large as compared to the CTOD. [This restriction on r is necessary because at radial distances smaller than several times the CTOD, the asymptotic field around the now blunted "circular" crack-tip is that of the logarithmic spiral (Rice, 1968b; Kachanov, 1974).] Furthermore, it is implicitly understood that such asymptotic fields are only valid in regions where their fundamental assumptions of linear kinematics and a mathematically sharp crack tip are not violated. It will be shown in Section 5.1 that use of linear kinematics is only valid in fan sectors for radial distances $R > \gamma_0$, where γ_0 , the initial shear yield strain, typically ranges from 10^{-4} to 10^{-2} for polycrystalline metals. For values of R smaller than γ_0 , the resulting strains are no longer small; i.e., less than unity. Henceforth, asymptotic SSY bi-material crack-tip fields shall be defined as those which emerge as $R \rightarrow \gamma_0$.

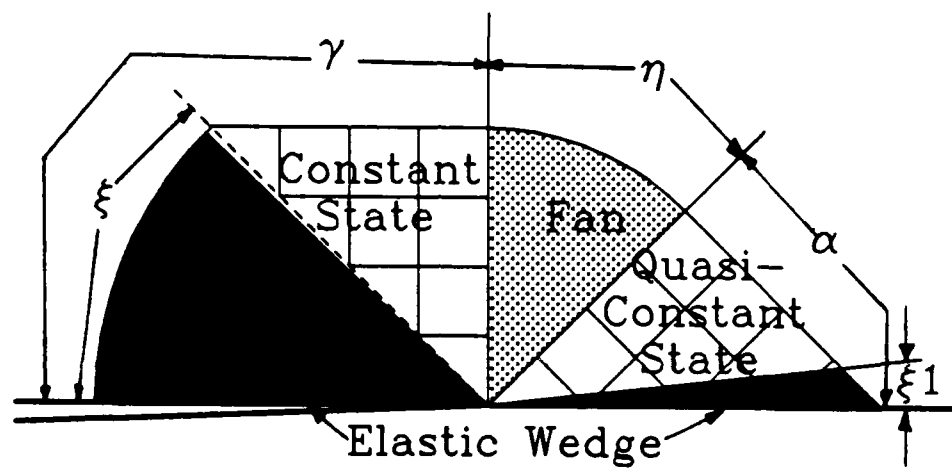


Figure 4.10 Slip-line field at a traction-free interfacial crack for an elastic/perfectly-plastic upper region bonded to a rigid (or elastic) substrate. See *Table 4.1* and *4.5* for numerical values of indicated angles.

Assemblage of Crack-Tip Fields

The asymptotic crack-tip fields are assembled from the numerical results in the following manner. The elastic wedge coefficients a_2 and c_2 along the crack face are obtained by matching the analytical elastic wedge expressions for stress and pressure with the numerical results over the range of θ where no prior inelastic deformation has occurred. With these coefficients, the elastically predicted location where $\bar{\sigma} = \sigma_{\nu\theta}$ is identified, and the corresponding angle is taken to be ξ . The stress state at ξ in the elastic and constant state sectors are assumed to be equal, and from the elastically predicted stress state at ξ , a Mohr's circle calculation is performed to estimate the rotation in the constant state region necessary to achieve a state of pure shear ($\sigma_{rr} = \sigma_{\theta\theta}$). This rotation angle is interpreted as $\gamma - \xi$. In making this estimate, it is assumed that σ_{rr} is continuous from the elastic-wedge/constant-state border through the entire constant state sector, up to the constant-state/fan border. To determine the angle η , the pressure distributions in the fan and the adjacent constant state sectors are fit to linear expressions (with respect to θ), and their extrapolated intersection defines the angle η . This approach circumvents problems associated with a lack of mesh refinement and numerical noise at boundaries between constant state and fan sectors. The angle α is then back calculated as $\alpha = \pi - \gamma - \eta$, and is compared to the angular location of the last node or integration point whose stress state is indicative of a centered fan.

In assembling the assumed asymptotic fields, the stress distribution in the unloaded elastic sector is obtained by projecting the stress distribution from the "virgin" elastic sector. Although such an extrapolation is not strictly acceptable since it does not account for the residual $\epsilon_{ss}^{Plastic}$ strain, modest agreement between the numerical and elasticity solutions does exist for the $\sigma_{r\theta}$ and $\sigma_{\theta\theta}$ components. This extrapolation is done for several reasons. For the smaller values of ζ_0 , it is not clear that the initial (numerical) transient period accumulates the same amount of strain as it would have had the analysis been initially started from a smaller value of ζ_0 . Second, if ζ_0 uniquely defines the assemblage of the asymptotic crack-tip fields independently of ν and ϵ , then

these results are directly applicable for negative values of ϵ . (For $\epsilon < 0$, ζ_0 decreases as $\|K\|$ increases, and no prior plastic deformation would occur in the elastic sector.)

Interfacial Traction and Crack-Tip Fields

Due to the elastic/perfectly-plastic constitutive assumption, the interfacial tractions are bounded and are constant as $R \rightarrow 0$. The maximum magnitude of the shear traction, t_s , is $|t_s| = k$, and for a fully plastic crack tip the maximum value of the normal traction, t_n , is $t_n = 3.298\sigma_{ys}$. The development of the asymptotic interfacial tractions is identical to that of the asymptotic crack-tip fields. At normalized radial distances several times greater than $R = 1$, the elastic interfacial tractions are recovered, and the asymptotic interfacial tractions are fully established at radial distances less than 2% to 10% of the actual plastic zone radius along the interface. The interfacial tractions appear to reach their steady state values slightly faster than the crack-tip fields, except when a cusp or an interfacial elastic sector is present. The stress state shown in *Figure 4.7* is indicative of the transient period necessary to establish asymptotic interfacial tractions when a cusp is present.

The assembled asymptotic crack-tip fields for six values of ζ_0 ranging from 1.34° to 30.04° are summarized for $R = \gamma_0$ in the *Table 4.1*. Included in the table are the far-field values of the J -Integral, the numerical values of the slip-line angles α , η , γ , ξ , and ξ_1 , the elasticity potential coefficients a_2 and c_2 for the interfacial elastic sectors denoted by the angle ξ , and the normalized hoop $[H \equiv \sigma_{\theta\theta}(\theta = \pi - \xi)/\sigma_{ys}]$ and shear stress $[K \equiv \sigma_{r\theta}(\theta = \pi - \xi)/\sigma_{ys}]$ components at $\theta = \xi_1$. The first value of η corresponds to the value obtained by the previously described procedure, and the value of η in parentheses represents the value based solely upon the last node or integration point whose stress state is that of a centered fan. Also included in the table are the normalized interfacial traction coefficients P and S which are related to the interfacial shear, t_s , and normal, t_n , tractions by

$$t_n(R = \gamma_0) \equiv P\sigma_{ys} \quad (4.21)$$

and

$$t_s(R = \gamma_0) \equiv S\sigma_{yy}. \quad (4.22)$$

From Table 4.1, the schematic bi-material crack-tip configuration shown in Figure 4.10, and the elasticity potential given in Appendix B, the stress distribution in the deformable upper half-plane is completely described.

ζ_0	J MPa m	α	η	γ	ξ	ξ_1
1.34°	1.12×10^{-5}	40°	90° (82°)	50°	45°	23°
8.72°	5.83×10^{-5}	26°	88° (79°)	66°	61°	6°
18.2°	4.49×10^{-4}	14°	68° (74°)	98°	92°	0°
25.7°	2.63×10^{-3}	13°	58° (59°)	109°	79°	0°
30.0°	6.90×10^{-3}	6°	64° (57°)	110°	87°	0°
ζ_0	a_2	c_2	P	S	H	K
1.34°	-0.234	-0.0348	2.89	0.103	2.71	0.448
8.72°	-0.104	-0.113	2.86	0.298	2.77	0.372
18.2°	0.063	-0.136	2.41	0.462	—	—
25.7°	0.157	-0.133	1.99	0.524	—	—
30.0°	0.185	-0.115	1.74	0.546	—	—

Table 4.1 Crack-tip slip-line angles, crack-face elastic wedge and interfacial traction coefficients, and the stress state at the interfacial elastic-wedge/constant state boundary; $R = \gamma_0$, $\epsilon = 0.07796$, and $\nu = 0.342$.

Comparison

The accuracy of the slip-line angles identified in the manner discussed previously is very good when no elastic sectors are nearby, however, the accuracy is significantly reduced when elastic sectors are present. The transition from an elastic sector to a fan sector usually spans only 2 to 4 elements (each element covers approximately 8°) and seldom occurs at an element boundary. Sector boundaries which occur within an element are poorly resolved because the deviatoric and hydrostatic stress states within an element are only bi-quadratically and bi-linearly represented, respectively. Consequently, accurate data from constant state sectors needed to precisely determine the elastic/constant-state/fan boundaries is not available.

The numerical and analytically inferred stress states are compared for $\zeta_0 = 30.0^\circ$ at $R = \gamma_0$ ($\epsilon = 0.07796$) and are plotted in *Figure 4.11*. Substantially away from the fan/elastic-wedge transition, little discrepancy exists between the inferred analytical solution, represented by solid lines, and the FE calculations, whose values at integration points are plotted with symbols. Near the constant-state elastic-wedge transition, accumulated residual strains influence the stress state, especially the σ_{rr} component, and the inferred stress state is not continuous at the actual boundary. In the construction of this figure, rigid-plastic slip-line theory is used in the plastically deforming regions, and the pressure distribution is arrived at by matching a point within the fan region. The constant-state elastic-wedge transition shown in the figure is not accurate because it fails to reflect the elastically compressible material behavior in the constant state region and the effect of residual strains in the elastic sector. Also, the stress states in elastic and plastic regions are matched from different conditions, and therefore continuity of stress is not guaranteed. Furthermore the apparent "almost continuous" stress state at $\theta = \pi - \gamma$ results from the technique used to approximate γ . Overall, the asymptotic crack-tip fields reproduce the stress distribution accurately near a fan/elastic-wedge transition, with the exception of the σ_{rr} component

Asymptotic Strain Distribution and CTOD

At plastically deforming crack tips, knowledge of the stress distribution is not sufficient to completely characterize the crack-tip regions because the strain distribution is not uniquely defined from the stress distribution. Unfortunately, convenient asymptotic forms to describe the strain distribution do not exist as they do to describe the stress distribution. Due to the asymptotic nature of deformation in a centered fan sector (i.e., $\dot{\gamma}_{r\theta}$ is the only non-zero strain rate component) $|\dot{\gamma}_{r\theta}|$ is generally large compared to all other strain components. In constant state regions, large strains are not anticipated since they must occur uniformly throughout the region or along crack-tip rays where $\sigma_{r\theta} = \pm k$ (Rice and Tracey, 1973), and, in general, strains in constant state regions are

Bi-material Crack-Tip Stresses $\zeta_0 = 30.0^\circ$ $\epsilon = 0.07796$ $R = \gamma_0$

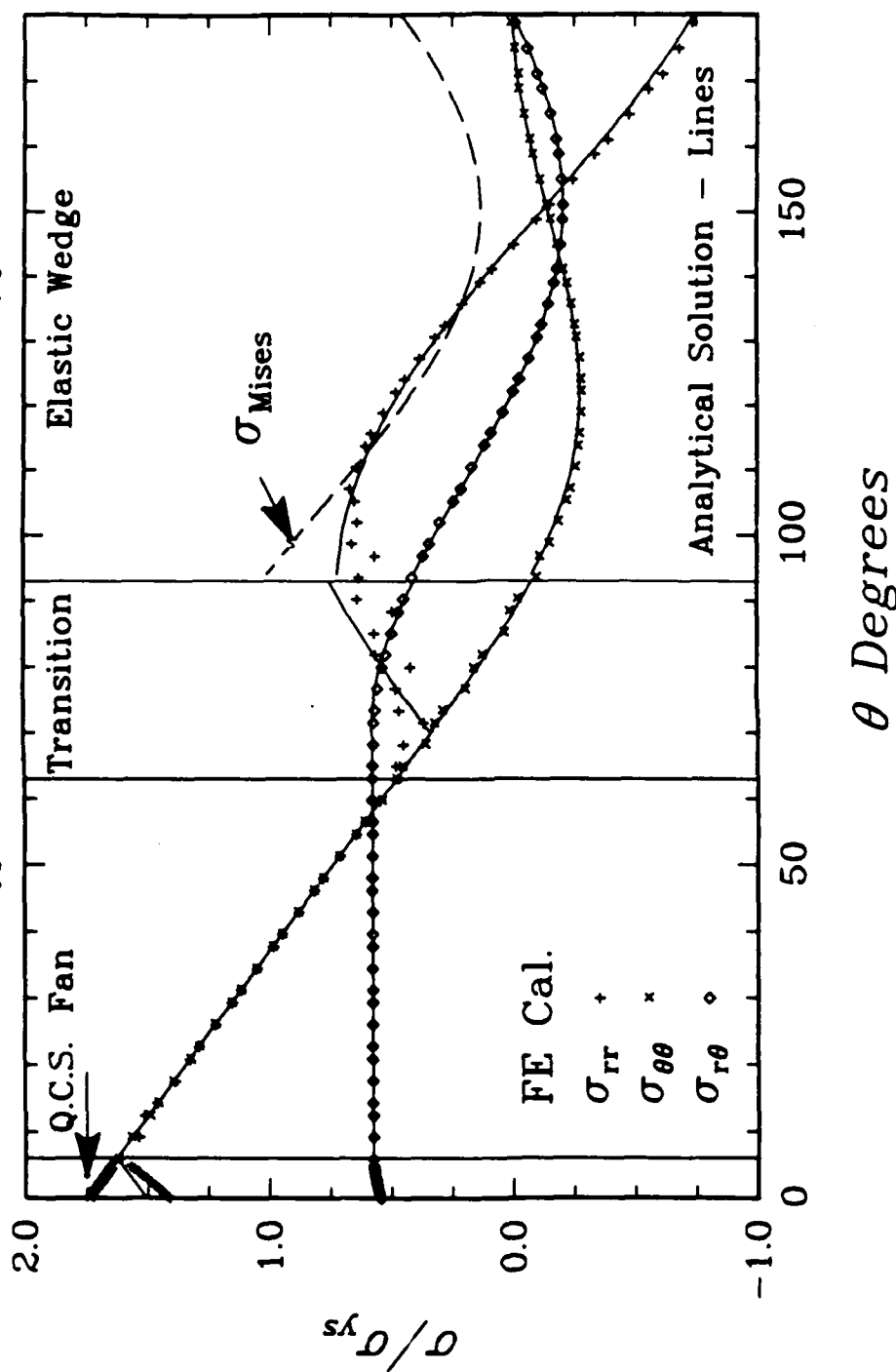


Figure 4.11 Normalized circumferential stress distribution for an elastic/perfectly-plastic upper region bonded to a rigid substrate at $R = \gamma_0$; $\epsilon = 0.07796$ and $\zeta_0 = 30.0^\circ$. Symbols represent the integration point stress states and the lines reproduce the inferred analytical solution. Included is the inferred Mises equivalent stress in the crack-face elastic wedge.

small compared to those found in centered fans. For these and other reasons, the most significant strain component in the crack-tip region is the $\gamma_{r\theta}$ component, and therefore $\gamma_{r\theta}$ is the only strain component considered.

The $\gamma_{r\theta}$ strain distribution is normalized by considering its functional form within a centered fan sector. From Eq.(4.10), the shear strain distribution is given approximately by $R\gamma_{r\theta}/\gamma_0 \approx A(\theta)$, when $R \ll 1$. Figure 4.12 shows the normalized distribution of $\gamma_{r\theta}$ for $\epsilon = 0.07796$ at six values of ζ_0 between 1.34° and 30.0° . Comparing the radial shear strain distributions with the asymptotic crack-tip forms, the largest strains occur in fan regions approximately 15° away from the fan-elastic boundary, and from Figure 4.12, the maximum shear strain increases as ζ_0 increases. Although not shown, the normalized shear strain distributions deep within the plastic zone ($R < 0.01$) are independent of R . Thus the presence of a cusp strongly influences the entire asymptotic crack-tip deformation, even in regions where the cusp is not present.

An additional quantity directly related to the strain field is the CTOD. The bi-material CTOD is defined as

$$\delta_{CTOD} \equiv u(R=0, \theta=\pi) - u(R=0, \theta=-\pi), \quad (4.23)$$

where u is the displacement vector. The CTOD physically represents the displacement of the crack faces relative to one another and also represents an integrated vector sum of the strain field on a path about the crack tip. To uniquely define δ_{CTOD} , both its magnitude and orientation are required. In Figure 4.13 a schematic crack tip and the associated coordinate system used to define δ_{CTOD} are sketched. Figure 4.14 shows the normalized magnitude of δ_{CTOD} and ω , the angle of δ_{CTOD} , for $\epsilon = 0.07796$ as a function of ζ_0 . Also plotted in the figure is the angle $\omega_{Elastic}$, which is the angle of δ_{CTOD} obtained from the elasticity solution by evaluating Eq.(P2.32) at $\zeta = \zeta_0$ and $r = r_p$. The difference between ω and $\omega_{Elastic}$ is less than 15° for the range of ζ_0 shown. The corresponding elastically-calculated magnitude of δ_{CTOD} , defined as

$$\left| \frac{\delta_{CTOD}\sigma_{ys}}{J} \right|_{Elastic} \equiv \frac{4\sqrt{2}}{\pi\sqrt{1+4\epsilon^2}}, \quad (4.24)$$

is $|\delta_{CTOD}\sigma_{ys}/J|_{Elastic} = 1.779$ for $\epsilon = 0.07796$ and is independent of ζ_0 .

Bi-material Crack-Tip Shear Strain

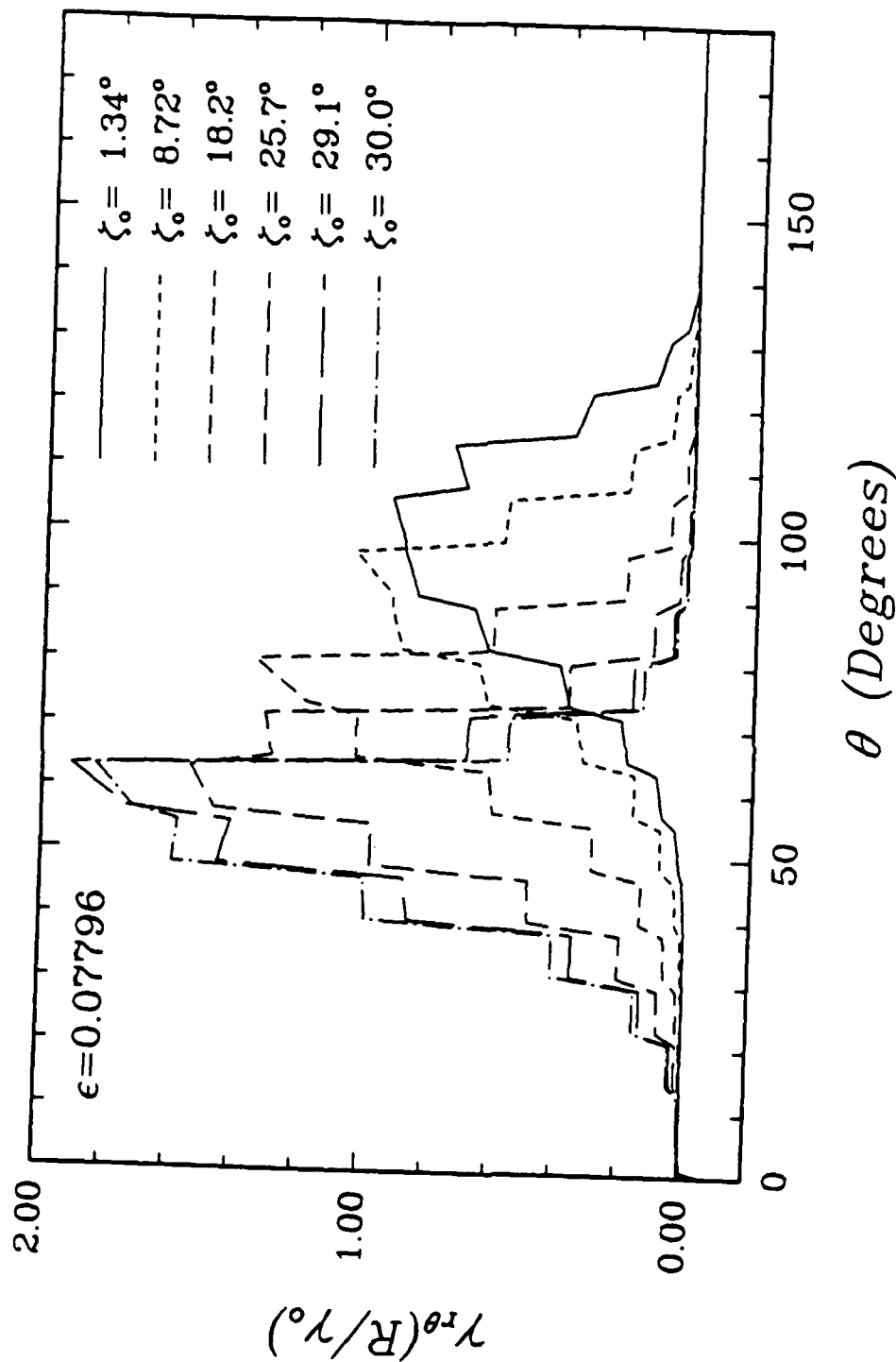


Figure 4.12 Circumferential variation of normalized $\gamma_{r\theta}$ shear strain deep in the plastic zone ($R = \gamma_0$) for an elastic/perfectly-plastic upper region bonded to a rigid substrate at various values of ζ_0 ; $\epsilon = 0.07796$.

Schematic Crack Tip

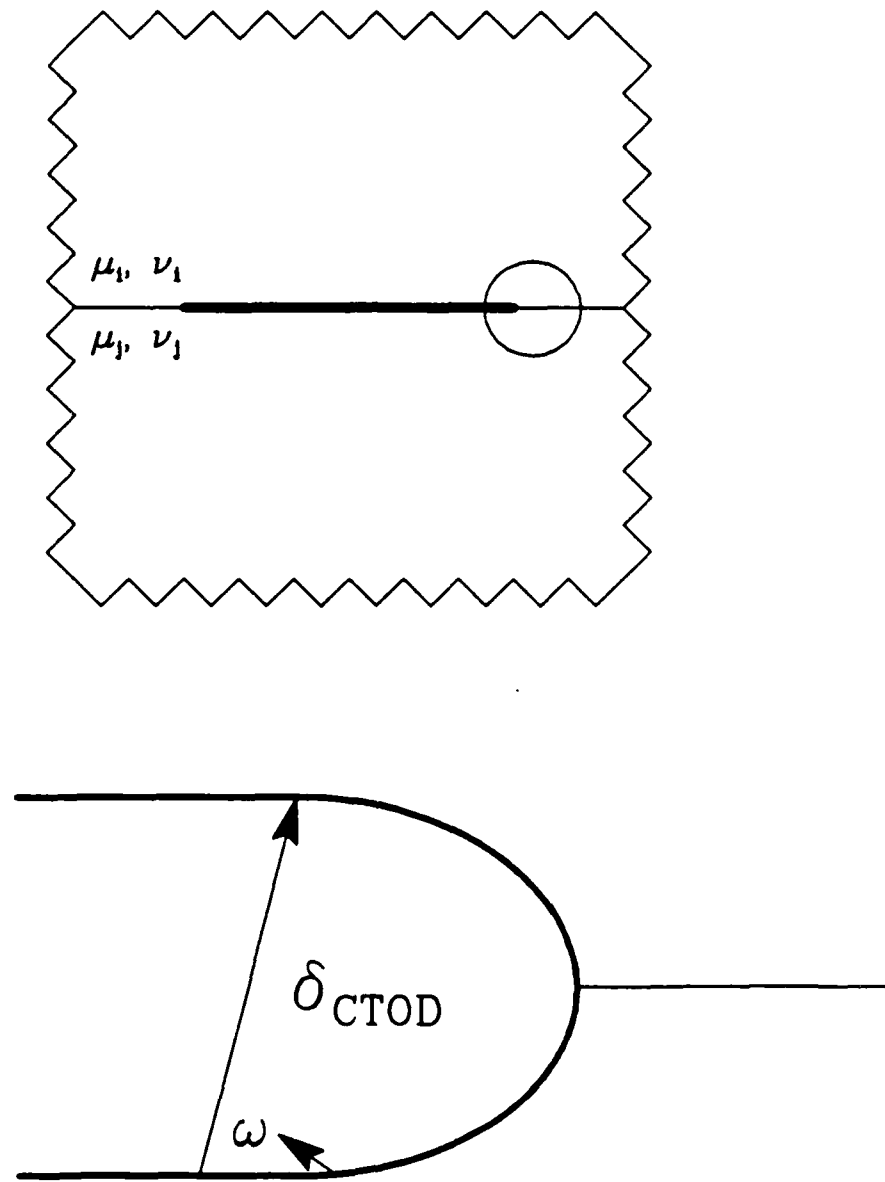


Figure 4.13 Schematic interfacial crack-tip region showing the crack-tip opening displacement (δ_{CTOD}) and its associated angle ω .

Bi-material Crack-Tip δ_{CTOD}

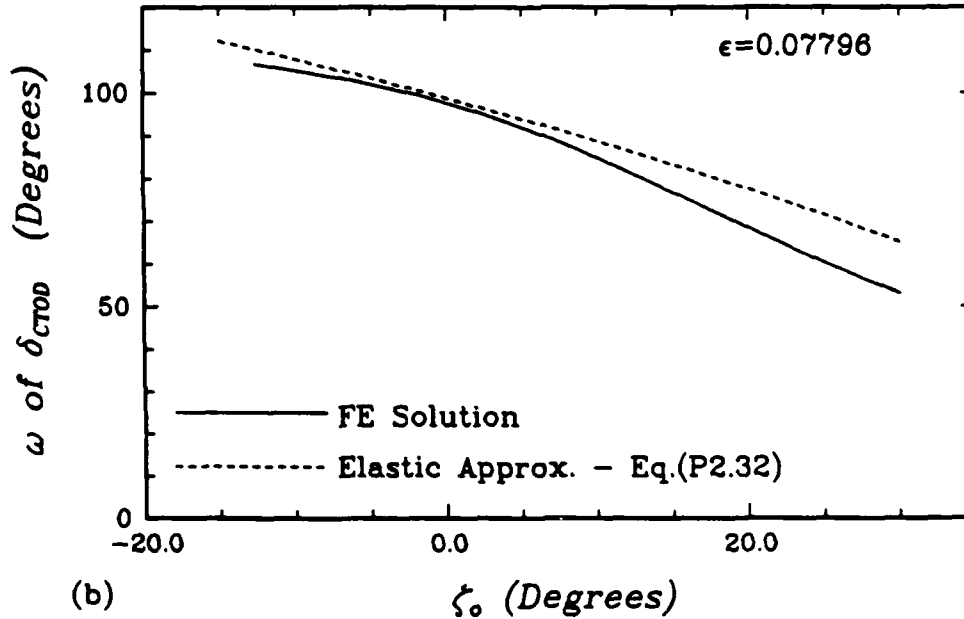
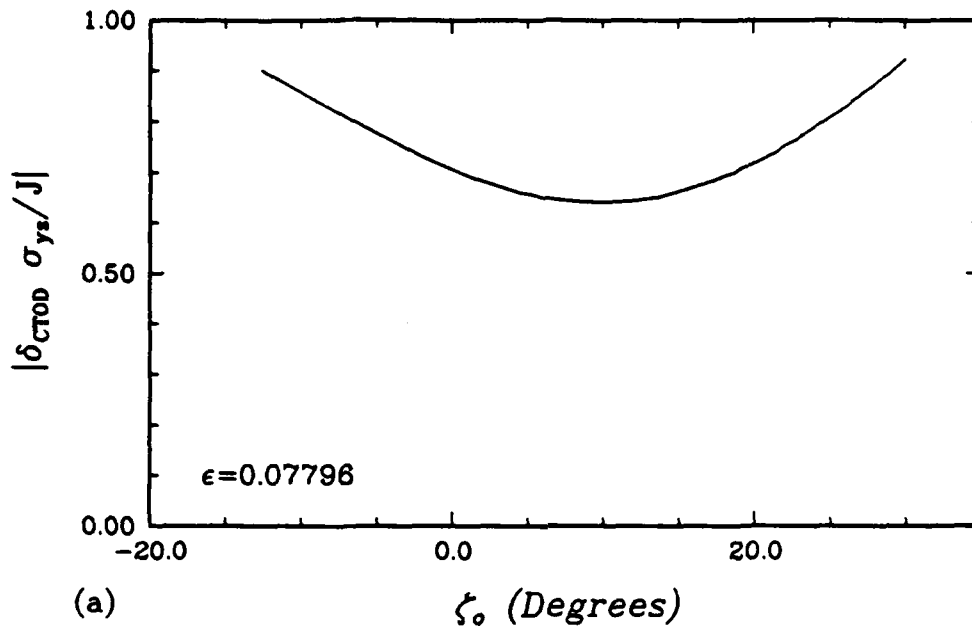


Figure 4.14 Traction-free bi-material δ_{CTOD} from a finite element calculation of an elastic/perfectly-plastic upper region atop a rigid substrate for ζ_0 between -20° and 30° ; $\epsilon = 0.07796$. (a) shows the magnitude normalized with respect to yield strength and the far-field elastic J -Integral and (b) shows the crack-tip angle ω from the finite element calculations and from Eq.(P2.32) evaluated at $r = r_p$ and $\zeta = \zeta_0$.

Path Dependence of J-Integral

The J -Integral is evaluated within the asymptotic crack-tip fields by considering the contributions to it from each of the various sectors. Rice (1968b) states that since the strains are bounded as $R \rightarrow 0$ in a constant region, constant state sectors produce no contribution to J . Extending this rationale, it is concluded that no contributions to J are made from either the rigid lower half or from any of the (non-singular) crack-tip elastic sectors. Therefore, the entire local contribution to J comes from the centered fan region(s) and is given by (Rice, 1967)

$$J = \int_{\theta_{fan}} r \gamma_{r\theta}(r, \theta) [k \cos \theta + \sigma_{rr}(r, \theta) \sin \theta] d\theta. \quad (4.25)$$

Here the integration path is chosen to be a circular arc about the crack tip, and in terms of the schematic slip-line field shown in *Figure 4.10*, the upper and lower limits of integration are $\theta = \eta$ and $\theta = \alpha + \eta$, respectively.

Local J -Integral estimates were calculated by the virtual crack extension method (VCEM). The VCEM uses the divergence theorem to convert the contour integral of J to a surface integral and then calculates the change in energy associated with a virtual extension of the crack front. The J estimate is interpreted as $J \approx -\Delta\pi/\Delta a$, where $\Delta\pi$ is the change in energy and Δa is the virtual increment of crack advancement. *Table 4.2* summarizes the local J_{VCEM} normalized by $J_{Elastic}$, the far-field elastic J -Integral, for $\epsilon = 0.07796$ and ζ_0 between 1.34° and 30.0° . Included in the table are the average values of the second, third, and fourth contour values of J . A considerable amount of non-proportional loading occurs, especially with the presence of the cusps and growth of the crack-face elastic wedge, thus local J values which are appreciably lower than the far-field J are expected. The contour values of J typically decreased slightly from the second contour to the ninth contour. Growth of J as $R \rightarrow 0$ is not anticipated, but may be attributable to both the stress and strain distributions asymptotically approaching a steady state as $R \rightarrow 0$.

ζ_0	$J_{VCEM}/J_{Elastic}$
30.0°	0.86
25.7°	0.75
18.2°	0.61
8.72°	0.49
1.34°	0.41

Table 4.2 Local J -Integral estimates, normalized by the elastic far-field value of J , obtained by the VCEM for various values of ζ_0 with $\epsilon = 0.07796$.

4.2.2 Solution in the Lower Elastic Half-Plane

Due to the use of a rigid material adjoint to the elastic/perfectly-plastic material in the quarter wave-length calculation, no results are obtained for the lower elastic half-plane. The nature of the elastic half space is instead obtained from one of the other, less focused, analyses. Because contact between the upper and lower half-planes is made only via the interface, the behavior of the asymptotic interfacial conditions very deep within the plastic zone, described previously, are reflective of the stress behavior in the elastic half-plane.

Unlike the upper yielding region, no significantly different behavior is observed in the elastic region at r_I , the plastic zone radius along the interface [$r_I \equiv r_p(\theta = 0^\circ)$], and at distances much closer to the crack-tip, $r \approx r_I/10$, certain dominant features begin to emerge. Consider the results obtained for the material combination of yielding aluminum in region 1 and graphite in region 2, ($\epsilon = -0.07923$) loaded until $\zeta_0 = -2.70^\circ$. (Table 4.4 contains the elastic properties of all material used.) Figure 4.15 shows the normalized stress components in the elastic interfacial region as a function of the logarithm of the normalized radial distance R_I ($R_I \equiv r/r_I$). The normalized hoop and shear components experience a transitional period from $\log_{10}(R_I) = 0$ up to $\log_{10}(R_I) = -1.0$, at which point they level off and achieve a steady state behavior as $R_I \rightarrow 0$. The normalized radial stress experiences a similar transitional period, but it increases linearly in the region where the other components reach their steady-state values ($R_I < -1$). This indicates that the radial stress component is logarithmically

Bi-material Crack-Tip Stresses $\epsilon = -0.07923$ $\theta = 0.0^\circ$

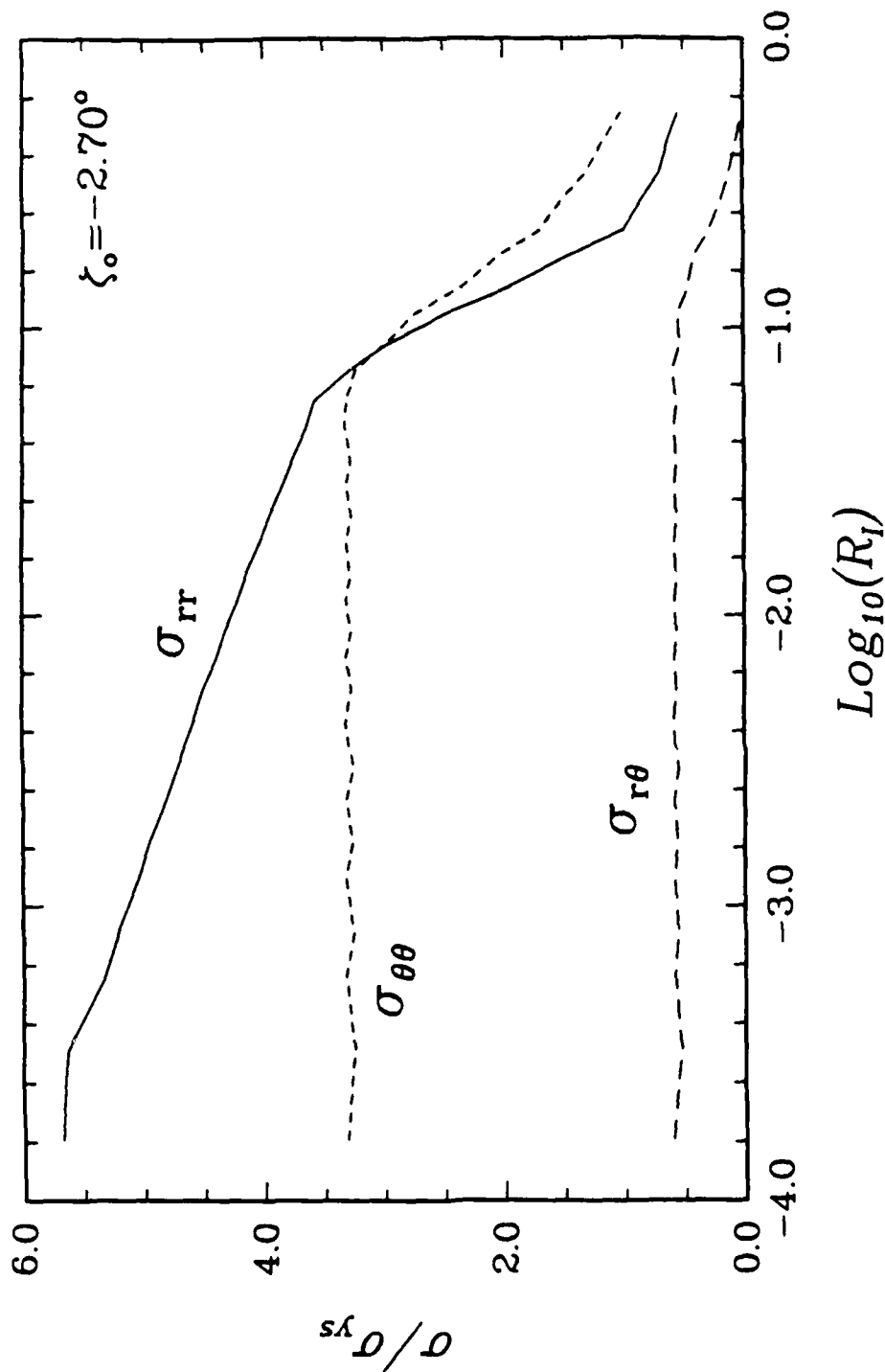


Figure 4.15 Normalized interfacial stress variation with normalized radial distance in the lower region for a traction-free bi-material crack-tip under SSY conditions; elastic/perfectly-plastic upper region bonded to a rigid substrate ($\zeta_0 = -2.70^\circ$, $\epsilon = -0.07923$, and $\theta = 0.0^\circ$).

singular. *Figure 4.16* shows the normalized elastic stress components plotted versus normalized radial distance R at $\theta = -86^\circ$. At this angle, all the stress components experience some transitional behavior at $R_I > -1$ before they reach a linear region. In *Figure 4.17* the angular distribution of the normalized stress components at $R = 0.00551$, $R = 0.0138$, and $R = 0.0551$ are plotted. It is obvious that the asymptotic stress distribution does not generally reach a steady-state as $R \rightarrow 0$ (or $R_I \rightarrow 0$), as is observed in the upper domain, nor does it reach a self similar distribution as is observed in homogeneous asymptotic elastic and plastic crack-tip fields (Rice and Rosengren, 1968; Hutchinson, 1968).

Formulation of an Elasticity Potential

To describe the stress field very near the crack tip, beneath the region where the solution in the upper domain has achieved a steady state, a closed form elasticity solution will be formulated. The planar elasticity solution will describe the asymptotic characteristic as $R \rightarrow 0$ in the lower field and will be expressed in the form of an elasticity potential.

It has been shown that any planar stress function, $\phi(x, y)$, which satisfies the differential equation

$$\frac{\partial^4 \phi}{\partial x^4} + 2 \frac{\partial^4 \phi}{\partial x^2 \partial y^2} + \frac{\partial^4 \phi}{\partial y^4} = 0, \quad (4.26)$$

also satisfies the basic equations of isotropic linear elasticity, namely the constitutive, equilibrium, and the compatibility equations (Timoshenko and Goodier, 1970). In addition to satisfying Eq.(4.26), the stress function must also satisfy all accompanying boundary conditions. The individual stress components for a body with stress function, ϕ (with negligible body forces) are:

$$\sigma_{xx}(x, y) = \frac{\partial^2 \phi(x, y)}{\partial y^2}, \quad (4.27)$$

$$\sigma_{yy}(x, y) = \frac{\partial^2 \phi(x, y)}{\partial x^2}, \quad (4.28)$$

and

Bi-material Crack-Tip Stresses $\epsilon = -0.07932$ $\theta = -86^\circ$

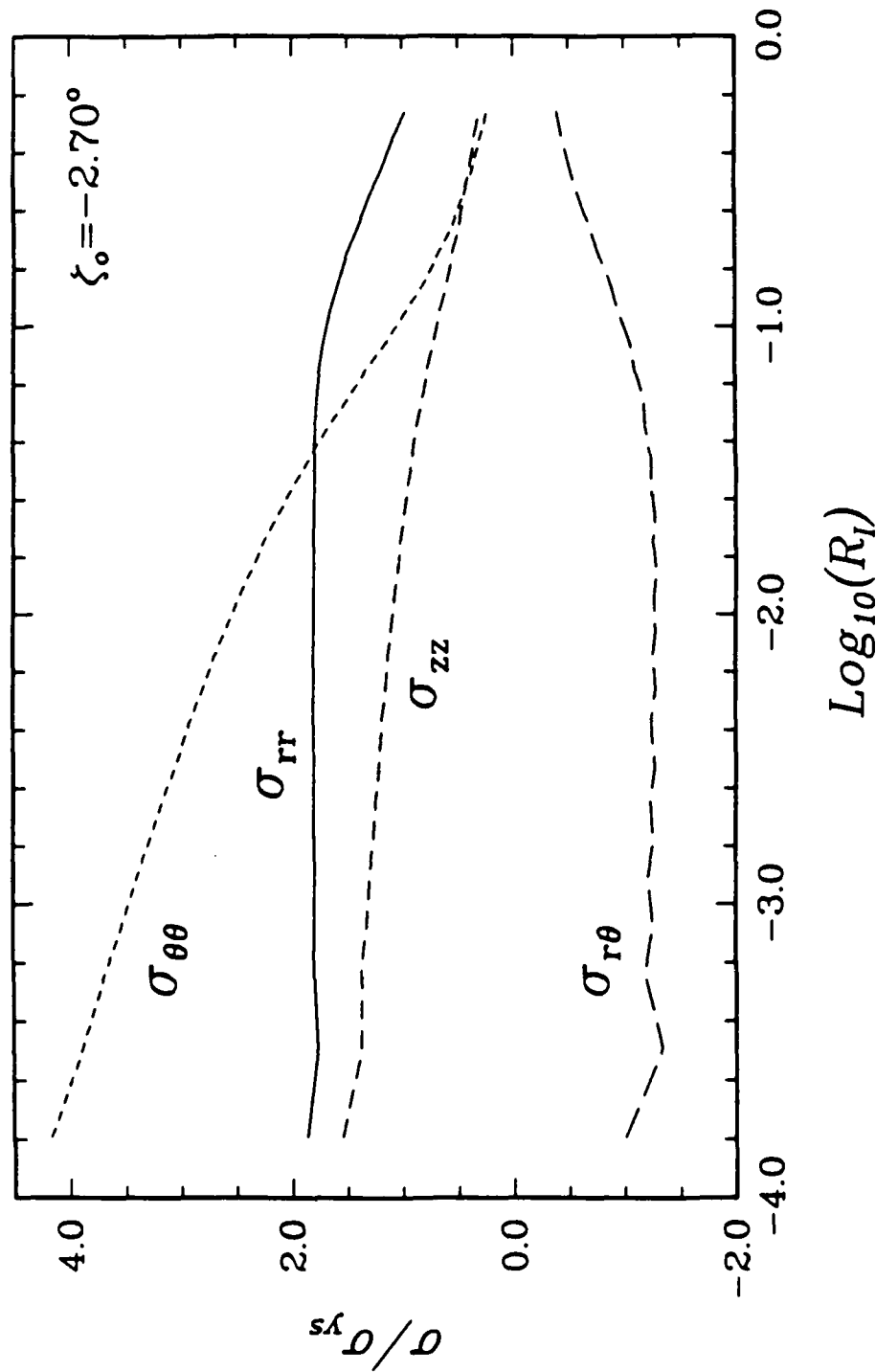


Figure 4.16 Normalized interfacial stress variation with normalized radial distance in the lower region for a traction-free bi-material crack-tip under SSY conditions; elastic/perfectly-plastic upper region bonded to a rigid substrate ($\zeta_o = -2.70^\circ$, $\epsilon = -0.07923$, and $\theta = -89^\circ$).

Bi-material Crack-Tip Stresses $\epsilon = -0.07932$ $\zeta_0 = -2.70^\circ$

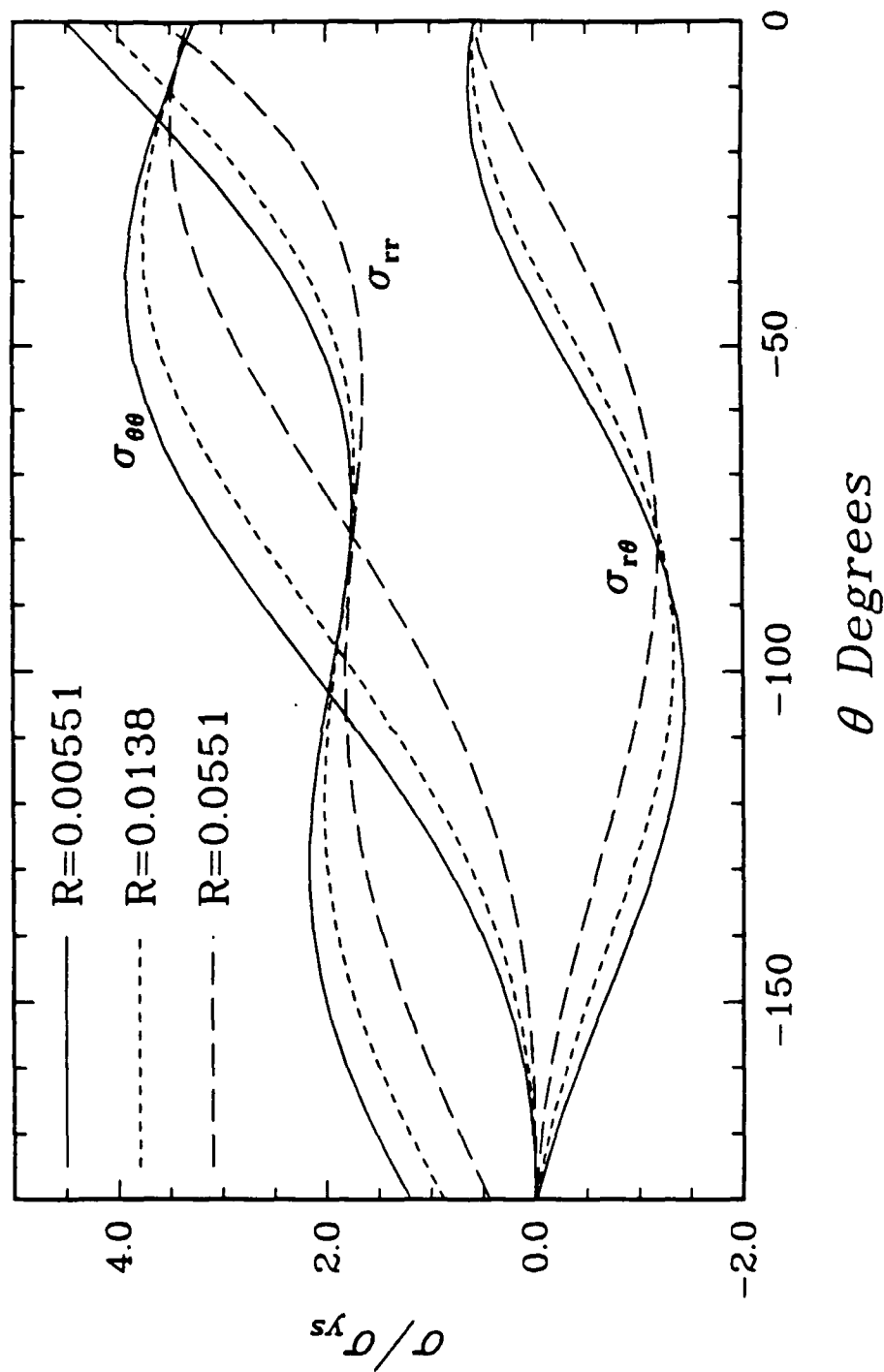


Figure 4.17 Normalized angular stress distribution in lower region for a traction-free bi-material crack-tip under SSY conditions at various radial distances; elastic/perfectly-plastic material bonded to an elastic substrate ($\zeta_0 = -2.70^\circ$ and $\epsilon = -0.07923$).

$$\sigma_{xy}(x, y) = -\frac{\partial^2 \phi(x, y)}{\partial x \partial y}. \quad (4.29)$$

The strain field is found by inverting the appropriate isotropic elasticity tensor, \mathcal{L} , defined in Eq.(3.14), and using it to operate directly on the stress field. Assumptions regarding plane-strain (or plane-stress) conditions are necessary to fully define the stress and strain fields. Integration of the strain field uniquely determines the displacement field, to within a rigid body motion. Therefore, the determination of ϕ , in conjunction with the planar assumptions and two elastic material properties, completely describes the elastic fields.

The stress function ϕ need not be expressed in Cartesian coordinates. It can be found in any coordinate frame and, via the proper coordinate transformation, transformed into any other coordinate frame. For example, it is more convenient to express the stress components around the crack tip in a polar coordinate frame. The polar stress components can be obtained from ϕ by (Timoshenko and Goodier, 1970):

$$\sigma_{\theta\theta}(r, \theta) = \frac{\partial^2 \phi(r, \theta)}{\partial r^2}, \quad (4.30)$$

$$\sigma_{r\theta}(r, \theta) = -\frac{\partial}{\partial r} \left(\frac{1}{r} \frac{\partial \phi(r, \theta)}{\partial \theta} \right), \quad (4.31)$$

and

$$\sigma_{rr}(r, \theta) = \frac{1}{r} \frac{\partial \phi(r, \theta)}{\partial r} + \frac{1}{r^2} \frac{\partial^2 \phi(r, \theta)}{\partial^2 \theta}, \quad (4.32)$$

where r is the radial coordinate and θ is the angular coordinate.

In general, the stress potential ϕ is obtained by considering the assorted boundary conditions and the desired asymptotic behavior. In an attempt to find ϕ for the problem at hand, the contributions to ϕ from the local crack-face and interfacial tractions are first examined.

The major factor which governs the behavior of the elastic domain is the interfacial traction. Because of the elastic/perfectly-plastic material idealization used in the upper domain, and to within the limits discussed previously, the asymptotic crack-face and interfacial tractions, t , as $R \rightarrow \gamma_0$, assume constant values of:

$$t_n = \begin{cases} P\sigma_{ys} & \theta = 0^\circ \\ 0 & \theta = -180^\circ, \end{cases} \quad (4.33)$$

and

$$t_s = \begin{cases} S\sigma_{ys} & \theta = 0^\circ \\ 0 & \theta = -180^\circ. \end{cases} \quad (4.34)$$

Here σ_{ys} refers to the yield strength of the material in the upper domain σ_{ys1} , and the subscripts n and s designate the normal and shear components, respectively. Although these asymptotic interfacial tractions extend only over a "short" distance within the plastic zone, the actual traction distribution is approximated by considering that these tractions exist over the entire interface within the plastic zone. Outside the plastic zone region, the asymptotic elastic stresses are small with respect to σ_{ys} and decay rapidly as the radial distance r increases. To describe the asymptotic behavior in the crack-tip region it is assumed that the interfacial tractions in the elastic portion of the upper region are negligible. The interfacial tractions are idealized as being equal to zero everywhere beyond the plastic zone and within the plastic zone are equal to t_n and t_s , as given by Eqs.(4.33) and (4.34). This idealized traction distribution around the crack tip is drawn in *Figure 4.18*.

By consideration of this idealized interfacial traction distribution, an elasticity potential is assembled which asymptotically reproduces the stress and strain state in the elastic lower domain as $r \rightarrow 0$. From the known solutions for semi-infinite bodies with constant normal and shear surface tractions across half of their free surface (Timoshenko and Goodier, 1970), the stress potential, ϕ , for the lower crack-tip domain is assembled by superposition of the various known solutions and is expressed as

$$\begin{aligned} \phi = & -\frac{S\sigma_{ys}}{\pi} \left[\frac{1}{2} y^2 \ln \left(\frac{x^2 + y^2}{(x + r_I)^2 + y^2} \right) + xy \arctan \left(\frac{y}{x} \right) \right. \\ & \left. + (x - r_I) y \arctan \left(\frac{y}{x + r_I} \right) \right] \\ & + \frac{P\sigma_{ys}}{2\pi} \left[(x^2 + y^2) \arctan \left(\frac{y}{x} \right) - xy + (x + r_I) y \right. \\ & \left. - ((x + r_I)^2 + y^2) \arctan \left(\frac{y}{x + r_I} \right) \right]. \end{aligned} \quad (4.35)$$

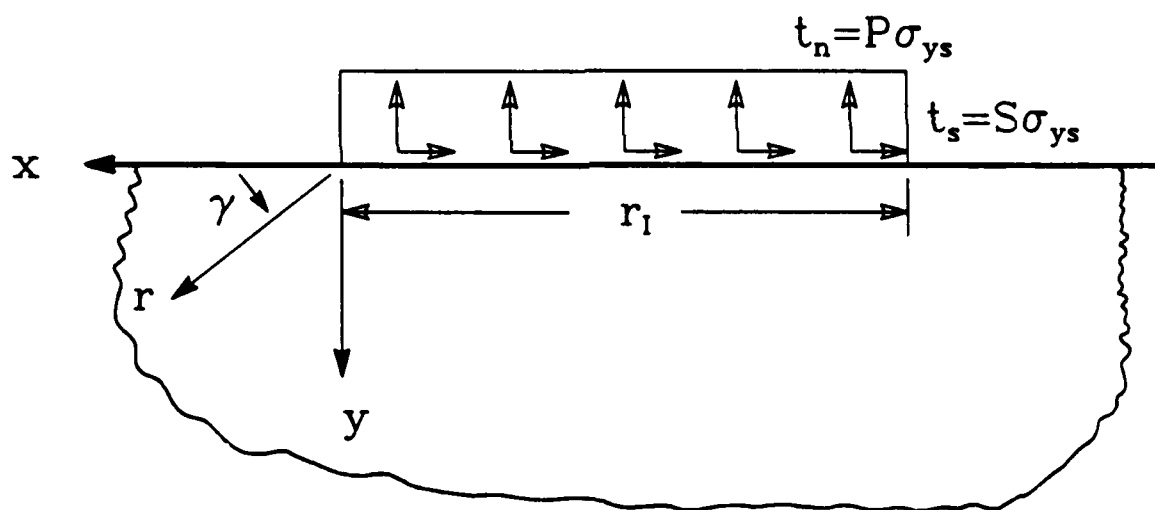


Figure 4.18 Idealized interfacial traction distribution for a traction-free crack-tip in SSY conditions, showing interfacial normal (t_n) and shear (t_s) tractions, plastic zone radius of upper material (r_I), and polar (r, γ) and Cartesian (x, y) coordinates.

Here r_I is the plastic zone radius along the interface. (The stress potential for a semi-infinite body is a special case of the general wedge solution with the enclosed wedge angle equal to 180° .) Since only the asymptotic crack-tip elastic stress field is desired and the traction distribution outside the crack-tip region is only approximate, attention is focused upon the very near crack-tip field. By dividing Eq.(4.29) by r_I^2 , defining two new relative coordinate measurements $X = x/r_I$ and $Y = y/r_I$, and by assuming $X \ll 1$ and $Y \ll 1$, the local asymptotic stress potential is obtained, as $R_I \rightarrow 0$ (where $R_I^2 = X^2 + Y^2$), and it is given by

$$\begin{aligned} \phi = & -\frac{S\sigma_{ys}}{\pi} \left[\frac{1}{2} Y^2 \ln(X^2 + Y^2) + XY \arctan\left(\frac{Y}{X}\right) - Y^2 \right] \\ & + \frac{P\sigma_{ys}}{2\pi} \left[(X^2 + Y^2) \arctan\left(\frac{Y}{X}\right) - XY \right]. \end{aligned} \quad (4.36)$$

At small distances along the interface relative to the interfacial plastic zone radius, r_I , the tractions appear to remain constant for increasing or decreasing x . Thus, by observation of the traction behavior, the stress potential for a semi-infinite body with constant normal and shear surface tractions across half of its free surface could be obtained directly. Note, Eq.(4.36) is the stress potential for such a semi-infinite body, except that the coordinates X and Y are normalized by the plastic zone radius along the interface.

Timoshenko and Goodier (1970) pointed out that prescribing only the surface tractions and determining their resultant stress potential does not always uniquely characterize the stress field. Stress fields which require no surface tractions or displacement boundary conditions on the free surface ($y = 0$) can be arbitrarily superimposed. Due to these boundary constraints, certain restrictions are imposed on the otherwise arbitrary fields. Since no free-surface shear tractions are allowed in these fields,

$$\sigma_{zy}(X, Y = 0) = 0 \quad \Rightarrow \quad -\frac{\partial^2}{\partial X \partial Y} \phi(X, Y = 0) = 0, \quad (4.37)$$

and because no normal tractions are admissible,

$$\sigma_{yy}(X, Y = 0) = 0 \quad \Rightarrow \quad \frac{\partial^2}{\partial X^2} \phi(X, Y = 0) = 0. \quad (4.38)$$

For small values of X and Y as $R_I \rightarrow 0$, the most dominant field which satisfies these conditions is that of a uniform stress field parallel to the interface, defined such that $\sigma_{zz} = T\sigma_{ys}$. The stress potential for this uniform field is given by

$$\phi = \frac{1}{2}T\sigma_{ys}[Y^2]. \quad (4.39)$$

The total asymptotic stress potential for the elastic lower domain as $R_I \rightarrow 0$ is now assembled. Summing the various stress potentials, Eqs.(4.30) and (4.33), the total stress potential, expressed in a polar coordinate frame, is

$$\begin{aligned} \phi = & -\frac{S\sigma_{ys}}{\pi} [R_I^2 \ln(R_I) \sin^2(\gamma) + R_I^2 \gamma \sin(\gamma) \cos(\gamma) - R_I^2 \sin(\gamma)] \\ & + \frac{P\sigma_{ys}}{2\pi} [R_I^2 \gamma - R_I^2 \sin(\gamma) \cos(\gamma)] + \frac{1}{2}T\sigma_{ys} [R_I^2 \sin^2(\gamma)]. \end{aligned} \quad (4.40)$$

Asymptotic Characteristic

The stress components are obtained from Eq.(4.40) using Eqs.(4.30) to (4.32), and are converted to the polar coordinate frame used shown in *Figures 1.1* and *2.1* (via $\theta = \gamma - \pi$). The normalized stress components are expressed as

$$\begin{aligned} \frac{\sigma_{\theta\theta}}{\sigma_{ys1}} = & -\frac{S}{\pi} [(1 + 2 \ln(R)) \sin^2(\theta) + (\pi + \theta) \sin(2\theta)] \\ & + \frac{P}{\pi} [\pi + \theta - \sin(\theta) \cos(\theta)] + T [\sin^2(\theta)], \end{aligned} \quad (4.41)$$

$$\begin{aligned} \frac{\sigma_{rr}}{\sigma_{ys1}} = & -\frac{S}{\pi} [2 \ln(R) \cos^2(\theta) - (\pi + \theta) \sin(2\theta) - \sin^2(\theta)] \\ & + \frac{P}{\pi} [\pi + \theta + \sin(\theta) \cos(\theta)] + T [\cos^2(\theta)], \end{aligned} \quad (4.42)$$

and

$$\begin{aligned} \frac{\sigma_{r\theta}}{\sigma_{ys1}} = & \frac{S}{\pi} \left[\frac{1}{2} (1 + 2 \ln(R)) \sin(2\theta) + (\pi + \theta) \cos(2\theta) \right] \\ & - \frac{P}{\pi} [\sin^2(\theta)] - T [\sin(\theta) \cos(\theta)]. \end{aligned} \quad (4.43)$$

It is assumed here that the plastic zone radius along the interface, r_I , can be approximated by the characteristic plastic zone dimension, r_p , such that $R_I \approx R$.

The total stress state at any point in the elastic domain can be decomposed into the three individual components which describe the entire field. From both a physical and mathematical point of view, the uniform T-stress produces no startling or unusual features. The field which results from a uniform normal interfacial traction ($P\sigma_y$) produces normalized stress components of order P/π which are solely a function of angular location. The third field which arises, due to the uniform interfacial shear traction, is logarithmically singular as $R \rightarrow 0$ (and mathematically as $R \rightarrow \infty^+$). The stress components behave as $\sigma \sim [(S/\pi)\sigma_y \ln(R)]$ as $R \rightarrow 0$, indicating that large stresses are present and that yielding in the lower material domain is expected near the crack tip. *This means that the inclusion of non-linear deformation in the upper region does not completely eliminate the stress singularity at the crack tip; rather it only changes the relative degree of singularity at the crack tip.*

The actual asymptotic stress field is completely defined by substituting in the appropriate numerical values for S , P , and T . The numerical values of S and P are solely determined by the deformation pattern of the upper domain; however, the value of T is a function of the local asymptotic deformation and the far-field loads. In the traction-free crack-tip analyses the $M = 0$ "T-term" and associated eigenmode directly correspond to the uniform in-plane T stress. (In the boundary layer formulation the coefficient of the T-term is set to zero.) The value of T arrived at here does not include far-field loading effects and only reflects the interaction of the local crack-tip elastic-plastic fields with the elastic K-fields. The elastic far-field contribution in homogeneous cracks is typically small compared to the yield stress, but as pointed out by Larsson and Carlsson (1973), a non-zero T-stress does alter the local plastic fields.

The individual elastic stress fields are completely characterized when the precise numerical values of P , S , and T are determined from the numerical analyses. From the slip-line model used to describe the plastically deforming upper region, the interfacial traction coefficients P and S are extracted, and the value of T is obtained by matching the predicted behavior in the lower elastic region with the actual numerical results.

To determine the value of T , any number of matches can be made which theoretically should produce identical results; *e.g.*, matching the radial strain, ϵ_{rr} , along the interface. In the work described herein, T represents the average of matching σ_{rr} at $\theta = 0^\circ$ and $\theta = -180^\circ$, typically at $R = 0.01$. This is done in an attempt to minimize the effects of numerical noise.

Comparison

Comparisons between the asymptotic fields based upon the elasticity potential and those numerically calculated are now made. *Figure 4.19* shows the angular distribution of the normalized stress components for the case of a deformable aluminum medium atop a graphite substratum loaded with $\angle K = 0$ until $\zeta_0 = -2.70^\circ$ ($\epsilon = -0.07923$). In judging this comparison, one should bear in mind that $\sigma_{\theta\theta}$ and $\sigma_{r\theta}$ are mathematically required to match by definition of the boundary conditions imposed in obtaining the stress potential. The radial strain along the interface as a function of the $\ln R$ is plotted in *Figure 4.20* for the same conditions as in *Figure 4.19*. Here development of the asymptotic "logarithmically singular" solution is evident. The fields described by the elasticity potential, Eq.(4.40), represent the actual crack-tip fields at radial distances where $R_I < 0.05$ or (in terms of the normalized radial distance R) where $R < 0.01$. The additional restriction on R , as compared to R_I , is necessary to compensate for any overestimation that the assumption $r_I \sim r_p$ causes, since the characteristic dimension in the lower half-plane is r_I , not r_p . Clearly, sufficient agreement exists between the numerical result and the stress potential to justify use of the stress potential for describing the lower half-plane asymptotic crack-tip fields in SSY.

4.2.3 Parametric Study

This section explores the dependence of the SSY asymptotic crack-tip field on the ILPA (ζ_0) and on material properties, namely ϵ and ν_1 . The stress intensity factor angle ($\angle K$) is varied in an attempt to cover the full range of admissible ILPA for several values

Bi-material Crack-Tip Stresses $\epsilon = -0.07923$ $\zeta_0 = -2.70^\circ$ $R = 0.00551$

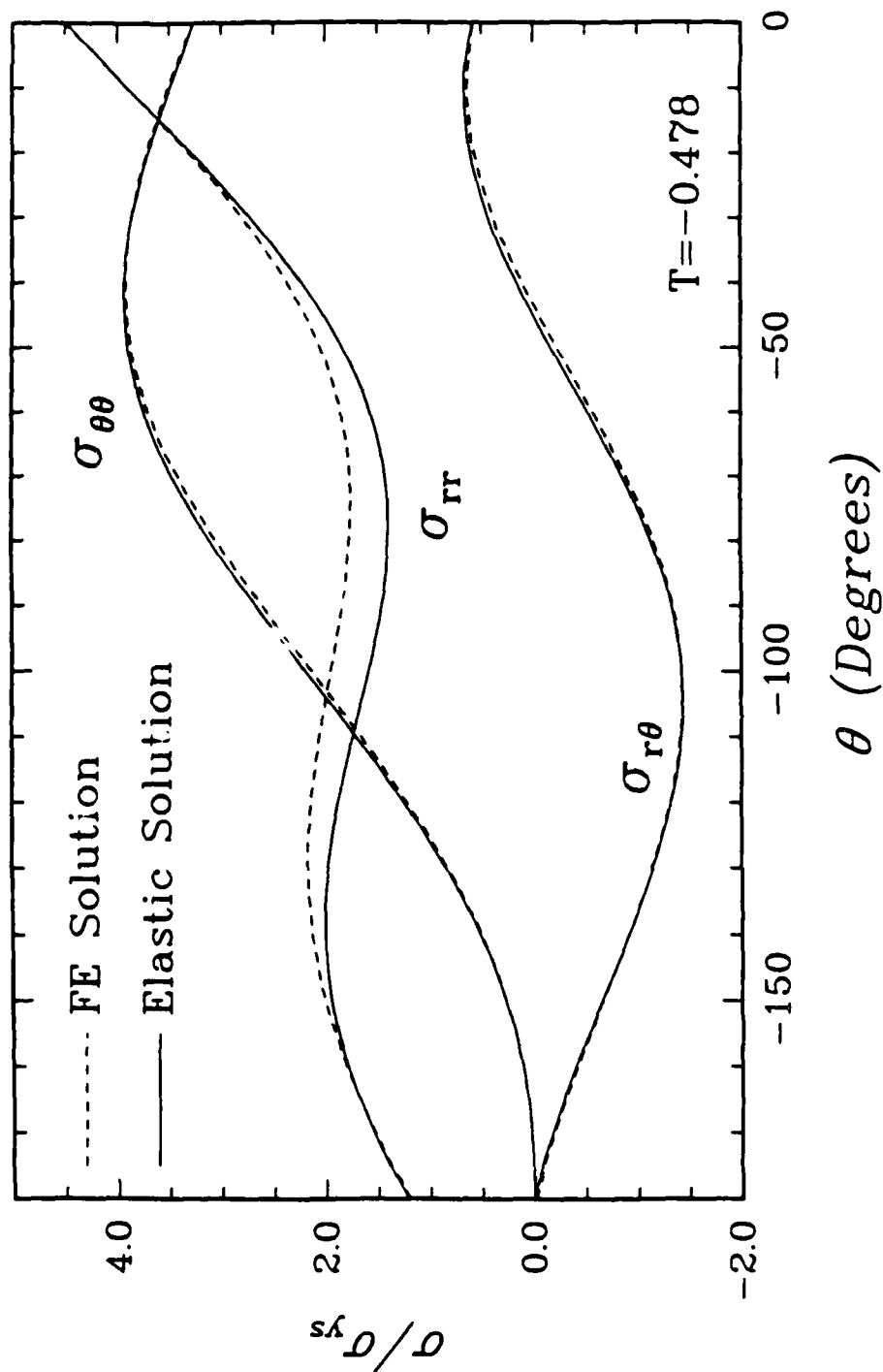


Figure 4.19 Normalized angular stress distributions in lower region of a traction-free interfacial crack-tip under SSY conditions; elastic/perfectly-plastic upper region bonded to an elastic substrate. Solid line solution obtained from finite element calculations and dashed line is inferred elasticity solution; $\epsilon = -0.07923$, $R = 0.00551$, and $\zeta_0 = -2.70^\circ$.

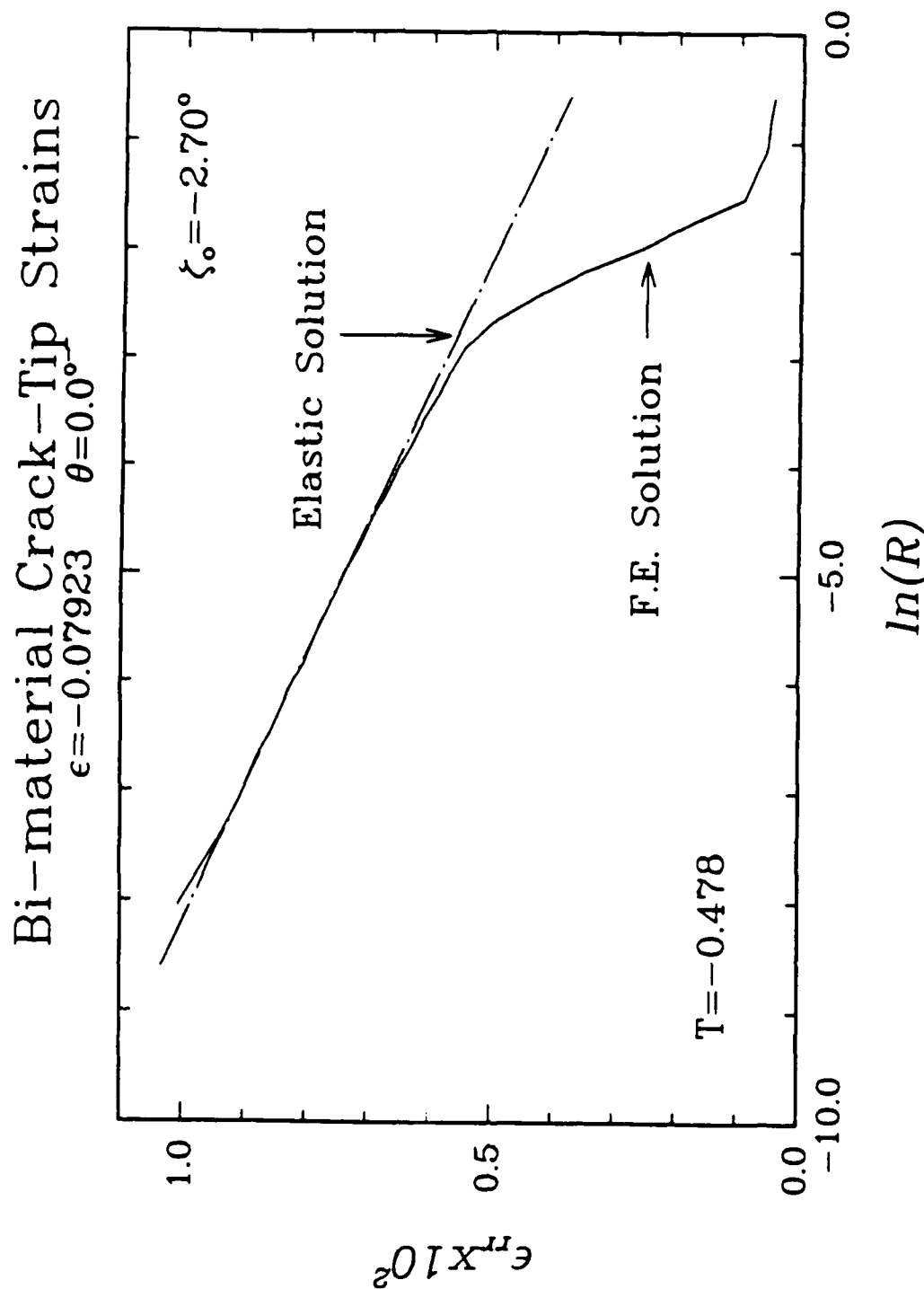


Figure 4.20 Interfacial radial strain variation with radial distance in lower region of a traction-free interfacial crack-tip under SSY conditions; elastic/perfectly-plastic material bonded to an elastic substrate. Solid line solution obtained from FE calculation and dashed line is inferred elasticity solution; $\epsilon = -0.07923$, $T = -0.478$, $\zeta_0 = -2.70^\circ$, and $\nu = 0.342$.

of ϵ . Various materials and material combinations are used to span nearly the entire plane strain range of ϵ for positive Poisson's ratio ($-0.170 < \epsilon < 0.170$). By use of six materials, whose isotropic elastic properties are listed in *Table 4.3*, the various values of ϵ obtained by pairing the materials are shown in *Table 4.4*. It is not possible to isolate the dependence upon the Poisson's ratio ν_1 , since varying ν_1 simultaneously alters ϵ , except in the degenerate case $\epsilon = 0$.

	μ (GPa)	E (GPa)	κ (GPa)	ν	Reference
"Soft"	1.00	2.04	0.708	0.02	Chamis, 1984 † Hertzberg, 1976 Hertzberg, 1976
Graphite	5.48	13.7	9.13	0.25	
Aluminum	26.1	70.1	73.9	0.342	
Steel	80.7	210.0	175.0	0.293	
"Stiff"	249.2	722.7	2409.0	0.45	
"Rigid"	∞	∞	∞	0.0	

† Approximate isotropic (transverse) properties from a Pitch-55 fiber.

Table 4.3 Idealized elastic material properties.

ϵ	β	Region 1 Upper Domain	Region 2 Lower Domain
-0.1700	0.4885	"Stiff"	"Soft"
-0.07923	0.2439	Aluminum	Graphite
0	0	Aluminum	Aluminum
0.03320	-0.1039	Aluminum	Steel
0.07796	-0.2400	Aluminum	"Rigid"
0.07923	-0.2439	Graphite	Aluminum
0.1700	-0.4885	"Soft"	"Stiff"

Table 4.4 Material combinations used in analyses to obtain the various ϵ .

For all the cases considered, the evolution of steady-state solutions, interfacial tractions, and strains are fundamentally the same as discussed previously. In the upper domain, the plastic zone boundary separates the elastic and yielding regions. The shape, size, and growth characteristics of this boundary, along with its dependence upon ϵ , $\angle K$, and ν_1 are essentially represented by the plastic zone approximation, Eq.(P2.6), and thus the ILPA, ζ_0 . The plastic zone grows in a periodic fashion with respect to ζ_0 , which,

along with ϵ , completely determines the plastic zone shape. *Figures P2.4 to P2.7* show the actual numerically calculated plastic zones for the various values of ζ_0 and ϵ along with the elastically approximated plastic zone shapes. The actual plastic zone features are always elongated ahead of the crack tip, as compared to the elastic approximation, while the features in the region along the crack face are "stunted" as compared to the elastic solution. In combinations of ζ_0 and ϵ in which the elastic approximation predicts small crack-face plastic zone lobes (usually $\zeta_0 > 0$), the elastic/perfectly-plastic material idealization totally suppresses the formation of any crack-face lobes. The suppression of these crack-face plastic zone lobes has a pronounced effect on the asymptotic SSY crack-tip fields, as elaborated upon earlier. Subsequent discussion is, therefore, limited to describing the asymptotic fields via representative forms and discussing unique or unusual features that arose in specific cases.

Plastic Crack-Tip Fields and Interfacial Traction

The tensile yield strength used for all analyses is 32.5 MPa, however, the numerical value used for σ_y is irrelevant in slip-line representation, because all stress components are linearly dependent upon σ_y . In the interpretation of these results, it is the initial shear strain to yield, γ_0 , which is important, since γ_0 is used to judge where the elastic strains are small relative to total strains, thereby defining the domain where the asymptotic slip-line solution accurately represents the stress field. In this parametric study the initial tensile yield strain ranges between 1.6% for the elastically "soft" material, and 0.0045% for the elastically "stiff" material.

The asymptotic crack-tip field can now be assembled for each individual case. From *Figure 4.10*, the schematic slip-line field, and *Table 4.5*, which lists the slip-line field angles, all the asymptotic stress fields considered are defined. As alluded to earlier, an elastic wedge with uniform surface tractions along its sides is necessary to complete some of the slip-line fields. Included in *Table 4.5* is the elastic far-field value of J . The stress potential and stress components for the elastic wedge are given in Appendix

B. Table 4.6 contains the values of the elastic wedge coefficients a_2 and c_2 required to match the numerical stress states. Although the general stress potential for such a wedge, Eq.(B.4), allows for singular radial stresses ($\sigma_{rr} \approx 1/r$), no such behavior is found in the numerical calculation. Because of this, the coefficients a_1 and c_1 in the potential, Eq.(B.4), are zero.

ϵ	ζ_0	$\angle K$	J MPa m	α	η	γ	ξ
-0.07923	29.1°	26.6°	7.713×10^{-2}	0°	83° (76°)	97°	84°
-0.07923	4.62°	0°	4.853×10^{-2}	0°	135°	45°	0°
-0.07923	-25.0°	-26.6°	9.552×10^{-3}	0°	135°	45°	0°
-0.07923	-41.4°	-45.0°	6.094×10^{-2}	61°	74°	45°	0°
-0.07923	-57.2°	-63.4°	3.428×10^{-2}	80°	55°	45°	0°
-0.07923	-81.8°	-90.0°	2.191×10^{-2}	90°	45°	45°	0°
0	0°	0°	5.066×10^{-2}	0°	129° (115°)	51°	49°
0.03320	0.127°	0°	2.986×10^{-2}	0°	123° (117°)	57°	56°
0.03320	-46.2°	-45.0°	1.453×10^{-2}	88°	47°	45°	0°
0.07923	-0.980°	0°	0.1159	47°†	83° (77°)	50°	44°
0.1700	-1.08°	0°	0.7291	74°	61°	45°	0°

ϵ	ζ_0	P	S	T
-0.07923	2.91°	1.83	$1/\sqrt{3}$	0.42
-0.07923	4.62°	3.22	$1/\sqrt{3}$	-0.48
-0.07923	-25.0°	3.22	$1/\sqrt{3}$	-2.3
-0.07923	-41.4°	1.99	-0.31	-0.9
-0.07923	-57.2°	1.88	-0.54	-1.2
-0.07923	-81.8°	1.48	$-1/\sqrt{3}$	-0.95
0	0°	3.21	$1/\sqrt{3}$	-1.10
0.03320	0.127°	3.14	$1/\sqrt{3}$	-1.56
0.03320	-46.2°	1.69	-0.57	-0.68
0.07923	-0.980°	2.68†	0†	-0.96
0.1700	-1.08°	2.11	-0.49	-0.55

Table 4.5 Traction-free crack-tip slip-line angles and traction coefficients for various values of ϵ and applied K . The slip-line angle $\xi_1 = 0$ except as noted; † - $\xi_1 = 20^\circ$.

Hydrostatic noise present in the deforming constant state sectors limited the analyses resolution for certain cases. Crack-tip fields which contained interfacial elastic wedges or interfacial constant state sectors (with $\alpha < 90^\circ$), probably contained cusps.

The stress state weakly depended upon R along the interfacial constant-state/fan border ($\theta = \alpha$), however conclusive verification of a cusp presence was not possible due to the limited extent of the mesh. For some cases hydrostatic noise in interfacial constant state regions perturbed interfacial normal tractions and stresses in the lower elastic region appreciably, and this limited the resolution of the T -stress. It should be noted that in inelastic sectors hydrostatic noise alone did not severely restrict identification of asymptotic crack-tip fields because deviatoric stresses and the shear strain, which were unaffected by hydrostatic pressure, were used.

The asymptotic traction-free crack-tip fields and interfacial tractions for an elastic/perfectly-plastic media adjoint to an elastic substratum are qualitatively identifiable for the full range of admissible ζ_0 , and are outlined for the material combination where the upper region is aluminum ($\nu = 0.342$). The following discussion is only schematic, and based upon the data, the actual asymptotic slip-line fields are (only) mildly dependent upon ν and ϵ . *Figure 4.21* qualitatively depicts the anticipated slip-line angles as a function of ζ_0 and (selective) known data points are represented by a "+". The associated assemblage of asymptotic crack-tip sectors, sketched schematically in *Figure 4.22*, shows the evolving generic crack-tip behavior with respect to the ILPA and simulates the crack-tip evolution for monotonically increasing proportional loading. For positive values of ϵ and fixed $\angle K$, the crack-tip fields evolve with increasing load in the direction of increasing ζ_0 . The arrows on the sector boundaries indicate the direction that each boundary moves as ζ_0 increases.

ϵ	ζ_0	a_2	c_2
-0.07923	29.1°	0.153	-0.113
0	0	-0.221	-0.053
0.03320	0.127°	-0.185	-0.080
0.07923	-0.980°	-0.228	-0.040

Table 4.6 Interfacial elastic wedge coefficients.

A natural separation in the asymptotic crack-tip fields occurs at $\zeta \approx 0^\circ$. For negative ILPA ($\zeta_0 < 0$) the crack-tip fields are fully plastic and consist of only fan and constant

Bi-material Crack-Tip Fields Schematic Evolution of Asymptotic Slip-Line Field

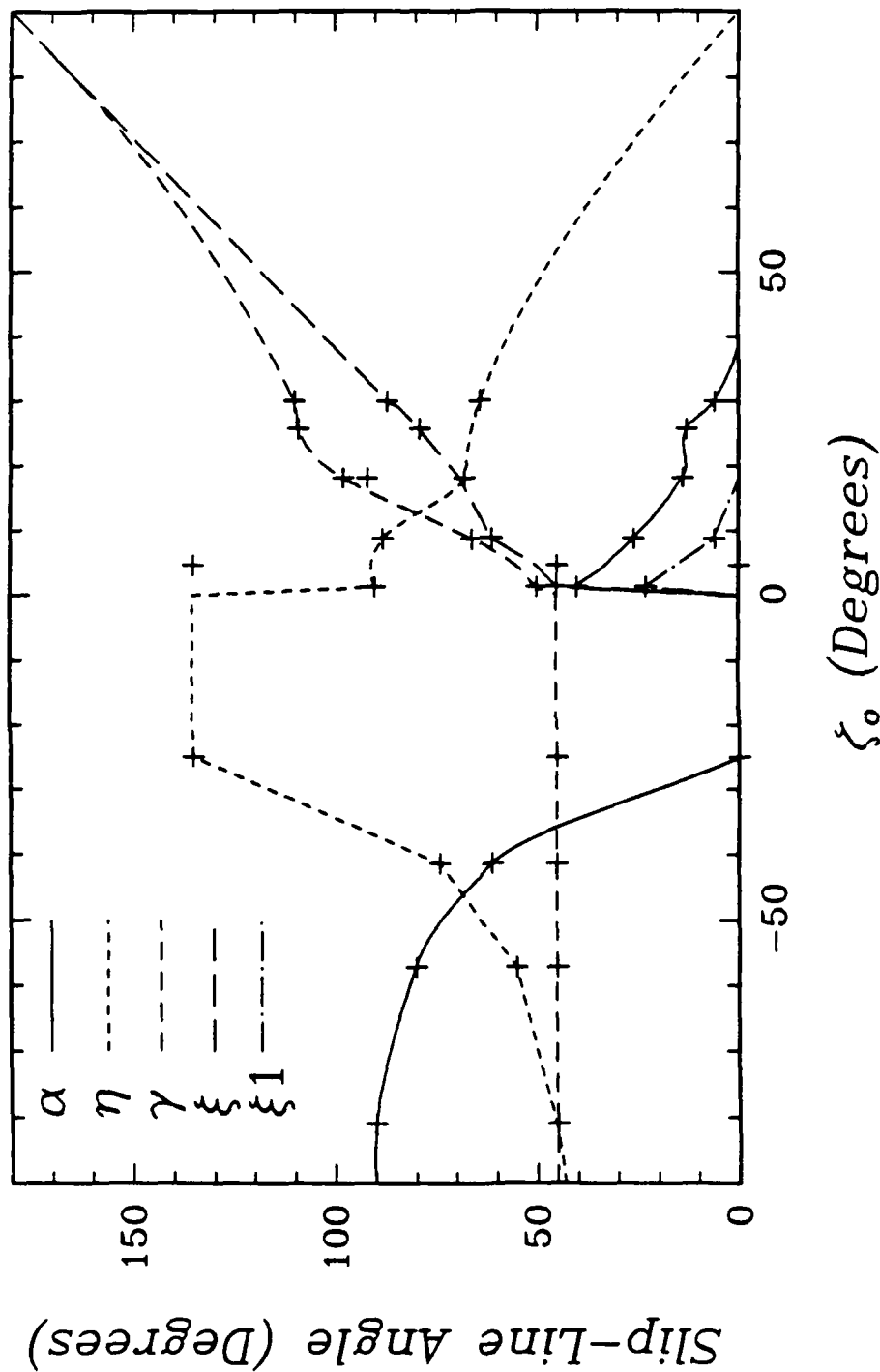


Figure 4.21 Schematic asymptotic slip-line angle evolution with the ILPA for an elastic/perfectly-plastic material ($\nu \approx 0.342$) atop an elastic substrate, for $\zeta_0 \leq 0$ ($\epsilon = -0.07923$), or atop a rigid ($\epsilon = 0.07796$) substrate, for $\zeta_0 > 0$. Known data points are shown by "+" marks.

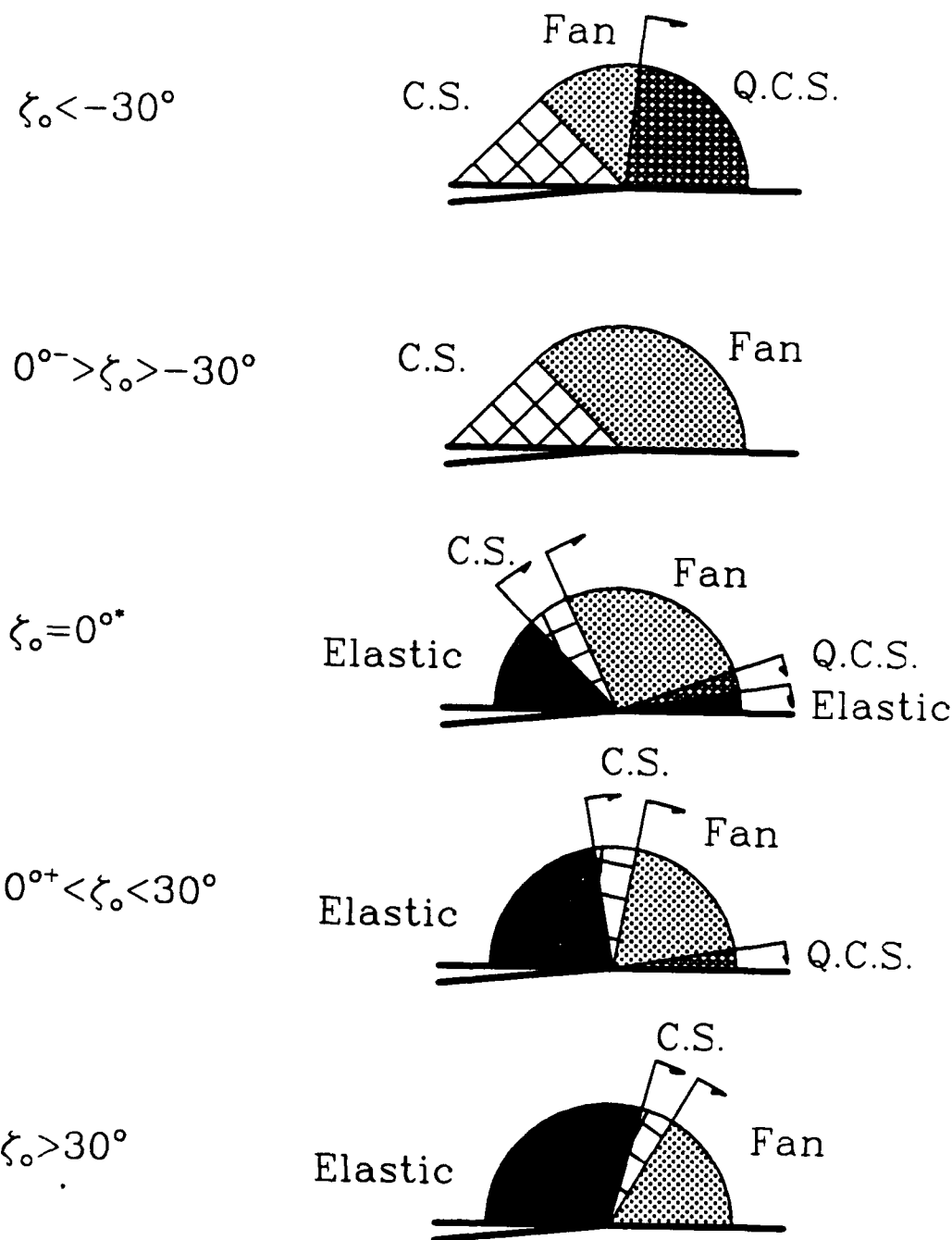


Figure 4.22 Schematic evolution of asymptotic slip-line, fields as a function of ζ_0 , for an elastic/perfectly-plastic material bonded atop an elastic or rigid substrate. Figure based upon data for $\epsilon = -0.07923$ when $\zeta \leq 0$ and $\epsilon = 0.07796$ when $\zeta_0 > 0$ with $\nu = 0.342$.

state sectors. To meet the traction-free crack-face boundary condition, a constant state sector always exists along the crack face which extends 45° ($\gamma = 45^\circ$). For ζ_0 between -90° and -30° , an interfacial quasi-constant state region is present whose angular extent (α) varies from 90° when $\zeta_0 = -90^\circ$ to 0° when $\zeta_0 \approx -30^\circ$. The interfacial tractions vary from their minimum ($t_s = -k$ and $t_n = 1.48\sigma_{ys}$) at $\zeta_0 = 90^\circ$ to their maximum ($t_s = k$ and $t_n = 3.22\sigma_{ys}$) when ζ_0 equals -30° . The interfacial tractions and assemblage of crack-tip sectors remain unchanged as the ILPA increases from $\zeta_0 \approx -30^\circ$ to some critical value near zero.

When the ILPA is positive, the crack-tip fields consist of both elastic and plastic sectors. It is speculated that as ζ_0 increases and approaches zero, the stress state everywhere in the crack-face constant state region falls simultaneously below the yield stress, and this produces a crack-face elastic wedge which extends a minimum of 45° . Along the interface an elastic sector, with a quasi-constant state sector adjacent to it, emerges and whose appearance is speculated to be linked with formation of a local plastic-zone boundary kink. [From Eq.(P2.6) it appears that both ζ_0 and the angular location at which this kink forms are dependent upon ν and ϵ .] Adjacent to both elastic wedges are constant-state regions which in turn border opposite sides of a centered fan. Near the interface, a cusp boundary separates the fan and the constant state region. The angular extent of the interfacial constant-state region approaches zero ($\alpha \rightarrow 0$) as $R \rightarrow 0$ and as ζ_0 increases to approximately 35° . The crack-face elastic wedge size increases with the ILPA from $\xi = 45^\circ$ at $\zeta_0 \approx 1^\circ$ to $\xi = 87^\circ$ at $\zeta_0 = 30^\circ$, and it is speculated that the size of the crack-face elastic wedge increases toward $\xi = 180^\circ$ as ζ_0 approaches 90° . Because various interfacial zones emerge, the interfacial tractions fluctuate appreciably over the range of positive ILPAs. The smallest interfacial shear traction, $t_s = 0.10\sigma_{ys}$, appears near $\zeta_0 = 1^\circ$, and then increases to its maximum value, $t_s = k$, for values of the ILPA equal to or greater than 35° . The normal interfacial traction decreases from its maximum value at $\zeta_0 = 0^\circ$ as the ILPAs increase.

Strain Distribution and CTOD

The strain fields are again represented by the $\gamma_{r\theta}$ distribution. The normalized strain distributions at six values of ζ_0 between -81.8° and 21.9° are plotted in *Figure 4.23* at $R = \gamma_0$ for $\epsilon = -0.07923$. To accommodate plotting, the minimum value on the ordinate axis is set to -15, which truncates two strain distributions. At $\theta = 0^\circ$ the values of $\gamma_{r\theta}(R/\gamma_0)$ are -899 and -49.8 when the ILPA (ζ_0) equals -57.2° and -81.8° , respectively. Drawn in *Figure 4.24* are the normalized strain distributions for four values of ϵ at $R = \gamma_0$ and $\zeta_0 \approx 0^\circ$. *Figure 4.24* (b) shows the strain distribution for $\epsilon = 0.03220$ when the ILPA equals -46.2° . In this figure, the truncated value of $\gamma_{r\theta}(R/\gamma_0)$ at $\theta = 0^\circ$ is -41.5.

To further summarize the strain fields, *Table 4.7* contains the numerically calculated magnitude of δ_{CTOD} , normalized by σ_{ys}/J , and its associated angle ω . (J is the far-field elastic J -Integral value.) For comparison, the elastically calculated CTOD angle, obtained by evaluating Eq.(P2.32) at $r = r_p$, is also given. The difference between ω and $\omega_{Elastic}$ is typically less than 30° , and ω is always less than $\omega_{Elastic}$.

ϵ	ζ_0	$\angle K$	J MPa m	$ \sigma_{ys}\delta_{CTOD}/J $	ω	$\omega_{Elastic}$
-0.07923	29.1°	26.6°	7.713×10^{-2}	1.008	21.4°	56.7°
-0.07923	4.62°	0°	4.853×10^{-2}	0.489	42.5°	76.7°
-0.07923	-25.0°	-26.6°	9.552×10^{-3}	0.621	83.1°	108.4°
-0.07923	-41.4°	-45.0°	6.094×10^{-2}	0.815	98.9°	130.1°
-0.07923	-57.2°	-63.4°	3.428×10^{-2}	1.086	107.2°	151.6°
-0.07923	-81.0°	-90.0°	1.867×10^{-2}	1.246	165.3°	179.9°
0	0°	0°	5.066×10^{-2}	0.598	81.2°	90°
0.03320	0.127°	0°	2.986×10^{-2}	0.668	88.8°	93.7°
0.03320	-46.7°	-45.0°	1.152×10^{-2}	1.364	130.7°	136.5°
0.07923	-0.980°	0°	0.1159	0.759	98.3°	99.9°
0.1700	-0.568°	0°	0.8387	0.876	107.3°	109.2°

Table 4.7 Traction-free crack-tip CTOD and CTOD angle (ω) for various values of ϵ and applied K .

From the information in the quarter wave-length analysis and this parametric study, the strain distribution in an aluminum upper region ($\nu = 0.342$) is qualitatively de-

Bi-material Crack-Tip Shear Strain $\epsilon = -0.07932$

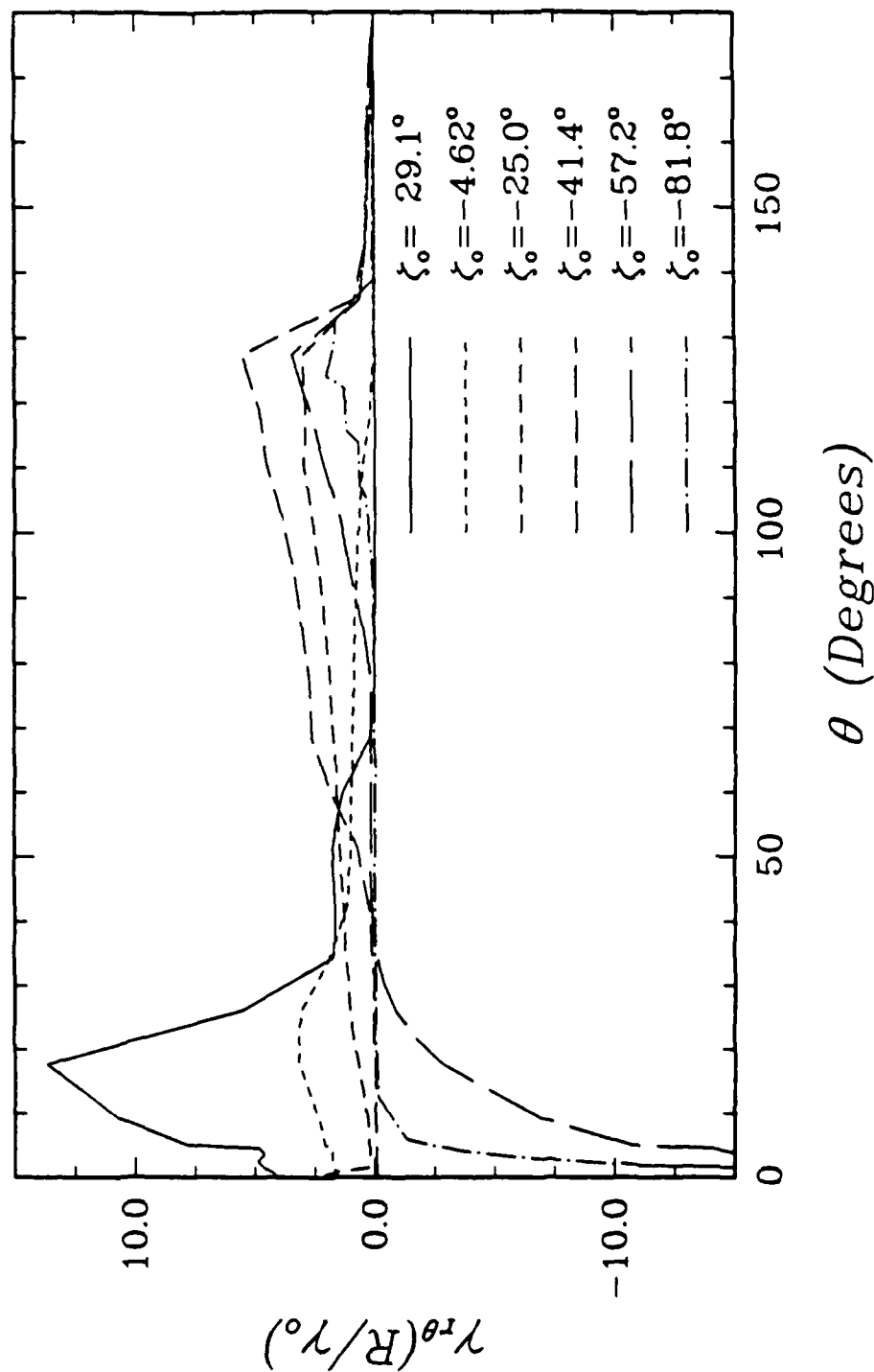


Figure 4.23 Angular variation of normalized $\gamma_{r\theta}$ shear strain deep in the plastic zone ($R \approx \gamma_0$) for a SSY traction-free interfacial crack-tip at various values of ζ_0 ; elastic/perfectly-plastic material atop a rigid substrate ($\epsilon = -0.07923$).

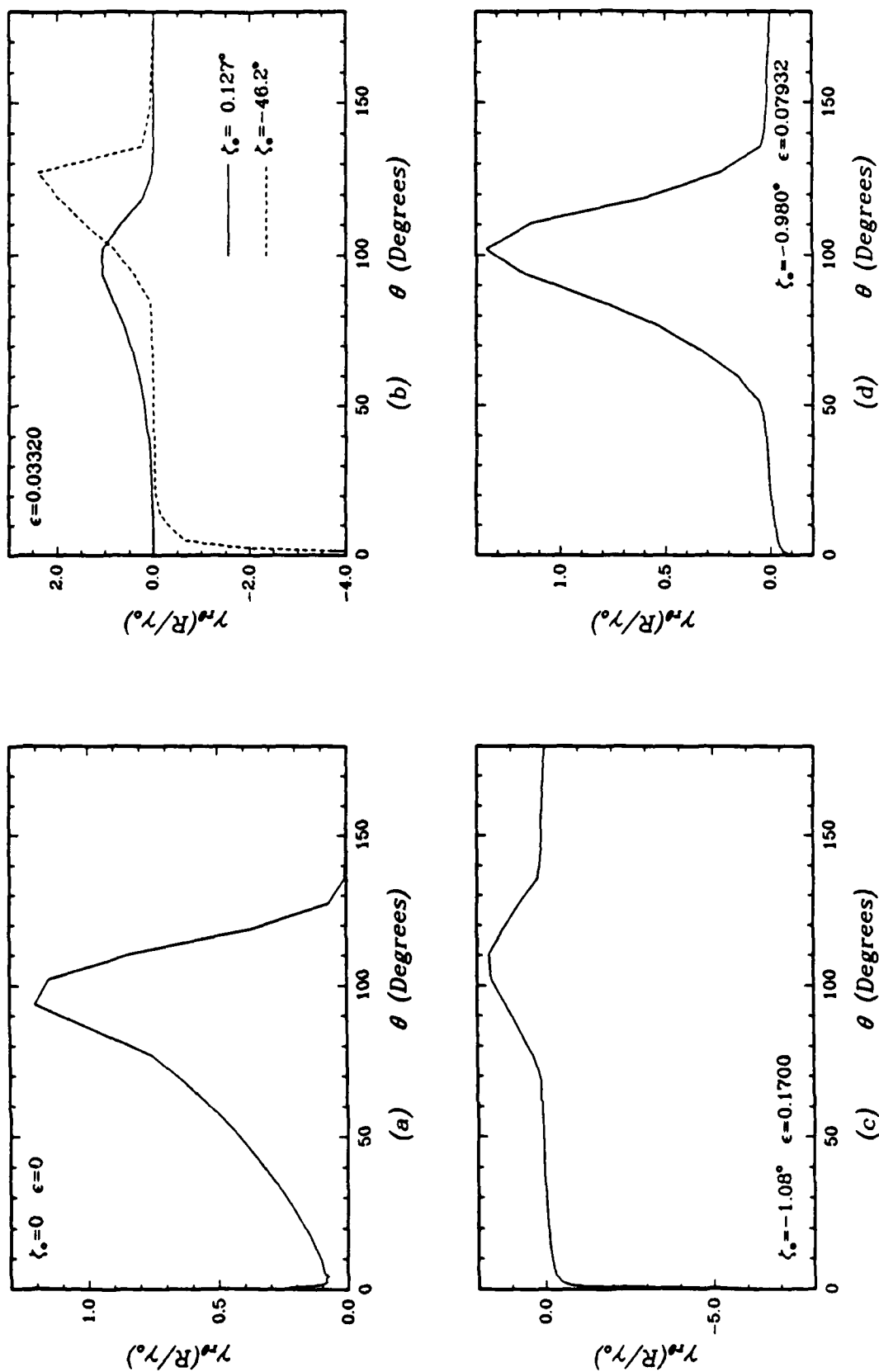


Figure 4.24 Angular distribution of normalized γ_{θ} shear strain deep within the plastic zone ($R \approx \gamma_0$) for SSY traction-free interfacial crack-tips; elastic/perfectly-plastic material atop a rigid substrate. (a) through (d) show distributions at various values of ζ_0 and ϵ .

scribed for the full admissible range of the ILPA. When the ILPA is between -90° and -50° , the largest strains (in magnitude) occur at the interface [$\gamma_{r\theta}(R/\gamma_0) < -40$], while modest positive strains [$\gamma_{r\theta}(R/\gamma_0) \approx 4$] are produced in the fan region near the crack-face constant-state sector ($\theta \approx 130^\circ$). As ζ_0 approaches zero, negligible interfacial strains are present and the location of maximum strains [$\gamma_{r\theta}(R/\gamma_0) \approx 3$] migrates from $\theta = 130^\circ$ to approximately $\theta = 90^\circ$. For positive ζ_0 , the location of maximum strains is in the centered fan, about 15° to 20° away from the crack-face elastic wedge, and moves toward the interface as the fan region shrinks. Finally, the maximum strains for ζ_0 between 0° and 30° are relatively small [$\gamma_{r\theta}(R/\gamma_0) \approx 2$].

When $\epsilon > 0$, large residual plastic shear strains would appear to accumulate and reside in portions of the non-singular sectors due to the continuously changing angular extent of the fan region. In centered fans the angular locations of the largest radial shear strains generally exist 10° to 15° away from the crack-face elastic-fan transition border, and for small to modest values of ϵ the asymptotic fields and ILPA change slowly with increasing magnitude of K ($\Delta\zeta_0/\Delta\|K\| = 2\epsilon/\|K\|$) as compared to the plastic zone size ($\Delta r_p/\Delta\|K\| = 2r_p/\|K\|$). Thus, by the time an elastic sector is positioned in a region previously occupied by a centered fan (where large strains existed), the plastic zone size and blunted crack-tip opening size would have grown by at least one order of magnitude or more. As the plastic zone size and CTOD grow, the inner limit of the radial extent of the "asymptotic crack-tip fields" ($r = r_p\gamma_0$), also grows. Therefore only a small portion of the elastic sector which is very near the crack tip could potentially contain large (previously singular) residual shear strains ($\gamma_{r\theta} \propto 1/r$), and, mathematically, these residual singular strains would be those that accumulated at $r \gg \gamma_0 r_p$.

Path Dependence of J -Integral

In the parametric study, local crack-tip J -Integrals were only estimated by the VCEM. Nine contours centered about the crack tip were evaluated, and the average of the second to fourth contours are tabulated in Table 4.8 for various ζ_0 and ϵ . The nine J

estimates typically vary by less than 5%, and except for the case where $\zeta_0 = -57.2^\circ$, no discernible trends are evident; i.e., J does not consistently increase or decrease as $R \rightarrow 0$. In the case where $\epsilon = -0.07923$ and $\zeta_0 = -57.2^\circ$, the J estimate increases by 89% from the ninth to the first contour (as $R \rightarrow 0$). However it is thought that this increase reflects the limited radial extent of the steady-state solution, and therefore it is insignificant. In general, the degree of crack-tip shielding or intensification is strongly dependent upon ζ_0 .

ϵ	ζ_0	$J_{VCEM}/J_{Elastic}$
-0.07923	29.1°	0.43
-0.07923	4.62°	0.77
-0.07923	-25.0°	0.94
-0.07923	-41.4°	1.06
-0.07923	-57.21°	1.11
-0.07923	-81.8°	0.25
0	0	0.90
0.03320	0.127°	0.92
0.03320	-46.2°	0.68
0.07923	-0.980°	0.97
0.1700	-1.08°	0.92

Table 4.8 Local J -Integral values, normalized by the elastic far-field value of J , estimated by the VCEM for various values of ζ_0 and ϵ .

Conclusion

The bi-material traction-free crack-tip fields for an elastic/perfectly-plastic material atop an elastic (or rigid) medium are represented by perfectly-plastic slip-line theory in the upper region and by an elasticity potential in the lower region. This representation is accurate at radial distances less than 1% to 5% of the characteristic plastic zone dimension r_p . The local stress and strain fields are strongly dependent upon the ILPA (ζ_0) and modestly dependent upon the bi-material constant (ϵ) and the Poisson's ratio of the plastically deforming media. No oscillations exist in elastic/perfectly-plastic bi-material crack-tip fields, however, cusps are found in some crack-tip fields which couple portions of the stress state to the radial distance from the crack-tip.

In the upper region, plastic deformation completely surrounds the crack tip for most values of ϵ when the ILPA is negative, thus the interfacial tractions are bounded between $|t_s| \leq k$ and $1.48 < t_n/\sigma_{ys} < 3.22$. In loadings where the ILPA is less than -50° , extremely large shear strains accumulate near the interface. The crack-tip behavior is significantly different for positive ILPA in the sense that elastic sectors are present. Interfacial elastic wedges are found embedded within the plastic zone, and a crack-face elastic sector grows (for $\epsilon > 0$) in angular extent as $|K|$ increases. Interfacial tractions vary between $0 \leq t_s \leq k$ and $1.7 < t_n/\sigma_{ys} < 2.9$, however, the interfacial strains are typically very small.

The asymptotic fields in the lower elastic region are represented by the superposition of three individual stress fields. The three stress fields are represented by a semi-infinite body with uniform:

1. Shear tractions ($t_s = S\sigma_{ys}$) across half of its free surface.
2. Normal tractions ($t_n = P\sigma_{ys}$) across (the same) half of its free surface.
3. Uniform stress (of magnitude $T\sigma_{ys}$) in the direction parallel to the free surface.

The free surface tractions simulate the conditions existing along the postulated intact interface in the immediate crack-tip proximity. Due to the jump in interfacial shear tractions, the elastic fields in the lower region are logarithmically singular and crack-tip yielding is expected. The radial strain along the interface is not zero, even though the interface is a line of zero extension (according to rigid-plastic slip-line theory).

The elastically-calculated and numerically obtained CTOD, the J -Integral, and the plastic zone shapes can differ appreciably. The CTOD angle ω was smaller than its elastic estimate, and no crack-face contact occurred over the range of ζ_0 explored. However, prior to establishing steady-state asymptotic crack-tip fields, oscillations present during initial plastic deformation may induce crack-face contact within the plastic zone for values of ζ_0 less than the elastically predicted critical values ζ_c , [Eq.(P2.35)]. Although plastic deformation reduces the range of admissible "traction-free crack-tip"

loadings, for many load states it also helps shield the crack-tip. The local J values are lower than the far-field elastic J -Integral by as much as 58%, but the significance of this is unclear.

4.3 Closed Crack-Tip Model

The local behavior around a closed bi-material crack tip varies much less than the local behavior around a traction-free crack tip. The approximated plastic zone shape in *Figure 2.2* is relatively independent of the precise values chosen for β and ν . Because a large lobe extends along the crack face, it is anticipated that the actual plastic zone in the upper medium will always completely surround the crack tip. Even if the same degree of plastic zone suppression occurs along the crack face, as seen in the traction-free model, the plastic zone should still completely engulf the crack tip. *Figure 2.3* shows the approximated plastic zone along with the location of actively yielding integration points from the numerical calculations, represented as black dots. To accommodate plotting, not all of the actively yielding integration points near the crack tip were drawn.

4.3.1 Plastic Fields

The transition from the remote K_{II}^c -field to the asymptotic plastic field is similar to that observed in the traction-free crack-tip model. A steady-state solution is achieved at radial distances less than 1% to 5% of the characteristic plastic zone dimension r_p^c . During this same transition period, the interfacial tractions and the now non-zero crack-face tractions also establish themselves. Similarity profiles of the normalized crack-face and interfacial tractions are shown as functions of the normalized radius, $R \equiv r/r_p^c$, in *Figure 4.25*. (The sign convention for positive normal traction is tensile stress, and shear traction has the same sign as σ_{re} .) No gaps open along the crack face, and the minimum crack-face traction occurs prior to reaching its steady state value near the plastic zone boundary.

Closed Crack-Tip Traction

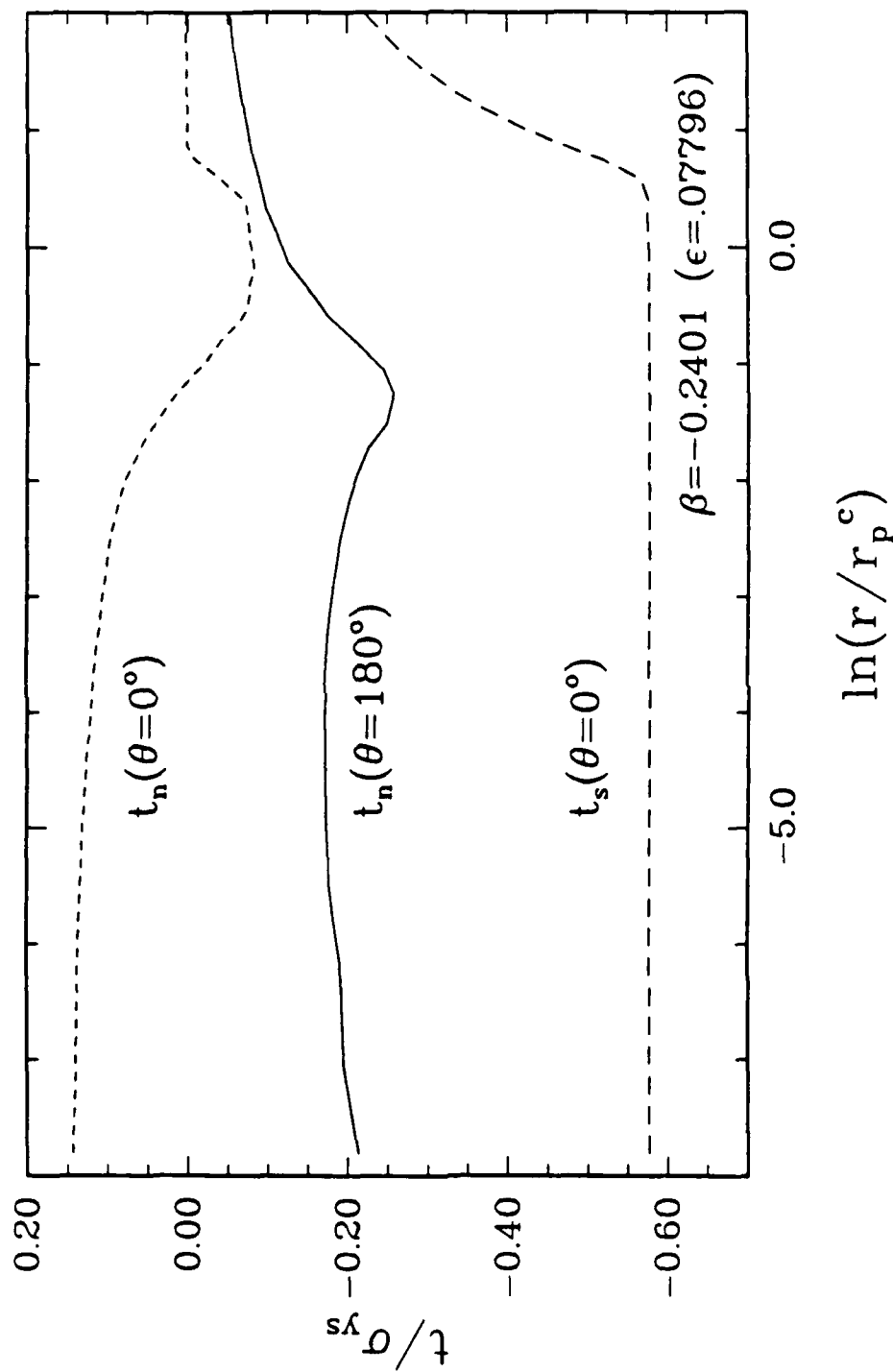


Figure 4.25 The interfacial $[t(\theta = 0^\circ)]$ and crack-face $[t(\theta = 180^\circ)]$ tractions for a closed bi-material crack tip under SSY conditions; elastic/perfectly-plastic upper region bonded to a rigid substrate.

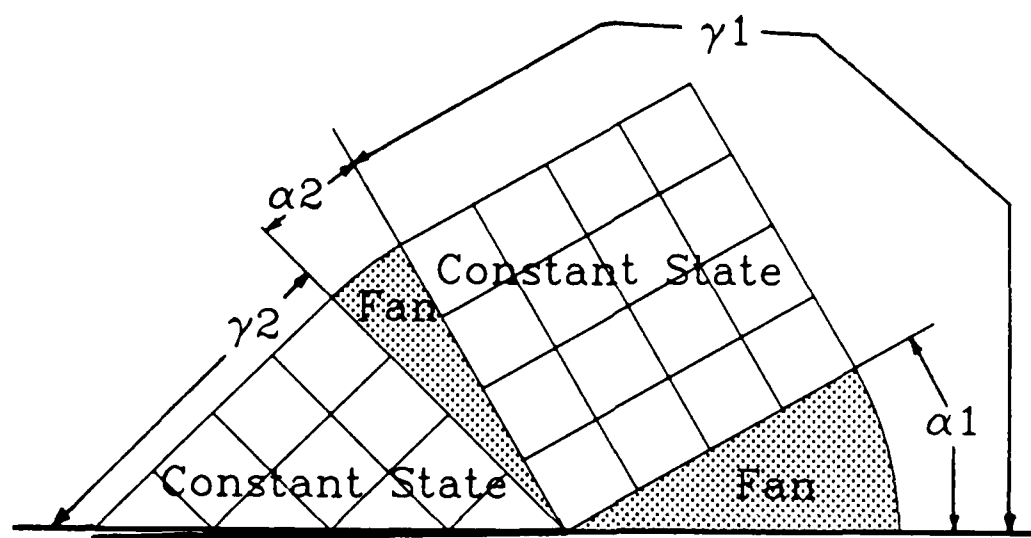


Figure 4.26 Slip-line field at a closed SSY interfacial crack for an elastic/perfectly-plastic upper region bonded to a rigid substrate. See *Table 4.9* for numerical values of indicated angles.

As $r \rightarrow 0$, the asymptotic interfacial and crack-face tractions t take on constant values of

$$t_n = \begin{cases} P\sigma_y, & \theta = 0^\circ \\ -Q\sigma_y, & \theta = -180^\circ, \end{cases} \quad (4.44)$$

and

$$t_s = \begin{cases} S\sigma_y, & \theta = 0^\circ \\ 0 & \theta = -180^\circ. \end{cases} \quad (4.45)$$

The asymptotic crack-tip stress state is completely constructed from fan and constant state regions. A schematic closed crack-tip slip-line field is sketched in *Figure 4.26*, while *Table 4.9* lists the schematic slip-line angles and the crack face and interfacial tractions obtained from the numerical calculations. (The slip-line angles for the closed crack-tip case were extracted from the numerical calculations in the same way as the traction-free crack-tip slip-line angles were.) Due to the crack-face contact, it is necessary to know the precise value of the normal traction on either the crack face or interface in order to construct the stress field in the upper domain. In this closed crack-face case, the crack-tip displacement represents sliding parallel to the interface, $\omega = 180^\circ$, and has a normalized magnitude of $|\delta_{CTOD}\sigma_y/J| = 1.914$.

β	ϵ	α_1	γ_1	α_2	γ_2	P	S	T	Q
-0.2401	0.07796	29°	119°	16°	45°	0.131	$-1/\sqrt{3}$	-	0.183

Table 4.9 Asymptotic SSY slip-line angles and traction coefficients for closed crack-tip model; elastic/perfectly-plastic material atop a rigid substrate.

Computationally, the shear strain at the fan near the crack face extends slightly beyond its purported angular extent. This is likely an artifact of the mesh discretization in this region, since the crack-face constant-state zone has no shear traction and there is no indication of an elastic wedge (see *Figure 2.9*). Thus the transition from constant state to centered fan must occur at $\theta = 135^\circ$. Indeed, the circumferential extent of the elements is nearly equal to the amount by which the shear zone in *Figure 4.27* extends beyond the fan/constant-state boundary. The numerical and assumed asymptotic stress

Closed Crack-Tip Strain Distribution

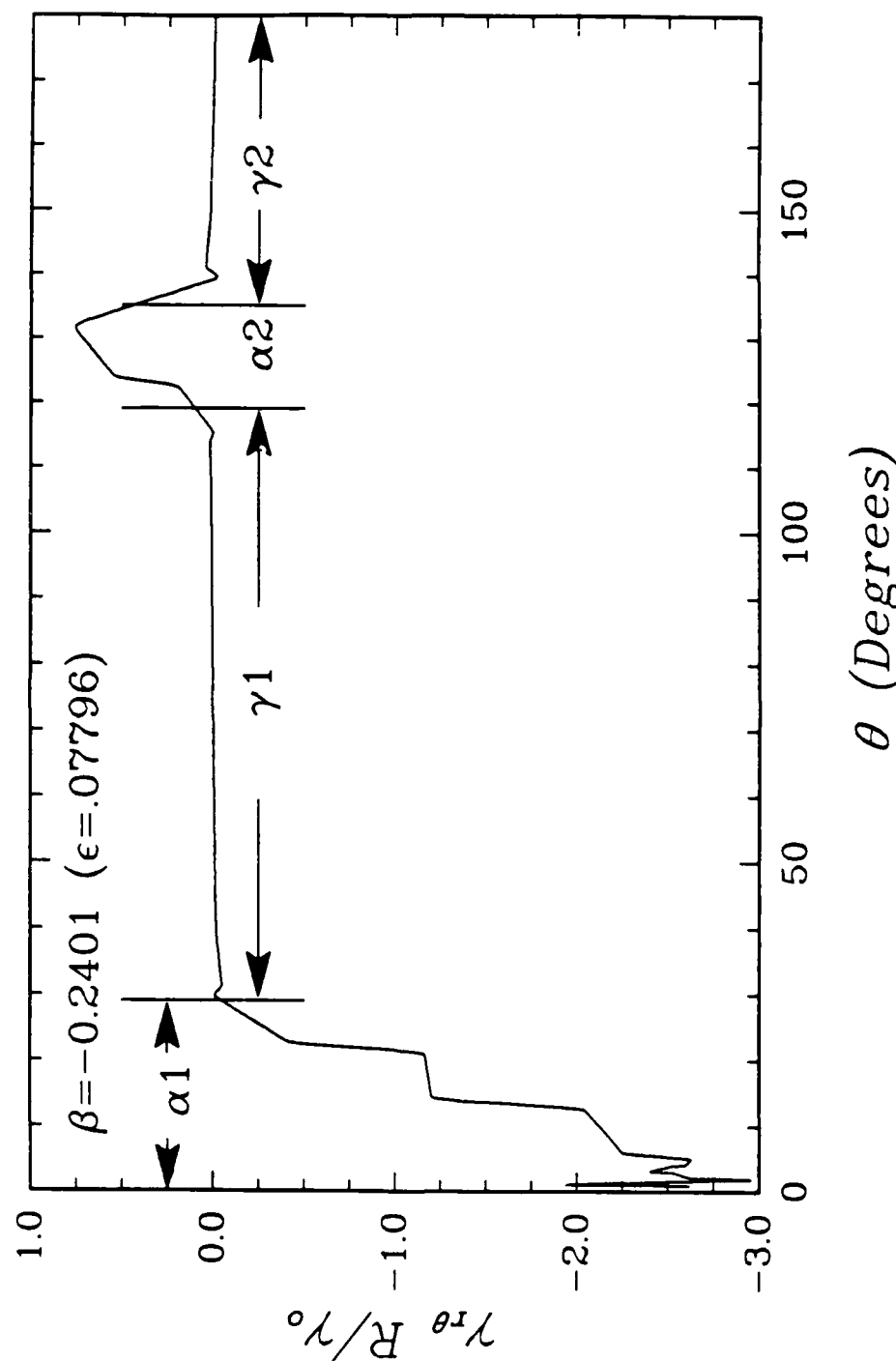


Figure 4.27 Circumferential variation of normalized $\gamma_{r\theta}$ shear strain deep in the plastic zone ($R = r/r_p^c = 3.12 \times 10^{-3}$), for an elastic/perfectly-plastic upper region bonded to a rigid substrate. Angular extents of centered fan and constant state regions of slip-line fields are also indicated.

distributions plotted in *Figure 4.28* differ only near the fan/constant-state borders, again over angular distances which correspond to the angular span of several elements. Excluding mesh discretization error, the assembled and numerically calculated crack-tip fields are in excellent agreement.

It is enlightening to compare the slip-line field, plastic zone shape, and the shear strain distribution. In *Figure 2.9*, the radial lines emanating from the crack-tip represent the slip-line field boundaries, and *Figure 4.27* is a plot of the asymptotic shear strain distribution. The shear strains are largest (in magnitude) at $\theta = 0^\circ$ (negative) and 130° (positive), which correspond to local maximum plastic zone radii. Near the center of the constant state regions the plastic zone radius exhibits a local minimum and the shear strain are nearly zero. It is evident that the radial shear strain distribution significantly influences the plastic zone shape and, to some extent, the local asymptotic stress field, and vice versa.

4.3.2 Elastic Field

Although the lower region was idealized in this work as being rigid, certain features of adjacent elastic fields can be ascertained in the same fashion as they were for the traction-free crack-tip model. Consider the conditions that exist along the common boundary of the elastic and plastic regions. The traction distribution beneath the plastic zone can be idealized such that they are described by Eqs.(4.22) to (4.23) and zero elsewhere. *Figure 4.29* is a schematic representation of the assumed traction distribution. The elastic stress potential for the closed crack-tip model is obtainable by superimposing an additional stress field, attributable to contact traction [$t_n(\theta = \pi) = -Q\sigma_{ys}$], to that previously obtained for the traction-free model Eq.(4.40). The total stress potential from the three individual traction contributions and the general uniform parallel stress field is

$$\phi = -\frac{S\sigma_{ys}}{\pi} \left[\frac{1}{2}y^2 \ln \left(\frac{x^2 + y^2}{(x + r_I)^2 + y^2} \right) + xy \arctan \left(\frac{y}{x} \right) + (x - r_I) y \arctan \left(\frac{y}{x + r_I} \right) \right]$$

Closed Bi-material Crack-Tip Stresses

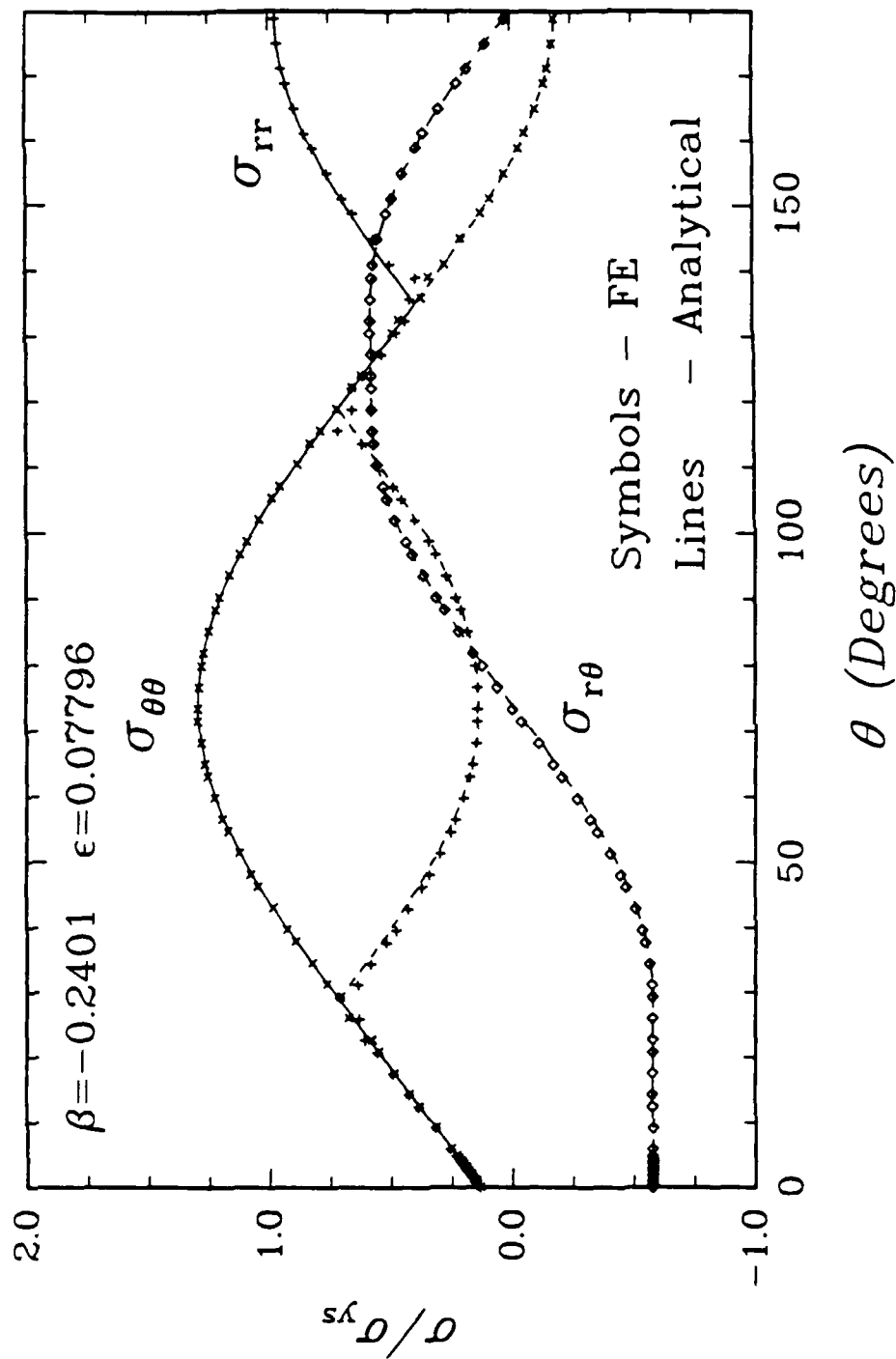


Figure 4.28 Normalized angular stress distribution, from a finite element calculation (plotted with symbols) of contact SSY in an elastic/perfectly-plastic upper region bonded to a rigid substrate and from the inferred slip-line field; $R = 3.12 \times 10^{-3}$, $\beta = -0.2401$ and $\epsilon = 0.07796$.

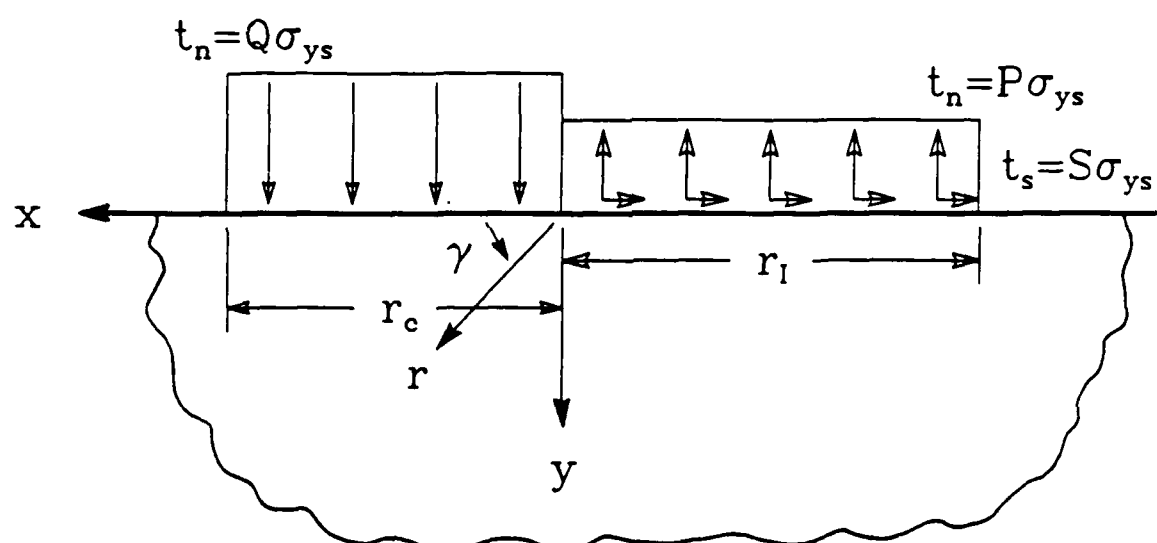


Figure 4.29 Idealized crack-face and interfacial traction distributions for a closed frictionless crack-tip in SSY, showing plastic zone radius along interface (r_I) and crack-face (r_c) and polar (r, γ) and Cartesian (x, y) coordinates.

$$\begin{aligned}
& + \frac{P\sigma_{vs}}{2\pi} \left[(x^2 + y^2) \arctan\left(\frac{y}{x}\right) - xy + (x + r_I) y \right. \\
& \left. - ((x + r_I)^2 + y^2) \arctan\left(\frac{y}{x + r_I}\right) \right] \\
& - \frac{Q\sigma_{vs}}{2\pi} \left[(x^2 + y^2) \arctan\left(\frac{y}{x}\right) + xy - (x - r_c) y \right. \\
& \left. - ((x - r_c)^2 + y^2) \arctan\left(\frac{y}{r_c - x}\right) \right] + \frac{1}{2} T\sigma_{vs} [y^2]. \tag{4.46}
\end{aligned}$$

Here r_c is the size of the plastic zone along the crack face ($\theta = 180^\circ$) and r_I is the size of the plastic zone along the interface ($\theta = 0^\circ$).

The asymptotic crack-tip behavior, as $r \rightarrow 0$, is found by defining $X = x/r_I$ and $Y = y/r_I$, assuming $r_c \approx r_I$, and assuming $X \ll 1$ and $Y \ll 1$. The asymptotic stress potential, as $R_I \rightarrow 0$, is given by

$$\begin{aligned}
\phi = & -\frac{S\sigma_{vs}}{\pi} \left[\frac{1}{2} Y^2 \ln(X^2 + Y^2) + XY \arctan\left(\frac{Y}{X}\right) - Y^2 \right] \\
& + \frac{P\sigma_{vs}}{2\pi} \left[(X^2 + Y^2) \arctan\left(\frac{Y}{X}\right) - XY \right] \\
& - \frac{Q\sigma_{vs}}{2\pi} \left[(X^2 + Y^2) \arctan\left(\frac{Y}{-X}\right) + XY \right] + \frac{1}{2} T\sigma_{vs} [Y^2], \tag{4.47}
\end{aligned}$$

or when expressed in a polar coordinate frame is given by

$$\begin{aligned}
\phi = & -\frac{S\sigma_{vs}}{\pi} \left[R_I^2 \ln(R_I) \sin^2(\gamma) + R_I^2 \gamma \sin(\gamma) \cos(\gamma) - R_I^2 \sin(\gamma) \right] \\
& + \frac{P\sigma_{vs}}{2\pi} \left[R_I^2 \gamma - R_I^2 \sin(\gamma) \cos(\gamma) \right] \\
& - \frac{Q\sigma_{vs}}{2\pi} \left[R_I^2 (\pi - \gamma) + R_I^2 \sin(\gamma) \cos(\gamma) \right] + \frac{1}{2} T\sigma_{vs} [R_I^2 \sin^2(\gamma)]. \tag{4.48}
\end{aligned}$$

The individual stress components can be obtained directly from the potentials via the relationships in Eqs.(4.2) to (4.4) or Eqs.(4.5) to (4.7).

In general, the elastic stress and strain field for the closed crack-tip model differs fundamentally only slightly from that derived for the traction-free crack-tip model. The addition of the crack-face tractions only contributes to the individual stress component terms of order $Q\sigma_{vs}/\pi$. For non-zero values of S , the stress field is logarithmically singular.

Comparison between the stresses based upon the elastic potential and the numerical calculations are not possible because the lower domain was idealized as being rigid. For

the same reason, explicit values for T were not expressed. As for agreement between the two solutions, one can only speculate that it would be comparable to that achieved in the traction-free crack-tip model (i.e., very good) and would be accurate at radial distances less than 1% of R .

4.3.3 Conclusion

The asymptotic stress field around a closed bi-material crack tip are completely represented by deforming slip-line fields in the upper domain and by an elastic potential in the lower domain. The asymptotic solution has interfacial shear tractions equal to the shear yield strength of the material (k) and small tensile normal tractions ($\sim 0.13\sigma_{ys}$). On the frictionless crack face, the asymptotic compressive normal tractions is also small ($\sim 0.18\sigma_{ys}$). The resulting plastic zone shape reflects certain features of the shear strain distribution and stress distribution.

Although no parametric study was performed, it is anticipated that asymptotic closed-face slip-line fields for an elastic/perfectly-plastic medium adjoint to a dissimilar elastic material are only weakly dependent on β . As discussed previously, the elastically-calculated plastic zone is rather insensitive to the precise values of β and ν used. In the degenerate case $\beta = 0$, the far-field elastic homogeneous mode II solution is recovered, it is therefore expected that as $\beta \rightarrow 0$, $t_n(\theta = \pm\pi) \rightarrow 0$. Finally, the homogeneous mode II slip-line field, whose slip-line angles are $\alpha_1 = 36.8^\circ$, $\gamma_1 = 126.8^\circ$, $\alpha_2 = 8.2^\circ$, and $\gamma_2 = 45^\circ$ for $\theta > 0$ (Hutchinson, 1968), does not differ substantially from the asymptotic field obtained for $\beta = -0.2401$.

4.4 Limitations

In this work the term "asymptotic crack-tip fields" has been extensively used to describe local crack-tip phenomena, but what are asymptotic fields? Webster (1979) defines an asymptote as "a line which continually approaches nearer to some curve, but, though infinitely extended, would never meet it." Fracture mechanics commonly

uses expressions to reproduce the dominant features and near-tip behavior which it terms as asymptotic. However these relationships are not truly asymptotic by definition in that they are only representative over a *discrete* interval because their underlying assumptions simplify and exclude a portion of the physics and mechanics. This section defines the limits for which the asymptotic characteristics are appropriate by identifying length scales for which the simplifications or omissions made in the mechanics are admissible.

In Chapter 2 it is established that the asymptotic elastic field equations [Eqs.(2.4) to (2.7)] represent SSY traction-free crack-tips for radial distances between $3r_p$ and $l/10$, where r_p is the characteristic plastic zone dimension and l is the characteristic geometric length. The outer limit defines the point where the local solution reproduces only 90% (in magnitude) of the full elasticity stress solution. (This happens because the asymptotic solution excludes the homogeneous far-field contribution.) The inner limit represents the point where the solution is significantly influenced by the exclusion of inelastic deformation. Deep within the plastic zone "steady-state inelastic" behavior appears at $r \approx 0.01r_p$, where deformation in plastic sectors is dominated by incompressible plasticity and the affects of compressible elasticity are generally negligible. Therefore inelastic (SSY) asymptotic crack-tip fields composed of some perfectly-plastic sectors describe the actual fields at radial distances less than $0.01r_p$. (Recall, it is necessary to account for compressible elasticity in constant state sectors when an elastic-wedge/fan transition exists.) Thus by examination of the mechanics or physics excluded, both bounds of the asymptotic elasticity solution and the outer bound of the inelastic asymptotic crack-tip solution have been quantified for SSY conditions. The minimum radial distance at which inelastic asymptotic crack-tip fields depict the actual crack-tip behavior is dependent upon various material attributes, mathematical assumptions, and micro or macro phenomena.

The discussion of limiting length scales, used to define the inner bound of the inelastic crack-tip fields, is divided into two parts. The first part identifies physical ma-

terial attributes in view of the necessary continuum assumptions to model them, and it qualitatively elaborates upon their associated mathematical length-scale restrictions. Quantitative results are not formally stated because the actual size varies considerably between different material systems. The second part quantitatively determines limitations imposed by modeling assumptions made and by the evolution of crack-tip features. The largest feature or mechanism is assumed to be the minimum distance for which inelastic asymptotic crack-tip fields are appropriate.

4.4.1 Physical Attributes

The physical material structure limits the representative element size necessary for continuum constitutive relationships to homogenize and accurately describe material behavior. For example, in crystalline materials deformation is produced by discrete movement of dislocations which each translate the crystal lattice by the interatomic distance. When many slip systems are active many discrete slip events must be averaged over a representative volume which is several hundred or thousand Burger's vectors per side, to achieve a continuum. Isotropy, as used in these analyses, poses additional restrictions because no macro preferential slip directions are allowed. Although many slip systems exist in metals [i.e., aluminum (FCC) has 12 possible independent slip directions], the representative volume must usually span many grain diameters to yield an isotropic response. Second phase and intermetallic particles restrict the minimum continuum volume size, when they exceed the primary grain size or if they preferentially impede directions of deformation. In non-metallic systems the minimum volume size is a function of some characteristic material dimension. For example, in particle reinforced composites the particle diameter or mean particle spacing is the characteristic material dimension, while in ceramics and polymers the characteristic dimensions are the grain size and length of the molecular chains, respectively.

In addition to the constraints associated with the bulk materials are those constraints which arise from the interfacial thickness and properties. Use of an ideal-

perfect interface assumes *a priori* that interfacial mechanical properties are equivalent or stronger and stiffer than the surrounding bulk media and that perturbations introduced by the actual interface, such as local crack-tip separation, are confined to a small region. As discussed in Chapter 1 the interfacial make-up and size scale varies widely and the interfacial resolution limits imposed must be assessed individually for each material system.

4.4.2 Mathematical and Evolutionary Limitations

When not restricted by physical attributes, it is anticipated that the inner range of the asymptotic solution is limited by:

1. The formation of a blunted crack-tip and the emergence of the CTOD as the characteristic length in the inelastic (SSY) asymptotic field.
2. The use of linearized kinematics.
3. The idealization that the lower domain behaves elastically.

To ascertain the limitations that these impose, an estimate for the critical length scale of each is made.

For planar homogeneous cracks, the CTOD (δ_{CTOD}) is typically estimated to be (Hellan, 1984)

$$\delta_{CTOD} = 0.6 \frac{J}{\sigma_{ys}}, \quad (4.49)$$

and an estimate of δ_{CTOD} for interfacial cracks is made by evaluating Eq.(P2.32) at $\zeta = \zeta_0$ and $r = r_p$ which yields

$$|\delta_{CTOD}| = \frac{4\sqrt{2}}{\pi\sqrt{1 + 4\epsilon^2}} \frac{J}{\sigma_{ys}}. \quad (4.50)$$

Equation (4.50) overestimates the homogeneous δ_{CTOD} by a factor of three, and, based upon the other data in Chapter 4 for an elastic/perfectly-plastic material atop an elastic medium, typically overestimates the actual $|\delta_{CTOD}|$ by a factor of 2 to 3. For

comparison purposes, it is convenient to compare δ_{CTOD} to r_p . Division of Eq.(4.50) by r_p and by a factor of 2 (to account for the overestimation) gives

$$\left| \frac{\delta_{CTOD}}{r_p} \right| = \frac{\sigma_{ys}}{2} \sqrt{\frac{2}{1+4\epsilon^2}} \left(\frac{1-\nu_1}{\mu_1} + \frac{1-\nu_2}{\mu_2} \right) \quad (4.51)$$

or

$$\left| \frac{\delta_{CTOD}}{r_p} \right| = \frac{\sqrt{6}}{2\sqrt{1+4\epsilon^2}} \gamma_0 \left[1 - \nu_1 + \frac{\mu_1}{\mu_2} (1 - \nu_2) \right]. \quad (4.52)$$

Here γ_0 is the initial yield strain of the material in the upper region and the subscripts 1 and 2 refer to the upper and lower domains, respectively. For many material combinations the normalized magnitude of the CTOD is of order $|\delta_{CTOD}/r_p| \approx O(\gamma_0)$.

Use of linearized kinematics fails when strains and rotations are no longer "small." To estimate the size of the strains and thereby infer the relative size of the rotations, the behavior of the largest strain component in a fan region, $\gamma_{r\theta}$, is considered. From Eq.(4.10) the asymptotic shear strain behavior in a fan region is approximately

$$\gamma_{r\theta} \approx A(\theta, t) \frac{\gamma_0}{R}, \quad (4.53)$$

where R is the normalized radial distance from the crack-tip and $A(\theta, t)$ is the angular distribution of shear strain. As stated previously, $A(\theta, t)$ is of order unity because at the edge of the plastic zone ($r = r_p$ or $R = 1$) the shear strain must just equal the yield shear strain ($\gamma_{r\theta} = \gamma_0$). With the assumption that $A(\theta, t) \approx 1$ and by use of the rather loose definition that strains of order unity are no longer small, the assumption of linearized kinematics is valid for radial distances such that

$$r > \gamma_0 r_p \quad \text{or} \quad R > \gamma_0. \quad (4.54)$$

For reference, a typical value of γ_0 for aluminum is 7.2×10^{-4} (Hertzberg, 1976).

In the lower domain use of an elastic material idealization is acceptable as long as the stress state is not sufficient to cause inelastic deformation. At the crack-tip the shear traction jumps by $|S\sigma_{ys}|$ from the crack-face to the interface, and this step-function jump in t , produces logarithmically singular stresses in the elastic domain

whenever $S \neq 0$. Plastic deformation is anticipated in the elastic half-plane for all non-zero values of S .

A "rough" interfacial plastic zone size is estimated by evaluating the elastic stress components at $\theta = 0^\circ$ and by determining the radial distance where the Mises equivalent stress equals σ_{ys2} , the yield stress of the "elastic" lower material. Substituting the stress components, Eqs.(4.41) to (4.23), into the Mises stress expression, Eq.(2.31) (retaining only the logarithmically singular portion of σ_{rr}), and solving for the radial distance r_{p2} at which $\bar{\sigma}_2 = \sigma_{ys2}$ yields (for $S \neq 0$)

$$\frac{r_{p2}}{r_p} \approx \exp \left\{ \frac{F P \pm \sqrt{(F P)^2 - 4D (3S^2 + D P^2 - (\sigma_{ys2}/\sigma_{ys})^2)}}{2DS/\pi} \right\}. \quad (4.55)$$

Here F and D are defined in Eqs.(P2.A.14) and (P2.A.15), respectively. For Eq.(4.55) to have physical significance, it is required that

$$\left(\frac{\sigma_{ys2}}{\sigma_{ys}} \right)^2 > 3S^2 + P^2 \left(D - \frac{F^2}{4D} \right). \quad (4.56)$$

When P and S take on their maximum observed values of $P = 3.27$ and $S = 1/\sqrt{3}$ the actual elastically inferred [not estimated by Eq.(4.55)] size of plastic deformation along the interface for $\nu = 0.3$ is $r_{p2}/r_p \approx 1.08 \times 10^{-2}$ for $\sigma_{ys2}/\sigma_{ys} = 3.0$ and $r_{p2}/r_p \approx 3.38 \times 10^{-5}$ for $\sigma_{ys2}/\sigma_{ys} = 4.0$. A more intuitive understanding is obtained from examination of *Figure 4.90*. By use of the stress expression, Eqs.(4.41) to (4.23) the elastically-calculated plastic zone in the lower half-plane is plotted for $P = 3.27$, $S = 1/\sqrt{3}$, and $T = -0.5$ for several ratios of σ_{ys2} to σ_{ys} ; i.e., $\sigma_{ys2}/\sigma_{ys} = 2.5, 3.0, 3.5, 4.0$, and 4.5 . The characteristic plastic zone size of the upper domain (r_p) is used to normalize the scale of this figure. Because the stress fields are logarithmically singular, the size of the plastic zone decays rapidly as σ_{ys2}/σ_{ys} increases. The elastically-calculated plastic zones for $\sigma_{ys2}/\sigma_{ys} \geq 3.5$ are not resolvable on this size scale. For material combinations where σ_{ys2}/σ_{ys} is greater than 3, the maximum plastic zone radius extends less than 0.1% of r_p for the extreme interfacial conditions and, for many metallic polycrystallines, $r_{p2}/r_p < \gamma_0$.

Lower-Elastic Plastic Zone

$$\nu=0.342 \quad P=3.27 \quad S=k \quad T=-0.5$$

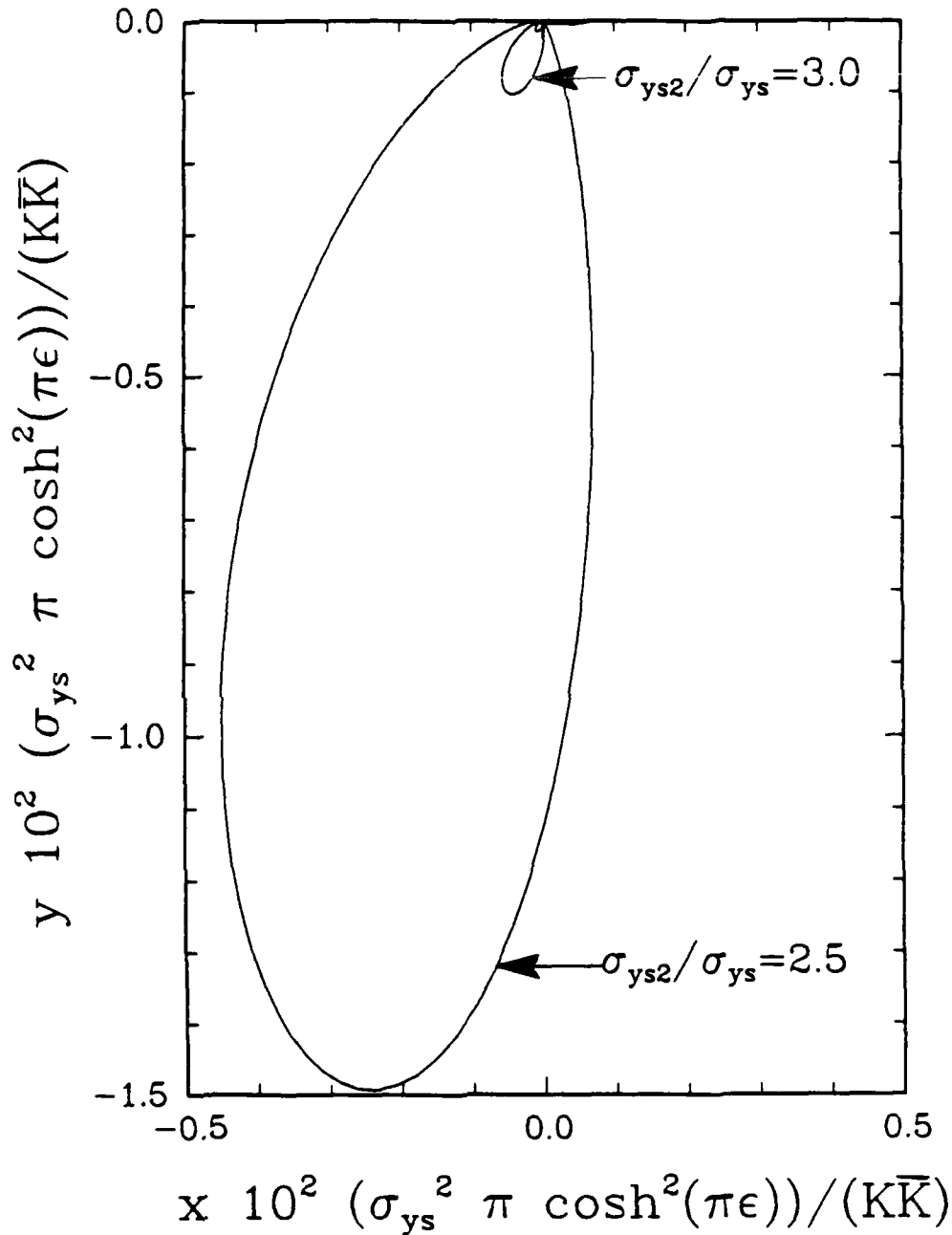


Figure 4.30 Elastically calculated yield zone for lower elastic half-space with constant normalized shear ($t_s = 0.57$) and normal ($t_n = 3.27$) tractions applied on $y = 0$ for $x \geq 0$. Scales are normalized with respect to the characteristic traction-free plastic zone radius.

When the specific material structure is excluded, it is evident that the SSY asymptotic crack-tip fields presented in sections 4.2 and 4.3 are usually applicable over the normalized radial range of $\gamma_0 < R < 0.05$. At radial distances smaller than this the assumptions of linearized kinematics and a mathematically sharp crack tip are violated, and the use of an elastic lower half-space may be inappropriate. When material structure is considered, the restrictions arise from the minimum representative element size necessary to model the material behavior as a continuum, and the actual limiting factor are only established after particular materials and their properties are identified.

Chapter 5

Summary and Discussion

In this final chapter, a brief summary qualitatively highlighting the major features of the two interfacial crack-tip models will be presented. It will touch on the major aspects of both the elasticity and plasticity solutions. Observations regarding some solution aspects and associated implications will also be discussed. This includes observations regarding crack-face conditions and the ILPA, and the anticipated effect that altering material combinations would have on interfacial separation. Finally, some suggestions regarding the direction of further work will be made.

5.1 Summary

Before reviewing specific details of the interfacial fracture mechanics, an overview of the various analyses and components which interconnect, forming a complete interfacial crack framework, is presented. Reviewing of the two commonly accepted interfacial crack-tip elasticity solutions identifies the parameters which quantify the asymptotic elastic fields, their admissible ranges, and the dominant features present in each. When appropriate, corresponding relationships between various elastic variables present in each idealization provide a link between the two models. Using the elasticity solutions, approximate descriptions of contained inelastic deformation embedded in a dominant asymptotic elastic crack-tip field (SSY) are given, along with the parameters needed to describe the plastic zone boundary. Presumably, the same variables which uniquely

relate the plastic zone shape to the asymptotic elastic solution also uniquely relate the asymptotic (inelastic) crack-tip behavior to the asymptotic elastic solution. Far-field loads producing physically admissible elastic crack-tip conditions are determined by excluding the crack-face behavior in regions where inelastic deformation is anticipated. Corresponding limits on the inelastic crack-tip parameters are then formulated, thereby reducing the spectrum of admissible inelastic crack-tip loadings. Finally, for a specific constitutive idealization, the complete range of asymptotic inelastic crack-tip fields is quantified as a function of the inelastic parameters. The discussion which follows details this schematic overview.

The asymptotic elastic behavior of interfacial cracks which occur between dissimilar isotropic media is reviewed. Traction-free crack-face boundary conditions result in oscillatory elastic fields as well as crack-face contact and mathematical interpenetration. Use of the complex traction-free bi-material stress intensity factor K requires defining both a magnitude and phase angle. (Two parameters are necessary to describe the elastic singularity of a traction-free interfacial crack.) Some ambiguity exists in expressing K because the phase angle of K changes when different length units are used. Physically inadmissible crack-face interpenetration is eliminated by considering a closed (frictionless) crack-tip model. This model contains no oscillatory fields, and its asymptotic nature is similar to that of the homogeneous mode II solution. The sign of the (scalar) closed bi-material stress intensity factor, K_{II}^c , is restricted to ensure compressive normal crack-face tractions. When defining the elastic singularity of a closed frictionless interfacial crack, only one parameter is required. Finally, both elastic crack-tip models predict unbounded stresses as the crack tip is approached.

For both crack-tip models, approximate SSY elastically-calculated plastic zones are obtained as the locus of points where the elastically-calculated Mises stress equals the tensile yield stress. This is the first time such an approach has been used to "semi-formally" extract the inelastic behavior around interfacial crack tips. From this approach, it is found that traction-free crack-tip plastic zones grow in a periodic manner,

with respect to the ILPA, $\zeta_0 = \angle \mathbf{K} + \epsilon \ln \frac{K\bar{K}}{\sigma_y^2 \pi \cosh^2(\pi\epsilon)}$, and scale approximately with the characteristic plastic zone dimension, $r_p = K\bar{K}/(\sigma_y^2 \pi \cosh^2(\pi\epsilon))$; however, the plastic zone shapes change continuously as $\|\mathbf{K}\|$ increases since ζ_0 also changes with increasing $\|\mathbf{K}\|$. The elastically-calculated plastic zone expression modestly represents the overall size and features of the plastic zone for strain hardening and elastic/perfectly-plastic materials atop rigid or elastic substrates.

For positive ζ_0 , the elastically-calculated plastic zone expression predicts crack-face plasticity; however, for elastic/perfectly-plastic materials bonded to an elastic or rigid substrate, no crack-face plastic deformation is observed. (This is an unexpected feature since in homogeneous plane-strain stationary and quasi-static growing crack tips, active plastic deformation occurs on the crack flanks.) The closed crack-tip plastic zone approximation weakly depends upon the bi-material constant and scales with the characteristic closed plastic zone dimension, $r_p^c = 3K_{II}^2/2\sigma_y^2$. No changes in the closed plastic zone shape occur with increased load, and the homogeneous mode II characteristics are completely recovered when the bi-material constant is equal to zero. It is learned from the elastically-calculated plastic zone expressions, that it is necessary to have both a phase angle and a load magnitude to describe the inelastic traction-free crack-tip fields, while only a load magnitude and the assurance that a sufficiently large contact length exists are required to quantify the closed crack-tip fields.

The crack-tip loads which provide traction-free or closed crack-tips are approximately identified by determining when crack-face contact occurs outside the elastically-calculated SSY plastic zone. Previously, discussions concerning the admissibility of the two elastic crack-tip models usually eliminated one crack-face idealization based upon so called "physical" reasons; *e.g.*, "the crack must be traction-free because the contact length is extremely small and on the order of the interatomic spacing distance," or "the crack tip is closed since interpenetration is predicted and is physically inadmissible." This unified approach shows that both interfacial idealizations are admissible for SSY, and provides explicit mathematical expressions to define the loads producing traction-

free or closed crack tips. For the right hand crack tip of a Griffith crack geometry, the far-field loads which produce open or closed elastic crack-face conditions are mapped. A region, termed SSC, exists where, simultaneously, the contact length is small compared to the crack length and the plastic zone size is small with respect to the contact length. Explicit relationships between K and K_{II}^c are established for SSC based upon equivalent energy release rates. In general, determination of the appropriate elastic crack-tip model can be made for most geometries, however, the precise contact length and closed form stress intensity factors are only known for a few geometries.

The numerical procedure used in identifying the SSY asymptotic interfacial crack fields between an elastic/perfectly-plastic material and an elastic or rigid material required implementation of an effective inelastic constitutive integration operator and extension of the boundary layer formulation to bi-materials. These numerical reduction techniques were necessary, especially when one considers that each parametric analysis represents an investment of one hundred to three hundred computational hours, and the quarter wave-length analysis consumed more than seven hundred computational hours on one computational element of an Alliant FX-8 mini super-computer. To demonstrate that the boundary layer formulation had indeed been extended correctly for bi-materials, an example point load elasticity problem was performed.

The asymptotic (inelastic) traction-free crack-tip fields contained some very unusual features. The cusp and elastic sectors found in the SSY traction-free crack-tip solutions have not been observed before in homogeneous plane-strain (stationary or quasi-static) crack fields. These cusps couple the stress state in the quasi-constant state sector to the radial distance from the crack tip and propagate as ζ_0 changes or, for proportional monotonic loading, as $\|K\|$ increases. The elastic crack-face and interfacial sectors evolve with ζ_0 and may or may not contain residual plastic strain depending upon ζ_0 and the sign of ϵ .

Qualitatively, the traction-free SSY asymptotic fields for the complete range of admissible ζ_0 are assembled, and from this the crack-tip behavior for proportional

monotonically increasing loads is described. At fixed radial locations deep within the plastic zone, the SSY asymptotic fields are assembled from centered fans, constant state, quasi-constant state, and elastic sectors. Excluding the cusp effects, the crack-tip stress and strain fields are not oscillatory for an elastic/perfectly-plastic material bonded to an elastic or rigid material, unlike those obtained by Shih and Asaro (1987) for deformation theory based strain hardening materials. The asymptotic crack-tip fields continuously evolve with ζ_0 , and, in general, only contain elastic sector(s) for positive ζ_0 . Crack-tip shielding lowers the local J -Integral, as compared to the far-field elastic J , by as much as 75%, but the degree of shielding varies considerably with ζ_0 . Moreover, for some values of ζ_0 the local J is actually larger than the far-field elastic J . As is anticipated, finite crack-tip opening displacements occur for all cases analyzed. However, the CTOD angle is always less than the elastic estimate, indicating that crack-face contact may occur within the plastic zone when no crack-face contact exists outside the plastic zone. Near the crack tip, deep within the plastically deforming interfacial region, the triaxiality, defined as $\sigma_{kk}/3\bar{\sigma}$, may exceed that of the Prandtl stress distribution and reach 3.22. Because of this, the interfacial tractions are bounded; i.e., $0 \leq t_n/\sigma_{ys} \leq 3.22$ and $|t_s| \leq k$, but depend strongly on ζ_0 .

No unusual features appear in the closed crack-tip model for a rigid medium beneath an elastic/perfectly-plastic medium. The asymptotic crack-tip fields are composed of two constant state and two centered fan sectors whose angular extent and arrangement are similar to homogeneous mode II fields. Compressive crack-face tractions extend from the elastic asymptotic fields, through the plastic fields, all the way to the crack-tip. Appreciable interfacial shear strains develop in the deforming medium.

For both crack-tip idealizations, asymptotic crack-tip fields in the lower elastic medium are completely described by the elastic potential for the closed crack-tip case. This potential is constructed by idealizing the interfacial tractions as constant beneath the plastic zone and zero elsewhere. It is also assumed that uniform compressive tractions exist along the crack-face within the plastic zone (the magnitudes of which are

zero in the traction-free crack-tip model). A uniform tensile field, oriented parallel to the interface, is superimposed to complete the potential. Due to the jump in shear traction at the crack-tip, the resulting field is logarithmically singular, and local crack-tip yielding is anticipated. However, for "elastic" materials with a yield strength three or more times greater than the yield strength of the perfectly-plastic material, "elastic" yielding does not restrict the application of these results.

The method used to identify the crack-tip idealization, in conjunction with the parameters necessary to define elastic and SSY inelastic crack-tip deformation, represents a rigorous framework usable in systematically quantifying interfacial crack-tip behavior. Via this framework one can determine the asymptotic stress, strain, and interfacial behavior, based upon the far-field loads and constitutive assumptions, and (by inference) provide the requisite interfacial properties necessary for sustaining the integrity of interfacial cracks. Evaluating the interfacial crack-tip conditions for a particular geometry (whose components' constitutive behavior can be idealized as elastic and elastic/perfectly-plastic, respectively) is made as follows. First the elastic crack-tip singularity and contact length must be quantified by either determining K or K_{II}^e (and/or \mathcal{G}) and δ via numerical solutions, tables containing known solutions, *etc.* Some parameters may not be directly obtainable, however their values might be inferred by using the approximations and relationships identified in Chapter 2; *e.g.*, approximating δ from K by Eq.(2.43). Based upon this information, the bi-material constant, and the yield strength of the material, the characteristic plastic zone dimension can be compared to the contact length, thereby establishing if and when either of the two models are appropriate. Alternatively, for certain geometries and loading conditions a load map might be consulted to determine the appropriate crack-tip idealization. If the crack tip is closed (and frictionless), the asymptotic crack-tip fields are those associated with the particular values of β (and ν). On the other hand if a traction-free crack tip exists, ζ_0 must be evaluated, and then, based upon the values of ζ_0 , ϵ , and ν , the asymptotic crack-tip fields can be "looked up." Section P2.B contains a numerical

example showing how SSY traction-free crack-tip conditions are established and how ζ_0 is evaluated for a particular geometry.

5.2 Discussion

As discussed in Chapter 1, the purpose of doing this work is to quantitatively describe the material state surrounding an interfacial crack tip. It is believed that since the largest stresses and strains evolve in this area, interfacial separation or crack deflection is completely governed by the behavior within the immediate crack-tip proximity. By analyzing and identifying the deformation patterns accompanying the maximum stresses, strains, and interfacial tractions, insight might be gained into the mechanisms and conditions which initiate separation. Unfortunately, this work only provides the conditions which must be sustained prior to unstable crack propagation and is limited to only one constitutive idealization. However, in conjunction with this study and experimental observations and measurements, the feasibility and admissibility of specific failure mechanisms postulated to be active in certain materials can be systematically evaluated.

Independent of the many observations and classifications made in regard to interfacial cracks, the present work is far from conclusive, even for elastic/perfectly-plastic materials bonded to elastic or rigid substrates. Some final comments will be made regarding interpretational aspects of the analyses, modifications to various quantities and definitions, and areas which warrant further investigation.

5.2.1 Crack-Face Contact

Various issues pertaining to the elastic and plastic crack-tip fields have been identified, with considerable attention to excluding the physically inadmissible phenomenon of crack-face interpenetration. *In SSY the complete asymptotic elasticity solution is recovered sufficiently far away from regions of inelastic crack-tip deformation, independent of whether the crack-faces are open or closed in the plastic zone.* Therefore,

crack-face contact within the plastic zone has no consequence upon the elastic crack-face conditions since it is the elastic solution which drives the inelastic deformation in SSY, and not vice versa. For proportional monotonically increasing far-field loads, conclusions based solely upon the asymptotic elasticity solutions are valid at distances larger than several times the characteristic plastic zone size, but still small compared to the next relevant characteristic geometric dimension. Within the limitations discussed in Section 2.3.3, the actual elastic crack face is *open* whenever crack-face contact or interpenetration is not predicted, independent of the crack-face conditions within the plastic zone.

In this study only frictionless closed bi-material crack-tips were considered. In actuality, frictionless crack-tips rarely occur in nature, and friction significantly alters crack-tip behavior. In the bi-material case Comninou (1977b) found that friction reduced the order of the elastic stress singularity for "closed" interfacial cracks. Obviously, the assumption of frictionless closed crack-tip faces represents a simplification which is inappropriate for many situations, and further studies which include crack-face friction are warranted.

5.2.2 Unifying ILPA

The ILPA (ζ_0) is a naturally-arising parameter which is convenient for studying and classifying plastically deformable traction-free crack tips, but it is not comprehensive in that it does not automatically compensate for different values of ϵ and ν . For example, in the elastic approximation for crack-face closure, the critical value of ζ_0 is different for different ϵ . Similarly, the asymptotic inelastic crack-tip fields, for given values of ζ_0 and ν , differ with ϵ . Deformation near open interfacial cracks is only periodic with respect to ζ_0 ; i.e., it is not harmonic. (This is apparent when the additive decomposition of ζ , Eq.(P2.21), is substituted back into the plastic zone approximation, Eq.(P2.6), and the trigonometric functions are expanded. Although ζ_0 appears only as the argument of trigonometric functions, the coefficients which multiply the functions of ζ_0 change

(periodically) as ζ_0 changes.) Thus a relative shift in ζ_0 is not expected to relate the crack-tip fields' evolution (with ζ_0) for different values of ϵ . The ILPAs of the results in Chapter 4 were modified in an attempt to compensate for the dependence of crack-face closure on ϵ , however, this procedure failed to unify the asymptotic crack-tip fields (probably for the reason just discussed).

5.2.3 Anticipated Experimental Observations

To aid in experimental identification of bi-material crack-tip behavior, a qualitative overview describing the anticipated visible crack-tip features follows. Upon application of load, the extent of crack-face contact should become evident. The contact length will depend upon the direction of the applied far-field load, the characteristic geometric dimension and material properties, and it should be independent of the applied load magnitude. Experimental techniques capable of resolving elastic stress or displacement states should allow for detection and identification of the elastic asymptotic crack-tip fields and crack-face displacements. Because the period of oscillation in the traction-free crack-tip model is so large and experimental resolution and specimen size are limited, the experimentally obtained near crack-tip fields will appear as having the conventional square-root dependence on radial distance, whether or not crack-face contact occurs. In materials capable of inelastic deformation, as the load magnitude is increased the next resolvable feature should be the plastic zone. Again, due to the large oscillation period and limited realistic specimen size, the plastic zone shape will appear independent of the applied load magnitude, however, varying the direction of the load on different specimen sizes should produce different plastic zone shapes. For materials whose constitutive behavior is similar to that idealized within this study, plastic zone shapes extending only partially around the crack-tip (in the deforming medium) could be expected for certain loadings.

Resolving the asymptotic inelastic fields is not a realistic expectation at this time. Some materials may localize, i.e., Fe-Si, polycarbonate, leaving traces indicative of the

asymptotic inelastic field. In addition, experimental observations of surface deformation are likely to reflect plane-stress conditions, rather than the plane-strain conditions primarily studied.

In designing experiments, it is important to keep in mind both the types of loads being applied (usually to simulate some real physical situation) and the particular materials, because altering either of these can drastically change the crack-tip conditions. For example, consider the ramifications of evaluating interfacial separation by an interfacial Griffith crack geometry loaded by far-field tension. Sketched in *Figure P2.11* is such a geometry. (To facilitate discussion, allow the magnitude of the far-field tensile load, σ_{yy}^{∞} , and material properties to be unspecified.) Following the example shown in Section P2.B, both K and ζ_0 can be evaluated for a specific set of material combinations and load level. Note that because no far-field shear tractions are applied, K and ζ_0 are the same at both crack tips. For convention, the material with the lower yield strength is always located in the upper region, and its yield strength is used in evaluating ζ_0 . The evolution of ζ_0 with monotonically increasing SSY loading is shown in *Figure 5.1* for several different values of ϵ . For material combinations whose constitutive behavior can be idealized as an elastic/perfectly-plastic material atop an elastic medium, the crack-tip fields are those which correspond to the particular values of ζ_0 , $(\nu,)$ and ϵ . Note the large range of ζ_0 produced from this one "simple" test configuration, and that the actual value of ζ_0 is strongly dependent upon the actual value of ϵ for a specific load level of $\sigma_{yy}^{\infty}/\sigma_{ys}$.

In light of the above example, experimentalists who simulate interfaces by using alternative material models, must insure that not only chemical similitude exists between the actual and model systems, but that mechanical properties (namely the elastic constants) are also scaled appropriately. Using only one model material which is elastically softer than its counterpart in the actual system can change ϵ , possibly even changing its sign, and produce asymptotic crack-tip fields in the model which differ drastically from those produced in the actual system. *Figure 5.1* clearly indicates how sensitive

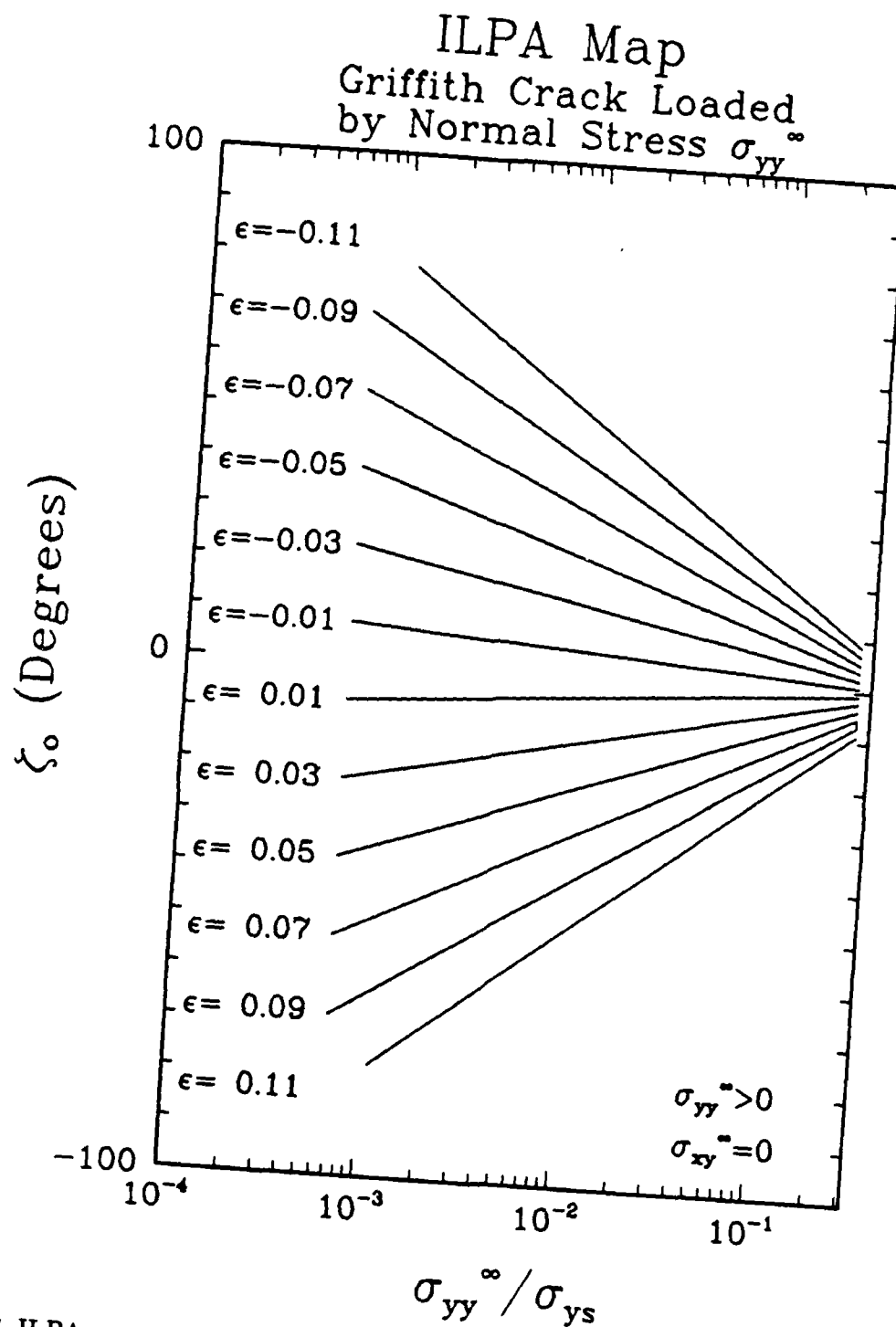


Figure 5.1 ILPA map for a Griffith crack geometry loaded with far-field tensile normal load σ_{yy} , for various values of ϵ .

the crack-tip parameter ζ_0 is to load levels and material combinations.

5.2.4 Influence of Material Properties on Separation

On the basis of the limited parametric study considered, it appears that particular material combinations do not alter the nature of the asymptotic fields produced, rather, they shift the fields in the same way that a change in ζ_0 would, and they distort the strain distribution. For an elastic/perfectly-plastic material bonded to an elastic substrate, the phase angle of the applied load, measured by ζ_0 , appears to affect the asymptotic crack-tip fields more than the choice of elastic material properties. However, for a specific set of traction-free loading conditions, altering the elastic material properties and changing the sign of ϵ can significantly alter both the asymptotic crack-tip stress and strain states, as demonstrated previously. This is extremely important when interfacial separation criteria are evaluated, because, for certain load states, it might be more advantageous to bond to a stiffer substrate or to orientate an anisotropic substrate in a different direction.

Generally, the material combination with the lowest perfectly-plastic flow strength produces the lowest tractions, since the asymptotic stress state scales with the flow strength. For a specific flow strength, minimum normal tractions occur when the material combination is subjected to the largest (positive) ζ_0 or when the crack-tip is closed. When the normal tractions are at their minimum level, substantial inelastic radial shear strains, which scale as $\gamma_{r\theta} \propto 1/R$, localize in a small band parallel to or slightly inclined from the interface. It is somewhat ironic that the minimum interfacial shear strains are present when normal interfacial tractions are at their maximum values and vice versa. Interfacial separation criteria for deformable media, which are only traction or (interfacial) strain based, may seem inappropriate in light of this trend.

In this crack-tip idealization, the resulting interfacial tractions are bounded. This implies that separation criterion for materials with strong interfaces, i.e., those capable of sustaining tractions greater than the maximum asymptotic crack-tip interfacial

tractions, must be strain controlled. (If the controlling mechanism is only a maximum traction criterion, and the tractions are less than the critical traction value, separation would never occur in SSY.) However, it is impossible to predict separation without a specific criterion in mind because most separation criteria require the traction and/or strain level to reach or exceed some threshold value over a critical distance before separation is said to commence.

Micro fracture mechanisms occurring in the interfacial proximity may be indistinguishable from interfacial decohesion. One can easily visualize small particles, whose size might be 10^{-8} to 10^{-6} m, embedded in continuum crack-tip fields and whose presence does not alter the continuum idealization. The high triaxiality near the interface which accompanies the maximum tractions will promote (ductile) micro-void formation and growth in the near crack-tip field. For traction-free crack-tip loadings the maximum triaxiality always occurs at or within $(+)\text{40}^\circ$ of the interface, while in the closed crack-tip case, the region where the triaxiality is the highest extends from $\theta \approx 30^\circ$ to $\theta \approx 120^\circ$. Cleavage of brittle particles, which can initiate macro-voids, and micro-cracking are typically thought to be governed by the maximum principal stress and its associated direction. The maximum principal stress occurs along the interface [when $\sigma_{rr}(\theta = 0^\circ) = k$] and its direction is orientated approximately 45° from the interface. Therefore, in the plastically deforming interfacial region one might expect to find microcracks and the direction of cleaved particles inclined $(+)\text{135}^\circ$ from the interface. In the lower elastic region failure associated with a maximum principal stress criterion may deflect the crack into the lower elastic medium. At radial distances very close to the crack tip such a failure criterion predicts crack deflection at an angle inclined approximately -90° from the interface, while at larger radial distances the deflection angle would be larger ($\approx -45^\circ$).

5.2.5 Suggested Additional Work

Several avenues need to be explored to establish concisely the complete bi-material crack-tip behavior even for the case of an elastic/perfectly-plastic material adjoint to an elastic or rigid material. An analytical expression defining the cusp in terms of the far-field load parameters is essential to fully ascertain the evolution of the interfacial tractions. Incorporation of finite deformation would allow identification of the crack-tip fields all the way to the blunted crack tip and extend the mathematical range for which asymptotic inelastic fields are appropriate. Of course, the material restrictions acknowledged earlier would still limit the applicability of the results from such analyses, but additional insight may suggest a mathematical bound for the singular interfacial and the crack-tip strains.

Finite element solutions such as these "roughly" estimate the actual slip-line angles, and are severely limited by mesh fineness. Analyses which use discretized representations must carefully refine and focus these representative elements to ensure that important details are not systematically excluded from the solution. For example, in this study, no jumps in σ_{rr} were resolved. It is unclear, however, whether jumps existed or were just unresolved. To this extent a more precise asymptotic numerical solution would resolve the issue of stress jumps.

In this study, incremental plasticity is utilized as opposed to deformation theory, as used by Shih and Asaro (1987). For the constitutive idealization of an elastic/perfectly-plastic medium atop a rigid or elastic substrate, unloading usually occurred in asymptotic crack-tip fields whenever $\epsilon > 0$ and $\zeta_0 > 0$. In light of this, utilization of deformation theory in investigating interfacial cracks which have large strain hardening exponents must insure that all "plastically deforming" material points do not unload; i.e., $\bar{\epsilon}(t + \Delta t) \geq \bar{\epsilon}(t)$; $\bar{\epsilon} = \sqrt{\frac{2}{3} \epsilon' \cdot \epsilon'}$.

As is usually the case, parametric studies are only of limited value, and there always exist additional material combinations and loadings for which information is sought. The major issues unresolved in this study which still need be addressed are how

and when does the crack-face constant-state sector become an elastic wedge; how and why does the interfacial elastic wedge and accompanying constant state region evolve; and what are the elastic and inelastic asymptotic crack-tip fields when the elastically-predicted crack-face contact zone is approximately the same size as the plastic zone. In addition to analyzing more material combinations, extending the assumed material idealization to include anisotropic material behavior (both elastic and inelastic), and strain-hardening would also be useful.

Although much attention has been focused upon determining the characteristics of fields very deep within the plastic zone (specifically, for the traction-free crack-tip model — nine orders of magnitude smaller than the plastic zone), such information is of little more than academic use unless it reveals the complete asymptotic structure. From a purely physical point of view, structures larger than geophysical plates must be considered before the characteristics of fields which are nine orders of magnitude smaller than the plastic zone would have meaning. [Picture the structure that would require the twelve orders of magnitude of resolution considered by Shih and Asaro (1987)!] Additionally, the limitations identified previously, (Section 4.4) would require very *unique* material properties in order to achieve a valid solution at that size scale. For most common engineering applications, resolution and identification of continuum fields three or four orders of magnitude smaller than the plastic zone should provide sufficient and (hopefully) meaningful information at that size scale.

References

- Atkinson, 1982 Atkinson, C., *Int. J. Fracture*, **18**, March 1982, pp. 161-177.
- Bathe, 1982 Bathe, K. J., Finite Element Procedures in Engineering Analysis, Prentice-Hall, Inc., Englewood Cliffs, 1982.
- Barenblatt, 1962 Barenblatt, G. I., Advances in Applied Mechanics, Eds. Dryden, H. L., and von Karman, T., Academic Press, New York, **7**, 1962, pp. 56-131.
- Bilby, Cottrell, and Swinden, 1963 Bilby, B. A., Cottrell, D. H., and Swinden, K. H., *Proc. Roy. Soc., A* **272**, 1963, pp.304-310.
- Buchholz and Herrman, 1983 Buchholz, F.G., and Herrman, K. P., Mechanical Behavior of Materials - IV, August 1983, pp. 3005-3013.
- Chamis, 1984 Chamis, C, *S.A.M.P.E. Quarterly*, **15**, No. 3, April 1984, p. 14.
- Comninou, 1979 Comninou, M., and Schmueser, D., *J.A.M.*, **46**, June 1979, pp. 345-348.
- Comninou, 1978 Comninou, M., *J.A.M.*, **45**, June 1978, pp. 287-290.
- Comninou, 1977a Comninou, M., *J.A.M.*, **44**, Dec. 1977, pp. 631-636.
- Comninou, 1977b Comninou, M., *J.A.M.*, **44**, Dec. 1977, pp. 780-782.
- Cooper and Kelly, 1969 Cooper, G.A., and Kelly, A., Interfaces in Composite Materials, ASTM STP 452, ASTM, Philadelphia, 1969, pp. 90-106.
- Dugdale, 1960 Dugdale, D. S., *J. Mech. Phys. Solids*, **8**, 1960, pp. 100-104.
- England, 1965 England, A. H., *J.A.M.*, **32**, June 1965, pp. 400-402.
- Erdogan, 1965 Erdogan, F., *J.A.M.*, **32**, June 1965, pp. 403-410.

- Everet, *et al.*, 1986 Everet, R., Henshaw, W., Simons, D. G., and Land, D. J., Composite Interfaces, Eds. Ishida, H., and Koenig, J. L., Elsevier Science Publishing Co., Cleveland, OH, 1986, pp. 231-240.
- Fried and Yang, 1972 Fried, I., and Yang, S. K., *AIAA J.*, 10, 1972, pp. 1244-1246.
- Fung, 1977 Fung, Y. C., A First Course in Continuum Mechanics, Prentice-Hall, Inc., Englewood Cliffs, 1977, pp.2-4.
- Gautesen and Dundurs, 1987 Gautesen, A. K., and Dundurs, J., *J.A.M.*, 54, March 1987, pp. 93-98.
- Gurtin, 1981 Gurtin, M. E., An Introduction to Continuum Mechanics, Mathematics Science and Engineering, 158, Academic Press, 1981.
- Hellan, 1984 Hellan, K., Introduction to Fracture Mechanics, McGraw-Hill Book Co., New York, 1984, p. 93.
- Hertzberg, 1976 Hertzberg, R. W., Deformation and Fracture Mechanics of Engineering Materials, J. Wiley, New York, 1976, p. 20.
- Hibbit, Karlsson, and Sorensen, 1987 Hibbitt, Karlsson, and Sorensen, Inc. (HKS), "ABAQUS User's Manual", Providence, RI, 1987.
- Hibbit, 1984 Hibbitt, H. D., *ABAQUS/EPGEN, Nuclear Eng. and Design*, 77, 1984, pp. 271-297.
- Hill, 1983 Hill, R., The Mathematical Theory of Plasticity, Clarendon Press, Oxford, 1983, pp. 132-163.
- Hilton and Hutchinson, 1971 Hilton, P. D. and Hutchinson, J. W., *Eng. Frac. Mech.*, 3, 1971, pp. 435-451.
- Hobbs, Means, and Williams, 1976 Hobbs, B. E., Means, W. D., and Williams, P. F., Outline of Structural Geology, J. Wiley, New York, 1976.

- Hult and McClintock, 1956** Hult, J., and McClintock, F. A., Proceedings of the 9th International Conference of Applied Mechanics, Brussels, 1956, pp. 51-58.
- Hutchinson, 1968** Hutchinson, J. W., *J. Mech. Phys. Solids*, **16**, 1968, pp. 13-31.
- Ioakimidis and Theocaris, 1979** Ioakimidis, N.I., and Theocaris, P. S., *Int. J. Fracture*, **15**, 1979, pp. 299-309.
- Johnson, 1985** Johnson, K. L., Contact Mechanics, Cambridge Univ. Press, New York, 1985.
- Kachanov, 1974** Kachanov, L. M., Fundamentals of the Theory of Plasticity, Trans. Konyaeva, M., Mir Publishers, Moscow, 1974.
- Kanninen and Popelar, 1985** Kanninen, M. F., and Popelar, C. H., Advanced Fracture Mechanics, Oxford University Press, New York, 1985.
- Krieg and Krieg, 1977** Krieg, R. D., and Krieg, D. B., *J. Pressure Vessel Tech.*, **99**, November 1977, pp. 510-515.
- Larsson and Carlsson, 1973** Larsson, S. G., and Carlsson, A. J., *J. Mech. Phys. Solids*, **22**, 1973, pp. 263-277.
- McMeeking, 1977** McMeeking, R. M., *J. Mech. Phys. Solids*, **25**, 1977, pp. 357-381.
- Mushelishvili, 1953** Mushelishvili, N. I., Some Basic Problems in the Mathematical Theory of Elasticity, Trans. Radok, J. R. M., Noordhoff, Gronngen, Holland, 1953.
- Narasimhan, Rosakis, and Hall, 1987** Narasimhan, R., Rosakis, A., J., and Hall, J. F., *J.A.M.*, **54**, Dec. 1987, pp. 838-845.
- Needleman and Sham, 1980** Needleman, A., Sham, T. L., "Final Report- General Electric Company, Subcontract to Brown University," Brown University, Providence, 1980.

- Nemat-Nasser and Obata, 1984 Nemat-Nasser, S., and Obata, M., *Mechanics of Materials*, 3, 1984, pp. 235-243.
- Nutt and Needleman, 1987 Nutt, S. R., and Needleman, A., *Scripta METALLURGIA*, 21, 1987, pp. 705-710.
- Ochiai and Murakami, 1981 Ochiai, S., and Murakami, Y., *Met. Trans.*, July 1981, pp. 1155.
- Ou and Bassani, 1988 Ou, J., and Bassani, J. L., "Cracks on Bimaterial and Bicrystal Interfaces," Univ. of Pennsylvania, Philadelphia, March 1988.
- Rice, 1988 Rice, J. R., *J.A.M.*, 55, March 1988, pp. 98-103.
- Rice, 1982 Rice, J. R., *Mechanics of Solids*, Eds. Hopkins, H. G., and Sewell, M. J., Pergamon Press, Oxford, New York, 1982, pp.539-562.
- Rice, 1974 Rice, J. R., *J. Mech. Phys. Solids*, 22, 1974, pp. 17-26.
- Rice, 1968a Rice, J. R., *J. A. M.*, 35, June 1968, pp. 379-386.
- Rice, 1968b Rice, J. R., *Fracture: An Advanced Treatise*, Ed. Liebowitz, H., Academic Press, New York, 2, 1968, pp. 191-311.
- Rice and Rosengren, 1968 Rice, J. R., and Rosengren, G. F., *J. Mech. Phys. Solids*, 16, 1968, pp. 1-12.
- Rice, Drugan and Sham, 1980 Rice, J. R., Drugan, W. J., and Sham, T. L., *Fracture Mechanics*, ASTM-STP 700, ASTM, Philadelphia, 1980, pp. 189-219.
- Rice and Sih, 1965 Rice, J. R., and Sih, G. C., *J.A.M.*, 32, June 1965, pp. 418-423.
- Rice and Tracey, 1973 Rice, J. R., and Tracey, D. M., *Numerical and Computer Methods in Structural Mechanics*, Academic Press, New York, 1973, pp. 585-623.

- Sham, 1983** Sham, T. L., Elastic-Plastic Fracture: Second Symposium Vol. 1 - Inelastic Crack Analysis, ASTM STP 803, ASTM, Philadelphia, 1983, pp. 52-79.
- Shields, 1982** Shields, R. T., *J.A.M.*, **49**, 1982, pp. 516-518.
- Shih and Asaro, 1987** Shih, C. F., and Asaro, R. J., "Elastic-Plastic Analysis of Cracks on Bimaterial Interfaces Part I: Small Scaling Yielding," Brown Univ., Div. of Eng., March 1987, Providence.
- Shih, 1974** Shih, C. F., Fracture Analysis, ASTM STP 560, ASTM, Philadelphia, 1974, pp. 187-210.
- Sih and Rice, 1964** Sih, G. C., and Rice, J. R., *J.A.M.*, **31**, 1964, pp. 477-482.
- Timoshenko and Goodier, 1970** Timoshenko, S. P., and Goodier, J. N., Theory of Elasticity, McGraw Hill, New York, 1970, pp. 90-145.
- Webster, 1979** Webster, N., Webster's Deluxe Unabridged Dictionary, Simon and Schuster, New York, 1979, p. 117.
- Williams, 1979** Williams, M.L., *Bul. Seis. Soc. Am.*, **49**, April 1959, pp. 199-204.
- Willis, 1971** Willis, J. R., *J. Mech. Phys. Solids*, **19**, 1971, pp. 353-368.

Appendix A

Boundary Layer Formulation

In order to impose Sham's boundary layer formulation (Sham, 1983), it is necessary to calculate consistent energy conjugate stiffnesses and boundary displacements. The first section derives the far-field stored energy, due to the lower order terms, and formulates an energy equivalent spring network to represent it. Appendix C contains the actual FORTRAN program used to determine the spring stiffness for a given material combination. The second section derives the imposed displacements in terms of the admissible eigenfunctions and coefficients (generalized degrees of freedom). These displacement constraints are then enforced on the FE boundary nodes via a user-written MPC subroutine. Again, Appendix C contains the actual FORTRAN coding used for the MPC subroutine.

In this appendix, the two stress potential functions used are ϕ and χ instead of the stress potentials ϕ and Ω , as used in the body of the text. Since χ is related to ϕ and Ω by

$$\chi'' = \Omega' - \phi' - z\phi'',$$

they produce equivalent results. However, the unknown coefficients a_n and b_n of Eqs.(3.4) and (3.5) are not the same. All Appendices, subroutines, and FORTRAN coding use $B_{(N)}$ and $D_{(N)}$ as the unknown coefficients, with the $B_{(0)}$ term being adjusted so that it is interpreted as $B_{(0)} = \bar{K}$.

A.1 Energy Considerations

A.1.1 Formulation of Equivalent Stiffness Matrix

Implementation of Sham's boundary layer formulation requires the evaluation and inclusion of the far-field energy, which is attributable to the T -field terms. This section evaluates the second term in Eq.(3.8) from its associated strain energy potential relationship.

The general series potential functions given by Sih and Rice, (1964) and Rice (1988), which satisfy the bi-material crack, are

$$\phi_1(z) = 2z^{-\frac{1}{2}-i\epsilon} \sum_N [(N + \frac{1}{2}) - i\epsilon] \bar{B}_{(N)} z^N + \frac{2C_2}{C_1 + C_2} \sum_M \frac{\bar{D}_{(M)}}{M+1} z^{M+1}, \quad (\text{A.1})$$

$$\phi_2(z) = 2e^{2\pi\epsilon} z^{-\frac{1}{2}-i\epsilon} \sum_N [(N + \frac{1}{2}) - i\epsilon] \bar{B}_{(N)} z^N + \frac{2C_1}{C_1 + C_2} \sum_M \frac{\bar{D}_{(M)}}{M+1} z^{M+1}, \quad (\text{A.2})$$

$$\begin{aligned} \chi_1(z) = & 2e^{2\pi\epsilon} z^{\frac{1}{2}+i\epsilon} \sum_N B_{(N)} z^N - 2z^{\frac{1}{2}-i\epsilon} \sum_N [(N - \frac{1}{2}) - i\epsilon] \bar{B}_{(N)} z^N \\ & - \frac{C_2}{C_1 + C_2} \sum_M D_{(M)} \bar{z}^M z^2 - \frac{2C_2}{C_1 + C_2} \sum_M \frac{\bar{D}_{(M)}}{M+2} z^{M+2}, \end{aligned} \quad (\text{A.3})$$

and

$$\begin{aligned} \chi_2(z) = & 2z^{\frac{1}{2}+i\epsilon} \sum_N B_{(N)} z^N - 2e^{2\pi\epsilon} z^{\frac{1}{2}-i\epsilon} \sum_N [(N - \frac{1}{2}) - i\epsilon] \bar{B}_{(N)} z^N \\ & - \frac{C_1}{C_1 + C_2} \sum_M D_{(M)} \bar{z}^M z^2 - \frac{2C_1}{C_1 + C_2} \sum_M \frac{\bar{D}_{(M)}}{M+2} z^{M+2}, \end{aligned} \quad (\text{A.4})$$

with

$$C_k = \frac{\eta_k + 1}{\mu_k} \quad (k = 1, 2). \quad (\text{A.5})$$

In these expressions the subscripts (1,2) indicate material domains, ϵ is the bi-material constant, $\eta_j = 3 - 4\nu_j$ for plane strain or $\eta_j = (3 - \nu_j)/(1 + \nu_j)$ for plane stress, μ_j and ν_j are the appropriate shear modulus and Poisson's ratio, respectively, and z is the complex variable measured from the crack tip. The desired lower order Laurent series displacements, u^T , and the associated stresses, σ^T , are obtained by letting $N = -1, -2, -3, \dots$ and $M = -2, -3, -4, \dots$. The $M = -1$ term is excluded from the

formulation since it represents an applied concentrated crack-tip force and produces infinite far-field elastic energy in the boundary layer formulation. For the ϕ and χ stress potentials, this represents the same modifications to the ϕ and Ω potentials as were made in Eqs.(3.4) and (3.5). From these potentials, the far-field elastic strain energy due to the lower modes, $\Phi(\xi^T)$, can be evaluated and incorporated directly.

Since u^T is an equilibrium solution in the far-field (Region \mathcal{R} of Figure 9.2),

$$2\bar{\Pi}(u^T) = 2 \int_{\mathcal{R}} \Phi(\xi^T) dS = \int_{\Gamma} t^T \cdot u^T ds. \quad (A.6)$$

Here $\bar{\Pi}$ is the total strain energy in \mathcal{R} , Φ is the strain energy density, Γ represents the entire boundary around \mathcal{R} (Γ_{∞} , $\Gamma_{Plastic}$, and Γ_c), and t^T is the resultant traction due to the lower order modes. Dividing the boundary into regions yields

$$2\bar{\Pi}(u^T) = \int_{\Gamma_{Plastic}} t^T \cdot u^T ds + \int_{\Gamma_{\infty}} t^T \cdot u^T ds + \int_{\Gamma_c} t^T \cdot u^T ds. \quad (A.7)$$

Recall the Kolosov-Muskhelishvili stress formulas (Sih and Rice, 1964),

$$\sigma_{rr} + \sigma_{\theta\theta} = 4\Re[\phi'] = 2[\phi' + \bar{\phi}'], \quad (A.8)$$

and

$$\sigma_{\theta\theta} - \sigma_{rr} + i2\sigma_{r\theta} = 2e^{i2\theta}[\bar{z}\phi'' + \chi''], \quad (A.9)$$

where a bar indicates the complex conjugate, and \Re signifies the real portion of the argument. Subtracting Eq.(A.8) from Eq.(A.9) gives

$$-2\sigma_{rr} + i2\sigma_{r\theta} = 2e^{i2\theta}[\bar{z}\phi'' + \chi''] - 2[\phi' + \bar{\phi}']. \quad (A.10)$$

The displacements obtained via Kolosov-Muskhelishvili transformation are

$$u + iv = \frac{1}{2\mu}[\eta\phi - z\bar{\phi}' - \bar{\chi}'], \quad (A.11)$$

where the shear modulus, μ , Poisson's ratio, ν , and η are those associated with the individual material domains. Transforming to a polar coordinate frame, Eq.(A.11) becomes

$$u_r + iu_\theta = \frac{e^{-i\theta}}{2\mu} [\eta\phi - z\bar{\phi}' - \bar{\chi}']. \quad (\text{A.12})$$

Examination of the potential functions shows that the stresses, σ_{rr}^T and $\sigma_{r\theta}^T$, behave as $z^{p-\frac{3}{2}-i\epsilon} + z^{-2-p}$ and the displacements, u_r^T and u_θ^T , behave as $z^{q-\frac{1}{2}-i\epsilon} + z^{-1-q}$, where $p = 0, -1, -2, \dots$ and $q = 0, -1, -2, \dots$. In general, the term $\mathbf{t}^T \cdot \mathbf{u}^T$ behaves like $z^{p+q-2-2i\epsilon} + z^{-3-p-q}$, while for large z the dominant component, $p = q = 0$, acts like $z^{-(2+2i\epsilon)}$. This means that as $r \rightarrow \infty$ on Γ_∞ ,

$$\int_{\Gamma_\infty} \mathbf{t}^T \cdot \mathbf{u}^T ds = 0. \quad (\text{A.13})$$

By the problem definition, "traction-free crack-tip faces," $\mathbf{t}^T = 0$ on Γ_c , so that Eq.(A.7) can now be written as

$$2\bar{\Pi}(\mathbf{u}^T) = \int_{\Gamma_{Plastic}} \mathbf{t}^T \cdot \mathbf{u}^T ds. \quad (\text{A.14})$$

The traction, \mathbf{t}^T , is by definition

$$\mathbf{t}^T = \boldsymbol{\sigma}^T \cdot \mathbf{n}, \quad (\text{A.15})$$

where \mathbf{n} is the unit outward normal. Choosing $\Gamma_{Plastic}$ to be a circle of radius r , ds becomes $r d\theta$, and the cylindrical components of \mathbf{n} are $(-1, 0, 0)$. Eq.(A.14) then becomes

$$2\bar{\Pi}(\mathbf{u}^T) = \int_{\Gamma_{Plastic}} [-\sigma_{rr}^T u_r^T - \sigma_{r\theta}^T u_\theta^T] r d\theta. \quad (\text{A.16})$$

For convenience, C in Eq.(A.12) is defined as

$$C = \frac{e^{-i\theta}}{2\mu} [\eta\phi - z\bar{\phi}' - \bar{\chi}'] = u_r + iu_\theta, \quad (\text{A.17})$$

and D is defined by dividing the complex conjugate of Eq.(A.10) by two, which results in the following:

$$D = e^{-i2\theta} [z\bar{\phi}'' + \bar{\chi}''] - [\phi' + \bar{\phi}'] = -\sigma_{rr} - i\sigma_{r\theta}. \quad (\text{A.18})$$

Eq.(A.16) can then be rewritten as

$$2\bar{\Pi}(\mathbf{u}^T) = \int_{\Gamma_{Plastic}} [\Re(C)\Re(D) + \Im(C)\Im(D)] r d\theta, \quad (\text{A.19})$$

or

$$2\bar{\Pi}(u^T) = \int_{\Gamma_{Plastic}} \Re(rC\bar{D})d\theta = \int_{\Gamma_{Plastic}} \Re(r\bar{C}D)d\theta, \quad (A.20)$$

where \Re and \Im designate real and imaginary parts, respectively. It is convenient to factor out the coefficients \mathbf{B} and \mathbf{D} (these are the vectors which contain $B_{(N)}$ and $D_{(M)}$ as their components, respectively), and to express the potential functions, Eq.(A.1) to Eq.(A.4), in terms of their individual components as

$$\phi = \sum_{i=1}^{N+M} \bar{P}_i \phi_i \quad (A.21)$$

and

$$\chi = \sum_{i=1}^{N+M} P_i N_i - \sum_{i=1}^{N+M} \bar{P}_i U_i, \quad (A.22)$$

where

$$\{\mathbf{P}\}_{N+M-1} = \left\{ \begin{array}{c} B_{(1)} \\ \vdots \\ B_{(N)} \\ D_{(2)} \\ \vdots \\ D_{(M)} \end{array} \right\}, \quad (A.23)$$

and the terms ϕ_i , N_i , and U_i correspond to the functional parts of Eq.(A.1) to Eq.(A.4). More specifically, this means that the functions (ϕ_1, \dots, ϕ_N) , (N_1, \dots, N_N) , and (U_1, \dots, U_N) all correspond to the functions associated with the \mathbf{B} coefficients and the functions $(\phi_{N+1}, \dots, \phi_{N+M-1})$, $(N_{N+1}, \dots, N_{N+M-1})$, and (U_1, \dots, U_{N+M-1}) correspond to the functions associated with the \mathbf{D} coefficients. (The subscripts indicating the material domains are implied by the value of z chosen.) Further, four matrices, $\mathbf{B}\mathbf{B}$, $\mathbf{B}\bar{\mathbf{B}}$, $\bar{\mathbf{B}}\mathbf{B}$, and $\bar{\mathbf{B}}\bar{\mathbf{B}}$, are defined whose components are given by

$$\mathbf{B}\mathbf{B}_{ij} = \bar{z}[-z\bar{\phi}'_i e^{i2\theta} N''_j + z\bar{\phi}'_i \bar{\phi}'_j + \bar{U}'_i e^{i2\theta} N''_j - \bar{U}'_i \bar{\phi}'_j], \quad (A.24)$$

$$\begin{aligned} \mathbf{B}\bar{\mathbf{B}}_{ij} = \bar{z}[-z\bar{\phi}'_i e^{i2\theta} \bar{z}\phi''_j + z\bar{\phi}'_i e^{i2\theta} U''_j + z\bar{\phi}'_i \phi'_j + \bar{U}'_i e^{i2\theta} \bar{z}\phi''_j \\ - \bar{U}'_i e^{i2\theta} U''_j - \bar{U}'_i \phi'_j], \end{aligned} \quad (A.25)$$

$$\bar{\mathbf{B}}\mathbf{B}_{ij} = \bar{z}[\eta\phi_i e^{i2\theta} N''_j - \eta\phi_i \bar{\phi}'_j - \eta\bar{N}'_i e^{i2\theta} N''_j + \bar{N}'_i \bar{\phi}'_j], \quad (A.26)$$

and

$$\begin{aligned}\bar{B} \bar{B}_{i,j} = & \bar{z}[\eta \phi_i e^{i2\theta} \bar{z} \phi_j'' - \eta \phi_i e^{i2\theta} U_j'' - \eta \phi_i \phi_j' - \bar{N}_i' e^{i2\theta} \bar{z} \phi_j'' \\ & + \bar{N}_i' e^{i2\theta} U_j'' + \bar{N}_i' \phi_j']. \end{aligned} \quad (A.27)$$

By using Eq.(A.17), Eq.(A.18), and Eqs.(A.20) to (A.27), Eq.(A.16) reduces to

$$2\bar{\Pi}(u^T) = \int_{R_{Plastic}} \frac{1}{2\mu} \Re[P \bar{B} B P + P \bar{B} \bar{B} \bar{P} + \bar{P} \bar{B} B P + \bar{P} \bar{B} \bar{B} \bar{P}] d\theta. \quad (A.28)$$

At this point, the integral $\int_R \Phi(\epsilon^T) dS$ has been recast in terms of the complex vector P , which represents the unknown coefficients, and four matrices containing functions of the original stress potentials. The remaining formulation consists of various algebraic manipulations used to recast Eq.(A.28) into an expression which, when integrated, contains *real* numbers only. First, the *real* vector q^{ϵ^T} is defined as

$$\{q^{\epsilon^T}\} = \left\{ \frac{\Re P}{\Im P} \right\} = \left\{ \begin{array}{c} \Re B_{(1)} \\ \vdots \\ \Re B_{(N)} \\ \Re D_{(2)} \\ \vdots \\ \Re D_{(M)} \\ \Im B_{(1)} \\ \vdots \\ \Im B_{(N)} \\ \Im D_{(2)} \\ \vdots \\ \Im D_{(M)} \end{array} \right\}. \quad (A.29)$$

Next, the stiffness matrix S is introduced and is defined such that

$$\bar{\Pi}(u^T) = \frac{1}{2} q^{\epsilon^T} S q^{\epsilon^T}. \quad (A.30)$$

Using the convention that $\bar{P}_j = e_j + i f_j$, factoring out the real components, and equating Eq.(A.28) to Eq.(A.30), we can express S as

$$S = \int_{R_{Plastic}} \frac{1}{2\mu} \left[\frac{\Re(B \bar{B} + \bar{B} B + \bar{B} \bar{B} + \bar{B} \bar{B})}{\Im(B \bar{B} + \bar{B} B - \bar{B} \bar{B} - \bar{B} \bar{B})} \middle| \frac{\Im(B \bar{B} - \bar{B} B + \bar{B} \bar{B} - \bar{B} \bar{B})}{\Re(-B \bar{B} + \bar{B} B + \bar{B} \bar{B} - \bar{B} \bar{B})} \right] d\theta. \quad (A.31)$$

After integration of Eq.(A.31), the integral $\int_R \Phi(\epsilon^T) dS$ can be replaced by $\frac{1}{2} q^{\epsilon^T} S q^{\epsilon^T}$.

A.1.2 Evaluation of Spring Constants

To incorporate this energy into the finite element code, a spring network, with appropriate stiffness, was constructed. The spring network vertices corresponded to "free" nodes and the displacements of these free nodes were governed by the value of the generalized coefficient vector q^{eT} . It was observed that, since q^{eT} both pre- and post-multiplied the stiffness matrix S [in Eq.(A.30)], a new upper triangular stiffness matrix C can be used to reduce the number of individual stiffnesses. When constructed correctly, C replaces S in Eq.(A.30) to produce identical results. The new stiffness matrix C is related to S (after evaluation of S) via

$$C_{ij} = \begin{cases} S_{ij} & i = j & i = 1, 2, 3, \dots, 2(N + M - 1) \\ S_{ij} + S_{ji} & i < j & j = i, i + 1, i + 2, \dots, 2(N + M - 1) \\ 0 & \text{otherwise.} \end{cases} \quad (A.32)$$

The energy associated with a spring is calculated in the finite element code as $\frac{1}{2} C_{ij} (q_i - q_j)^2$ as opposed to $\frac{1}{2} C_{ij} q_i q_j$, as assumed in Eq.(A.30). To rectify this situation, a further modified spring stiffness matrix C' is defined whose components are

$$C'_{ij} = \begin{cases} -\frac{1}{2} C_{ij} & i \neq j \\ \frac{1}{2} \sum_{k=1}^i C'_{kj} + \frac{1}{2} \sum_{l=j}^{2(N+M-1)} C'_{il} & i = j \end{cases} \quad \begin{matrix} i = 1, 2, 3, \dots, 2(N + M) \\ j = i, i + 1, i + 2, \dots, 2(N + M - 1). \end{matrix} \quad (A.33)$$

Finally, the far-field elastic strain energy can now be expressed in terms of spring constants, C'_{ij} , as

$$\Phi(u^T) = \frac{1}{2} (q_i - q_j) C'_{ij} (q_i - q_j), \quad (A.34)$$

with the clarification that the term $(q_i - q_j)$ is interpreted as q_i , when $i = j$.

The actual spring stiffnesses for a particular choice of material properties were obtained by numerically integrating Eq.(A.31) using Simpson's 1/3 Rule with $\Delta\theta = \pi/100$. The $\Gamma_{Plastic}$ boundary was chosen to be a circle, with radius $r_{Plastic} = 1.0$ m, centered about the crack tip. This prevented numerical noise associated with evaluating $r_{Plastic}$ raised to large power. To reduce other numerical noise, the integration path was divided and integrated from $\theta = \pm\pi$ to $\theta = 0$ simultaneously. The *complex* FORTRAN coding used to evaluate C' is included in Appendix C.

A.2 Boundary Considerations

The boundary conditions required for Sham's boundary layer formulation are those of the general bi-material crack problem. Using the general series potential functions, Eqs.(A.1) to (A.4), and the Kolosov-Muskhelishvili relation Eq.(A.11), the displacements can be expressed in terms of the complex coefficients $B_{(N)}$ and $D_{(M)}$, and the location $z = re^{i\theta}$. To maintain the K-field dominance at the boundary, again only the series terms corresponding to $N = 0, -1, -2, \dots$ and $M = -2, -3, -4, \dots$, are used to determine the displacements. After some algebra, the displacements for the upper half can be written as:

$$u = \sum_N \frac{r^Q}{\mu} (Fe1_N e_N + Fe2_N f_N) + \sum_M \frac{Cr^{M+1}}{2\mu} (Ge1_M c_M + Ge2_M d_M) \quad (A.35)$$

and

$$v = \sum_N \frac{r^Q}{\mu} (Fe3_N e_N + Fe4_N f_N) + \sum_M \frac{Cr^{M+1}}{2\mu} (Ge3_M c_M + Ge4_M d_M), \quad (A.36)$$

where (subscripts dropped for brevity),

$$P = N + 3/2, \quad (A.37)$$

$$Q = N + 1/2, \quad (A.38)$$

$$R = PQ - \epsilon^2, \quad (A.39)$$

$$S = \epsilon(P + Q), \quad (A.40)$$

$$T1 = \cos[\epsilon \ln(r)] \cos(Q\theta) + \sin[\epsilon \ln(r)] \sin(Q\theta), \quad (A.41)$$

$$T2 = \cos[\epsilon \ln(r)] \sin(Q\theta) - \sin[\epsilon \ln(r)] \cos(Q\theta), \quad (A.42)$$

$$T3 = \cos[\epsilon \ln(r)] \cos(2Q\theta) - \sin[\epsilon \ln(r)] \sin(2Q\theta), \quad (A.43)$$

$$T4 = \cos[\epsilon \ln(r)] \sin(2Q\theta) + \sin[\epsilon \ln(r)] \cos(2Q\theta), \quad (A.44)$$

$$T5 = \cos[\epsilon \ln(r)] \cos(Q\theta) - \sin[\epsilon \ln(r)] \sin(Q\theta), \quad (A.45)$$

$$T6 = \cos[\epsilon \ln(r)] \sin(Q\theta) + \sin[\epsilon \ln(r)] \cos(Q\theta), \quad (A.46)$$

$$Fe1 = \eta e^{i\theta} [P \times T1 + \epsilon \times T2] - e^{i\theta} [R \times T3 - S \times T4]$$

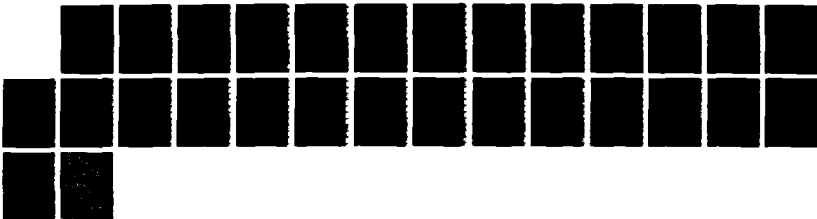
NO-A190 746

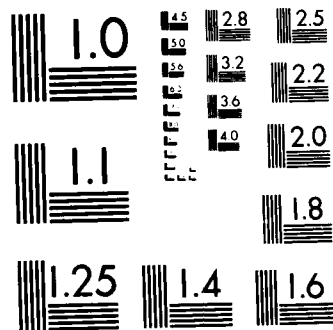
ENGINEERING INTERFACES IN METAL MATRIX COMPOSITES
(VOLUME 3)(U) MASSACHUSETTS INST OF TECH CAMBRIDGE
J A CORNIE 10 JUN 88 N00014-84-K-0495

575

UNCLASSIFIED

F/G 11/6.1 ML





$$-e^{2\pi\epsilon}e^{-\epsilon\theta}[P \times T5 + \epsilon \times T6] + e^{\epsilon\theta}[\mathcal{R} \times T1 + S \times T2], \quad (\text{A.47})$$

$$\begin{aligned} Fe2 &= \eta e^{\epsilon\theta}[\epsilon \times T1 - P \times T2] - e^{\epsilon\theta}[S \times T3 + \mathcal{R} \times T4] \\ &\quad - e^{2\pi\epsilon}e^{-\epsilon\theta}[P \times T6 + \epsilon \times T5] - e^{\epsilon\theta}[\mathcal{R} \times T2 - S \times T1], \end{aligned} \quad (\text{A.48})$$

$$\begin{aligned} Fe3 &= \eta e^{\epsilon\theta}[P \times T2 - \epsilon \times T1] - e^{\epsilon\theta}[S \times T3 + \mathcal{R} \times T4] \\ &\quad + e^{2\pi\epsilon}e^{-\epsilon\theta}[P \times T6 + \epsilon \times T5] - e^{\epsilon\theta}[\mathcal{R} \times T2 - S \times T1], \end{aligned} \quad (\text{A.49})$$

and

$$\begin{aligned} Fe4 &= \eta e^{\epsilon\theta}[P \times T1 + \epsilon \times T2] + e^{\epsilon\theta}[\mathcal{R} \times T3 - S \times T4] \\ &\quad - e^{2\pi\epsilon}e^{-\epsilon\theta}[P \times T5 - \epsilon \times T6] - e^{\epsilon\theta}[\mathcal{R} \times T1 + S \times T2]. \end{aligned} \quad (\text{A.50})$$

The coefficients of the integer powers are defined as

$$\bar{D}_{(j)} = c_{(j)} + id_{(j)}, \quad (\text{A.51})$$

and the accompanying terms associated with the integer powers are

$$Ge1 = \frac{\eta + M + 1}{M + 1} \cos[(M + 1)\theta], \quad (\text{A.52})$$

$$Ge2 = -\frac{\eta + M + 1}{M + 1} \sin[(M + 1)\theta], \quad (\text{A.53})$$

$$Ge3 = \frac{\eta - M - 1}{M + 1} \sin[(M + 1)\theta] + 2 \sin[(M - 1)\theta], \quad (\text{A.54})$$

$$(\text{A.55})$$

and

$$Ge4 = \frac{\eta - M - 1}{M + 1} \cos[(M + 1)\theta] + 2 \cos[(M - 1)\theta]. \quad (\text{A.56})$$

By using the definition proposed by Rice and Sih for the stress intensity factors and the convention $\bar{B}_{(0)} = e_{(0)} + if_{(0)}$, $B_{(0)}$ can be expressed in terms of K as

$$e_{(0)} = \frac{\Re K(.75 - \epsilon^2) + \Im K 2\epsilon}{4e^{\epsilon\pi}\sqrt{2\pi} [.75 + 3\epsilon^2] \cosh(\pi\epsilon)} \quad (\text{A.57})$$

and

$$f_{(0)} = \frac{\Re K 2\epsilon - \Im K (.75 - \epsilon^2)}{4e^{\epsilon\pi}\sqrt{2\pi} [.75 + 3\epsilon^2] \cosh(\pi\epsilon)}. \quad (\text{A.58})$$

It should be noted that the original Rice and Sih (1965) work does not give the appropriate energy release rate unless the definition relating k_I and k_{II} to K , given by Hutchinson *et al.* (1987) [Eq.(2.15)], is used.

The displacement relations (A.34) and (A.35) were "coded up" as constraint equations and used along the $\Gamma_{Plastic}$ -model boundary of the finite element mesh. Appendix C contains the user MPC which was used to enforce the nodal displacement boundary conditions in terms of imposed the $K(t)$ and the unknown vector q^{eT} .

Appendix B

Elastic-Wedge Stress Potential

The elastic stress potentials for a semi-infinite wedge loaded by constant tractions on each of its faces is given. The individual stress components are obtained from ϕ , the stress potential, by using the definitions (Timoshenko and Goodier, 1970)

$$\sigma_{\gamma\gamma} = \frac{\partial^2 \phi}{\partial r^2}, \quad (\text{B.1})$$

$$\sigma_{r\gamma} = -\frac{\partial}{\partial r} \left(\frac{1}{r} \frac{\partial \phi}{\partial \gamma} \right), \quad (\text{B.2})$$

and

$$\sigma_{rr} = \frac{1}{r} \frac{\partial \phi}{\partial r} + \frac{1}{r^2} \frac{\partial^2 \phi}{\partial \gamma^2}. \quad (\text{B.3})$$

The stress potential for a wedge loaded along its faces by constant tractions is found from the general solution given by Timoshenko and Goodier (1970):

$$\phi = b_0 r^2 + d_0 r^2 \gamma + \frac{a_1}{2} r \gamma \sin \gamma - \frac{c_1}{2} r \gamma \cos \gamma + a_2 r^2 \cos 2\gamma + c_2 r^2 \sin 2\gamma. \quad (\text{B.4})$$

For the specific problem shown in *Figure B.1*, the stress potential constants are

$$b_0 = \frac{W}{2} - a_2, \quad (\text{B.5})$$

$$d_0 = -2c_2 - T, \quad (\text{B.6})$$

$$c_2 = \frac{(H + 2T\psi - W) \sin 2\psi - (K - T)(\cos 2\psi - 1)}{2(\cos 2\psi - 1)^2 + 2(\sin 2\psi) \times (\sin 2\psi - 2\psi)}, \quad (\text{B.7})$$

and

$$a_2 = \frac{(H + 2T\psi - W)(\cos 2\psi - 1) + (K - T)(\sin 2\psi - 2\psi)}{2(\cos 2\psi - 1)^2 + 2(\sin 2\psi) \times (\sin 2\psi - 2\psi)}. \quad (\text{B.8})$$

Using Eqs. (B.1) to (B.3) and Eq. (B.5), the stress components are

$$\sigma_{\gamma\gamma} = 2a_2(\cos 2\gamma - 1) + 2c_2(\sin 2\gamma - 2\gamma) + W - 2T\gamma, \quad (\text{B.9})$$

$$\sigma_{r\gamma} = 2a_2 \sin 2\gamma - 2c_2(\cos 2\gamma - 1) + T, \quad (\text{B.10})$$

and

$$\begin{aligned} \sigma_{rr} = & -2a_2(\cos 2\gamma + 1) - 2c_2(\sin 2\gamma + 2\gamma) + W - 2T\gamma \\ & + \frac{1}{r}(a_1 \cos \gamma + c_1 \sin \gamma). \end{aligned} \quad (\text{B.11})$$

The σ_{rr} component is singular with respect to r , and that two constants a_1 and c_1 remain unspecified from the boundary conditions prescribed. The values of these two constants are determined by matching the σ_{rr} stress, and for non-zero values of a_1 and c_1 concentrated forces must exist at $r = 0$.

A note of caution, when the coordinate frame is rotated to coincide with the crack-tip coordinate frame (via $\gamma = \pi - \theta$), the sign of the $\sigma_{r\theta}$ component must also be changed.

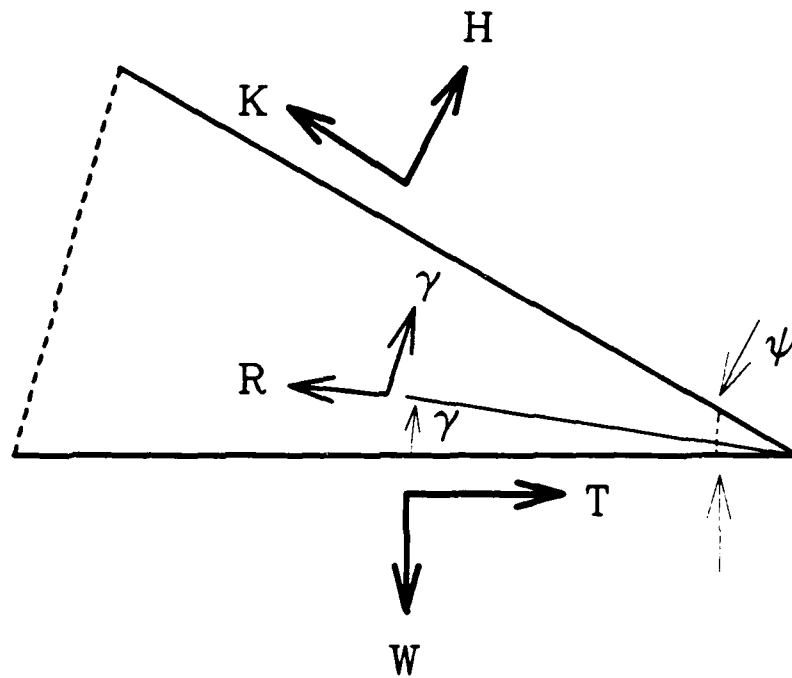


Figure B.1 Elastic wedge showing constant normal [$W = t_n(\gamma = 0)$] and shear [$T = t_s(\gamma = 0)$] tractions on its lower surface, constant normal [$H = t_n(\gamma = \psi)$] and shear [$K = t_s(\gamma = \psi)$] on its upper surface, and polar (r, γ) coordinates.

Appendix C

User-Written Software

This appendix contains the the FORTRAN coding for the user-written elastic/perfectly-plastic constitutive relationship subroutine UMAT as well as the program used to calculate the spring coefficients for the traction-free crack-tip model derived in Appendix A. The user-written MPC subroutines which impose the boundary displacements are included for both the traction-free and (frictionless) closed crack-tip models.

C.1 Elastic/Perfectly-Plastic UMAT

This routines original framework was written by Allen Lush. The author modified the original subroutine from its radial return operator to the Rice-Tracey mean normal integration operator.

```
C*****>
C                                     >
C               ABAQUS USER MATERIAL FOR   >
C               RATE INDEPENDENT PERFECT PLASTICITY >
C                                     >
C*****>
C                                     >
C  Properties common to all material models: >
C    PROPS(1) = yield stress TAU   Tensile >
C    PROPS(2) = MU >
C    PROPS(3) = KAPPA >
C                                     >
C*****>
C  Notes: >
```

```

C
C
C      1.  Compile with FORTRAN 77 only.
C      2.  Do not use this version for plane stress.
C      3.  Use with the *STATIC procedure.
C
C*****>
      SUBROUTINE UMAT(STRESS,STATEV,DDSDDE,SSE,SPD,SCD,STRAN,DSTRAN,
1  TIME,DTIME,TEMP,DTEMP,PREDEF,DPRED,MATERL,NDI,NSHR,NTENS,
2  NSTATV,PROPS,NPROPS,COORDS)
      IMPLICIT REAL*8(A-H,O-Z)
      REAL*8 MU,KAPPA
      DIMENSION STRESS(NTENS),STATEV(NSTATV),DDSDDE(NTENS,NTENS),
1  STRAN(NTENS),DSTRAN(NTENS),Stressf(6),Sn(6),Gamma(6),
2  COORDS(3),PREDEF(1),DPRED(1),PROPS(NPROPS)

C
      DATA ZERO,ONE,Onep,TWO,THREE/0.0D0,1.0000000D0,1.0200000D0
      *      ,2.0000000D0,3.0000000D0/

C
      NDIPL1=NDI+1

C
      TAU=32.5D0 !PROPS(1)
      MU=5.48D3 !PROPS(2)
      KAPPA=0.13333333333D3 !PROPS(3)
C*****
C  Calculate the beginning state SIG1 and P1.
C  Note that UMINV converts STRESS to its deviatoric part.
C*****
      CALL UMINV (STRESS,P1,SIG1,NDI,NTENS)
C*****
C  Calculate the trace of the strain increment.
C*****
      TRACE=ZERO
      DO 10 I=1,NDI
10  TRACE=TRACE+DSTRAN(I)
C*****
C  Convert to deviatoric tensor strain components.
C*****
      DO 15 I=1,NDI
15  DSTRAN(I)=DSTRAN(I)-TRACE/THREE
      DO 20 I=NDIPL1,NTENS
20  DSTRAN(I)=DSTRAN(I)/TWO
C*****
C  Calculate the new trial stress.
C*****
      DO 30 I=1,NTENS

```

```

30 SN(I)=TWO*MU*DSTRAN(I)+STRESS(I)
C*****
C Calculate SIGTRL.
C*****
      CALL UMINV (SN,PDUMMY,SIGTRL,NDI,NTENS)
C*****
C Calculate the pressure at the end of the increment.
C*****
      P2=P1-KAPPA*TRACE
C*****
C Determine the state of the initial and final conditions.
C*****
      Iflag=0
      Close=(.99999999DO*Tau)
      If(Sigtrl.Lt.Close) Then
C The final state is elastic.
      ETA=ONE
      C1=TWO*MU
      C2=KAPPA-C1/THREE
      C3=ZERO
C Check if the initial state is non-yielding, but the final state is.
      Else IF (SIGTRL.Gt.Close.and.SIG1.Lt.Close) then
      Iflag=1
      Else
C Both initial and final states are plastic. (Use Rice-Tracey)
      Iflag=2
      End if
C*****
C Decide what method should be used to calculate the stresses and the
C Jacobian. The following section is used if the final state is
C elastic.
C*****
      If(Iflag.Eq.0) Then
C*****
C Calculate the deviatoric stress at the end of the increment.
C*****
      DO 100 I=1,NTENS
      100 STRESS(I)=ETA*Sn(I)
C*****
C Calculate the Jacobian.
C*****
      DO 200 I=1,NTENS
      DO 200 J=1,NTENS
      200 DDSDDDE(I,J)=-C3*STRESS(I)*STRESS(J)
      DO 210 I=1,NDI

```

```

      DDSDE(I,I)=DDSDDE(I,I)+C1
      DO 210 J=1,NDI
210    DDSDE(I,J)=DDSDDE(I,J)+C2
      DO 220 I=NDIPL1,NTENS
220    DDSDE(I,I)=DDSDDE(I,I)+C1/TWO
C*****
C  Convert deviatoric stress to complete stress.
C*****
      DO 225 I=1,NDI
225    STRESS(I)=Stress(I)-P2
C*****
      Else If (IfIag.Eq.2) Then
C*****
C  This section is used to implement the Rice-Tracey Mean Normal Operator
C*****
C*****
C  Calculate the trail stress and the needed direction.
C*****
      Do 230 I=1,Ntens
230    Sn(i)=Two*Stress(i)+Two*Mu*Dstran(i)
C*****
C  Normalize the trail stress and the needed direction.
C*****
      Call Euminv(Sn,Taustar,Ndi,Ntens)
C*****
C  Calculate the dot product between the strain increment and stress
C  direction.
C*****
      RNdotE=Zero
      Do 240 I=1,Ndi
240    RNdotE=RNdotE + Sn(i)*Dstran(i)
      Do 250 I=(Ndi+1),Ntens
250    RNdotE=RNdotE + Sn(i)*Dstran(i)*Two
C*****
C  Calculate the final stress state
C*****
      Do 260 I=1,Ntens
260    Stressf(i)=Stress(I) + Two*Mu*Dstran(i)
      *    - Two*Two*Mu*RNdotE*Sn(i)
C*****
C  Calculate the Jacobian - It is symmetric.
C*****
      Alpha=Two*Mu*(One-Two*Mu*RNdotE/Taustar)
      Do 290 I=1,Ntens
      Do 290 J=1,Ntens

```

```

      Ddsdde(i,j)= -Two*Alpha*Sn(i)*Sn(j)
*      -(Mu/Taustar)*Sn(i)*(Stressf(j)-Stress(j))
*      -(Mu/Taustar)*Sn(j)*(Stressf(i)-Stress(i))
      If(I.Le.Ndi.and.J.Le.Ndi)
*      Ddsdde(i,j)= Ddsdde(i,j) + Kappa - Alpha/Three
      If(I.Eq.J.and.I.Le.Ndi)
*      Ddsdde(i,j)= Ddsdde(i,j) + Alpha
      If(I.Eq.J.and.I.Gt.Ndi)
*      Ddsdde(i,j)= Ddsdde(i,j) + Alpha/Two
290      Continue
C*****
C To prevent numerical drift, the stress will be normalized and the
C equivalent stress scaled to be exactly the yield stress, Tau.
C*****
      CALL UMINV (Stressf,Pug,Scale,Ndi,Ntens)
      Factor=Tau/Scale
C If the new stress is not close to the yield surface, signal it!
      If (Factor.lt.(.99).or.Factor.Gt.(1.01)) then
        Print *,'Scaling factor is ',Factor,
*        'and Initial Equiv. stress is ',Sig1
      End if
      Do 295 I=1,Ntens
295      Stress(i)=Stressf(i)*Factor
C*****
C Convert deviatoric stress to complete stress.
C*****
      DO 300 I=1,NDI
      300 STRESS(I)=Stress(I)-P2
C*****
      Else
C*****
C This section is used to implement the Rice-Tracey Mean Normal Operator
C when the initial solution is elastic and the final is plastic.
C*****
C*****
C Calculate the dot product between the strain increment and itself.
C*****
      DEdotDE=Zero
      Do 305 I=1,Ndi
305      DEdotDE=DEdotDE + Dstran(i)**Two
      Do 310 I=(Ndi+1),Ntens
310      DEdotDE=DEdotDE + Dstran(i)*Dstran(i)*Two
C*****
C Calculate the dot product between the strain increment and initial
C stress.

```

```

C*****
    DEdotS=Zero
    Do 315 I=1,Ndi
315      DEdotS=DEdotS + Stress(i)*Dstran(i)
        Do 320 I=(Ndi+1),Ntens
320      DEdotS=DEdotS + Stress(i)*Dstran(i)*Two
C*****
C Calculate the dot product between the initial stress and initial
C stress.
C*****
    SIdotSI=Sigi*Dsqrt(Two/Three)
C*****
C Find beta, the fraction of the elastic strain needed to cause yield
C In the text beta is called alpha.
C*****
    Quad2=Dsqrt((DEdotS**Two)
    *          -DEdotDE*(SIdotSI-Two*Close*Close/Three))
    Quad3=Two*Mu*DEdotDE
    Ibeta1=0
    Ibeta2=0
    Beta1=(-DEdotS - Quad2)/Quad3
    Beta2=(-DEdotS + Quad2)/Quad3
c      Logic to find maximum exceptable root.
    If(Beta1.Lt.Zero.or.Beta1.Gt.One) Ibeta1=1 !Unexceptable value
    If(Beta2.Lt.Zero.or.Beta2.Gt.One) Ibeta2=1 !Unexceptable value
    If(Ibeta1.Eq.1.and.Ibeta2.Eq.1) Then
        Beta=One
        Print *, 'Beta roots exceed the allowable range. Beta1 ',Beta1
    *   ', Beta2 ',Beta2
    Else If(Ibeta1.Eq.1.and.Ibeta2.Eq.0) Then
        Beta=Beta2
    Else If(Ibeta1.Eq.0.and.Ibeta2.Eq.1) Then
        Beta=Beta1
    Else
        Beta=Beta1
        If(Beta2.Gt.Beta1) Beta=Beta2
    End if
C*****
C Calculate the star stress state.
C*****
    Do 325 i=1,Ntens
325      Sn(i)=Two*Stress(i) + (One+Beta)*Two*Mu*Dstran(i)
C*****
C Find the N star-bar direction and it's magnitude. Normalization is
C done in the subroutine.

```

```

C*****
      Call Euminv(Sn,Taustar,Ndi,Ntens)
C*****
C Calculate the dot product between the strain increment and N star-bar
C*****
      SNdotDE=Zero
      Do 330 I=1,Ndi
330      SNdotDE=SNdotDE+ Sn(i)*Dstran(i)
      Do 335 I=(Ndi+1),Ntens
335      SNdotDE=SNdotDE+ Sn(i)*Dstran(i)*Two
C*****
C Calculate the final stress state.
C*****
      Do 340 I=1,Ntens
340      Stressf(i)=Stress(i) + Two*Mu*Dstran(i)
          *   - (One-Beta)*Two*Two*Mu*Sn(i)*SNdotDE
C*****
C Calculate the Gamma tensor. Determines the change in beta wrt. Dstran
C*****
      Gammacon=(Two*Beta*Mu*DEdotDE+DEdotS)*(-One)
      Do 345 I=1,Ntens
345      Gamma(i)=((Two*Mu*(Beta)**Two)*Dstran(i)
          *   +Beta*Stress(i))/Gammacon
C*****
C Calculate the Jacobian - It is symmetric.
C*****
C*****
C Useful constants for the Jacobian
C*****
      C1=ENdotDE
      D1=(One-Beta)*Two*Mu
      E1=D1*Two*Mu/Taustar
      F1=DEdotDE
      G1=Two*Mu-E1*C1*(One+Beta)
      G2=Two*Two*(Mu*(Beta-One)+E1*C1*(One+Beta))
      G3=Two*Two*Mu*C1+Two*Two*C1*C1*E1-E1*F1
      G4=(-E1)*(One+Beta)
      G5=(-C1*E1)
      Do 390 I=1,Ntens
      Do 390 J=1,Ntens
          Ddsdde(i,j)=
          *   G2*Sn(i)*Sn(j)
          *   +G3*Sn(i)*Gamma(j)/Two
          *   +G4*Sn(i)*Dstran(j)/Two
          *   +G5*Dstran(i)*Gamma(j)/Two

```



```

* +G3*Sn(j)*Gamma(i)/Two
* +G4*Sn(j)*Dstran(i)/Two
* +G5*Dstran(j)*Gamma(i)/Two
  If(I.Le.Ndi.and.J.Le.Ndi)
*   Ddsdde(i,j)= Ddsdde(i,j) + Kappa - G1/Three
  If(I.Eq.J.and.I.Le.Ndi)
*   Ddsdde(i,j)= Ddsdde(i,j) + G1
  If(I.Eq.J.and.I.Gt.Ndi)
*   Ddsdde(i,j)= Ddsdde(i,j) + G1/Two
390   Continue
C*****
C   To prevent numerical drift, the stress will be normalized and the
C   equivalent stress scaled to be exactly the yield stress, Tau.
C*****
  CALL UMINV (Stressf,Pug,Scale,Ndi,Ntens)
  Factor=Tau/Scale
C   If the new stress is not close to the yield surface, signal it!
  If (Factor.lt.(.99).or.Factor.Gt.(1.01)) Then
    Print *,'In mod R-T: Scaling factor is ',Factor,
    *      'and Initial Equiv. stress is ',Sig1
  End if
  Do 395 I=1,Ntens
395   Stress(i)=Stressf(i)*Factor
C*****
C   Convert deviatoric stress to complete stress.
C*****
  DO 400 I=1,NDI
    400 STRESS(I)=Stress(I)-P2
C*****
  End if
C*****
  RETURN
  END
C*****

C*****
  SUBROUTINE UMINV (X,XINV1,XINV2,NDI,NTENS)
  IMPLICIT REAL*8 (A-H,O-Z)
  DIMENSION X(NTENS)
C*****>
C   This subroutine calculates: >
C   XINV1=-(1/3)*trace(X), >
C   converts X to its deviatoric part X', and calculates >
C   XINV2=DSQRT(1.5*X'*X') >
C*****>

```

```

      NDIPL1=NDI+1
      XINV1=0.0DO
      XINV2=0.0DO
C
      DO 10 I=1,NDI
10    XINV1=XINV1-X(I)
      XINV1=XINV1/3.0DO
      DO 20 I=1,NDI
20    X(I)=X(I)+XINV1
      DO 30 I=1,NDI
30    XINV2=XINV2+0.5DO*X(I)*X(I)
      DO 40 I=NDIPL1,NTENS
40    XINV2=XINV2+X(I)*X(I)
      XINV2=3.0DO*XINV2
      XINV2=DSQRT(XINV2)
      RETURN
      END
C*****
C*****
      SUBROUTINE Euminv (X,Xinv2,NDI,NTENS)
      IMPLICIT REAL*8 (A-H,O-Z)
      DIMENSION X(NTENS)
C*****>
C  This subroutine calculates:                >
C     $X_{ij} = X_{ij} / (2.0 * (.5 * X_{ij} \text{ Dot } X_{ij})^{.5})$     >
C*****>
      NDIPL1=NDI+1
      XINV2=0.0DO
C
      DO 10 I=1,NDI
10    XINV2=XINV2+0.5DO*X(I)*X(I)
      DO 20 I=NDIPL1,NTENS
20    XINV2=XINV2+X(I)*X(I)
      XINV2=DSQRT(XINV2)
      Xinv=2.0000000DO*Xinv2
      DO 30 I=1,NTENS
30    X(I)=X(I)/Xinv
      RETURN
      END
C*****

```



```

*          *Dlog((F1+F2)/(F3+F4))
Pa1=3.000000000D0-(Two*Two*P1) !Plain strain Poisson's ratio
Pa2=3.000000000D0-(Two*Two*P2) !Plain strain Poisson's ratio
C1=(Pa1+1.000000000D0)/G1 !Constants needed for the integer terms.
C2=(Pa2+1.000000000D0)/G2
Cc1=Two*C2/(C1+C2)
Cc2=Two*C1/(C1+C2)
Epitheta=Dexp(6.28318530717958D0*Epsil)
R=.1000000D1
C This sets up the integration rules for Simpson's 1/3 Rule.
Ninv=50 !Number of intervals per half/should be even
Nsteps=(Ninv*2)+1 !Number of steps
Tinc=3.14159265358979D0/Dble(Ninv*2) !Integration step size.
C The integration step is one-half the interval size.
Do 50 i=1,Mterms !Zero out the matrix
Do 50 j=1,Mterms
  AiAj(i,j)=Dcmplx(Zero,Zero)
  AiBj(i,j)=AiAj(i,j)
  BiAj(i,j)=AiAj(i,j)
  BiBj(i,j)=AiAj(i,j)
50 Continue
Do 300 KKK=1,Nsteps !Begin the major do loop of the intergration
Do 300 M1=1,2
c This loop is set to integrate the lower half from -pi to zero
c while at the same time integrate the upper half from pi to zero.
c The 'logic' of this is that terms of similar magnitude will be
c accumulated at the same time so that in the case of an anti-
c symmetric term it should contain less error. I hope!
If (M1.Eq.1) then !Lower half first.
  Theta =(-3.14159265358979D0)+((Dble(KKK-1))*Tinc)
  G=G2
  Cposs=Dcmplx(Pa2,Zero)
  Cc=Cc2
Else !Upper half second.
  Theta =(3.14159265358979D0)-((Dble(KKK-1))*Tinc)
  G=G1
  Cposs=Dcmplx(Pa1,Zero)
  Cc=Cc1
End if
Dthe=Dcmplx((Dcos(Two*Theta)),
* (Dsin(Two*Theta)))
Z=Dcmplx((R*Dcos(Theta)), (R*Dsin(Theta)))
Zb=Dconjg(Z)
Do 100 i=1,Mterms
  P=.500000000D0+(1-i)

```

```

Q=(1-i)-.5000000000D0
Con1=Dcmplx(P,(-1.0000000D0*Epsil))      !P-1e
Con2=Dcmplx(P,(Epsil))                    !P+1e
Con3=Dcmplx(Q,(-1.0000000D0*Epsil))      !Q-1e
Con4=Dcmplx(Q,Epsil)                      !Q+1e
Con5=Con3-Dcmplx(1.0000000D0,Zero)        !Q-1-1e
Call Power(R,Theta,Con3,Ans)
Phi(i)=Dcmplx(Two,Zero)*Con1*Ans
  If (M1.Eq.1) Phi(i)=Phi(i)*Dcmplx(Epitheta,Zero)
C      !This adjusts for the lower half potential function.
PhiI(i)=Phi(i)*Con3/Z
PhiII(i)=PhiI(i)*Con5/Z
Call Power(R,Theta,Con2,Ans)
X1(i)=Dcmplx(Two,Zero)*
*      Dcmplx(Epitheta,Zero)*Ans
Call Power(R,Theta,Con1,Ans)
X2(i)=Dcmplx(Two,Zero)*Con3*Ans
  If (M1.Eq.1) then
    X1(i)=X1(i)/Dcmplx(Epitheta,Zero) !This adjusts the potential
    X2(i)=X2(i)*Dcmplx(Epitheta,Zero) !functions for being on the
    End If                               !lower half.
X1I(i)=X1(i)*Con2/Z
X2I(i)=X2(i)*Con1/Z
X1II(i)=X1I(i)*Con4/Z
X2II(i)=X2I(i)*Con3/Z
  If(i.GT.(Mterms-Nterms)) Then
c      This section calculates out the terms associated with the integer
c      powers of the series expansion starting out at n=-2.
    jj=Nterms-1-i
    Call Power (R,Theta,(Dble(jj+1)),Ans)
    X1I(i)=Dcmplx(-Cc,Zero)*Conjg(Ans/Z)*Z
    X1II(i)=X1I(i)/Z
    X2I(i)=Dcmplx(Cc,Zero)*Ans
    X2II(i)=Dcmplx((Dble(jj+1)),Zero)*X2I(i)/Z
    PhiI(i)=Dcmplx(Cc,Zero)*Ans/Z
    PhiII(i)=Dcmplx((Dble(jj)),Zero)*PhiI(i)/Z
    Phi(i)=PhiI(i)*Z/Dcmplx((Dble(jj+1)),Zero)
    End if
100  Continue
Do 200 i=1,Mterms !The following are the individual terms
c      associated with the complex variable bb and its conjugates.
Do 200 j=1,Mterms
  BB(i,j)=Zb*(
*      (Z*Dconjg(PhiI(i)*PhiI(j)))
*      -(Z*Dconjg(PhiI(i))*Dthe*X1II(j))

```

```

*      -(Dconjg(X2I(i)*PhiI(j)))
*      +(Dconjg(X2I(i))*Dthe*X1II(j)))
BcB(i,j)=Zb*(
*      (Z*Dconjg(PhiI(i))*Dthe*X2II(j))
*      -(Z*Dconjg(PhiI(i))*Dthe*Zb*PhiII(j))
*      +(Z*Dconjg(PhiI(i))*PhiI(j))
*      +(Dthe*Zb*Dconjg(X2I(i))*PhiII(j))
*      -(Dthe*Dconjg(X2I(i))*X2II(j))
*      -(Dconjg(X2I(i))*PhiI(j)))
cBB(i,j)=Zb*(
*      (Phi(i)*Dthe*X1II(j)*Cposs)
*      -(Phi(i)*Dconjg(PhiI(j))*Cposs)
*      -(Dconjg(X1I(i))*Dthe*X1II(j))
*      +(Dconjg(X1I(i))*PhiI(j)))
cBcB(i,j)=Zb*(
*      (Phi(i)*Dthe*Zb*PhiII(j)*Cposs)
*      -(Phi(i)*Dthe*X2II(j)*Cposs)
*      -(Phi(i)*PhiI(j)*Cposs)
*      -((Dconjg(X1I(i))*Dthe*Zb*PhiII(j)) !The Problem Term.
*      +(Dconjg(X1I(i))*Dthe*X2II(j))
*      +(Dconjg(X1I(i))*PhiI(j)))

```

200 Continue

C This section adjusts the weighting factor applied to each point.

C This is in accordance with Simpson's 1/3 rule.

If (KKK.Eq.1.or.KKK.Eq.Nsteps) Then

Rinc=Tinc/Three

Else

K1=KKK/2

K2=K1*2

If (K2.Eq.KKK) Then !KKK is an even number

Rinc=Two*Two*Tinc/Three

Else

Rinc=Two*Tinc/Three

End If

End If

Do 300 i=1,Mterms

Do 300 j=1,Mterms

AiAj(i,j)=Dreal(BB(i,j)+cBB(i,j)+BcB(i,j)+cBcB(i,j))*Rinc/(G*Two)

* + AiAj(i,j)

BiBj(i,j)=Dreal(BcB(i,j)-BB(i,j)+cBB(i,j)-cBcB(i,j))*Rinc/(G*Two)

* + BiBj(i,j)

BiAj(i,j)=Dimag(BB(i,j)+BcB(i,j)-cBB(i,j)-cBcB(i,j))*Rinc/(G*Two)

* + BiAj(i,j)

AiBj(i,j)=Dimag(BB(i,j)-BcB(i,j)+cBB(i,j)-cBcB(i,j))*Rinc/(G*Two)

* + AiBj(i,j)

```

300 Continue      !End of the integration.
Do 400 i=1,Mterms !Form the global stiffness matrix.
Do 400 j=1,Mterms
  C(i,j)=AiAj(i,j)
  C(i,(j+Mterms))=AiBj(i,j)
  C((i+Mterms),j)=BiAj(i,j)
  C((i+Mterms),(j+Mterms))=BiBj(i,j)
400 Continue
Do 500 i=1,(2*Mterms) !Upper triangularize the global stiffness
Do 500 j=1,(2*Mterms) !matrix. Use only one spring per node set.
  D(i,j)=C(j,i)+C(i,j) !The other half is being filled in for
  If(i.Ne.j) D(j,i)=D(i,j) !convenience only.
  If(i.Eq.j) D(j,i)=D(j,i)/Two
500 Continue

C      This section adjusts for the springs working on the difference
C      between the two degrees of freedom, instead of the degree's
C      of freedom's product. It becomes very important to determine
C      at this time how many terms are actually going to be used.
Do 550 i=1,(2*Mterms)
Do 550 j=1,(2*Mterms)
  If(i.Ne.j) then
    E(i,j)=(-.500000000000)*D(i,j)
  Else
    E(i,j)=D(i,j)*(.500000000000)
    Do 525 K=1,(Mterms*2)
      E(i,j)=E(i,j)+(.500000000000)*D(i,k)
525 Continue
    End If
550 Continue
      Ncount=8999 !Set up elset numbering counter.
Do 600 i=1,Mterms
Do 600 j=1,Mterms
  Ncount=Ncount+1
  II=i+1
  JJ=j+1
  If (Dabs(E(i,j)).Gt.Zepo) then
    If(i.Ne.j) then
      Write (30,1012) Ncount,Ncount,II,JJ
      Write (30,1016) Ncount,E(i,j)
    Else
      Write (30,1011) Ncount,Ncount,II
      Write (30,1015) Ncount,E(i,j)
    End If
  End If
End If

```

```

600  Continue
    Do 700 i=1,Mterms
    Do 700 j=(Mterms+1),(2*Mterms)
        Ncount=Ncount+1
        II=i+1
        JJ=j-Mterms+1+Isec
        If (Dabs(E(i,j)).Gt.Zepo) then
            Write (30,1012) Ncount,Ncount,II,JJ
            Write (30,1016) Ncount,E(i,j)
        End If
700  Continue

    Do 800 i=(Mterms+1),(2*Mterms)
    Do 800 j=1,(2*Mterms)
        Ncount=Ncount+1
        II = i+1-Mterms + Isec
        JJ = j+1-Mterms + Isec
        If (Dabs(E(i,j)).Gt.Zepo) then
            If(i.Ne.j) then
                Write (30,1012) Ncount,Ncount,II,JJ
                Write (30,1016) Ncount,E(i,j)
            Else
                Write (30,1011) Ncount,Ncount,II
                Write (30,1015) Ncount,E(i,j)
            End If
        End If
800  Continue
1011  Format('*ELEMENT,TYPE=SPRING1,ELSET=SP',I4,/,3I5 )
1012  Format('*ELEMENT,TYPE=SPRING2,ELSET=SP',I4,/,3I5 )
1015  Format('*SPRING,ELSET=SP',I4 ,/, '1',/,E17.11,',' )
1016  Format('*SPRING,ELSET=SP',I4 ,/, '1,1',/,E17.11,',' )
    End

    Subroutine Power(R,Theta,Con,Ans)
C      This subroutine calculates a complex number Z,( R,Theta),
C      raised to a another complex number Con.
    Complex*16 Z,Con,Ans
    IMPLICIT REAL*8 (A-H,O-Z)
    Ans=Dcmplx( ( R*Dreal(Con) ) ,0.00000000000000D0)
    * Dcmplx( (Dexp(-1.00000000D0*Theta*Dimag(Con))),0.00000000000000D0)
    * Dcmplx((Dcos(Dimag(Con)*Dlog(R))), (Dsin(Dimag(Con)*Dlog(R))))
    * Dcmplx((Dcos(Dreal(Con)*Theta)), (Dsin(Dreal(Con)*Theta)) )
    Return
    End

```


C.2.2 MPC Subroutine

```

Subroutine MPC (Ue,A,Jdof,N,Jtype,X,U,Nmpce)
IMPLICIT REAL*8 (A-H,O-Z)
DIMENSION A(n),JDOF(n),X(6,n),U(6,n)
C      This program imposes the asymptotic bi-material crack tip
C      displacements as an MPC. The order of the MPC as it should
C      appear in the deck is MPC#,Node#,Knode,Knode. Here MPC#
C      should be 1 for dof 1 and 2 for dof 2 in the upper half.
C      While 11 should be used for dof 1 and 12 for dof 2 in the
C      lower half. Note, this means that for every node to be tied
C      it has to be entered in twice; once for each dof. Node# is
C      the number of the constrained node while Knode is the number
C      of the extra node. The desired Ki strength should be given
C      as Knode's dof 1 displacement while the Kii should be given
C      as Knode's dof 2 displacement. The subscript 1 and 2 refer to
C      the upper (1) and lower (2) materials respectively. The
C      Knode numbering are arranged with the first lnteg minus one
C      terms corresponding to the square-root order terms while the
C      following terms correspond to the integer terms. (Starting from
C      the n=-2 term.)
      lnteg=7 !# of square-root terms including the K terms.
      Rone =(-1.000000000000000D0) ! Useful constants
      Zone =1.000000000000000D0
      Two =2.000000000000000D0
      Three=3.000000000000000D0
      Pie =3.14159265358979D0
C      Determine the R and theta coordinates.
      Theta=Datan2( X(2,1),X(1,1) )
      If(X(1,1).Lt.(0.0D0).and.Dabs(X(2,1)).Lt.(0.0001D0)) Theta=Pie
      Theta =Dabs(Theta) ! This always gives a positive theta.
      If(Jtype.Eq.11.or.Jtype.Eq.12) Theta=Theta*Rone
      R=Dsqr(X(1,1)*X(1,1)+X(2,1)*X(2,1))
C      Set up the material properties
      Em2=70.1D03
      Em1=13.7D03
      P2=.342D0
      P1=.250D0
C      Determine the bi-material displacements
      G1=Em1/((Zone+P1)*Two) !Shear Modulus
      G2=Em2/((Zone+P2)*Two) !Shear Modulus
      F1=(Three-(Two*Two*P1))/G1
      F2=(Zone/G2)
      F3=(Three-(Two*Two*P2))/G2
      F4=(Zone/G1)

```

```

Epsil=(Zone/(Two*Pie))*Dlog((F1+F2)/(F3+F4))
C1=F1+F4           !These are constants used in the integer
C2=F3+F2           !function expansion.
Cc1=Two*C2/(C1+C2)
Cc2=Two*C1/(C1+C2)
If (Jtype.EQ.11.OR.Jtype.EQ.12) then
  G=G2 !This adjust for the material being on the down side.
  Rnj=Three-(Two*Two*P2)
  Cc=Cc2
Else
  G=G1 ! Assume that the node is on the upper half
  Rnj=Three-(Two*Two*P1) !Plain strain Poisson's ratio
  Cc=Cc1
End If
Uit=0.0D0          !Initialize the displacements before the do loop.
Vit=Uit
A(1)=Zone
MM=(N-1)/2          !Adjustment for the due loop
Coshpe=((Dexp(Epsil*Pie))+(Dexp(Epsil*(Rone*Pie))))/
* Two) !Correction of Rice's original solution.
Etheta=Dexp(Epsil*Theta)
Epitheta=Dexp(Two*Pie*Epsil)
Re=Epsil*(Dlog(R))
Con3=(Three/(Two*Two)) - Epsil*Epsil
Con4= Two * Epsil
Con7=10.026513D0 * Dexp(Pie*Epsil) *
* ( Con4 * Con4 + Con3 * Con3)
Do 200 I=1,MM ! The number of terms involved is the second limit
  If (I.LE.Iinteg) then !These terms are used for the square-
    !root expansion.

    II=2-I
    P=Dble(II)+(Zone/Two)
    Q=Dble(II)-(Zone/Two)
    CRe=DCos(Re)
    SRe=DSin(Re)
    CQt=DCos(Q*Theta)
    SQt=DSin(Q*Theta)
    CQ2t=DCos((Two-Q)*Theta)
    SQ2t=DSin((Two-Q)*Theta)
    Tern1=CRe*CQt+SRe*SQt
    Tern2=CRe*SQt-SRe*CQt
    Tern3=CRe*CQ2t-SRe*SQ2t
    Tern4=CRe*SQ2t+SRe*CQ2t
    Tern5=CRe*CQt-SRe*SQt
    Tern6=CRe*SQt+SRe*CQt

```

```

Con1=(P*Q)-(Epsil*Epsil)
Con2=(P+Q)*Epsil
End If
C The terms Fe1 and Fe3 are associated with the e_n term in my expan.
C The terms Fe2 and Fe4 are associated with the f_n term in my expan.
If((Jtype.EQ.11.or.Jtype.EQ.12).and.I.LE.Iinteg) then
c   These are done for the lower half.
Fe1=(P*Term1 + Epsil*Term2)*(Etheta)*Rnj*Epitheta -
*   (Con1*Term3 - Con2*Term4)*(Etheta)*Epitheta -
*   (P*Term5 - Epsil*Term6)/Etheta +
*   (Con1*Term1 + Con2*Term2)*Etheta*Epitheta
Fe2=(Epsil*Term1 - P*Term2)* Etheta*Rnj*Epitheta -
*   (Con2*Term3 + Con1*Term4)* Etheta*Epitheta -
*   (P*Term6 + Epsil*Term5)/Etheta -
*   (Con1*Term2 - Con2*Term1)*Etheta*Epitheta
Fe3=(P*Term2 - Epsil*Term1)*(Etheta)*Rnj*Epitheta -
*   (Con2*Term3 + Con1*Term4)*(Etheta)*Epitheta +
*   (P*Term6 + Epsil*Term5)/Etheta -
*   (Con1*Term2 - Con2*Term1)* Etheta*Epitheta
Fe4=(Epsil*Term2 + P*Term1)*(Etheta)*Rnj*Epitheta +
*   (Con1*Term3 - Con2*Term4)*(Etheta)*Epitheta -
*   (P*Term5 - Epsil*Term6)/Etheta -
*   (Con1*Term1 + Con2*Term2)*(Etheta)*Epitheta
Rcon=(Zone/(G*Coshpe))*(R**Q)
Else If ((Jtype.EQ.1.or.Jtype.EQ.2).and.I.LE.Iinteg) then
! These are done for the upper half.
Fe1=(P*Term1 + Epsil*Term2)*(Etheta)*Rnj -
*   (Con1*Term3 - Con2*Term4)*(Etheta) -
*   (P*Term5 - Epsil*Term6)*Epitheta/Etheta +
*   (Con1*Term1 + Con2*Term2)*Etheta
Fe2=(Epsil*Term1 - P*Term2)* Etheta * Rnj -
*   (Con2*Term3 + Con1*Term4)* Etheta -
*   (P*Term6 + Epsil*Term5)*Epitheta/Etheta -
*   (Con1*Term2 - Con2*Term1)*Etheta
Fe3=(P*Term2 - Epsil*Term1)*(Etheta)*Rnj -
*   (Con2*Term3 + Con1*Term4)*(Etheta) +
*   (P*Term6 + Epsil*Term5)*Epitheta/Etheta -
*   (Con1*Term2 - Con2*Term1)* Etheta
Fe4=(Epsil*Term2 + P*Term1)*(Etheta)*Rnj +
*   (Con1*Term3 - Con2*Term4)*(Etheta) -
*   (P*Term5 - Epsil*Term6)*Epitheta/Etheta -
*   (Con1*Term1 + Con2*Term2)*(Etheta)
Rcon=(Zone/(G*Coshpe))*(R**Q)
Else If (I.GT.Iinteg) Then !This begins the integer
! section of the expansion.

```

```

Mno=Iinteg-I-1
Rmno1=Dble(Mno-1)
Rmno3=Dble(Mno+1)
Rcon=Cc*(R**Rmno3)/(Two*G)
Argp=Theta*Rmno3
Argn=Theta*Rmno1
Fe1=((Rnj+Rmno3)/Rmno3)*Dcos(Argp)
Fe2=(-(Rnj+Rmno3)/Rmno3)*Dsin(Argp)
Fe3=((Rnj-Rmno3)/Rmno3)*Dsin(Argp) + Two*Dsin(Argn)
Fe4=((Rnj-Rmno3)/Rmno3)*Dcos(Argp) + Two*Dcos(Argn)
Else
Print *, 'Your are in deep.....'
End if

```

C The U(*,*) are the stress intensity factors. Therefore an adjustment
 C must be made to convert them into the proper form. What follows are
 C the derivatives of the displacements with respect to the Stress
 C Intensity factors. Or the unknown degrees of freedom.
 C The conversion to the Stress Intensity Factors only occurs for
 C the square root term. The remaining terms are left as the unknowns
 C a+ib. This is done because the evaluation of the far-field is much
 C easier using aj+ibj instead of Kij+iK2j. Another separation is
 C given to the integer terms and the square-root order terms.

```

If(I.Eq.1) then
  UK1= Rcon*(Fe1*Con3 + Fe2*Con4)/Con7
  UK2= Rcon*(Fe2*Con3 - Fe1*Con4)/Con7
  VK1= Rcon*(Fe3*Con3 + Fe4*Con4)/Con7
  VK2= Rcon*(Fe4*Con3 - Fe3*Con4)/Con7

```

```

Else If(I.Gt.Iinteg) then

```

```

  UK1=Rcon*Fe1
  UK2=Rcon*Fe2
  VK1=Rcon*Fe3
  VK2=Rcon*Fe4

```

```

Else

```

```

  UK1= Rcon*Fe1*Coshpe
  UK2= Rcon*Fe2*Coshpe
  VK1= Rcon*Fe3*Coshpe
  VK2= Rcon*Fe4*Coshpe

```

```

End If

```

```

  Jdof(2*I+1)=1      ! node in the expansion.

```

```

  Jdof(2*I)=1 !Give the correct degree of freedom for each free

```

```

IF (Jtype.Eq.1) then

```

```

  JDOF(1)=1

```

```

  A(2*I)=Rone*UK1

```

```

  A(2*I+1)=Rone*UK2

```

```

Else IF (Jtype.Eq.11) then

```

```

      JDOF(1)=1
      A(2*I)=Rone*UK1
      A(2*I+1)=Rone*UK2
ELSE IF (Jtype.Eq.2) then
      JDOF(1)=2
      A(2*I)=Rone*VK1
      A(2*I+1)=Rone*VK2
ELSE      !      (Jtype.Eq.12)
      JDOF(1)=2
      A(2*I)=Rone*VK1
      A(2*I+1)=Rone*VK2
END IF
      Uit=Uit+(U(1,(2*I))*A(2*I) + U(2,(2*I+1))*A(2*I+1))
      Vit=Vit+(U(1,(2*I))*A(2*I) + U(2,(2*I+1))*A(2*I+1))
200      Continue
C      Figure out which dof is being sought and is it in the upper or
C      lower half. Also, give the total displacement.
      IF (JTYPE.EQ.1.OR.JTYPE.EQ.11) THEN
      JDOF(1)=1
      UE=Uit
ELSE      ! IF (Jtype.Eq.2.or.Jtype.Eq.12) THEN
      JDOF(1)=2
      UE=Vit
END IF
      Return
      End

```

C.3 Closed Crack-Tip : MPC Subroutine

```

      Subroutine MPC (Ue,A,Jdof,N,Jtype,X,U,Nmpce,Kstep,Kinc,Time)
      IMPLICIT REAL*8 (A-H,O-Z)
      DIMENSION A(n),JDOF(n),X(6,n),U(6,n)
C      For      ABAQUS - VERSION 4.6
C      This program imposes the asymptotic bi-material crack-tip
C      displacements as an MPC. This is the routine used to enforce
C      the CLOSED crack-tip model. The order of the MPC as it should
C      appear in the deck is MPC#,Node#,Knode. Here MPC#
C      should be 1 for dof 1 and 2 for dof 2 in the upper half.
C      While 11 should be used for dof 1 and 12 for dof 2 in the
C      lower half. Note, this means that for every node to be tied
C      it has to be entered in twice; once for each dof. Node# is
C      the number of the constrained node while Knode is the number
C      of the extra node. The desired Kii strength should be given
C      as Knode's dof 1 displacement. The subscript 1 and 2 refer to

```

```

C   the upper (1) and lower (2) materials respectively.
    Rone =(-1.000000000000000D0) ! Useful constants
    Zone =1.000000000000000D0
    Two  =2.000000000000000D0
    Three=3.000000000000000D0
    Pie  =3.14159265358979D0

C   Determine the R and theta coordinates.
    Theta=Datan2( X(2,1),X(1,1) )
    If(X(1,1).Lt.(0.0D0).and.Dabs(X(2,1)).Lt.(0.0001D0)) Theta=Pie
    Theta =Dabs(Theta) ! This always gives a positive theta.
    If(Jtype.Eq.11.or.Jtype.Eq.12) Theta=Theta*Rone
    R=Dsqrt(X(1,1)*X(1,1)+X(2,1)*X(2,1))

C   Determine the bi-material constant. Caution: use Comninou's
C   ordering. Give Beta with 1 in the lower region!
    Beta=-0.240120000D0

C   Set up the material properties
    Em1=70.1D03
    Em2=211.4D16
    P1=.342D0
    P2=.300D0

C   Solve for the shear modulus
    G1=Em1/((Zone+P1)*Two) !Shear Modulus upper domain
    G2=Em2/((Zone+P2)*Two) !Shear Modulus lower domain
    If (Jtype.EQ.11.OR.Jtype.EQ.12) then
        G=G2 !This adjust for the material being on the down side.
        Rnj=Three-(Two*Two*P2)
    Else
        G=G1 ! Assume that the node is on the upper half
        Rnj=Three-(Two*Two*P1) !Plain strain Poisson's ratio
        Beta=Beta*Rone !Adjust for Beta in the upper domain.
    End If
    A(1)=Zone
    F1=Rone*((Dsqrt(Two*R))/((Two*Two*Two*G))
    F2=(Two*Rnj-Zone)*(Zone-Beta)*Dsin(Theta/Two)
    F3=(Three+Beta)*Dsin(Three*Theta/Two)
    Ur=F1*(F2-F3)
    F4=(Two*Rnj+Zone)*(Zone-Beta)*Dcos(Theta/Two)
    F5=(Three+Beta)*Dcos(Three*Theta/Two)
    Uo=F1*(F4-F5)

C   Rotate the displacements into the Cartesian Coordinate frame.
    Jx=(Ur*Dcos(Theta))-(Uo*Dsin(Theta))
    Uy=(Uo*Dcos(Theta))+(Ur*Dsin(Theta))
    Jdof(2)=i !Imposing DOF of K_II node.
    IF ((Jtype.Eq.1).or.(Jtype.Eq.11)) then
        JDOF(1)=1

```

```

      A(2)=Rone*Ux
ELSE IF ((Jtype.Eq.2).or.(Jtype.Eq.12)) then
      JDOF(1)=2
      A(2)=Rone*Uy
ELSE
      Print *, 'You goofed up!'
END IF
      Uit= U(1,2)*A(2) !Get the actual displacement
      Vit= U(1,2)*A(2)
C      Figure out which dof is being sought and is it in the upper or
C      lower half. Also, give the total displacement.
      IF (JTYPE.EQ.1.OR.JTYPE.EQ.11) THEN
      JDOF(1)=1
      UE=Uit
ELSE      ! IF (Jtype.Eq.2.or.Jtype.Eq.12) THEN
      JDOF(1)=2
      UE=Vit
END IF
      Return
      End

```